amU
Aix Marseille Université

NNT : 2024AIXM0001

THÈSE DE DOCTORAT

Soutenue à AMU — Aix-Marseille Université,
le 10 décembre 2024 par

Quentin POTIRON

Advanced solid state neutron detectors for fast neutron measurement and monitoring in fusion and fission environments

Discipline

Physique et Sciences de la Matière

Spécialité

Instrumentation

École doctorale

ED 352

Laboratoire/Partenaires de recherche

AMU, Institut Sciences de la Fusion et de l'Instrumentation en Environnements Nucléaires (ISFIN)

CEA, Direction des Energies (DES), Institut de REcherche sur les Systèmes Nucléaires pour la production d'Energie bas carbone (IRESNE)

CEA, Direction de la Recherche Fondamentale (DRF), Institut de Recherche sur la Fusion par Confinement Magnétique (IRFM)

AMU, Institut Matériaux Microélectronique Nanosciences de Provence (IM2NP)

Composition du jury

Giuseppe BERTUCCIO Professor at Politecnico di Milano, Italy	Rapporteur
Ludo VERMEEREN Researcher at SCK.CEN research center, Belgium	Rapporteur
Andrea ŠAGÁTOVÁ Associate Professor at Bratislava Institute of Nuclear and Physical Engineering, Slovakia	Examinatrice
Benedikt BERGMANN Head of the department of Electronics and Software at Prague Technical University, Czech Republic	Examinateur
Malcolm JOYCE Professor of Nuclear Engineering at Lancaster University, United Kingdom	Président du jury
Stanislav POSPISIL Senior Researcher at Prague Technical University, Czech Republic	Examinateur
Abdallah LYOUSSI Directeur de Recherche, Senior Fellow, CEA - DES | IRESNE | DER, France	Directeur de thèse
Christelle REYNARD-CARETTE Professeure des Universités, Aix Marseille Université	Co-Directrice de thèse
Christophe DESTOUCHES Chercheur, Expert Senior, Chef de projets, CEA - DES | IRESNE | DER, France	Membre invité
Michaël HOURY Chercheur, Chef de Service, CEA - DRF | IRFM | STEP, France	Membre invité

Institut Sciences de la Fusion et de l'Instrumentation en Environnements Nucléaires Aix Marseille Université

cea iresne

cea irfm

im2np Institut Matériaux Microélectronique Nanosciences Provence

Affidavit

Je soussigné, Quentin Potiron, déclare par la présente que le travail présenté dans ce manuscrit est mon propre travail, réalisé sous la direction scientifique de Abdallah Lyoussi et Christelle Reynard-Carette, dans le respect des principes d'honnêteté, d'intégrité et de responsabilité inhérents à la mission de recherche. Les travaux de recherche et la rédaction de ce manuscrit ont été réalisés dans le respect à la fois de la charte nationale de déontologie des métiers de la recherche et de la charte d'Aix-Marseille Université relative à la lutte contre le plagiat.

Ce travail n'a pas été précédemment soumis en France ou à l'étranger dans une version identique ou similaire à un organisme examinateur.

Fait à Aix-en-Provence le 10 octobre 2024

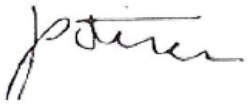

Cette œuvre est mise à disposition selon les termes de la Licence Creative Commons Attribution - Pas d'Utilisation Commerciale - Pas de Modification 4.0 International.

Liste de publications et participation aux conférences

Liste des publications et/ou brevets réalisées dans le cadre du projet de thèse:

1. Q. Potiron, C. Destouches, M. Houry, O. Llido, A. Lyoussi, C. Reynard-Carette, (2024). Evaluating Solid-State Neutron Detectors for Measuring 14 MeV Neutrons at High Temperatures. Conference proceeding submitted to Fusion Engineering and Design, SOFT 2024 special issue. https://www.sciencedirect.com/journal/fusion-engineering-and-design/about/call-for-papers

2. Q. Potiron, C. Destouches, L. Dubus, M. Houry, O. Llido, A. Lyoussi, L. Ottaviani, C. Reynard-Carette, F.H. Ruddy, (2024). Estimation of the Fast-Neutron Fluence Rate with a 4H-SiC Based Detector in a 14.1 MeV Mono-Energetic Field. IEEE Transactions on Nuclear Science. PP. 1-1. 10.1109/TNS.2023.3348147. https://ieeexplore.ieee.org/document/10376152

3. Q. Potiron, C. Destouches, L. Dubus, M. Houry, O. Llido, A. Lyoussi, L. Ottaviani, C. Reynard-Carette (2023). Modelling of a SiC Based Detector for the Interpretation of 14.1 MeV Neutrons Measurements. EPJ Web of Conferences. 288. 03001. https://www.epj-conferences.org/articles/epjconf/abs/2023/14/epjconf_animma2023_03001

Participation aux conférences et écoles d'été au cours de la période de thèse :

1. Oral Presentation. Q. Potiron, C. Destouches, M. Houry, O. Llido, A. Lyoussi, C. Reynard-Carette, Comparison of Solid-State Neutron Detectors at 14 MeV up to 500°C. 33rd Symposium on Fusion Technology, Dublin City University, Ireland. https://soft2024.eu/

2. Training program. Organized by the Jožef Stefan Institute, under the management of the European Nuclear Experimental Educational Platform (ENEEP) and in cooperation with the European Nuclear Educational Network (ENEN). Fundamentals of Neutron Detection, JSI, Ljubljana, Slovenia. https://www.eneep.org/courses/previous-courses/eneep-autumn-reactor-physics-courses-2023/neutron-detection-jsi/

3. Oral Presentation. Q. Potiron, C. Destouches, L. Dubus, M. Houry, O. Llido, A. Lyoussi, L. Ottaviani, C. Reynard-Carette. Modelling of a SiC Based Detector for the Interpretation of 14.1 MeV Neutrons Measurements. 8th International conference on Advancements in Nuclear Instrumentation Measurement Methods and their Applications, Real Collegio, Lucca, Italy. https://animma2023.caen.it/

Résumé

Les neutrons de fusion produits dans les tokamaks sont une source d'énergie clé pour la production d'électricité et sont essentiels à la production de tritium, nécessaire à l'auto-alimentation en combustible des réacteurs de fusion. Pour l'industrie de la fission nucléaire, bien que les neutrons rapides ne représentent qu'une faible fraction du spectre total des neutrons, le suivi de ces neutrons est essentiel pour la surveillance des dommages des matériaux. Disposer de capteurs sensibles aux neutrons rapides, mais insensibles aux neutrons thermiques, est donc essentiel pour connaitre précisément les flux neutronique et les spectres associés pour les expériences prévues sur ITER et le RJH, tout en tenant compte des contraintes environnementales partagées, avec des températures supérieures à 200°C et des niveaux de radiation élevées. Cette thèse se concentre ainsi sur l'étude, le test et la qualification de détecteurs de neutrons miniaturisés à l'état solide utilisant du carbure de silicium (4H–SiC). L'estimation du flux de neutrons rapides, ainsi que l'étude des effets des contraintes environnementales sur la réponse du détecteur représentent les objectifs principaux de ce travail. Initialement, la réponse du capteur dans un champ de neutrons rapides mono-énergétiques a été utilisée pour estimer le flux de neutrons rapides. S'en est suivi la construction d'une matrice de réponse expérimentale du détecteur pour un champ de neutrons continu de 1 à 40 MeV, nécessaire à l'estimation du flux neutronique dans un champ mixte de neutrons multiénergétiques. Enfin, des expériences dans des environnements de fusion, en utilisant les capteurs jusqu'à 500°C dans un champ de neutrons rapides, ont été menées.

Ces études de R&D s'inscrivent au sein du partenariat entre le CEA[1] (IRESNE[2], IRFM[3]) et l'Université Aix-Marseille (ISFIN[4], IM2NP[5]) via le laboratoire commun LIMMEX[6].

Keywords: instrumentation nucléaire, détection de rayonnement, neutrons rapides, détecteurs semi-conducteurs, carbure de silicium

[1] *Commissariat à l'Énergie Atomique et aux énergies alternatives (CEA)*
[2] *Institut de REcherche sur les Systèmes Nucléaires pour la production d'Energie bas carbone (IRESNE)*
[3] *Institut de Recherche sur la Fusion Magnétique (IRFM)*
[4] *Institut Sciences de la Fusion et de l'Instrumentation en Environnements Nucléaires (ISFIN)*
[5] *Institut Matériaux Microélectronique Nanosciences de Provence (IM2NP)*
[6] *Laboratoire d'Instrumentation et de Mesures en Milieux EXtrêmes (LIMMEX)*

Abstract

The fusion neutrons produced in tokamaks are a key source of energy for power generation, and are essential for the production of tritium, which is needed to fuel fusion reactors. For the nuclear fission industry, although fast neutrons represent only a small fraction of the total neutron spectrum, fast neutron measurements is essential for monitoring material damage. Sensors that are sensitive to fast neutrons, but insensitive to thermal neutrons, are therefore essential for accurate knowledge of neutron fluxes and associated spectra for the experiments planned on ITER and the RJH, while taking into account shared environmental constraints, with high temperatures above 200°C and radiation levels. This thesis focuses on the study, testing and qualification of miniaturized solid-state neutron detectors using silicon carbide (4H–SiC). The main objectives of this work are to estimate the flux of fast neutrons, and to study the effects of environmental constraints on detector response. Initially, the sensor response in a mono-energetic fast neutron field was used to estimate the fast neutron flux. This was followed by the construction of an experimental detector response matrix for a continuous neutron field from 1 to 40 MeV, required to estimate neutron flux in a mixed field of multi-energy neutrons. Finally, experiments were carried out in fusion environments, using the sensors up to 500°C in a fast neutron field.

These R&D studies were conducted through a strong partnership between CEA (IRFM, IRESNE) and Aix-Marseille University (ISFIN, IM2NP) via the LIMMEX joint Lab.

Keywords: nuclear instrumentation, radiation detector, fast neutrons, semiconductor detector, silicon carbide

Résumé Étendu

Le travail de recherche présenté dans cette thèse a été consacré à l'étude, au test et à la qualification de détecteurs de neutrons miniaturisés à l'état solide basés sur le carbure de silicium de type 4H–SiC, pour la détection et le suivi des neutrons dans un environnement représentatif de la fusion et de la fission nucléaire. Les principaux objectifs étaient de proposer une méthode pour estimer le flux de neutrons rapides, ainsi que d'évaluer l'effet des contraintes environnementales sur la réponse du détecteur. Une attention particulière a été accordée à chaque étape du développement du détecteur, de la conception à la caractérisation dans un environnement représentatif des réacteurs de fusion et de fission.

Le 4H–SiC comme détecteur de rayonnement

L'état de l'art réalisé sur les détecteurs de neutrons rapides a montré que les semi-conducteurs à large bande interdite ou gap sont des matériaux prometteurs pour la détection de neutrons dans des environnements contraints. Ces derniers sont des candidats de choix pour les applications de suivi de flux neutroniques dans les réacteurs de fusion et de fission nucléaire, du fait de leurs capacités intrinsèques à surmonter les limitations des détecteurs neutroniques actuels, tout en offrant des performances prometteuses en termes de spectroscopie et de miniaturisation. Le choix du carbure de silicium 4H–SiC a été motivé par sa stabilité thermique et sa compatibilité avec les hautes températures et les champs magnétiques présents dans les réacteurs de fusion. Ses propriétés font du 4H–SiC un candidat prometteur pour ces environnement contraints par rapport aux autres semi-conducteurs, comme illustré dans la Fig. 1, en comparant les propriétés des matériaux à température ambiante.

Ensuite, l'utilisation du carbure de silicium comme détecteur de rayonnement a été discutée, avec une description détaillée de l'interaction des particules chargées avec le capteur et leur transport en son sein, puis des modes d'interaction mis en jeu pour la détection de neutrons. La complexité de la réponse du capteur à une irradiation par des neutrons a été soulignée, tout en présentant des capacités spectroscopiques intéressantes en raison des nombreuses réactions nucléaires à seuil en énergie. Par la suite, des exigences de dimensionnement ont été définies pour développer un détecteur de neutrons rapides dans la gamme d'énergie de 1 à 20 MeV, ainsi que les spécifications techniques requises pour la fabrication du détecteur. Après une description du processus de fabrication, les détecteurs conçus et présentés sur la Fig. 2 ont été caractérisés d'un point de vue électrique et ont montré des performances en adéquation avec les spécifications requises pour la détection de rayonnement, avec un courant d'obscurité de l'ordre de 10 nA à 300 °C.

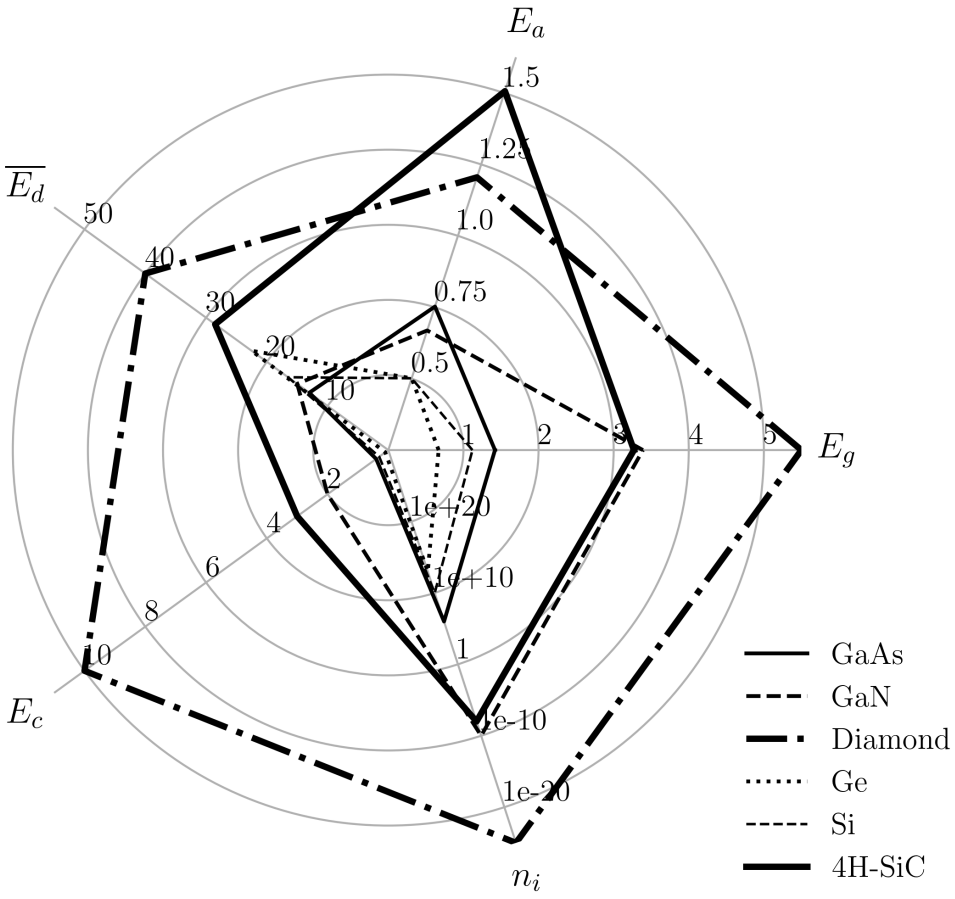

Fig. 1. Comparaison des principaux paramètres des semi-conducteurs étudiés à 300 K. Avec E_d en [eV] l'énergie moyenne de déplacement atomique, E_a en [eV] l'énergie d'activation des pièges de niveau profond, E_g en [eV] la largeur de la bande d'énergie interdite, n_i en [cm^{-3}] la concentration de porteurs intrinsèques et E_c [MV/cm] le champ électrique critique. Les valeurs tabulées proviennent de différents travaux [1, 2], regroupant les articles de référence pour les mesures des différents paramètres.

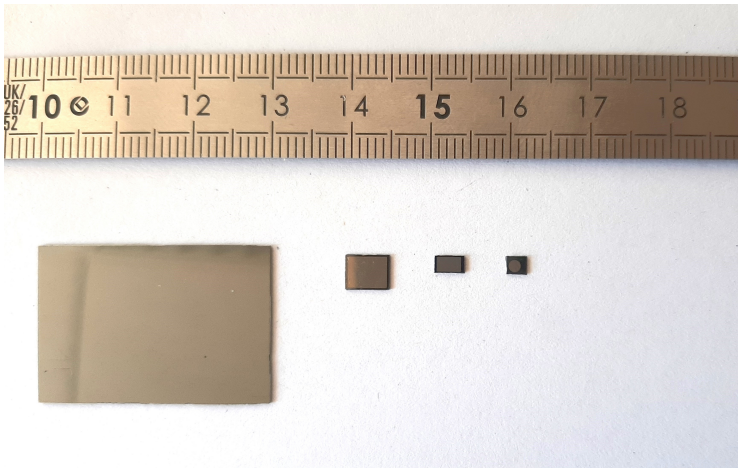

Fig. 2. Diodes 4H–SiC à jonction *p*-*n* fabriquées durant cette thèse. De gauche à droite, le wafer 4H–SiC, les diodes après le dépôt du contact ohmique et la découpe, avec plusieurs surfaces de $4 \times 5\text{mm}^2$ et $2 \times 3\text{mm}^2$ et un diamètre de 1.6 mm.

La qualification du détecteur dans un champ neutronique mono-énergétique

La méthodologie utilisée pour estimer le flux de neutrons en utilisant un capteur 4H–SiC a tout d'abord été présentée dans le cadre d'une utilisation dans un champ de neutrons monoénergétiques. La description des interactions des neutrons avec le capteur a été décrite à l'appui d'une étude de la cinématique des multiples réactions mises en jeu. Cette dernière a montré que la réponse du capteur est complexe et que l'interprétation de la réponse du capteur n'est pas directe puisque qu'un faisceau de neutrons monoénergétiques engendre une distribution d'énergie déposée dans le capteur. L'utilisation d'un modèle Monte-Carlo a été proposée pour simuler la réponse du capteur à une irradiation neutronique. Les motivations de l'utilisation du code GEANT4 ont été discutées, afin de simuler la génération de particules chargées secondaires dans la zone active de détection du capteur ainsi que leurs dépots d'énergie, en suivant le transport des particules primaires et secondaires.

Les résultats numériques ont été comparés au modèle analytique afin de valider l'utilisation du modèle Monte-Carlo sur la gamme d'énergie considérée, de 1 à 20 MeV. Cependant, les sections efficaces de désintégrations séquentielles des états excités du béryllium-9 et du noyau de carbone-12 ne sont pas correctement évaluées dans les données nucléaires de référence. La distribution d'énergie déposée dans le capteur obtenue par simulation Monte-Carlo a donc été comparée à celle obtenue expérimentalement afin de valider les hypothèses de modélisation introduites pour décrire les réactions à la cinématique complexe. Pour ce faire, une chaîne d'acquisition dédiée à la mesure impulsionnelle rapide a été présentée, et déployée lors d'une campagne d'irradiation auprès d'un générateur de neutrons utilisant une source d'ion deutérium et une cible tritiée générant ainsi des neutrons de 14 MeV d'énergie. Enfin, le modèle a servi à évaluer les coefficients de correction liés à la géométrie du capteur pour estimer les effets de bords, ainsi que la contribution de toutes les réactions dans le pic d'intérêt de la réponse du capteur, observé à 8.3 MeV dans la Fig. 3, en prenant en compte des neutrons de 14 MeV.

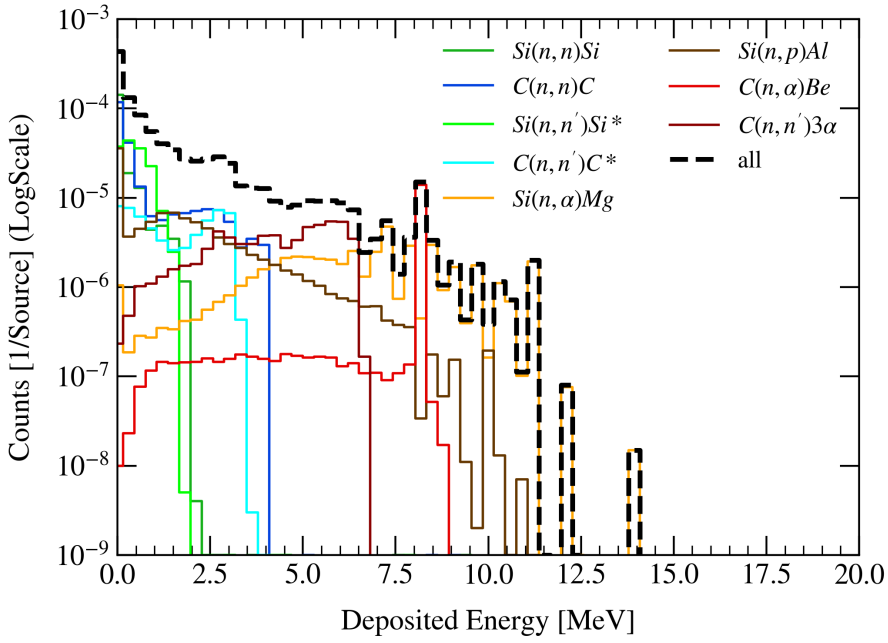

Fig. 3. Simulation GEANT4 de l'énergie déposée par les particules chargées produites dans un capteur SiC. Le calcul a été réalisé en considérant un faisceau incident monoénergétique de $1 \cdot 10^9$ neutrons de 14 MeV.

L'estimation expérimentale du flux de neutrons a été comparée à la valeur théorique de référence. Les incertitudes des flux expérimentaux et théoriques ont également été estimées et comparées. Les résultats montrent que le flux expérimental est dans la plage d'incertitude de la valeur de référence, avec un ratio de 1,04 et une incertitude relative de 22,2% à 1σ à l'emplacement du capteur.

La qualification du détecteur dans un champ neutronique multi-énergétique

L'utilisation du capteur dans un champ mono-énergétique a montré des résultats encourageants. Cette méthode est applicable aux sources de neutrons quasi mono-énergétique comme les générateurs de neutrons ou encore, pour les scénarios deuterium–tritium des tokamaks. Cependant, la qualification de la réponse du capteur sur une large plage d'énergie dans un champ multi-énergétique se révèle complexe. Une solution a été proposée en utilisant des fonctions réponses pour déconvoluer le spectre neutronique. En raison des limitations de l'outil de simulation, qui repose sur des données nucléaires évaluées avec de grandes incertitudes pour les réactions étudiées, les données expérimentales se sont révélées nécessaires pour les méthodes de déconvolution utilisant une matrice de réponse. La calibration de ces fonctions réponses aurait pu être réalisée dans des installations comme AMANDE de l'IRSN [3], ou au Tendetron du PTB [4], avec des faisceaux de neutrons mono-énergétiques. Cependant, la mesure de temps de vol dite ToF pour Time of Flight, s'est montrée avantageuse dans la mesure où celle-ci permet d'obtenir une matrice de réponse avec suffisamment de canaux en énergie pour satisfaire les exigences des méthodes de déconvolution itérative. Ainsi, une chaîne d'acquisition dédiée aux mesures de neutrons par temps de vol sur l'installation NFS du GANIL [5] a été développée. Les données expérimentales ont été interprétées, permettant la construction d'une matrice de réponse pour le capteur 4H–SiC, présentée dans la Fig. 4.

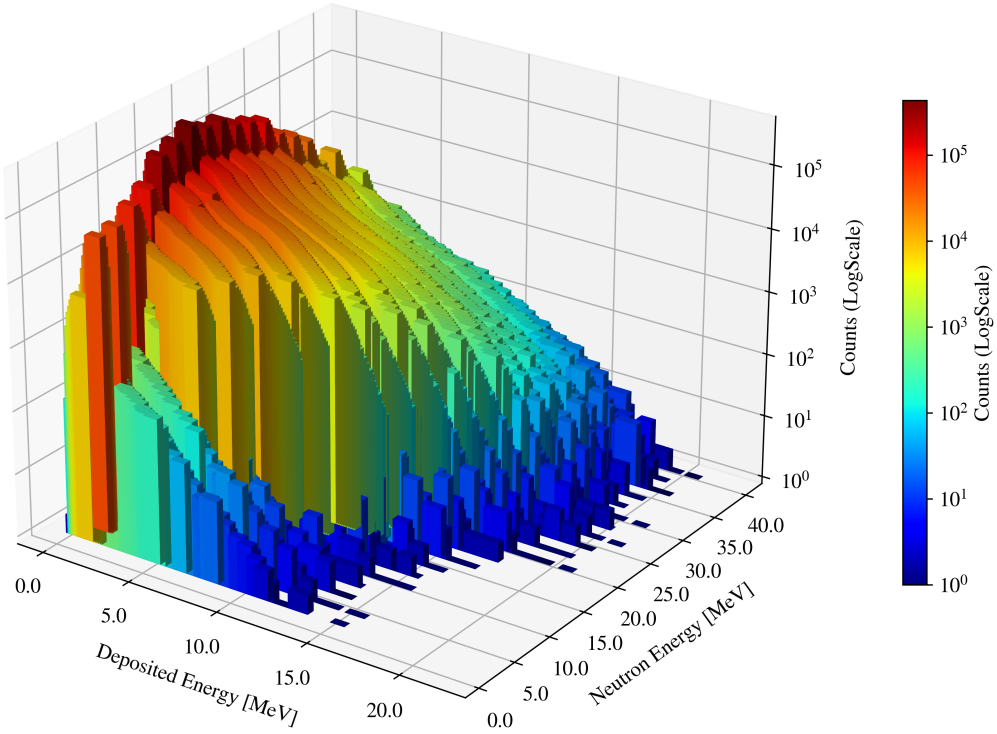

Fig. 4. Matrice de réponse expérimentale du capteur 4H–SiC d'épaissseur 60 µm. Les données sont calculées à partir d'un échantillon de résultats de mesure de la campagne réalisée sur l'installation NFS du GANIL.

Enfin, une méthode de déconvolution pour la dérivation du spectre a été appliquée pour estimer le flux de neutrons en utilisant la matrice de réponse construite expérimentalement. Le dépliage du spectre de neutrons obtenu avec le capteur 4H–SiC de 60 µm d'épaisseur dans le champ neutronique de NFS est montré dans la Fig. 5 en considérant des canaux en énergie de 2 MeV de largeur.

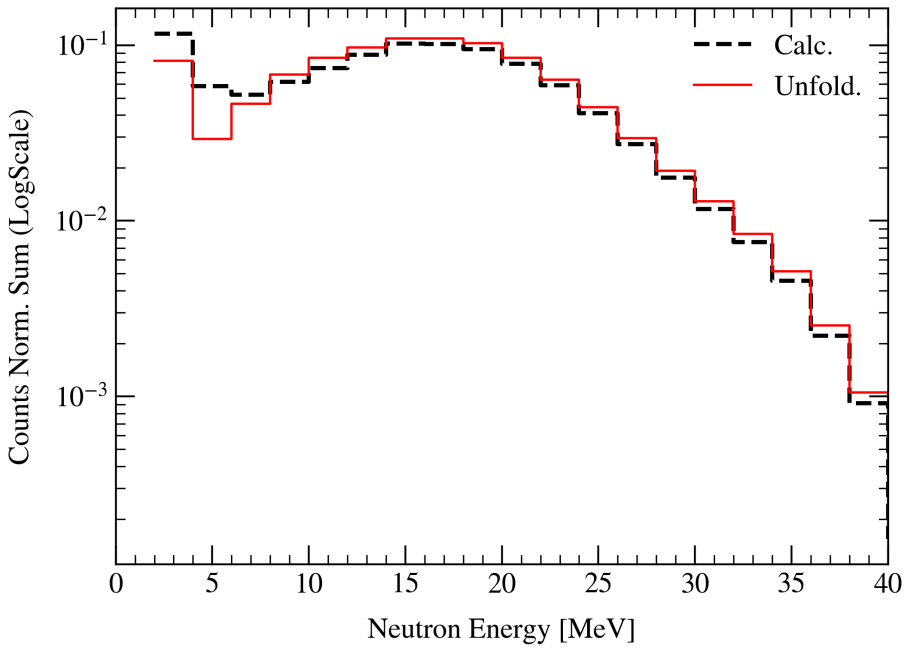

Fig. 5. NFS neutron spectrum comparison. The spectrum are normalized to the sum of the spectrum. Comparaison du spectre neutronique calculé avec MCNP et du spectre neutronique obtenu par dépliage itératif pour le capteur SiC de 60 µm d'épaisseur.

Les résultats présentés sont prometteurs sur toute la plage d'énergie du spectre neutronique, démontrant la capacité du capteur à estimer le flux de neutrons dans un champ de neutrons de haute énergie avec des écarts faibles, de l'ordre de 10 % sur la majeure partie de la plage d'énergie du spectre. L'objectif principal de la construction d'une matrice de réponse dans ce travail avait pour but de démontrer la faisabilité de la méthode de déconvolution. Idéalement, un écart nul aurait dû être obtenu en comparant le résultat du dépliage itératif avec le spectre théorique dérivé des calculs du modèle Monte-Carlo de l'installation. Cependant, des écarts subsistent à la fin de ce test initial. Aussi, un travail supplémentaire est nécessaire pour améliorer le processus de résolution numérique et pour intégrer des incertitudes réalistes dans l'étape de traitement finale. La campagne expérimentale a ainsi démontré la capacité du capteur à mesurer le flux de neutrons dans un champ de neutrons continu en utilisant une matrice de réponse expérimentale construite avec des mesures par temps de vol.

L'étude des effets de la température

Au regard des températures élevées dans les environnements visés de fusion et de fission nucléaire, une étude dédiée à l'effet de la température sur la réponse du capteur a été menée. Premièrement, un modèle analytique de la dynamique des porteurs de charges dans le 4H–SiC a été présenté, fournissant les modèles physiques nécessaires à l'interprétation des résultats expérimentaux. Concernant la dégradation de la mobilité avec l'augmentation de la température due à la diffusion des porteurs de charges, plusieurs études ont examiné la mobilité de ces porteurs dans le 4H–SiC. Cependant, les modèles empiriques avec des coefficients calibrés décrivant cet effet de température, en tenant compte de la concentration de porteurs de charge et de la concentration de dopage, sont moins courants par rapport aux modèles existants pour le silicium, et notamment pour les températures supérieures à 200 °C. Pour obtenir des résultats de simulation fiables pour la collecte de porteurs de charges, les coefficients des modèles empiriques ont été ajustés pour la structure du dispositif 4H–SiC étudié dans la plage de température allant jusqu'à 500 °C. Ainsi, l'analyse des données expérimentales a été utilisée pour déterminer les paramètres et les coefficients de ces modèles avec l'augmentation de la température. Enfin, un modèle numérique utilisant la méthode des éléments finis a permis de simuler la collecte d'un nuage de charges générées dans le capteur, illustré avec la Fig. 6.

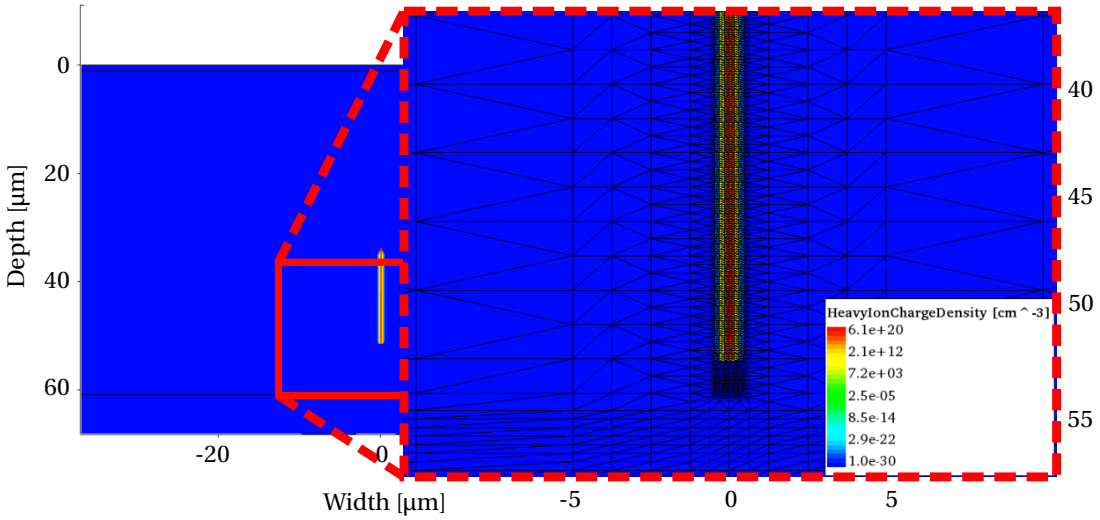

Fig. 6. Distribution de la densité de charges créées par une particule alpha de 5 MeV dans le 4H-SiC. L'image de gauche est une coupe du profil de densité de charges au centre du capteur, et l'image de droite est une vue zoomée de la maille de calcul.

Ce schéma a permis de mettre en évidence la complexité de la dynamique de collecte des porteurs de charges avec l'augmentation de la température, offrant des informations sur les performances du dispositif en calculant et en représentant visuellement des profils internes tels que les champs, les concentrations de porteurs de charges et les densités de courant, qui sont souvent inaccessibles expérimentalement.

Les objectifs de cette étude sur l'effet de la température ont été atteints. Premièrement, l'étude de la forme des impulsions de courant avec l'augmentation de la température a décrit l'effet de la dégradation de la mobilité sur la dynamique de collecte de charges. Ensuite, la stabilité des performances de détection du 4H–SiC dans la plage de température d'intérêt a été observée, et cela jusqu'à une température de 500 °C, comme le montre la Fig. 7.

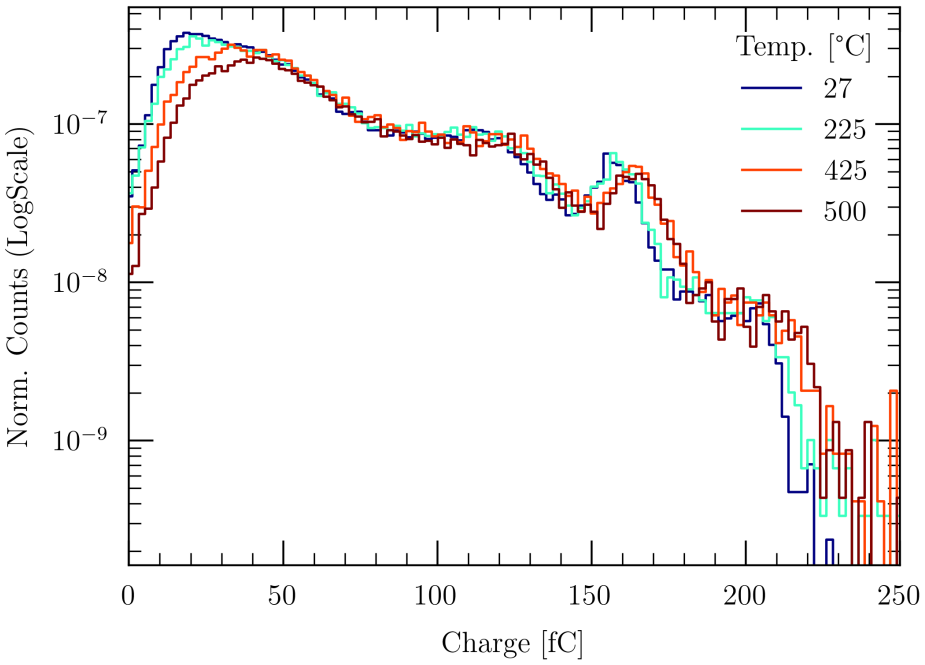

Fig. 7. Distribution de la charge collectée en fonction de la température pour un capteur 4H–SiC de 60 µm d'épaisseur. Les taux de comptage sont normalisés par rapport à l'intensité du faisceau de neutrons source.

La stabilité de la réponse du capteur jusqu'à 500 °C, illustrée par la position constante du pic associé aux évènements issus des réactions de captures neutroniques, montre que le SiC n'est pas sujet à des dégradations significatives de son efficacité de collection de charges dans la plage de température d'intérêt. Ainsi, ces résultats permettent d'envisager l'utilisation du 4H–SiC pour le suivi de flux neutroniques dans des environnements de haute température.

L'étude des effets des défauts sur la mesure

Enfin, le problème des défauts dans le capteur a été abordé. Le modèle analytique de création de défauts a été présenté, suivi de l'application de la simulation par éléments finis pour étudier les mécanismes induits par l'activation des défauts. Ensuite, en présentant les résultats d'expériences sur les défauts induits sous irradiation neutronique pour le 4H–SiC et sur les défauts activés thermiquement pour le diamant, les limitations de la réponse du capteur à l'irradiation neutronique dans l'environnement spécifique des réacteurs de fusion et de fission ont été identifiées. Les résultats ont montré que les défauts induits par l'irradiation neutronique dans le 4H–SiC ont un impact sur la réponse du capteur. Ils induisent une diminution de l'ordre de 35% de l'efficacité de détection après une fluence neutronique équivalente 1 MeV de $2.4 \cdot 10^{15}\,\mathrm{cm}^{-2}$, comme illustré dans la Fig. 8. Cela pouvant être problématique pour des applications à long terme dans des environnements à fort flux de rayonnement.

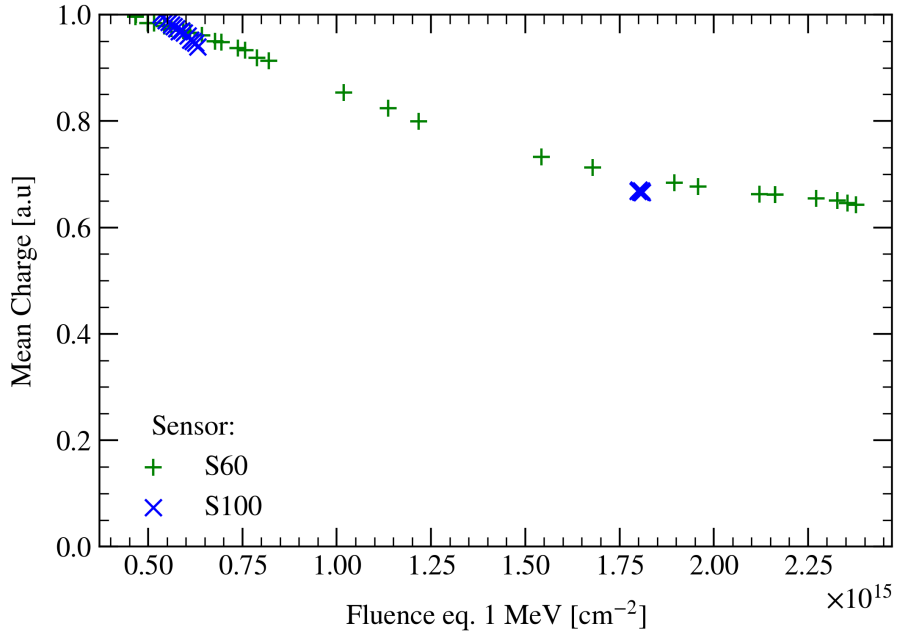

Fig. 8. Variation de la charge moyenne collectée en fonction de la fluence équivalente à 1 MeV. Les données ont été acquises avec des capteurs 4H–SiC de 60 µm et 100 µm d'épaisseur lors d'une campagne d'irradiation sur l'installation NFS du GANIL.

Cependant, le problème des défauts natifs activés thermiquement n'a pas été mis en évidence en utilisant le 4H–SiC, au contraire du diamant. En effet, une étude a été menée sur un capteur en diamant, montrant une diminution de l'efficacité de détection de l'ordre de 60% à 300 °C, en étudiant la distribution de la charge collectée, comme illustré dans la Fig. 9.

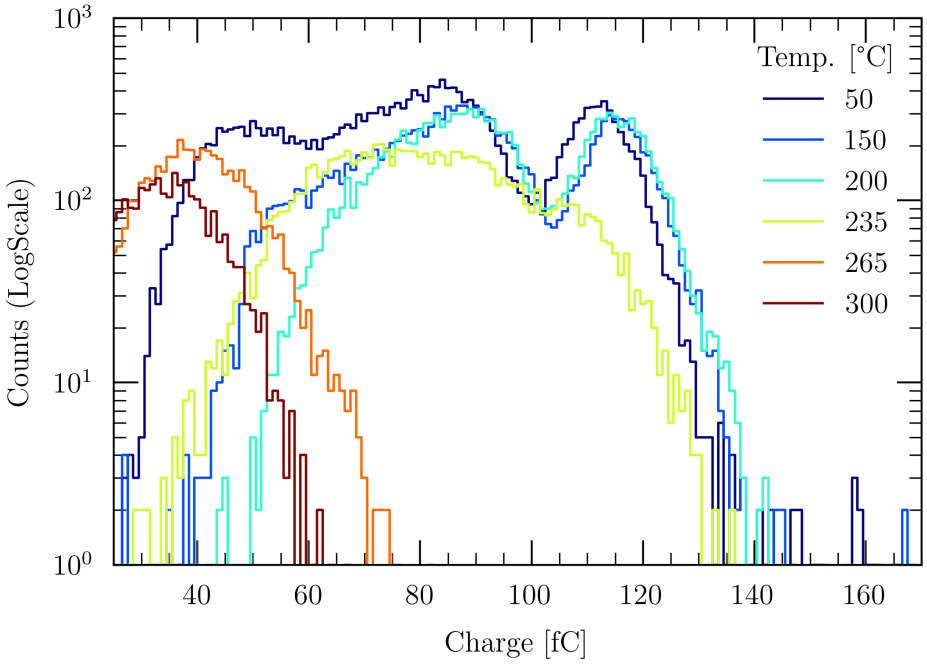

Fig. 9. Distribution de la charge collectée en fonction de la température pour un capteur en diamant dans un champ neutronique mono-énergétique de 14 MeV.

De plus, ces défauts ont été révélés comme étant quasi-irréversibles, dans la mesure où les porteurs de charges piégés dans les défauts profonds ne sont libérés qu'après une durée de treize heures, associée à la constante de temps d'émission du défaut. Ainsi, l'utilisation du capteur en diamant en régime stationnaire dans un environnement à haute température ne permet pas de suivre le flux neutronique, au contraitre du 4H–SiC qui reste un candidat potentiel pour des applications de surveillance et monitoring dans des environnements contraints, comme les TBM pour ITER.

Perspectives

Au final, les résultats des travaux de cette thèse sont prometteurs pour le déploiement à terme de détecteurs de neutrons à semi-conducteurs à base de carbure de silicium pour la détection et le suivi des neutrons dans un environnement représentatif de la fusion et de la fission nucléaire. Les méthodes proposées pour estimer le flux de neutrons rapides en utilisant un détecteur en carbure de silicium de type 4H–SiC représentent une étape significative vers le développement d'un détecteur de neutrons fiable, robuste et précis permettant de fournir des résultats spectrométriques sur plusieurs groupes en énergie, dans des environnements hostiles avec un champ neutronique et photonique mixte, des températures supérieures à 200°C et des contraintes technologiques d'intégration.

Une méthode a été proposée pour estimer le flux de neutrons rapides en utilisant un modèle Monte-Carlo. Toutefois, faute de temps, l'analyse de sensibilité finale, cruciale pour identifier les incertitudes des données d'entrée les plus influentes, n'a pas pu être réalisée. Des logiciels spécialisés comme URANIE [6] pourront être utilisés pour automatiser cette analyse. De plus, une nouvelle évaluation des sections efficaces de capture de neutrons par le carbone pourrait contribuer à réduire l'incertitude globale de l'estimation du flux de neutrons. Les résultats expérimentaux obtenus sur l'installation NFS du GANIL ont montré que les mesures par temps de vol au moyen de détecteur 4H–SiC permettent de construire une matrice de réponse spectrale du capteur permettant de déconvoluer un spectre de neutrons continu en énergie, par des méthodes itératives. Des mesures complémentaires, comme avec des sphères de Bonner, des chambres à fission ou des techniques d'activation neutronique, permettraient d'améliorer les résultats obtenus, grâce à une meilleure connaissance des spectres de neutrons à l'emplacement du capteur. L'application de la méthode de déconvolution itérative à des champs neutroniques typiques de réacteurs de fission est encourageante, même si elle nécessiterait une matrice de réponse axée sur les basses énergies.

Ensuite, concernant la résistance du capteur en environnement hostile, les résultats ont montré que le capteur 4H–SiC est stable jusqu'à 500 °C, tandis que les capteurs en diamant montrent une limitation due aux défauts natifs représentant des niveaux de piégeage profonds. Concernant les défauts induits par l'irradiation neutronique, une diminution de l'efficacité de détection a été observée, qui doit être prise en compte pour des applications à long terme dans des environnements à fort flux de rayonnement. Néanmoins, Les études sur l'effet de la température montrent des résultats prometteurs pour l'intégration des capteurs de neutrons rapides 4H–SiC dans des environnements à haute température.

Enfin, une utilisation couplée des schémas de modélisation GEANT4 et TCAD utilisés dans ce travail de thèse pour simuler d'une part l'interaction des neutrons et celle des particules chargées, et d'autre part les mécanismes d'ionisation et de collecte de charges menant à la génération du signal, représenterait une méthode efficace pour l'identification et la discrimination des particules. Cette approche ouvre ainsi la voie à une modélisation complète du capteur, permettant d'envisager une analyse en ligne de la forme des signaux en utilisant des techniques d'apprentissage automatisée pour identifier et classifier les interactions neutroniques dans le capteur.

Remerciements

Je souhaite remercier tout d'abord les personnes à l'origine de ce projet de thèse. Abdallah Lyoussi, Christelle Reynard-Carette, pour leur implication dans les activités de recherche inter-institutionnels. Durant ces trois ans, j'ai découvert une thématique riche et pluridisciplinaire, ainsi qu'un cadre stimulant avec une émulation certaine autour de nombreux projets en soutien à la décarbonation.

Je remercie Nicolas Thiollay, chef du Laboratoire de Dosimétrie Capteurs et Instrumentation du CEA, et Oliver Palais, responsable de l'équipe Interaction Rayonnement Matière et PhotoVoltaïque de AMU, de m'avoir accueilli dans leur laboratoire respectif.

Je suis très reconnaissant envers les membres du jury, Messieurs et Mesdames, Bertuccio, Vermeeren, Šagátová, Bergmann, Joyce et Pospisil, qui ont accepté d'évaluer mon travail de thèse, témoignant de leur intérêt pour mes travaux de recherche.

Cette thèse n'aurait pas été menée à bien sans l'encadrement de Messieurs Destouches et Houry. Merci, Christophe et Michael, pour vos nombreux conseils et remarques toujours constructives. Ce fut un plaisir de travailler à vos côtés. J'ai beaucoup appris durant ces trois années, et je compte appliquer ces enseignements dans mes futurs projets.

Merci aussi à tous les collègues de mes différents laboratoires d'accueil, du LDCI et du GP3 de l'institut IRESNE et IRFM de Cadarache, mais aussi à ceux de l'équipe IRMPV de l'institut IM2NP de AMU. Merci à Laurent Ottaviani de m'avoir accompagné dans l'apprentissage des technologies à base de matériaux semiconducteurs. Merci à Karine Coulié et Alexandre Subercaze de m'avoir formé à l'utilisation des codes de simulation Synopsys et GEANT4. Je souhaite remercier Léo Dubus pour son aide précieuse dans le développement des programmes d'acquisition des données, ainsi que Olivier Llido pour son accompagnement continu dans la réalisation des expériences et montages expérimentaux. Je remercie également Véronique Munusami et Christelle Maitre pour l'assistance administrative et logistique dans le cadre des nombreuses missions que j'ai pu effectuer durant ma thèse.

À ce titre, je remercie les équipes et opérateurs des installations de recherche, qui m'ont accueilli et accompagné lors de mes expériences. Merci à Joel Loridon et Philippe Malard pour leur assistance, respectivement sur les installations DANAIDES et WEST du CEA Cadarache. Je souhaite remercier également les équipes du LPSC à Grenoble, et notamment Benjamin Cheymol, responsable de la plateforme GENESIS. Je remercie aussi les équipes du GANIL à Caen et en particulier Sébastien Gautrot, Jean-Claude Foy et Xavier Ledoux, pour leur accueil et leur aide précieuse lors de mon expérience sur l'installation NFS.

Je n'oublie pas mes collègues doctorants, Marc, Elsa, André et Quentin, avec qui j'ai eu le plaisir de travailler, et pour la convivialité et l'entraide qui ont toujours régné dans nos bureaux. Un grand merci également à tous les autres doctorants, ingénieurs, chercheurs et enseignants, rencontrés lors de conférences, séminaires ou à l'occasion de préparation de travaux pratiques et dirigés. La diversité de leurs profils et compétences a été pour moi une véritable source d'inspiration et de motivation.

Enfin, je remercie mes amis, ma famille et Amélia, pour leur soutien indéfectible et leur patience durant ces trois années.

Contents

Affidavit 2

Liste de publications et participation aux conférences 3

Résumé 4

Abstract 5

Résumé Étendu 6

Remerciements 15

1 Introduction 21
- 1.1 ITER facility . . . 21
  - 1.1.1 The objectives . . . 21
    - 1.1.1.1 Neutrons production in ITER . . . 21
    - 1.1.1.2 Neutrons are involved in self-fuelling process . . . 25
  - 1.1.2 The needs . . . 25
    - 1.1.2.1 The tritium self-sufficiency challenge . . . 25
    - 1.1.2.2 The characterization of the neutron spectrum . . . 28
- 1.2 JHR facility . . . 31
  - 1.2.1 The objectives . . . 31
    - 1.2.1.1 Intense neutron flux in a mixed field . . . 31
    - 1.2.1.2 Monitoring of the material damages . . . 34
- 1.3 The technological limitations . . . 35
  - 1.3.1 Hostile fusion and fission environments . . . 35
  - 1.3.2 Dedicated neutron instrumentation . . . 36

I Choice of the sensor 38

2 Review of the main candidates 39
- 2.1 Fission Chambers . . . 39
  - 2.1.1 Operating principle . . . 39
  - 2.1.2 Operating experience . . . 41
- 2.2 Self Powered Neutron Detectors . . . 42
  - 2.2.1 Operating principle . . . 42
  - 2.2.2 Operating experience . . . 44
- 2.3 Scintillator neutron detectors . . . 45
  - 2.3.1 Operating principle . . . 45
  - 2.3.2 Operating experience . . . 46
- 2.4 Solid State sensors . . . 47
  - 2.4.1 Operating principle . . . 47

2.4.2 Operating experience . . . 48

3 The Silicon Carbide 54
3.1 Inherent parameters . . . 54
3.1.1 The properties of semiconductor materials . . . 54
3.1.1.1 Atomic bonds and crystal lattices . . . 54
3.1.1.2 Native and induced defects . . . 56
3.1.1.3 Semiconductor junction devices . . . 57
3.1.2 Electrical characterization of the sensor . . . 60
3.1.2.1 The movement speed of charge carriers . . . 60
3.1.2.2 The lifetime of charge carriers . . . 63
3.1.2.3 The resultant current . . . 63
3.1.3 Signal Formation . . . 65
3.1.3.1 Charge Induction . . . 65
3.1.3.2 Pulse Shape . . . 66
3.1.3.3 Space Charge . . . 67
3.2 Response to external parameters . . . 67
3.2.1 The effects on the sensor . . . 67
3.2.1.1 The effects on charge carrier current . . . 68
3.2.1.2 The effects on charge carrier lifetime . . . 69
3.2.2 Comparison of semiconductors . . . 71
3.3 The SiC as a radiation sensor . . . 73
3.3.1 Interaction with photons . . . 73
3.3.1.1 Photon reactions . . . 73
3.3.1.2 Attenuation of photons . . . 76
3.3.2 Interaction with charged particles . . . 77
3.3.2.1 Interaction mechanisms with electrons and positrons . . . 77
3.3.2.2 Interaction mechanisms with ions . . . 79
3.3.3 Interactions with neutrons . . . 85
3.3.3.1 Neutron scattering . . . 85
3.3.3.2 Neutron capture . . . 87
3.3.4 Sensor response is complex . . . 88
3.4 Manufacturing of 4H–SiC sensors . . . 90
3.4.1 Diodes manufacturing . . . 90
3.4.2 Sensor design requirements . . . 90
3.4.2.1 Bias voltage operational range . . . 90
3.4.2.2 Active region thickness . . . 91
3.4.2.3 Cleanroom manufacturing processes . . . 92
3.4.2.4 Electrical characterisation . . . 93
3.4.3 Description of the detector . . . 97

II Using a 4H-SiC sensor to estimate a fast neutron flux 99

4 Using a 4H-SiC sensor to estimate fast neutron flux in a mono-energy field 100
4.1 Study of the analytical model of neutron interactions in the sensor . . . 100
4.1.1 Carbon Neutron capture . . . 103
4.1.1.1 Case of the fundamental state . . . 103
4.1.1.2 Case of excited levels: sequential two-body decay . . . 106
4.1.2 Silicon neutron inelastic scattering . . . 112
4.1.3 Silicon neutron captures . . . 115
4.1.4 Neutron elastic scattering . . . 119

4.2 Development of a numerical model to simulate the generation of secondary particles . . . 121
4.2.1 Modeling scheme based on GEANT4 . . . 121
4.2.2 Model Construction . . . 123
4.2.2.1 Nuclear Data . . . 123
4.2.2.2 GEANT4 Physics List . . . 123
4.2.3 Analytical versus Monte-Carlo model comparison . . . 125
4.2.3.1 Neutron scattering modelling . . . 125
4.2.3.2 Neutron capture modelling . . . 127
4.3 Realization of a dedicated measurement campaign on a 14 MeV neutron generator 131
4.3.1 The GENESIS Installation . . . 131
4.3.2 Implementation of an acquisition chain dedicated to pulse mode measurement . . . 134
4.3.2.1 Dedicated electronic acquisition system . . . 134
4.3.2.2 Digitizing the signal . . . 136
4.3.3 Measurements results . . . 138
4.3.3.1 Context . . . 138
4.3.3.2 Determining the depletion bias voltage . . . 138
4.3.3.3 Data processing and energy calibration . . . 140
4.4 Validation of the charged particle transport modeling scheme in the sensor . . . 142
4.4.1 Calculation versus experiment comparison . . . 142
4.4.1.1 Presentation of the method . . . 142
4.4.1.2 Detector simulation within the neutron field . . . 143
4.4.2 Assessment of the experimentally estimated fluence rate and associated uncertainties . . . 144
4.4.2.1 Uncertainty of the detector count rate . . . 145
4.4.2.2 Uncertainty of the real time . . . 146
4.4.2.3 Uncertainty of the reaction deconvolution . . . 147
4.4.2.4 Uncertainty of the detector edge effects . . . 149
4.4.2.5 Uncertainty of the number of target nuclei . . . 150
4.4.3 Assessment of the theoretically estimated flux and associated uncertainties 150
4.4.4 Discussion about the sources of uncertainties . . . 151
4.4.4.1 Uncertainty of the reference flux value . . . 151
4.4.4.2 Uncertainty of the experimental flux value . . . 151
4.4.5 Comparison of theoretical and experimental results . . . 152

5 Using a SiC sensor to estimate fast neutrons flux in a multi-energy field 155
5.1 Complexity of the sensor response . . . 155
5.2 Calibration method for the sensor response function . . . 158
5.2.1 Direct simulation of the response functions . . . 158
5.3 Review of numerical unfolding methods . . . 160
5.3.1 Comparison of the methods . . . 160
5.3.2 Iterative Unfolding . . . 161
5.4 ToF measurement campaign . . . 163
5.4.1 The GANIL NFS facility . . . 163
5.4.2 Experimental set-up . . . 164
5.4.3 Tof principle . . . 165
5.4.4 Acquisition chain requirements . . . 166
5.5 ToF measurement results . . . 168
5.5.1 Context . . . 168
5.5.2 Experimental data . . . 169

5.5.3 Data analysis . . . 170
5.5.3.1 Distribution of the events according to the trigger timestamps. 170
5.5.3.2 Energy calibration . . . 171
5.5.4 Construction of a response matrix . . . 174
5.5.5 Calculation versus Experiment comparison . . . 175
5.6 Application of the deconvolution method and calculation versus experiment comparison . . . 180
5.6.1 Deposited energy distribution . . . 180
5.6.2 Calculation versus experiment comparison . . . 180
5.6.3 JHR spectrum . . . 182

III Evaluation of the Sensor response to Integration Constraints 186

6 Study of the effects of temperature on measurements 187
6.1 Study of the analytical model of the charge carriers dynamics in the SiC . . . 187
6.1.1 Bandgap energy . . . 187
6.1.2 Intrinsic carrier concentration . . . 189
6.1.3 Carrier mobility . . . 190
6.2 Development of a numerical model to simulate the charge carriers collection . . . 193
6.2.1 Finite element simulation . . . 193
6.2.1.1 TCAD programs . . . 193
6.2.1.2 TCAD worflow . . . 193
6.2.2 Sensor geometry . . . 194
6.2.2.1 Abrupt junction . . . 194
6.2.2.2 Ohmic contacts . . . 194
6.2.3 Structuring numerical resolution . . . 195
6.2.3.1 Electrostatic potential and transport equation . . . 195
6.2.3.2 Finite differences method . . . 196
6.3 Study of mechanisms induced by an ionizing particle via finite element method 197
6.3.1 Simulating a charged particle . . . 197
6.3.1.1 Linear energy transfer . . . 197
6.3.1.2 Generation rate computation . . . 197
6.3.2 Charge carrier collection simulation . . . 200
6.3.2.1 Simulation of the mechanisms involved in energy deposition . 200
6.3.2.2 Simulation of the current pulse . . . 202
6.4 Dedicated 14 MeV neutron generator measurement campaign with a heating device 203
6.4.1 Protocole and Methodology . . . 203
6.4.1.1 Experimental protocol . . . 204
6.4.2 Quantification of the effects - SiC . . . 206
6.4.2.1 Pulse Shape Analysis at room temperature . . . 206
6.4.2.2 Increasing temperature - Overall view of the results . . . 213
6.4.2.3 Count rate study . . . 215
6.4.2.4 Pulse Shape Analysis as a function of the temperature . . . 216
6.5 Evaluation of the model for the charge carrier collection . . . 220
6.5.1 Charge carrier dynamics and Temperature . . . 220
6.5.1.1 Full Width at Half Maximum Study . . . 220
6.5.1.2 Mobility models comparison . . . 222
6.5.2 TCAD results . . . 222
6.6 Perspectives . . . 224

7 Study of the effects of defects on measurements 226

7.1 Study of the analytical model of defect creation . . . 226
7.1.1 Neutron induced defects . . . 227
7.1.2 Thermally activated defects . . . 227
7.2 Application of finite element simulation to study defect activation mechanisms 228
7.2.1 Recombining and trapping . . . 228
7.2.1.1 Recombination processes . . . 228
7.2.1.2 Carrier lifetime . . . 229
7.2.1.3 Trapping and stationary charges . . . 230
7.2.2 Dynamics of trap occupation . . . 230
7.3 Neutron induced defects experimental results . . . 232
7.3.1 Counts rate evolution with irradiation . . . 232
7.3.2 Pulse shape analysis with irradiation . . . 235
7.3.3 Charge collection efficiency study with irradiation . . . 237
7.4 Application of thermally activated defect analysis to diamond . . . 239
7.4.1 Counts rate evolution with temperature . . . 239
7.4.2 Pulse shape analysis with temperature . . . 240
7.4.3 Charge collection efficiency study with temperature . . . 241
7.5 Evaluation of the model for the charge carrier trapping . . . 244
7.5.1 Traps distribution . . . 244
7.5.2 Electric field modification . . . 245
7.6 Perspectives . . . 248

General Conclusion **250**

Bibliography **254**

List of acronyms **271**

Appendices **275**
A SiC Junction - Demonstrating the main variables . . . 275
A.1 Space Charge Region . . . 275
A.2 Free carriers concentration . . . 282
B Kinematic study - Demonstrating the main expressions . . . 284
B.1 Two bodies . . . 284
C NovaSiC Epitaxy quotation - technical details . . . 287
D Reaction Products level scheme and de-excitation . . . 288
D.1 Be . . . 288
D.2 Mg . . . 290
D.3 Al . . . 300
E NFS Campaign: Ghost Events . . . 301
F TCAD Modeling . . . 303
F.1 Mobility Models . . . 303
F.1.1 Phonon Scattering . . . 303
F.1.2 Doping Dependant . . . 303
F.1.3 High-Field Saturation Models . . . 304
F.2 Recombination Rate . . . 305
F.2.1 Shockley-Read-Hall Recombination Rate . . . 305
F.2.2 Carriers lifetime doping dependance . . . 305

1. Introduction

ITER[1] and JHR[2] present major challenges for fusion and fission research programs for the next few decades. Both these installations are thus used in this chapter as examples to illustrate the issues surrounding nuclear instrumentation and measurement in current and futur reactors. In light of these similarities, the challenges facing by these spear-heading are presented, and significantly regarding the scope of the neutrons study highlighting some shared needs. Then, with respect to these shared goals and objectives, the shared constraints and requirements for such nuclear installations are displayed. To this end, major neutron detectors available in industry are reviewed and examined according to the technical specifications for this hostile environment. Namely, with respect to the stable use of such sensors to estimate a fast neutron flux as well as the ability to meet integration and miniaturisation constraints. All things considered, large bandgap semiconductors are introduced and depicted as one of the most suitable sensors to achieve such goals regarding the constraints.

1.1. ITER facility

1.1.1. The objectives

1.1.1.1. Neutrons production in ITER

Currently under construction in southern France, the main objective of ITER reactor, shown in Fig. 1.1, is to demonstrate the scientific and technical feasibility of a thermonuclear reactor based on the fusion of light nuclei such as hydrogen isotopes[3].

Quantitatively, the initial main objective is to produce a 500 MW thermonuclear power and to maintain an amplification regime with a gain factor of around 10. It means that fusion power produced with the nuclear fusion has to be ten times superior to the power required to maintain the plasma in steady state. Technological studies of components, focusing on their integration and performance, particularly in terms of power extraction and tritium regeneration, are also major objectives of the program.

Finally, beyond the feasibility objective, the next stage of the industrial demonstrator tokamak[4] reactor will require experimental data for the issue of self-sustaining fuel. This last point is discussed in details in Section 1.3.

[1] *International Tokamak Experimental Reactor (ITER)*
[2] *Jules Horowitz Reactor (JHR)*
[3] *This generic information is devoted to the presentation of the installation. For a full discussion of the general concepts relating to magnetically controlled fusion, please refer to the references [7] and [8].*
[4] *TOroidalnaïa KAmera s MAgnitnymi Katouchkami (TOKAMAK)*

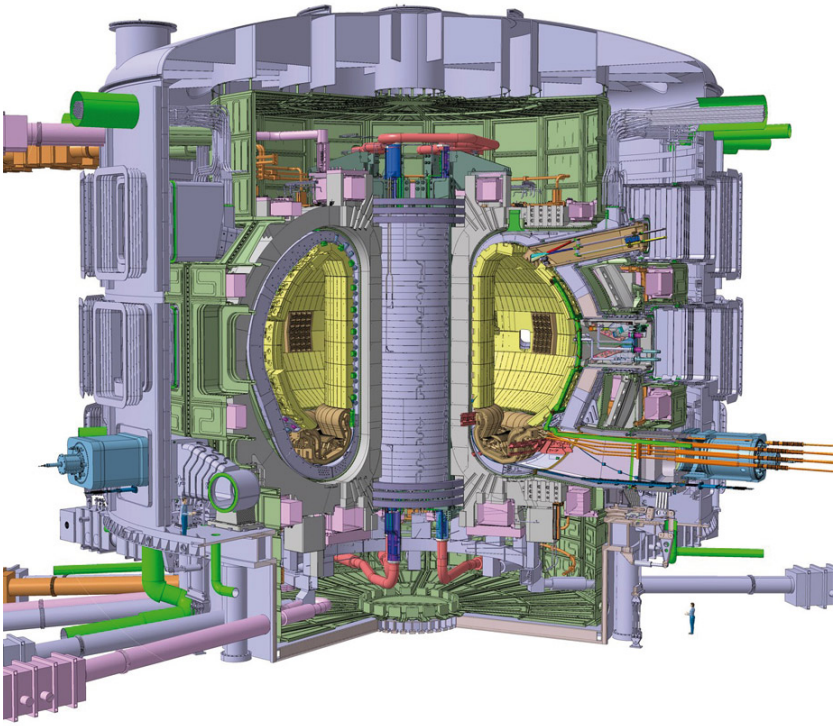

Fig. 1.1. ITER cutting scheme [9].

Several fusion reaction of light nuclei[5] such as deuterium (D) and tritium (T) were identified and studied at the outset of plasmas studies for fusion machine design:

$$D + T \rightarrow \underbrace{^4He}_{3.52\,\text{MeV}} + \underbrace{n}_{14.06\,\text{MeV}} \rightarrow Q_{DT} = 17.58\,\text{MeV} \tag{1.1}$$

$$D + D \rightarrow \underbrace{^3He}_{0.82\,\text{MeV}} + \underbrace{n}_{2.45\,\text{MeV}} \rightarrow Q_{DD_n} = 3.27\,\text{MeV} \tag{1.2}$$

$$D + D \rightarrow \underbrace{T}_{1.01\,\text{MeV}} + \underbrace{p}_{3.03\,\text{MeV}} \rightarrow Q_{DD_p} = 4.04\,\text{MeV} \tag{1.3}$$

$$T + T \rightarrow {}^4He + 2n \tag{1.4}$$

However, since the cross section[6] is higher for the D–T reaction, as seen in Fig. 1.2, this is the reaction being studied with the aim of demonstrating fusion for industrial production —although an initial operating phase is taking place with D–D fuel—such that:

$$D + T \rightarrow {}^4He + n \tag{1.5}$$

The ^4He nuclei[7], as charged particles stay confined in the plasma under the effect of the magnetic field lines and transmit their energy by colliding with other particles. The latter contribute to self-heating the plasma and to maintain a steady-state combustion regime.

[5] *D and T stand respectively for hydrogen isotopes, deuterium for two neutrons and one proton, and tritium for three neutrons and one proton.*

[6] *Used to describe the probability of a specific nuclear interaction to occur, expressed in barn,* $1\,\text{b} = 1 \cdot 10^{-24}\,\text{cm}^2$.

[7] *The* ^4He *nuclei are currently called alpha denoted* α *in the following.*

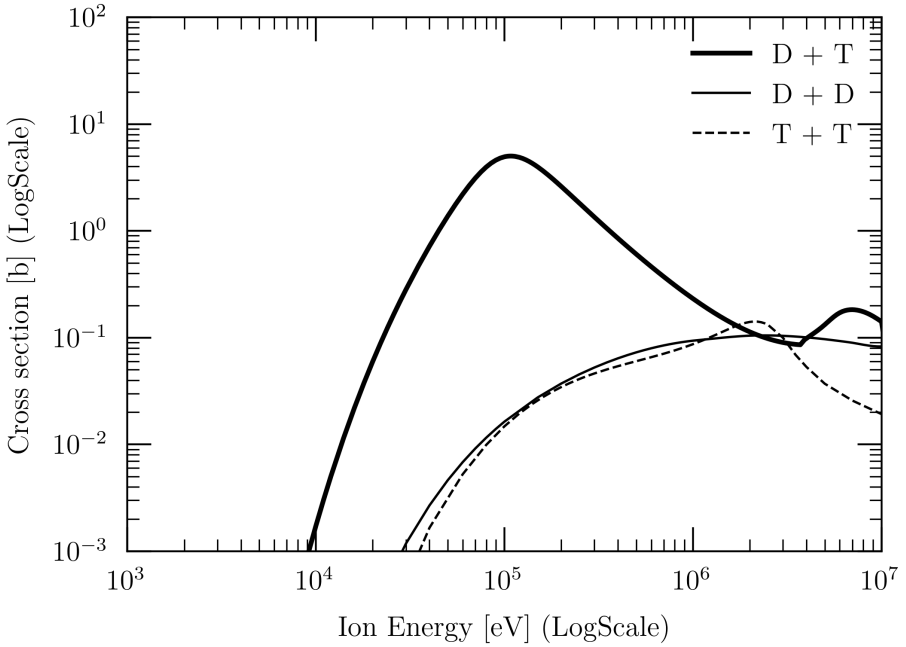

Fig. 1.2. Cross sections for the main thermonuclear fusion reactions of light nuclei. The nuclear data used comes from the latest ENDF/B-VIII.0 library [10].

The D–D fusion reaction (1.2), with two equally likely channels, and T–T reaction (1.4) will also appear in the reactor, but within lower proportion since the cross section is lower than the one of D–T as seen in Fig. 1.2. In addition to these, atoms that are not part of the D–T fuel may also be involved in neutron generation. For fusion plasmas, such impurities may come from the ashes of thermonuclear like ^{3}He and ^{4}He particles respectively from D–D and D–T reactions, from the walls of the enclosure and other structures, or may have been injected deliberately, for example for additional heating. These different fusion reactions, which obviously involve deuterium and tritium ions of different energies, can be estimated by simulations. Theoretically, neutrons of different energies emitted by previous fusion reactions could be discerned [11]. However, the neutrons emitted by these thermonuclear reactions will diffuse widely over the walls of the installation through elastic and inelastic collisions. The neutron flux distribution by lethargy[8] unit u on the first wall of ITER is therefore more complex as seen with Fig. 1.3.

During the full-power discharges planned for ITER, $1 \cdot 10^{21}$ fusion neutrons will be produced per second in the vessel with neutron flux ranging from $1 \cdot 10^{9}$ to $1 \cdot 10^{14}$ cm^{-2}s^{-1} depending on the location as seen in Fig. 1.4 from the work of Juarez et al. [12], computed with E–lite[9].

[8] *For both practical (plotting spectra) and theoretical reasons, the logarithm of the kinetic energy of neutrons is introduced with a variable called lethargy defined by* $u = \ln \frac{E_{ref}}{E}$.

[9] *E–lite is a 360° heterogeneous and detailed MCNP model of the ITER tokamak.*

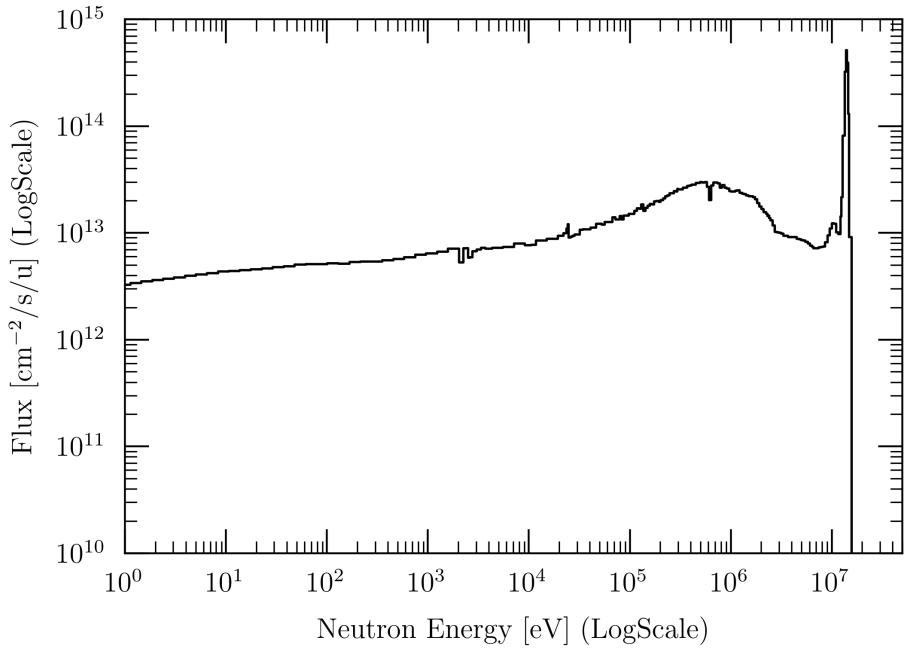

Fig. 1.3. ITER neutron flux spectrum by lethargy unit u at the first wall location. Data from FISPACT–II nuclear database for ITER D–T campaign [13].

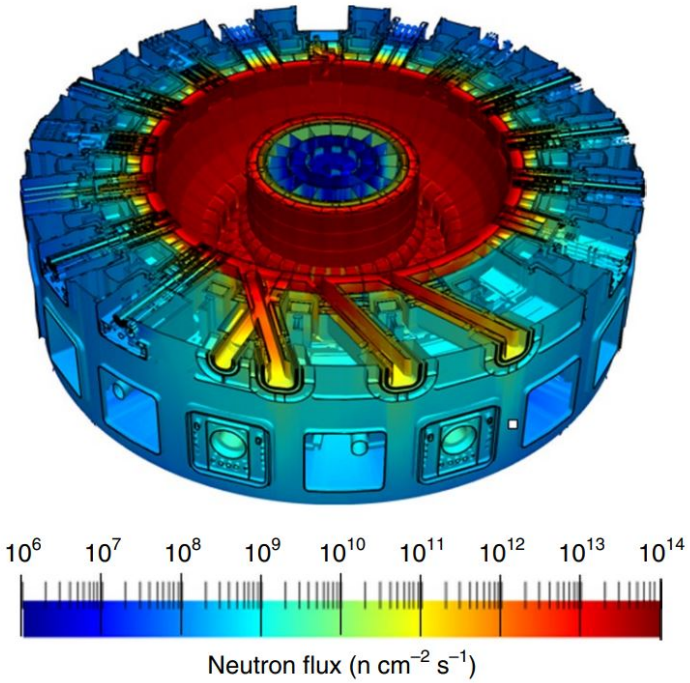

Fig. 1.4. Neutron flux projected onto the surfaces of the ITER tokamak with a horizontal cut through the centre at the L1 level. All energies are considered. From the article of [12].

1.1.1.2. Neutrons are involved in self-fuelling process

Secondly, with a view to an industrial fusion reactor, another challenge lies in ensuring that the reactor is self-sufficient in tritium. Tritium is a very rare element on Earth due to its short half-life of 12.3 years. Therefore, the tritium that will be used in a power reactor has to be produced in situ. The prototype concept that will be experimentally evaluated on ITER is the development and test of a tritium blanket module, positioned opposite the plasma. The neutrons produced by the D–T fusion reaction could then be captured by this blanket. These are the Test Blanket Modules (TBM) as illustrated with Fig. 1.5.

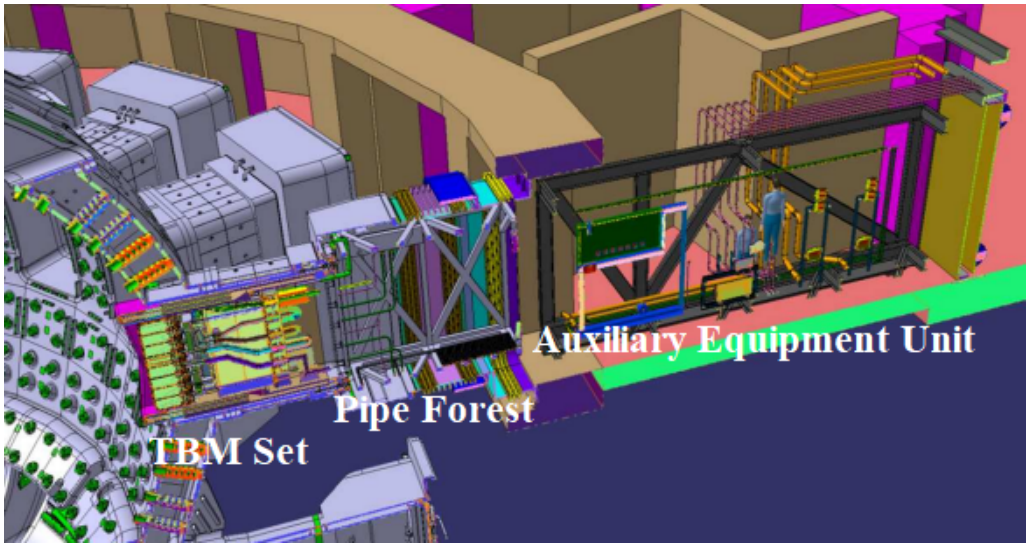

Fig. 1.5. Representation of the configuration of one of ITER's three equatorial ports (aperture 1.75-2.2 m), allocated to TBM testing.

1.1.2. The needs

1.1.2.1. The tritium self-sufficiency challenge

Lithium has been identified as an element that can generate tritium by neutron capture. The two stable isotopes of lithium can generate a tritium nucleus on the way out following neutron capture such as:

$$^{6}Li + n \rightarrow \alpha + T \tag{1.6}$$

$$^{7}Li + n \rightarrow \alpha + T + n' \tag{1.7}$$

The lithium-7 isotope is the most abundant in nature[10]. However, although the cross section of the threshold reaction $(n, n'\alpha)$ with the ^{7}Li is greater than the one with the ^{6}Li in the fast neutron energy range, both remain relatively low in the fast neutron energy range as shown with Fig. 1.6.

[10] *93% of abundance in the natural lithium.*

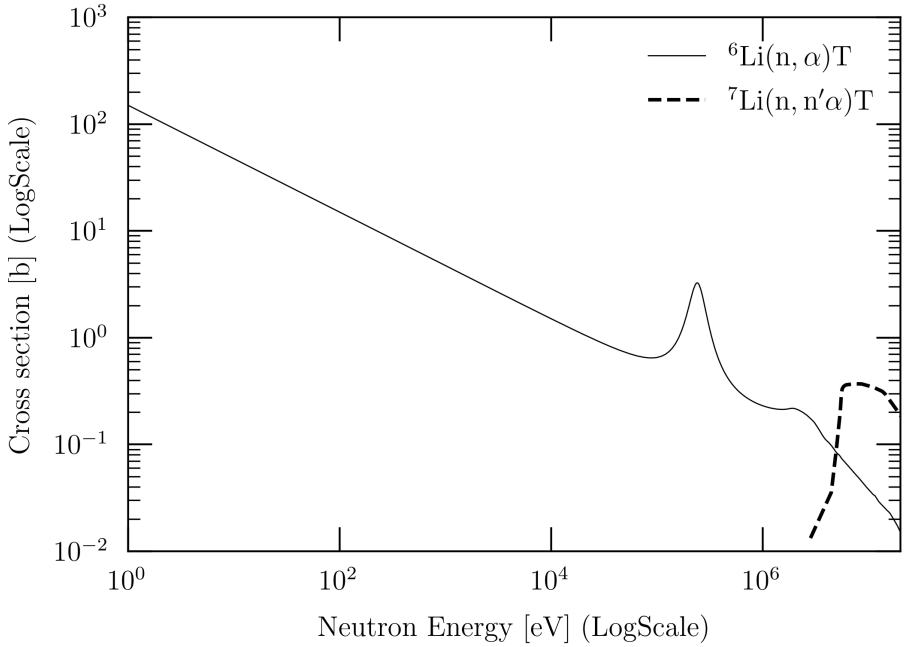

Fig. 1.6. Cross sections in barn for the two neutron capture with the two stable isotopes of lithium. Data are from EAF-2010 database.

Hence, reactions with lithium-6 are more effective at thermal neutron energies. The use of lithium-6 isotope, under several form will be studied in many TBM modules like the LLCB[11] as shown in Fig. 1.7, as an illustrative example in this paragraph. To achieve the neutron thermalization, the blanket is designed to slow down fast neutrons increasing the likelihood of the fast neutrons being captured and converted into thermal neutrons which can effectively interact with the lithium-6.

Finally, the neutron is captured[12] by the lithium nucleus, generating a helium nucleus and a tritium nucleus. The tritium will be then extracted from this blanket, processed in a dedicated facility and injected into the plasma as fuel for the fusion reaction.

The problem of self-sufficiency in fuel is therefore theoretically solved from the point of view of physics. However, a fusion neutron cannot systematically generate a tritium atom. Experimentally, the tritium production ratio is less than 1 for two reasons:

- Neutrons from thermonuclear reactions will be lost when they interact with the structure of the reactor
- The low cross section of the neutron capture reactions with lithium isotopes as seen in Fig. 1.6, regarding the neutron energy spectrum at first wall before, will limit the production of tritium.

As Luciano Giancarli[13] explains in an interview [15]:

> *"The first challenge is the ratio between the neutrons generated by the fusion reaction and the tritium atoms actually produced. For the system to work, the ratio must be higher than 1 meaning that —between the neutron and its lithium target —we'll need a 'neutron multiplier' like lead or beryllium."*

[11] *Lithium-Lead Ceramic Breeder (LLCB)*

[12] *The physical description of the kinematics of these capture reactions will be presented in detail in the second part of this work.*

[13] *Head of the Tritium Breeding Blanket ITER group.*

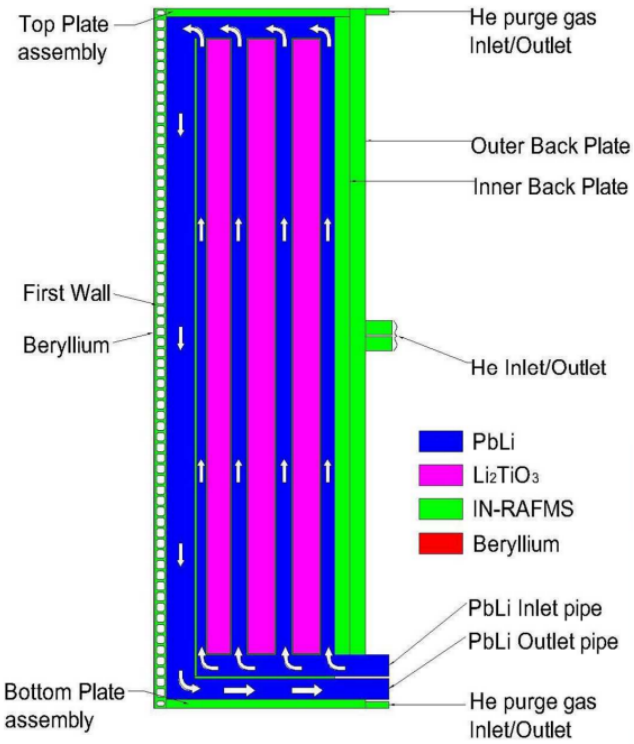

Fig. 1.7. Representative diagram of the TBM LLCB module supplied by India [14].

Theoretical solutions have been proposed to multiply the neutrons using $(n,2n)$ reactions and recover the energy deposited during elastic and inelastic collisions. The idea would be to place a suitable breeder material, such as lead or beryllium, around the vacuum chamber so that the neutron is absorbed by the breeder material and then multiplied as follow, with reaction cross section about a barn above neutron energy of 2.5 MeV for (1.8) and above 8 MeV for (1.9):

$$^{9}Be + n \rightarrow {}^{8}Be + 2n \tag{1.8}$$

$$^{204}Pb + n \rightarrow {}^{203}Pb + 2n \tag{1.9}$$

In reality, this solution will take the form of a blanket with appropriated materials and geometry associated to a cooling fluid. What remains to be done is to implement the various technological solutions needed to move from the demonstration of the physical concept to the production system, and thus achieve self-sufficiency in tritium for fusion facilities. The aim of tritium production, one of the major challenge of the next fusion reactor DEMO[14] is therefore to meet the challenge of fuel self-sufficiency. A tritium nuclei consumed by a fusion reaction as seen in (1.1) gives a neutron around 14 MeV energy which, once slowed down and multiplied such as in (1.8) and (1.9), should produce several tritium nucleus such as in (1.6). Therefore, to achieve the goal of tritium self-regeneration, it is essential to characterize the neutron spectrum at different positions in the facility.

[14] *DEMOnstration power plant (DEMO)*

1.1.2.2. The characterization of the neutron spectrum

In order to characterize neutron spectra, Monte-Carlo modeling codes such as MCNP6[15] [16] or TRIPOLI–4[16] [17] are used to simulate neutrons and photons transport. It enables to carry out exact geometric and material modelling of the configuration in question and to solve the transport equation in an approximate that is to say stochastic and statistical manner. In that respect, these codes provide a realistic estimate of neutron and photon fluxes at a given location and for a given geometry. Such an estimation can be illustrated with a study for the HCPB[17] ITER TBM, taken into account several locations as seen in Fig. 1.8. An estimation of neutron and photon fluxes are respectively represented in Fig. 1.8a and in Fig. 1.8b. These figures underline the discrepancy in the neutron and photon fluxes at different locations in the TBM module.

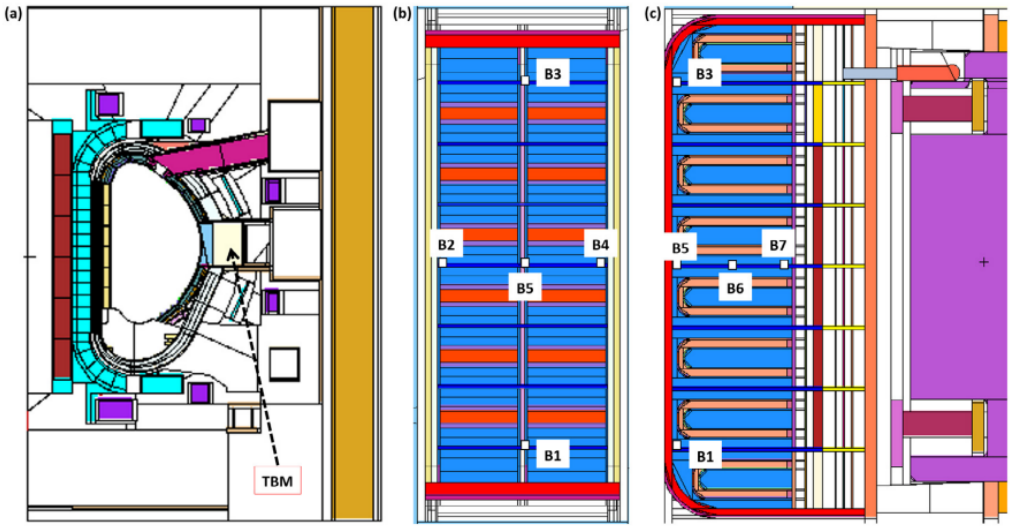

Fig. 1.8. (a) Cross-section of the "MCNP ITER A-lite" model, showing the equatorial port for TBM insertion; (b) front view (looking at the plasma side), and (c) side view of the HCPB [18].

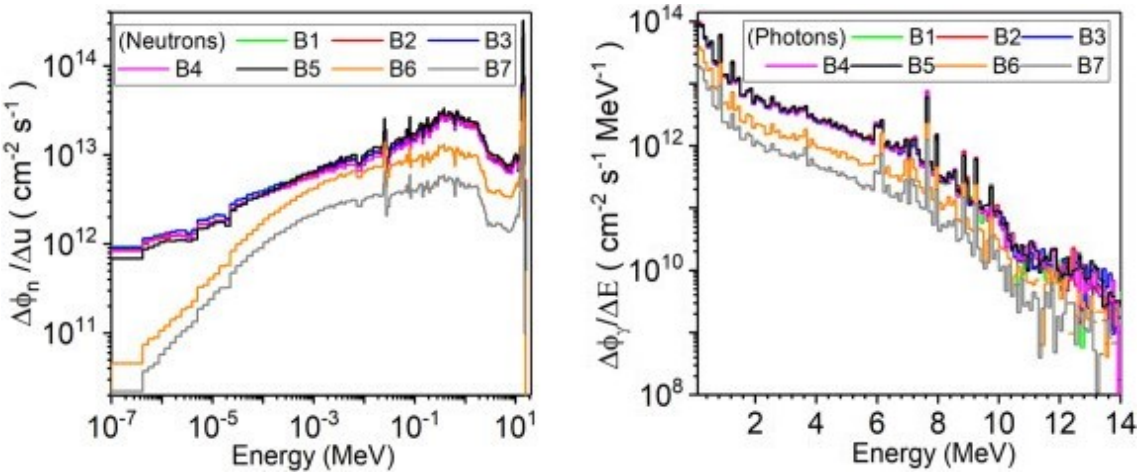

(a) Neutron flux spectra.

(b) Photon flux spectra.

Fig. 1.9. Calculated spectra from seven locations according to Fig. 1.8 for the HCPB ITER TBM [18]. The flux are given in lethargy units.

[15] *Monte Carlo N-Particle (MCNP)*
[16] *TRIdimensionnel POLIcinétique (TRIPOLI)*
[17] *Helium Cooled Pebble Beds (HCPB)*

It should be pointed out that all the scattered neutrons will have their energy downgraded. Indeed, the main interaction processes being elastic and inelastic collisions due to the high cross section, in both cases, the neutron emitted on the exit path will have a lower energy than the incident neutron. The neutron calculation prediction must be then validated with experimental measurements. In fact, in situ measurements will make it possible to verify uncertainties of several kinds linked to:

- Neutrons losses in the structures
- Variability in the fusion plasma scenarios, with heating by Neutral Beam Injection (NBI) and radio frequency or plasma disruption[18]
- Neutron energy fluctuations produced by multiplication.

Measurements systems that will be integrated to the TBM must therefore provide information regarding the neutrons fluxes and the associated energy in order to validate by the experiments the various simulation results in the outputs of the models of these prototype concepts. As the head of the Tritium Breeding Blanket group explained in 2011 during an interview [20]:

> *"We don't need a thousand measurements but we do need measurements that are simple, reliable, and independent."*

In summary, the challenge lies in identifying a suitable detector to characterize the neutron spectrum, particularly the fast component at the first wall, as illustrated in Fig. 1.3, which will interact with the TBMs. However, as the thermal neutron component in the TBM location is significant due to thermalization processes, the aim is to have a detector that is sensitive and selective to fast neutrons in a mixed field of fast neutrons, thermal neutrons and gamma radiation.

To this end, the fast neutron online measurements must be precise in order to provide information linked to:

- The initial neutron population, since fast neutrons influence the number of thermal neutrons generated after moderation
- The tritium production since the number of tritium atoms produced can be affected by fast neutrons though their interaction with materials in the blanket including losses or additional production pathways with multiplication reactions
- The damage on materials, since fast neutrons interact with structural materials and can lead to damage affecting the overall integrity and lifetime of the reactor components.

This appears to be critical for tritium fuel self-sustaining. Indeed, the target set is to reach a Tritium Breeding Ratio (TBR) greater than 1. The latter is defined as the number of tritium atoms produced per second in the blanket, divided by the number of neutrons emitted per second during fusion reactions in the plasma, such that:

$$TBR = \frac{\int \tau_{^6Li} dV + \int \tau_{^7Li} dV}{N_\phi} \tag{1.10}$$

With N_ϕ the number of neutrons emitted per second during fusion reaction in the plasma, τ the reaction rate defined as the number of interactions between a flux of particles ϕ and the

[18] *Sudden appearance of magnetohydrodynamic instabilities in the vacuum chamber, capable of generating electrons of several* MeV *[19].*

nuclei number per centimeter cube of a matter N, per unit of time and volume for a given reaction with a microscopic cross section σ such that:

$$\tau = N \cdot \sigma \cdot \phi \tag{1.11}$$

The latter can be calculated for multi-groups neutron energy spectrum with the neutron captures cross sections for the two isotopes of the lithium ^6Li and ^7Li, presented previously in Fig. 1.6. To give an estimation in a neutron spectrum characteristic of the first wall presented in Fig. 1.3, computational tools can be used, like the preparation code for nuclear database ECORCES[19] developed at the CEA. The results are illustrated in Fig. 1.10

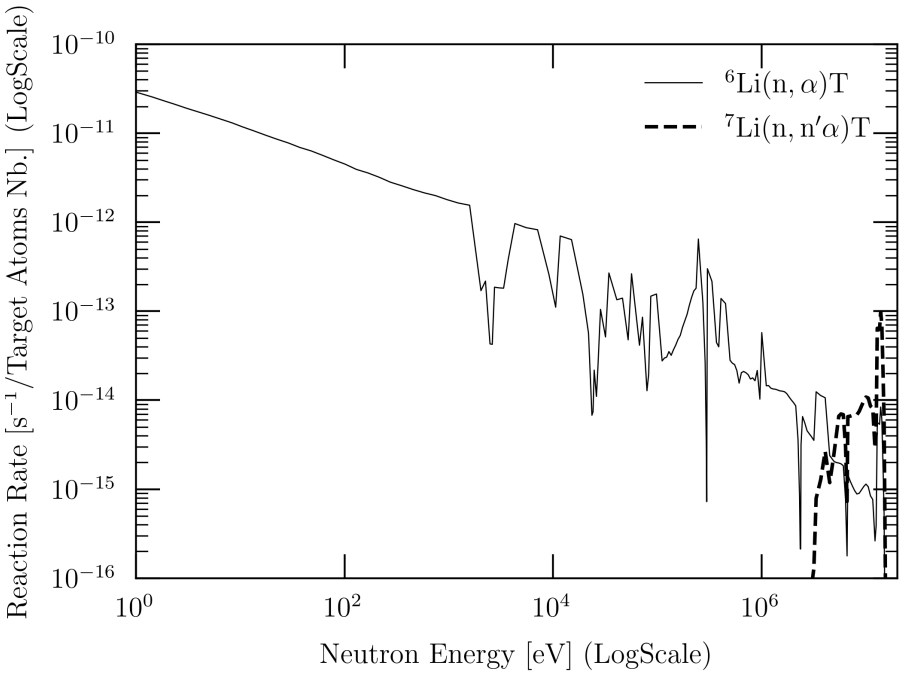

Fig. 1.10. Reaction rates per number of target atoms, for the energy groups of the first wall neutron flux spectrum and for the two neutrons captures for the lithium isotopes. Computed with ECORCES code using JEFF-3.3 nuclear data library and FW ITER neutron spectrum.

As a conclusion, the process of self-sustaining of the tritium and the issues correlated for the neutrons measurements is represented schematically with the diagram below, Fig. 1.11.

[19] *Energetic COmputation of Reaction rate from Cross section and nEutron Spectrum (ECORCES)*

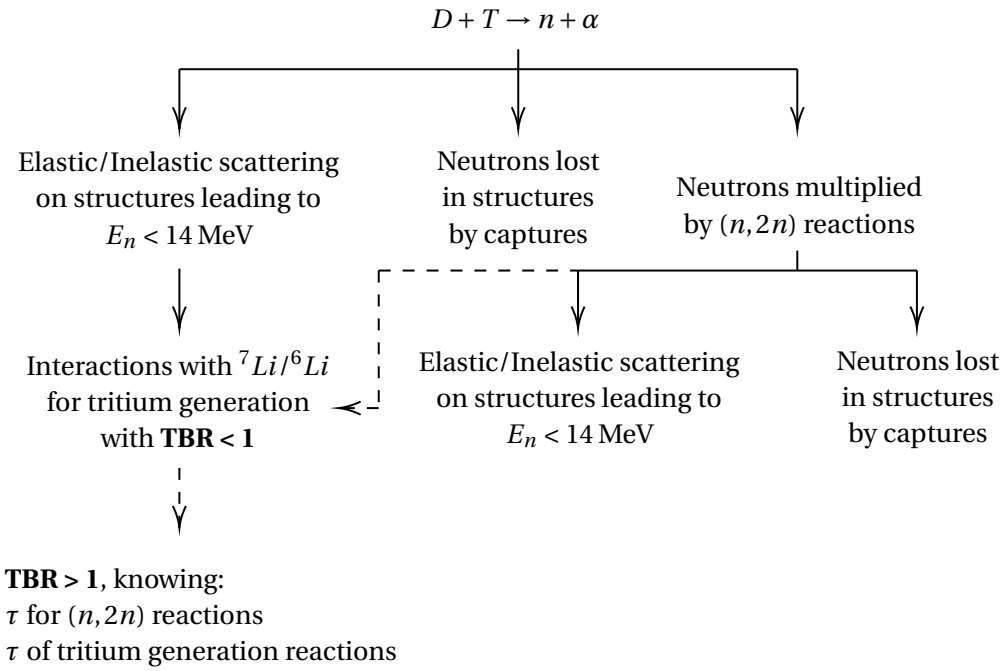

Fig. 1.11. Diagram of tritium regeneration from D-T fusion reaction

1.2. JHR facility

1.2.1. The objectives

1.2.1.1. Intense neutron flux in a mixed field

Tests of materials and nuclear fuel under irradiation for nuclear fission power reactors are at the heart of research group programs developed by numerous countries since sixty years. In that respect, these programs have led to a significant improvement of dedicated experimental devices and the associated instrumentation both for experimental measurements and for control and monitoring of the test conditions and parameters in the dedicated Material Testing Reactors (MTR).

As Gilles Bignan[20] explains in an interview [21] dealing with the French MTR reactor JHR under construction in Cadarache CEA research center:

> *"All European Material Testing Reactors were built in the 60s. By 2015-2020, they will have reached their age limit. We needed at least one facility to cope with the growing needs of our community."*

For power reactors, like for experimental reactors, neutron studies require precise and reliable measurements. To this end, a dedicated in-core or ex-core instrumentation is needed. To correctly qualify the experimental test conditions in which these measurements are achieved, sensors capable to measure photons and neutrons flux locally are needed.

JHR which is described in Fig. 1.12, as a powerful, modular, and highly versatile facility, will be able to accommodate simultaneous experiments. This plurality of experiments will once more, require the key insights of the environmental conditions as claimed by the JHR facility interface manager:

> *"The instrumentation which has been developed will allow us to do real-time analysis. Until now, with the existing installations, we could mainly do 'post-mortems' [...] "*

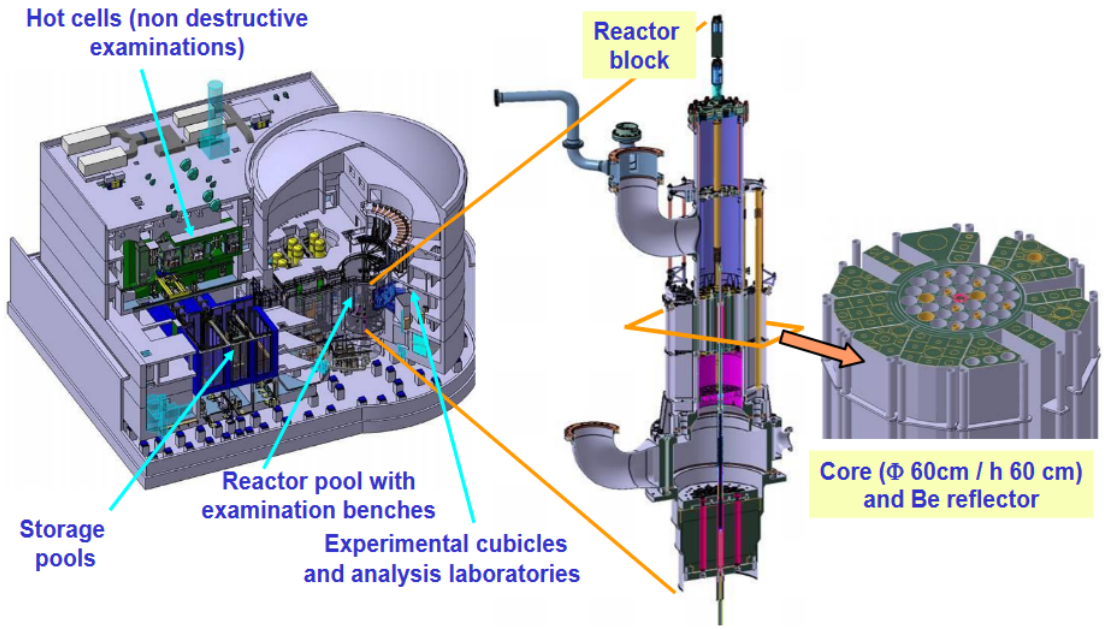

Fig. 1.12. View of the the JHR facility and the reactor core [22].

Various kind of devices have been developed and used for MTR experiments. Since their early development phase, numerous sensors had been progressively improved [23]. A growing interest has recently appeared regarding the improvement of existing instrumentation in reactors but also regarding the enlargement of measurement capacities in MTR. This is for instance the case in France, where the CEA has engaged the construction of the JHR, shown in Fig. 1.12. Operated at 100 MWtH, this reactor will be able to generate irradiation levels that should be noticeably higher than those of the previous french MTR OSIRIS[21] definitively stopped in 2015. The thermal neutron flux, with energy below 0.625 eV, at the irradiation locations of the JHR is expected to reach levels of around $5 \cdot 10^{14} \mathrm{cm}^{-2} \cdot \mathrm{s}^{-1}$. The in-core fast neutrons flux, with energy above 0.907 MeV, for its part, is expected to reach the same levels, enabling the study of the ageing of materials up to 16 displacement per atom (dpa) per year [24].

However, the fast neutron region of interest regarding the neutrons with energy above 1 MeV represents only few percents of the total reactor neutron flux as seen in Fig. 1.14. In addition, it appears currently difficult to access this information because the interaction cross-sections of thermal neutrons are several decades larger than those of fast neutrons.

At present, only activation measurements can provide this kind of information on neutron fluence in the fast neutron energy range. However, this measurement has the disadvantage that it cannot be carried out on-line during reactor operation. In order to be able to extract an on-line signal proportional to fast neutron flux with energies of 2 to 20 MeV and thus monitor the measurement of fast neutron flux directly, it would appear necessary to be equipped with a device that is sensitive to fast neutrons while being insensitive to thermal neutrons. In the same way as for fusion, it would also be advisable to have a device capable of carrying out spectrometric studies in order to obtain a relative response of fast neutrons over several energy groups.

[20] *User's facility interface manager at JHR.*
[21] *Origins, Spectral Interpretation, Resource Identification, and Security (OSIRIS)*

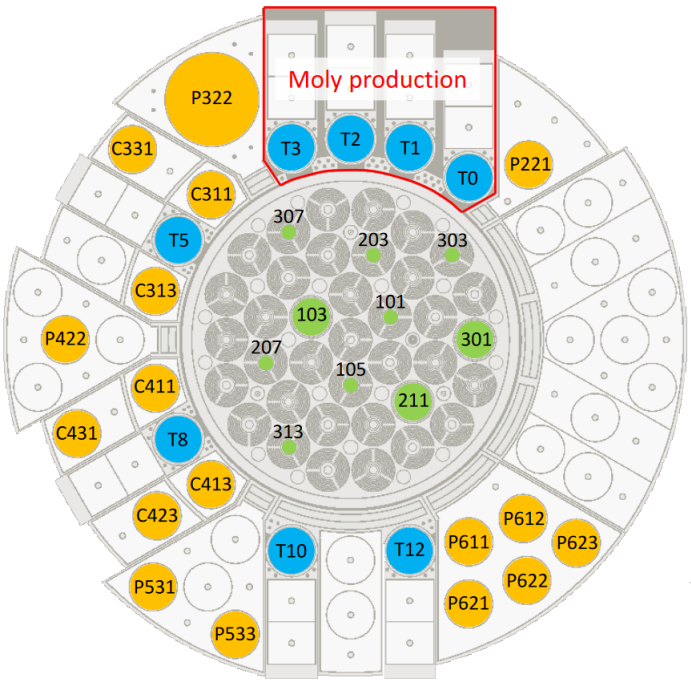

Fig. 1.13. Diagram of the horizontal irradiation ports, and the volumes of interest for each port, in which the neutron fluxes are calculated [22].

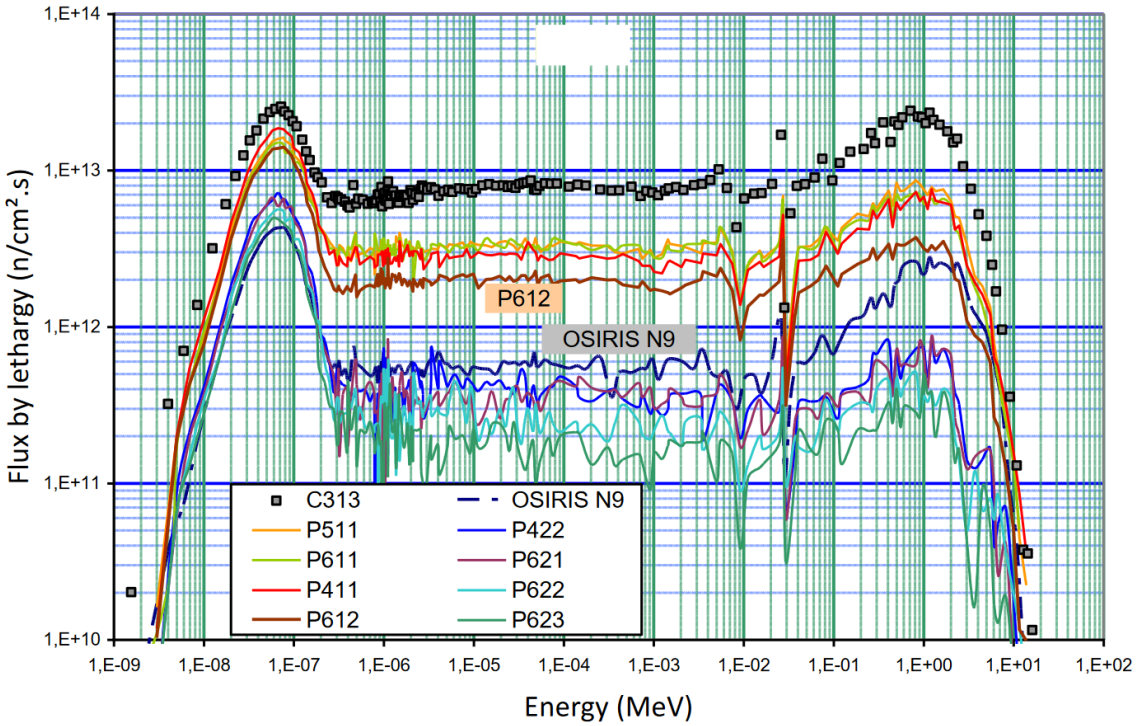

Fig. 1.14. Neutron flux spectra by lethargy unit within several irradiation locations in JHR regarding Fig. 1.13 [22]. The calculation have been carried out using the TRIPOLI Monte-Carlo radiation transport code.

Furthermore, the challenge lies in transitioning from a MTR neutron spectrum, where components are irradiated, to a fusion reactor spectrum, that accurately mirrors the anticipated conditions at ITER. The neutron spectrum at ITER is primarily composed of fast neutrons from the DT fusion reaction, as illustrated in Fig. 1.15. In contrast, the JHR spectrum does not share this characteristic. However, the JHR reactor, with its high neutron flux levels, is capable of testing material resistance to high neutron fluxes and studying material behavior under irradiation. This is achieved by using neutron fluence rates equivalent to those expected in ITER, thereby linking the irradiation capabilities of the JHR reactor to the needs of fusion reactors like ITER.

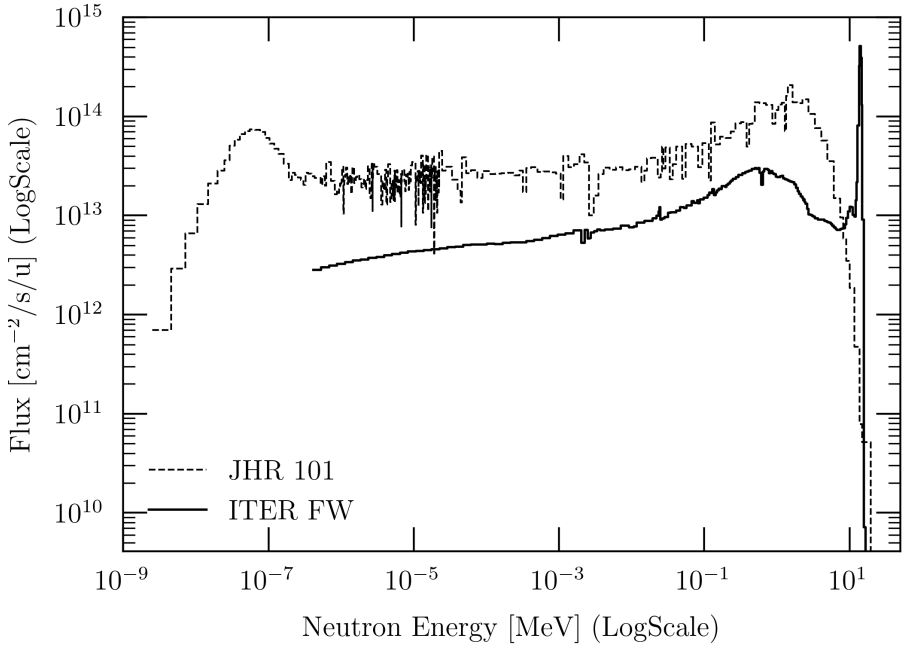

Fig. 1.15. JHR and ITER neutron fluence rate spectra by lethargy unit u in the 101 fuel slot and at the first wall location. Data from FISPACT-II nuclear database for ITER FW neutron spectrum for D–T campaign [13] and from CEA technical note for JHR 101 fuel slot [25].

1.2.1.2. Monitoring of the material damages

A collaborative project between the CCFE[22] and the CEA has started in 2015 in order to examine the needs in the fusion field and to develop dedicated JHR experimental devices. The aim is therefore to help solve the future challenges facing the fusion community in terms of materials science behavior and aging under irradiation [26]. In order to design these different components successfully, it is important to know how their structural and functional characteristics change as a function of irradiation.

For example, the performance of superconducting magnets in tokamaks and their evolution under both neutron and photon irradiation need to be assessed. The conductive and insulating materials need also to be tested in an environment of high neutron and photon flux, representative of the expected one in nuclear fusion reactors. To summarize, several objectives are defined for R&D programs planned on the JHR, for the qualification of materials linked to nuclear fusion needs such as FUSERO:

- Irradiating various innovative materials

[22] *Culham Centre for Fusion Energy (CCFE)*

- Measuring physical properties under high neutron flux
- Reproducing the environmental conditions of thermonuclear fusion reactors.

To meet these objectives, a number of requirements have been identified:

- The accurate control of environmental conditions (stationary and transient phenomena) particularly regarding fast neutrons
- Long term irradiation to study dpa effects.

1.3. The technological limitations

1.3.1. Hostile fusion and fission environments

One of the specificities for the nuclear instrumentation used for fission or fusion reactor resides in the special features required by this constraint environment in which measurements are performed. The implementation of neutrons sensors in ITER TBMs is for instance constrained due to the operating conditions and specific features of this outstanding environment in the context of radiation detection [27]:

- Temperature reaching 600 °C
- Magnetic field of few T
- EMC[23] issues due to the auxiliary heating device with radio-frequency
- Thermomechanical and ultra-high vacuum stresses that can lead to mechanical deformation or structure failures
- Radiation levels reaching $1 \cdot 10^{14} \mathrm{cm}^{-2} \cdot \mathrm{s}^{-1}$ to the entrance of TBM
- Damage to materials of up to 30 dpa per year during continuous operation of a future power reactor.

Thus, a number of precautionary aspects regarding the choices of the sensors devices used or whether the choice concerning the materials and insulators used for the sensor conditioning must be considered. To summarize, a sensor dedicated to the fast neutrons measurement in a fusion or fission environment must be able to meet a set of specifications covering a number of precise and crucial characteristics.

Related to the device response:

- With a fast neutrons selectivity in a mixed field composed of fast and thermal neutrons, with gamma rays
- With spectrometric results on several neutron energy groups.

Related to the system implementation:

- Resistance to a hostile environment, summarized in the Table 1.1
- A need for miniaturisation to meet integration requirements, like the experimental devices integrated into MTRs as seen for instance in Fig. 1.16 for the experimental device CALIPSO[24] for the JHR.

[23] *ElectroMagnetic Compatibility (EMC)*
[24] *Core Advanced Loop for Irradiation in Potassium SOdium (CALIPSO)*

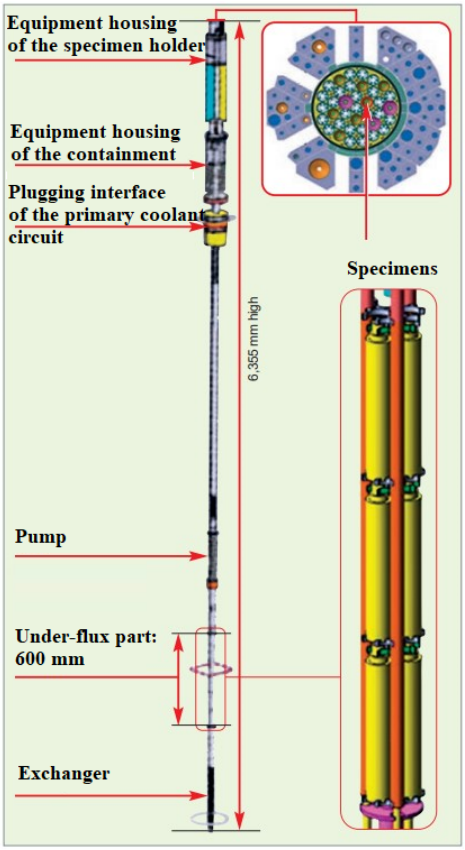

Fig. 1.16. Representation of the CALIPSO experimental set-up for studying the thermomechanical behavior of fuel under irradiation in the JHR [28].

1.3.2. Dedicated neutron instrumentation

A selection of candidates has been identified to meet the requirements for fast neutron detection and monitoring, specifically for the implementation of TBMs on ITER or JHR instrumentation needs. Gaz filled detectors and micro Fission Chamber (FC), or scintillators and solid-state based detectors have the shared advantages of good detection efficiency, robustness and resistance to radiation. An important feature of the successful candidate is the dependence of its response on the energy of the incident neutron. In other words, the detector's ability to reconstruct a neutron flux spectrum in detail from signals coming from the measurement device. This property differentiates devices dedicated to counting from those capable of providing neutron spectrometric results.

The requirements for a neutron detector designed for monitoring applications fall into two categories. Firstly, there are requirements relating to the active component itself, with a defined detection efficiency, the ability to discriminate the background contribution of gamma photons, stability of the device over time with a linear response as a function of reactor power, and resistance to radiation. Secondly, the device implementation requirements include operation and stability of the detector response over a wide range of temperatures and magnetic fields as listed in Table 1.1, tolerance to mechanical and thermal shocks, and consideration of data acquisition, device geometry and device maintenance needs.

Criteria	ITER FW	JHR core	ITER external	JHR reflector
Fast neutron flux [$cm^{-2}{\cdot}s^{-1}$]	$3\cdot10^{14}$ [a]	$5\cdot10^{14}$ [g]	$3\cdot10^{9}$ [b]	$5\cdot10^{12}$ [g]
Photon flux [$cm^{-2}{\cdot}s^{-1}$]	$7\cdot10^{14}$ [h]	$3\cdot10^{14}$ [a]	$1\cdot10^{8}$ [b]	$2\cdot10^{13}$ [h]
Temperature [°C]	800 [e]	up to 600 [i]	350-550 [j]	up to 600 [i]
dpa [per year]	8 [c]	16 [g]	4 [d]	11 [g]
Magnetic field [T]	5 [f]	∅	0.5 [f]	∅

[a] *For the peak neutron flux in FW inboard region, from [29].*
[b] *For the peak neutron flux in magnet location, from [29].*
[c] *For the radiation damage in Fe for FW inboard region, from [29].*
[d] *For the radiation damage in Fe for blanket location, from [29].*
[e] *Constraint based on safety considerations, from [30].*
[f] *Considering the upper port, from [31].*
[g] *From [32].*
[h] *From [25].*
[i] *Depending of the experimental device, from [33].*
[j] *From [34].*

Table 1.1. Comparison of the main environmental constraints in ITER and JHR facilities in two different locations.

Conclusion

The requirements relating to active components can be met by choosing appropriate detection physics, in particular through an appropriate choice of materials, optimization of the detector geometry or the properties of the acquisition system. The work presented in this manuscript proposes to address each of these requirements.

In a first part, the choice of the detection physics is discussed, by reviewing candidate detectors for measuring fast neutrons in hostile environments. This review results in the selection of the wide bandgap semiconductor detector, identifying silicon carbide as a promising material. Its properties as a semiconductor and its potential for fast neutron detection are discussed in detail. The design of the selected sensor, resulting in a manufactured prototype, is used in the second part of the manuscript to estimate the fast neutron flux in a mono-energetic and multi-energetic neutron field. After evaluating the detection performances, the final part of this thesis examines the behavior of the sensor in hostile environments. Experiments are conducted in high-temperature conditions and under high neutron irradiation levels to assess the reponse of the sensor and its limitations. Finally, according to the broad spectrum of the work presented, in terms of quantitative methods of fast neutron flux estimation, and regarding the sensor behavior in hostile environment, the perspectives are discussed and the potential for future work is outlined.

Part I.

Choice of the sensor

2 Review of the main candidates **39**
2.1 Fission Chambers 39
2.2 Self Powered Neutron Detectors 42
2.3 Scintillator neutron detectors 45
2.4 Solid State sensors 47

3 The Silicon Carbide **54**
3.1 Inherent parameters 54
3.2 Response to external parameters 67
3.3 The SiC as a radiation sensor 73
3.4 Manufacturing of 4H–SiC sensors 90

2. Review of the main candidates

The detection of neutrons, photons and direct ionizing radiation requires the use of a medium capable of interacting with the particle to be detected and converting the interaction effects into an electrical charge that can be amplified and transformed into a measurable signal. Much of the development of radiation detection methods has focused in the past on the discovery of such conversion mechanisms and on the optimum means of implementing them, particularly with a view to developing ever more sensitive devices. As a result of the interaction of radiation, for a large category of detectors, a given quantity of electrical charges can be measured in the active volume of the detector. The time required to collect the charge completely varies considerably from one detector to another and may require the use of several modes of operation.

Several criteria have to be taken into account in the choice of a neutron sensor. First, in order to use it in a mixed field with fast and thermal neutrons but also gamma radiation, the detection device should be the most sensitive to fast neutrons. In addition, there is a need to get some results of spectrometry in order to get information of detailed characterization of the neutron energy spectrum. Depending of the sensitivity of the sensor, the sensor response has to be fast enough to provide precise estimation of the neutron flux in pulse mode up to 1 MHz events rate for instance, before the signal experienced a pile-up effect. Finally, as well as the consideration concerning the hostile environment, the operating mode can be different from one to another and also give some different insights. For very high event rates, pulse mode can no longer be used in practice. This is because the time between two successive events may become too short in relation to the acquisition time to perform an adequate analysis, or these successive pulses may overlap in time. In this case, alternative measurement techniques that process the time average taken over many individual events are used, such as current mode or Campbell mode.

The constraints and requirements linked to the need for fast neutron measurements in nuclear fusion and fission environments were identified in the Section 1.1, page 21. At present, only neutron activation measurement is used to obtain information on the integrated neutron fluence in the fast neutron energy range. However, this measurement has the disadvantage that it cannot be carried out on-line during reactor operation. It is therefore necessary to study the various candidates for on-line measurement of fast neutrons in the hostile environment of nuclear fusion and fission. After reviewing the main on-line measurement devices, a comparison table can be drawn up, taking into account both the constraints identified above and feedback from operating experiences.

2.1. Fission Chambers

2.1.1. Operating principle

Filled with inert gas, the FC is a gaseous ionization chamber that consists of two electrodes, at least one of which is covered with a fissile material deposit as seen in Fig. 2.1. Incident neutrons then induce fission reactions generating highly energetic fission products, around 80 MeV each, which ionize the inert gas as they leave the deposit. Finally, a potential difference applied between the two electrodes collects the resulting charges.

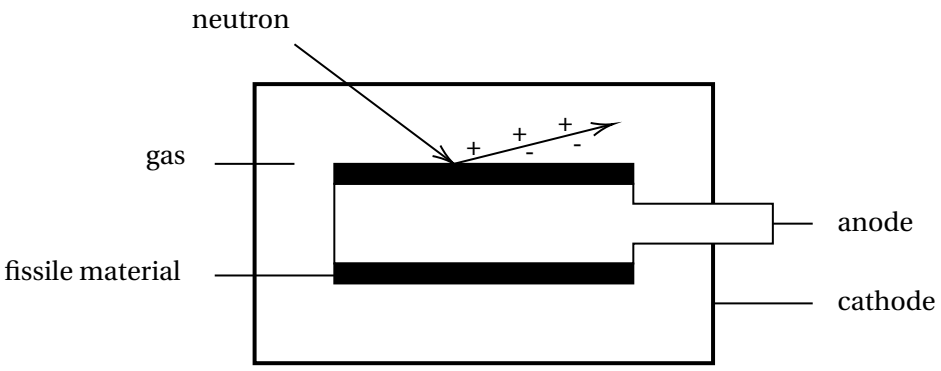

Fig. 2.1. Basic operating diagram of a FC detector.

The choice of fissile deposit takes into account two considerations:

- The interaction cross section for fission reactions is generally much larger for thermal neutrons than for fast neutrons. Moreover, even for the few isotopes with an energy threshold close to 1 MeV, such as ^{238}U or ^{242}Pu, it remains of the order of a few barns as seen in Fig. 2.2 for fast neutrons with energies greater than 1 MeV.
- These few isotopes can then undergo radiative capture of mainly thermal neutrons. This process, either directly or after certain radioactive decays, then leads to new isotopes, which in turn are likely to undergo fission preferentially with thermal neutrons. The sensitivity to thermal neutrons of a chamber based on these isotopes therefore increases progressively.

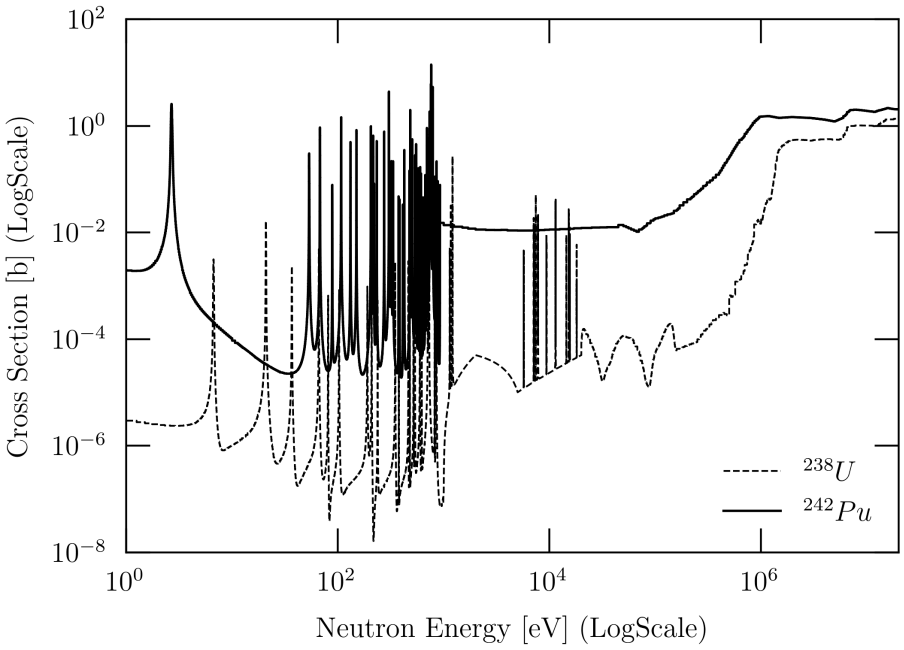

Fig. 2.2. Fission cross section of ^{238}U and ^{242}Pu. Nuclear data from ENDF/B-VIII.0.

2.1.2. Operating experience

Selectivity of fast neutrons in mixed fields

In the context of the detection of fast neutrons, the importance of using ^{242}Pu as a fissile deposit to measure the fast component of a high neutron flux in the case of a significant thermal contribution was highlighted by Filliatre et al. [35]. Thus, in order to meet the needs of the online fast neutron fluence rate monitoring, a measurement system called FNDS[1] was developed by the CEA and the SCK-CEN[2] within the framework of their common instrumentation laboratory. This device, allowing the measurement of the fast neutron component is based on two sensors. A FC with a ^{242}Pu deposit for the fast or thermal neutron fluence rate, in which is coupled a FC with a ^{235}U deposit as a reference for the thermal neutron fluence rate. The fast neutron fluence rate component can thus be obtained, subtracting the responses of the two FC. However, the measure obtained does not give a detailed characterization of the neutron energy spectrum since the ^{242}Pu deposit is sensitive only to neutrons with energies greater than 1 MeV.

Concerning classical FC, miniaturized micro FC have been utilized for several years for online monitoring of thermal neutron flux and flux mapping in MTR [36]. However, although the latter are proposed as means of neutron diagnosis for total neutron yield measurement on ITER by the JAERI[3] [37] [38], the results obtained does not give a detailed characterization of the neutron energy spectrum. MPFD[4] are another concept of miniaturized FC proposed for online control of neutron flux on MTR [39, 40, 41]. However, although these MPFDs are able to distinguish neutron signals from gamma signals, they are still dedicated to the total neutron yield measurement and are not suitable for the selective measurement of fast neutron flux in mixed fields.

Regarding the FNDS device, Vermeeren et al. [42] demonstrated the effectiveness of supressing the gamma component of the signal using a FC with a ^{242}Pu deposit coupled to a FC with a ^{235}U deposit, in Campbell mode during irradiation campaigns on the BR2[5]. The qualification of the FNDS system for online detection of fast neutrons with energy greater than 100 keV in the presence of a high thermal neutron field in the order of $2 \cdot 10^{14} \mathrm{cm}^{-2} \cdot \mathrm{s}^{-1}$ and a high gamma dose rate was described. However, no information on the energy distribution of these fast neutrons is available using this device.

Behavior versus temperature

FC available in industry are designed to operate at temperatures up to 600 °C [43]. However, during the operation of the sensor at temperature higher than 400 °C, with elevated bias voltage inducing electric field greater than $200\,\mathrm{V} \cdot \mathrm{mm}^{-1}$, an additional signal, independent of the neutron source was observed by Jammes et al. [44]. It brought up the fact that FC is subject to partial discharges[6] which gave rise to pulses similar in shape and amplitude to those resulting from neutron interactions, which can cause biases in the measurement.

Post-treatment analysis has enabled Hamrita et al. to discriminate pulses induced during partial discharges from the ones induced by the neutrons, using the FWHM[7] as a discrimination criteria [47]. To get rid of this post-processing task, it had been considered adding a new electrode to the FC in order to physically eliminate partial discharges. However, the addition of this new electrical cable would make it more difficult to integrate the FC into the MTR. Dedicated

[1] *Fast Neutron Detection System (FNDS)*
[2] *StudieCentrum voor Kernenergie-Centre d'étude de l'Énergie Nucléaire (SCK-CEN)*
[3] *Japan Atomic Energy Research Institute (JAERI)*
[4] *Micro-Pocket Fission Detectors (MPFD)*
[5] *Belgian Reactor 2 (BR2)*
[6] *Theoretical studies have defined the phenomenon of partial discharges in gases and solids, also known as "electron avalanches" [45, 46].*
[7] *Full Width at Half Maximum (FWHM)*

FNDS studies for high temperature applications were carried out in the scope of the ASTRID[8] project [48], but up to now, no results have been published since the decision to stop the project in 2019.

Influence of magnetic fields

The effects of a strong magnetic field on FC have been studied by Nishitani et al. [49]. They measured the current induced by the electrons from ionization by the fission fragments and then calculated the electron drift orbit in a magnetic field. Numerical applications of their model, in the case of a FC with 14.6 atm of Argon gas, with an applied voltage of 200 V in a magnetic field of 5.7 T gave a very low value for the drift angle of the charge carriers. The effect of a strong magnetic field of around 5.7 T on the electron drift speed is therefore theoretically negligible.

Concerning the fusion environment, an initial measurement was carried out on the JT-60[9] by Hayashi et al. [50]. However, electromagnetic noise signals were measured. These were observed during breakdowns in the NBI process. Nevertheless, no spurious signals were observed during plasma disruptions[10]. Nor was any effect of the magnetic field observed up to 2 T.

The influence of a magnetic field on the FC operation is therefore theoretically negligible, but this point could be validated experimentally with FCs used in fields greater than 2 T. In addition, initial measurements on the JT-60 tokamak have shown that FCs are highly sensitive to electromagnetic noise when deuterium injection is stopped, which is a notable weakness. As far as the FNDS concept is concerned, no study dedicated to the influence of the device's magnetic field has been referenced to date.

Conclusion

- Classical FC are not suitable for the detection of fast neutrons in a mixed field.
- In a mixed field, FNDS devices have shown a capacity to estimate a fast neutron. fluence rate by suppressing the gamma interference component.
- However, FNDS are not suitable for fast neutron spectrometry or detailed characterization of the neutron energy spectrum.
- Moreover, FNDS impose additional integration constraints with the implementation of two FC.
- Finally, the manufacturing cost of this device, which consists of two coupled FC could be greater than 50 k$.

2.2. Self Powered Neutron Detectors

2.2.1. Operating principle

Collectron or SPND[11] takes the form of a coaxial cable made up of two electrodes, the emitter in the centre and the collector on the outside, separated from each other by an insulating material as seen in Fig. 2.3. When subjected to photon or neutron radiation, the electrode, made of a carefully chosen material, will emit electrons. As the electrons travel from the emitter to the collector, they produce a current proportional to the flux of the incident radiation.

[8] *Advanced Sodium Technological Reactor for Industrial Demonstration (ASTRID)*
[9] *JAERI - Tokamak 60 (JT-60)*
[10] *Sudden appearance of magnetohydrodynamic instabilities in the vacuum cavity.*
[11] *Self Powered Neutron Detectors (SPND)*

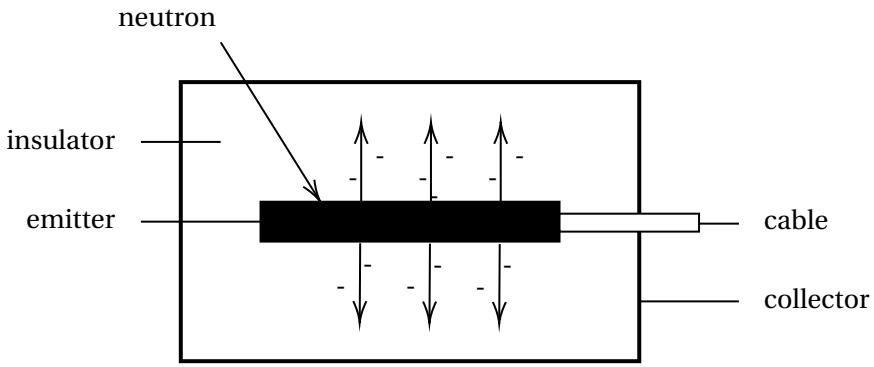

Fig. 2.3. Basic operating diagram of a SPND detector.

SPND are divided in two categories:

- SPND based on delayed beta decay
- SPND based on prompt gamma rays.

In the first category, the absorbed neutron produces a nuclide that emits an electron as it decays with beta-minus emission. This electron has enough energy to pass through the insulating material between the emitter and the collecting electrode. The collection of beta particles then produces the signal. SPNDs based on beta decay therefore give only delayed responses compared with SPNDs based on prompt gamma rays. This second category uses the gamma prompt emitted after the radiative capture of a neutron by a nucleus. The gamma rays then interact with the collecting and insulating materials through the photoelectric effect, the Compton effect, and the electron-positron pair production.

The use of SPND in a mixed field therefore requires the effect of gamma radiation on the emitter to be taken into account. In a mixed field, the response of SPND detectors is mainly due to three important factors [51]:

- Photon/matter interactions, mainly Compton scattering in the insulator
- Radiative capture of thermal neutrons which emits gamma radiation, which subsequently induces Compton scattering and/or the photoelectric effect
- β^- decay of an unstable isotope in the detector leading to the emission of gamma radiation again inducing Compton scattering and/or the photoelectric effect; or leading to the emission of a β^- particle behaving like a highly energetic free electron, of the order of a few MeV.

To meet the need for on-line measurement of fast neutron flux in a mixed field, the sensitivity of the SPND to gamma rays must be as low as possible in order to reject its contribution, which interferes with the measurement of the current proportional to the neutron flux [52]. It is possible to design SPND devices with gamma sensitivities of less than 1%, provided that the electrode pair materials are chosen correctly. SPNDs have a number of interesting properties in terms of their ability to withstand high radiation fluxes, their compactness and the absence of external polarization. However, the use of SPNDs to measure fast neutron flux in a mixed field is limited since the effective cross-sections for the production of beta emitters are much lower in a fast neutron spectrum.

2.2.2. Operating experience

Selectivity of fast neutrons in mixed fields

There is little experience of SPNDs based on prompt gamma rays. These have mainly been used in thermal and epithermal flux conditions. Experiments with SPNDs based on delayed beta have been carried out under thermal, epithermal and fast flux conditions. A study was done comparing three SPND marketed [53] composed of three different materials: rhodium, cobalt and vanadium. The possible nuclear reactions induced by neutrons in the three materials used as emitters in these SPNDs were studied by Angelone et al. [54]. The analysis was carried out for neutrons from 0 to 15 MeV at the facility TAPIRO[12] of the ENEA[13] in Rome, covering the entire neutron energy range in a TBM.

The results then showed that in the presence of a complex neutron spectrum extending up to around 15 MeV, the number of reactions induced is not negligible and most of the reaction products may be stable or decay with a long half-life, the latter point not being favourable to the use of SPNDs for monitoring fast neutrons in a mixed field. This first attempt to study the feasibility of using SPNDs therefore demonstrated that the devices currently available commercially are not suitable for such use because of the sharp reduction in the current measured.

Operating experience from various projects has shown the need to study new emitting materials suited to the operation of SPND in neutron spectra in mixed field with a low component of fast neutrons [55]. With regard to SPNDs based on prompt gamma, an innovative use of prompt-SPND detectors for measuring the flux of fast neutrons in mixed fields has been proposed by Lepore et al. [56], but no experimental validation of the method presented has yet been carried out. Finally, with regard to the spectrometric capabilities of such a device, the main limitation lies in the small number of materials — with threshold nuclear reactions — that can be introduced during the assembly process.

Behavior in temperature

Particular attention must be paid to the materials chosen for the SPND emitter. For applications in hostile environments, SPNDs must not only operate at high temperatures but also be able to follow variations in neutron flux, while remaining sensitive to high-energy neutrons. In addition to the compromise on the choice of emitter material, the problem of choosing a suitable insulating material must also be addressed. Indeed, regarding the operation in high temperature environments, low melting point materials must be avoided. SPND currently used as in-core flux monitors in the nuclear industry are designed to operate at temperatures up to 300 °C [57]. Few studies have been conducted on the resistance of SPNDs to high temperatures. Bock et al. studied one SPND with a platinum emitter and one SPND with a rhodium emitter, up to 800 °C [58]. They observed an increase in the electrical conductivity of the SPNDs with temperature [59]. A non-linear behavior was noted above 400 °C, with a decrease in signal with increasing temperature.

Influence of magnetic fields

No studies dedicated to the influence of an intense magnetic field on SPND performance have been referenced.

[12] *TAratura PIla Rapida di potenza 0 (TAPIRO), Fast Pile Calibration at 0 Power*

[13] *Energia Nucleare ed Energie Alternative (ENEA), Italian National Agency for New Technologies, Energy and Sustainable Economic Development*

Conclusion

- Gamma sensitivity depends on the choice of materials for the electrode pair.
- SPND concepts proposed for fast neutron flux monitoring in mixed field are still under development.
- With regard to the spectrometric capabilities of SPNDs, the transmitter/receiver assembly process imposes integration constraints.
- Lastly, there are no studies to date on the influence of high temperatures and/or magnetic fields.

2.3. Scintillator neutron detectors

2.3.1. Operating principle

Scintillators consist of a detector medium whose role is to convert the energy deposited by the incident radiation into detectable light with a high scintillation efficiency as described in Fig. 2.4. The intensity of these scintillation photons, which is proportional to the energy deposited by the incident particle, is emitted by the de-excitation of atoms in the scintillator medium. These photons then generate electrons via a photomultiplier, and the resulting electrical signal is measured after amplification.

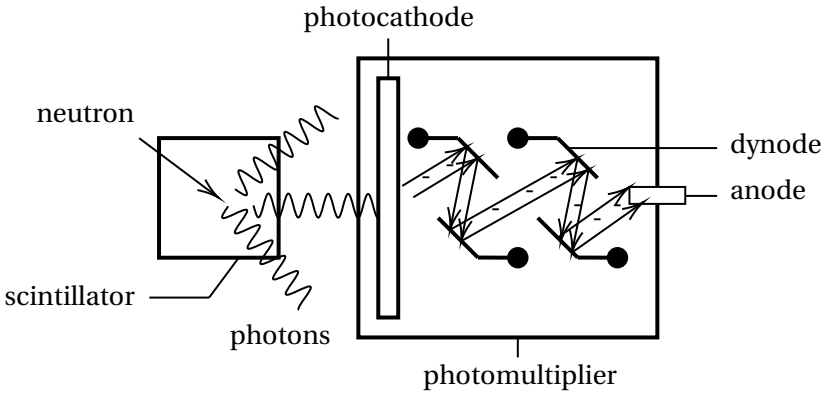

Fig. 2.4. Basic operating diagram of a scintillator detector.

Organic scintillators are mainly used for the detection of fast neutrons and are rarely used for X-ray or gamma-ray spectrometry because of their composition, which is essentially carbon and hydrogen with low atomic numbers. Because of the low atomic masses of the elements making up these organic scintillators, a fast incident neutron is able to transfer some or all of its energy by scattering. When the incident neutron strikes a nucleus of the hydrogen compounds, a recoil nucleus — in this case, a proton — excites or even ionizes the molecules in the detector medium, resulting in the emission of de-excitation photons [51]. The main challenge in detecting fast neutrons with scintillators is to separate the response resulting from neutron interactions from that from gamma. However, while neutrons are detected by elastic/inelastic scattering on the target nuclei, gamma photons are detected via electrons generated by Compton scattering or the photoelectric effect. Since the ionization mechanisms are different, it is possible to distinguish between these two contributions by studying the shape of the electrical pulses.

2.3.2. Operating experience

Selectivity of fast neutrons in mixed fields

The Pulse Shape Discrimination (PSD) was chosen very early as a technique to separate and attribute the individual contributions which come from a neutron or a gamma. As early as 1960, Brook et al. emphasized the ability of a plastic scintillator to discriminate the pulses shapes resulting from neutron and gamma interaction [60]. However, a deterioration in performance was observed after six months of use, with in particular a structural deformation of the edges of the device. Recently, another concept was studied by Hamel et al. in 2014 [61]. They have taken into account threshold neutron capture reactions $^{19}F(n,p)^{19}O$ and $^{19}F(n,\alpha)^{16}N$ in order to detect energetic neutrons. This concept had already been demonstrated by Gozani et al. as a mean to detect hidden nuclear materials, using prompt neutrons with an energy of 3 MeV emitted during ANI[14] with induced photofissions [62]. These plastic scintillators have made it possible to obtain a spectrum of recoils protons, with low resolution, during an exposition with fast neutrons as well as modest PSD for the discrimination of neutron/gamma interactions.

Fast neutrons detection with scintillator by removing the gamma component using several methods was also studied by Ryzhikov et al. [63]. The first, which consists of installing lead shielding, provides good suppression of gamma background noise, but sensitivity to fast neutrons is then reduced by an order of magnitude. A second approach is an active protection method coupling two scintillators. Discrimination between gamma and neutron radiation is achieved by observing the difference in scintillation decay times of the two devices. This type of detector is suitable for specialized scientific research, but its complex design makes it unsuitable for industrial applications. Finally, a mathematical processing method has made it possible to deduce the gamma spectral component in a mixed field without reducing the sensitivity of the neutron response recording. While this last method is the most promising, it is currently under development and requires further investigation, particularly as regards its feasibility under high fluxes of neutron and photon radiation.

It should also be mentioned that two stilbene scintillators were also used to characterize the neutron spectra from 0.8 MeV to 10 MeV and photonic from 0.2 MeV to 10 MeV, in multiple positions within an irradiation channel of LR-0[15] at Prague [64].

Behavior versus temperature

The temperature dependence of conventional scintillators has already been studied [65]. Scintillators characteristics such as the pulse height, the energy resolution and the decay time of monocristal of NaI doped with Tl, of Lu2SiO5 doped with Ce, of YAlO3 doped with Ce, Gd3(Al,Ga)5O12 doped with Ce, Lu3Al5O12 doped with Pr, LuAG undoped and transparent ceramics Y3Al5O12 doped with Ce have been compared from 25 °C to 150 °C. While temperature increases, Yanagida et al. have shown that the light output of scintillators decreases. Among these samples, the LuAG-based sample gave the best scintillation performances at 150 °C.

Another study from Kawaguchi et al. [66] demonstrated the influence of temperature on the responses of LiCaAlF6 scintillators compared with those of Ce-doped lithium silicate. Pulse height spectra were measured under thermal neutron irradiation over a temperature range from 25 °C to 150 °C. The peaks height at 150 °C decreased by 60 % in comparison to the measurement achieved at 25 °C for the lithium silicate and by 25 % for the LiCaAlF6. Moreover, the stable response in the temperature range of 25 °C to 150 °C has led the authors to conclude that lithium silicate scintillators can be effectively used within this temperature range, up to 150 °C.

[14] *Active Neutron Interrogation (ANI)*
[15] *Light water zero power Reactor (LR-0)*.

Influence of magnetic fields

A calorimeter concept consisting of a plastic scintillator with silicon photomultipliers has been developed by Graf et al. [67]. A measurement campaign on the electron beam at DESY[16] research center was carried out to test the prototype's performance in a powerful magnetic field. Data was acquired for different incident electron beam energies with and without a 1.5 T magnetic field. The researchers observed that the detector's response to the magnetic field increased by around 10%. This effect is due to a combination of several phenomena, including the fact that the path of the particles through the scintillator is longer because of the curvature of the magnetic field, inducing a greater number of interactions and thus depositing more energy in the scintillator. An increase in the luminous efficiency of scintillators of around 4% has been observed.

A stilbene scintillator has been proposed as a neutron diagnostic system for measuring the characteristics of fusion reactor neutrons KSTAR[17]. The effect of magnetic shielding on this scintillator was studied by Lee et al. [68]. They demonstrated that the detection efficiency of the neutron detector was better using a 10 mm soft iron magnetic shield in magnetic fields of 0.1 T and 0.4 T.

Conclusion

- The signals resulting from interactions with neutrons can be distinguished from the response to gamma by a post-processing step using the PSD method.
- Stilbene scintillators were used to detect fast neutrons.
- Work has been carried out on temperature resistance and the influence of the magnetic field, but more needs to be done in order to improve the operational domain above 150 °C and 0.5 T.

2.4. Solid State sensors

2.4.1. Operating principle

Neutron detection mechanisms using detectors based on semiconductor materials are achieved through indirect methods in which neutrons interact with atomic nuclei in the lattice and produce ionizing charged particles[18]. The effective cross-section of the incident neutron's interaction with the atomic nucleus is a function of the neutron's energy, the nature of the nucleus, the nuclear reaction involved and the temperature. Consequently, various reactions can be induced by fast neutrons, leading to energetic and charged reaction products which, as they slow down, ionize the detector medium. The effects of radiative capture, such as ionization by gamma rays, can also be measured. In the case of fast neutron detection, the later interact directly with the nuclei of the atoms in the active detection zone as depicted in Fig. 2.5. On the contrary, thermal neutron require the use of a Neutron Converter Layer (NCL) composed of elements with a high interaction cross-section with thermal neutrons and which emit charged particles.

[16] *Deutsches Elektronen-SYnchrotron (DESY)*
[17] *Korea Superconducting Tokamak Advanced Research (KSTAR)*
[18] *This general information is presented here by way of comparison, but will be expanded and discussed in detail in later chapters.*

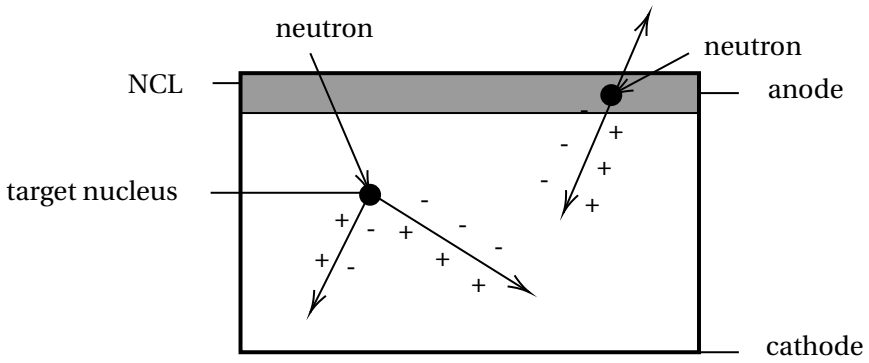

Fig. 2.5. Basic operating diagram of a semiconductor neutron detector.

Solid state sensors based on wide band-gap semiconductors as diamond Chemical Vapor Deposition (CVD) or Silicon Carbide (SiC) can be used[19] for the detection of fast neutrons over a wide energy range, which gives them interesting spectrometric properties. In a mixed field of fast and thermal neutrons characteristic of a nuclear fission environment, the response of a diamond or SiC semiconductor detector will be dominated by the detection of ^{12}C and ^{28}Si energy recoil nuclei in the case of SiC, because the average energy of fission neutrons is around 2 MeV. These energetic recoil nuclei from elastic scattering reactions will therefore contribute to the majority of the measured signal since the average energy of fission neutrons is below the threshold energy of the main neutron capture reactions on ^{12}C and ^{28}Si nuclei. It can also be mentioned that threshold neutron capture reactions on silicon and carbon nuclei can also be studied in order to detect the fast neutrons of higher energy[20].

2.4.2. Operating experience

Selectivity of fast neutrons in mixed fields

In the framework of the European project I_SMART in 2012 [69], new radiation sensor based on SiC semiconductor material were developed and tested in mixed radiation fields. A first PhD thesis proved the ability for such sensors to detect fast and thermal neutrons [70], in hostile environments described previously. Within this context, several measurements have been carried out with several particle sources as described in Fig. 2.6 at the CEA Cadarache using a LINAC[21] and at technical university of Dresden using a DT neutron generator of 14 MeV.

During fast neutrons sources measurements, pulses with high amplitude due to induced reactions by fast neutrons on ^{28}Si and ^{12}C nuclei were recorded with such sensors [71]. A comparison of responses to thermal and fast neutrons for SiC sensors was presented in 2006 by Ruddy et al. as seen in Fig. 2.7.

[19] *The reasons that led to the choice of diamond and SiC for the neutron detection application will be explained in Chapter 3.*

[20] *Information on these neutron captures and will be presented in more detail in Chapter 3 and their relevance will be demonstrated in Part II.*

[21] *LINear ACcelerator (LINAC)*

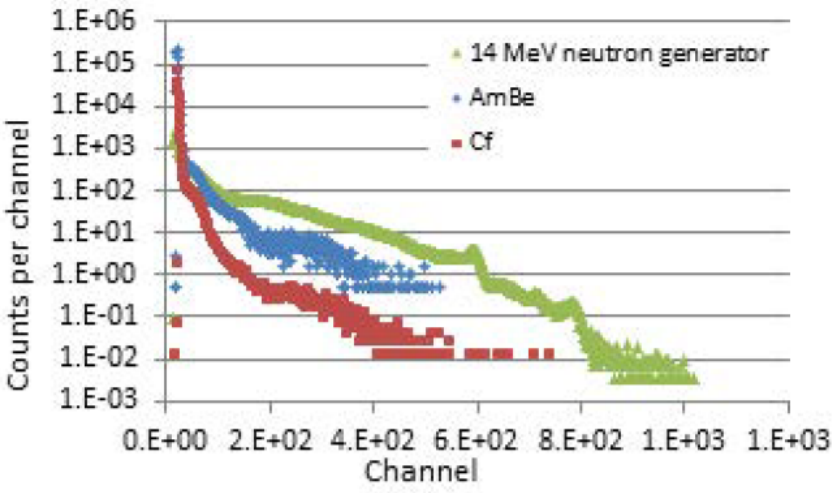

Fig. 2.6. Pulse height analysis for three neutrons sources [71].

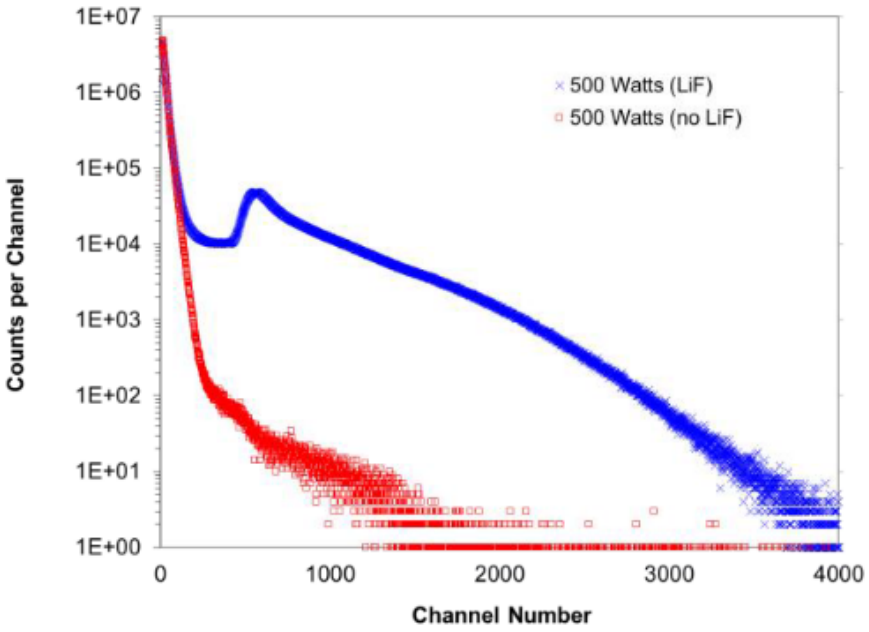

Fig. 2.7. Neutron response comparison of a SiC Schottky diode of 500 µm of diameter × 3 µm to neutrons from fission reactor with and without ^{6}LiF based NCL of 24.2 µm [72].

Within the I_SMART project ion implanted ^{10}B as NCL has shown the capability to study the sensor response at several reactor power at BR1 [73], and more recently up to 250 kW power at the JSI[22] TRIGA Mark II reactor [74]. Hence, using a ^{6}LiF or ^{10}B based NCL, it had been demonstrated the ability to discriminate the sensor response to thermal and fast neutrons. Regarding the quantitative analysis of SiC sensor neutron response, a numerical tool has been described by Cetnar et al. [75] to obtain sensor responses to each type of radiation. A methodology for deconvoluting the incident fast neutron energy spectrum and fluence rate from measured pulse height spectra in SiC semiconductor radiation detectors is still under development [76] and a method has been recently proposed for diamond sensors [77].

[22] *Jožef Stefan Institute (JSI)*

The approach adopted by Franceschini et al., involves firstly the simulation of the interactions between fast neutrons and the generation of recoil nuclei and capture products in the detector. Secondly, the energy deposition of these charged particles is analyzed using the SRIM[23] [78] code. Validation of the methodology with a 14 MeV single-energy neutron source showed a quite good agreement between the predicted and experimental responses.

Behavior versus temperature

SiC semiconductor sensors at high temperatures were first used in 1963 by Bacock et al. [79] for measuring ionizing radiation. Results from the measurement of 5 MeV alpha particles at ambient temperatures up to 700 °C showed a broadening of the alpha peak with temperature and a shift of the alpha peak towards higher energy channels. Then, measurements at 700 °C showed a background level reaching the signal level showing limitations of the device under study. More extensive experiments have been carried out more recently by Kalinina et al. [80] using SiC pn diodes to detect alpha particles from 3 MeV to 8 MeV from room temperature to 375 °C. The effect of external temperature on the diode signal as well as different thermal noise and current values were investigated showing ability to operate at temperature at least up to 300 °C with a quite good energy resolution.

The applicability of single-crystal diamond CVD sensors for particle spectrometry at ambient temperatures of up to 200 °C has also been reported in 2020 by Kraus et al. [81]. The results indicate that high-temperature spectrometry with diamond-based solid-state detectors is feasible at least up to 473 K, after which signal degradation occurs. A study of the temperature behaviour of alpha particle detection by diamond CVD and 4H–SiC sensors was recently presented by Weiss et al. over a temperature range of up to 500 °C [82]. For the diamond detector, the collected charge measured as a function of temperature showed a constant distribution up to 250 °C, where an immediate drop of around 30% occurred. Above this temperature threshold, a decrease in the charge measured with increasing temperature was observed. Measurements with the diamond CVD sensor show a reduction in signal amplitude and an increase in signal FWHM, which can be linked to the increase in electron drift time.

Concerning the sensor response as a function of temperature for 4H–SiC sensors, it was shown that the collected charge was constant up to 350 °C and showed a decrease from around 70% to 500 °C. This decrease, which was not sufficiently explained by the authors, requires further investigation. The results presented are part of ongoing research work, which aims to systematically study the high-temperature performance of CVD and SiC diamond sensors for particle spectrometry. In order to validate these observations and questions related to the increase in charge carrier drift time, in-depth studies are required, in particular using larger active detection thicknesses. This is one of the objective of the third Part of this manuscript, to propose a model for quantitative interpretation of the effect of increasing temperature on charge carrier drift velocity in Chapter 6. In addition, a comparison of the performance of SiC and diamond sensor up to 500 °C is required, and is subject to an in-depth study of the sensor performances degradation in Chapter 7. The influence of temperature on the generation energy of electron-hole pairs with 4H–SiC detectors irradiated by alpha particles has been studied by Garcia et al. [83]. It was shown that the FWHM of the measured alpha energy peaks increases with temperature due to an exponential increase in the leakage current. The temperature dependence of electron-hole pair creation energy was also quantified. Moreover, no degradation in detector parameters based on repeated heating and cooling of the detector for 13 cycles was observed.

[23] *Stopping and Range of Ions in Matter (SRIM)*

High-temperature measurements with 4H–SiC detectors were subsequently extended to the fast neutron detection setting in work presented by Szalkai et al. [84]. Due to the increased effects of thermal noise at high temperatures, the applied bias voltages had to be decreased to avoid sensor deterioration. A decrease in count rate was then observed at different temperatures as seen in Fig. 2.8. For the energy calibration of the recorded histograms, the energy peak observed in the high channels of the analyzer, which the authors identify with the reaction $^{12}C(n,\alpha)^{9}Be$ was considered, using the same procedure as in the work presented by Ruddy et al. [85].

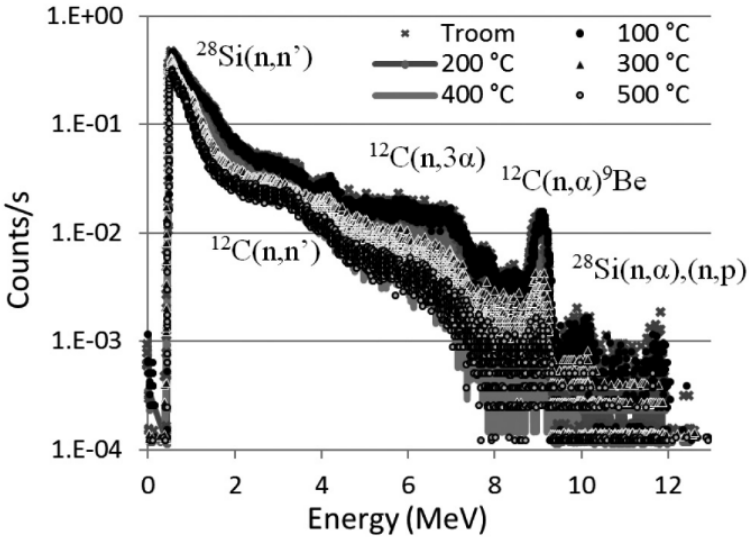

Fig. 2.8. Deposited energy spectrum recorded during 14 MeV irradiation and several temperatures [84].

At the same time, a significant increase in the count rate per micrometer value was observed due to the additional scattering effect of minority charge carriers generated outside the depletion zone. The stability of the detector's count rate was examined during repeated long-term measurements over the ambient temperature range 22 °C up to 500 °C. Stable operation of the detector was observed during the tests over the temperature range investigated. After repeated increases in temperature up to 500 °C, deterioration of the metal contacts on the diode electrodes was observed, causing a disturbance in the detector signal, necessitating replacement of the contacts.

The quality and shape of the metal contact must therefore be considered in future work in order to offer a detector capable of withstanding high temperatures and environmental conditions over a long operating lifetime.

Influence of magnetic fields

During the JET[24] tokamak experimental campaign achieved in 2013, two natural and cvd diamond sensors were installed in the torus hall, at a distance of approximately 3 m of the plasma center [86]. The detectors were used to evaluate the flux of fast neutrons with energies greater than 0.2 MeV. Hence, the D–D and D–T neutron fluxes at the detector location were estimated and these measurements were compared with the signals measured by JET's main neutron diagnostic based on a FC with a high degree of accuracy.

A SiC-based detector covered with a ^{6}LiF NCL and another covered with a 1.5 mm layer of polyethylene were installed on a porthole outside the vacuum vessel of the EAST[25] tokamak and

[24] *Joint European Torus (JET)*
[25] *Experimental Advanced Superconducting Tokamak (EAST)*

were operated continuously throughout an experimental campaign [87]. The results were again compared with those obtained with ^{235}U FCs. Despite their small active volumes, the 4H–SiC detectors were able to measure neutron emission as a function of time with good reliability and stability compared with the FC. The results of this work demonstrated the satisfactory performance of the 4H–SiC detector in the harsh environment of a high mixed neutron-gamma radiation field and an electromagnetic field.

Conclusion

- The performance of SiC and CVD diamond detectors in detecting fast neutrons and their spectrometric capabilities regarding the reaction products have been evaluated.
- Work has been carried out on the behavior at high temperatures and on the influence of the magnetic field, but more work is needed.
- The operational limits, in terms of fast neutron fluence requires further investigation to be clearly established.
- Integration constraints are reduced by the miniaturization of solid-state detectors based on semiconductor materials.

In conclusion further studies are required, concerning the environment constraints in order to quantify the effect of the temperature and magnetic field variation, as well as expanding its operational scope. Regarding the spectrometric capabilities, no methodology has been presented for estimating the absolute value of the neutron flux. The latter, as well as the capability of the sensors to estimate a multi-energy neutron flux, are the subject of the second part of this manuscript.

Conclusions on ITER or JHR applications

As a summary of the various operating experiences, a comparison table of the candidates selected for on-line fast neutron measurements in the hostile environments of nuclear fusion and fission is presented below in Table 2.1, taking into account the constraints identified previously in Table 1.1. When values cannot be provided, the corresponding cell is referenced as N/A[26].

Parameter	FC	SPND	Scintill.	SemiCon.
T [°C]	400[a]	300[b]	150[c]	500[d]
B [T]	2[e]	N/A	0.4[f]	0.5[g]

[a] *Spurious signals observed for T above* 400 °C *[44, 47].*
[b] *Approximate value, depending on the choice of insulator/emitter materials [57].*
[c] *Approximate value, depending on the choice of scintillator/photomultiplier materials.*
[d] *Value for a SiC detector above which deterioration of the metal contacts was observed, disturbing the signal measurement [84].*
[e] *Value for a FC placed between the vacuum enclosure and the toroidal field coils of the JT-60U tokamak [50].*
[f] *Value for a scintillator placed on the KSTAR tokamak [68].*
[g] *Approximate value for a SiC sensor placed on the EAST tokamak [87].*

Table 2.1. Summary of the various fast neutron detectors with the constraints imposed by the ITER/RJH installations. (cf. Table 1.1)

To meet the needs identified above, FNDS devices consisting of two FCs may appear suitable, enabling the measurement of fast neutrons by discriminating the gamma contribution in pulse mode and in Campbelling mode. However, the latter is not suitable for neutron spectrometry results and exhibits limitations in terms of high temperature applications. SPNDs, which are considered to be suitable alternatives to FCs for monitoring the thermal neutron flux for in-core instrumentation of nuclear fission reactors, are also the subject of research work at CEA Cadarache[27] to explore the possibility of developing special types of SPND for monitoring the fast neutron flux [88].

Finally, semiconductor detectors same as SPNDs are also being studied for their ability to measure fast neutrons. Although further investigations are required for these two devices with regard to the influence of a high magnetic field and high temperatures, the device based on semiconductor materials has the particular advantage of offering spectrometric capabilities by exploiting threshold nuclear reactions, as detailed in the next Chapter 3. The promizing performances in terms of neutron spectrometry capabilities are presented in a second Part through methods to estimate the fast neutron flux in monoenergetic and continuous neutron fields. Then, regarding the environmental constraints, the stability of the sensor performances in harsh conditions is presented in a third Part through the study of the sensor response to temperature and irradiation. All things considered, in this manuscript a comprehensive overview of the measurements methodologies is provided as well as critical aspects of sensor design necessary for developing a fast neutron sensor suitable for extreme conditions like JHR and ITER.

[26] *Not Assessed (N/A)*
[27] *A thesis on the subject is currently being prepared at the Laboratoire de Dosimétrie, Capteurs et Instrumentation (LDCI) at CEA Cadarache.*

3. The Silicon Carbide

The constraints of the hostile environments represented by nuclear fusion and fission facilities have been studied and highlighted. The semiconductor-based detector has been identified as a promising concept for meeting the constraints and requirements set out in Table 2.1.

In order to compare the performance of semiconductor materials with respect to the applications considered in hostile environments, it is first necessary to introduce several properties. These brief explanations are intended to introduce the important concepts related to semiconductor physics and nuclear physics for an application to radiation detection. For a full discussion of the general concepts relating to the intrinsic properties of semiconductor materials, see references [89, 90, 91] useful for this study.

3.1. Inherent parameters

3.1.1. The properties of semiconductor materials

3.1.1.1. Atomic bonds and crystal lattices

In solids, as a reminder, the atoms are bonded to each other and their respective positions are fixed. In a molecule containing a small number of atoms or in a crystal, the valence electrons contribute to the bonds between the atoms and influence the electrical properties. In a crystal lattice, electrons are pooled to form covalent bonds. Under the influence of the potential of neighboring atoms, their energy levels group together into continuous energy bands[1] separated by forbidden bands. The last energy levels allowed for localized electrons are termed Valence Band (VB), and Conduction Band (CB), the next highest energy band. The width of the band gap between CB and VB is referred to as the gap. This gap is of the order of an electronvolt for intrinsic semiconductors and is therefore intermediate between that of conductors and insulators as seen in Fig. 3.2 representing schematically the energy band gap.

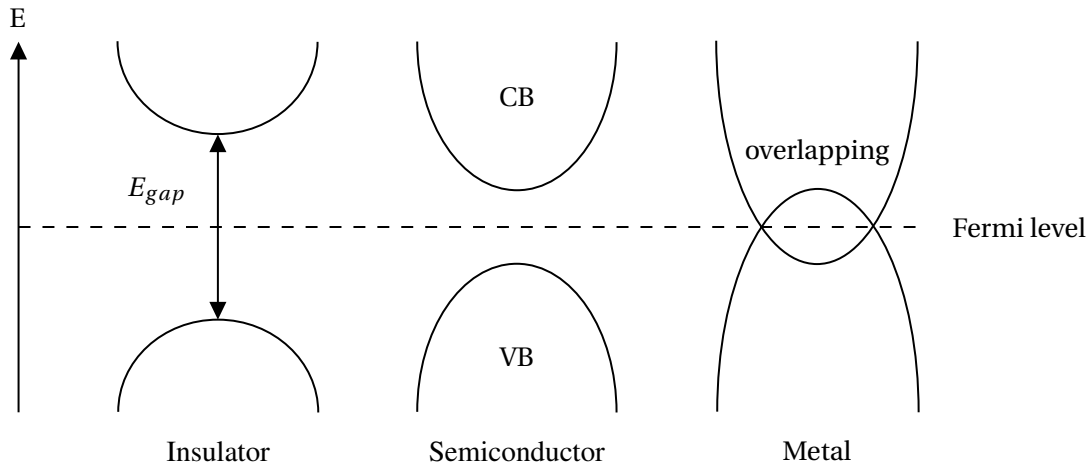

Fig. 3.1. Schematic diagram of energy band theory.

[1] *For the sake of brevity and to simplify the discussion, the basic notions of electron distribution on the energy levels at thermal equilibrium are not reintroduced in this paragraph. The energy band distribution is based on the known principles of Pauli exclusion and Klechovsky's principle.*

In many applications, semiconductors are doped in order to modify their electrical properties, increasing their conductivity by increasing the number of majority carriers. This is achieved by introducing impurities into the crystal lattice, which can be substituted for atoms of the base material in the crystal lattice. These are called extrinsic semiconductors. To dope IV valence materials such as silicon or germanium corresponding to the 4th column of the periodic table as seen in Fig. 3.2, III or V valence atoms are used. The later are respectively called *p* impurities such as Boron and Aluminum or respectively *n* impurities such as Phosphorus and Nitrogen elements.

	III	IV	V	VI
	5 B	6 C	7 N	8 O
II	13 Al	14 Si	15 P	16 S
30 Zn	31 Ga	32 Ge	33 As	34 Se
48 Cd	49 In	50 Sn	51 Sb	52 Te

Fig. 3.2. Positions of semiconductor materials in the periodic classification of the elements.

Semiconductors are found in column IV of the periodic table or in "III-V" or "II-VI" alloys mixing elements from these columns[2]. Hence, there are very few semiconductors in the state of simple elements. In column IV, it goes from germanium (Ge), which is a semiconductor, to tin (Sn) and lead (Pb), which are metals. The doping rate is defined as the ratio of the number of substituted impurity atoms to the number of atoms in the base material per unit volume. For the valence V atoms introduced, there is an additional valence electron loosely bound to the neighbouring valence IV atoms as shown schematically in Fig. 3.3(a). It can then easily be set in motion by the effect of an electric field. Conductivity is thus achieved by these negative charges being set in motion. A valence III atom, on the other hand, is able to capture an electron belonging to a bond of a neighbouring atom in order to complete its own bonds as visually represented in Fig. 3.3(b).

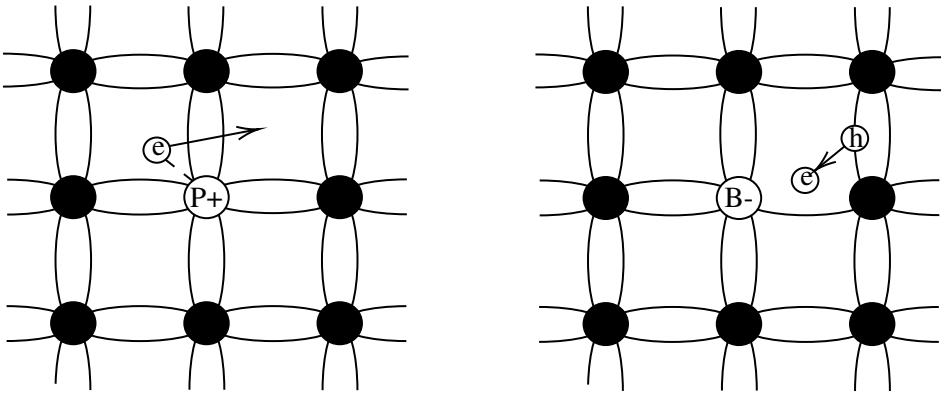

(a) Phosphorus atom acting as a donor **(b)** Boron atom acting as an acceptor

Fig. 3.3. Diagram of atomic bonds in a simplified 2D crystal lattice.

[2] *As atoms get bigger from one line to the next, peripheral electrons become less bound and move more easily.*

However, as this bond is in turn broken, it can only be re-established by itself borrowing an electron from another bond. This absence of a bonding electron is called a hole with a positive charge, and the resulting current, under the effect of an electric field, is called a hole current.

In conclusion, depending on the impurities introduced into the crystal, the electrical properties are different, since conductivity is achieved by negative charges in the case of valence V impurities in the n-doped regions and positive charges in the case of valence III impurities in the p-doped regions. In addition, by doping the crystal with specific impurities as seen above, the creation of charge carriers will be favoured as schematically represented in Fig. 3.4, because the impurities are more likely to be ionized than the lattice atoms.

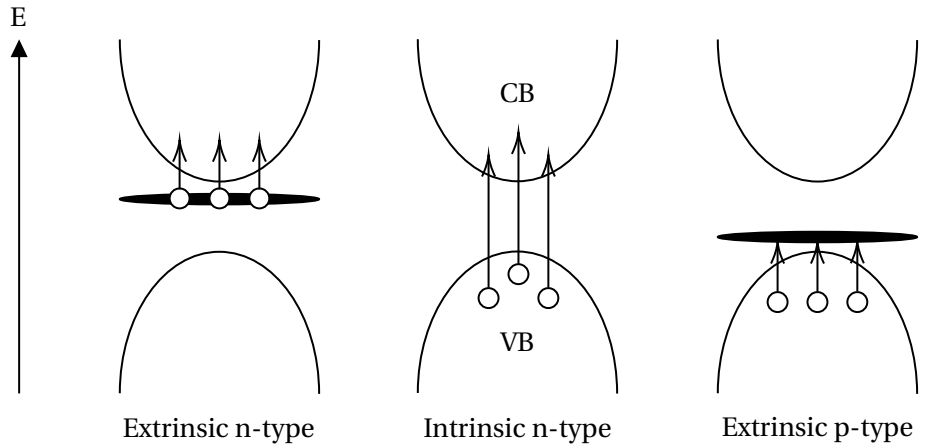

Fig. 3.4. Schematic diagram of energy band representation. In the case of an intrinsic semiconductor in the middle an electron must pass from the VB to the CB to conduct the current. In the case of an extrinsic semiconductor, the introduction of "ad hoc" impurities, whose energy level is located in the gap, near one of the two bands, enables electrons to be transferred either from the impurity level to the CB (n-doped, left) or from the VB to the impurity level (p-doped, right).

3.1.1.2. Native and induced defects

By presenting these crystal lattices it is important to bear in mind that they are not perfect single crystals without defects. The native defects of crystals can be divided into several categories:

- Point defects relating to isolated atomic positions
- Extended defects, which include dislocations involving atoms that are more or less aligned and occur at great distances, or stacking defects.

Under the effect of temperature, the crystal lattice undergoes oscillations. As a result of these oscillations, one atom may acquire sufficient energy to detach itself from its neighbouring atoms. When this atom has left its initial place in the lattice, several types of induced defects can occur through the crystal:

- An interstitial when the atom is isolated in its structure
- A vacancy when an atom is missing
- A Frenkel pair when these two defects recombine to give the crystal its normal structure [92].

The several defects defined are summarized in Fig. 3.5 below.

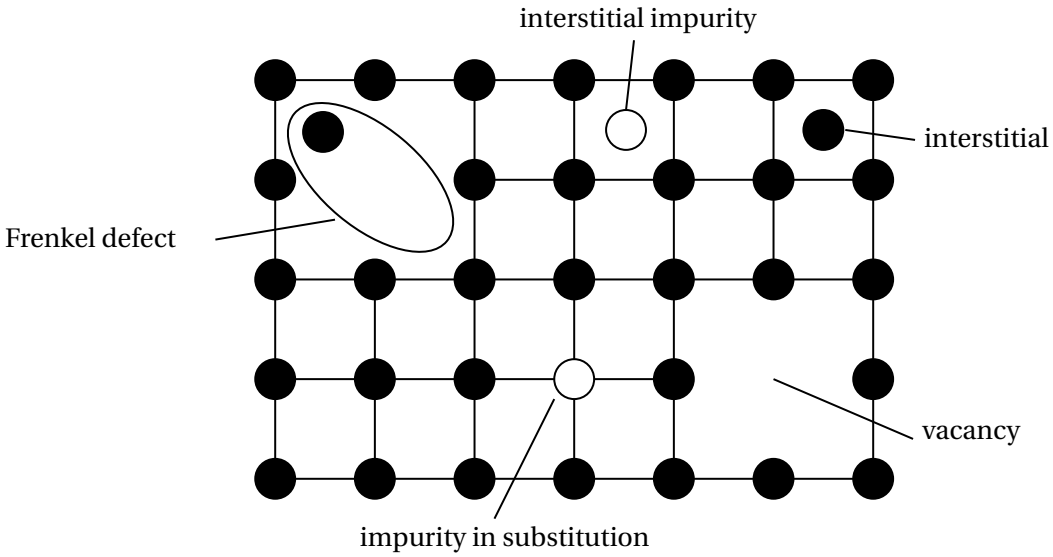

Fig. 3.5. Schematic diagram of the different types of point defect in a crystal lattice.

Other phenomena can also produce isolated displacements of atoms, such as high-energy radiation. It is nevertheless possible to repair these defects. In fact, by heating the crystal, the mobility of the vacancies/interstitials pairs created is such that the recombination phenomena of these pairs become more probable, thus eliminating the defects [93].

3.1.1.3. Semiconductor junction devices

As understood previously, there is little purpose in using a single semiconductor material, whether doped with *p* or *n*. In fact, it is the combination of several doped semiconductors that makes it possible to create components based on semiconductor materials. The abrupt junction between two *p*-*n* regions, commonly known as a bipolar diode, is the simplest of these components, as opposed to the Schottky diode, which is a device consisting of a junction between a semiconductor and a metal.

Semiconductors devices under study are essentially constituted by mono-crystal within which it can be distinguished regions characterised by the type and the level of impurity. Hence, p-type region and n-type region are dissociated. The surface between two regions is called a junction, in another words a surface defined such that:

$$N_A - N_D = 0 \tag{3.1}$$

With N_D and N_A respectively the concentration of donor atoms and acceptor atoms in [cm^{-3}]. In fact, the junction often refers to the region between p-type and n-type regions, including the surface defined above, where it exists a strong variation in concentration with distance.

In this introductory part it is mandatory to establish the existing relations between the applied bias voltage and the carrier concentration close to the junction, and more precisely close to the transition area that will be defined. In that way, the nature of the currents flowing through the junction, and their interdependence with the bias voltage or the current variations with increasing temperature and voltage will be put in perspective.

Taking the case of a single crystal at thermal equilibrium, in the absence of applied voltage, in which it can be distinguished a p-type and n-type region. The diffusion phenomenon causes carriers to move from areas with high concentration to areas with low concentration. This means that carriers near a junction will spread into nearby areas where they are less common. So, on either side of the junction, the majority carriers tend to move from one zone to the other. However, the movement of these carriers leaves a thin layer of crystal on either side of the junction that is almost empty of majority carriers, known as the transition zone, depletion zone or more commonly Space Charge Region (SCR). Inside these transition zones, charge neutrality is therefore lacking and so:

- p-type material, where the impurities are all negatively ionized, tends to be negatively charged
- n-type material, where the impurities are all positively ionized, tends to be positively charged.

If a polarization voltage V_r is applied to the ends of the pn-junction, it will be added to the potential barrier ϕ_0 such that:

$$V_{PN} = V_r - \phi_0 \tag{3.2}$$

As a result, the potential barrier is raised or lowered depending on the sign of the polarization voltage. The junction is then said to be polarized by a reverse voltage and a very low current, known as the reverse or saturation current, flows through it. Similarly, when the potential barrier is lowered, the junction is said to be polarized by a forward voltage.

Hence, it is interesting to give more insights regarding the interpretation of the direct and reverse currents from the variations in energy undergone by the carrier as they pass through the junction. As a reminder, as the carriers increase their energy, they rise in the CB for -q carriers and fall in the VB for +q carriers. It is therefore easy to see that the initially majority carriers have to increase their potential energy by the quantity $q(V_r - \phi_0)$ to cross the junction, whereas the initially minority carriers lower their potential energy as they cross the junction. The reverse current is precisely equal to the number of initially minority carriers that cross the junction per time unit. Hence, a summary of the situation is presented here after in Fig. 3.6.

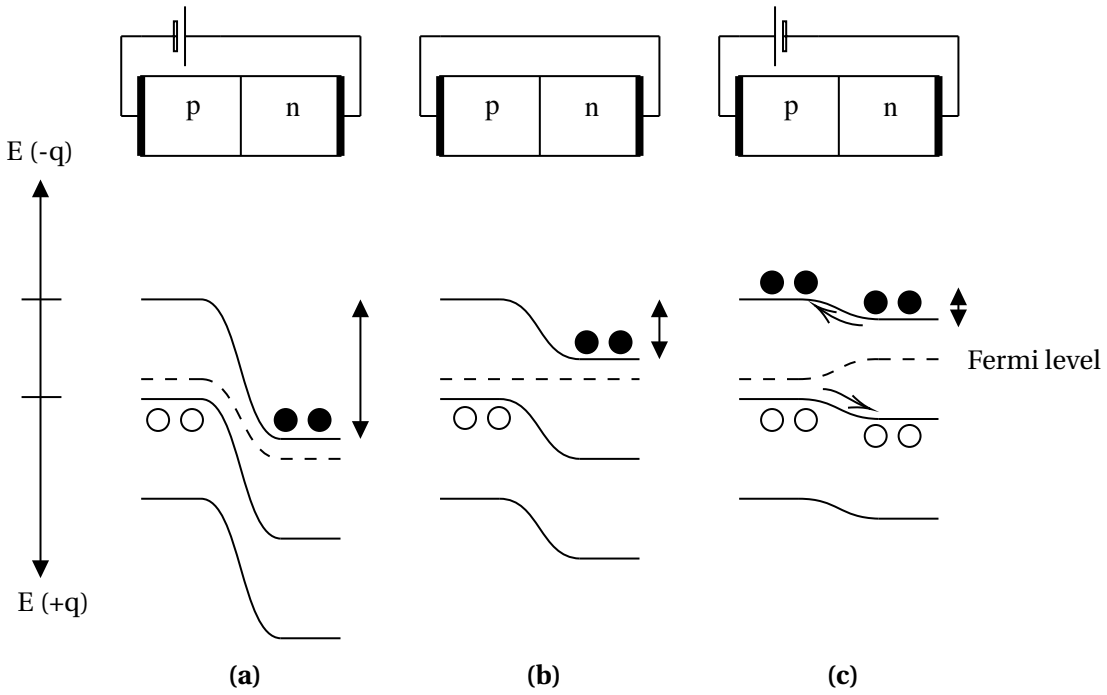

(a) When $V_{app} < 0$, no carrier, initially a majority, crosses the junction in this case.

(b) When $V_{app} = 0$, the current of initially minority carriers which flow in one direction is balanced by the current of the initially majority carriers which goes in the opposite direction. No current flows in the circuit.

(c) When $V_{app} > 0$, the current of initially minority carriers continues as before across the junction. But on this current is superimposed in the opposite direction a current of initially majority carriers coming from each of the materials P and N which will have sufficient kinetic energy to cross the reduced barrier $q(V_{app} - \phi_0)$.

Fig. 3.6. Description of the behavior of carriers within polarized junction.

Then when a positive potential is applied, the reverse current of minority carriers continues to cross the junction. But this time, this current is superimposed, in the opposite direction to the current of majority carriers from each of the p-type and n-type regions. Hence, these carriers will have sufficient kinetic energy to cross the reduced barrier $q(V_r - \phi_0)$. Crossing is rare, but becomes increasingly probable as V_r increases. Finally, when V_r is null, i.e., at thermal equilibrium, the total current is also null. Indeed, the current of the initially minority carriers flowing in one direction is balanced by the current of the initially majority carriers flowing in the opposite direction. Therefore, no external current flows in the circuit, as shown schematically.

The previous consideration in terms of induced electric field variation as well as charge carriers density with applied reverse bias voltage leads to the following expression of the SCR thickness W_{SCR} in [µm], demonstrated in Appendix A.1:

$$W_{SCR} = \sqrt{\frac{2\epsilon}{q} \cdot \left(\frac{N_D + N_A}{N_D N_A} \right) \cdot V_0} \tag{3.3}$$

With ϵ the dielectric permittivity in [F/m], q the elementary charge in [C] and V_0 the contact

potential at the junction in [V] defined such that:

$$V_0 = \frac{k_B T}{q} \ln\left(\frac{N_D N_A}{n_i^2}\right) \tag{3.4}$$

With k_B the Boltzmann constant in [$m^2 \cdot kg/s^2/K$] equals to $1.38 \cdot 10^{-23}$, T the temperature in [K] and n_i the intrinsic carrier concentration in [cm^{-3}].

3.1.2. Electrical characterization of the sensor

3.1.2.1. The movement speed of charge carriers

To simplify the discussion, the phenomenological Drude model [94], which is based on the kinetic theory of gases, is used here. Hence, an electron colliding with ions in the crystal lattice is then considered in the following.

When a valence electron leaves a covalent bond, an electrical imbalance is created in the vicinity of the atom. In an ionized state, this is equivalent to a charge of opposite sign that can move. In an intrinsic material, free conduction charges are generated in pairs of free electron/hole carriers likely to contribute to a possible electric current.

In the case of a crystalline lattice at room temperature, with no significant vibrational phenomena, a valence electron freed from its bond and launched into the lattice at a great distance from its nodes normally follows a straight trajectory. However, if the lattice is subjected to thermal agitation, the free carrier will bounce off the deformations in the lattice caused by the thermal agitation and move in another direction[3]. When there is no electric or magnetic field applied to the semiconductor, the trajectories of the carriers consist of broken lines made up of segments of straight lines. There are also bends in the carrier trajectories that occur when a charge passes in the vicinity of an ionized impurity atom of the same or opposite sign[4] or a nucleus.

With the thermal agitation motion, the following expressions are established for the thermal agitation velocity v_{th} and the mean free path l between two collisions in the crystal lattice, as defined in (3.5):

$$\begin{cases} \frac{1}{2} m v_{th}^2 = \frac{3}{2} k_B T \\ l = v_{th} \cdot \tau \end{cases} \tag{3.5}$$

With v_{th} the thermal agitation velocity, equals to the average electronic velocity in [m/s], m the electron effective mass in [kg], and T the temperature in [K]. Then τ in [s] stands for the average relaxation time between two collisions with l in [m] the mean free path between two collisions.

The following Table 3.1 is shown as an example for the the defined quantities in germanium at 300 K.

	$v_{th.}$ [m/s]	τ [s]	l [m]
Germanium	$1 \cdot 10^5$	$1 \cdot 10^{-12}$	$1 \cdot 10^{-7}$

Table 3.1. Germanium thermal agitation velocity, relaxation time and mean free path at 300 K, from [95].

[3] *Then the carrier will bounce off another deformation and set off again: the electron is thus driven by a thermal agitation movement.*

[4] *Provided that when a charge passes in the vicinity of an ionized impurity atom of opposite sign, the energy of the carrier is such that it does not recombine.*

The trajectory changes are due to thermal deformations of the crystal lattice, which partially reflect the waves associated with the electrons as depicted schematically in the first scheme of Fig. 3.7. The charge carrier is therefore subject to a random movement of thermal agitation at a very high velocity, but since the latter bounces randomly on the deformations of the lattice, the velocity associated to the motion of the carrier through the sensor can be considered as zero. In other words this carrier will not contribute to the current of collected electrons.

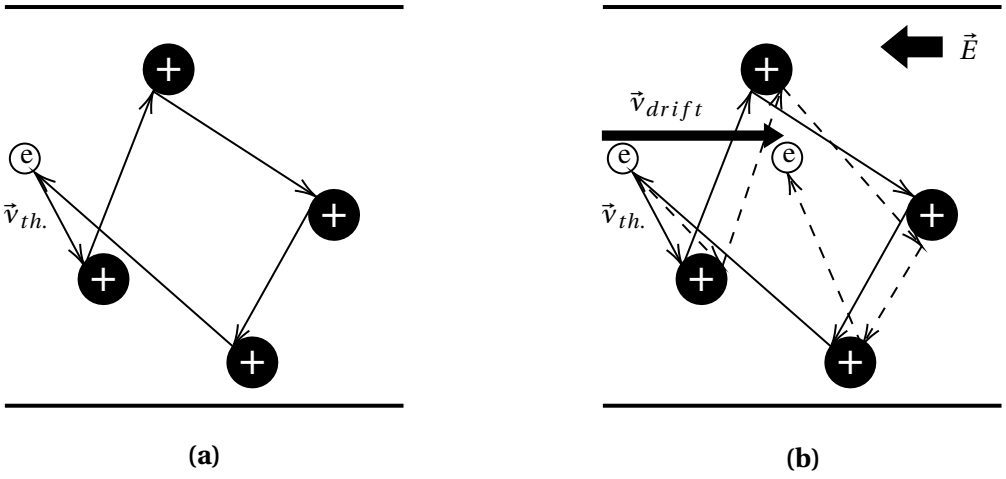

(a) **(b)**

(a) Thermal agitation of the electron.

(b) Electron drift displayed by the dashed lines.

Fig. 3.7. Schematic diagrams of the movement of the electron in the sensor.

Then, when an electric field $\vec{E}$ is applied, a force $\vec{F}$ of same direction or opposite direction is exerted on charge carriers $\pm q$ such that:

$$\vec{F} = q\vec{E} \tag{3.6}$$

Hence charge carriers are accelerated and consequently will experience a drift of their trajectory in the direction of the electric force for which they are subjected to, as depicted in the second scheme of Fig. 3.7. The whole deformed trajectories have then an average drift velocity v_{drift} defined in (3.7) parallel to the electric field which enable to the charge carriers to contribute to the electric current.

$$\vec{v}_{drift} = \mu \cdot \vec{E} \tag{3.7}$$

With v_{drift} in [m/s], the mobility μ in [$\mathrm{cm \cdot s^{-1}/V \cdot m^{-1}}$] and the electric field E in [V/m].

So, in a semiconductor, the action of a field $\vec{E}$ is to impose on the erratic movements of the mobile charges, an average component of speed parallel to $\vec{E}$, in the same or opposite direction and whose value is constant and proportional to $\vec{E}$. Considering the path traveled by the previous charge carrier when no field is applied. The disordered trajectory follows the laws of chance and is made up of straight line segments, since each elementary trajectory takes place between two collisions of the carriers on thermally induced deformations of the crystal lattice. However, after a large number of elementary trajectories, the laws of chance will mean that the charge carrier will return to the vicinity of its initial position such that:

$$\sum_{i=1}^{n} \vec{l}_i = 0 \tag{3.8}$$

The application of a field $\vec{E}$ provides a force that is always directed away from the field as the charge carrier moves. The elementary trajectories then have an elementary mean drift of length $\vec{u}$. Finally, considering n elementary trajectories, there is a drift length $\vec{X}$ as described in Fig. 3.8 and defined such that:

$$\vec{X} = \sum_{i=1}^{n} \vec{l}_i = n\vec{u} \tag{3.9}$$

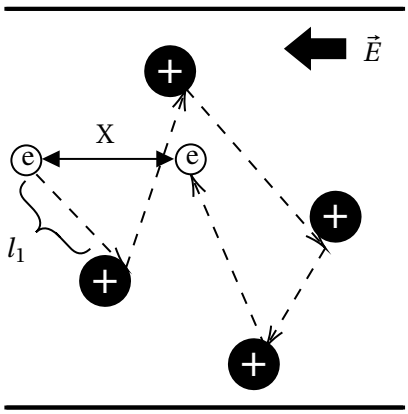

Fig. 3.8. Deviation of the trajectory of a carrier in a crystal under the effect of an applied electric field.

To assess the value of $\vec{u}$, the fundamental relation of dynamics is applied, introducing the notion of the effective mass of the carrier m^* within the crystal lattice. This effective mass takes into account the internal forces exerted by the crystal lattice's own potential, such as:

$$m^* \frac{d^2}{dt^2} = -q\vec{E} \tag{3.10}$$

Next, the value of the drift $\vec{u}$ is obtained by integrating the equation between the time at $t = 0$ and $t = \tau_e$ which represents the average time required to cover an elementary trajectory l_i such that:

$$\vec{u} = -\frac{q\vec{E}\tau_E^2}{2m^*} \tag{3.11}$$

As the elementary segments are not equal, it is necessary to take into account an average statistical length. The average drift $\vec{u'}$ is then calculated by multiplying by a factor of 2 the drift produced by the $\vec{E}$ field and leads to the average drift velocity such that:

$$\vec{v}_{drift} = \frac{\vec{u'}}{\tau_e} = \frac{-q\vec{E}\tau_e}{m^*} \tag{3.12}$$

This velocity is then constant for a given $\vec{E}$ field and the mobility of the charges is then defined by a scalar in order to express the drift velocity as a function of a constant as in (3.7) such as:

$$\boxed{\mu = \frac{q\tau_e}{m^*}} \tag{3.13}$$

This definition of mobility is valid for both electrons and holes. Mobility will always occur in the same direction as the applied $\vec{E}$ field, but the effective mass is different depending on the type of carrier considered. Indeed, the drift velocity v_{drift} is independent of time for a material at a given temperature. However, this depends on the intensity of the applied electric field. In a semiconductor, the mobility of electrons called "conduction electrons" is greater

than that of holes indirectly called "valence electrons" due to the different band structures and diffusion mechanisms of these two types of carriers. The free electrons then move in the CB and the holes in the VB. When an electric field is applied, holes cannot move as freely as free electrons because their movement is restricted due to their lower mobility which is of the order of 800 $cm \cdot s^{-1}/V \cdot m^{-1}$ for the electrons in the SiC and 115 $cm \cdot s^{-1}/V \cdot m^{-1}$ for the holes at 300 K. The expression of mobility as a function of the temperature or the impurity concentration will be introduced in detail and studied precisely later in the scope of the Chapter 6.

3.1.2.2. The lifetime of charge carriers

Once electrons and holes have been generated in the semiconductor, they will tend to migrate either spontaneously by diffusion, or under the influence of an applied electric field, until they are collected at an electrode or until recombination takes place. According to some models, as presented by Yamashita et al. [96], the average lifetime of charge carriers before recombination in perfectly pure semiconductors could be as long as one second. In practice, lifetimes of at least three or four orders of magnitude below one second are actually observed [97].

The trapping length in the material, i.e., the diffusion length[5], must be taken into account in the charge carrier collection process in the sensor. This quantity simply represents the mean free path traveled by a charge carrier before being trapped or recombined and is given by the product of the average lifetime[6] and the average drift velocity such that:

$$l_d = \tau_l \cdot v_{drift} \tag{3.14}$$

With l_d the diffusion length in [m], τ_l the lifetime in [s] and v_{drift} the drift velocity in [m/s].

Hence, in order to develop a high-performance detector, the trapping length must be large in comparison to the physical dimensions on which the charge must be collected. The product which quantifies the degree of charge loss is expressed in [cm/Vcm^{-1}] such that:

$$\frac{l_d}{E} = \mu \cdot \tau_l \quad \text{with (3.7)} \tag{3.15}$$

And once multiplied by the electric field intensity in [V/cm] gives the trapping length.

3.1.2.3. The resultant current

The quantity of charge carriers passing through the sensor per second will depend firstly on the drift velocity of the latter. This quantity also depends on the dimensions of the sensor. The free carriers density per unit volume in the intrinsic material is called n_i. Adding p or n type impurities to a material barely changes its band-gap width. Therefore, the product of p and n type free carriers, equal to n_i^2 (shown in Appendix A.2), remains constant, depending only on temperature and not on the concentration of impurities. Hence, the concentration of free carriers represents the amount of electrons available to contribute to the conduction of current. This concentration of intrinsic carriers represents the number of electrons in the CB and the number of holes in the VB such that:

$$n_i = \sqrt{N_C N_V} \cdot \exp\left(-\frac{E_{gap}}{2k_B T}\right) \tag{3.16}$$

[5] *Not to be confused with the mean free path between two collisions.*

[6] *Not to be confused with the relaxation time i.e. the average time between two collisions of the carrier with the atoms of the lattice.*

With N_C and N_V the respective effective densities of states of electrons in the CB and holes in the VB, $k_B T$ the thermal energy, product of the Boltzmann constant and the temperature, and E_{gap} the band-gap energy between the CB and VB.

While the free carrier concentration is of the order of $1 \cdot 10^{22}$ cm^{-3} in metals where the VB and the CB are overlapping, the later is weaker in semiconductors — of the order of $1 \cdot 10^{6}$ cm^{-3} for undoped SiC, and $1 \cdot 10^{-9}$ cm^{-3} for doped SiC[7] — due to the forbidden band-gap energy E_{gap} of the order of the electronvolt.

The occupied sensor volume in one second by the free carriers as described in Fig. 3.9 is obtained by multiplying the sensor surface by the drift velocity. The resulting current intensity is then the product of the occupation volume per time unit by the number of carriers per unit volume such that:

$$I = q \cdot n_i \cdot S \cdot v_{drift} \tag{3.17}$$

With v_{drift} defined previously in (3.7), it comes the expression of the surface current $\vec{j}$ such that:

$$\vec{j} = q \cdot n_i \cdot \mu \cdot \vec{E} \tag{3.18}$$

$$= q \cdot n_i \cdot \frac{q\tau}{m} \cdot \vec{E} \quad \text{with (3.13)} \tag{3.19}$$

$$= \frac{n_i q^2 \tau}{m} \cdot \vec{E} \tag{3.20}$$

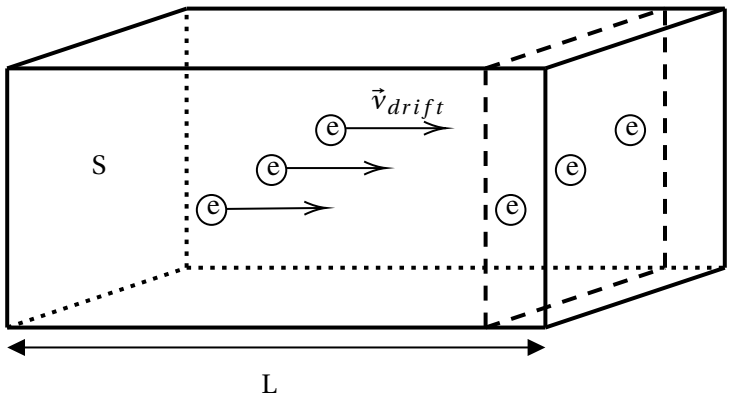

Fig. 3.9. Schematic diagram of the circulation of free carriers in a semiconductor material.

Hence, the Ohm law is obtained by introducing the electrical conductivity σ which characterizes the ability of a material to allow free charge carriers to move such that:

$$\vec{j} = \sigma \cdot \vec{E} \tag{3.21}$$

Therefore, the surface current of charge carriers within the sensor depends on the intensity of the applied electric field and of the electrical conductivity of the material. This conductivity in turn depends on the concentration of free carriers in the material as well as the mobility of the carriers within it.

[7] *Note that these order of magnitude values vary widely depending on the n-type or p-type SiC and the doping levels and also on the polytype of the SiC as presented in Section 3.2.2.*

3.1.3. Signal Formation

3.1.3.1. Charge Induction

To comprehend how pulses are generated in semiconductor-based detectors, the Ramo-Shockley theorem has to be introduced [98, 99]. Let's consider a detector comprising a layer between two metal electrical contacts. When a charged particle interacts at position x, excess charges under an external electric field $\vec{E}$ move apart. These charges drift, either getting trapped in materials traps or heading toward the electrodes. Notably, for the electrical current measured by the external circuit, it's unnecessary for the free charge carriers to reach the electrodes due to the Ramo-Shockley theorem. The drifting charges, if untrapped, eventually reach the electrodes, contributing to pulse timing depending on their initial position and drift velocity.

To calculate the instantaneous current I, let L be the thickness of the detector and V_0 the biasing potential applied, resulting in a constant[8] electric field such that $E_0 = V_0/L$. According to Ramo and Shockley, the instantaneous current induced by a moving point charge q at position x in the inter-electrode region and the induced charge Q are given such that:

$$\begin{cases} I &= q v_{drift} E_w(x) \\ Q &= q \phi_w(x) \end{cases} \tag{3.22}$$

With E_w and ϕ_w the weighting electric field and weighting potential considered at the instantaneous charge position x.

This weighting field is calculated under specific boundary conditions, facilitating the computation of induced current or charge:

- No space charge is considered
- The electrode for which is calculated the induced charge has a potential of 1 V
- The other electrode is set to zero.

The later conditions have to be applied to the geometry under study. If no space charge is present, Poisson's equation leads to $\nabla^2\phi = 0$ under these conditions, forming the basis for the Ramo-Shockley theorem.

According to their definition, both $E_w(x)$ and $\phi_w(x)$ do not represent the actual electric field and potential within the detector; they are instead employed to calculate induced current or charge. Once $\phi_w(x)$ is determined from (3.22), the induced charge on the electrode of interest can be computed by simply evaluating the difference between its values at the starting point x_1 and the end point x_2 of the moving charge. The trajectory $x(t)$ along with the drift velocity v_{drift} of the moving charge must be derived from the real external electric field E_0. It's noteworthy that the utilization of $\phi_w(x)$ is realistic because induced charge is independent of the drift velocity v_{drift} of the moving particles under the assumption of the second hypothesis, with a potential set 1 V. Hence v_{drift} relies on the actual electric field, rather than the weighting electric field. And under these conditions, the solution of the Poisson's equation leads to a constant value of the weighting electric field of magnitude equals to $1/L$. Consequently (3.22) can be simplified such that:

$$I = q \frac{dx}{dt} \frac{1}{L} \tag{3.23}$$

Finally, it appears manifest that if the position $x(t)$ of the charge q is known as a function of time, the induced charge $Q(t)$ can also be determined. Therefore, this enables the derivation of the output pulse shape from the detector.

[8] *By assuming a constant electric field, the theorem simplifies the analysis while still providing insights into the motion of charges.*

3.1.3.2. Pulse Shape

The electrical signals generated by a semiconductor device exhibit rapid response, with the rising time of the electrical pulse typically on the order of several nanoseconds depending on the thickness of the semiconductor layer. The rise time depends also on many factors such as the applied bias voltage, the type and energy of radiation and entrance window. The collection time of the measured pulse can then be defined as the duration required for excess carriers to drift towards the electrodes under the influence of the external electric field. As a result, the collected charge exhibits a baseline timing corresponding to the longest drifting time of the free carriers.

When irradiating a semiconductor detector from the top of the negative electrode, considering a charged particle created close to the top electrode, holes generated are hence rapidly collected by the negative electrode, while electrons drift towards the positive electrode. This scenario generally holds true for localized ionization events occurring near one of the electrodes. Consequently, each individual electron or hole induces a rectangular pulse on the electrode, with its amplitude determined by (3.23), and its width governed by its drifting velocity. Since electrons and holes have different drifting velocities as introduced in the previous section, if an electron-hole pair is produced at a point x_0 in the detector such that electrons and holes reach their respective electrodes simultaneously , they contribute equally to the induced current. The resultant current exhibits a rectangular shape, representing the superposition of these two rectangular signals as depicted schematically in Fig. 3.10.

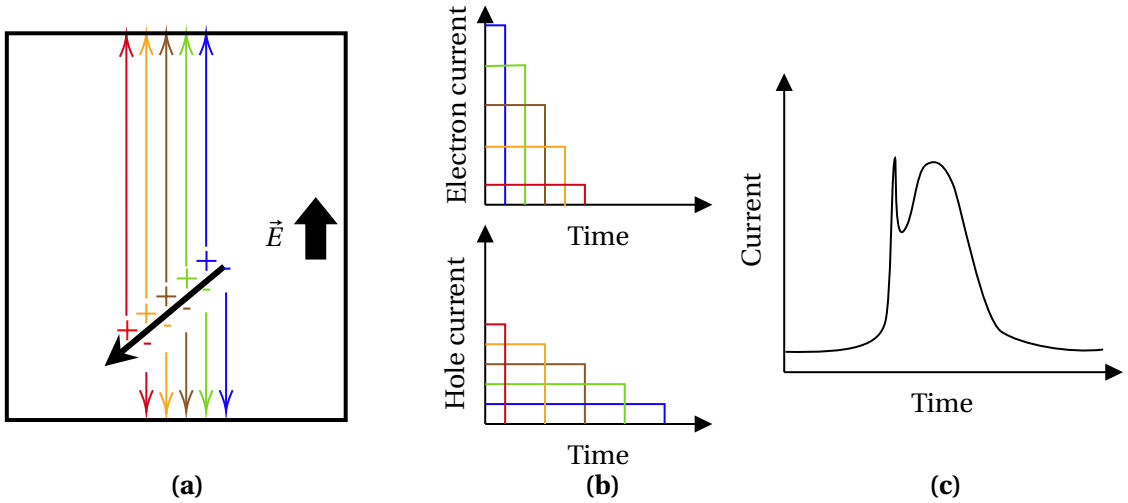

(a) Ionization of the medium along the trajectory of the charged particle and drifts of the carriers under the effect of an electric field

(b) Induction of electron and holes currents on the collection electrode considered

(c) Induction of the total current by summing the currents of the two charge carriers.

Fig. 3.10. Schematic diagram of the induction of a current signal in a solid detector when a charged particle is generated.

In practice the first component is not observed due to a shaping effect under the influence of the RC time constant of the system after the current to voltage conversion of the transimpedance [9]. Hence, the induced capacitance of the detector must be taken into account as it

[9] *This effect will be discussed in detail in a pulse shape analysis section in Chapter 6.*

tends to disturb the shape of the signal when the time constant τ_{RC} is greater than the pulse duration. The capacitance of the junction acts as a low-pass filter and helps to spread out the pulse in time. This effect is more important for sensors with larger active areas since the intrinsic capacitance of the detector increases with the surface area of the detector, such as:

$$C_{junction} = \epsilon_0 \epsilon_r \cdot \frac{S}{W_{SCR}} \tag{3.24}$$

With ϵ_0 the vacuum permittivity, ϵ_r the relative permittivity of the material, S the surface area of the detector and W_{SCR} the thickness of the space charge region.

3.1.3.3. Space Charge

Several studies have highlighted a significant increase or decrease in the drift for electrons or holes [100]. The convoluted effect of trapping charges with lifetime and with negative (resp. positive) space charge concentration $N_{eff.}$ in the sensor bulk, lead to a non ohmic field which explains the increase of decrease of the current during the carrier drift. Indeed, due to the presence of defects or foreign chemical species in the crystalline structure, the effective field is partially shielded by a local field such that:

$$\vec{E}_{eff.} = \vec{E}_0 + \vec{E_{loc}} \tag{3.25}$$

With $\vec{E}_{eff.}$ the effective electric field and $\vec{E}_0$ the local electric field.

Depending on the carrier type and the polarity of the effective space charge, the latter can contribute to increase or decrease the velocity drift of charge carriers within the thickness of the sensor due to the decrease of the electric field describes in (3.25). The variation in current observed in the charge drift phase is therefore, not due to a variation in momentum but to a variation in drift velocity. This effect is generally small, but it is important to keep in mind since it can lead to a dramatic deformation of the pulse shape.

3.2. Response to external parameters

The objective of this study is to examine how external parameters influence the response of the sensor. To achieve this, the important parameters are firstly introduced, focusing on their behavior under environmental constraints. This approach is required to select the most suitable semiconductor by comparing the sensor characteristics in relation to their performance in harsh environments. The motivations behind this selection and the key variables is discussed. A more detailed analysis of the environmental constraints' impact on sensor performance is presented in the last Part of the manuscript.

3.2.1. The effects on the sensor

It has been discussed previously, the ideal process of electron hole pairs charge generation due to the ionization by a charged particle. After the drift under an external electrical field as seen in Section 3.1.2.1, these pairs induced the current collected at the electrode as explained in Section 3.1.2.3. In order to choose a semiconductor material that is suitable for radiation detection applications in a hostile environment, it is necessary to study the effects on the sensor, such as the reduction in the current collected or the reduction in the lifetime of the carriers.

3.2.1.1. The effects on charge carrier current

As previously presented with the resultant current in Section 3.1.2.3, the electrons which will contribute to the conduction of the current are denoted as free carriers. The concentration of these carriers in an intrinsic material is defined as:

$$n_i = \sqrt{N_C N_V} \cdot \exp\left(-\frac{E_{gap}}{2k_B T}\right) \tag{3.26}$$

With N_C and N_V the respective effective densities of states of electrons in the CB and holes in the VB.

This amount of free carriers is function of the energy gap and as explained, also function of the temperature [101, 102]. Indeed, under the effect of temperature —like the process of generating defects in the semiconductor —the crystal lattice undergoes vibrational phenomena of expansion and contraction. It can then happen that an electron in the VB acquires enough kinetic energy to overcome the potential energy which holds it in its valence bond, by crossing the forbidden energy band E_{gap}. The generation rate of free charge carriers per unit of time increases with temperature [103]. Indeed, the higher the temperature, the lower the width of the forbidden energy band to be crossed as observed in Fig. 3.11.

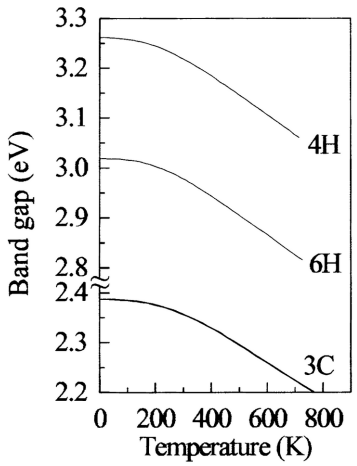

Fig. 3.11. SiC band-gap energy as a function of temperature [104].

The valence electron which leaves an interatomic bond is therefore qualified as a free conduction charge and will be likely to make its contribution to a possible electric current: this is the leakage current. This effect, rooted in band theory, is observed across all semiconductor materials. This notion of leakage current is a problem to take into account in applications where the non-thermal generation of charge carriers is studied, in particular for applications linked to the detection of ionizing radiation in harsh environment described in the first Chapter 1. These effects will be carefully described, and taken into account in the last part of the manuscript, in Chapter 6, when a numerical approach will be developed to model this effect on charge collection dynamic, and validated through experimental results obtained.

Then the second point that must be emphasized in this introductory approach presenting the effects on charge carrier current is to present the influence of increasing temperature on charge carrier collection. Indeed, increasing temperature leads to an increase of the thermal agitation. Hence, since the thermal velocity increases the random vibrational movement of the carriers increases and collisions are therefore more numerous. The relaxation time τ of charge carriers decreases and will be responsible for a decrease of the mobility μ of the charge carriers as observed in Fig. 3.12a. As a result, carrier drift is delayed as seen in Fig. 3.12b.

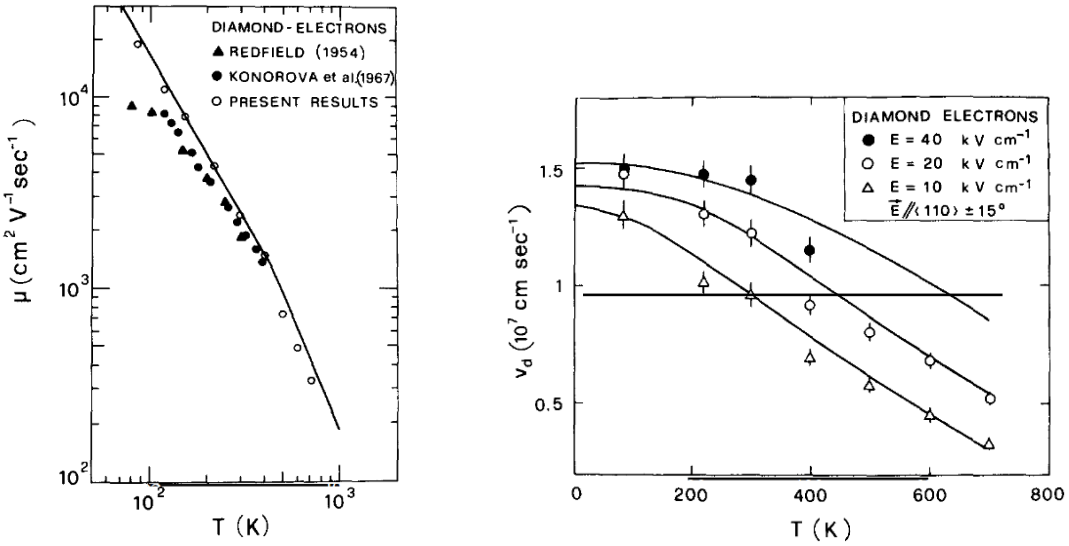

(a) (b)

Fig. 3.12. Electron mobility (a) and drift velocity (b) in diamond as a function of temperature [105].

Therefore, dedicated measurements or analysis must be performed in order to quantify the evolution of charge carrier velocity drift as a function of the applied bias voltage and with increasing temperature. Finally, this effect of charge carrier drift diminution and so current diminution must be quantified to address the proper electric field to correct this effect using the sensor in harsh environment.

3.2.1.2. The effects on charge carrier lifetime

Two phenomenon usually tend to reduce the charge carrier lifetime and thus to contribute to a decrease in the Charge Collection Efficiency (CCE) and therefore to a loss of signal:

- Recombination
- Charge carriers trapping.

Usually, the equation governing the hole lifetime is defined such that:

$$\frac{dp}{dt} = -\frac{p}{\tau_h} \tag{3.27}$$

With τ_h the characteristic hole lifetime and p the hole density in the VB.

This equation is strictly applicable at a local level, and for measurements at the macroscopic scale, the variables within it represent averages across the entire sample. In this context, the influence of the trap centers on the limited values of CCE are linked through the Hecht equation [106], defined if the electric field and the carrier generation are uniform across the sample, such that:

$$CCE = \frac{\tau_e}{t_{drift,e}}\left[1 - \frac{\tau_e}{t_{drift,e}}\left(1 - \exp\left\{-\frac{t_{drift,e}}{\tau_e}\right\}\right)\right] + \frac{\tau_h}{t_{drift,h}}\left[1 - \frac{\tau_h}{t_{drift,h}}\left(1 - \exp\left\{-\frac{t_{drift,h}}{\tau_h}\right\}\right)\right] \tag{3.28}$$

With $\tau_{drift,i}$ the transit time across the sensor thickness d, which in case of a junction with a

SCR is defined for a carrier i drifting on the whole thickness such that:

$$\tau_{drift,i} = \frac{d}{v_{drift,i}} = \frac{W_{SCR}}{\mu_i E} \tag{3.29}$$

Therefore, for short lifetime it comes the simplified Hecht expression such that:

$$CCE = \frac{\tau_i}{t_{drift,i}} \tag{3.30}$$

Hence, for lifetime smaller than the charge carrier transit time, a decrease in the CCE is expected. The equation governing the trap carrier for an hole trap can be defined such that:

$$\frac{dp_t}{dt} = -\frac{dp}{dt} = N_t(c_h + e_e) - p_t(c_h + e_e + c_e + e_h) \tag{3.31}$$

With N_t the trap concentration, e the emission coefficients and c the capture coefficients for charge carriers defined such as:

$$\begin{cases} c_h &= \sigma_h \langle v_h \rangle p \\ c_e &= \sigma_e \langle v_e \rangle n \end{cases} \tag{3.32}$$

With σ the cross section capture, v the thermal velocity, and p or n respectively the hole and electron density in the VB and CB.

When the free charge carriers concentration can be considered constant in time, the equation governing the hole trap can be obtained solving the previous differential equation (3.31) such that:

$$p_t(t \to \infty) = N_t \cdot \frac{c_h + e_e}{c_h + e_e + c_e + e_h} \tag{3.33}$$

The complex issue of a trap interacting with carriers via the capture and emission process cannot be resolved with an analytical approach. Some semi-analytical expressions related to this problem can be found in literature [107]. Nevertheless, a practical correlation can be derived under two conditions:

- The condition $p \ll N_t$ holds true at all times
- The only factor limiting the carrier lifetime is the capture of trap of a single species, like the holes.

In that matter, the primary rate equation (3.31) is simplified such that:

$$\frac{dp_t}{dt} = -\frac{dp}{dt} = N_t \cdot e_e = N_t \sigma_h \langle v_h \rangle p \tag{3.34}$$

With these hypothesis, the emission process can be considered as uncoupled from the capture process. It can be noted that simplified differential equation governing the trap of holes is the same as the equation (3.27) governing the hole lifetime. The capture time constant can thus be defined such that:

$$\tau_c = \frac{1}{N_t \sigma_h \langle v_h \rangle} \tag{3.35}$$

As a conclusion regarding this first analytical approach, the consequences concerning CCE and trapping issues are twofold:

- According to (3.30), a charge carrier lifetime smaller than the charge carrier transit time will be responsible for a decrease in the CCE
- According to (3.27) and (3.34), The capture time constant determines the maximum speed at which a trap can limit the accumulation of charges.

To this end, a careful study of these two quantities, i.e., charge carrier lifetime and capture time constant, must be carried out each time a reduction in CCE is observed using solid-state sensor in harsh environment. Therefore, the selection of the appropriate material must take into account the conclusions drawn above.

3.2.2. Comparison of semiconductors

According to the described effects linked to the charge carrying current, it was pointed out that for high temperature application, higher is the band-gap energy, the better. Indeed, free conduction charges concentration tends to increase with the temperature which contribute to leakage current presented above. At the same time, charge carriers experiment a decrease in their drift velocity with increasing temperature. Hence to counter this decrease, higher electric field might be applied. The correlation of such effects is the reason why the relevant parameters to take into account in order to define the most suitable material for high-temperature applications are the band gap energy E_{gap}, the concentration of intrinsic carriers n_i and the critical electrical field E_c. These parameters are compared in Fig. 3.13 for diamond, SiC, GaN and Si at room temperature.

Regarding the problematic of charge carriers trapping and recombination, it can be understood that greater displacement energy yields improved outcomes. Indeed, to move an atom from its site in a crystal lattice, a certain amount of recoil energy is required. This can be provided by the elastic scattering of a high-energy charged or neutral particle. By looking at the displacement probability as a function of the recoil energy, the atomic displacement energy E_d can be quantified. This is the energy at which the probability of the atom moving from its site is approximately 50%. Recoil energies below E_d lead mainly to lattice vibrations only, while values above E_d also create a Frenkel pair. Concerning the choice of the SiC polytype, the 4H–SiC is the most suitable for high-temperature applications, as it exhibits the highest band gap energy, the lowest intrinsic carrier concentration, and the highest thermal conductivity according to the comparison presented in Table 3.2.

Parameter	3C	4H	6H
Lattice structure	face-centered cubic	hexagonal	hexagonal
Thermal conductivity [W$\dot{c}$m^{-1}K^{-1}]	3.6	4.9	2.6
Bandgap energy [eV]	2.4	3.2	3.0
Intrinsic carrier concentration [cm^{-3}]	$1.5 \cdot 10^{-1}$	$5.6 \cdot 10^{-9}$	$1.6 \cdot 10^{-6}$

Table 3.2. Material properties at 300 K of the three currently used SiC polytypes, from [108].

All things considered, this is the reason why wide band gap semiconductors materials such as diamond and 4H–SiC are considered promising candidates for application in constrained environments, according to the big picture depicted with Fig. 3.13 comparing the previous parameters at room temperature.

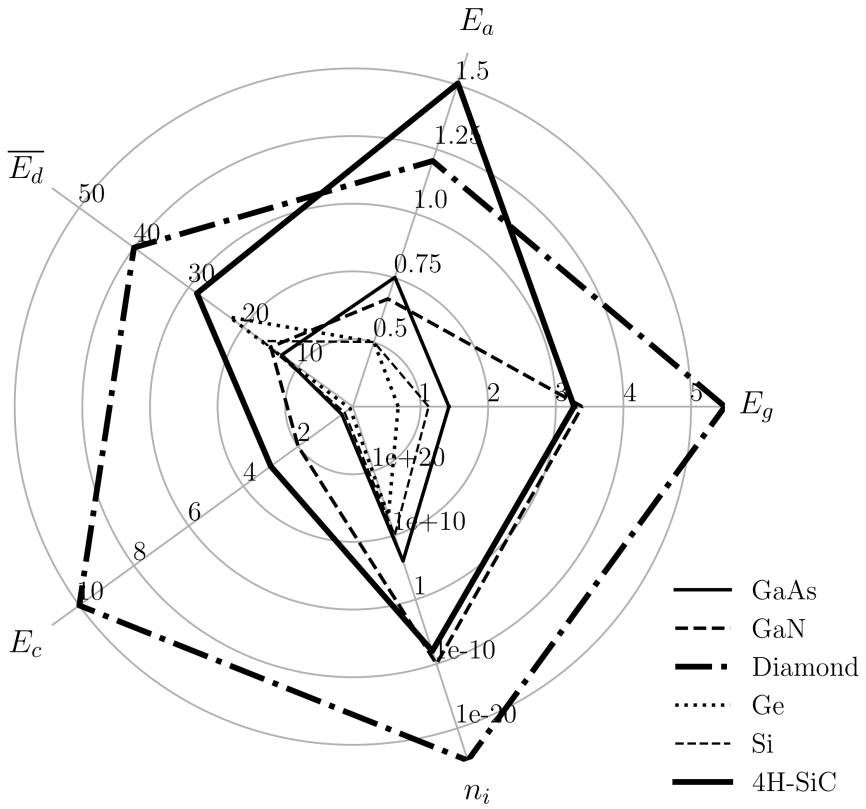

Fig. 3.13. Comparison of the main semiconductor parameters under study at 300 K. With E_d in [eV] the average atomic displacement energy, E_a in [eV] the deep level traps activation energy, E_g in [eV] the width of the forbidden energy band, n_i in [cm^{-3}] the intrinsic carrier concentration and E_c [MV/cm] the critical electric field. Tabulated values come from different works [1, 2], bringing together the reference articles for the measurements of the different parameters.

Finally, the effects on charge carrier lifetime described in the previous Section 3.2.1.2 introducing traps capture time constant, must be considered for the high temperatures encountered in the fusion and fission environments, above 200 °C. In general, traps within the semiconductor lattice act as localized electronic states between the VB and CB, capturing and releasing excess carriers with a random time delay as they drift towards the electrodes. This process influence the dynamics of both electron and hole carriers, and alters the collected signal by reducing its amplitude and distorting its shape. In terms of activation energy E_a, the shallow traps, such that E_a <0.3 eV are empty at room temperature. But deep traps, such that E_a >1 eV, activate[10] at high temperature, above 250 °C for diamond sensor [109]. However regarding the expected temperature encountered in the fusion and fission environments presented in Chapter 1, Section 1.3, sensors must be used in locations where temperatures can reach 500 °C, which is therefore a critical point to consider.

These introductory remarks provide a better understanding of the importance of 4H–SiC in terms of its thermal properties, in comparison to diamond. However, due to the lack of data for both materials in high temperature environments exceeding 200 °C, a dedicated qualification is necessary. The stability of its performance will be studied up to 500 °C in Part III, by comparing it with diamond.

[10] *These mechanisms will be discussed in more detail in the second part of the manuscript, in Chapter 7.*

3.3. The SiC as a radiation sensor

In this section, the basis of neutron and photon interaction with matter is introduced. The following explanations, in terms of phenomenons is needed for the kinematic study used for data interpretation, which is presented in the second part of the work, in Chapter 4.

3.3.1. Interaction with photons

3.3.1.1. Photon reactions

While neutrons interact with atomic nuclei, photons interact mainly with electrons in the electron cloud[11] for the energy range of interest in this study.

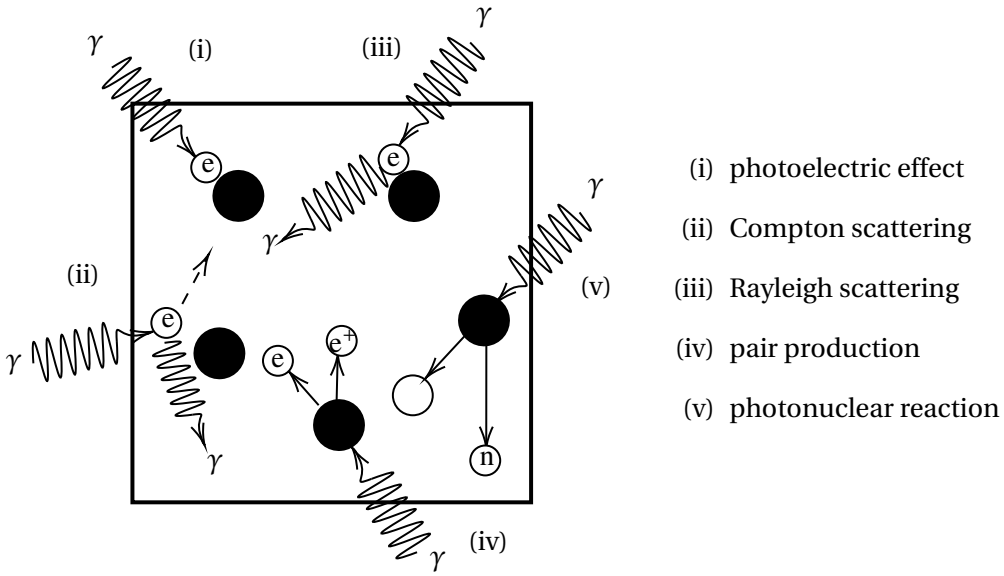

Fig. 3.14. Schematic diagram of photon interactions with matter.

Therefore, several interactions can take place as schematically depicted in Fig. 3.14:

- The photoelectric effect. An electron is ejected from the electron nucleus after acquiring sufficient energy by absorbing a photon of energy E_γ. In this process, the electron carries the excess energy regarding its binding energy E_B such that:

$$E_{e^-} = E_\gamma - E_B \tag{3.36}$$

  With E_B the binding energy of the electron in a specific shell n of the atom of atomic number Z such that:

$$E_B = \frac{Z^2 e^4 m_e}{32\pi^2 \epsilon_0^2 \hbar^2 n^2} \tag{3.37}$$

  With e the elementary charge, m_e the electron mass, ϵ_0 the vacuum permittivity, and $\hbar$ the reduced Planck constant.

- Compton scattering. A loosely bound electron of rest mass m_e, is ejected after receiving part of the energy of the incident photon of energy E_γ. Hence, the amount of energy transferred to the electron depends on the scattering angle of the incident photon and its

[11] *Photons can interact with the nucleus, but this interaction is negligible compared to the interaction with electrons since it concerns photons energy much larger than the MeV, which is not the case in the context of this study.*

initial energy such that:

$$E_{e^-} = E_\gamma - E_{\gamma'} \tag{3.38}$$

With $E_{\gamma'}$ the scattered photon energy, and θ the photon scattering angle such that the energy of the scattered photon is given by:

$$E_{\gamma'} = \frac{E_\gamma}{1 + \frac{E_\gamma}{m_e c^2}(1 - cos\theta)} \tag{3.39}$$

- Rayleigh scattering. No electrons are ejected, but the incident photon changes direction without giving up energy by scattering elastically.
- Pair creation. An electron/positron pair is emitted after absorption of a photon of energy greater than 1.022 MeV. Hence, the energy given to the electron or positron in pair production is equal to the energy of the incoming photon minus the rest mass energy of the electron or positron such that:

$$E_{e^-/e^+} = E_\gamma - 2m_e c^2 \tag{3.40}$$

  Then, the resulting positron will annihilate with an electron in the medium, producing two photons of annihilation.
- The photonuclear reaction. A neutron is emitted after absorption of a photon of energy greater than the binding energy of the last neutron in the target atom[12].

The relative significance of these interactions depends on both the energy of the photon and the atomic number of the material. For example, the photoelectric effect is the dominant interaction for low-energy photons, while Compton scattering is the dominant interaction for intermediate photons as displayed in Fig. 3.15. Compton scattering has an effective cross-section of a few barns on carbon and silicon atoms. The other interactions have relatively small cross sections over the energy range 1 to 20 MeV as shown in Fig. 3.16 considering SiC material.

[12] *This reaction is not considered in the context of this study since the energy of the photons is not sufficient to induce this reaction.*

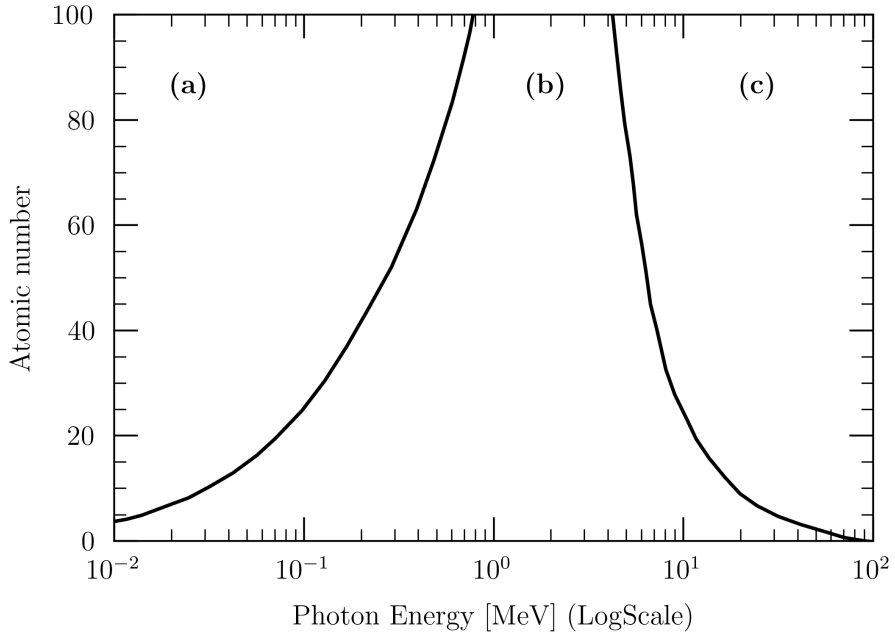

Fig. 3.15. Relative importance of photon interactions as a function of the photon energy and atomic number of the material: (a) Photoelectric effect, (b) Compton scattering, (c) Pair production. Figure adapted from [110].

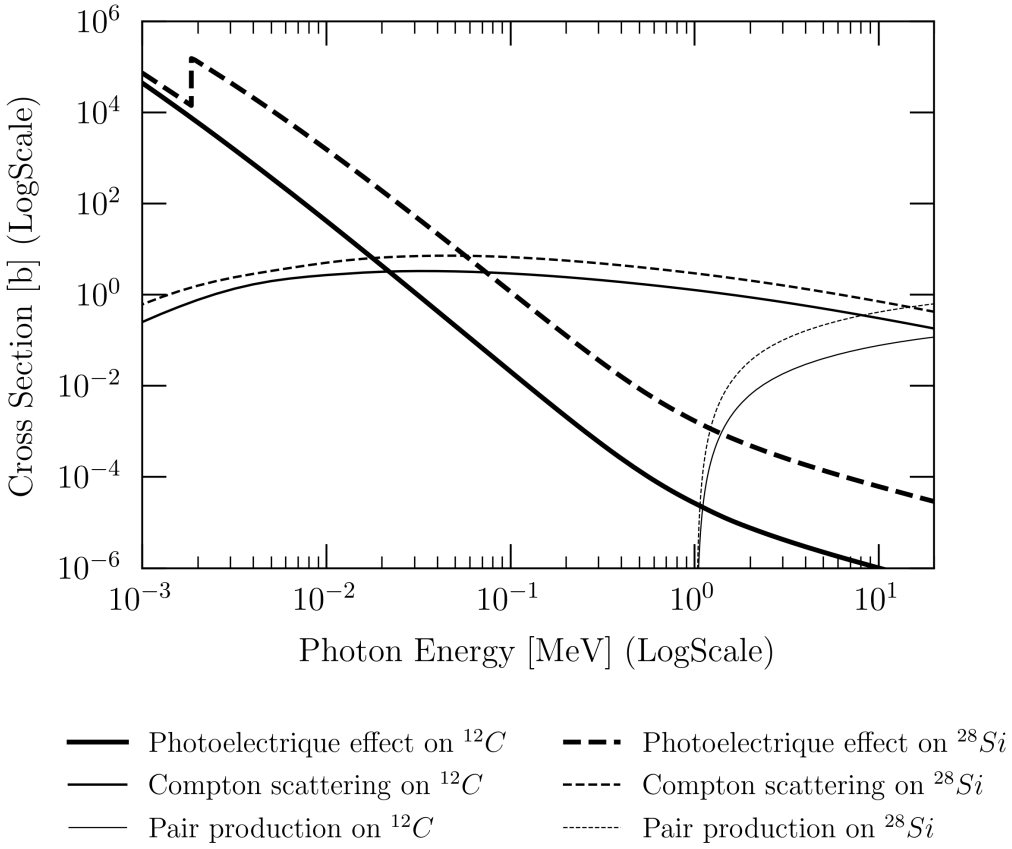

Fig. 3.16. Effective cross section interaction for photon reactions. Data are from EPICS2017 [111].

3.3.1.2. Attenuation of photons

Photons, as electrically neutral particles interact randomly within a detector depending on their energy and the medium of interaction. As a result, energy deposition is indirect either partially or entirely by electrons, occurring through the attenuation of photons. The probability of photon interaction in a medium is related to its mass attenuation coefficient, which is energy-dependant since it is inherently linked to the notion of cross section. The lineic attenuation coefficient represents the macroscopic cross section. The exponential decay (random law) is applicable only if the photons have the same energy. The amount of photons traversing a material is then defined such that:

$$I(x) = I_0 \exp\left(-\mu x\right) \tag{3.41}$$

With I_0 the incident population of photon, I the number of photons traversing a thickness of material x, and μ the attenuation coefficient in $[\mathrm{cm}^2\mathrm{g}^{-1}]$.

Hence, the amount of photons interacting within the sensor on a thickness x is obtained such that:

$$I_{int.}(x) = I_0\left(1 - \exp\left(-\mu x\right)\right) \tag{3.42}$$

Then, taking into account all the photon reactions introduced previously, the total mass attenuation coefficient is therefore the sum of the terms for the different phenomena. The different distributions including the total attenuation coefficient are represented in Fig. 3.17.

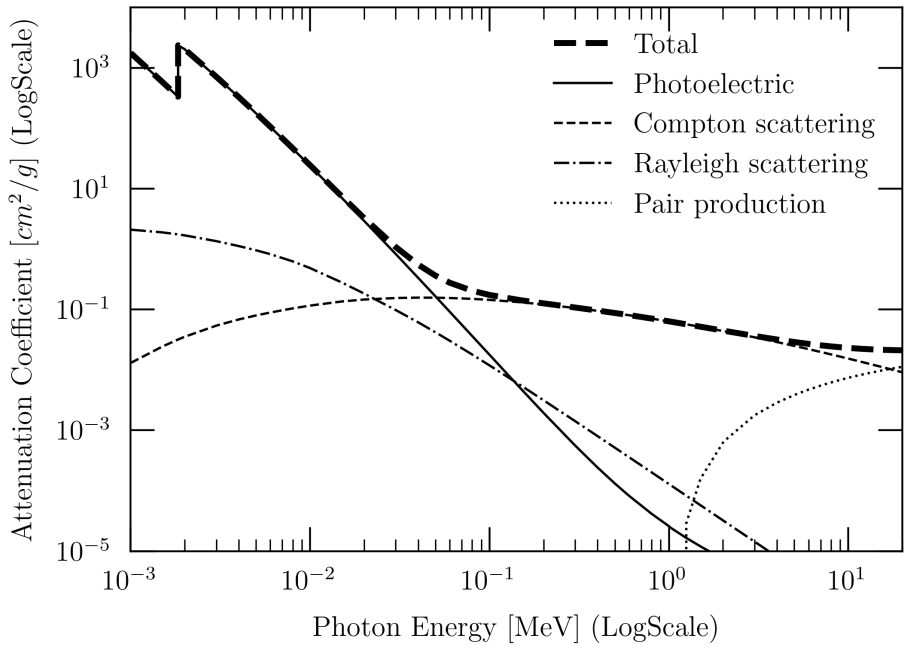

Fig. 3.17. Attenuation coefficient within 4H–SiC as a function of photon energy. Data are from NIST XCOM database [112]. The resonance peaks are due to the K-edge of carbon and silicon, when the photon energy is sufficient to eject an electron from the K-shell.

The caracteristic length traveled by the photon in the material is the approximate length before undergoing an interaction resulting in the absorption of its energy. Moreover, since the relationship between the attenuation coefficient and this caracteristic length is described using an exponential decay model (3.42), it leads to the following approximation, taking into account

the density ρ in [g/cm^{-3}] of the material:

$$X = \frac{1}{\mu} \tag{3.43}$$

With X the attenuation length which represents the average distance traveled by the photon in the material before its intensity decreased by a factor $1/e$.

Hence, it is understood that the distance traveled by the photon in the material before its intensity decreases significantly is relatively high for photons of several MeV of energy according to Fig. 3.18. Therefore, this property is therefore an advantage when using such a thin sensor in a mixed field with a photon spectrum of the same order of magnitude as that of fast neutrons.

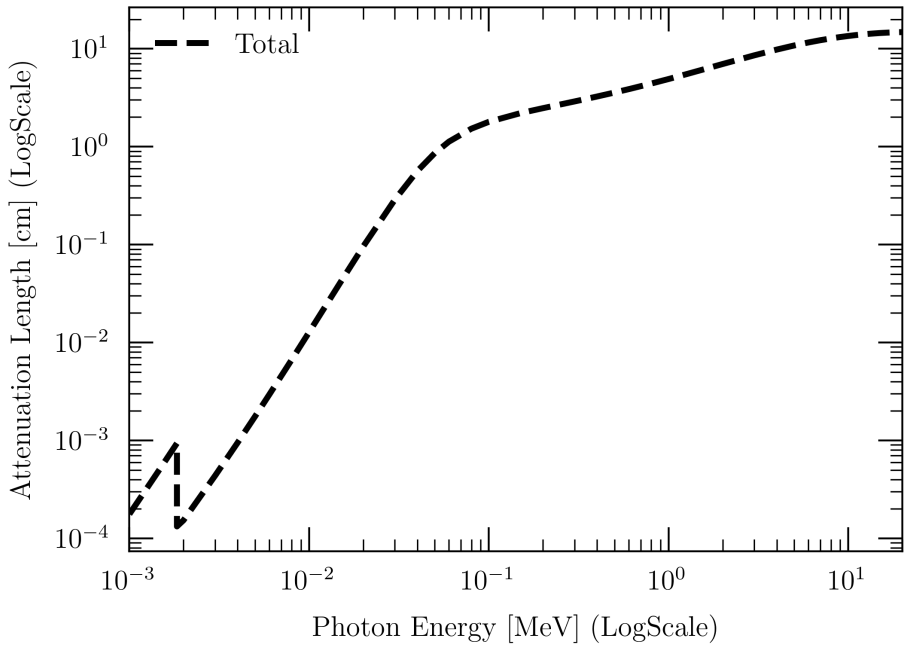

Fig. 3.18. Approximate characteristic attenuation length range within 4H–SiC as a function of photon energy. Data are from NIST XCOM database [112].

3.3.2. Interaction with charged particles

3.3.2.1. Interaction mechanisms with electrons and positrons

The interaction of electrons or positrons with matter is governed by Coulomb interactions, ionization, and radiative losses. Indeed, in addition to energy loss through ionization, energy loss due to Bremsstrahlung must be considered for these light charged particles. As a result of the light electron interaction with orbital electrons, for each interaction involving a transfer of energy, a much larger fraction of its energy is transferred to the target electron. As electrons are much more easily deflected during collisions with target electrons, the propagation of projectile electrons is therefore much less rectilinear than ions. Electrons are also likely to lose energy through electromagnetic radiation in the vicinity of a target nucleus at very high energies, resulting in the emission of remsstrahlung radiation. Hence, the energy loss of electrons in the material is thus the sum of the collisional stopping power and the radiative stopping power related to Bremsstrahlung.

The linear stopping power of these charged particles in an absorbing medium is then simply given as the differential energy loss for that particle within the material divided by the

corresponding differential path length such that:

$$S = -\frac{dE}{dx} \tag{3.44}$$

With S the linear stopping power in [MeV/µm]. The classic expression which describes this energy loss is known as the Bethe formula [113] and is defined for non relativistic charged particles such that:

$$-\frac{dE}{dx} = \frac{4\pi}{m_e v^2} \cdot n \cdot \left(z \cdot \frac{q^2}{4\pi\epsilon_0} \right)^2 \cdot \left[\ln\left(\frac{2m_e v^2}{I} \right) \right] \tag{3.45}$$

With v the charged particle velocity in [m/s] and z its charge, m_e the electron mass at rest in [kg] and q the elementary charge in [C], ϵ_0 the dielectric permittivity in [F/m], I the average excitation potential of the material in [eV] and n the electronic density of the material such that:

$$n = \frac{Z \cdot \mathcal{N}_A \cdot \rho}{A \cdot M_u} \tag{3.46}$$

With ρ the density material, Z its atomic number and A its mass number, $\mathcal{N}_A$ the Avogadro number in [/mol] and M_u the molar mass constant in [g/mol].

The collisional term is described with (3.45). Then, as electrons are considered, it must be applied with a projectile charge set to -1. Finally the energy loss per unit length depends solely on the velocity of electrons, and the electronic density of the material. Indeed, as seen in Fig. 3.19, at low energies, the energy loss of electrons is exclusively due to collisions. Then the stopping power decreases until it reaches a minimum, known as the ionization minimum.

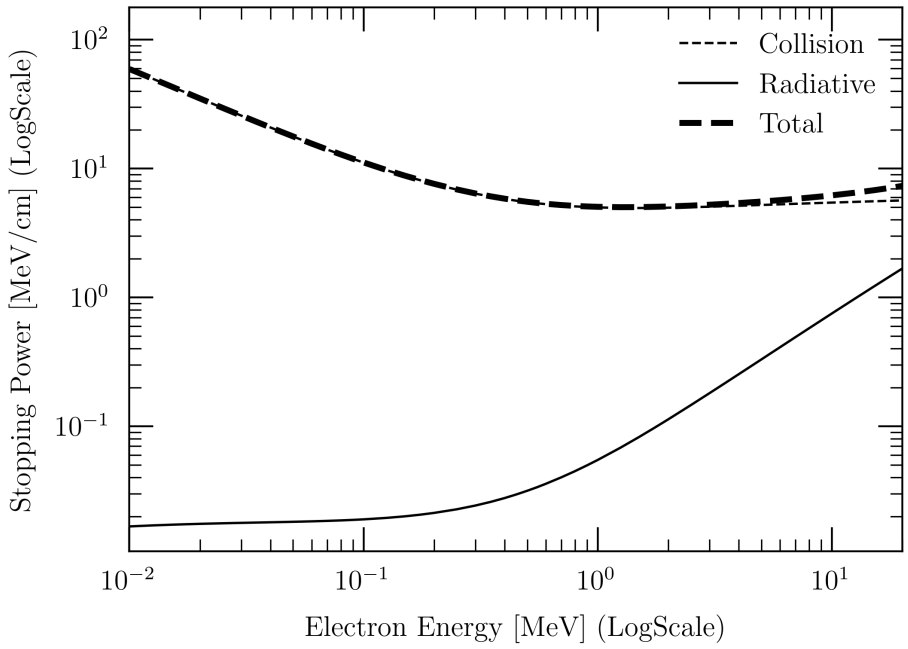

Fig. 3.19. Electron stopping power in the 4H–SiC as a function of their energy. Data are from ESTAR database [114].

Then using the Continuous Slowing Down Approximation (CSDA) approximation range calculated by integrating the reciprocal of the total stopping power with respect to energy, it comes as represented in Fig. 3.20 the average distance that an electron travel in the 4H–SiC before it comes to a halt.

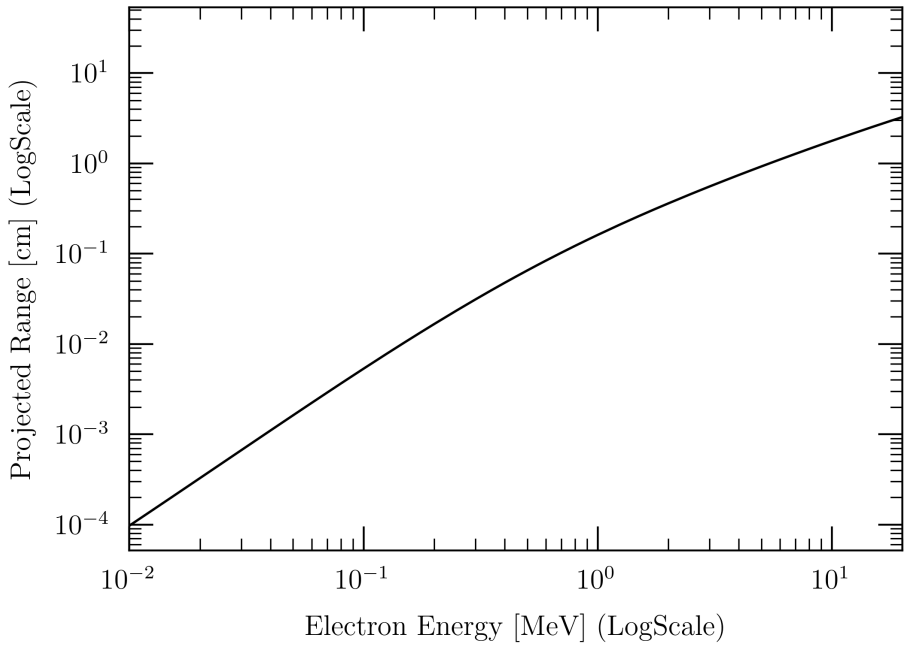

Fig. 3.20. Electron projected range in the 4H–SiC as a function of their energy. Data are from ESTAR database [114].

3.3.2.2. Interaction mechanisms with ions

All the secondary charged particles on their way out, whether recoil nuclei from elastic/inelastic collisions or charged particles produced by neutron capture, like the case of using NCL, interact mainly with the orbital electrons of the target atoms, leaving a dense trail of excited and ionized atoms in their wake.

Electronic stopping power refers to the slowing down of an incident ion due to inelastic collisions between the bound electrons of the medium and the ion passing through it. The energy of the incident ion is then lost during processes such as collisions, which can lead to both excitations of the bound electrons in the medium and excitations of the ion's electron cloud. The electronic stopping power as a function of the kinetic energy of the incident ion is represented in Fig. 3.21, using the SRIM software [115]. Since the number of collisions that an ion undergoes with electrons is large, and since the charge state of the ion as it passes through the medium can change frequently, it is very difficult to describe all the possible interactions for all the possible charge states of the ion. Instead, the electronic stopping power is often given as a simple function of energy that is an average taken over all the energy loss processes for different charge states. It can be determined theoretically to an accuracy of a few percent in the energy range above several hundred keV per nucleon from theoretical models. The best known is Bethe's formula (3.45). At energies below about 100 keV per nucleon, it becomes more difficult to determine the electronic stopping using power analytical models [116]. Recently, a new theoretical model has been proposed to accurately determine the electronic stopping power for various ion-target systems over a wide range of energies, including the low-energy regime [117, 118].

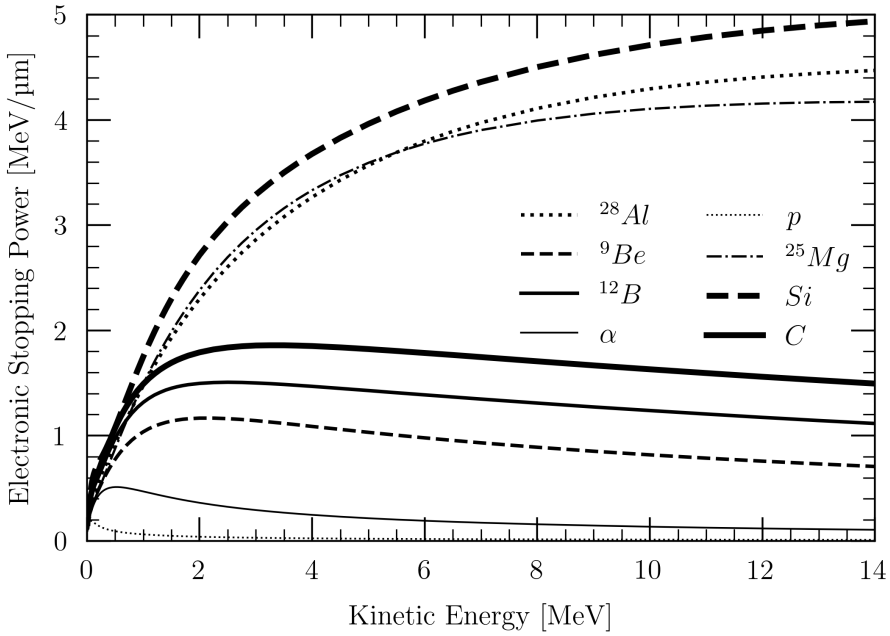

Fig. 3.21. Electronic stopping power in the 4H–SiC as a function of kinetic energy. Data are from SRIM software [115] computation.

Nuclear stopping power[13] refers to the elastic collisions between the projectile ion and the atoms in the medium. If the form of the potential energy of repulsion (3.47) between two atoms is known, the nuclear stopping power can be calculated.

$$V(r) = \frac{1}{4\pi\epsilon_0}\frac{Z_1 Z_2 e^2}{r}\phi(r/a) \tag{3.47}$$

With $V(r)$ the repulsion potential, Z_1 et Z_2 the charges of interacting nuclei, $\phi(r/a)$ a screening function[14] with a the screening parameter.

The nuclear stopping power is negligible for the various charged particles and recoil nuclei in 4H–SiC, except at the lowest energy as seen in Fig. 3.22.

A large number of different repulsion potentials and screen functions have been proposed, some determined semi-empirically, others from theoretical calculations. A widely used repulsion potential is that given by Ziegler, Biersack and Littmark, known as the repulsive potential ZBL [119]. The nuclear stopping power is negligible for the various charged particles and recoil nuclei in SiC, except at the lowest energy as seen in Fig. 3.22. The nuclear stopping power increases as the mass of the ion increases.

With regard to the comparison of the stopping power of the same charged particle in different materials, again with regard to Bethe's expression (3.45), the stopping power is only a function of n (3.46) which represents the electron density of the absorbing material. Materials with a high atomic number and high density will therefore give the greatest linear stopping power as observed previously in Fig. 3.21 for the comparison of stopping power of the various reactions products in 4H–SiC simulated with the SRIM software.

[13] *The term nuclear does not refer here to the stopping of an incident ion due to nuclear forces, but this nuclear stopping power implies only the interaction of an ion with a target nucleus.*

[14] *At very small distances between the nuclei, the repulsive interaction can be considered to be essentially Coulombic, but at larger distances, the electron clouds form a screen between the nuclei.*

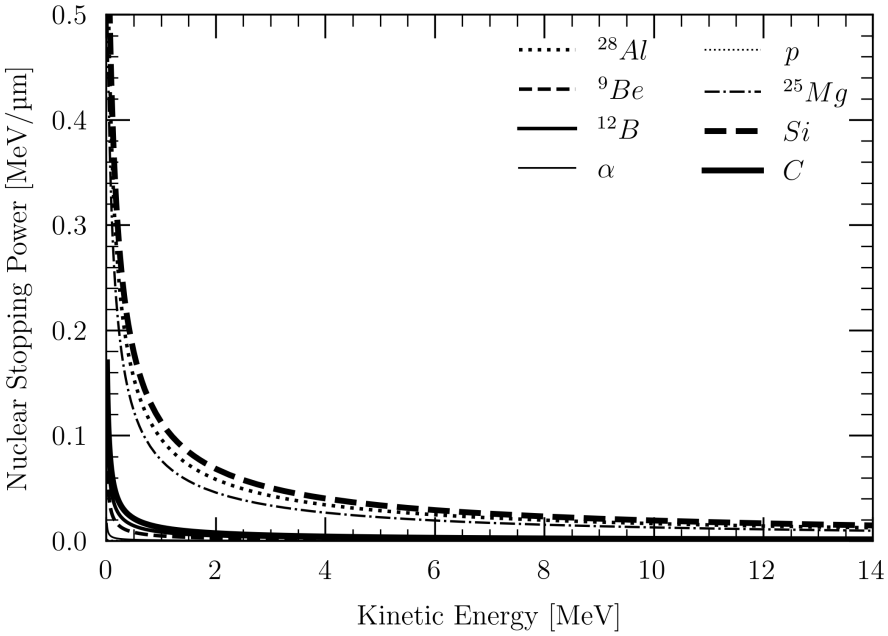

Fig. 3.22. Nuclear stopping power in the 4H–SiC as a function of kinetic energy. Data are from SRIM software [115] computation.

The loss of specific energy along the trajectory of a charged particle can be represented as follows with Fig. 3.23 using the TRIM software [115]. This example is given as an illustration[15] for an alpha particle and a beryllium of 5 MeV. It should be remembered that the stopping power of secondary charged particles varies approximately according to $1/v^2$ as seen in (3.45), that is to say, according to $1/E$ in terms of kinetic energy. On reaching the maximum depth of penetration into the material, i.e. at the end of the trajectory, the charged particle captures orbital electrons from the atoms of the absorbing medium and the stopping power curve collapses: this is the Bragg peak as seen in Fig. 3.23. The plots are shown both for a single alpha particle track and for the average behaviour of a parallel beam of alpha particles of the same initial energy as represented in Fig. 3.24. The two curves differ somewhat due to straggling effects, discussed here after.

[15] *The case-by-case study for real energy on the way out will be presented later in Chapter 4.*

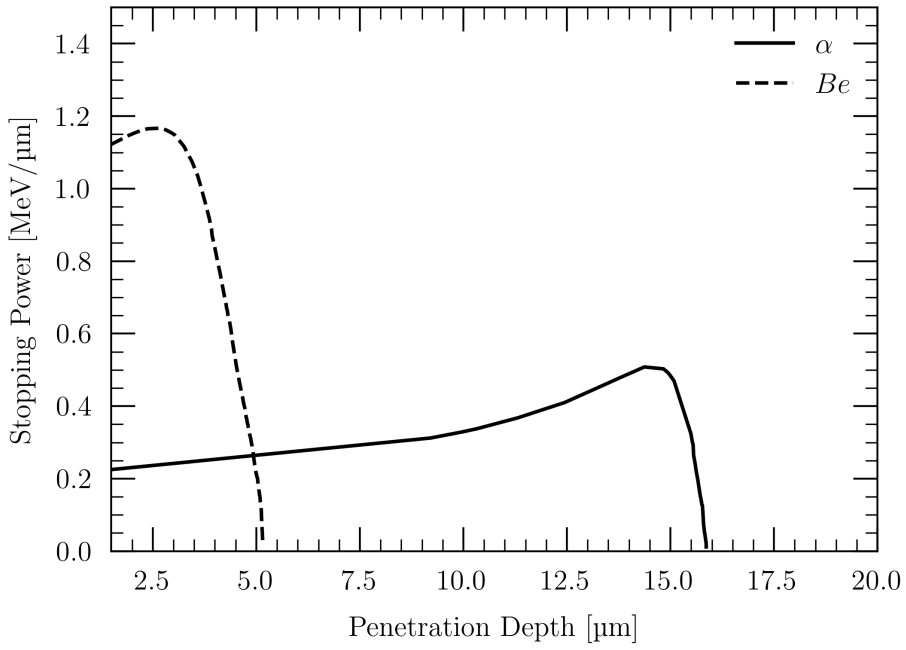

Fig. 3.23. Stopping power for one charged particles with a kinetic energy of 5 MeV in the 4H–SiC as a function of penetration depth. Data are from TRIM software [115] computation.

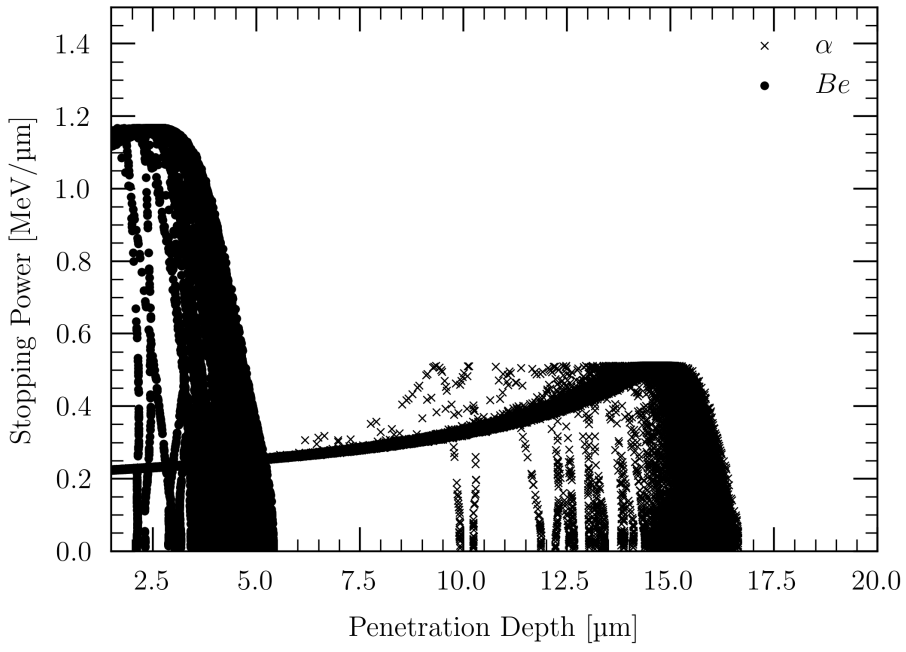

Fig. 3.24. Stopping power for 10000 charged particles with a kinetic energy of 5 MeV in the 4H–SiC as a function of penetration depth. Data are from TRIM software [115] computation.

Since the interactions undergone by a charged particle in an absorbing material vary randomly, its energy loss, characterised by the stopping power, is a stochastic process. Consequently, in the case of a large number of monoenergetic charged particles passing through a given thickness of a material, the deposited energy will be distributed: this is the energy "straggling" [120]. The width of this energy distribution is then a measure of the spread of the energy, which varies with distance along the trajectory of the particles. In the first part, the distribution becomes wider and more asymmetric with penetration distance, showing the increasing importance of energy spreading. Towards the end of the range, the distribution narrows again because the average energy of the particles has been greatly reduced.

In the sensor, secondary charged particles have a quasi-rectilinear trajectory. The notion of path corresponds then to the length of the trajectory of a given charged particle emitted at a certain energy as described previously with the penetration depth. For a particle of given energy, this path is expressed as a function of the stopping power defined above, such that:

$$R_p = \int_{E_{part.}}^{0} dx = \int_{0}^{E_{part.}} \frac{dE}{-\frac{dE}{dx}} = \int_{0}^{E_{part.}} \frac{dE}{S} \tag{3.48}$$

With R_p the projected range in [µm], $E_{part.}$ the energy of the secondary charged particle in [MeV], S the stopping power in [MeV$\cdot$µm^{-1}].

Therefore, the secondary charged particles lose their energy progressively in a very large number of collisions with the orbital electrons of the atoms in the medium encountered. The first curves represented with Fig. 3.25 and Fig. 3.26 show the projected range of the secondary charged particles as a function of the initial energy computed with the TRIM[16] software [115]. Thus it gives a first insight of the width needed for a SiC sensor to stop a secondary particle generated.

In the end, when a charged particle deposits energy in a semiconductor detector whether it be heavy or light charged particle, an equal number N_{e^-,h^+} of conduction electrons and holes are formed in a few picoseconds along the trajectory of the charged particle, such that:

$$N_{e^-,h^+} = \frac{E_{dep.}}{E_W} \tag{3.49}$$

With $E_{dep.}$ the deposited energy of the incident charged particle and E_W the ionisation energy for the material.

Then, as explained earlier in Section 3.1.3, under the effect of an internal electric field, the charge carriers will feel electrostatic forces causing them to drift in opposite directions. The movement of the electrons or holes then forms a current that persists in the junction until the charge Q defined as follows is collected at the sensor electrodes:

$$Q = N_{e^-,h^+} \cdot q \tag{3.50}$$

[16] *TRansport of Ion in Matter (TRIM)*

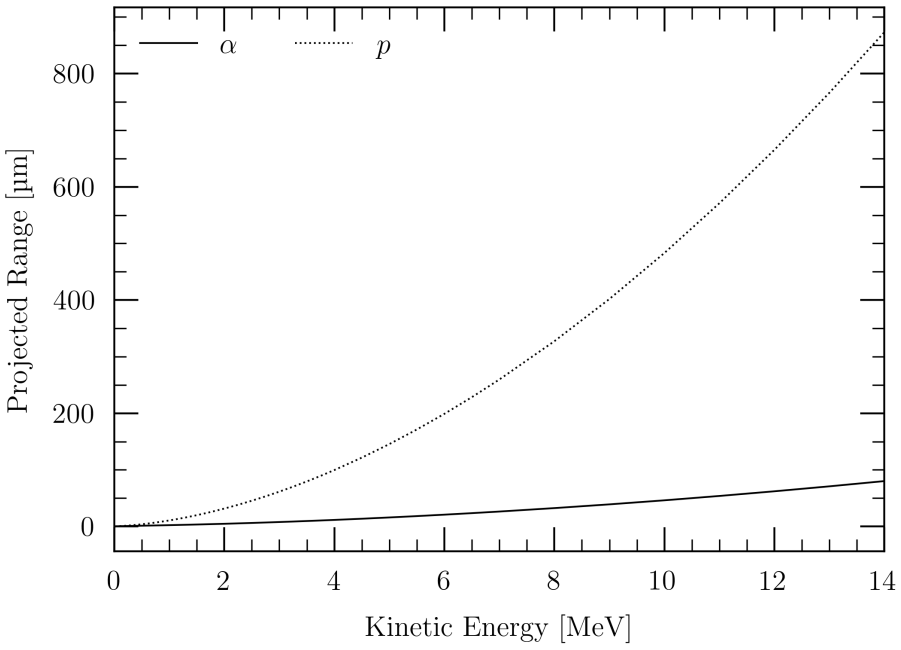

Fig. 3.25. Projected range of proton and alpha particle in the 4H–SiC as a function of kinetic energy. Data are from TRIM software [115] computation .

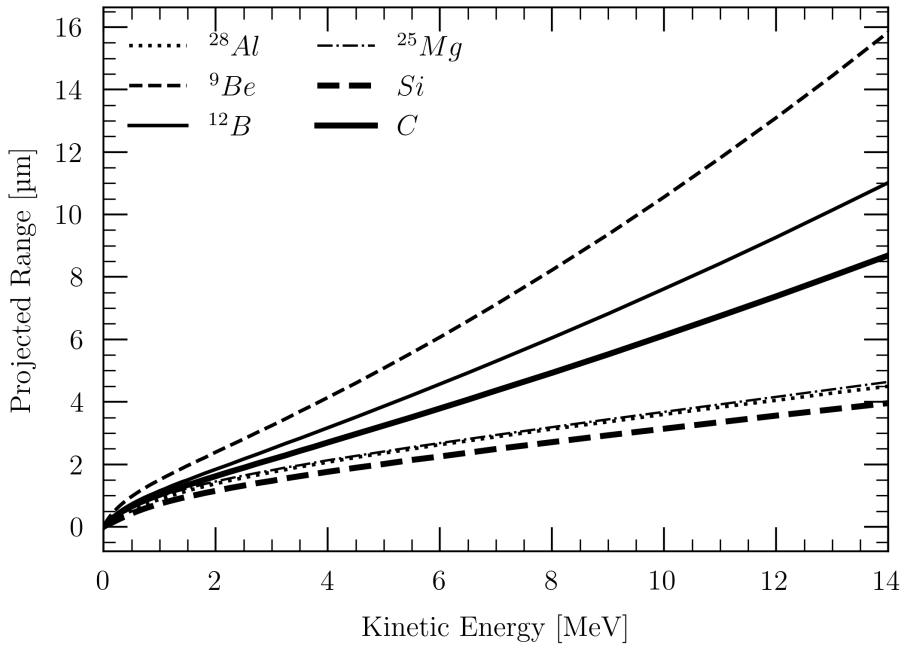

Fig. 3.26. Projected range of secondary particles in the 4H–SiC as a function of kinetic energy. Data are from TRIM software [115] computation.

3.3.3. Interactions with neutrons

Neutrons, as uncharged particles, do not interact with the orbital electrons of SiC[17] but react through various processes[18] schematically represented in Fig. 3.27, and explained below.

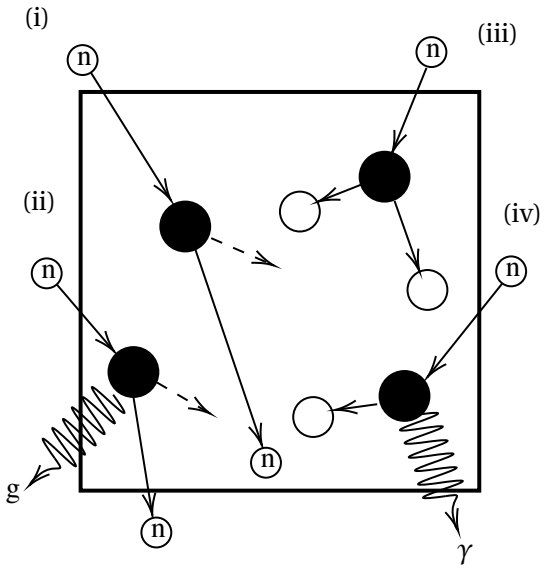

(i) elastic scattering

(ii) inelastic scattering

(iii) non-radiative neutron capture

(iv) radiative neutron capture

Fig. 3.27. Schematic diagram of possible neutron interactions with SiC.

3.3.3.1. Neutron scattering

Two types of neutron scattering can be distinguished. From a phenomenological point of view, the scattering processes of an incident neutron on a target nucleus are depicted to:

- Elastic scattering
- Inelastic scattering.

Elastic scattering is always possible, whatever the target nucleus and the energy of the incident neutron. Inelastic scattering, on the other hand, is a threshold reaction. The incident neutron leaves the residual nucleus target in an excited state after ejecting a neutron[19].

Considering such scattering reactions, describing the relation between a particle on its way out and the angle at which it is emitted, the following kinetic energy expressions are obtained according to the demonstration presented in Appendix B.1 for the scattered neutron:

$$\sqrt{E_3} = C \pm \sqrt{C^2 + B} \tag{3.51}$$

$$\begin{cases} C = \dfrac{\sqrt{m_1 E_1 m_3}}{m_3 + m_4} \cdot cos\theta \\ B = \dfrac{Q m_4 - (1 - m_4) E_1}{m_3 + m_4} \end{cases} \tag{3.52}$$

[17] *As a reminder, the doping levels typical of p-type or n-type semiconductors are so low that the impurity atoms introduced play no significant role in determining the nature of radiation interactions in semiconductors.*

[18] *These brief explanations are intended to introduce the main concepts associated with neutron and photon interactions. For a full discussion of radiation/matter interactions, please refer to the following references [110, 121].*

[19] *The threshold energy is then the energy of the excited state considered.*

With E_3 the kinetic energy of a product of the reaction, and m_3 and m_4 the reaction products masses, Q the amount of energy absorbed, and θ the emission angle of a reaction product with respect to the incident neutron of energy E_1 and mass m_1.

The later can be simplified in the case of elastic scatterings such that:

$$Q = 0 \qquad m_1 = m_3 \qquad m_2 = m_4 \tag{3.53}$$

The only charged particle emitted in the case of these reactions is the recoiled nucleus of the target atom whose energy denoted E_r is simply determined (3.55) using the energy balance (3.54) considering the target atom at rest such that:

$$E_{inc} + E_{target} = E_r + E_n \quad \text{with } E_{target} = 0, \tag{3.54}$$

$$\begin{cases} E_r = E_{inc} - E_n & \text{for the elastic scattering,} \\ E_r = E_{inc} - E_n - E_\gamma & \text{for the inelastic scattering}[20]. \end{cases} \tag{3.55}$$

Neutron scattering cross sections on silicon and carbon atoms are approximately constants and of the order of few barns as seen in Fig. 3.28.

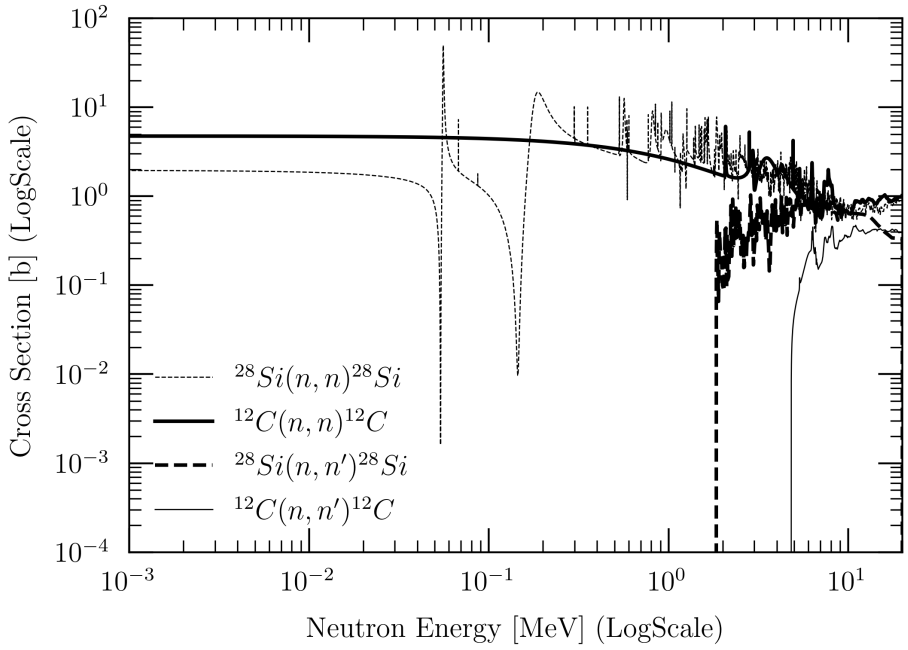

Fig. 3.28. Effective cross section interaction for scattering reactions. Data from ENDF/B-VIII.0.

The two inelastic collisions on carbon and silicon are threshold reactions. In the same way, the maximum energy for the recoiled nucleus such that $cos(\theta) = -1$ can be determined for a given incident neutron energy. Hence, the kinetic energy of the recoiled nucleus is then distributed as a function of the incident neutron energy and the emission angle of the recoiled nucleus. Summary of results is presented in Table 3.3 below, as an illustration[21] of the maximum energy of the recoiled nucleus for an incident neutron energy of 14 MeV, for the inelastic reactions under study.

[20] *Assuming that the energy carried away by the photons is simply the forward binding energy.*

[21] *The complete study of the energy of the recoiled nucleus for the different scattering reactions will be presented in Chapter 4.*

Reaction	E_{thresh} [MeV]	$E_{r_{max}}$ [MeV]
$^{12}C(n,n)^{12}C$	0	3.98
$^{28}Si(n,n)^{28}Si$	0	1.86
$^{12}C(n,n')^{12}C$	4.8	3.26
$^{28}Si(n,n')^{28}Si$	1.8	1.73

Table 3.3. Computed threshold energy $E_{thresh.}$ from the conservation of energy and momentum in Appendix B.1 and maximum energy of the recoiled nucleus $E_{r_{max}}$ for an incident neutron with energy E_{inc} of 14 MeV.

3.3.3.2. Neutron capture

Finally, neutrons can react through a capture process, radiative when the excitation energy of the nucleus is released in the form of a gamma photon or non-radiative when a charged particle is emitted, when the incident neutron enters the nucleus of the target atom.

This reaction can be described in three stages by the compound nucleus model:

- Firstly, the neutron is absorbed by the target nucleus. The latter acquires an excitation energy E_{exc} such that:
$$E_{exc} = E_{inc} + E_l \tag{3.56}$$
With E_{inc} the kinetic energy of the incident neutron and E_l the binding energy of the additional neutron.

- Secondly, the target nucleus becomes a higher order isotope. Its lifetime is short on our scale, of the order of magnitude of $1 \cdot 10^{-14}$ s but long on the nuclear scale. The excitation energy can then become uniform within the compound nucleus. In other words, de-excitation will be independent of the process that created the compound nucleus.

- Thirdly, the compound nucleus de-excites with the energy acquired during neutron absorption. This can lead to immediate de-excitation, indicated by the emission of a prompt gamma capture photon, as well as delayed emission processes where one or more secondary particles can be emitted.

Considering one more time the two bodies kinematic study in Appendix B.1, the Q value expression as a function of kinetic energies of capture products is obtained. This Q value corresponds to the amount of energy released by a reaction. Then, by solving the second degree quadratic equation describing the relationship between a particle on its way out and the angle at which it is emitted, the maximum energy associated with the reaction products as a function of the energy of the incident neutron is expressed.

Regarding such interactions within the SiC, the effective cross sections of non-radiative[22] neutron captures on silicon and carbon atoms are of the order of a few millibarns as seen in Fig. 3.29.

[22] *This non-radiative designation means that there are no prompt gamma photons emitted, but only reaction products emitted in fundamental or excited states.*

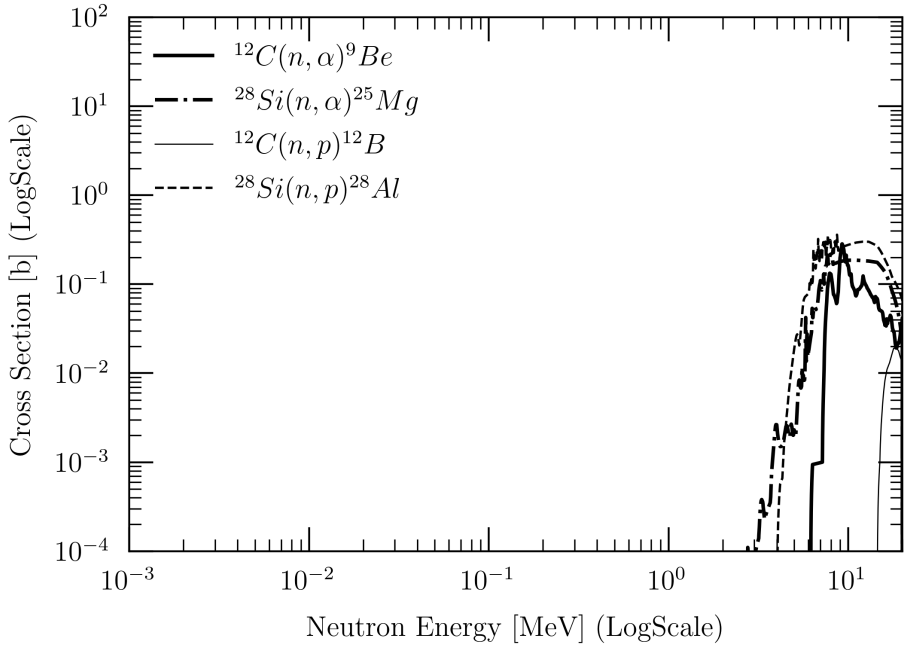

Fig. 3.29. Effective cross section interaction for the main non-radiative capture reactions. Data from ENDF/B-VIII.0.

For these reactions, the threshold energy is computed using the previous expression (3.51). These values and the maximum kinetic energy of the secondary charged particles on the way out of the reactions are summarized in Table 3.4 below.

Reaction	$E_{tresh.}$ [MeV]	$E_{tot_{max}}$ [MeV]
$^{12}C(n,\alpha)^{9}Be$	6.2	8.3
$^{28}Si(n,\alpha)^{25}Mg$	2.8	11.3
$^{28}Si(n,p)^{28}Al$	4.0	10.1

Table 3.4. Computed threshold energy values $E_{tresh.}$ from the conservation of energy and momentum in Appendix B.1, and maximum kinetic energy of reaction products $E_{tot_{max}}$ in ground state on the way out of captures reactions, for a 14 MeV incident neutron.

3.3.4. Sensor response is complex

The previous description of the interactions of several types of particles with the SiC material shows that the sensor response is complex and depends strongly on the neutron energy. Neutrons or gamma photons can interact with the SiC material in various ways, leading to the production of secondary charged particles. Then the charge carriers are collected at the sensor electrodes as described in Section 3.1.3. These interactions are schematically illustrated in Fig. 3.30. The scheme summarizes the interaction of a gamma photon generating an electron, a charged particle produced by thermal neutron capture by the NCL, threshold capture reactions for fast neutrons generating charged particles, and neutron scattering in the bulk. These particles can then deposit their energy in the sensor, creating electron-hole pairs along their trajectory taking into account the stopping power of the material. The electron-hole pairs then

drift under the effect of an internal electric field, creating a current that persists in the junction until

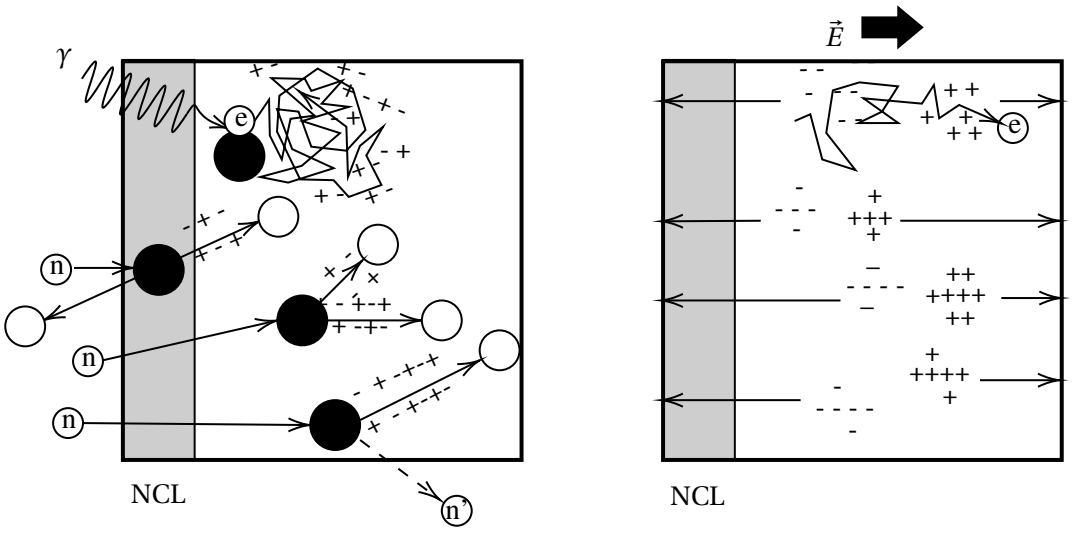

(a) Without electric field.

(b) With an applied electric field.

Fig. 3.30. Schematic synthesis of the interactions between the particles in the absence and presence of an electric field.

Finally, the response of the sensor can be described as a function of the energy of the incident particle, the nature of the particle, and the nature of the absorbing material. The sensor response to a monoenergetic incident primary particle is schematically depicted in Fig. 3.31.

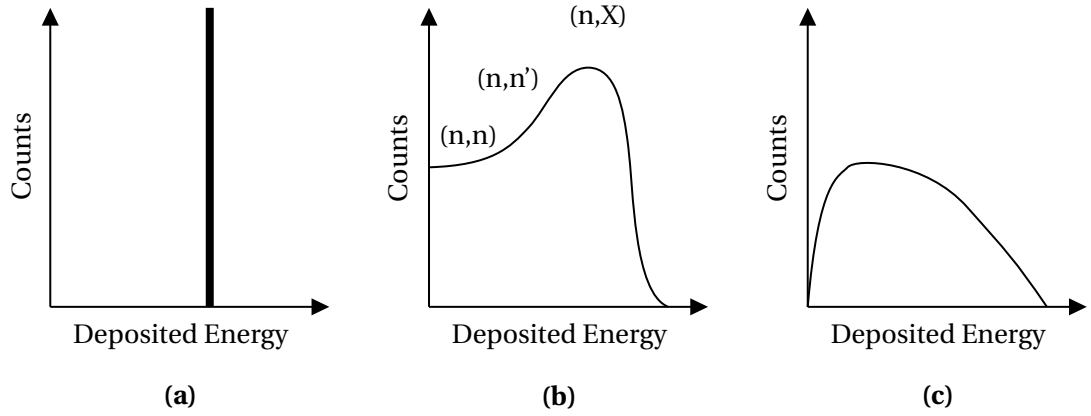

(a) Ideal case for monoenergetic incident neutron

(b) Real case for monoenergetic incident neutron

(c) Real case for monoenergetic incident gamma

Fig. 3.31. Scheme of the sensor response distribution, according to the incident particle type.

While the ideal case is considering an unique signature to a given particle, the sensor response is complex and depends strongly on the probability of interaction of the incident particle with

the material which lead to different charged particle produced. Then these charged particles are responsible for several ionisation profil according to their stopping power and straggling effects.

Therefore, the use of such sensor to estimate the energy of the incident particle is a complex task that requires a detailed understanding of the interactions between the particles and the material. Hence, it requires the development of a model that can predict the sensor response as a function of the incident particle energy, and dedicated experiments to validate the model.

3.4. Manufacturing of 4H–SiC sensors

3.4.1. Diodes manufacturing

It has been previously identified in the Section 3.2.2, that the SiC material is the most promising candidate for the applications of fast neutron detection in fission and fusion nuclear environment. Preliminary studies were needed in order to design new devices presented in Section 3.1.1.3, optimized for the detection of fast neutron through energetic charged particles described in the previous Section.

3.4.2. Sensor design requirements

Two motivations are at the origin of the elaboration of the chosen design:

- Firstly, the ionization profiles of the secondary particles created in a fast neutron field of several MeV depicted in Section 3.3.2.2 have a path through the material of several tens of microns
- Secondly, the low neutron capture cross-sections presented in Section 3.3.3.2 reduce the sensitivity of the detectors.

A sensor of sufficient thickness is then required to stop the secondary charged particles, but with small surfaces to limit the capacitance effect on the pulses shapes.

3.4.2.1. Bias voltage operational range

It has been explained previously in Section 3.1.1.3 that the application of a reverse bias voltage on a p-n junction diode allows the latter to be depleted, which is required to fully collect generated charge carriers. This SCR thickness corresponding to the active detection area of the sensor increases with reverse bias according to the following expression demonstrated previously:

$$W_{SCR} = \sqrt{\frac{2\epsilon}{q} \cdot \left(\frac{N_D + N_A}{N_D N_A}\right) \cdot (V_0 + V_R)} \tag{3.57}$$

With N_D and N_A respectively the concentration of donor atoms and acceptor atoms in [cm^{-3}], V_0 and V_R respectively the conctact potential at the junction and the reverse bias in [V], ϵ the dielectric permittivity in [F/m] and q the elementary charge in [C].

It can be highlighted that the depletion thickness is directly proportional to the square root of the applied voltage and inversely proportional to the square root of the dopant concentration. Therefore, to obtain large active volumes with thick SiC doped layers, low impurity concentrations of n-type are required and/or apply high reverse bias voltages V_R as depicted in Fig. 3.32.

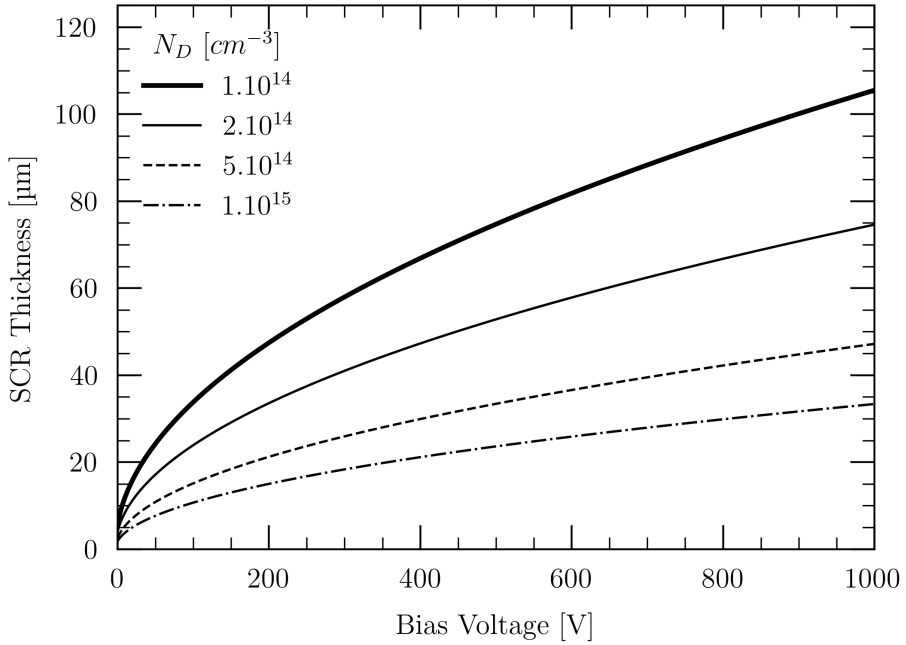

Fig. 3.32. Variation of the SCR region thickness as a function of the applied reverse bias voltage for different concentrations of donor atoms. The given acceptor atoms concentration is equals to $1 \cdot 10^{19}$ cm^{-3}.

In practice, the reverse bias voltage applied in current instrumentation is less than 1000 V in order to protect the electronics of the acquisition chain from electrostatic discharges. Consequently, it is desirable to obtain 4H–SiC layers with the lowest possible dopant concentrations in order to reach the highest possible thicknesses with the lowest possible reverse bias voltages as depicted in Fig. 3.32. But currently, doping in donor atoms is limited to a concentration of approximately $1 \cdot 10^{13}$ cm^{-3}.

3.4.2.2. Active region thickness

When designing a solid-state sensor for the application of fast neutron detection, the range of charged particles produced must be taken into account as explained previously. In order to measure the total energy deposited by a secondary charged particle, the thickness of the SiC sensor's SCR must be greater than the range of the particles emitted as a result of interactions with the primary particles in the material. The previous introduction of ionisation mechanisms and generation of charge carriers within the material leads to the a first order of magnitude for the required active region thickness so that the charged particles deposit the global kinetic energy they have at their creation within the SCR. Indeed, according tho the kinematic study that will be explicitly presented in detail in the following Chapter, the maximum kinetic energy of charged particles produced lead to a projected range of at least 20 µm.

Taking into account geometrical effects reducing the sensor sensibility as well as bias voltage operational range, epitaxial thicknesses of 60 µm and 100 µm with doping concentration in donor atoms of $1 \cdot 10^{14}$ cm^{-3} were processed at the start of this phD project, according to the functional specifications transmitted to NOVASiC [122] company[23]. The technical details of the epitaxy quotations are provided in Appendix C.

[23] *Since 2022, Soitec [123] has acquired NOVASiC to strengthen its silicon carbide substrate technology.*

3.4.2.3. Cleanroom manufacturing processes

The current method of fabricating a *p*-*n* junction diode is based on a simplified sequence of several steps depicted in Fig. 3.33 as follows:

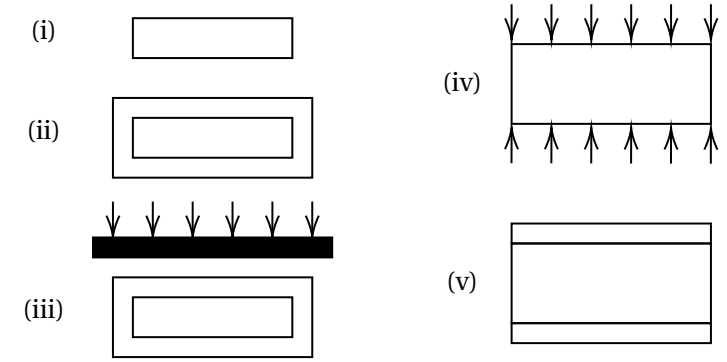

(i) Clean crystal

(ii) Oxidation

(iii) Illumination, mask and wafer

(iv) Impurity implantation

(v) Aluminum deposition

Fig. 3.33. Manufacturing process of the proposed sensor.

- A lightly doped *n* crystal is chemically cleaned to remove organic and metallic contaminants [124] and oxidised by heating the compound in an oxygen atmosphere at approximately 1000 °C. During a first step of photo-lithography[24], the type *n* layer is covered with a thin layer of photosensitive resin, which is then illuminated through a mask.
- Donor impurity atoms are implanted over the entire back surface. It is followed by an annealing step [25] to repair damage to the crystal and properly integrate the implanted atoms into the lattice. Aluminisation by evaporation or sputtering on both surfaces provides the ohmic back contact and electrical connection to the diode.
- A photolithographic etching step of the top aluminium layer gives it its final shape. Heating to a temperature slightly below the melting point of the aluminium completes the production sequence in order to obtain a good connection between the aluminium and the crystal type *n*. The depth of the p^+ layer of the diode can be controlled by varying the implantation energy and/or dopant dose.

Key factors to be maintained during growth are the silicon/carbon ratio which is necessary to control the formation of native point defects such as carbon/silicon atom vacancies and interstitials and other complex defects presented in Section 3.1.1.2 as well as the growth rate, which determines the uniformity of the crystalline nature of the layers. The later is typically maintained by the control of the temperature and the pressure, as well as the flow rates of the precursors. Regarding the ohmic contact realization, the later were made at Troyes Technical University, following the results obtained during the doctoral thesis work of F. Laariedh who focused on overcoming technological obstacles to produce transistor-type components by integrating them into 4H–SiC substrates [125]. The ohmic contact on n-type silicon carbide is often made with nickel, a metal that enables achieving specific contact resistances lower

[24] *Refers to the process of transferring a structure from a mask to the wafer by optical means.*
[25] *Heating up to* 1700 °C.

than $1 \cdot 10^{-5} \Omega \cdot cm^2$. Other metals like titanium or tungsten are also used, resulting in relatively low specific resistances. A wide variety of metals can be selected for this contact. The process usually involves depositing the metal onto a heavily doped layer with a concentration exceeding $1 \cdot 10^{18} cm^{-3}$, and then annealing at approximately 1000 °C to establish a stable ohmic contact suitable for component application.

Aluminum acts as a p-type dopant for SiC, making it one of the most commonly used metals in ohmic contact formation, often combined with another metal. Resistance levels achieved are typically around $1 \cdot 10^{-4} \Omega \cdot cm^2$, depending on doping levels and annealing temperatures, an order of magnitude compared to n-type contacts. Then, as mentioned, nickel is the most frequently used metal for n-type contacts. But ohmic contacts on p-type are also feasible, although resistances obtained are around $1 \cdot 10^{-3} \Omega \cdot cm^2$. For the Al-Ti alloy, ohmic behavior is achieved but remains highly sensitive to the quality of the aluminum layer. Presently, ohmic contacts on p-type SiC are generally made with a ternary alloy based on Ni, Ti, and Al. Hence, this choice was made for the realization of the ohmic contacts on the diodes produced during this thesis shown in Fig. 3.34 because of the low specific contact resistances obtained with this alloy, the stability of the contacts, and the ease of engraving such alloy.

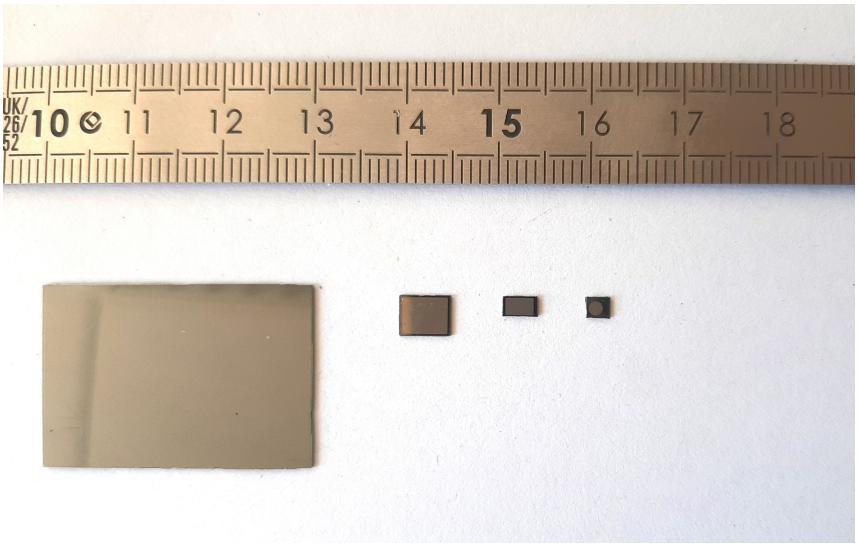

Fig. 3.34. SiC *pn* junction diodes manufactured during this thesis. From left to right, the SiC wafer, the diodes after the ohmic contact deposition and cutting, with several surface areas of $4 \times 5 mm^2$ and $2 \times 3 mm^2$ and 1.6 mm diameter.

3.4.2.4. Electrical characterisation

In order to verify the quality of the diodes produced, the electrical characteristics of the diodes were measured using a Keithley 4200A-SCS Parameter Analyzer. The main objectives of these measurements are to verify the diode's rectifying behavior, to determine the leakage current, and to measure the capacitance-voltage characteristics to determine the doping profile of the diode.

Hence, a straightforward approach to studying electrical contact performance before exposure to radiation is to measure the I-V characteristics as a function of the applied voltage. The resulting I-V curve presented in Fig. 3.35 displays the typical rectifying junction diode behavior with a leakage current of 10 nA in reverse bias.

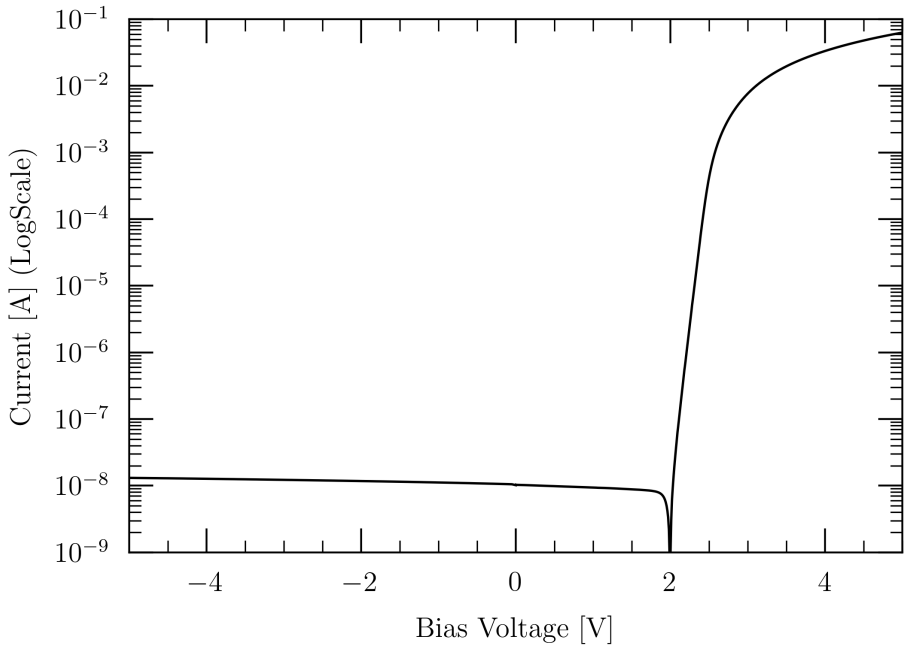

Fig. 3.35. Current-Voltage characteristics behaviour for reverse up to forward polarization for the 60 µm thick device. Data obtained using a Keithley 4200A-SCS Parameter Analyzer.

When a diode is forward-biased, the current voltage relationship does not show a sharp change at 0 V. Instead, the diode requires a certain forward voltage to overcome the potential barrier and allow current to flow significantly as seen in the reverse bias with Fig. 3.35. Hence, in forward bias, the I-V curve shows a region where the current starts to increase exponentially as the voltage exceeds the diode's forward voltage threshold. This exponential increase leads to a characteristic "knee" or "turn-on" voltage.

In the case of *pn* junction usually studied, with a very high doping acceptor atoms concentration and a low doped donor concentration, the space charge region can be assumed to be contained in the low doped substrate of type n. The capacitance-voltage characteristics are derived for an one-dimensional doping profile. Thus, the change in voltage and surface charge can be considered in the region of type p when the space charge region goes from x to $x + dx$. By integrating from $x = 0$ up to $x = W_{SCR}$, it comes the surface charge and surface voltage such that:

$$Q_p = -\int_0^{W_{SCR}} qN_D(x)\,dx \tag{3.58}$$

$$V_p = \int_0^{W_{SCR}} \frac{qN_D(x)}{\epsilon} x\,dx \tag{3.59}$$

With W_SCR, ϵ, N_A and N_D the previously defined quantities. For sake of clarity in the following derivative, W is used instead of W_{SCR} quantity.

The potential difference for the *p*-*n* junction is defined by the difference between the built-in voltage V_0 and the applied bias voltage V_r such that:

$$V = V_0 + V_r = \frac{kT}{q}\ln\left(\frac{N_A N_D}{{n_i}^2}\right) + V_r \tag{3.60}$$

The measured capacitance shown in Fig. 3.36 as a function of the applied bias voltage for the 60 µm *pn* junction can be expressed as a function of the charge Q_p such that:

$$C = \frac{\partial Q_p}{\partial V} = \frac{\partial Q_p/\partial W}{\partial V/\partial W} \tag{3.61}$$

Hence, computing the partial derivatives it comes:

$$\frac{\partial Q_p}{\partial W} = -qN_D(W) \tag{3.62}$$

$$\frac{\partial V}{\partial W} = -\frac{\partial V_p}{\partial W} + \frac{\partial V_r}{\partial W} = -\frac{qN_D(W)}{\epsilon}W + \frac{kT}{q}\frac{1}{N_D(W)}\frac{\partial N_D}{\partial W} \tag{3.63}$$

It comes then, since the variation of the built-in voltage is generally negligible regarding to the reverse bias voltage the expression of the capacitance such that:

$$C = \frac{\epsilon}{W} \tag{3.64}$$

Hence, looking at the variation of the inverse square of capacitance variation with the bias voltage, it gives the insight of the doping concentration. Indeed, neglecting once again the variation of V_0 with increasing W_{SCR}, it comes the equation characteristic doping concentration slope such that:

$$\frac{\partial(1/C^2)}{\partial V} = \frac{\partial(1/C^2)/\partial W}{\partial V/\partial W} \tag{3.65}$$

$$= \frac{2W/\epsilon^2}{qN_D W/\epsilon} \tag{3.66}$$

$$= \frac{2}{qN_D\epsilon} \tag{3.67}$$

Finally, the doping concentration at depth $x = W_{SCR}$ is then expressed such that:

$$N_D = \frac{2}{q\epsilon\,\partial(1/C^2)/\partial V} \tag{3.68}$$

The current diode manufactured during these project has been presented and electrically characterised in order to quantify the leakage current just as the doping concentration profile shown in Fig. 3.37. The measurements show a leakage current of 10 nA in reverse bias, and a doping concentration of few $1 \cdot 10^{13}$ cm^{-3} which is in agreement with the expected values for the diodes manufactured according to the uncertainties of the process provided by NOVASiC company, shown in Appendix C.

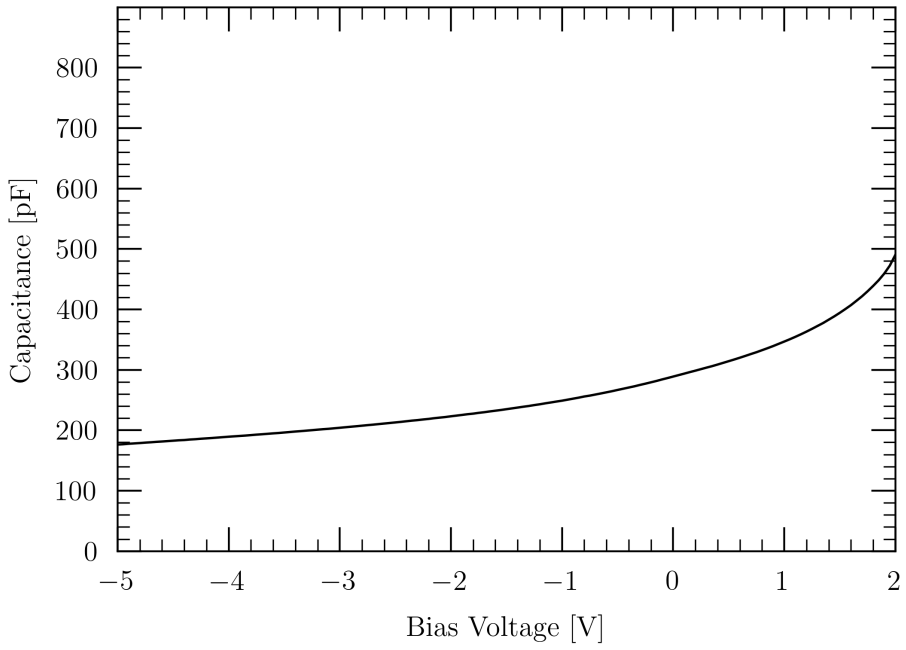

Fig. 3.36. Capacitance as a function of the applied bias voltage for the 60 µm *pn* junction. Data obtained using a Keithley 4200A-SCS Parameter Analyzer.

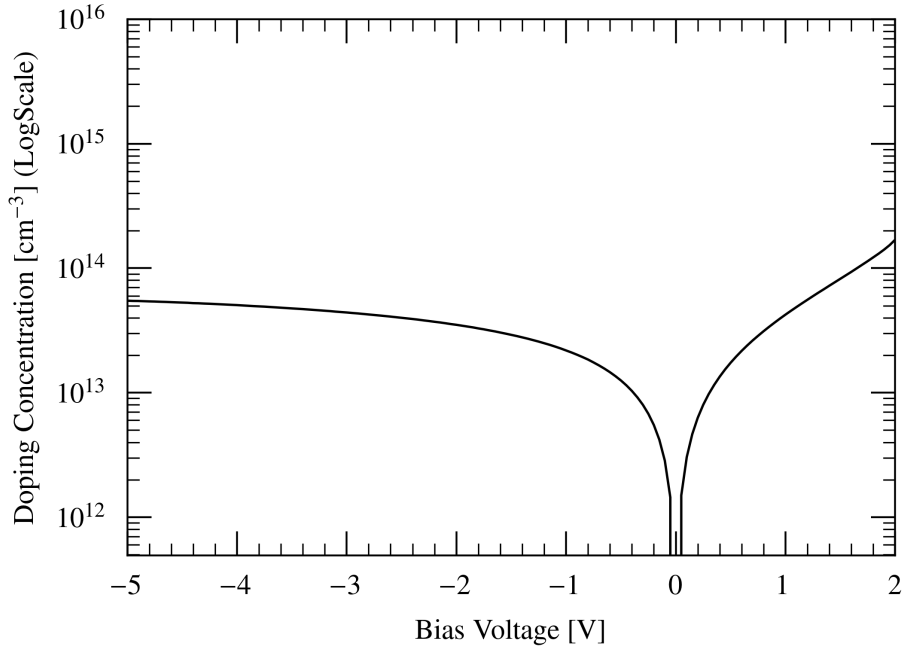

Fig. 3.37. Computed doping concentration as a function of the applied bias voltage for the 60 µm *pn* junction. Data obtained using a Keithley 4200A-SCS Parameter Analyzer.

3.4.3. Description of the detector

In order to ensure the best possible signal transmission, the sensor is encapsulated in a Polytetrafluoroethylene (PTFE) package as seen in the Fig. 3.38. The dimensions of the package are chosen to ensure a 50 ohm impedance matching with the coaxial cable such that the signal is not distorted during transmission. The dimensions considered are such that the ratio between the inner and outer diameters of the coaxial cable are in agreement with the following expression, obtained from the characteristic impedance of a coaxial line:

$$\frac{b}{a} = \exp\left(\frac{Z_0}{60}\sqrt{\frac{\epsilon_r}{\mu_r}}\right) \tag{3.69}$$

With Z_0 the characteristic impedance of the coaxial cable in [Ω], μ_r the relative permeability of the dielectric material in [H/m], ϵ_r the relative permittivity of the dielectric material in [F/m], a the inner diameter of the collection electrodes, b the outer diameter of the collection electrodes in [m].

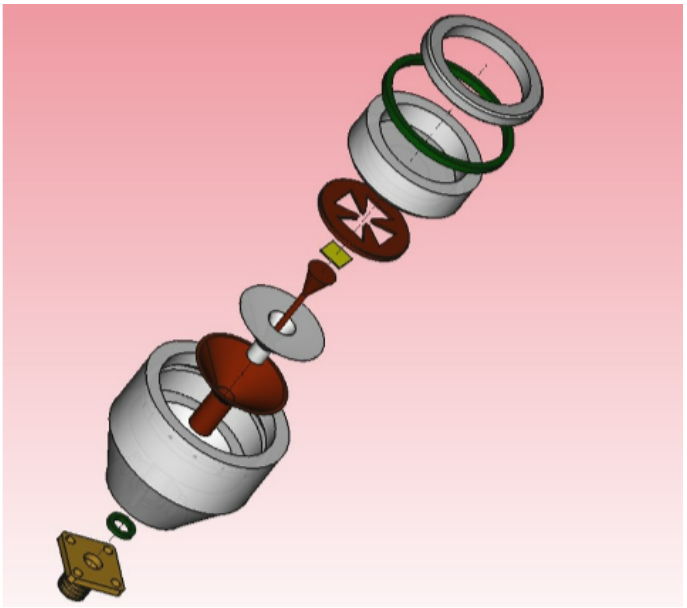

Fig. 3.38. Scheme of the encapsulated semiconductor sensor within PTFE insulator. From [126] design fabrication. The sensor is represente in yellow.

The manufacturing of the sensor is completed by the connection of the sensor to the acquisition chain. All the necessary steps have now been taken to proceed with data collection with the detector.

Conclusion

Finally after going through the environmental constraint in a first introductory chapter, the semiconductor devices has been presented. First intrinsic semiconductors parameters have been introduced, in order to compare materials in terms of characteristics evolution with external parameters related to experimental conditions. This preliminary discussion is mandatory for the choice of the most promising semiconducting material for the application of fast neutron detection in fusion and fission environment. Moreover design requirements to use it in a fast neutron field, as well as the technical specifications of the device under study were presented, leading to the selection of 4H–SiC as the most promising candidate for the application. Finally, the manufacturing process of the diodes was described, as well as the electrical characterisation of the diodes. Then, the use of such semiconductor based sensor as a radiation sensor was presented, introducing the prerequisites for the next Part of the manuscript which is about the estimation of the fast-neutron fluence rate, using such sensors.

This first Part, led to the selection of the most promising semiconductor material for the application of fast neutron detection in fusion and fission environments. Although the response of the sensor in such a field is complex, the advantages of using SiC as a sensor material have been highlighted. The next Part of this work is dedicated to the presentation of methodologies, experiments, and models developed to estimate the fast neutron flux using such sensors.

Part II.

Using a 4H-SiC sensor to estimate a fast neutron flux

4 Using a 4H-SiC sensor to estimate fast neutron flux in a mono-energy field 100

4.1 Study of the analytical model of neutron interactions in the sensor 100

4.2 Development of a numerical model to simulate the generation of secondary particles 121

4.3 Realization of a dedicated measurement campaign on a 14 MeV neutron generator 131

4.4 Validation of the charged particle transport modeling scheme in the sensor . . . 142

5 Using a SiC sensor to estimate fast neutrons flux in a multi-energy field 155

5.1 Complexity of the sensor response 155

5.2 Calibration method for the sensor response function 158

5.3 Review of numerical unfolding methods 160

5.4 ToF measurement campaign 163

5.5 ToF measurement results 168

5.6 Application of the deconvolution method and calculation versus experiment comparison 180

4. Using a 4H-SiC sensor to estimate fast neutron flux in a mono-energy field

In this chapter, the interactions between impinging fast neutrons and silicon carbide are presented. A first analytical model based on the kinematic study is provided to estimate the energy deposited by charged particles in the sensor. This is required in order to establish a numerical model to simulate the generation of secondary particles. Hypotheses and nuclear process used in the Monte-Carlo model are introduced. Then in order to estimate the fast neutron flux in a approximate mononoenergetic neutron field, the dedicated acquisition chain is presented as well as the associated experimental protocol. The experimental results are then discussed and compared with the numerical model ones. Finally, using the numerical model for experimental interpretation, the absolute flux value is obtained. The comparison with the reference value is discussed, providing a first quantitative measurement approach to obtain the integral value of a fast neutron flux and its uncertainties, as well as a a first evaluation of a 4H-SiC based sensor Monte-Carlo model.

4.1. Study of the analytical model of neutron interactions in the sensor

In Chapter 3, Section 3.3, dedicated to the use of the SiC as a radiation sensor, preliminary remarks were introduced in order to describe the indirect methods of neutron detection, through several neutron interactions involving a wide variety of charged particles. Such reactions, especially threshold energy reactions, must be clearly analyzed with the aim of using the deposited energy response spectra to quantify the fast neutron flux. The objective behind the calculative approach presented here is twofold:

- Firstly, to interpret experimental measurements of the energy deposited by the secondary charged particles generated
- Secondly, to validate the results at the output of the Monte-Carlo transport codes used to model the solid state sensor response.

To do this, the analytical model presented hereafter is based on reference data distributed by the National Nuclear Data Center (NNDC), which collects, evaluates and disseminates nuclear physics data for fundamental nuclear research and applied nuclear technologies. The demonstrations behind the solutions presented for the expressions of the various kinetic energies are available in the appendix. These have been re-demonstrated using reference works [127], enabling the mechanical characteristics of the particles to be calculated in the reference frames associated with the center of mass and the laboratory.

These reactions are all the more complex in that they are associated with different decay paths, with emission and settlement probabilities that also vary. Concerning the branching ratio for charged particles emissions, they are evaluated experimentally using nuclear reactions studies. In the following study about carbon neutron capture , reactions channels are based on a study conducted by Antolkovic and Dolenec [128]. They performed a kinematic analysis using nuclear emulsions and identified the contributing channels. Furthermore, they provided a quantitative discussion on the $C(n,n')3\alpha$ reaction channels in a separate publication [129]. These studies

involve measuring the energy spectra and intensities of emitted charged particles to deduce the relative probability of populating the different excited states of the residual nucleus.

But regarding the Isomeric Transition (IT), following neutron elastic scattering or neutron capture, the probability that a particular excited state will decay into a specific lower energy state or ground state via photon emission can be determined. For a given excited state j that decays via photo emission to a lower state i, the following branching ratio is computed:

$$b_{j\to i} = \frac{A_{j\to i}}{\sum_k A_{j\to k}} \tag{4.1}$$

With $A_{j\to i}$ the Einstein coefficient for the transition from state j to state i, and $\sum_k A_{j\to k}$ the total Einstein A coefficient for all possible transitions from state j to all lower states k.

The Einstein coefficients are related by definition to the half life of the excited state j as follows:

$$A_{j\to i} = \frac{1}{T_{1/2,j}} \tag{4.2}$$

With the excited state decay half-life defined as:

$$T_{1/2} = \frac{\hbar \cdot \ln 2}{\Gamma} \tag{4.3}$$

With $\hbar$ the reduced Planck constant such that $\hbar = h/2\pi$ with h equals to $6.62 \cdot 10^{-34}$ J$\cdot$s and Γ corresponding to the width at half maximum of the energy curve representing the probability of obtaining a particle with a specific energy during a decay.

Finally, the description of the several neutron reactions, listed in Table 4.1, is required to provide a better understanding of the sensor response to fast neutrons in order to interpret the experimental measurements of deposited energy in the sensor.

Reaction	Q value [MeV]	Branching ratio [%]	De-excitation mode	$T_{1/2}$ [fs]	Q value [MeV]	Products	Branching ratio [%]	De-excitation mode	$T_{1/2}$ [fs]	Q value [MeV]	Products
$^{28}Si(n,n)^{28}Si$	0	/	stable	/	/	/	/	/	/	/	/
$^{12}C(n,n')^{12}C^{(1^{st})*}$	-4.439	?	IT = 100%	42	4.439	$^{12}C^{(g.s)}+\gamma$	100	stable	/	/	/
$^{12}C(n,n')^{12}C^{(2^{nd})*}$	-7.654	4	IT = $4.16\cdot10^{-2}$% $\alpha\approx100$%	$4.9\cdot10^{-2}$	0.288	$^{8}Be^{(g.s)}+\boldsymbol{\alpha}$	100	$\alpha\approx100$%	$8.3\cdot10^{-2}$	0.09	$\boldsymbol{\alpha+\alpha}$
$^{12}C(n,n')^{12}C^{(3^{rd})*}$	-9.641	33	IT = $4.1\cdot10^{-5}$% $\alpha\approx100$%	$9.92\cdot10^{-6}$	2.275	$^{8}Be^{(g.s)}+\boldsymbol{\alpha}$	100	$\alpha\approx100$%	$8.3\cdot10^{-2}$	0.09	$\boldsymbol{\alpha+\alpha}$
$^{12}C(n,n')^{12}C^{(4^{th})*}$	-10.30	16	IT = $7.1\cdot10^{-6}$% $\alpha\approx100$%	$5.38\cdot10^{-7}$	2.934	$^{8}Be^{(g.s)}+\boldsymbol{\alpha}$ $^{8}Be^{(1^{st})*}+\boldsymbol{\alpha}$	50 50	$\alpha\approx100$%	$8.3\cdot10^{-2}$ $3.0\cdot10^{-7}$	0.09 3.12	$\boldsymbol{\alpha+\alpha}$
$^{12}C(n,n')^{12}C^{(5^{th})*}$	-10.847	6	?	$1.68\cdot10^{-7}$	3.481 0.451	$^{8}Be^{(g.s)}+\boldsymbol{\alpha}$ $^{8}Be^{(1^{st})*}+\boldsymbol{\alpha}$	69 31	$\alpha\approx100$%	$8.3\cdot10^{-2}$ $3.0\cdot10^{-7}$	0.09 3.12	$\boldsymbol{\alpha+\alpha}$
$^{12}C(n,n')^{12}C^{(6^{th})*}$	-12.71	4	$\alpha\approx100$%	$1.5\cdot10^{-7}$	5.344 2.314	$^{8}Be^{(g.s)}+\boldsymbol{\alpha}$ $^{8}Be^{(1^{st})*}+\boldsymbol{\alpha}$	32 68	$\alpha\approx100$%	$8.3\cdot10^{-2}$ $3.0\cdot10^{-7}$	0.09 3.12	$\boldsymbol{\alpha+\alpha}$
$^{12}C(n,\boldsymbol{\alpha})^{9}Be^{(1^{st})*}$	-7.386	24^{a}	IT = $1.4\cdot10^{-6}$% n ≈100%	$2.1\cdot10^{-6}$	0.02	$^{8}Be^{(g.s)}+n$	100	$\alpha\approx100$%	$8.3\cdot10^{-2}$	0.02	$\boldsymbol{\alpha+\alpha}$
$^{12}C(n,\boldsymbol{\alpha})^{9}Be^{(2^{nd})*}$	-8.131	-	IT = $1.2\cdot10^{-4}$% n > 7% $\alpha>1$%	$5.5\cdot10^{-4}$	0.765	$^{5}He^{(g.s)}+\boldsymbol{\alpha}$	100	$\alpha\approx100$% n =?%	0.704	0.735	$\boldsymbol{\alpha}+n$
$^{12}C(n,\boldsymbol{\alpha})^{9}Be^{(3^{rd})*}$	-8.482	-	n ≈100%	$4.1\cdot10^{-7}$	1.116	$^{8}Be^{(g.s)}+n$	100	$\alpha\approx100$%	$8.3\cdot10^{-2}$	0.09	$\boldsymbol{\alpha+\alpha}$
$^{12}C(n,\boldsymbol{\alpha})^{9}Be^{(4^{th})*}$	-8.751	-	IT = $1.0\cdot10^{-6}$% n > 87%	$4.1\cdot10^{-7}$	1.385	$^{8}Be^{(g.s)}+n$	100	$\alpha\approx100$%	$8.3\cdot10^{-2}$	0.09	$\boldsymbol{\alpha+\alpha}$
$^{12}C(n,\boldsymbol{\alpha})^{9}Be^{(5^{th})*}$	-10.406	13	IT = $1.6\cdot10^{-6}$% n < 100%	$6.1\cdot10^{-7}$	0.01	$^{8}Be^{(1^{st})*}+n$	100	$\alpha\approx100$%	$3\cdot10^{-7}$	3.12	$\boldsymbol{\alpha+\alpha}$
$^{12}C(n,\alpha)^{9}Be^{(g.s)*}$	-5.7	/	stable	/	/	/	/	/	/	/	/

[a] *For the sum of the branching ratio for the next four excited states of* ^{9}Be

Table 4.1. De-excitation modes of excited states of ^{9}Be and ^{12}C and associated half-life. Computations of branching-ratio are considering 14 MeV incident neutrons. Data are from NNDC. The bold characters highlight the three α particles emitted.

4.1.1. Carbon Neutron capture

4.1.1.1. Case of the fundamental state

As an illustration, lets take the reaction $C(n,\alpha)^9Be^*$ as an example in this paragraph. Then with the total energy conservation equation it comes:

$$m_n c^2 + E_{k_n} + m_{^{12}C}c^2 + E_{k_{^{12}C}} = m_\alpha c^2 + E_{k_\alpha} + m_{^9Be}c^2 + E_{k_{^9Be}} + E^*_{exc_{^9Be}} \tag{4.4}$$

With E_{k_i} and $m_i c^2$ respectively the kinetic energy and the rest mass of particle i, $E^*_{exc_{^9Be}}$ the excited state energy of ^9Be. Then, considering the target nucleus at rest, therefore with $E_{k_{^{12}C}} = 0$, it comes the following Q value expression:

$$Q = (m_n + m_{^{12}C} - m_\alpha - m_{^9Be})c^2 - E^*_{exc_{^9Be}} = E_{k_\alpha} + E_{k_{^9Be}} - E_{k_n} \tag{4.5}$$

In addition, considering the emission of ^9Be in fundamental state denoted $(g.s)$ for ground state with an associated alpha particle denoted α_0, it comes the total kinetic energy $E_{k_{tot.}}$ such that:

$$E_{k_{tot.}} = E_{k_{\alpha_0}} + E_{k_{^9Be^{(g.s)}}} = Q + E_{k_n} \tag{4.6}$$

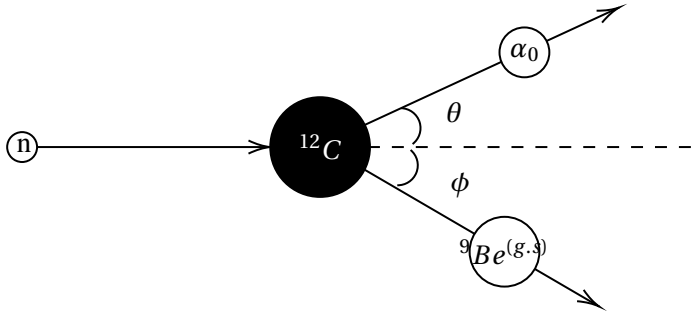

Fig. 4.1. Basic diagram of the $^{12}C(n,\alpha_0)^9Be^{(g.s)}$ two bodies reaction.

Considering the case of the two-body kinematic problem schematically depicted in Fig. 4.1, the equation for the heat of reaction Q as a function of the kinetic energies of the capture products and that of the incident neutron is computed. Then, by solving the second degree quadratic equation describing the relationship between a particle on its way out and the angle at which it is emitted, the energy associated with the reaction products as a function of the energy of the incident neutron is determined such that:

$$\sqrt{E_\alpha} = C \pm \sqrt{C^2 + B} \tag{4.7}$$

$$\begin{cases} C = \dfrac{\sqrt{E_n m_{\alpha_0}}}{m_{\alpha_0} + m_{Be^{(g.s)}}} \cdot cos(\theta) \\ \\ B = \dfrac{Q m_{Be^{(g.s)}} - (1 - m_{Be^{(g.s)}})E_n}{m_{\alpha_0} + m_{Be^{(g.s)}}} \end{cases} \tag{4.8}$$

With E_{α_0} and $E_{Be^{(g.s)}}$ then m_{α_0} and $m_{Be^{(g.s)}}$ respectively kinetic energy and mass of reaction products, and θ the emission angle of the α_0 particle emitted compared to the incident neutron direction. By performing numerical applications in the extreme case where $\theta = 0$ or $\theta = \pi$, the maximum values of the kinetic energy distributions of each of the reaction products are found as depicted in Table 4.2, according to the distribution shown in Fig. 4.2. This analytical description is then more simple in the case of the emission of charged particle in ground state since the

kinetic energy of the reaction products is then directly related to the energy of the incident neutron, without the need to take into account any transition energy level in decay.

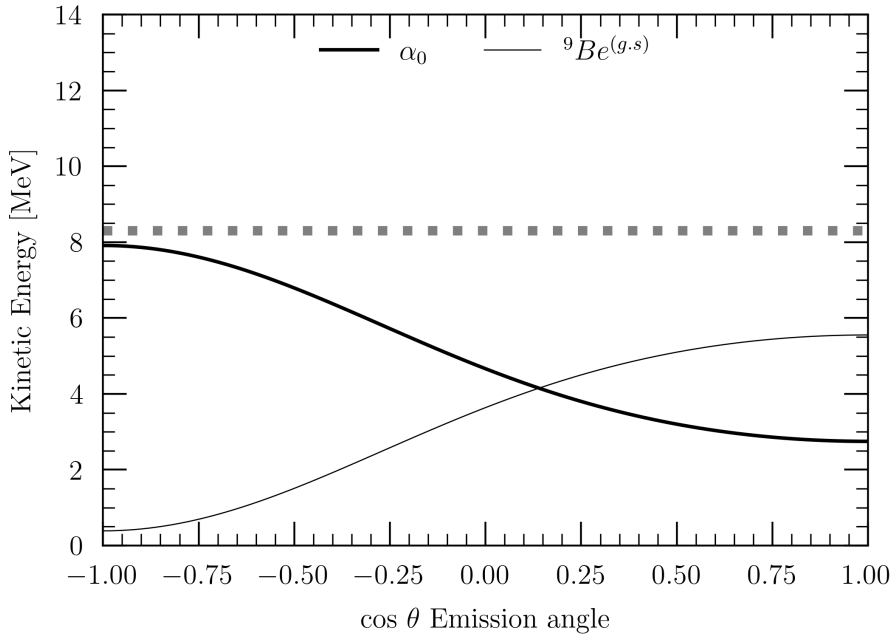

Fig. 4.2. Kinetic energy distribution of reaction products of $^{12}C(n,\alpha_0)^9Be^{(g.s)}$ for 14 MeV incident neutron, as a function of the emission angle of the produced particle, computed using (4.7). The dotted line represent the sum of the kinetic energy of the two reaction products.

	$E_{k_{min}}$ [MeV]	$E_{k_{max}}$ [MeV]
α_0	2.74	7.91
$^9Be^{(g.s)}$	0.39	5.55

Table 4.2. Minimum and maximum kinetic energy in [MeV] of reaction products $^{12}C(n,\alpha_0)^9Be^{(g.s)}$ for $\theta = 0$ or $\theta = \pi$ between the incident neutron direction and the emitted alpha, considering 14 MeV incident neutrons.

In order to understand the issues involved in studying the kinematic model, the hypothesis of a thick active detection zone for the SiC device is considered. Then the time $t_{part.}$ in [s] associated with the lifetime of the charged particles produced before being stopped can be approximated as the ratio of the projected range R_p in the device in [µm] and the velocity $v_{part.}$ in [m/s] of the particle such that:

$$t_{part.} = \frac{R_p}{\sqrt{2 \cdot \frac{E_k}{m}}} \tag{4.9}$$

This formula provides a rough estimate of the lifetime of the particle in the material based on its kinetic energy E_k and projected range. This estimation assesses that the particle energy loss is primarily due to ionization and that the material properties are homogeneous over the range of the particle. In reality, other factors such as scattering, nuclear reaction and non uniformities in the material could affect the actual lifetime of the particle. By considering the lower and upper bounds of the kinetic energy distribution of each of the products, the distances and travel times of the capture products are determined in Table 4.3.

	E_k [MeV]	$v_{part.}$ [m/s]	R_p [µm]	$t_{part.}$ [s]
α_0	7.91	$1.95 \cdot 10^7$	31.87	$1.63 \cdot 10^{-12}$
$^9Be^{(g.s)}$	0.39	$2.89 \cdot 10^6$	0.82	$2.83 \cdot 10^{-13}$
α_0	2.75	$1.15 \cdot 10^7$	6.99	$6.06 \cdot 10^{-13}$
$^9Be^{(g.s)}$	5.55	$1.09 \cdot 10^7$	5.62	$5.15 \cdot 10^{-13}$

Table 4.3. Comparison of distances and travel times of charged particles produced in their ground state by neutron capture $^{12}C(n,\alpha_0)^9Be^{(g.s)}$ in the case where the kinetic energy is maximum or minimum, for 14 MeV impinging neutron. Projected ranges data are obtained from SRIM calculation presented Section 3.3, Chapter 3.

The two charged particles produced travel a short distance in matter in sub-pico to picosecond duration, generating two clouds of charge carriers. These charges, created by ionization from beryllium and helium nuclei, are collected as a single cloud, resulting in a single current pulse. The experimental signal, which is the sum of these collected charge clouds, corresponds to the total kinetic energy of the two particles. This results in a single peak representing the energy deposited by the reaction $^{12}C(n,\alpha_0)^9Be^{(g.s)}$ in their ground state. This peak is commonly observed in the literature for sensors composed of carbon in a field of 14 MeV as observed with Fig. 4.3. This observation consistently occurs, independently of the kinetic energy distribution of the charged particles in their ground state. When all the kinetic energy from the reaction is released in the active zone, the response of the sensor correlates directly with the constant total kinetic energy of the reaction products. However, to know precisely the energy deposited in the sensor, it is necessary to study the individual processes of generation of charged particles leading to different kinetic energy distributions, for which the maximum and minimum values are depicted in Table 4.3.

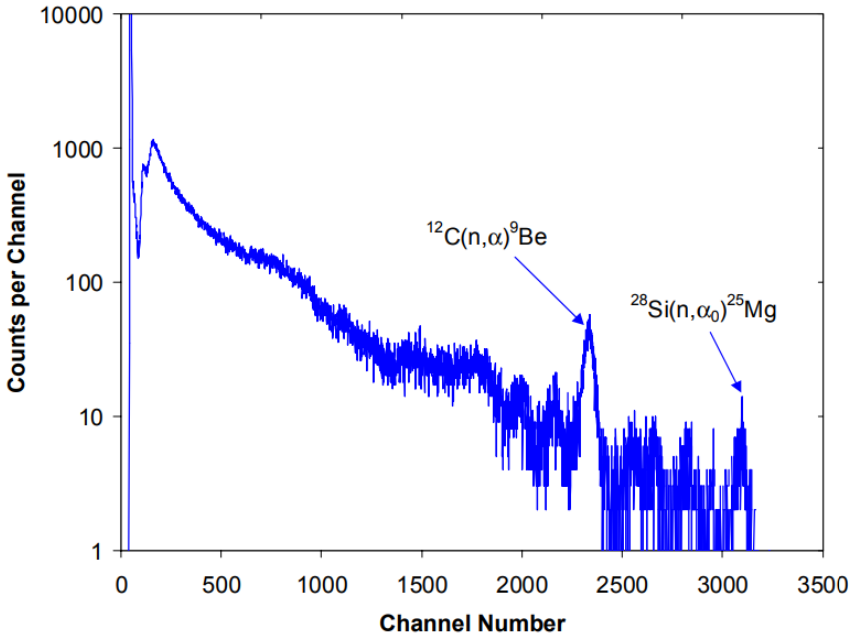

Fig. 4.3. Spectrum of the response of a SiC Schottky diode to 14 MeV neutrons [130].

4.1.1.2. Case of excited levels: sequential two-body decay

In this model, the incident neutron is incorporated into the target nucleus forming an unstable nucleus. In the following, the case of the first excited state of ^{9}Be is considered as a first example.

$$\begin{aligned} n + {}^{12}C \rightarrow {}^{9}Be^{(1^{st})*} + \alpha_a \\ \hookrightarrow {}^{8}Be^{(g.s.)} + n \\ \hookrightarrow \alpha_b + \alpha_c \end{aligned}$$

According to Table 4.1 the half-life of the first excited state of ^{9}Be is equals to $2.1 \cdot 10^{-6}$ fs. These excited states, with decay modes and associated branching ratios also listed in Table 4.1, decay in a very short time in ^{8}Be by emission of a neutron. Then in turn, the ^{8}Be will spontaneously decay into two α particles. Regarding the kinetic energy distribution of the 1st excited state, as for the ground state presented previously, by considering the case of the two-body kinematics problem, the equation of the heat of reaction Q is obtained as a function of the kinetic energies of the capture products. The total kinetic energy distribution of reaction products of the 1st excited state of $^{9}Be^{1^{st}*}$ can then be estimated, knowing the Q value associated such that $Q = -7.38$ MeV according to the first excited state energy level. Considering an incident neutron of 14 MeV, the maximum and minimum values of the kinetic energies of each of the products are shown in Table 4.4. The description of the distribution is this time more complex since the kinetic energy of the reaction products is not only related to the energy of the incident neutron and emission angle as for the ground state case, but also to the energy of the excited state of the daughter nucleus. And since the later can decay into different lower energy states or ground state, it leads to a more complex kinetic energy distribution. A proper description of the energy deposited in the sensor requires then to consider the different decay modes of the excited state, and associated branching ratio considering the half-life of the excited state to estimate the Einstein coefficient needed to compute the level diagram settlement probabilities.

Making the numerical applications in the limiting cases where $\theta = 0$ or $\theta = \pi$ the maximum and minimum values of the kinetic energies of each of the products are obtained according to Table 4.4.

	$E_{k_{min}}$ [MeV]	$E_{k_{max}}$ [MeV]
α_1	1.90	6.43
$^{9}Be^{(1^{st})*}$	0.19	4.72

Table 4.4. Minimum and maximum kinetic energy of reaction products $^{12}C(n,\alpha_1)^{9}Be^{(1^{st})*}$ for $\theta = 0$ or $\theta = \pi$, considering 14 MeV incident neutrons.

The $^{9}Be^{(1^{st})*}$ excited state de-excite by neutron emission and can only decay into the ground state of ^{8}Be, as shown in Table 4.1, such that:

$$Q = (m_{^{9}Be} - m_{^{8}Be} - m_n)c^2 + E^*_{exc._{^{9}Be}} \tag{4.10}$$

It comes:

$$^{9}Be^{(1^{st})*} \xrightarrow[T_{1/2} = 2.1 \cdot 10^{-6}\,\text{fs}]{\text{Q = -1.66 + 1.68 = 0.02 MeV}} {}^{8}Be^{(g.s)} + n \tag{4.11}$$

Taking the case where the kinetic energy of $^{9}Be^{1^{st}*}$ is maximal, the maximum total kinetic energy on the way out of (4.11) is then such that:

$$E_{k_{tot.max}} = Q + E_{k_{^{9}Be^{(1^{st})*}}} = 4.74\,\text{MeV}$$

Likewise for a minimum kinetic energy it comes $E_{k_{tot.max}}$ =0.21 MeV.

Considering a two bodies decay where the energy surplus Q is distributed between the two bodies. If $^{9}Be^{(1^{st})*}$ is at rest, the distribution of the energy between the two reaction products by conservation of the angular moments (4.12) is obtained such that:

$$m_{^{8}Be}v_{^{8}Be} = m_n v_n \tag{4.12}$$

$$E_{k_{^{8}_{Be}}} = E_{k_n}\left(\frac{m_n}{m_{^{8}Be}}\right) \tag{4.13}$$

The distribution of the kinetic energy of the decay products thus follows the ratio of the respective masses (4.13) of the nuclei of ^{8}Be and neutrons such as:

$$E_{k_{^{8}_{Be}}} = Q\cdot\frac{m_n}{m_{^{8}Be}+m_n} \quad \text{and} \quad E_{k_n} = Q\cdot\frac{m_{^{8}Be}}{m_{^{8}Be}+m_n} \tag{4.14}$$

However, considering the emission of $^{9}Be^{(1^{st})*}$ endowed with kinetic energy such that $E_{k_{^{9}_{Be^{(1^{st})*}}}}$ =4.72 MeV, according to Table 4.4, equally distributed between the two decay products (4.15). The following kinetic energies $E_{k_{^{8}_{Be}}}$ and E_{k_n} are then obtained as a function of the emission angles θ and ϕ and the energy of the particle in its excited state which decays such that:

$$\begin{cases} E_{k_n} = \dfrac{m_{^{8}Be}}{m_{^{9}Be}}Q\cdot\left(1+\left(\dfrac{m_n}{m_{^{8}Be}Q}E_{k_{^{9}Be}}\right)+2\left(\dfrac{m_n}{m_{^{8}Be}Q}E_{k_{^{9}Be}}\right)^{1/2}cos(\theta)\right) \\ E_{k_{^{8}_{Be}}} = \dfrac{m_n}{m_{^{9}Be}}Q\cdot\left(1+\left(\dfrac{m_{^{8}Be}}{m_nQ}E_{k_{^{9}Be}}\right)+2\left(\dfrac{m_{^{8}Be}}{m_nQ}E_{k_{^{9}Be}}\right)^{1/2}cos(\phi)\right) \end{cases} \tag{4.15}$$

Numerical application, in the upper boundary for the kinetic energy for the decay (4.11) :

$$E_{k_{^{8}_{Be}}} = 4.29\,\text{MeV} \quad \text{and} \quad E_{k_n} = 0.45\,\text{MeV}$$

Then since $^{8}Be^{(g.s)}$ is unstable, it decays spontaneously by emission of two α particles as detailed in Table 4.1 such that:

$$Q = (m_{^{8}Be^{(g.s)}} - m_\alpha - m_\alpha)c^2 \tag{4.16}$$

It comes then:

$$^{8}Be \xrightarrow[T_{1/2}=8.3\cdot10^{-2}\,\text{fs}]{\text{Q = + 0.09 MeV}} \alpha_b + \alpha_c \tag{4.17}$$

Numerical application, still in the cases of upper boundaries:

$$E_{k_{\alpha_b}} = 2.39\,\text{MeV} \quad \text{and} \quad E_{k_{\alpha_c}} = 1.78\,\text{MeV}$$

The energy deposited on the way out of the reaction $^{12}C(n,\alpha_1)^{9}Be^{(1^{st})*}$ is therefore intrinsically linked to the distribution of the energy of the scattered neutron. This is the reason why no defined peak, representative of the emission of a $^{9}Be^{*}$ in first excited state with an associated α is experimentally observed as seen previously in Fig. 4.3.

Analogical reasoning is carried out for the other aroused states of the $^{9}Be^{*}$ which can decay by neutron emission emitting ^{8}Be in its ground state such that:

$$^{9}Be^{(2^{nd})*} \xrightarrow{\text{Q = -1.66 + 2.43 = 0.77 MeV}} {}^{8}Be^{(g.s)} + n \tag{4.18}$$

$$^{9}Be^{(3^{rd})*} \xrightarrow{\text{Q = -1.66 + 2.78 = 1.12 MeV}} {}^{8}Be^{(g.s)} + n \tag{4.19}$$

$$^{9}Be^{(4^{th})*} \xrightarrow{\text{Q = -1.66 + 3.05 = 1.39 MeV}} {}^{8}Be^{(g.s)} + n \tag{4.20}$$

Hence, studying the case of neutron de-excitation of ^{9}Be emitted in its first four excited states in Table 4.5, or the Hoyle state decaying into ^{8}Be in its ground state in Table 4.6, or in its first

excited state in Table 4.7, it is seen with that the kinetic energy of the three alphas emitted is widely distributed. Moreover, considering the sum of the kinetic energy of these alphas — which corresponds to the maximum energy that can be deposited in the sensor when the detection thickness is sufficient — the kinetic energy distribution goes from few MeV to almost 7 MeV. This first distribution explains a part of the continuum observed experimentally in Fig. 4.3.

	$E_{k_{\alpha_a}}$	$E_{k_{^9Be}}$	$E_{k_{^8Be^{(g.s)}}}$	E_{k_n}	$E_{k_{\alpha_b}}$	$E_{k_{\alpha_c}}$	$\sum E_k$
$^{12}C(n,\alpha)^9Be^{(g.s)}$	7.91 2.75	0.39 5.55	/	/	/	/	8.3
$^{12}C(n,\alpha)^9Be^{(1^{st})*}$	1.9	4.71	4.28	0.45	{2.5, 1.88}	{1.87, 2.5}	6.27
			4.09	0.64	{2.39, 1.79}	{1.79, 2.39}	6.08
	6.42	0.19	0.19	0.02	{0.21, 0.08}	{0.08, 0.21}	6.71
			0.15	0.06	{0.18, 0.06}	{0.06, 0.18}	6.66
$^{12}C(n,\alpha)^9Be^{(3^{rd})*}$	1.38	4.14	4.48	0.78	{2.60, 1.97}	{1.97, 2.60}	5.95
			3.12	2.13	{1.87, 1.34}	{1.34, 1.87}	4.59
	5.43	0.09	0.31	0.90	{0.28, 0.12}	{0.12, 0.28}	5.83
			0.11	1.10	{0.15, 0.05}	{0.05, 0.15}	5.63
$^{12}C(n,\alpha)^9Be^{(4^{th})*}$	1.26	3.99	4.44	0.94	{2.58, 1.95}	{1.95, 2.58}	5.79
			2.96	2.42	{1.78, 1.27}	{1.27, 1.78}	4.31
	5.18	0.07	0.32	1.14	{0.29, 0.12}	{0.12, 0.29}	5.59
			0.12	1.34	{0.16, 0.05}	{0.05, 0.16}	5.39
	$E_{k_{\alpha_a}}$	$E_{k_{^9Be}}$	$E_{k_{^8Be^{(1^{st})*}}}$	E_{k_n}	$E_{k_{\alpha_b}}$	$E_{k_{\alpha_c}}$	$\sum E_k$
$^{12}C(n,\alpha)^9Be^{(5^{th})*}$	0.55	3.05	2.76	0.295	{4.41, 1.47}	{1.47, 4.41}	6.43
			2.65	0.405	{4.32, 1.45}	{1.45, 4.32}	6.32
	3.59	$1\cdot10^{-4}$	0.002	0.009	{1.60, 1.52}	{1.52, 1.60}	6.71
			0.001	0.009	{1.59, 1.53}	{1.53, 1.59}	6.71

Table 4.5. Minimum and maximum kinetic energy in [MeV] of reaction products of $^{12}C(n,\alpha)^9Be^*$ and intermediate states for $\theta = 0$ or $\theta = \pi$ for 14 MeV impinging neutrons, in the case where ^9Be is emitted.

	$E_{k_{n'}}$	$E_{k_{^{12}C}}$	$E_{k_{^{8}Be^{(g.s)}}}$	$E_{k_{\alpha}}$	$E_{k_{\alpha_b}}$	$E_{k_{\alpha_c}}$	$\sum E_k$
$^{12}C(n,n')^{12}C^{(2^{nd})*}$	3.66	2.69	2.30	0.67	$\begin{cases}1.42\\0.97\end{cases}$	$\begin{cases}0.97\\1.42\end{cases}$	3.06
			1.47	1.50	$\begin{cases}0.96\\0.60\end{cases}$	$\begin{cases}0.60\\0.96\end{cases}$	3.06
	6.21	0.13	0.27	0.14	$\begin{cases}0.26\\0.10\end{cases}$	$\begin{cases}0.10\\0.26\end{cases}$	0.5
			0.09	0.33	$\begin{cases}0.14\\0.05\end{cases}$	$\begin{cases}0.05\\0.14\end{cases}$	0.5
$^{12}C(n,n')^{12}C^{(3^{rd})*}$	2.10	2.26	3.33	1.20	$\begin{cases}1.99\\1.44\end{cases}$	$\begin{cases}1.44\\1.99\end{cases}$	4.63
			1.20	3.34	$\begin{cases}0.81\\0.48\end{cases}$	$\begin{cases}0.48\\0.81\end{cases}$	4.63
	4.11	0.25	1.28	1.24	$\begin{cases}0.86\\0.52\end{cases}$	$\begin{cases}0.52\\0.86\end{cases}$	2.62
			0.57	1.96	$\begin{cases}0.44\\0.22\end{cases}$	$\begin{cases}0.22\\0.44\end{cases}$	2.62
$^{12}C(n,n')^{12}C^{(4^{th})*}$	1.60	2.10	3.55	1.49	$\begin{cases}2.10\\1.54\end{cases}$	$\begin{cases}1.54\\2.10\end{cases}$	5.13
			1.21	3.83	$\begin{cases}0.81\\0.48\end{cases}$	$\begin{cases}0.48\\0.81\end{cases}$	5.13
	3.40	0.30	1.62	1.61	$\begin{cases}1.05\\0.66\end{cases}$	$\begin{cases}0.66\\1.05\end{cases}$	3.32
			0.74	2.50	$\begin{cases}0.54\\0.28\end{cases}$	$\begin{cases}0.28\\0.54\end{cases}$	3.32
$^{12}C(n,n')^{12}C^{(5^{th})*}$	1.19	1.96	3.70	1.74	$\begin{cases}2.18\\1.61\end{cases}$	$\begin{cases}1.61\\2.18\end{cases}$	5.53
			1.24	4.2	$\begin{cases}0.83\\0.50\end{cases}$	$\begin{cases}0.50\\0.83\end{cases}$	5.53
	2.79	0.36	1.93	1.93	$\begin{cases}1.22\\0.80\end{cases}$	$\begin{cases}0.80\\1.22\end{cases}$	3.94
			0.87	2.97	$\begin{cases}0.62\\0.34\end{cases}$	$\begin{cases}0.34\\0.62\end{cases}$	3.94
$^{12}C(n,n')^{12}C^{(6^{th})*}$	0.02	1.27	3.85	2.76	$\begin{cases}2.27\\1.68\end{cases}$	$\begin{cases}1.68\\2.27\end{cases}$	6.7
			1.40	5.21	$\begin{cases}0.92\\0.57\end{cases}$	$\begin{cases}0.57\\0.92\end{cases}$	6.7
	0.53	0.76	3.24	2.86	$\begin{cases}1.94\\1.40\end{cases}$	$\begin{cases}1.40\\1.94\end{cases}$	6.2
			1.34	4.77	$\begin{cases}0.89\\0.54\end{cases}$	$\begin{cases}0.54\\0.89\end{cases}$	6.2

Table 4.6. Minimum and maximum kinetic energy in [MeV] of reaction products of $^{12}C(n,n')^{12}C^*$ and intermediate states for $\theta = 0$ or $\theta = \pi$ for 14 MeV impinging neutrons, in the case where ^{12}C is emitted in Hoyle state and decay by alpha emission.

	$E_{k_{n'}}$	$E_{k_{^{12}C}}$	$E_{k_{^8Be^{(1st)*}}}$	E_{k_α}	$E_{k_{\alpha_b}}$	$E_{k_{\alpha_c}}$	$\sum E_k$
$^{12}C(n,n')^{12}C^{(4^{th})*}$	1.60	2.10	1.42	0.68	3.32 1.22	1.22 3.32	5.22
			1.38	0.72	3.29 1.21	1.21 3.29	5.22
	3.40	0.30	0.21	0.09	2.07 1.26	1.26 2.07	3.42
			0.19	0.11	2.04 1.27	1.27 2.04	3.42
$^{12}C(n,n')^{12}C^{(5^{th})*}$	1.19	1.96	1.9	0.51	3.73 1.29	1.29 3.73	5.53
			1.01	1.40	2.96 1.18	1.18 2.96	5.53
	2.79	0.36	0.58	0.23	2.52 1.18	1.18 2.52	3.93
			0.2	0.61	2.06 1.27	1.27 2.02	3.93
$^{12}C(n,n')^{12}C^{(6^{th})*}$	0.02	1.27	2.43	1.16	4.15 1.40	1.40 4.15	6.70
			0.81	2.77	2.76 1.17	1.17 2.76	6.70
	0.53	0.76	1.91	1.17	3.73 1.29	1.29 3.73	6.19
			0.65	2.42	2.60 1.17	1.17 2.60	6.19
	$E_{k_{\alpha a}}$	$E_{k_{^9Be}}$	$E_{k_{^5He^{(g.s)}}}$	$E_{k_{\alpha_b}}$	$E_{k_{\alpha_c}}$	E_{k_n}	$\sum E_k$
$^{12}C(n,\alpha)^9Be^{(2^{nd})*}$	1.54	4.33	3.65	1.44	3.72 2.41	0.67 1.98	6.70 5.39
			1.84	3.25	2.08 1.15	0.49 1.42	6.87 5.94
	5.75	0.12	0.56	0.33	0.85 0.34	0.44 0.96	6.93 6.42
			0.26	0.63	0.53 0.18	0.47 0.81	6.91 6.56

Table 4.7. Minimum and maximum kinetic energy in [MeV] of reaction products of $^{12}C(n,n')^{12}C^*$ and intermediate states for $\theta = 0$ or $\theta = \pi$ for 14 MeV impinging neutrons, in the case when the products decay by emitting a particle in excited state.

Regarding this analytical study which led to the computation of the kinetic energy distribution boundaries of the reaction products from sequential decay of carbon nuclei, two conclusions can be drawn:

- The sensor response to this nuclear capture reaction is complex with various kinetic energy distributions according to the emission angle and the decay pathway, as displayed in Fig. 4.4 for the decay modes described in Table 4.1. But, it does not represent a limit for the interpretation of the experimental results, since the only available output data corresponds to the amount of collected charged produced by the ionization of the active zone by all the charged particles generated. In other words, the experiment sensor response is directly related to the sum of the kinetic energies of three alpha particles emitted, regardless the decay pathway.
- However, the development of a modeling scheme requires particular caution, since the description of the several decay-mode pathway exhibits a complex sequential decay with branching ratio still discussed in the literature today [131].

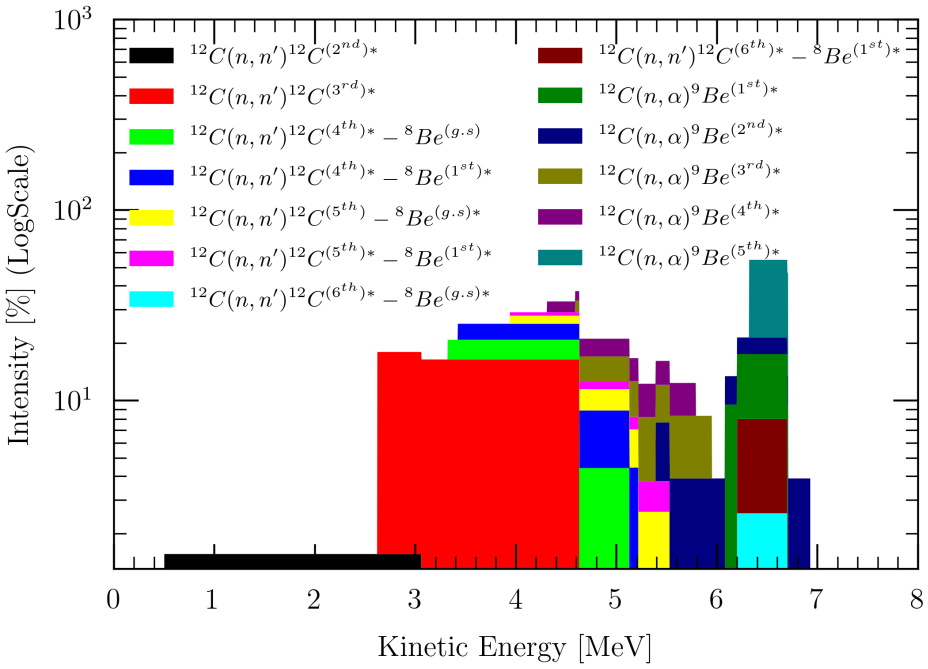

Fig. 4.4. Kinetic energy distribution obtained analytically for the reactions leading to the emission of three alphas, considering 14 MeV impinging neutrons. The distributions are obtained for the different excited states of the ^{9}Be and ^{8}Be. The sum of the kinetic energies of the three alpha particles is displayed for each pathway, and normalized according to the branching ratio regarding Table 4.1.

4.1.2. Silicon neutron inelastic scattering

In the case of the neutrons reactions with silicon, the branching ratio is also determined experimentally. The following study is based on the last evaluations of the NNDC [132] using ENDFB-VIII.0 [133] library. The latter provides the probability of populating the different excited states of the residual nucleus, as well as the probability of decay of these excited states. All these data are summarized in Table 4.8, according to the several decay pathways of the excited states as depicted in the comparison of the individual and total cross sections of the $^{28}Si(n,n')^{28}Si^{*}$ reaction in Fig. 4.5.

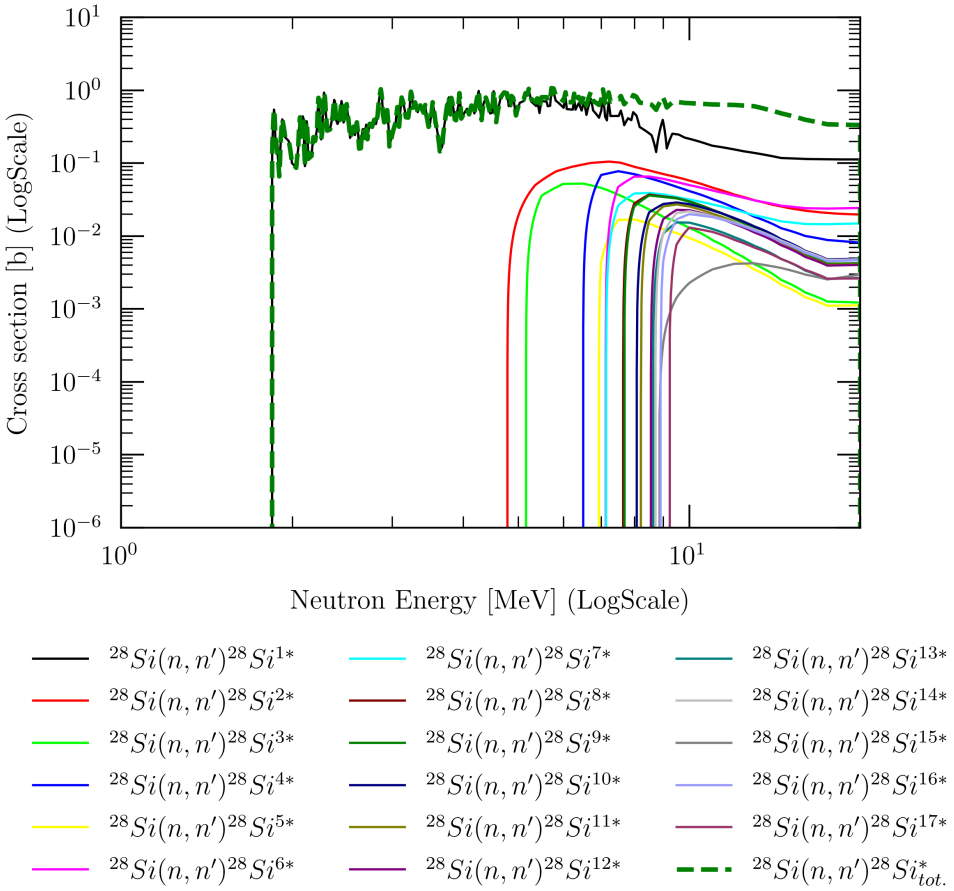

Fig. 4.5. Comparison of the individuals and total cross sections of the $^{28}Si(n,n')^{28}Si^{*}$ reaction [133].

The kinetic energy of the recoil nucleus can be estimated analytically using the previously introduced two-body kinematics problem, and taking into account the different pathway depicted in Fig. 4.5 and summarized in Table 4.8. These information give also the possibility to compute the photon emission energy of the decay of the excited states of the recoiled nucleus. For sake of simplicity, only the first IT decay is considered in the following in the presentation of the analytical approach of the kinetic energy distribution of the reaction products. Hence only the decay leading to the emission of a recoil in the ground state are considered which are displayed in Table 4.8 with a grey cell color background.

Reaction	Q value [MeV]	Branching ratio [%]	$T_{1/2}$ [fs]	$E_{k_{n'}}$	$E_{k_{^{28}Si}}$	Q value [MeV]	Products	Branching ratio [%]	$\sum E_k$
$^{28}Si(n,n')^{28}Si^{(1^{st})*}$	-1.779	23.82	475	10.5 12.2	1.7 0.002	1.779	$^{28}Si^{(g.s)}+\gamma$	100	1.7 0.002
$^{28}Si(n,n')^{28}Si^{(2^{nd})*}$	-4.617	5.15	37			2.838	$^{28}Si^{(1^{st})*}+\gamma$	100	
$^{28}Si(n,n')^{28}Si^{(3^{rd})*}$	-4.979	0.58	35			3.2	$^{28}Si^{(1^{st})*}+\gamma$	100	
$^{28}Si(n,n')^{28}Si^{(4^{th})*}$	-6.276	2.81	780			1.659 4.497	$^{28}Si^{(2^{nd})*}+\gamma$ $^{28}Si^{(1^{st})*}+\gamma$	11.8 88.2	
$^{28}Si(n,n')^{28}Si^{(5^{th})*}$	-6.69	0.50	147			4.911	$^{28}Si^{(1^{st})*}+\gamma$	100	
$^{28}Si(n,n')^{28}Si^{(6^{th})*}$	-6.878	5.30	$1.9\cdot10^{3}$	5.76 7.08	1.36 0.042	2.261 5.099 6.878	$^{28}Si^{(2^{nd})*}+\gamma$ $^{28}Si^{(1^{st})*}+\gamma$ $^{28}Si^{(g.s)}+\gamma$	2.7 27.3 70	1.36 0.042
$^{28}Si(n,n')^{28}Si^{(7^{th})*}$	-6.887	3.26	33			2.27 5.108	$^{28}Si^{(2^{nd})*}+\gamma$ $^{28}Si^{(1^{st})*}+\gamma$	1.3 98.7	
$^{28}Si(n,n')^{28}Si^{(8^{th})*}$	-7.38	1.86	5	5.30 6.57	1.32 0.05	2.763 5.601 7.380	$^{28}Si^{(2^{nd})*}+\gamma$ $^{28}Si^{(1^{st})*}+\gamma$ $^{28}Si^{(g.s)}+\gamma$	0.3 63.4 36.3	1.32 0.05
$^{28}Si(n,n')^{28}Si^{(9^{th})*}$	-7.416	1.85	29	5.27 6.53	1.31 0.05	5.637 7.416	$^{28}Si^{(1^{st})*}+\gamma$ $^{28}Si^{(g.s)}+\gamma$	6 94	1.31 0.05
$^{28}Si(n,n')^{28}Si^{(10^{th})*}$	-7.799	2.02	225			0.921 1.523 3.182 6.02	$^{28}Si^{(6^{th})*}+\gamma$ $^{28}Si^{(4^{th})*}+\gamma$ $^{28}Si^{(2^{nd})*}+\gamma$ $^{28}Si^{(1^{st})*}+\gamma$	0.1 32.6 1.3 66	
$^{28}Si(n,n')^{28}Si^{(11^{th})*}$	-7.933	1.74	11	4.80 6.01	1.27 0.06	1.657 2.954 3.316 6.154 7.933	$^{28}Si^{(4^{th})*}+\gamma$ $^{28}Si^{(3^{rd})*}+\gamma$ $^{28}Si^{(2^{nd})*}+\gamma$ $^{28}Si^{(1^{st})*}+\gamma$ $^{28}Si^{(g.s)}+\gamma$	2.4 4 4.7 5.5 83.4	1.27 0.06
$^{28}Si(n,n')^{28}Si^{(12^{th})*}$	-8.258	1.67	10	4.50 5.68	1.24 0.07	3.279 3.641 6.479 8.258	$^{28}Si^{(3^{rd})*}+\gamma$ $^{28}Si^{(2^{nd})*}+\gamma$ $^{28}Si^{(1^{st})*}+\gamma$ $^{28}Si^{(g.s)}+\gamma$	17 4 70 9	1.24 0.07
$^{28}Si(n,n')^{28}Si^{(13^{rd})*}$	-8.328	1.09	347	4.44 5.60	1.23 0.068	2.052 6.549 8.328	$^{28}Si^{(4^{th})*}+\gamma$ $^{28}Si^{(1^{st})*}+\gamma$ $^{28}Si^{(g.s)}+\gamma$	16 26 58	1.23 0.068
$^{28}Si(n,n')^{28}Si^{(14^{th})*}$	-8.413	1.89	324			1.535 3.796 6.634	$^{28}Si^{(6^{th})*}+\gamma$ $^{28}Si^{(2^{nd})*}+\gamma$ $^{28}Si^{(1^{st})*}+\gamma$	80.1 2.8 17.1	
$^{28}Si(n,n')^{28}Si^{(15^{th})*}$	-8.543	0.73	11.4			3.926	$^{28}Si^{(2^{nd})*}+\gamma$	100	
$^{28}Si(n,n')^{28}Si^{(16^{th})*}$	-8.588	1.82	11			0.789 1.701 2.312 3.971 6.809	$^{28}Si^{(10^{th})*}+\gamma$ $^{28}Si^{(7^{th})*}+\gamma$ $^{28}Si^{(4^{th})*}+\gamma$ $^{28}Si^{(2^{nd})*}+\gamma$ $^{28}Si^{(1^{st})*}+\gamma$	0.5 0.3 6.9 4.3 88	
$^{28}Si(n,n')^{28}Si^{(17^{th})*}$	-8.904	1.06	8	3.92 5.01	1.18 0.08	7.125 8.904	$^{28}Si^{(1^{st})*}+\gamma$ $^{28}Si^{(g.s)}+\gamma$	52.9 47.1	1.18 0.08

Table 4.8. IT de-excitation modes of excited states of ^{28}Si and associated half-life. The last column shows the sum of the kinetic energy of the produced particles. Computations are considering 14 MeV incident neutrons. Data are from NNDC [132].

Therefore, the kinetic energy of the reaction products of the $^{28}Si(n,n')^{28}Si^*$ reaction is distributed according to the different excited states of the residual nucleus, from few keV up to 1.7 MeV for the first excited state as shown in Fig. 4.6. Even if the angular distribution of the emitted particles is not considered in this schematic analytical approach, it is pointed out that the amount of kinetic energy released in the the matter comes mainly from the recoiled nucleus emitted in the first excited state. Considering a 14 MeV incident neutron, regarding the branching ratio, it means that almost 24% of the kinetic energy released with the $^{28}Si(n,n')^{28}Si^*$ reaction is consecutive to the emission of the recoiled nucleus in the first excited state, associated with a photon of 1.779 MeV as displayed in Fig. 4.6 and Fig. 4.7. Therefore, it is expected that the response function of the sensor within a monoenergetic field of 14 MeV neutrons will exhibit a peak complex distribution for the lower energy bins.

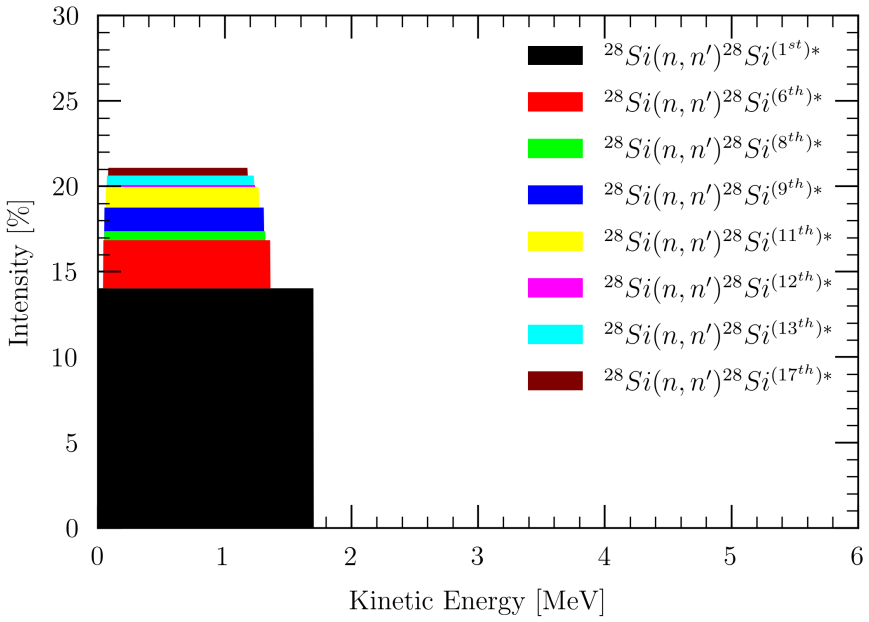

Fig. 4.6. Kinetic Energy distributions obtained analytically for several inelastic neutron scattering on ^{28}Si leading to the emission of a recoiled nucleus in excited state that decays directly into the ground state.

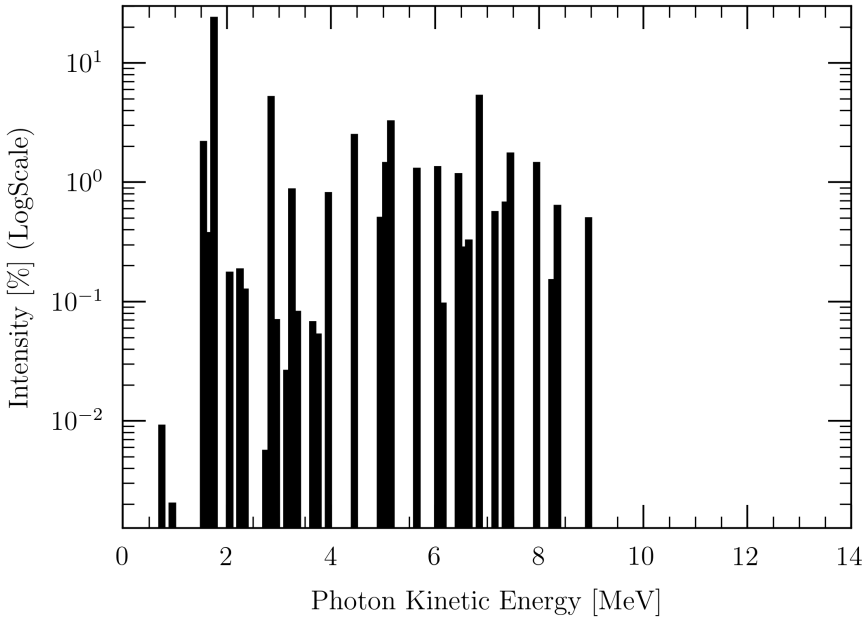

Fig. 4.7. Photon emission energy distribution obtained analytically for the first IT decay of the excited states of ^{28}Si.

4.1.3. Silicon neutron captures

The same approach is adopted regarding the silicon neutron capture reactions below:

$$n + {}^{28}\mathrm{Si} \rightarrow {}^{25}\mathrm{Mg}^{*} + \alpha \hookrightarrow \gamma \qquad n + {}^{28}\mathrm{Si} \rightarrow {}^{28}\mathrm{Al}^{*} + p \hookrightarrow \gamma$$

The description of silicon neutron capture is simpler than the previous carbon neutron capture description regarding the kinematic of the reaction products, with a nucleus emitted in excited state which decays by emitting a gamma. But the description of decay paths is particularly thorny due to the numerous excited states of the residual nucleus. Indeed, whether for the $^{28}Si(n,\alpha)^{25}Mg$ or $^{28}Si(n,p)^{28}Al$ reactions, the excited states of the emitted particle can decay into different lower energy excited states or ground state, leading to a more complex kinetic energy distribution due to the different branching ratios as depicted respectively in Fig. 4.8 and Fig. 4.9 with the evaluated cross sections from ENDFB-VIII.0 [133]. It should be noticed that all the excited states of the residual nuclei are not considered in the following, since nuclear data are not available for all of them. Then, as explained previously, the kinetic energy of the reaction products is distributed according to the emission angle and the energy of the excited state of the emitted particle. The results of the analytical approach are displayed in Table 4.9 and Table 4.10 for the $^{28}Si(n,\alpha)^{25}Mg$ and $^{28}Si(n,p)^{28}Al$ reactions respectively. Considering the maximum kinetic energy released in the matter as the sum of the kinetic energies of the two reaction products, discrete values are obtained for each excited state of the emitted particles with branching ratio computed with the transition probabilities. All things considered, it has been shown, even in the simple case of monoenergetic incident neutrons of 14 MeV, that the kinetic energy distribution of the reaction products is complex and widely distributed. In practice, while excited state emissions can de-excite to the ground state, resulting in defined energy peaks, the reality is more complex. The numerous and successive decay pathways of the excited states leading to the emission of several gammas, make the interpretation of the sensor response intricate, with an expected continuum in the energy distribution.

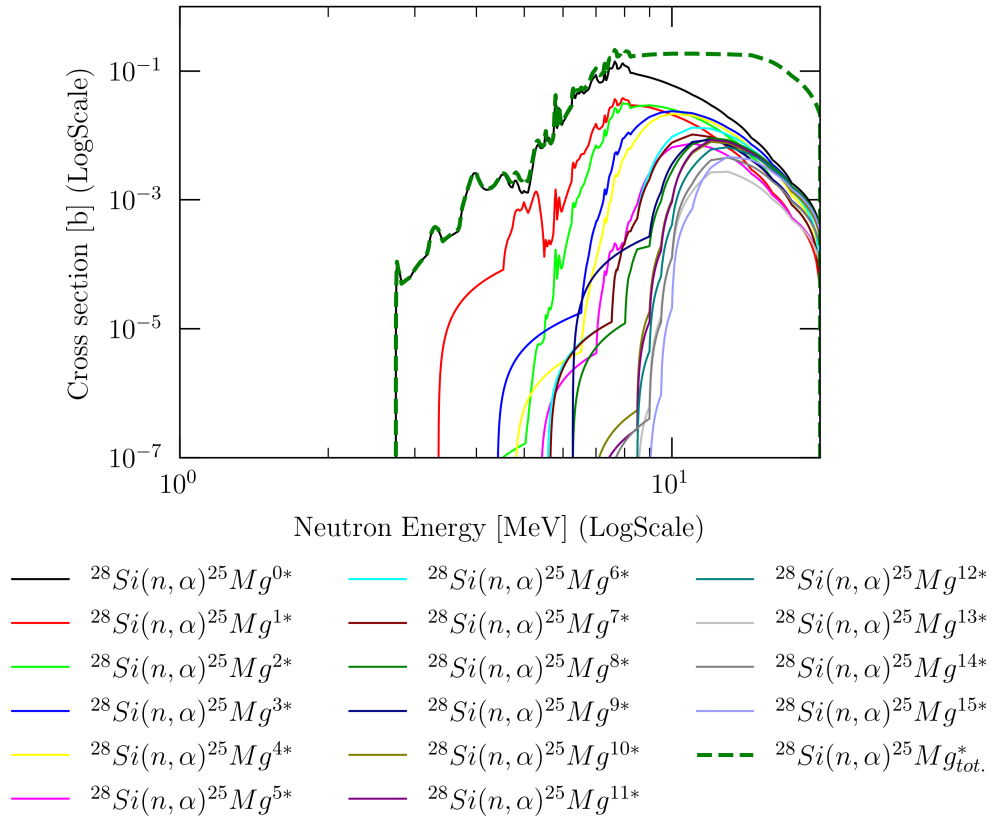

Fig. 4.8. Cross sections of the $^{28}Si(n,\alpha)^{25}Mg$ reaction. Data from ENDFB-VIII.0 [133].

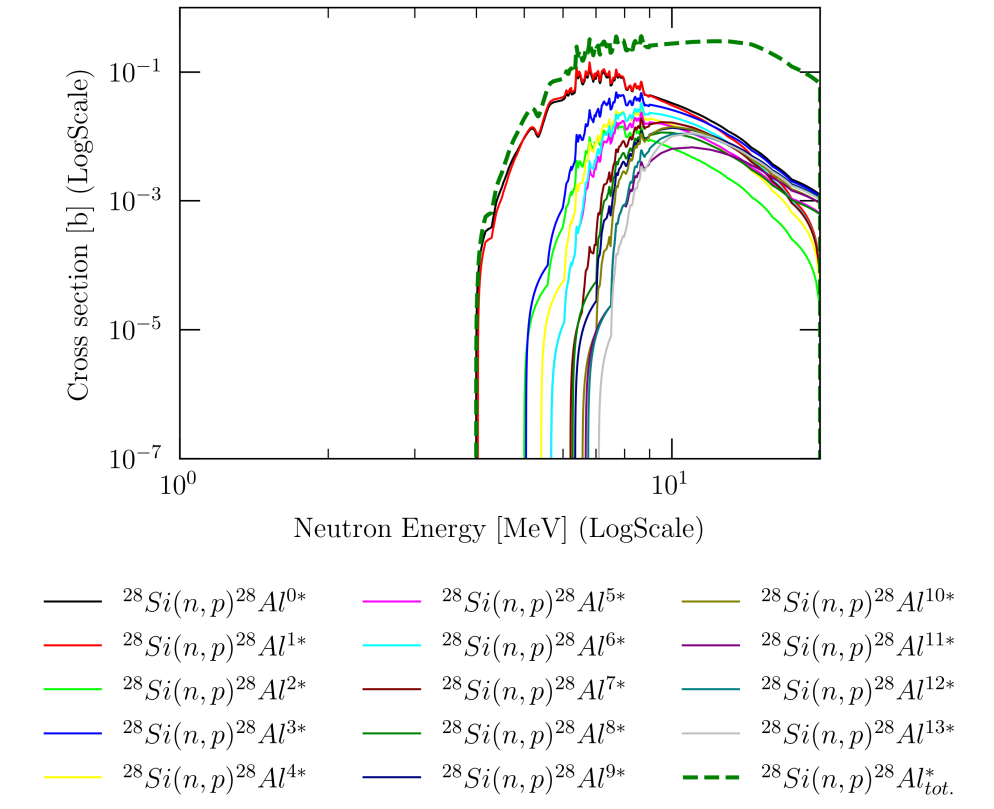

Fig. 4.9. Cross sections of the $^{28}Si(n,p)^{28}Al$ reaction. Data from ENDFB-VIII.0 [133].

Reaction	Q value [MeV]	Branching ratio [%]	$T_{1/2}$ [fs]	E_{k_α}	$E_{k_{^{25}Mg}}$	Q value [MeV]	Products	Branching ratio [%]	$\sum E_k$
$^{28}Si(n,\alpha)^{25}Mg^{(g.s)}$	-2.65	7.03	stable	7.84 11.01	3.51 0.33	/	$^{25}Mg^{(g.s)}+\gamma$	100	11.35
$^{28}Si(n,\alpha)^{25}Mg^{(1^{st})*}$	-3.24	2.30	$3.38\cdot10^{6}$	7.38 10.47	3.38 0.29	0.585	$^{25}Mg^{(g.s)}+\gamma$	100	10.76
$^{28}Si(n,\alpha)^{25}Mg^{(2^{nd})*}$	-3.63	3.52	$10.1\cdot10^{3}$	7.07 10.10	3.30 0.27	0.385 0.974	$^{25}Mg^{(1^{st})*}+\gamma$ $^{25}Mg^{(g.s)}+\gamma$	45.9 54.1	10.37
$^{28}Si(n,\alpha)^{25}Mg^{(3^{rd})*}$	-4.26	5.16	17	6.57 9.50	3.16 0.23	1.611	$^{25}Mg^{(g.s)}+\gamma$	100	9.73
$^{28}Si(n,\alpha)^{25}Mg^{(4^{th})*}$	-4.62	4.50	$0.70\cdot10^{3}$	6.30 9.17	3.08 0.21	0.99 1.379	$^{25}Mg^{(2^{nd})*}+\gamma$ $^{25}Mg^{(1^{st})*}+\gamma$ $^{25}Mg^{(g.s)}+\gamma$	30.5 42.5 27	9.38
$^{28}Si(n,\alpha)^{25}Mg^{(5^{th})*}$	-5.22	1.86	10	5.83 8.60	2.95 0.18	1.589 4.979 2.563	$^{25}Mg^{(2^{nd})*}+\gamma$ $^{25}Mg^{(1^{st})*}+\gamma$ $^{25}Mg^{(g.s)}+\gamma$	20.4 75.8 3.8	8.78
$^{28}Si(n,\alpha)^{25}Mg^{(6^{th})*}$	-5.39	4.21	290	5.70 8.44	2.91 0.17	0.733 1.763 2.737	$^{25}Mg^{(4^{th})*}+\gamma$ $^{25}Mg^{(2^{nd})*}+\gamma$ $^{25}Mg^{(g.s)}+\gamma$	7 87 6	8.61
$^{28}Si(n,\alpha)^{25}Mg^{(7^{th})*}$	-5.45	2.93	26	5.65 8.38	2.90 0.17	0.837 1.827 2.801	$^{25}Mg^{(4^{th})*}+\gamma$ $^{25}Mg^{(1^{st})*}+\gamma$ $^{25}Mg^{(g.s)}+\gamma$	42.1 37.9 20	8.55
$^{28}Si(n,\alpha)^{25}Mg^{(8^{th})*}$	-6.06	3.75	7.7	5.18 7.81	2.76 0.13	1.794 3.405	$^{25}Mg^{(3^{rd})*}+\gamma$ $^{25}Mg^{(g.s)}+\gamma$	81.5 18.5	7.94
$^{28}Si(n,\alpha)^{25}Mg^{(9^{th})*}$	-6.07	2.87	7	5.17 7.80	2.76 0.14	0.85 2.439 2.828 3.413	$^{25}Mg^{(5^{th})*}+\gamma$ $^{25}Mg^{(2^{nd})*}+\gamma$ $^{25}Mg^{(1^{st})*}+\gamma$ $^{25}Mg^{(g.s)}+\gamma$	0.22 14.03 73.48 12.27	7.93
$^{28}Si(n,\alpha)^{25}Mg^{(10^{th})*}$	-6.56	3.33	6	4.79 7.33	2.65 0.11	1.106 1.17 2.933 3.907	$^{25}Mg^{(7^{th})*}+\gamma$ $^{25}Mg^{(6^{th})*}+\gamma$ $^{25}Mg^{(2^{nd})*}+\gamma$ $^{25}Mg^{(g.s)}+\gamma$	10 13 66 11	7.44
$^{28}Si(n,\alpha)^{25}Mg^{(11^{th})*}$	-6.71	3.51	22	4.67 7.18	2.61 0.10	2.006 2.359 3.970	$^{25}Mg^{(4^{th})*}+\gamma$ $^{25}Mg^{(3^{rd})*}+\gamma$ $^{25}Mg^{(g.s)}+\gamma$	15.3 2 82.7	7.28
$^{28}Si(n,\alpha)^{25}Mg^{(12^{th})*}$	-6.93	3.11	47	4.50 6.98	2.56 0.09	0.654 2.448 4.059	$^{25}Mg^{(8^{th})*}+\gamma$ $^{25}Mg^{(3^{rd})*}+\gamma$ $^{25}Mg^{(g.s)}+\gamma$	1 39 60	7.06
$^{28}Si(n,\alpha)^{25}Mg^{(13^{rd})*}$	-7.01	1.22	4	4.44 6.90	2.55 0.09	0.864 1.716 3.303 3.692	$^{25}Mg^{(9^{th})*}+\gamma$ $^{25}Mg^{(5^{th})*}+\gamma$ $^{2}Mg^{(2^{nd})*}+\gamma$ $^{2}Mg^{(1^{st})*}+\gamma$	4 12 79 5	
$^{28}Si(n,\alpha)^{25}Mg^{(14^{th})*}$	-7.36	2.11	7	4.17 6.56	2.46 0.07	1.796 3.385 3.774	$^{25}Mg^{(5^{th})*}+\gamma$ $^{25}Mg^{(2^{nd})*}+\gamma$ $^{25}Mg^{(1^{st})*}+\gamma$	1 47 52	
$^{28}Si(n,\alpha)^{25}Mg^{(15^{th})*}$	-7.38	2.45	26	4.16 6.55	2.46 0.07	1.974 3.332	$^{25}Mg^{(6^{th})*}+\gamma$ $^{25}Mg^{(4^{th})*}+\gamma$	6 94	

Table 4.9. IT de-excitation modes of excited states of ^{25}Mg and associated half-life. The last column shows the sum of the kinetic energy of the produced particles. Computations are considering 14 MeV incident neutrons. Data are from NNDC with level scheme in Appendix D.2.

Reaction	Q value [MeV]	Branching ratio [%]	$T_{1/2}$ [fs]	E_{k_p}	$E_{k_{^{28}Al}}$	Q value [MeV]	Products	Branching ratio [%]	$\sum E_k$
$^{28}Si(n,p)^{28}Al^{(g.s)}$	-3.86	3.05	stable	8.54 10.13	1.60 0.01	/	$^{28}Al^{(g.s)}+\gamma$	100	10.14
$^{28}Si(n,p)^{28}Al^{(1^{st})*}$	-3.89	2.39	$2.07\cdot10^6$	8.51 10.10	1.60 0.01	0.030	$^{28}Al^{(g.s)}+\gamma$	100	10.11
$^{28}Si(n,p)^{28}Al^{(2^{nd})*}$	-4.83	0.54	$33\cdot10^3$	7.64 9.15	1.53 0.02	0.942	$^{28}Al^{(1^{st})*}+\gamma$	45.9 54.1	
$^{28}Si(n,p)^{28}Al^{(3^{rd})*}$	-4.87	2.72	103	7.61 9.11	1.52 0.02	0.983 1.013	$^{28}Al^{(1^{st})*}+\gamma$ $^{28}Al^{(g.s)}+\gamma$	62 38	9.13
$^{28}Si(n,p)^{28}Al^{(4^{th})*}$	-5.23	1.36	223	7.27 8.75	1.49 0.02	0.359 0.4 1.342 1.372	$^{28}Al^{(3^{rd})*}+\gamma$ $^{28}Al^{(2^{nd})*}+\gamma$ $^{28}Al^{(1^{st})*}+\gamma$ $^{28}Al^{(g.s)}+\gamma$	0.3 35.3 56 8.4	8.76
$^{28}Si(n,p)^{28}Al^{(5^{th})*}$	-5.48	1.47	92	7.05 8.50	1.47 0.02	0.248 0.607 0.648 1.590 1.620	$^{28}Al^{(4^{th})*}+\gamma$ $^{28}Al^{(3^{rd})*}+\gamma$ $^{28}Al^{(2^{nd})*}+\gamma$ $^{28}Al^{(1^{st})*}+\gamma$ $^{28}Al^{(g.s)}+\gamma$	1.9 1.9 3.8 87.2 5.2	8.52
$^{28}Si(n,p)^{28}Al^{(6^{th})*}$	-5.48	1.98	63	7.04 8.50	1.47 0.02	0.250 0.609 0.650 1.592 1.622	$^{28}Al^{(4^{th})*}+\gamma$ $^{28}Al^{(3^{rd})*}+\gamma$ $^{28}Al^{(2^{nd})*}+\gamma$ $^{28}Al^{(1^{st})*}+\gamma$ $^{28}Al^{(g.s)}+\gamma$	3.4 2.6 1.7 6 86.3	8.51
$^{28}Si(n,p)^{28}Al^{(7^{th})*}$	-6.00	1.84	8	6.57 7.97	1.43 0.03	0.516 0.518 0.766 1.125 1.166 2.108 2.138	$^{28}Al^{(6^{th})*}+\gamma$ $^{28}Al^{(5^{th})*}+\gamma$ $^{28}Al^{(4^{th})*}+\gamma$ $^{28}Al^{(3^{rd})*}+\gamma$ $^{28}Al^{(2^{nd})*}+\gamma$ $^{28}Al^{(1^{st})*}+\gamma$ $^{28}Al^{(g.s)}+\gamma$	2.9 1.9 1 6.3 1.9 48 38	8.0
$^{28}Si(n,p)^{28}Al^{(8^{th})*}$	-6.06	1.35	32	6.51 7.90	1.43 0.03	0.063 0.579 0.581 0.829 1.188 1.229 2.171 2.201	$^{28}Al^{(7^{th})*}+\gamma$ $^{28}Al^{(6^{th})*}+\gamma$ $^{28}Al^{(5^{th})*}+\gamma$ $^{28}Al^{(4^{th})*}+\gamma$ $^{28}Al^{(3^{rd})*}+\gamma$ $^{28}Al^{(2^{nd})*}+\gamma$ $^{28}Al^{(1^{st})*}+\gamma$ $^{28}Al^{(g.s)}+\gamma$	2.9 4.0 2.1 2.1 3.8 13.4 67 4.7	7.94
$^{28}Si(n,p)^{28}Al^{(9^{th})*}$	-6.13	2.15	22	6.45 7.84	1.42 0.03	0.133 0.649 1.258 2.241	$^{28}Al^{(7^{th})*}+\gamma$ $^{28}Al^{(6^{th})*}+\gamma$ $^{28}Al^{(3^{rd})*}+\gamma$ $^{28}Al^{(1^{st})*}+\gamma$	4.3 4.3 3.4 1.8 86.2	
$^{28}Si(n,p)^{28}Al^{(10^{th})*}$	-6.35	1.94	66	6.25 7.62	1.40 0.03	0.215 0.348 0.864 0.866 1.114 1.473 1.514 2.456 2.486	$^{28}Al^{(9^{th})*}+\gamma$ $^{28}Al^{(7^{th})*}+\gamma$ $^{28}Al^{(6^{th})*}+\gamma$ $^{28}Al^{(5^{th})*}+\gamma$ $^{28}Al^{(4^{th})*}+\gamma$ $^{28}Al^{(3^{rd})*}+\gamma$ $^{28}Al^{(2^{nd})*}+\gamma$ $^{28}Al^{(1^{st})*}+\gamma$ $^{28}Al^{(g.s)}+\gamma$	0.9 0.9 10.1 56.3 1.9 1.9 5.6 3.8 18.6	7.65
$^{28}Si(n,p)^{28}Al^{(11^{th})*}$	-6.44	1.48	313	6.16 7.52	1.40 0.04	0.31 1.568 2.581	$^{28}Al^{(9^{th})*}+\gamma$ $^{28}Al^{(3^{rd})*}+\gamma$ $^{28}Al^{(g.s)}+\gamma$	5.4 4.5 90.1	7.56
$^{28}Si(n,p)^{28}Al^{(12^{th})*}$	-6.52	2.02	22	6.09 7.45	1.39 0.04	0.385 0.518 1.034 1.643 2.626 2.656	$^{28}Al^{(9^{th})*}+\gamma$ $^{28}Al^{(7^{th})*}+\gamma$ $^{28}Al^{(6^{th})*}+\gamma$ $^{28}Al^{(3^{rd})*}+\gamma$ $^{28}Al^{(1^{st})*}+\gamma$ $^{28}Al^{(g.s)}+\gamma$	0.9 0.9 2.8 69 3.7 22.7	7.48
$^{28}Si(n,p)^{28}Al^{(13^{rd})*}$	-6.85	2.01	62	5.79 7.11	1.36 0.04	1.365 1.974 2.987	$^{28}Al^{(6^{th})*}+\gamma$ $^{28}Al^{(3^{rd})*}+\gamma$ $^{28}Al^{(g.s)}+\gamma$	52.4 3.6 44	7.15

Table 4.10. IT de-excitation modes of excited states of ^{28}Al and associated half-life. The last column shows the sum of the kinetic energy of the produced particles. Computations are considering 14 MeV incident neutrons. Data are from NNDC with level scheme in Appendix D.3.

4.1.4. Neutron elastic scattering

Neutron inelastic scattering, as referring to the formation of a compound nucleus, was studied in the previous section with the description of neutron capture reaction. Concerning the elastic scattering, the kinetic energy and momentum are conserved with the interaction, and no compound nucleus is formed.

This time, as for charged particles scattering off the coulomb field of atomic nuclei, the differential cross section of neutron elastic scattering is described by the Rutherford scattering formula [134], given by:

$$\frac{d\sigma}{d\Omega} = \left(\frac{Ze^2}{4\pi\epsilon_0 E_n}\right)^2 \frac{1}{sin^4(\theta/2)} \tag{4.21}$$

With Z the atomic number of the target nuclei, e the elementary charge, E_n the kinetic energy of the impinging neutron, and θ the emission angle of the scattered neutron depicted in Fig. 4.10.

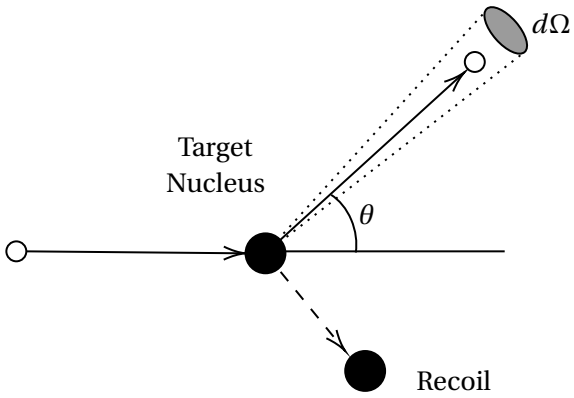

Fig. 4.10. Schematic diagram of scattering angle and solid angle for a neutron scattering reaction. The neutron scattering angle θ is the angle between the target and the incident neutron trajectory. The solid angle $d\Omega$ is then the angle subtended by the scattered neutron at the target.

Therefore, the angular differential cross section can be understood as the quantity describing how the scattering intensity is distributed with respect to the scattering angle. The angular distribution of the differential cross section of the scattered neutrons on ^{28}Si and ^{12}C nucleus is displayed in Fig. 4.11, while the kinetic energy distribution of the ^{28}Si and ^{12}C recoiled nucleus for 14 MeV neutron elastic scattering is displayed in the Fig. 4.12. Hence, the neutron emission is anisotropic, with a maximum intensity at small angles close to θ =0°. The kinetic energy distribution of the recoiled nucleus is also anisotropic, with a maximum intensity at angles close to θ =180°. Hence, it results in the addition of a new angular parameter further complicates the analytical description of the sensor response.

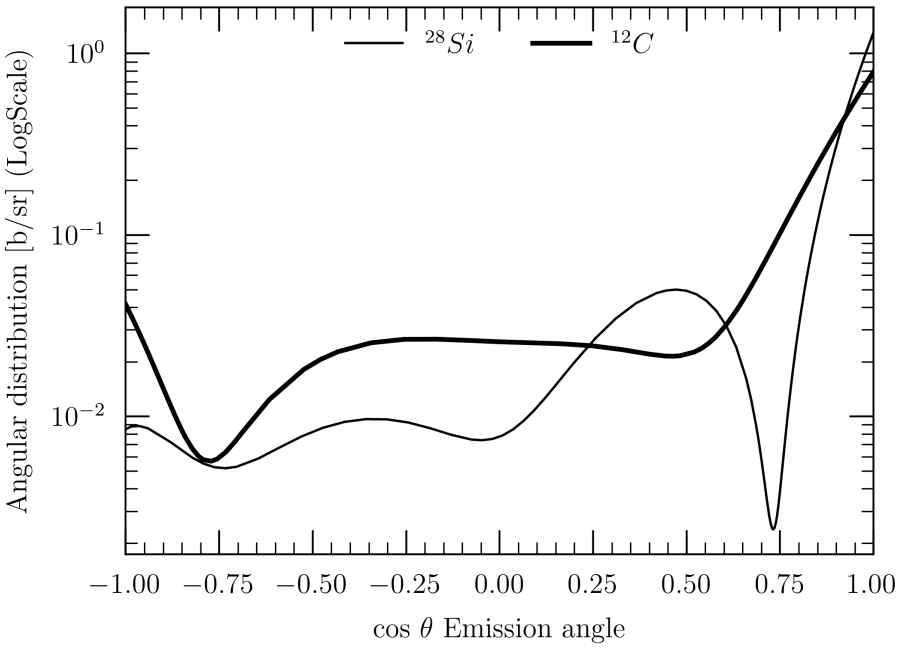

Fig. 4.11. Angular distribution of the differential cross section of the scattered neutron on ^{28}Si and ^{12}C nucleus. The distribution are obtained for a neutron energy of 14 MeV from the ENDF/B-VIII.0 library.

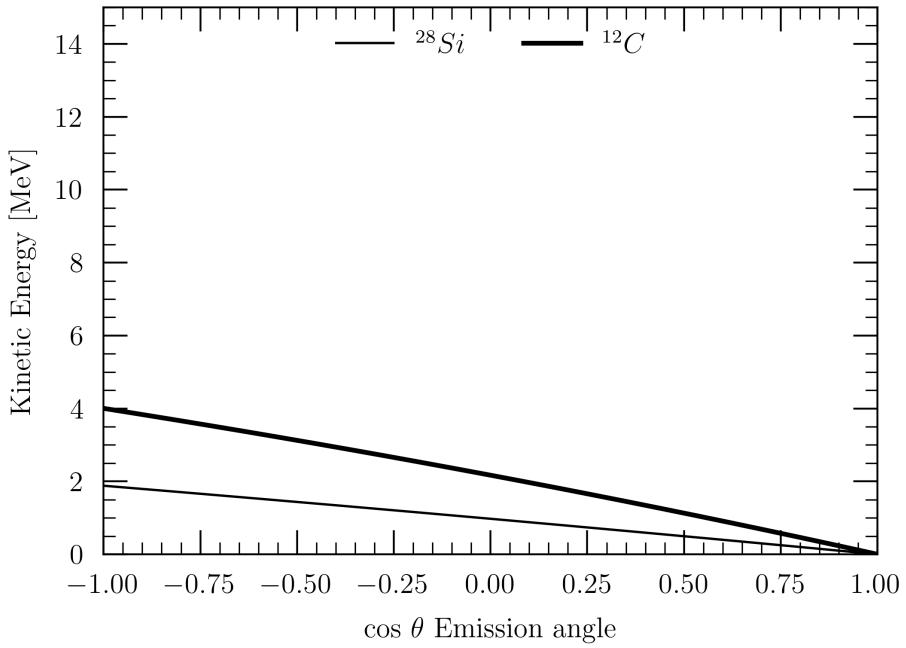

Fig. 4.12. Kinetic energy distribution of the ^{28}Si and ^{12}C recoiled nucleus versus the neutron angular scattering for 14 MeV neutron elastic scattering

The analytical description of the sensor response has been presented, pointing out the first results for the interpretation of the experimental data regarding the kinetic energy distribution of the reaction products. Firstly, the kinetic energy of the reaction products has been computed for the different nuclear reactions showing a wide distribution of the kinetic energy of the reaction products as a function of emission angle. Secondly, the angular distribution of the differential cross sections of the scattered neutrons has been discussed, showing a maximum intensity at small angles close to θ =0° for the neutron elastic scattering on ^{28}Si and ^{12}C nucleus. Finally, the kinetic energy of the reactions products from neutron captures has been computed for all the possible decay pathways. It showed all the complexity of the sensor response to the nuclear reactions according to the several decay modes and the associated branching ratio still under discussion in the literature today, leading to a complex analytical description of the sensor response.

Several limitations have been identified, such as the uncertainties regarding the branching ratio of the excited states, related to the nuclear data evaluation. The variety of charged particles produced, each with different stopping powers and ranges, complicates the analytical description of the sensor response. Due to this complexity and the sensor's geometrical configuration, a numerical model is required to simulate both neutron transport and the generation of secondary particles. As described in Section 3.3.2 on page 77, neutron capture produces various charged particles with different stopping powers and ranges. Tracking the individual trajectories inside and outside the sensor is essential for accurately describing the kinetic energy released in the sensor.

The following objective is to validate the numerical model by comparing its results with simple analytical cases. By looking at the min and max bounds of the energy distributions, on the energies of the de-excitation gamma rays, the results of the Monte-Carlo simulations are compared with the analogical results presented.

4.2. Development of a numerical model to simulate the generation of secondary particles

4.2.1. Modeling scheme based on GEANT4

Unlike analytical or numerical strategies, Monte-Carlo methods employ the technique of repeated random sampling based on a predefined probability distribution to estimate a particular measure such as the neutron transport in the matter, or the generation of secondary particles tracking their trajectories. Hence, Monte-Carlo transport codes are widely used in the field of nuclear physics, and is particularly suitable for the simulation of the generation of secondary particles in the matter in order to reconstruct the deposited energy distribution. Such reconstructions are made possible through the use of specific codes like MCNP[1] [135], FLUKA[2] [136] GEANT4[3] [137] or PHITS[4] [138].

Works that have been published on modeling nuclear interactions in SiC [139], do not incorporate the effects of sensor geometry or the precise locations of secondary particles generation. Additionally, the MCNP code is inadequate for accurately simulating heavy charged particle transport in SiC or diamond sensors, although it can offer a qualitative understanding of deposited energy spectra [140]. Regarding PHITS, it is a versatile code that can simulate a wide range of nuclear reactions, but it is not optimized for the precise tracking of secondary particles in the sensor. In contrast, the below GEANT4 application tracks primary particle trajectories and

[1] *Monte Carlo N-Particle eXtended (MCNPX)*
[2] *FLUktuierende KAskade (FLUKA)*
[3] *GEometry ANd Tracking (GEANT)*
[4] *Particle and Heavy Ion Transport code System (PHITS)*

energies within the material, enabling deduction of secondary charged particle characteristics resulting from neutron-atom interactions.

Therefore, the GEANT4 toolkit is chosen for simulating the generation of secondary particles in the sensor, as it is particularly suitable for modeling the passage of particles through matter. After a brief introduction to the GEANT4 toolkit, the construction of the model is presented in the following section.

GEANT4 is a toolkit for simulating the passage of particles through matter, based on the Monte-Carlo method. All aspects of the simulation are handled by the GEANT4 kernel:

- The geometry of the detector
- The materials from which it is made
- The tracking of particles through the detector
- The generation of primary and secondary particles
- The creation of events data and storage
- The visualization of the detector and the particles trajectories in the environment

Users can then construct their own simulation by selecting the appropriate options from the GEANT4 toolkit. The GEANT4 toolkit is divided into several packages, each of which is dedicated to a specific aspect of the simulation as described in the following diagram in Fig. 4.13.

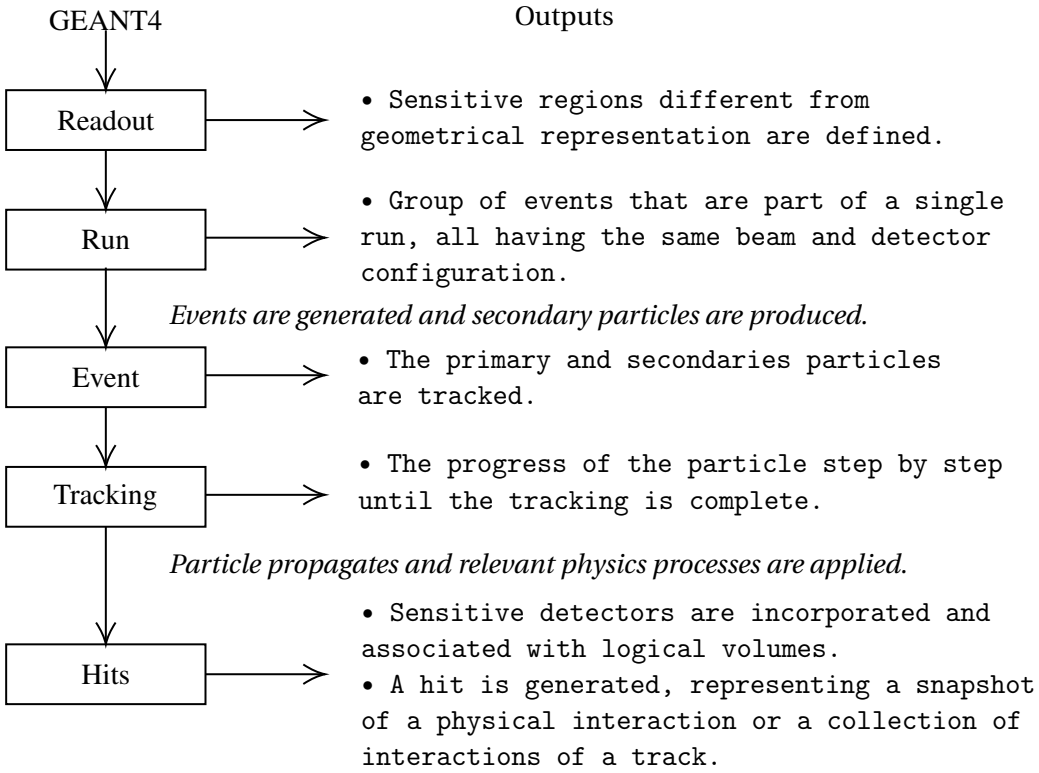

Fig. 4.13. Workflow diagram of the GEANT4 toolkit.

In numerous Monte-Carlo codes such as GEANT4, particle transport is modeled by breaking down the path of a particle into a sequence of minor steps between two interaction points. Both recoils and secondary particles are statistically tracked as they engage with the material they traverse. In this manner, each process linked to a particle suggests a step length, which statistically represents the distance to the next interaction. The smallest proposed step length is selected and the corresponding interaction is triggered.

4.2.2. Model Construction

4.2.2.1. Nuclear Data

GEANT4, originally developed for particle physics experiments, has been extended for neutron applications, including a dedicated high precision package called G4Neutron_HP for effective cross-section evaluation up to 20 MeV down to thermal energies. Using high-precision cross-section data and detailed nuclear models to simulate nuclear interactions, it includes the description of capture, fission and elastic scattering processes with high accuracy. Furthermore, a nuclear processing tool has been created to expand the compatibility of GEANT4 with various nuclear data libraries such as ENDF/B-VIII.0 [10] and JEFF-3.3 [141], with these enhancements planned for a future GEANT4 release [142]. This approach will grant GEANT4 users access to a comprehensive range of standard evaluated neutron data libraries for Monte-Carlo simulations, expands the available isotopic database, and facilitates the estimation of systematic uncertainties in results by accounting for uncertainties in nuclear data. In the present study, such neutron HP precision package is used to model accurately the neutron interactions evaluated in the nuclear database.

4.2.2.2. GEANT4 Physics List

The PhysicsList class is responsible for defining the physics processes that will be used in the simulation. It is one of the three mandatory classes that must be implemented in a GEANT4 application, along with the DetectorConstruction and PrimaryGeneratorAction classes. Their main role is summarized as follows:

- The DetectorConstruction, defining the geometry of the detector and the material composition
- The PrimaryGeneratorAction, defining the primary particles that will be used in the simulation as well as their energy and direction
- The PhysicsList, defining the physics processes that will be used in the simulation and which are the more relevant for the simulation of physical interactions.

Within the PhysicsList class, all the interactions and the particles are initialized, and parameters such as the energy thresholds for the interactions are set. The PhysicsList class is also responsible for defining the electromagnetic and hadronic processes that are used in the simulation. The most frequently used intra-nuclear cascade models are the Binary Cascade (BIC) [143] and the Bertini Cascade (BERT) [144]. In this study, the high-precision intranuclear cascade BIC_HP model that propagates primary particles and secondary particles through the nucleus is used since it is the most appropriate for neutron interactions up to 20 MeV. Hence, the interactions are considered between a primary particle or a secondary particle and an individual nucleon of the nucleus.

The $C(n,\alpha)$ reaction under examination in the presented GEANT4 model is derived from the ENDF/B-VI [145] library. It is important to note that the previously mentioned G4Neutron_HP library does not provide a comprehensive description of the kinematics of neutron interactions for energies below 20 MeV. Hence, although G4Neutron_HP is considered one of the most accurate GEANT4 models for simulating neutron interactions up to 20 MeV due to its use of evaluated nuclear data, it has limitations. Incomplete or missing data in the libraries and an incomplete model implementation mean that some reactions are only partially represented or not represented at all. This is particularly true for decay reactions that occur in multiple steps, especially those exhibiting a two-body sequential decay described in the first Section 4.1 such

that:

$$n + {}^{12}C \rightarrow {}^{12}C^{(2^{nd})*} + n' \hookrightarrow {}^{8}Be^{(g.s.)} + \alpha \hookrightarrow 2\alpha \tag{4.22}$$

$$n + {}^{12}C \rightarrow {}^{9}Be^{(1^{st})*} + \alpha \hookrightarrow {}^{8}Be^{(g.s.)} + n' \hookrightarrow 2\alpha \tag{4.23}$$

As previously described in detail in Section 4.1.1, when a carbon-12 nucleus is created in the second excited state (4.22), also known as the Hoyle state [146, 147], it de-excites to produce an alpha particle and a ground state beryllium-8, which further disintegrates into two alpha particles. Similarly, when a beryllium-9 nucleus is formed in an excited state (4.23), it de-excites by releasing a neutron, resulting in beryllium-8, which then disintegrates into two alpha particles. Various descriptions of these processes have been proposed in scientific literature, including the one by Caswell and Coyne [148], which outlines the multiple interaction modes for reactions that yield three alpha particles.

Although the model uses nuclear data from evaluated libraries such as ENDB/B.VIII.0 [133] or JENDL-4 [149] to represent the interactions, these libraries do not contain data on the sequential decay reaction leading to (4.22) and (4.23) for neutrons with energies below 20 MeV, as shown in Fig. 4.14.

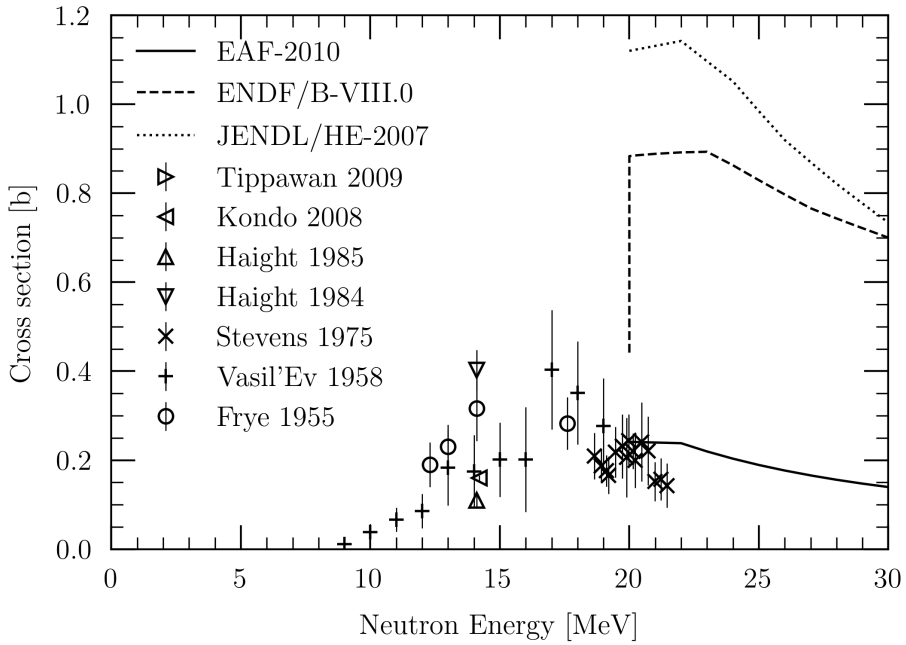

Fig. 4.14. Effective interaction cross section for the sequential decay reaction. The dashed lines represent the total cross section from evaluated nuclear data libraries while the crosses and geometrical marker represent experimental measurements.

Hence, the GEANT4 model has been be adjusted to accommodate the multistage decay mode outlined in NRESP7.1 [150]. Initially, the cross-section data for these neutron-induced reactions on carbon were sourced from ENDF/B-VI. Over time, this data was partially supplanted by results from dedicated experiments conducted at the Federal Institute of Physics and Technology PTB[5] in Berlin. This substitution was done while readjusting the balance with other reactions

[5] *Physikalisch-Technische Bundesanstalt (PTB)*

to maintain the total cross-section constant. These results have been recently cross-verified with simulations conducted with NRESP and validated against time-of-flight measurements performed at PTB [151].

All things considered, the model developed in this study based on the GEANT4 toolkit, uses the high-precision intranuclear cascade BIC_HP aswell as the G4Neutron_HP library to simulate the generation of secondary particles in the sensor. Nuclear data from END/B/VIII.0 are used to represent the interactions, with the model adjusted to accommodate the multistage decay mode outlined in NRESP7.1 [150].

4.2.3. Analytical versus Monte-Carlo model comparison

In order to verify the hypothesis of the model according to the options used to simulate the neutron interactions with fast neutrons, and especially the neutron capture leading to the sequential break-up of the ^{9}Be nucleus, the results obtained with the GEANT4 simulation are compared with the analytical study carried out in the previous Section 4.1.

4.2.3.1. Neutron scattering modelling

Firstly, regarding the neutron inelastic scattering, the kinetic energy distribution of the ^{28}Si nucleus is compared with the analytical results presented in Section 4.1.2. The results are displayed in Fig. 4.15.

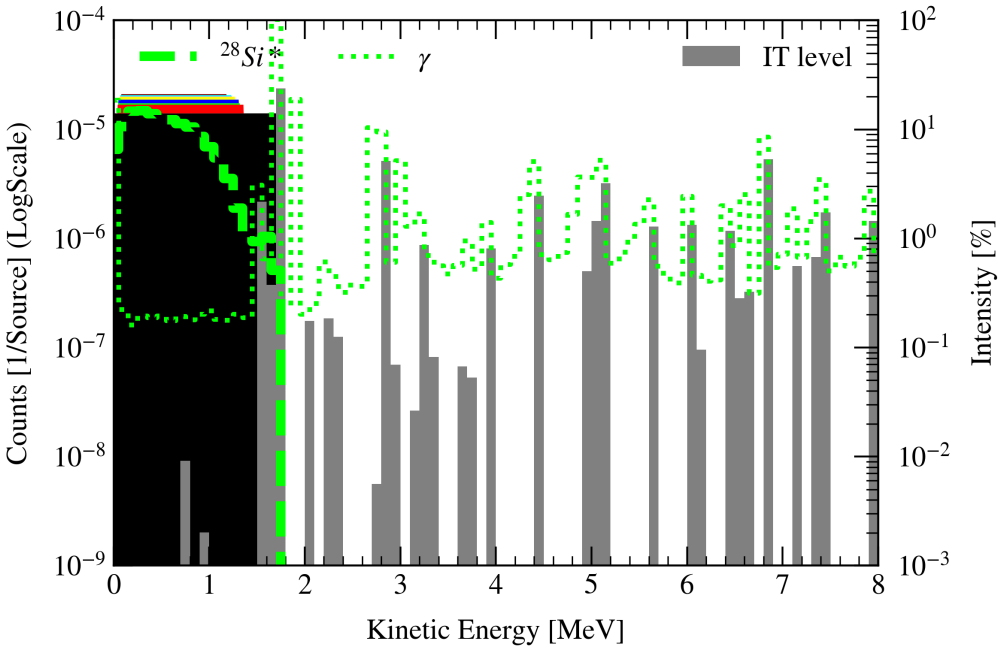

Fig. 4.15. Kinetic energy distribution of the ^{28}Si inelastic neutron scattering and associated energy distribution of the de-excitation gamma rays using GEANT4 model. The green curve is associated to calculated distribution results on the left axes and is superposed to the previous analytical results on the right axes. The colored squared boxed represent the analytical kinetic energy of the several ^{28}Si nucleus emitted in ground states as shown in Fig. 4.6, and the gray bars represent the energy of the de-excitation gamma rays computed analytically.

In a first qualitative comparison, the maximum and minimum bounds of the kinetic energy distribution are in agreement between the analytical and numerical results, even though no scaling factor was applied and the analytical approach did not consider angular distribution. Indeed, the kinetic energy of the recoiled nucleus displayed with a green bold line, ranges from a few keV up to 1.7 MeV for a 14 MeV incident neutron beam. In addition, the calculated distribution shows a maximum intensity for kinetic energies below 1 MeV, consistent with the neutron inelastic scattering reaction described in Table 4.8, page 113. Here, numerous successive IT processes result in the emission of several gamma rays and a recoiled nucleus with kinetic energy below 1 MeV. While the emission of a ^{28}Si nucleus in its first excited state is most probable, with a branching ratio of nearly 24%, decaying by IT process to emit a gamma ray of 1.779 MeV and a recoiled nucleus with 1.7 MeV kinetic energy, other excited states of the ^{28}Si nucleus are also possible. According to the previous Table 4.8, the agreement between the main peaks of the isomeric transitions into the ground state is observed, in the superposition of dotted lines and grey bars. However, the numerical results exhibit a continuum, reflecting the complexity of the decay pathways and the successives IT processes.

The Rutherford scattering was presented in Section 4.1.4, showing that the emission angle of the scattered neutron has preferential directions. The numerical results obtained with the GEANT4 simulation are compared in Fig. 4.16, with the evaluated data from ENDF/B-VIII.0 used previously.

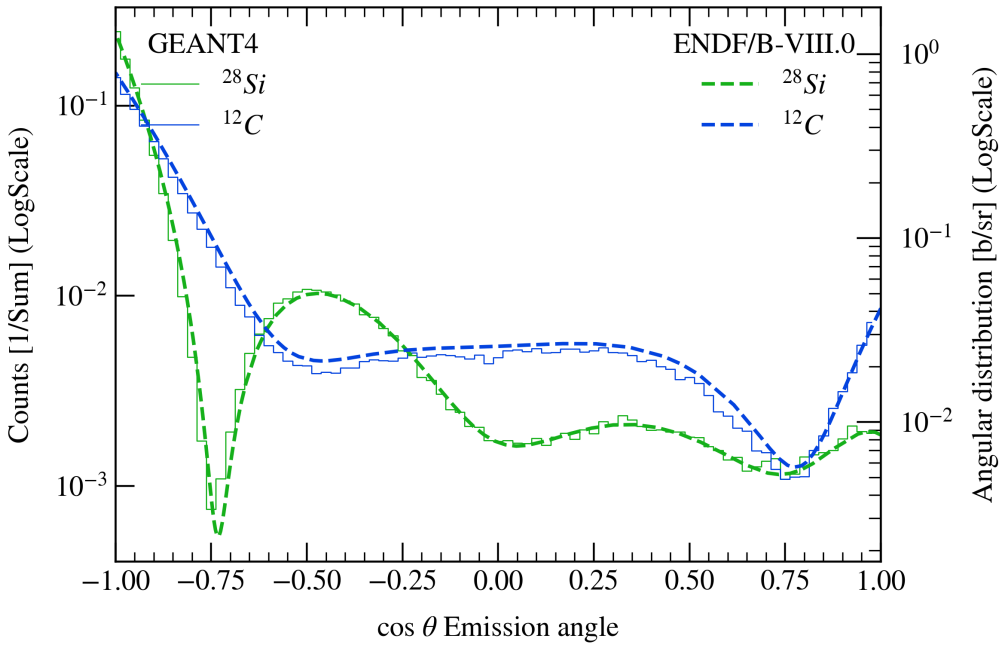

Fig. 4.16. Angular distribution of the differential cross section of the scattered neutrons on ^{28}Si and ^{12}C nucleus.

The good agreement between the two distributions confirmed that the neutron elastic scattering is well modeled in the GEANT4 simulation in the energy range under study. This preferential angular distribution explains the shape of the kinetic energy distribution of the recoiled nucleus, which is distributed with a maximum intensity at angles close to θ =180° as shown in Fig. 4.17.

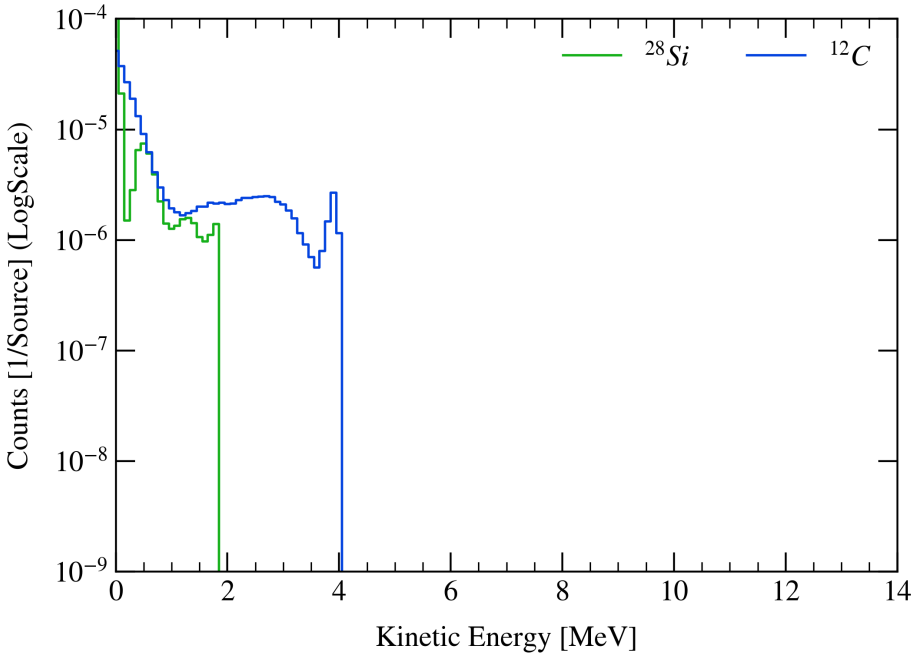

Fig. 4.17. Results from GEANT4 calculations showing the kinetic energy distribution of particles in the way out of the neutron elastic scattering with ^{28}Si and ^{12}C nuclei.

4.2.3.2. Neutron capture modelling

Regarding the silicon neutron capture, the sum of the kinetic energy of the particles in the way out of the $^{28}Si(n,\alpha)^{25}Mg$ reaction is computed using the GEANT4 simulation model. The results are presented in Fig. 4.18. The distribution of the sum of kinetic energy displayed with the dark orange curve, exhibits peaks whose intensity is directly related to the branching ratio of the decay pathways as discussed in the previous Section 4.1.3. In parallel, the sum of the kinetic energy of the particles computed for the first twelve excited states in Table 4.9 is displayed by superposing representative dashed lines to numerical results. The good agreement between the analytical and numerical results is observed, when comparing the peaks of the kinetic energy distribution for the twelve first excited states of the ^{25}Mg nucleus, which decay directly in the ground state according to Table 4.9, by emitting a gamma ray.

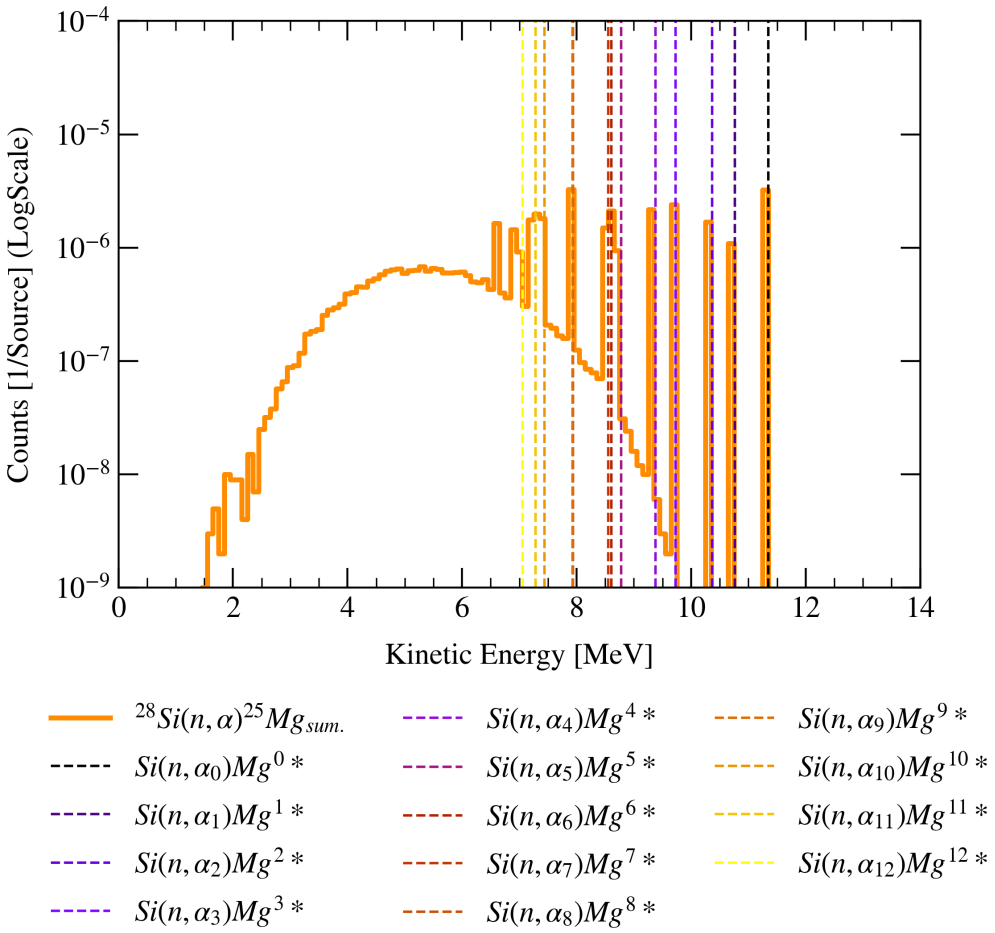

Fig. 4.18. Sum of the kinetic energy of the particles in the way out of the $^{28}Si(n,\alpha)^{25}Mg$ neutron capture. The dashed lines represent the sum of the kinetic energy of the produced particles computed analytically in Table 4.9.

In the same manner, the sum of the kinetic energy of the particles in the way out of the $^{28}Si(n,p)^{28}Al$ reaction is computed. The results are presented in Fig. 4.19. The distribution of the sum of the kinetic energy displayed with the maroon curve, exhibits once again peaks whose intensity is directly related to the branching ratio of the decay pathways. The sum of the kinetic energy of the particles computed for the first thirteen excited states, which decay directly in the ground state according to Table 4.10 is displayed by superposing representative dashed lines to numerical results. The good agreement between the analytical and numerical results is observed once again.

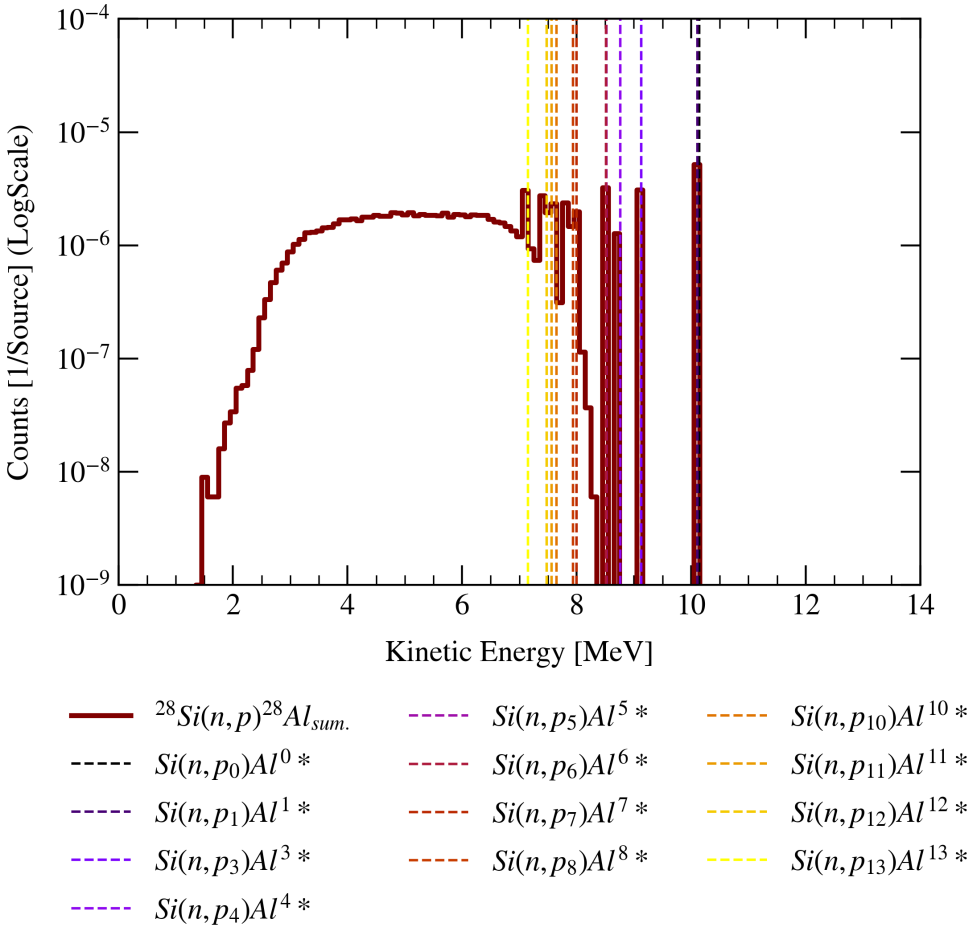

Fig. 4.19. Sum of the kinetic energy of the particles in the way out of the $^{28}Si(n,p)^{28}Al$ neutron capture. The dashed lines represent the sum of the kinetic energy of the produced particles computed analytically in Table 4.10.

Analytical and numerical results for neutron inelastic scattering, neutron elastic scattering, and neutron capture have been compared. The agreement between these results demonstrates that the GEANT4 simulation model is effective for simulating the generation of secondary particles in the sensor. Tracking the individual trajectories of the secondaries particle, inside and outside the sensor is essential for accurately describing the kinetic energy released in the sensor since they carry the most part of the energy released by the neutron capture reaction as explained in the previous sections and displayed in Fig. 4.20 and Fig. 4.21. It is particularly important in the case of the neutron capture reaction emitting light charged particles such as protons and alphas, because due to their higher projected range, they are more likely to escape the sensor.

Therefore, it has been demonstrated that the GEANT4 simulation model is well suited for simulating the generation of secondary particles in our application. Consequently, the model is used to reconstruct the deposited energy distribution in the sensor, in order to deconvolute the experimental sensor response. The next section is dedicated to the presentation of the dedicated experimental campaign.

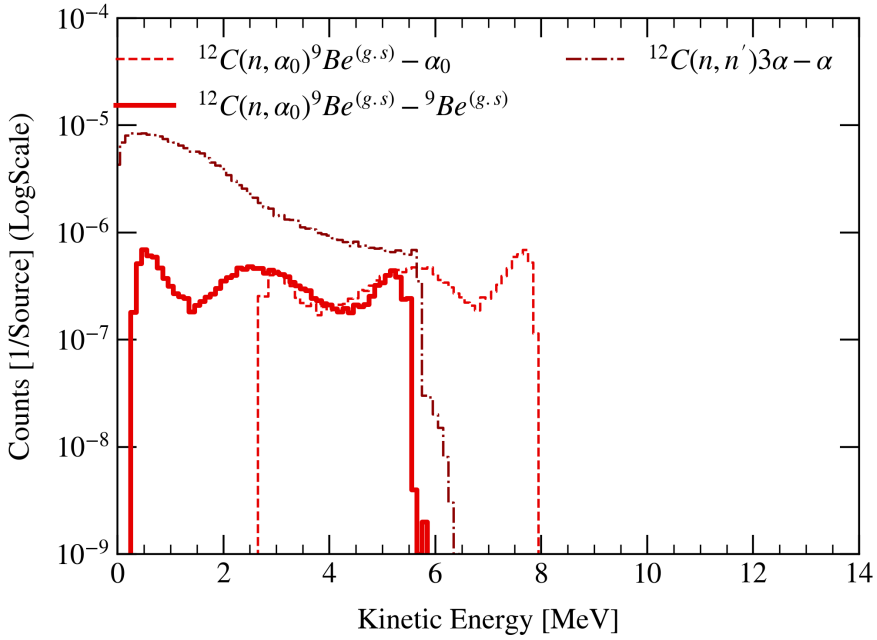

Fig. 4.20. Kinetic Energy distribution obtained with GEANT4 for the particles emitted in the way out of the carbon neutron capture reaction.

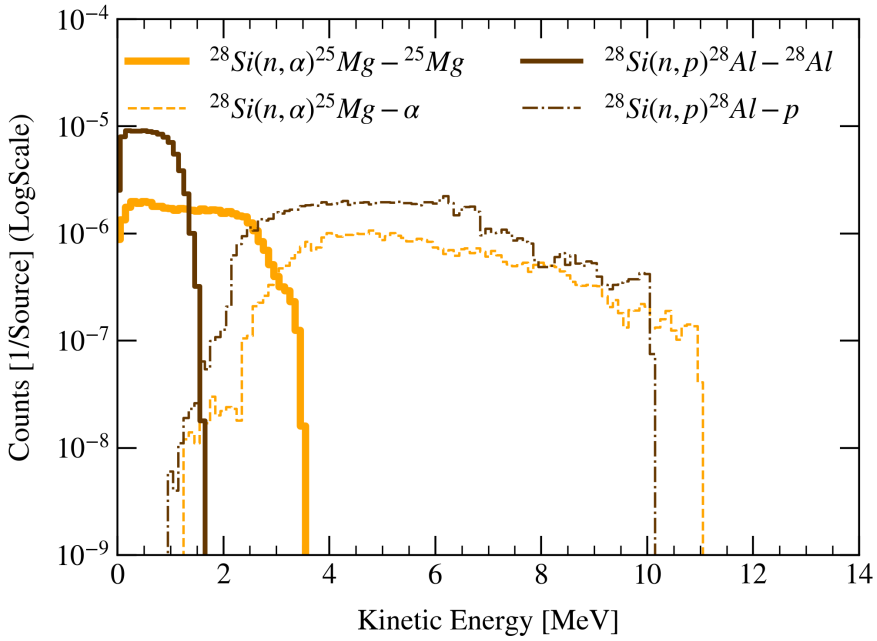

Fig. 4.21. Kinetic Energy distribution obtained with GEANT4 for the particles emitted in the way out of the silicon neutron capture reaction.

4.3. Realization of a dedicated measurement campaign on a 14 MeV neutron generator

4.3.1. The GENESIS Installation

In the early 2000s, the Reactor Physics group at LPSC[6] Grenoble, France, established the PEREN[7] platform for nuclear data evaluation experiments, including innovative reactor development. Initially commissioned in 2003, it featured a D-T generator named GENEPI2[8] and neutron slowing down assemblies like graphite [152]. Upgraded in 2014 to support academic and industrial neutron irradiation experiments, the platform was renamed GENESIS[9] in 2018, becoming part of the French national network under IN2P3[10].



Fig. 4.22. GENEPI2 electrostatic accelerator on the left and ECR source on the right.

The neutron generator is composed of an electrostatic accelerator delivering a continuous deuteron ion beam generated by a continuous ECR[11] source positioned in a Faraday cage as seen in Fig. 4.22. The source and the platform are then raised to a high voltage of 220 kV, it should be noticed that, while the fusion cross section is maximal at 150 kV, the deuteron beam is usually accelerated up to 250 kV in order to provide a sufficient penetration of the target. After extraction, the deuteron beam emitted is accelerated in a accelerating tube schematically represented in Fig. 4.23, to a kinetic energy of 220 keV reaching a current at the target location in a range from 10 µA to 2 mA.

[6] *Laboratoire de Physique Subatomique et Cosmologie (LPSC)*
[7] *Plateforme d'Etude et de Recherche sur l'Energie Nucléaire (PEREN)*
[8] *GEnérateur à NEutrons Pulsés Intenses (GENEPI2)*
[9] *GEnerator of NEutrons for Science and IrradiationS (GENESIS)*
[10] *Institut National de Physique Nucléaire et de Physique des Particules (IN2P3)*
[11] *Electron Cyclotron Resonance (ECR)*

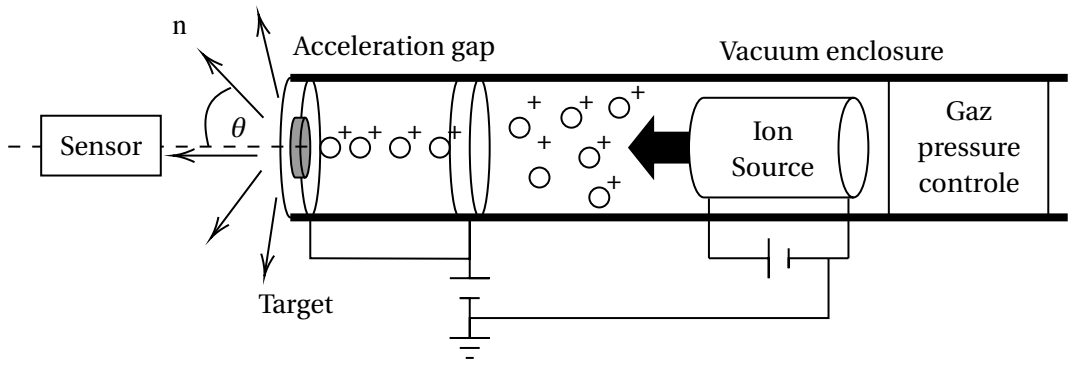

Fig. 4.23. Schematic diagram of the GENEPI2 ion source. The angle θ is the neutron emission angle with respect to the incident deuteron beam.

Deuteron ions are then guided to a target using a series of electrostatic quadrupoles in order to focus the beam. On this line, a bipolar magnet is used to select the deuteron acting as a mass spectrometer. Advanced vacuum packing of the order of 10^{-7} mbar is required to avoid the beam loss due to the interaction with the residual gas. The deuteron beam is then directed to a target made of titanium tritide. The target is composed of copper disk of 3 mm thickness and 38 mm diameter. The tritium coating is deposited on the copper disk by a chemical process leading to a quantity of 250 µg/cm^2. Hence, the active surface area of the target is a disk of 24 mm diameter, as shown in Fig. 4.24 and Fig. 4.25. In order to avoid too fast desorption of the tritium, which would lead to a decrease of the neutron flux, but also to avoid the tritium diffusion in the copper, the target is maintained at low temperature. To do so:

- Beam intensity is controlled
- The target is cooled by injecting compressed air at the rear of the target.

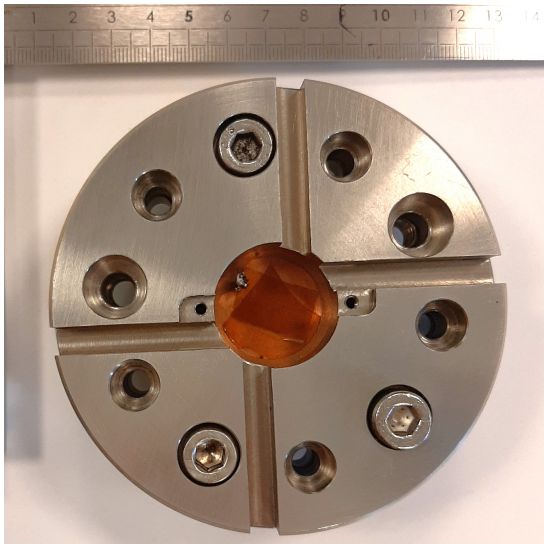

Fig. 4.24. Tritiated target backside. Cooling cavities are visible as perpendicular lines.

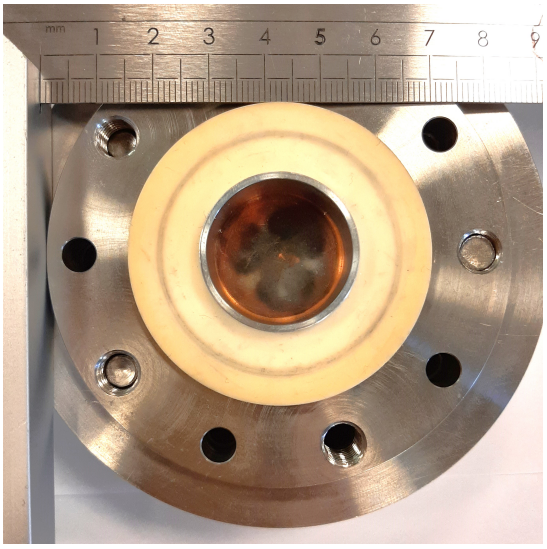

Fig. 4.25. Tritiated target frontside after removal, showing the aging.

Due to the kinetic moment of the impinging deuteron, the neutron flux is not uniform and the neutron flux is spread in the space. The neutron flux map at a distance of 5 cm from the neutron source is shown in Fig. 4.26.

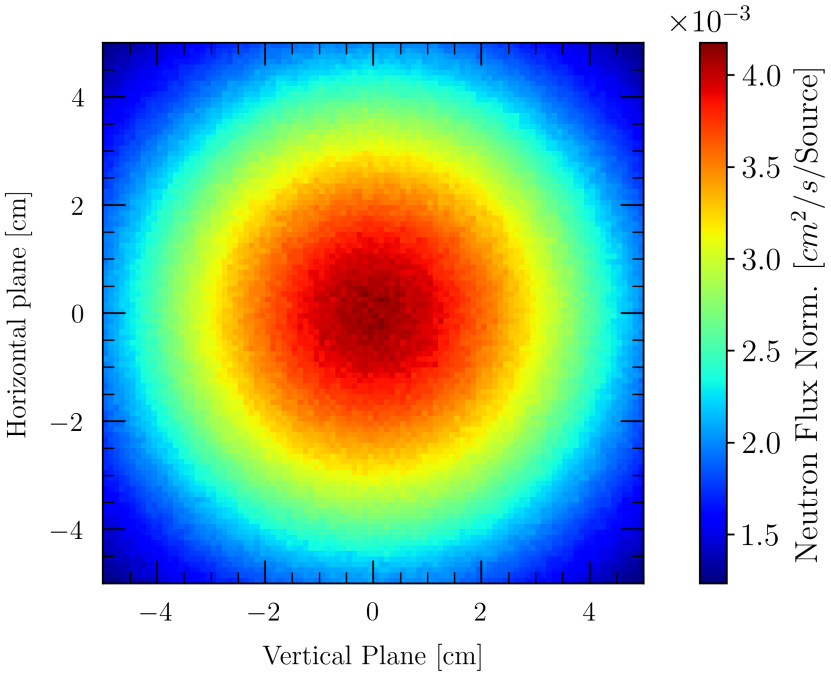

Fig. 4.26. Neutron flux map at distance of 5 cm from the neutron source. Results are obtained from FLUKA simulation using the GENESIS model [153].

Hence, it can be seen that the neutron flux intensity is higher in the center of the beam and decreases as the distance from the source increases. Considering the neutron flux distribution, it should be noticed that the neutron source is not isotropic. Particular attention is paid in the definition of the anisotropy of the source in the community of neutron generator users. Indeed, the neutron yield is a function of the deuteron energy and the angle of incidence on the target. According to the two body reaction analysis, the neutron energy is spread, depending on the angle of emission as seen in Table 4.11.

Target	E_n [MeV] (180 °)	E_n [MeV] (0 °)
Tritiated	13.12	15.26
Deuterated	2.01	3.14

Table 4.11. Neutron energy distribution according to the neutron emission angle in the laboratory frame, schematically represented in Fig. 4.23, for a given deuteron ion energy of 250 keV.

All the physical and technical aspects of the neutron source and sensor can be considered in Monte-Carlo simulations such as:

- The deuterons scattering
- The deuterons interacting with the target and energy loss
- The anisotropy of fusion cross Section [154].

The neutron spectrum, as observed in Fig. 4.27, is nearly monoenergetic, with the neutron energy varying based on the neutron emission angle, which is measured in relation to the direction of deuteron flight within the accelerator tube. The broadening of the spectrum is also dependent on the angle. The neutron spectrum spreading at a fixed detection angle is influenced by the energy and angular distributions of incident deuterons within the target.

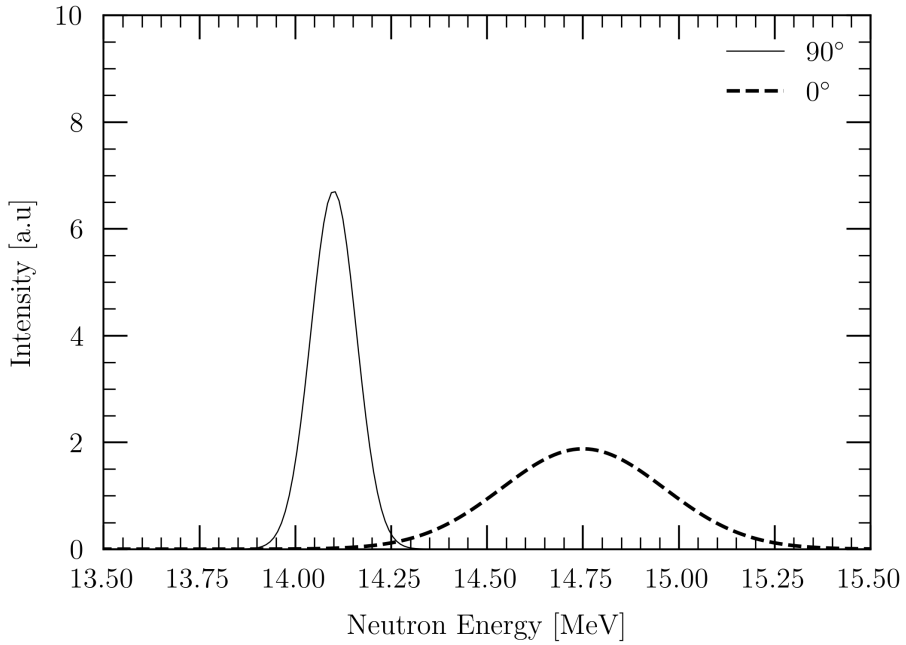

Fig. 4.27. Theoretical neutron spectrum of a D-T generator for two normal and perpendicular positions. The area under the curve is normalized to unity. The neutron spectrum spreading at a fixed detection angle is influenced by the energy and angular distributions of incident deuterons within the target according to the description adapted from [155].

The overall spectrum broadening at various angles is influenced by factors such as kinematics factors with the straggling of the deuteron within the tritiated/deuterated target [156], the velocity distribution of the accelerated deuterons, and the angular distribution of incident deuterons. The contributions presented are crucial for the understanding of the neutron spectrum and it should be pointed out that the MCNP simulation cannot provide the same level of accuracy for neutron emission and deuteron transport with incident energy of few hundreds of keV. Some upgraded D-T source model have been validated through the reproduction of the theoretical angle-dependent neutron energy and yields, as well as through cross-validation of the cell flux with point detector. The distribution of outgoing neutron angles in the center of mass system characterized by Legendre polynomials is also taken into account in the simulation leading to Fig. 4.27.

4.3.2. Implementation of an acquisition chain dedicated to pulse mode measurement

In Chapter 3, the indirect detection of fast neutrons via the collection of charge carriers generated in a thin SiC sensitive region was presented. The charge cloud produced by the ionization of this region by a secondary charged particle drifts under the influence of an electric field towards the sensor electrodes over a few nanoseconds. The acquisition chain must therefore be designed to capture the transient signals in pulse mode generated by the collection of these charge carriers in the sensor.

4.3.2.1. Dedicated electronic acquisition system

The acquisition chain is installed in the experimental hall, as displayed in Fig. 4.28.

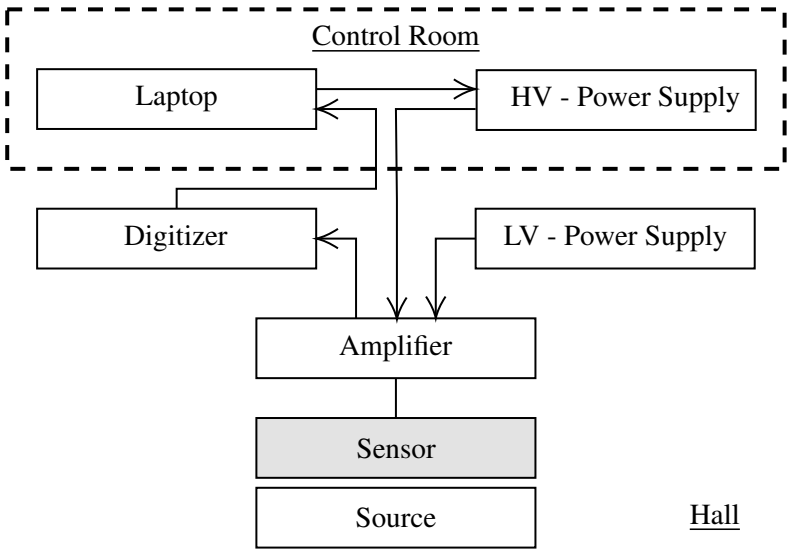

Fig. 4.28. Acquisition chain of the neutron detection system. The dashed rectangle represents the devices in the control room.

High voltage power supply

The collection of electrons and holes generated in the sensor is done by applying a HV[12] bias to the sensor. The HV is provided by a power supply manufactured by CAEN company. The DT5533E power supply is capable of delivering a voltage up to 4 kV with a current up to 3 mA. The power supply is connected to the sensor via a SHV connector. Four independent channels are available, allowing the biasing of several sensors simultaneously with positive, negative or mixed polarity. Outputs are provided in the form of SHV connectors. The HV output ramp is adjustable independently for each channel in the range 2 mV/s which is particularly useful at high voltage to avoid sparks and breakdowns.

A power supply able to deliver a high voltage is required to ensure that the charge carriers generated in the sensor are collected efficiently but particularly to ensure that sensitive regions is fully depleted as described in Section 3.4, Chapter 3.

Amplifier

A current amplifier sells by Cividec Instrumentation company [157] provides optimized coupling between the detector output and the rest of the counting system. This 40 dB broadband amplifier C2 HV is a low-noise current amplifier featuring an analog bandwidth of 2 GHz, making it ideally suited as a front-end amplifier for semiconductor based detectors due to its optimized speed. It includes a bias-tee for supplying bias to the detector HV input. Finally, this transimpedance amplifier, converts the current signal into a voltage signal.

This amplifier was chosen as regard to the requirements of the study, as it is particularly well suited for the detection of low-energy particles with its high gain. Its wide bandwith allows in addition, a high rate signal sampling. In a first approximation, the sensor capacitance C can be calculated as:

$$C = \frac{\epsilon \cdot S}{d} \tag{4.24}$$

With ϵ the permittivity of the material, S the surface of the sensor and d the thickness of the sensitive region.

[12] *High Voltage (HV)*

With the dimensions of the sensor under study of surface of 0.2 cm^2 and thickness of 60 µm it leads to a capacitance of the order of few dozen of pico-farads. The bandwith B being defined as:

$$B = \frac{1}{2\pi \cdot RC} \tag{4.25}$$

With R the input impedance of the amplifier.

It comes a bandwidth of the order of few hundreds of MHz for an input impedance of the amplifier of 50 Ω. The amplifier is then well suited for the detection of low-energy particles with a high bandwidth sampling.

4.3.2.2. Digitizing the signal

Device description

The SA230E digitizer from Aquiris company [158] is used to capture the transient signals generated by the sensor. The SA230E is a 14-bit digitizer capable of sampling at a rate of 4 Gsample/s with a bandwidth of 2 GHz. The digitizer is equipped with a single channel and a long acquisition memory of 2 Gsample. The digitizer is connected to the acquisition computer via a PCIe[13] bus which enables high-speed data transfer between the digitizer and the computer at up to 2 GB/s. The SA230E includes a Xilinx Kintex UltraScale FPGA[14] offering real-time signal processing capabilities such as waveform averaging or peak detection. All ADC boards and modules in the SA2 family implement a low-noise integrated real-time processing as displayed in Fig. 4.29. Hence, the dedicated device is capable of acquiring signals with a high dynamic range, which is essential for the detection of low-energy particles and requiring high bandwidth sampling.

The good Signal-to-Noise Ratio (SNR) performance allowed by the amplifier in the high frequencies allows then fast and accurate tracking of current pulses.

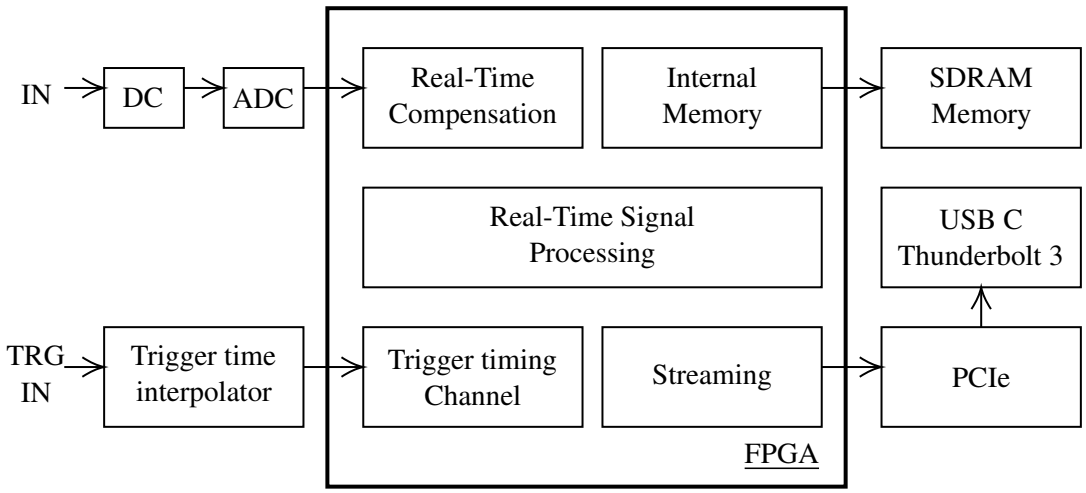

Fig. 4.29. SA230E Acqiris Digitizer Block Diagram.

[13] *Peripheral Component Interconnect Express (PCIe)*
[14] *Field-Programmable Gate Array (FPGA)*

Digitizer acquisition mode

The ADC[15] modules are designed to optimize sampling rates and memory usage, offering both single and multi-record modes. In these modes, data from all active channels is collected simultaneously, with all ADC gathering data concurrently, within a small fraction of the maximum sampling rate. The single record acquisition mode displayed in Fig. 4.30, which is the standard operation for most ADC module products, involves recording a waveform with a single trigger.

The ADC modules also provides a multi-record acquisition mode, which allows for the capture and storage of successive single waveforms. This mode displayed in Fig. 4.30, is beneficial as it can optimize the sampling rate of the ADC module and memory needs for applications where only specific parts of the signal under analysis are significant. This mode is particularly useful in nearly all impulse-response type applications such as RADAR, Time-of-Flight, and in the detection of neutrons for measurements in pulse mode in high flux environments, where signals have to be captured in a short time frame with a high sampling rate. In this mode, the acquisition memory is divided into a predetermined number of records, and waveforms are stored in consecutive memory records as they are received. Each waveform requires its own unique trigger. The multi-record acquisition mode allows for the capture and storage of successive events that occur within a very short frame duration, without any loss. A fast trigger rearm time is essential for multi-record acquisitions.

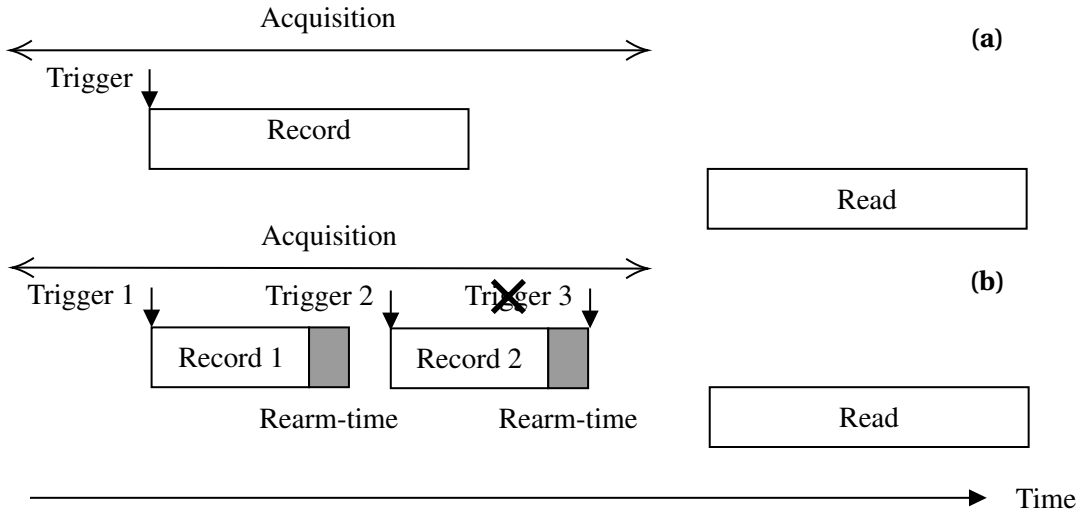

(a) Single-record mode

(b) Multi-record mode.

Fig. 4.30. Acqiris digitizer modes.

The digitizer is controlled by the Acqiris software. A dedicated Human-Computer Interface (HCI) was developed to control the digitizer and to set the acquisition parameters which allows the user to set the acquisition parameters such as the sampling rate, the number of samples, the trigger mode, and the trigger level. The later developped on LabVIEW[16] provides a user-friendly interface as seen in Fig. 4.31, to control the digitizer and to visualize the acquired waveforms as well as the on-line analysis of the data with Pulse Height Analysis (PHA) algorithms.

[15] *Analog to Digital Converter (ADC)*
[16] *Laboratory Virtual Instrument Engineering Workbench (LabVIEW)*

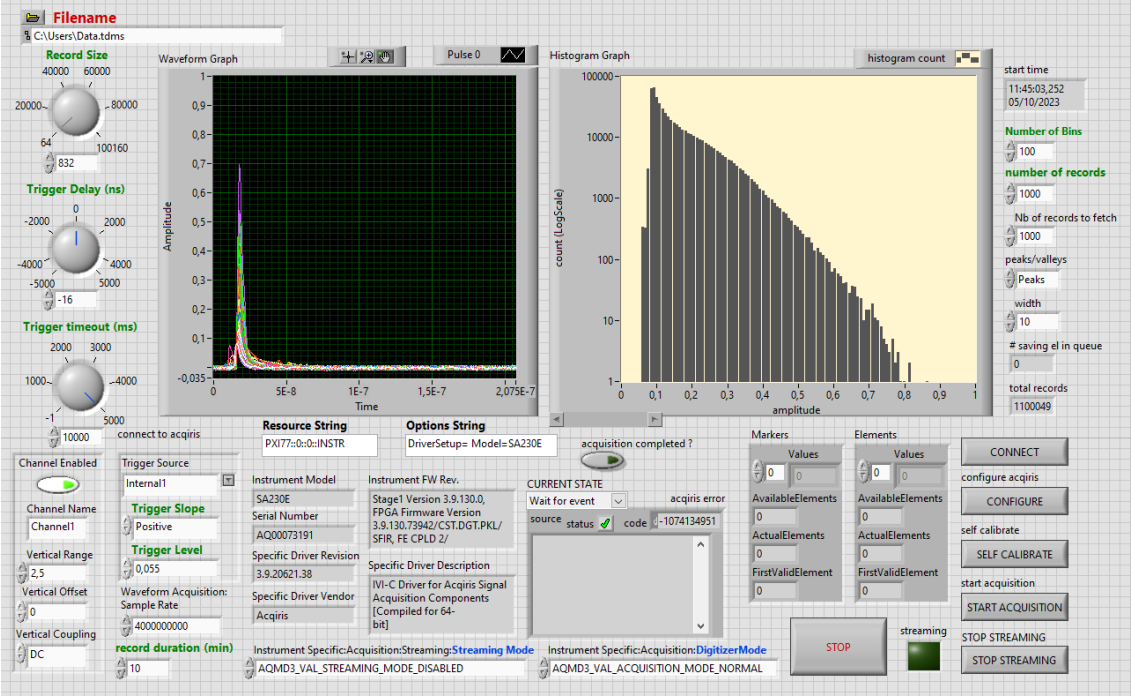

Fig. 4.31. LabVIEW HCI for the control of the Acqiris digitizer.

All in all, the specification of the presented acquisition chain has been presented. The performances have been evaluated in the context of the study of the detection of fast neutrons, and are deployed for the realization of a dedicated measurement campaign on a 14 MeV generator.

4.3.3. Measurements results

4.3.3.1. Context

The measurements carried out and the experiments performed on GENESIS facility are referenced below in Table 4.12. In the following, the presented results are obtained from the measurements performed on the specifically designed and manufacted sensor S60, at room temperature and room pressure. A cumulative duration of one hour of data had been recorded, with a stable neutron beam.

4.3.3.2. Determining the depletion bias voltage

In order to perform the measurements, the sensor is biased with a high voltage. The depletion voltage is determined by measuring the total counts as a function of the bias voltage. It should be noticed that study of the count rate as a function of the bias voltage is required to confirm the bias voltage needed to fully deplete the sensor. However, the influence of the induced electric field on the current flowing in the sensor will be described in a dedicated pulse shape analysis section in Chapter 6, dedicated to the charge carriers drift and collection dynamics study. The total counts are then normalized to the neutron fluence. The saturation curve is shown in Fig. 4.32 for the sensor S60[17] at room temperature. A sufficient depletion voltage of 300 V is determined for subsequent measurements based on the saturation curve. This value is set slightly higher than the beginning of the plateau to ensure full depletion of the sensor, even if changes in the electric field occur during the measurements.

[17] *To be noted that the notation S60 and S100 refer to the sensor of thickness* 60 µm *and* 100 µm *respectively.*

	S20	S60	S100
May 2022	Acquisitions at room temperature[b]. Validation of the measurement system.	∅	∅
Sept. 2023	∅	Acquisitions at room temperature[c], and up to 500 °C at room pressure[d].	Acquisitions at room temperature[a], and up to 500 °C at room pressure[a].
June 2024	Acquisitions at room temperature[a]	Acquisitions up to 300 °C under vacuum[e].	∅

[a] *Data not presented in this manuscript.*
[b] *Data not presented in this manuscript. Study presented at a conference [159].*
[c] *Data presented in Section 4.4.*
[d] *Data presented in Chapter 6.*
[e] *Data not presented in this manuscript. Study presented at a conference [160].*

Table 4.12. Summary of measurements carried out on GENESIS facility. The notation S20, S60, S100 are used to refer to the sensor of thickness 20 µm, 60 µm and 100 µm respectively.

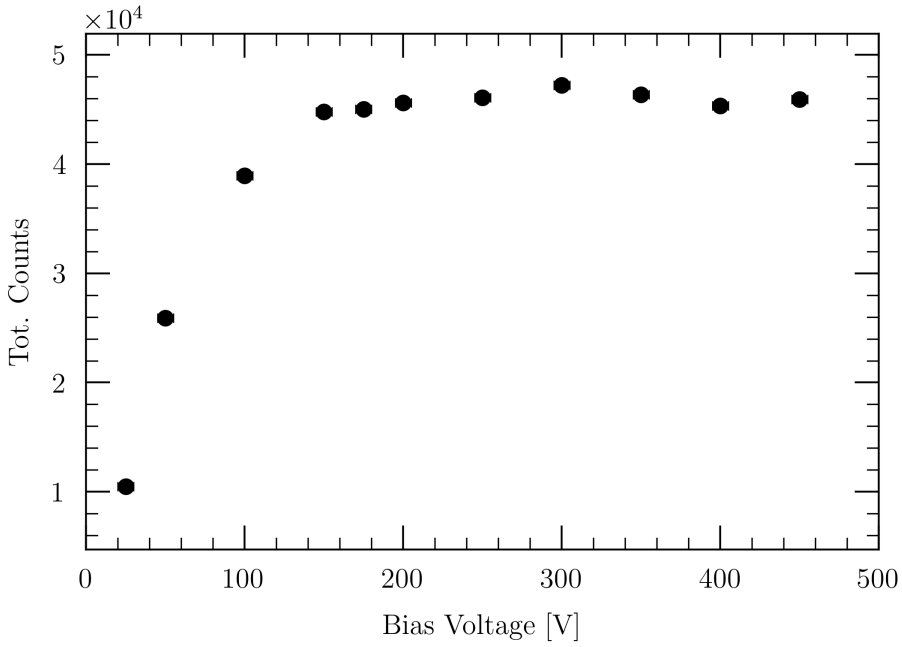

Fig. 4.32. Depletion voltage curve for the sensor S60 at room temperature.

4.3.3.3. Data processing and energy calibration

The objectives of the measurements using the dedicated acquisition chain presented previously were to record the current pulses generated by the collection of charge carriers in the sensor. These current pulses saved in binary format TDMS[18] are then converted to ASCII for subsequent processing. Each output file corresponds to a single trigger threshold within a preselected acquisition window on the Acqiris card. To individually analyze the pulses collected during the irradiation campaign, automated processing scripts are developed using the Python programming language and its associated libraries. Several quantities are extracted from the recorded signals as displayed in Fig. 4.33, such as the amplitude, which is determined relative to the baseline. The baseline is previously established by averaging the points before the trigger threshold. Additionally, the integral, representing the area under the peak, is determined using the trapezoidal method.

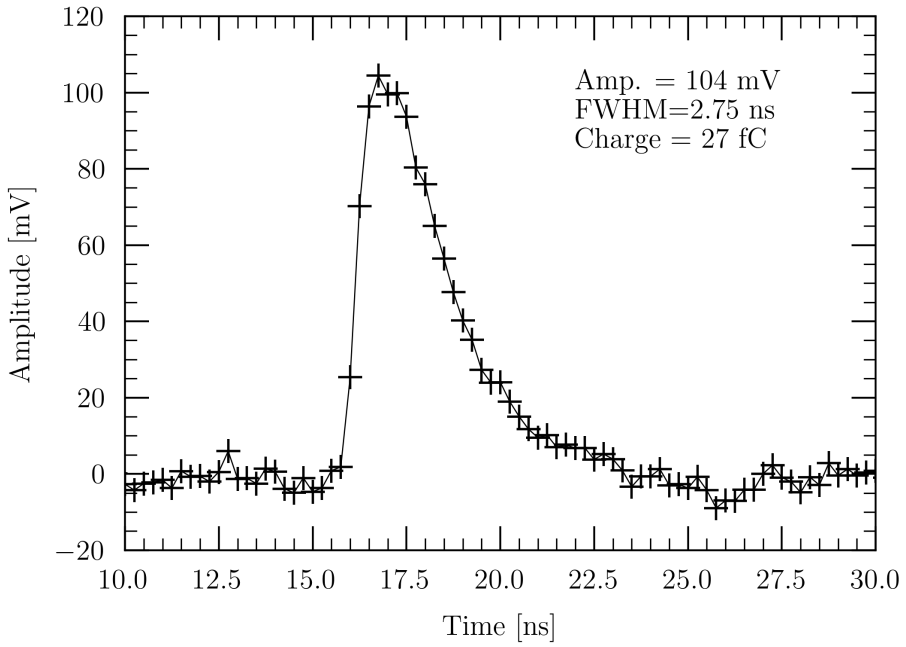

Fig. 4.33. Single current pulse recorded with the sensor S60.

Hence, using the current preamplifier internal gain A and the input impedance Z, the voltage signals are converted to the corresponding collected charges Q such that:

$$Q = \frac{1}{A \cdot Z} \int v(t)\,dt \tag{4.26}$$

The collected charge distribution obtained gives first insights into the secondary particles generated in the sensor, as seen in Fig. 4.34 paying attention to the peaks of interest depicted.

[18] *Technical Data Management System format (TDMS)*

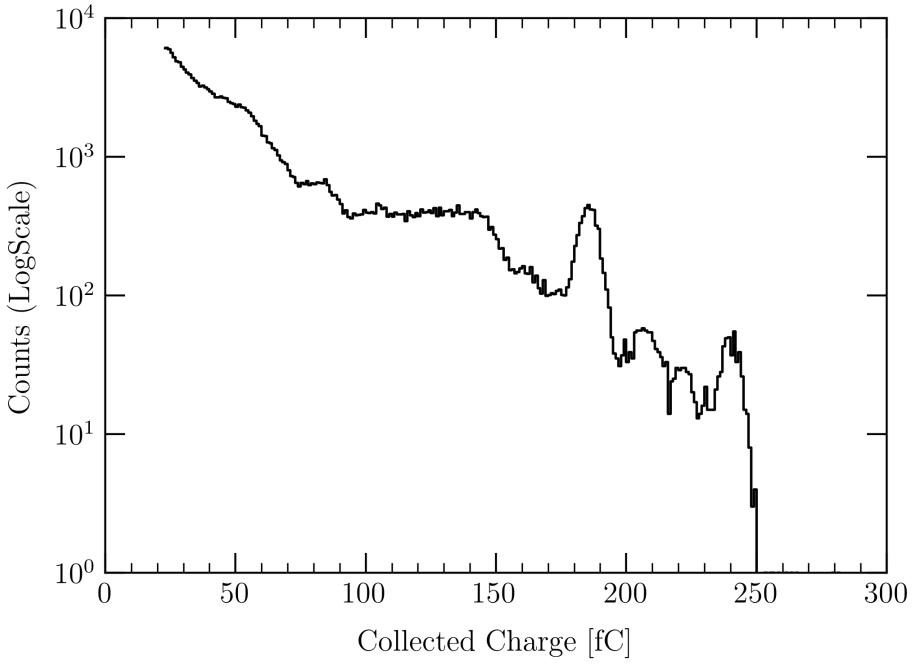

Fig. 4.34. Collected charge distribution obtained in 10 min duration. The experimental data are obtained with the sensor S60.

Then, from the distribution of the collected charges obtained, the energy deposited in the sensor is estimated. Indeed, in a preliminary approximation, the energy deposited in a semiconductor material by a charged particle is equivalent to the product of the number of generated electron-hole pairs N_{e^-,h^+} and the first ionization energy E_W. Furthermore, the number of produced electron-hole pairs is equal to the ratio of the charge collected upon reaching the electrodes, divided by the elementary charge q. Therefore, the expression for the deposited energy is derived such that:

$$E_{dep} = N_{e^-,h^+} \cdot E_W = \frac{Q}{q} \cdot E_W \tag{4.27}$$

The deposited energy distribution is computed based on the collected charge distribution obtained in the previous step. The next step is to compare the experimental data with the simulation results obtained using the GEANT4 code in order to validate the modeling scheme for the transport of charged particles in the sensor, and to use it to deconvolute the complex response of the deposited energy spectrum in the SiC sensor.

4.4. Validation of the charged particle transport modeling scheme in the sensor

4.4.1. Calculation versus experiment comparison

4.4.1.1. Presentation of the method

The objective of the method introduced here is to use the number of counts recorded in pulse mode for a specific reaction of interest to estimate the value of the neutron fluence incident on the sensor through the reaction rate evaluation. The various neutron interactions outlined in Section 4.1 will either directly or indirectly produce different charged particles at varying reaction rates. These need to be interpreted to trace the neutron flux as estimated by the solid-state sensor. To achieve this, a modeling scheme using the Monte-Carlo transport code GEANT4 was established to distinguish interactions in the SiC and to estimate edge effects related to the geometry of the sensor as described in Section 4.2. A first attempt to model the neutron interactions in the SiC sensor was made using the NRESP option [159], and a first estimation of the neutron flux was obtained using a 20 µm SiC sensor [161]. In the previous Section 4.2, it has been introduced a dedicated GEANT4 model, suited for simulating the generation of secondary particles in the SiC sensor to construct the response of the sensor. The provided GEANT4 model is hence used to simulate the SiC sensor under study as shown in Fig. 4.35, within the mono-energetic neutron field of the GENESIS facility, considering a planar source perpendicular to the sensor surface.

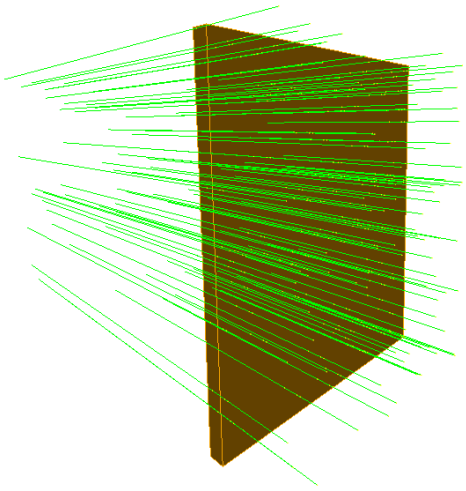

Fig. 4.35. GEANT4 model of the SiC sensor under study. The green lines represent the neutron beam.

The model is then employed to estimate two noticeable contributions to the interpretation of the experimental deposited energy spectrum obtained in Section 4.3:

- The distinction between reactions refers to the ratio of secondary particles from the $C(n,\alpha_0)$ reaction in the observed peak compared to those from the $Si(n,\alpha)$ and $Si(n,p)$ reactions.
- The edge effects, which pertain to the proportion of secondary particles from $C(n,\alpha_0)^9Be$ reaction, that will not deposit the full kinetic energy they possess at the time of their creation.

4.4.1.2. Detector simulation within the neutron field

It should be noted at this point that the input neutron spectrum used for the simulation is a result of FLUKA simulation presented in Section 4.3.1. The previous neutron flux distribution at 0°, displayed in Fig. 4.27, is then used as input for the GEANT4 simulation. However, the reference neutron spectrum at the location of the sensor is not derived from an exact modeling of the source. Consequently, an underestimation of the contribution of scattered neutrons is expected.

A comparison between the shapes of the experimental deposited energy spectrum and a simulated spectrum using the NRESP option incorporated into GEANT4 is shown in Fig. 4.36. The observed discrepancies at low energies, below 3 MeV, are due to the underestimation of the theoretical model of the number of scattered neutrons at the location of the sensor. The observed discrepancies at higher energies, for the events associated to the $^{28}Si(n,\alpha_0)^{25}Mg^{(g.s)}$ and $^{28}Si(n,\alpha_1)^{25}Mg^{(1^{st})*}$ reactions would be due to the uncertainties in the ENDF/B-VIII $^{28}Si(n,\alpha)$ evaluated data, for the fundamental and first excited states of the ^{25}Mg nucleus. However, for the rest of the distribution, like the continuous plateau observed from 4 MeV to 6.3 MeV, the differences between the GEANT4 model and the experimental distribution is within the ±25% deviation as displayed in Fig. 4.37. This result indicates that the representation of the complex sequential decay outlined in Section 4.1 is encouraging. As a result, this model is employed for the remainder of the study, although discrepancies are observed at high energies after the peak of interest. These discrepancies can be initially attributed to the uncertainties in the ENDF/B-VIII $Si(n,\alpha)$ reaction cross sections for excited states, especially regarding the first peak of deposited energy around 11.75 MeV associated to the emission of alpha particle and magnesium ion in fundamental state. It is important to note that the nuclear data used has not been cross-compared for neutron capture reactions. The data from ENDF/B-VIII.0 was used for the simulation, as it is commonly employed in the field of fast neutron detection.

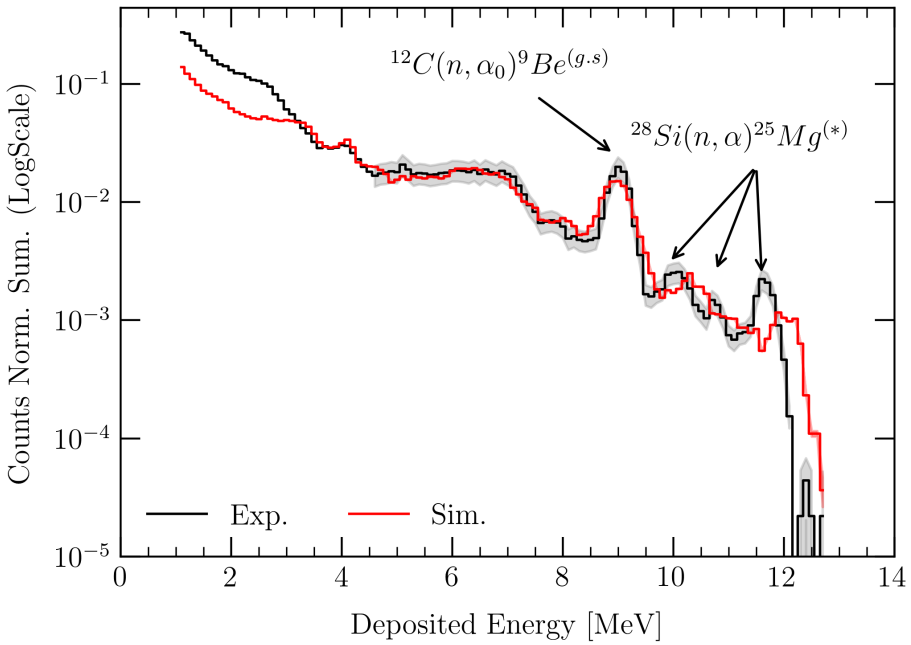

Fig. 4.36. Deposited energy spectrum comparison between the experimental and simulated data. The distributions are normalized based on the sum of counts above 4 MeV of deposited energy. This approach allows for comparison of the distribution shapes without considering discrepancies at low energy caused by the underestimation of scattered neutrons at the sensor's location.

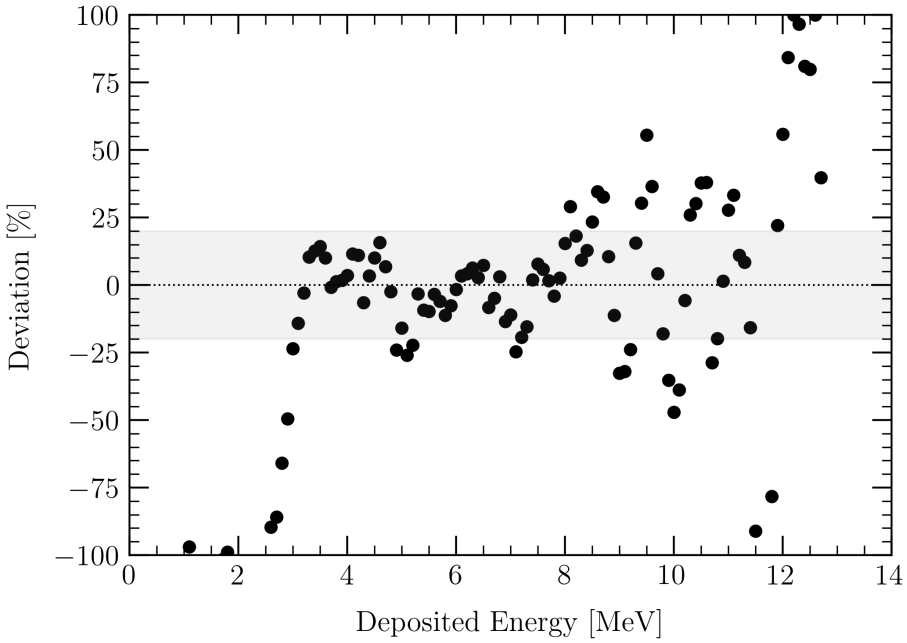

Fig. 4.37. Deviation percentage between the experimental and simulated data. The ratio is calculated as the difference between the experimental and simulated data divided by the experimental data.

4.4.2. Assessment of the experimentally estimated fluence rate and associated uncertainties

The procedure for determining uncertainties in data usually consists of three primary stages:

- Identifying uncertainty sources in the input data
- Propagating these uncertainties to estimate the uncertainties in the output data
- Performing sensitivity analysis with the goal of reducing the latter.

The following sections introduce, measure, and analyze sources of uncertainties derived from the comprehensive equation (4.30) shown below. Initially, regarding the thickness of the active region of the sensor, the reaction rate R at a specific energy E, is defined as follows:

$$R = N \cdot \sigma \cdot \phi \tag{4.28}$$

With σ the equivalent neutron cross section at energy E in [cm^2], ϕ the neutron flux in [cm^{-2}s^{-1}], and N the number of target nuclei defined such that:

$$N = \frac{\mathcal{N}_A \cdot \rho}{M} \cdot V \tag{4.29}$$

With $\mathcal{N}_A$ the Avogadro number in [1/mol], ρ the density of the target material in [g/cm^3], M the molar mass in [g/mol], and V the volume in [cm^3].

The fast neutron fluence rate from the mono-energetic beam can therefore be determined through measurements. By applying several correction factors to the reaction rate of the experimentally observed peak for $C(n,\alpha)$ reaction, we can establish the experimental flux as follows:

$$\phi_{exp.} = \frac{R_{peak,\,exp.} \cdot C^{-1}_{time,\,exp.} \cdot C_{diff.,\,num} \cdot C^{-1}_{edge,\,num.}}{N \cdot \sigma_{C(n,\alpha_0)}} \tag{4.30}$$

With $R_{peak,\ exp.}$ the number of counts under the experimental resolved peak of the reaction of interest $C(n,\alpha_0)$, $C_{time,\ exp.}$ the experimental irradiation time, $C_{diff.,\ num.}$ the reaction differentiation coefficient, $C_{edge,\ num.}$ the edge effects coefficient, and $\sigma_{C(n,\alpha_0)}$ the neutron cross section for the reaction $^{12}C(n,\alpha_0)^9Be^{(g.s)}$ at energy E.

Therefore, it comes the estimation of the experimental flux value of $2.7 \cdot 10^6$ cm^{2}s^{-1}. In the following paragraphs, the uncertainties associated with the experimental flux estimation are identified, evaluated, and discussed.

4.4.2.1. Uncertainty of the detector count rate

Since the objective of the method is to use the reaction of interest $C(n,\alpha_0)$, the initial step is to quantitatively estimate the number of $C(n,\alpha_0)$ reaction products that have deposited all the available kinetic energy at the time of their creation. In other words, experimentally, the number of counts involved in the growth of the peak observed.

Understanding the detector's energy resolution is crucial for these energy distribution measurements. In an ideal scenario, two particles of the same energy would result in pulses of the same amplitude distributed in the same energy bin of the deposited energy spectrum. However, in reality, the detection of particles of the same energy deposit approximates a Gaussian amplitude distribution across the spectrum as depicted in Fig. 4.38. The Gaussian approximates is also further complicated by the neutron spectrum's spread, which results in a broadening of the deposited energy spectrum.

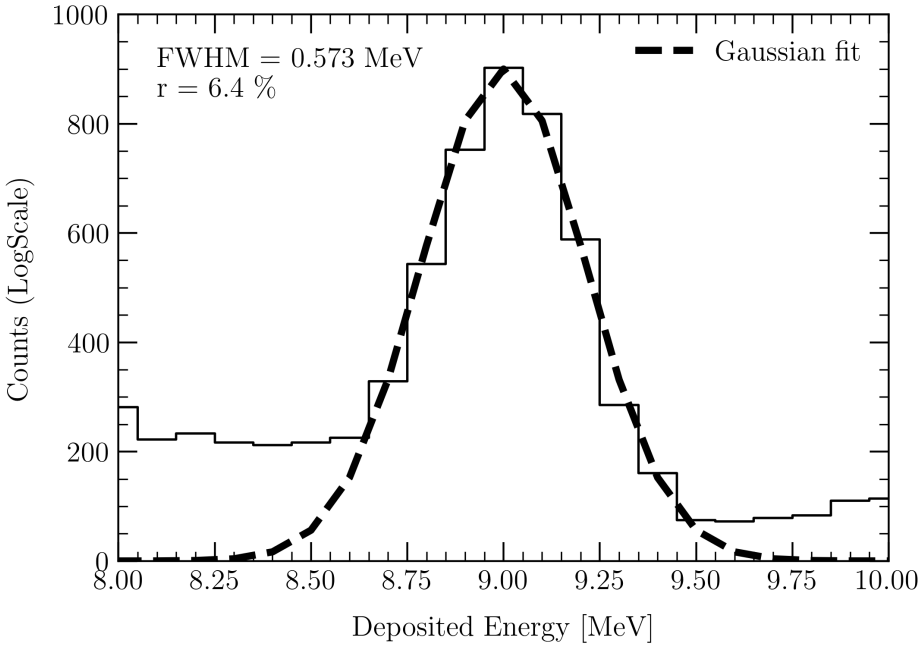

Fig. 4.38. Energetically resolved peak centered at 9 MeV.

The maximum energy resolution of the sensor is determined such that:

$$r = \frac{FWHM}{E_{max}} \tag{4.31}$$

With $FWHM$ in [MeV] and E_{max} the maximum energy deposited by the charged particles produced by the neutron reactions.

Several source of uncertainties can be identified in the determination of the FWHM of the peak :

- The uncertainty introduced by the electronic noise of the measurement chain bearing in mind that the most important part of the measurement chain is the detector-preamplifier part
- The uncertainty linked to the energy of the incident neutrons with the spread of the neutron beam energy
- The uncertainty associated with the collection of charges
- The uncertainty u_{Fano} in the generation of electron-hole pairs in the semiconductor based detector, defined such that [162]:

$$u_{Fano} = 2.355 \cdot \sqrt{E_W \cdot E_{max} \cdot F} \tag{4.32}$$

  Where, E_W is the average electron–hole pair creation energy of 7.78 eV for SiC [163], E_{max} is the maximum deposited energy by the reaction and F is the Fano factor[19] of 0.128 estimated for 5.485 MeV alpha particles from an ^{241}Am source using SiC [164]. But since the observed peak at 9 MeV is produced as a result of the sum of the ionization produced by the two reaction products, the Fano factor used is thus a rough estimate. Indeed, the energy distribution between ionizing processes, which contribute to the detector signal, and non-ionizing processes, which result in lattice heating and do not contribute to the detector response, will significantly differ for alphas and beryllium-9 ions. Sensors with a redesigned structure would necessitate the identification of a new appropriate Fano factor. This could entail, for instance, a new measurement campaign with an alpha source, complemented by modeling efforts. This point has not been addressed in the present study due to time constraints related to other thesis objectives.

A value of 573 keV is found for the FWHM with a peak resolution of 6.4% from 8.25 MeV to 9.75 MeV. This is an approximate estimation since silicon peaks contribute to the observed FWHM for the $^{12}C(n,\alpha_0)^9Be^{(g.s)}$ reaction peak as depicted in first Section 4.1. dedicated to the kinematics study and illustrated in the following Section 4.4.2.3

The parallel use of a silicon sensor with similar geometry and irradiation conditions would improve this estimate [165]. These upper and lower bounds for the peak are used to estimate the count number under the peak in the deposited energy spectrum obtained experimentally. A number of counts under the peak is estimated for which a statistical uncertainty must be taken into account. It varies as the square root of the total count numbers. It remains below 1.5% since the number of counts in the peak under study is greater than $5 \cdot 10^3$.

4.4.2.2. Uncertainty of the real time

In this section, the storage time of the data acquisition system is considered. Indeed, the complex behavior of a particular counting system can be affected by the physical processes occurring within the detector, as well as by the delays caused by pulse processing and recording electronics. Basic models, derived from experimental techniques, can be employed to ascertain the system's dead time [166]. Regarding the physical processes within the detector, it is important to note that the charge collection time in these thin detectors is of the order of a few nanoseconds, leading to current pulses with a FWHM of less than 5 ns after shaping and amplification. Hence, pile-up is not a significant issue in the present study with counts rates of the order of 1000 counts

[19] *The Fano factor is a measure of the fluctuations in the number of electron-hole pairs created by a high-energy particle passing through the semiconductor material.*

per second. Regarding the losses due to the pulse processing and recording electronics, it is noteworthy that the Acqiris SA230E digitizer used for data acquisition is a high-performance device as described in Section 4.3.2.2, equipped with a 4 GSample/s sampling rate and a 14-bit resolution. It can seize current pulse shapes up to 2 GHz and comes with a Xilinx Kintex Ultra-Scale FPGA for real-time signal processing. The standout feature of the digitizer is its extensive 8 GB acquisition memory, which allows it to store a significant amount of data. To optimize the memory usage and the sampling rate, the digitizer provides a multi-record acquisition mode, as described in Section 4.3.2.2. Within this mode, the acquisition memory is divided into several segments, which represent a predefined number of records, allowing then to store the data in a circular buffer. Hence, it allows the digitizer to record consecutive pulses waveform without any loss. The fast trigger re-arm time of approximately 100 ns ensures minimal dead time between records, enabling rapid successive events. Finally, The multi-record mode allows for consecutive accumulations of N records, making it extremely applicable for a variety of data collection situations, like the one being examined with a neutron generator for pulse mode measurements. The uncertainty in the experimental count rate is deemed insignificant in this context.

4.4.2.3. Uncertainty of the reaction deconvolution

It is worth noting that secondary particles from $Si(n,\alpha)$ and $Si(n,p)$ also contribute to the peak of interest observed in Fig. 4.39, which is associated with the maximum energy deposited by the products of $^{12}C(n,\alpha_0)^9Be^{(g.s)}$, as depicted in Fig. 4.40. Indeed, based on the kinematics study, the maximum energy deposited by the products of $^{12}C(n,\alpha_0)^9Be^{(g.s)}$ falls between the energy deposited by the products in the case of the two excited states of $^{28}Si(n,\alpha)^{25}Mg^*$, as outlined in the summary Table 4.13.

Reaction	Max. deposited energy [MeV]
$^{28}Si(n,\alpha_8)^{25}Mg^{(8^{th})*}$	8.69
$^{12}C(n,\alpha_0)^9Be^{(g.s)}$	9.04
$^{28}Si(n,\alpha_7)^{25}Mg^{(7^{th})*}$	9.30

Table 4.13. Maximum kinetic energy of the products contributing to the observed peak in deposited energy. Neutrons of 14.75 MeV are considered in the calculation, which correspond to the center of the neutron distribution spectrum.

For a given neutron energy, the kinetic energy of particles from $Si(n,\alpha)$ reaction is comparable to that from $C(n,\alpha_0)$ reaction. Consequently, the $Si(n,\alpha)$ events will invariably influence the observed FWHM for the $^{12}C(n,\alpha_0)^9Be^{(g.s)}$ peak, regardless of the junction design and thickness. Hence, it is necessary to quantify in the observed peak the fraction of events originating from $^{12}C(n,\alpha_0)^9Be^{(g.s)}$ reaction by subtracting those originating from neutron captures on silicon nuclei. The differentiation coefficient for the reaction of 61%, is then determined using the GEANT4 model. The intensity associated with the $^{12}C(n,\alpha_0)^9Be^{(g.s)}$ and $^{28}Si(n,\alpha_8)^{25}Mg^*$ reactions contributing to the peak of interest is based on branching ratio estimation. This estimation depends on the nuclear data used and its associated uncertainties, as well as the neutron energy distribution. For simplicity, a 10% uncertainty is assumed for the reaction differentiation coefficient, although a dedicated study would be required for a precise assessment.

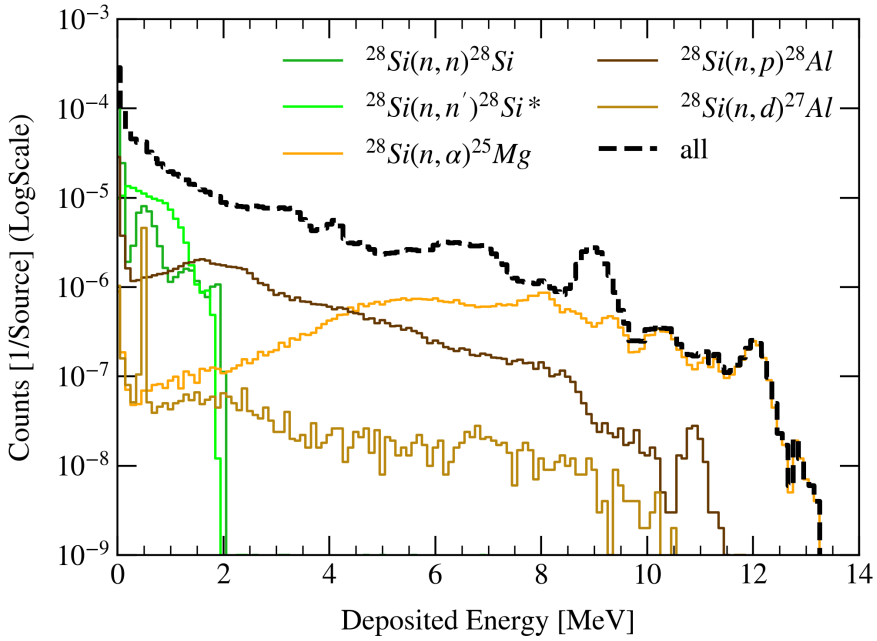

Fig. 4.39. Deposited energy distribution of the particles in the way out of the ^{28}Si nucleus neutron captures.

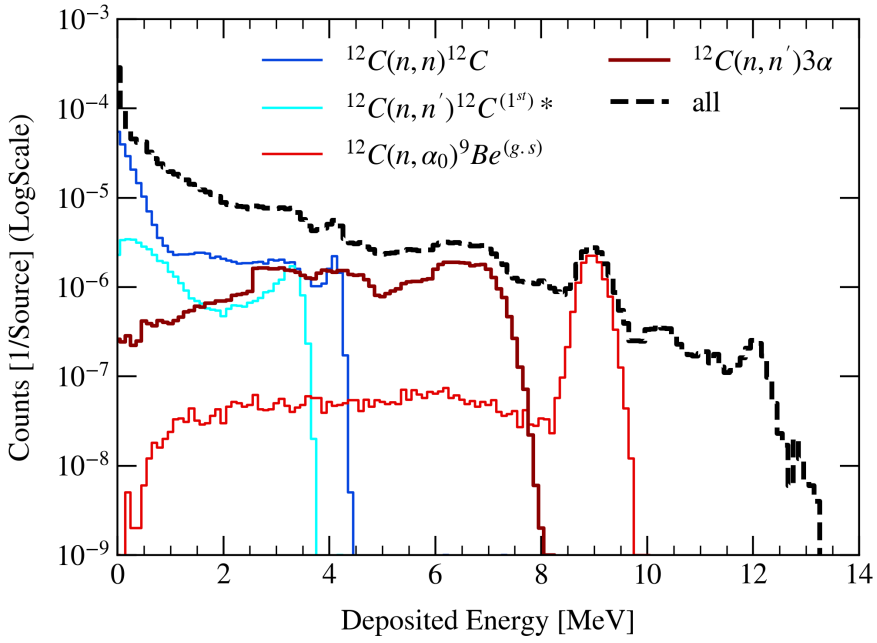

Fig. 4.40. Deposited energy distribution of the particles in the way out of the ^{12}C nucleus neutron captures.

4.4.2.4. Uncertainty of the detector edge effects

It has been previously established that events related to the $^{12}C(n,\alpha_0)^9Be^{(g.s)}$ reaction produce a distinct peak at a maximum energy of 9 MeV, as depicted in Fig. 4.40. This scenario corresponds to instances where the total kinetic energy of the secondary particles from the $^{12}C(n,\alpha_0)^9Be^{(g.s)}$ reaction is fully absorbed in the sensor as schematically described in Fig. 4.41(c). For events observed in the histogram where the deposited energy is less than this maximum 9 MeV value, the influence of edge effects on the results is considered at this point.

Hence, in the case of neutron interactions such as captures, it is understood that events occurring on the edges of the thin solid state sensor's rear side generate charged particles that traverse only a minimal distance in the active detection area, as schematically shown in Fig. 4.41(b). For example, the energy distribution of alpha particles produced in $C(n,\alpha_0)$ reactions ranges from 2.8 MeV to 7.9 MeV for an 14 MeV incident neutron, as shown in Section 4.1. According to SRIM calculations, these particles can deposit energy along their path from 7 to 32 µm.

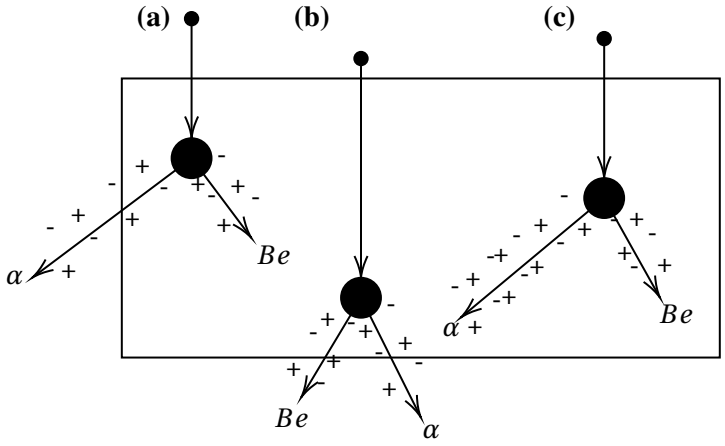

(a) Just a fraction is deposited

(b) Particles hardly deposit any energy

(c) All the energy is deposited in the SCR.

Fig. 4.41. Schematic representation of edge effects for the energy deposited by charged particles at the reaction outlet $^{12}C(n,\alpha_0)^9Be^{(g.s)}$. The plus and minus signs show the electron-hole pairs created along the trajectory of the charged particle. Their density along the trace represents schematically the ion's stopping power, associated with its linear energy transfer.

The energy deposited by these particles fluctuates based on the interaction location, particularly where the particle ceases movement. This is because the stopping power is most significant at the end of its path, as depicted by the Bragg peak for alpha-particle stopping power. Therefore, in certain instances, particles do not expend all their kinetic energy at the point of creation since the Bragg peak is situated outside the SCR, as depicted schematically in Fig. 4.41(a). These events contribute to the total energy spectrum deposited, but they do not aid in forming the characteristic peak that represents maximum energy deposition. The model results produced a count of 58% from the $^{12}C(n,\alpha_0)^9Be^{(g.s)}$ reactions that falls within the peak. This provides the correction factor needed to account for the sensor edge effects on the measured count. As for the previous correction factor, a 10% uncertainty is considered for the edge effects coefficient as a first approximation.

4.4.2.5. Uncertainty of the number of target nuclei

Given that the quantity of target nuclei is determined by the volume of the sensor's ac66666tive region as per (4.29), it is necessary to consider the uncertainty associated with defining this volume. In semiconductor-based *p-n* junction detectors, the thickness W_{SCR} of the active region, is influenced by the polarization bias voltage and intrinsic parameters as expressed in Section 3.1, Chapter 3.

However, since the optimal bias voltage applied was ascertained using a polarisation curve, a value exceeding the analytical requirement was utilized to deplete the SCR. Consequently, the uncertainty for the SCR volume is approximately equivalent to the *p*+ layer thickness uncertainty, which is estimated to be 10% during the manufacturing process, as indicated in Appendix C. This uncertainty is employed to estimate the number of target atoms, as the uncertainties of the other terms in (4.29) are negligible.

4.4.3. Assessment of the theoretically estimated flux and associated uncertainties

Initially, under the assumption that the distance from the detector to the source exceeds the linear dimensions of the detector aperture, we can establish the formula for the reference neutron flux emitted in the scenario of an isotropic point source as follows:

$$\phi_{ref.} = \frac{I_n}{4\pi d^2} \tag{4.33}$$

With I_n the neutron source intensity in [s^{-1}], and d the distance between the tritiated target and the detector in [cm].

Therefore, it comes an estimation of the reference flux value of $2.6 \cdot 10^6$ $cm^2 s^{-1}$. Although the hypothesis of an isotropic point source is not entirely accurate as presented previously in the source description, Section 4.3.1, it is a reasonable first approximation for the reference flux to be compared with the flux estimated experimentally. In a metrological context, the reference flux value would need to be assessed with a high level of accuracy.

The uncertertainty of the neutron source intensity is estimated considering the following parameters:

- The uncertainty of the gamma monitor, which is used to measure the neutron source intensity
- The uncertainty of the deuteron acceleration, which is directly linked to the neutron source intensity
- The uncertainty in the deuteron slowing down in the target, which is related to the aging and composition of the non-rotating target.

In the case being examined, the neutron generator which provides an average neutron source intensity of $2.54 \cdot 10^9$ s^{-1}, is estimated to have a source intensity uncertainty of 5%.

The encapsulation of the sensor in the experimental setup presented in Section 3.4.3 is designed to ensure that the distance between the sensor and the source is constant. The thicknesses of the several materials interfaces used in the setup between the active region of the sensor and the source are measured with a precision of 0.1 cm. Regarding the location of the tritiated target, the distance between the sensor and the source is measured with a precision of about 6%.

4.4.4. Discussion about the sources of uncertainties

4.4.4.1. Uncertainty of the reference flux value

A simplified transport calculation was used, assuming an isotropic point source at a specified distance d. The computation of the intensity of the source is independent from the distance at which this reference flux is assessed. The terms of (4.33) are presumed to be statistically independent. The quadratic summation method is then used to calculate the total relative uncertainty using the individual uncertainties introduced in the previous sections.

Consequently, by applying the general law of uncertainty propagation, the variance of the experimental flux, which is a function of other variables such that $\phi_{ref.} = f(x_i)$, can be articulated as follows:

$$\sigma^2 = \sum_{i=1}^{m} \left(\frac{\partial f}{\partial x_i}\right)^2 \sigma_{x_i}^2 \tag{4.34}$$

The individual uncertainties introduced in the previous sections are listed in Table 4.14. A relative uncertainty of 12.7% in the estimation of the reference flux value results, after the propagation of uncertainties taking the derivation of (4.33) with respect to I_n and d into account.

Symbol	Contribution	Relative uncertainty at 1σ [%]
I_n	source intensity [$n \cdot s^{-1}$]	5
d	sensor axial position [mm]	5.7

Table 4.14. Results and comparison of uncertainty sources in the theoretically estimated flux.

4.4.4.2. Uncertainty of the experimental flux value

In a primary analysis [161], it has been assumed as a first approximation that the m terms in (4.30) are only weakly correlated and are therefore considered to be statistically independent. However, the number of counts in the peak, the edge effects coefficient, the reaction differentiation coefficient, and the number of target nuclei are all interdependent in the calculation of the experimental flux since they are all derived from the sensor thickness for which the announced uncertainty is 10%. Therefore, considering the interdependence of these terms, the propagation of uncertainties has to take into account the covariance between the terms. The total relative uncertainty in the estimation of the experimental fluence rate is then evaluated using the general expression for the propagation of uncertainties considering m correlated terms as follows:

$$\sigma^2 = J \cdot \Sigma \cdot J^T \tag{4.35}$$

With J the Jacobian matrix of $\phi_{exp.}$ with respect to x as the vector of m variables where $J_{i,j} = \partial f / \partial x_i$ with $\phi_{exp.} = f(x_i)$ and Σ as the covariance matrix of x. With:

$$cov(x_i, x_j) = \frac{1}{n} \cdot \sum_{k=1}^{n} (x_{i,k} - \bar{x_i})(x_{j,k} - \bar{x_j}) \tag{4.36}$$

With n the number of measurements, $x_{i,k}$ the kth measurement of x_i and $\bar{x_i}$ the mean of x_i.

In the description of the corrective factor for reaction dissociation and deconvolution, it was noted that the current study is based on a single modeling scheme of a sensor, considering a specific reference neutron spectrum. A comprehensive metrological study would require a more extensive investigation to determine the covariance between terms, involving more measurements and a detailed sensor model, necessitating a dedicated modeling scheme. This study focuses on providing an initial estimation of the flux, emphasizing the methodological

approach and uncertainty estimation rather than detailed uncertainty propagation among interdependent terms. Such propagation would require specialized tools and more time than allocated for this part of the study.

Consequently, the covariance between terms is neglected, and the total relative uncertainty is estimated using the quadratic summation method. The individual uncertainties discussed in previous sections are listed in Table 4.15, leading to an estimated relative uncertainty of 18.2% at 1σ for the experimental flux.

Symbol	Contribution	Relative uncertainty at 1σ [%]
$R_{peak,\,exp.}$	number of counts[a]	1.3
$C_{time,\,exp.}$	experimental irradiation time	1.0
$C_{edge,\,num.}$	the edge effects coeff	10.0
$C_{diff.,\,num.}$	the reaction differentiation coeff.	10.0
N	the number of target nuclei	10.2
$\sigma_{C(n,\alpha_0)}$	the neutron cross section[b]	4.9

[a] *Under the experimental resolved peak at* 9 MeV.
[b] *For the* $C(n,\alpha_0)$ *reaction at* 14.7 MeV *using ENDF/B-VIII nuclear database.*

Table 4.15. Results and comparison of uncertainty sources in the experimentally estimated flux under the assumption of weak correlation.

4.4.5. Comparison of theoretical and experimental results

In conclusion, the comparison between the theoretical reference value and the experimental one includes distinct terms, clearly identifying experimental components like the count numbers under the peak in the SiC sensor, and purely computational elements such as the reaction rate correction factors for edge effects and reactions differentiation estimated through the Monte-Carlo code GEANT4. The raw experimental result equates to to the count numbers under the peak, while the calculated value yields to the reaction rate per source neutron. Therefore, the experimental flux value cannot be regarded as purely experimental, as it integrates additional factors like the correction factors from the Monte-Carlo calculation. These integrated values must also consider covariance due to the uncertainty associated with the cross section used in both the GEANT4 model and the calculation of the experimental flux value, as well as the other covariance terms. In this first approach, the covariance between the terms were neglected.

Regarding the experimental versus theoretical flux comparison, the fact that the solid angle covered by the detector surface relative to the neutron source is less than 10^{-4}rad suggests that the incident particles can be treated as uniformly distributed across the surface and moving through the same thickness. Therefore, the simulations used to compute correction factors are independent of the sensor location. The uncertainties of the corrective terms are thus decoupled from the transport calculation for the reference value of the flux, which was analytically simplified by considering the strong assumption of an isotropic point source. consequently, the uncertainty associated with the ratio of the measured value to the reference value can then be determined by propagating the uncertainties through quadratic summation, as shown in Table 4.16.

The estimated value for the experimental flux of $2.7 \cdot 10^6$ cm^{-2}·s^{-1} is within the 1σ uncertainty range of the reference value of $2.6 \cdot 10^6$ cm^{-2}·s^{-1} at the location of the sensor. Therefore, the discrepancy between the two values falls within the range that can be ascribed to the uncertainty in their measurements, with a relative uncertainty for the ratio of 22.2% at 1σ. This initial result is encouraging for a first attempt at estimating the neutron flux using a SiC sensor.

Flux	Value [$cm^{-2} \cdot s^{-1}$]	Relative uncertainty at 1σ [%]
Exp.	$2.7 \cdot 10^6$ [a]	18.2
Ref.	$2.6 \cdot 10^6$	12.7
Ratio	1.04	22.2

[a] *Computed by integrating values of the cross section for the $C(n,\alpha_0)$ reaction over the neutron energy distribution.*

Table 4.16. Comparison of measured and theoretical neutron fluxes.

Conclusion

The calibration method for the SiC sensor currently in use is based on creating correction factors that link the energy deposition in the sensor to the geometry of the active region of the sensor. This approach was developed by taking into account the detection principle and the parameters that can be achieved. An evaluation of the combined uncertainties in the experimental and calculated reaction rates for estimating a measured flux against a theoretical flux used as a reference was carried out. This was done by estimating various sources of uncertainty and biases during the model verification process. The process of determining uncertainties in data processing is multi-staged. It begins with identifying uncertainties in the input data, followed by propagating these uncertainties to ascertain the uncertainties in the output data. The final stage involves conducting a sensitivity analysis.

However, this study does not cover the latter stage, which is essential for pinpointing the most influential input data uncertainties that affect the output data uncertainties. This information is essential in identifying the input data that has the most potential to reduce uncertainty. Dealing with uncertainties in this context is challenging due to the high degree of interconnection among many entries. Therefore, assessing output uncertainties necessitates the use of advanced methods. Specialised software tools like URANIE [6] can be employed to simplify the uncertainty determination process by automating tasks such as Monte-Carlo uncertainty propagation and sensitivity analysis. Furthermore, to finalize the analysis, a Monte-Carlo sensitivity study based on Sobol indexes [167], could be conducted. This study would aid in identifying the most critical input uncertainties that significantly impact the overall results. This last step, although important, was not conducted in this study due to time constraints.

This chapter has presented the methodology used to estimate the neutron flux using a SiC sensor. In a first section, the study of the sensor's response to mono-energetic neutrons was conducted in terms of kinematics and energy deposition, according to the plurarity of the reaction products. The later showed that the sensor's response is complex and that the interpretation of the deposited energy spectrum is not straightforward. The second section was dedicated to the development of a Monte-Carlo model using GEANT4 to simulate the generation of charged particles in the sensor's active region and the energy deposition. The numerical results were basically compared to the analytical model presented in the first section. However, the hypothesis introduced to simulate the sequential decay of the excited states of the berillium-9 and carbon-12 nucleus as well as the description of the silicon neutron capture reactions, required experimental validation. The third section was dedicated to the realization of an irradiation campaign using a deuterium-tritium neutron generator. The experimental results were used to validate the Monte-Carlo model and to estimate the effects of the sensor's geometry on the energy deposition. The last section was dedicated to the estimation of the experimental neutron flux, and the comparison with the theoretical value. The uncertainties associated with the experimental and theoretical flux values were estimated and compared. The results showed that the experimental flux value is within the 1σ uncertainty range of the reference value at the sensor's location with a relative uncertainty for the ratio of 22.2% at 1σ.

In the pursuit of enhancing the ratio between the observed and reference flux values, employing diodes with a thicker SCR with a denser has mitigated the geometry effects on energy deposition from charged particles, as seen in the results obtained with the sensor with a 60 µm SCR compared to the 20 µm SCR. Nonetheless, a noticeable enhancement is observed in the effective cross-section used for estimating the flux and calibrating the sensor independently could be necessary. In terms of the reference measurement, it might be worth considering the use of a flux measurement acquired using a dosimeter at the location of the sensor location, to circumvent biases associated with the neutron source generator. The methodology developed for modeling the response of a SiC detector facilitated the evaluation of correction factors necessary for the quantitative assessment of the neutron flux. The validation of this approach in a mono-energetic field marks the initial phase in the creation of a tool for deconvoluting energy spectra deposited in mixed and complex neutron fields. It also signifies the first step towards unfolding multi-energy neutron flux and energy spectra using SiC sensors.

5. Using a SiC sensor to estimate fast neutrons flux in a multi-energy field

The previous Chapter 4 underlined the ability of the sensor to measure the neutron flux in a mono-energetic field. The use of a threshold reaction in the sensor allowed a first encouraging estimation of the neutron flux. This first method can be applied to a mono-energetic field, such as neutron generator, or tokamak neutron source in a D–T scenario as depicted in Chapter 1 However, providing a qualification of the sensor response on a large energy scale of incident neutrons in a multi-energy field is a more complex task.

This second Chapter presents the complexity of the sensor response in a multi-energy field, and the method to estimate the absolute neutron flux using the sensor response functions. Regarding the limitations of the simulation scheme, the experimental data are required for neutron spectrum deconvolution. Therefore, the implementation of an acquisition chain dedicated to neutrons measurements using Time oF Flight (ToF) at the NFS[1] facility at GANIL[2] in Caen, France is presented. Finally, the experimental data are interpreted and a deconvolution is presented based on the method for spectrum derivation to eventually estimate the neutron flux in a multi-energy field, using the sensor response matrix developed.

5.1. Complexity of the sensor response

In the literature and using the state of the art of the fast neutron detectors presented in Chapter 1, several approaches are usually used to measure the neutron flux in a multi-energy field. The latter can be described in the context of our study with the following:

- If the shape of the neutron spectrum does not vary. As discussed in Chapter 4, the neutron flux can be estimated using the area under a peak of the sensor response function for quasi-monoenergetic neutrons. The number of fast neutrons detected above a certain energy is proportional to the reaction rate, which is determined by the area of interest in the response function, as illustrated in Fig. 5.2a. This method of estimating fast neutron flux relies heavily on the assumption of a constant neutron spectrum when reactor power increases, as it is based on the proportionality between the count rate in the response function and the power, as shown in Fig. 5.1. This approach is only valid for a specific location with a well-known neutron spectrum. The method and the response function results cannot be applied to a different location with a varying neutron spectrum, as it requires a calibrated location with a reference measurement from a secondary sensor.

[1] *Neutron For Science (NFS)*
[2] *Grand Accélérateur National d'Ions Lourds (GANIL)*

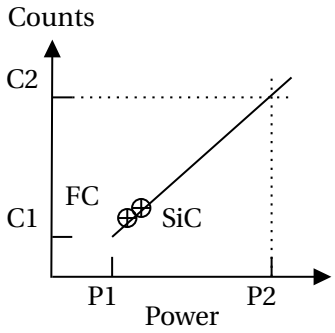

Fig. 5.1. Schematic diagram of the relative approach of flux estimation.

- In contrary, if the neutron spectrum shape varies. The objective results in the following bijection. A deposited energy spectrum is recorded by the sensor in an unknown neutron field, and the goal is to estimate the neutron flux using the sensor response, as illustrated by the bold arrow in Fig. 5.2. However, since the response of the sensor is a convolution of the neutron energy, the proportionality between the deposited energy and the neutron flux is not straightforward.

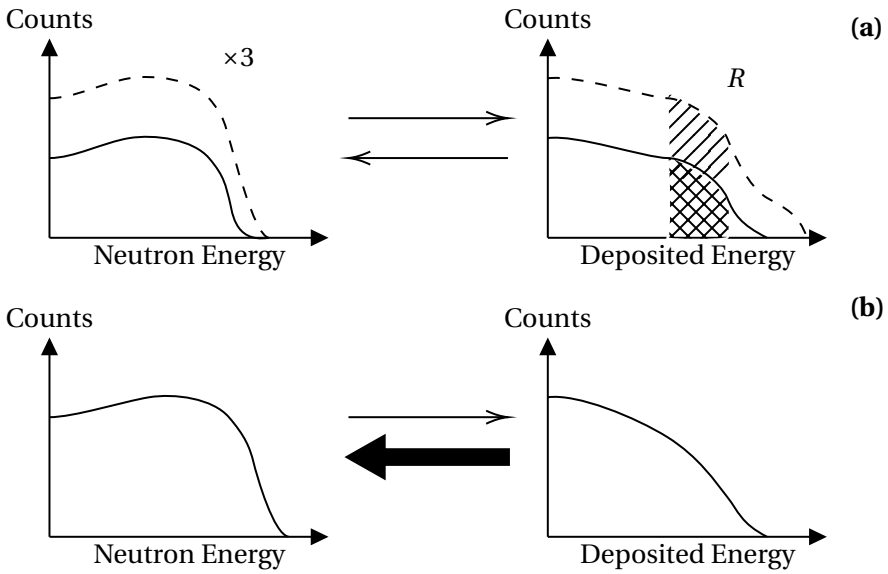

(a) Constant neutron spectrum shape

(b) Neutron spectrum subject to changes

Fig. 5.2. Schematic diagram of the use of the sensor in the two modes of operation.

All in all, the approach proposed to estimate the neutron flux in a multi-energy field is to proceed with the construction of the unitary response functions of the sensor for a multigroups neutron field. The overall approach is schematically depicted in Fig. 5.3, for a simple case considering three energy groups.

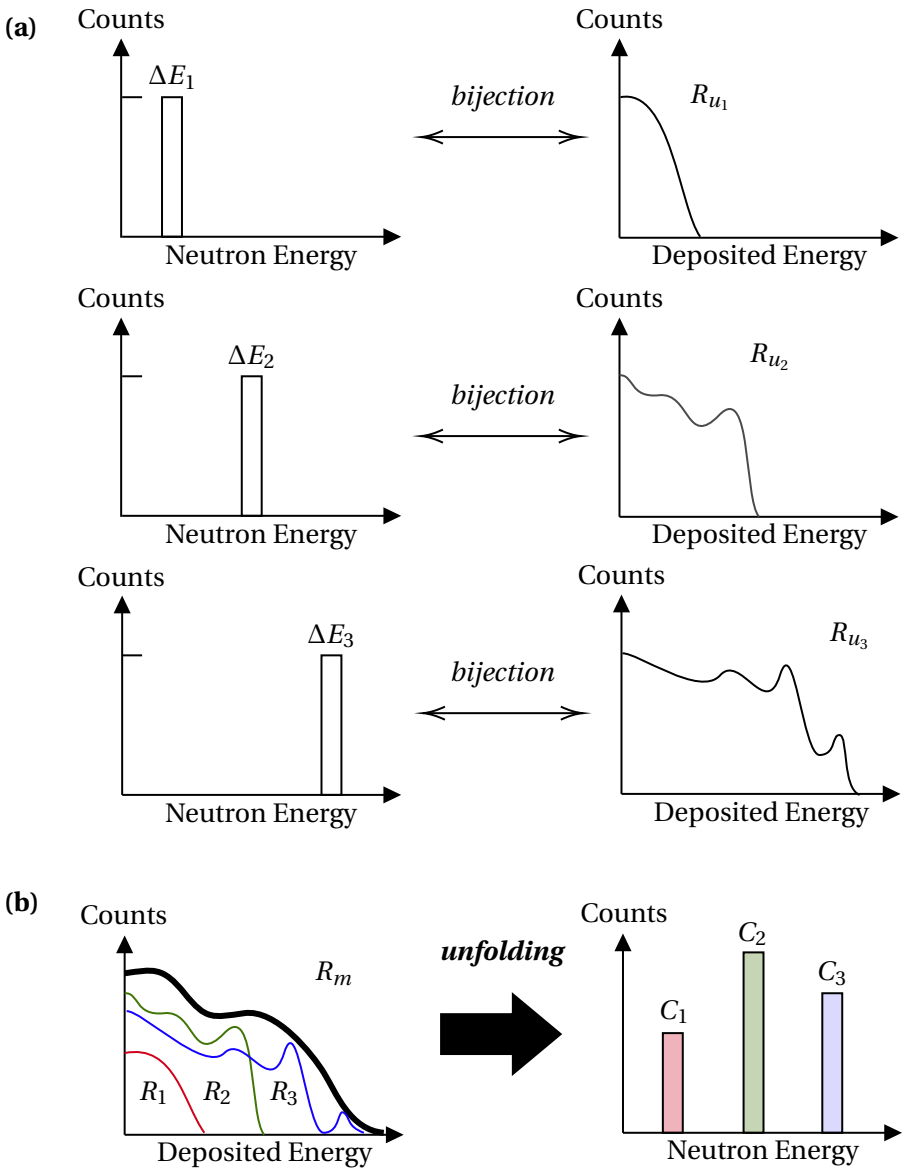

Fig. 5.3. Schematic diagram of the use of the sensor in case of a neutron spectrum subject to variation. (a) Three unitary neutron spectra $S_{\Delta E_i}$ and their corresponding response functions R_{u_i}. (b) The measured response R_m in the case of a multi-energy neutron spectrum, and the unfolding process to retrieve the neutron spectrum.

Hence, the bijection between the measured sensor response and the neutron flux of the multi-energy spectrum can be represented using a convolution function, such that:

$$R_m = R_1 \times C_1 + R_2 \times C_2 + R_3 \times C_3 \tag{5.1}$$

5.2. Calibration method for the sensor response function

In order to construct the bijection between the deposited energy spectrum and the neutron flux described above, the response functions must be built. This approach is commonly used in the field of neutron spectrometry, as for the scintillator detectors, and led to recent developments for fast neutron detectors using stilbene material [168, 169]. The later can be addressed through simulation with some limitations discussed in a next section, or through experimental data using mono-energetic neutron beam of different energies, or using the neutron time of flight technique in a multi-energy beam.

Since the mathematical operator that links the neutron flux to the sensor response is a convolution, the response matrix is built by the convolution of the neutron flux and the deposited energy in the sensor. When the response functions based on the pulses recorded through the ADC of digitizer is built, the relation between the differential energy vector and the neutron flux spectrum takes the discrete form of a matrix such that:

$$C_i = \sum_{j=1} R_{i,j}\phi_j \tag{5.2}$$

Which can be written in matrix form as :

$$\left(C_1, C_2, \ldots, C_n\right)^T = \begin{bmatrix} R_{1,1} & R_{1,2} & \cdots & R_{1,n} \\ R_{2,1} & R_{2,2} & \cdots & R_{2,n} \\ \vdots & \vdots & \ddots & \vdots \\ R_{m,1} & R_{m,2} & \cdots & R_{m,n} \end{bmatrix} \left(\phi_1, \phi_2, \ldots, \phi_m\right)^T \tag{5.3}$$

Where R the response matrix of size $m \times n$ which relates the response of the sensor to the neutron flux ϕ at energy i and the counts number in the energy bin j.

Each column of the response matrix R represents the sensor's response to a mono-energetic neutron field, obtained through simulations or experimental data, either with a mono-energetic neutron field or using the ToF technique. Then, to derive the neutron spectrum from the deposited energy distribution, it is necessary to invert the previous equations (5.2) and (5.3). This process effectively translates the measured data from an n-dimensional detector response space to an m-dimensional neutron energy flux space. Identifying the unknown ϕ from the observable C is a challenging, ill-conditioned problem. The response matrix R often has a high condition number, leading to large variations in the estimated ϕ due to small changes in the measured data C, making the problem sensitive to measurement errors or noise. This ill-conditioning arises from the presence of small singular values in R, causing its eigenvalues to vary widely in magnitude and indicating near-singularity. Numerically, this is reflected in the condition number of R, the ratio of its largest to smallest singular value. The ill-conditioning of the problem is further illustrated in the section dedicated to the study of the response matrix. Consequently, various mathematical techniques and computational algorithms, including least-squares and Monte Carlo methods, are employed to unfold the spectra.

5.2.1. Direct simulation of the response functions

Although the simulation scheme presented in Chapter 4 Section 4.2, through Monte Carlo calculation is able to provide a good estimation of the sensor response for a quasi mono-energetic field of 14 MeV, the simulation scheme is not able to provide a complete response matrix on the range of the neutron energy spectrum. The simulation scheme is limited by the nuclear data libraries evaluated on the range from 2 MeV up to 20 MeV, and the uncertainties associated.

In the Chapter 4, it was shown that the nuclear reactions induced by a fast neutron flux are numerous and complex. It is particularly the case for the reactions on the carbon with a sequential decay of the excited states of the beryllium and carbon nucleus, leading to the emission of alpha particles with several branching ratios and energy as detailed in Section 4.1. The uncertainties associated with the nuclear data libraries are significant for neutron capture reactions, such as $^{28}Si(n,\alpha)^{25}Mg$, as shown in Fig. 5.4.

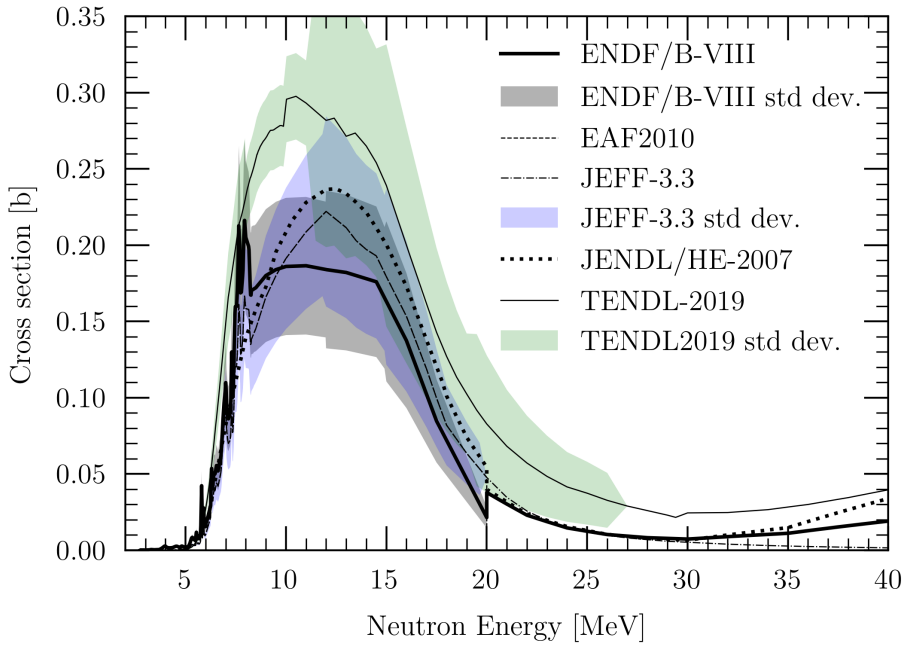

Fig. 5.4. Total effective interaction cross section of the $^{28}Si(n,\alpha)^{25}Mg$ reaction. The colored boxes represent the 1σ standard deviation of the cross section from evaluated nuclear data libraries .

The cross-section uncertainty is around 35% for the neutron energy range under study, regardless of the library used. In the following, ENDF/B-VIII.0, nuclear data are used since it is the most recent and widely used in the nuclear community, but comparing the cross-sections with other libraries such as JENDL-4.0, or JEFF-3.3 on the entire energy range is a perspective to consider. Additionally, the simulation scheme cannot provide a complete response matrix across the neutron energy spectrum. The covariance matrix of the nuclear data libraries is unavailable for the reactions under study, and there are significant uncertainties associated with the branching ratios and the energy of the emitted particles.

In the previous Chapter 4, dealing with quasi-monoenergetic neutron spectra, the nuclear data libraries were available, excluding the sequential description of the $^{12}C(n,n')3\alpha$ reaction, for the reactions under study and for the neutron energy spectrum between 2 MeV and 20 MeV. The later are typically obtained through experimental measurements and theoretical models providing reliable information for nuclear reactions and interactions within that energy range. However, for energies above 20 MeV, the nuclear data libraries are not evaluated and several approaches may be used including empirical extrapolation to extend the data to higher energies, or theoretical models such as optical model using fundamental principles of nuclear physics and statistical mechanics to predict reaction cross-sections. Hence, data above 20 MeV are not considered evaluated and the cross sections considered might be subject to high uncertainties. It is in particular the case for the high energetics neutrons capture reactions as the reaction $^{28}Si(n,n'+\alpha)^{24}Mg$, with cross section depicted in Fig. 5.5 for several libraries. This point is particularly important for neutron spectra such as the one at the NFS facility at GANIL, since the

neutron energy spectrum is in the range of few MeV up to 40 MeV.

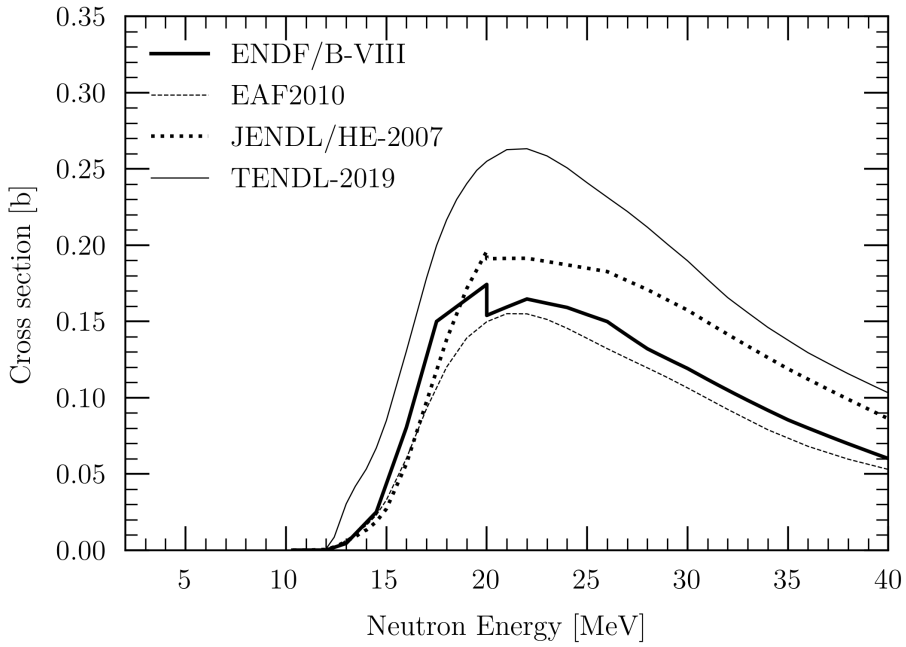

Fig. 5.5. Effective interaction cross section of the $^{28}Si(n,n'+\alpha)^{24}Mg$ reaction.

All in all, the simulation scheme is not able to provide a complete response matrix on the entire range of the neutron energy spectrum. The construction of the response matrix is then a challenging task, and the experimental data are required to estimate the neutron flux in a multi-energy field. This is the reason why an important experimental campaign was conducted at the NFS facility at GANIL in Caen, in october 2023 and is presented in the following sections of this Chapter.

5.3. Review of numerical unfolding methods

5.3.1. Comparison of the methods

Considering a matrix that links the number of events generated in one bin to the number of events observed in other bins, inverting this matrix and applying it to the measured distribution can lead to problems if the matrix is singular. Probabilistically, there is no guarantee that the inverse matrix exists. For instance, if two bins of the true quantities have the same probability of being observed in each of the measured bins, matrix inversion becomes problematic. To address ill-conditioned problems in unfolding measurements, the process typically starts by constructing a response matrix that captures how a theoretical "true" distribution, such as a neutron flux vector, is transformed into an observable distribution, like a deposited energy distribution vector, due to the measurement process. The goal is to use this matrix to reverse the transformation and approximate the original true distribution from the observed data. Direct matrix inversion is a common method to solve the equation (5.2), but it is challenging when the response matrix is ill-conditioned. Therefore, additional methods to stabilize the inversion process are required.

When choosing a method to solve an ill-conditioned problem, several factors must be considered. Regularization techniques, such as Tikhonov regularization [170], can stabilize solutions by adding a penalty term to handle noise and ill-conditioning, but require careful selection of the regularization parameter, which can introduce bias. Regarding other methods, the truncated

Singular Value Decomposition method [171], effectively manages numerical instability by focusing on significant singular values, but it can be computationally expensive and may lead to information loss.

Finally iterative methods are scalable for large problems and can be adapted to incorporate regularization, though they may face challenges with convergence and computational complexity. The best choice depends on the problem's size, matrix condition, noise level, and computational resources, often leading to a combination or hybrid approach to balance accuracy and stability.

5.3.2. Iterative Unfolding

The previous Tikhonov regularization method is a powerful tool for solving ill-posed inverse problems and can be particularly useful for unfolding neutron spectra from measured data. However, the method requires careful selection of the regularization parameter to balance the trade-off between fitting the data and smoothing the solution. Hence, the results obtained with this method shown large discrepancies with the true neutron flux. Indeed, in some cases, the regularization parameter may not be known a priori, and selecting an appropriate value can be challenging. To address this issue, an iterative unfolding approach can be used, which iteratively updates the solution based on the data and the response matrix, without the need for a fixed regularization parameter. Previous approach using stilbenes detectors have shown that iterative unfolding methods such as GRAVEL code can provide accurate results for unfolding gamma ray spectra [168, 169]. However discrepancies with the unfolded spectrum and the true neutron flux spectrum were observed, leading to unsatisfactory results. Therefore, D'Agostini's iterative unfolding technique [172], as a popular method specifically tailored for correcting data distortions is used in this study.

In the introductory section, the relationship (5.2) between true causes and observable effects was simplified through the use of a response matrix and its estimated inverse. Hence, (5.2) leads to the following expression:

$$\phi_j = \sum_{j=1} M_{i,j} C_i \tag{5.4}$$

To deduce the inverse matrix M, the understanding of the cause-effect dynamics via the response matrix is merged with an initial guess of the cause distribution. Using Bayes' theorem the following scenario is initiated:

$$P(c_j|e_i) = \frac{P(e_i|c_j)\, P(c_j)}{\sum_k^{n_c} P(e_i|c_k)\, P(c_k)} \tag{5.5}$$

This formula implies that upon observing effect associates to the number of counts in the deposited energy bin, the likelihood that it stems from cause associated to the neutron flux of a specific energy bin is directly related to the multiplication of the prior likelihood of that cause and its probability to obtain that effect. Therefore, the elements $P(e_i|c_j)$ denote the probability that a specific c_j leads to effect e_i, forming the known or simulated response matrix R. The prior $P(c_j)$ reflects the best or current understanding of the true and normalized distribution of causes. Following this, a connection between the observed effects and their causes is established using the following equation:

$$\phi(c_j) = \sum_{i=1}^{n_e} P(c_j|e_i)\, n(e_i) \tag{5.6}$$

However, it is important to note that a cause might not always lead to an observable effect, meaning there is a specific efficiency ϵ_j linked to each cause:

$$0 \leq \epsilon_j = \sum_{i=1}^{n_e} P(e_i|c_j) \leq 1 \tag{5.7}$$

With this consideration, the estimation of $\phi(c)$ is adjusted as follows:

$$\phi(c_j) = \frac{1}{\epsilon_j} \sum_{i=1}^{n_e} P(c_j|e_i)\, n(e_i) \tag{5.8}$$

$$= \sum_{i=1}^{n_e} M_{ji}\, n(e_i) \tag{5.9}$$

In this context, the detailed structure of M is outlined as:

$$M_{ij} = \frac{P(e_i|c_j)\, P(c_j)}{[\sum_k^{n_e} P(e_k|c_j)] \left[\sum_{k'}^{n_c} P(e_i|c_{k'})\, P(c_{k'})\right]} \tag{5.10}$$

The elements of M_{ij} are defined such that $P(e_i|c_j)$ established response matrix, $n(e_j)$ the observed distribution of effects, and $P(c_j)$ the initial distribution of causes.

After deriving the structure of M and estimating $\phi(c)$, the understanding of the cause distribution is improved. By using $\phi(c)$ as an updated prior, the accuracy of the cause distribution estimate is enhanced. The next iteration $(t+1)$ allows to compute $\phi(c)^{t+1}$ through the process denoted by the following expressions:

$$\phi_j^{t+1} = \sum_j M_{\mu j}^t n_j \tag{5.11}$$

$$M_{ji}^t = \frac{P_{ji}\phi_j^t}{\epsilon_j \sum_l P_{li}\phi_l^t} \tag{5.12}$$

Where ϕ_t represents the cause distribution at iteration t, and P_{ji} denote the elements of the response matrix.

By employing a suitable test statistic, like the Kolmogorov-Smirnov test, to compare ϕ_j^t and ϕ_j^{t+1}, the point at which further iterations yield minimal enhancements is determined. At this juncture, the unfolding process is considered to have converged. This powerful iterative unfolding method is retained for the following study. The mathematical framework has then to be implemented in a software package to be used in the unfolding process. The PyUnfold package [173] was chosen to implement the iterative unfolding method.

The package was initially designed to assess the impact of measurement effects on physical distributions, featuring an intuitive API[3] adaptable for various experimental scenarios, and the capability to seamlessly integrate both statistical and systematic uncertainties. It is especially designed to perform an iterative unfolding process on observed data to correct for distortions introduced by a response matrix and detection efficiencies. This process is widely used in fields like particle physics to infer the true distribution of a quantity from measured data. The package has been successfully applied in various scientific fields, including cosmic-ray energy spectrum measurements by the HAWC observatory [174].

The function takes into account uncertainties in the data, response matrix, and efficiencies, and allows for the use of different prior distributions and test statistics to guide the unfolding process. It supports stopping the iteration based on a test statistic threshold and can return either the final unfolded result or the results from each iteration. The function also supports the application of callbacks for additional customization of the unfolding process. The objectives involve several computationally intensive steps. Starting with validating user inputs and setting up a prior distribution scaled to the data sum, initializing a Mixer object[4] with provided data, errors, response matrix, and efficiencies, and setting a statistical test with stopping tolerance.

[3] *Application Programming Interface (API)*

[4] *A Mixer object is used to combine multiple datasets facilitating the integration of various inputs.*

The process iterates until the test statistic meets the tolerance or the maximum iterations are reached. Each iteration involves unfolding the distribution using a Mixer object updating the iteration status with the unfolded distribution, errors, and unfolding matrix, and calculating the test statistic for the next iteration. These steps are computationally demanding and require careful management of computational resources. Due to the size of our problem, the iterative unfolding method is particularly well-suited for the neutron flux unfolding process, and low computational resources are required to achieve convergence, which is a significant advantage as the unfolding process is usually computationally expensive.

All things considered, the iterative unfolding method is retained in the following study, using the PyUnfold package for the unfolding process. Low computational resources required are interesting, in the context of online unfolding process, where the neutron flux has to be estimated in real-time in nuclear facilities.

5.4. ToF measurement campaign

5.4.1. The GANIL NFS facility

GANIL stands as a prominent global laboratory specializing in ion beam research. Since 1983, it has provided beams for diverse scientific investigations, including atomic nucleus structure, nuclear fission or nuclear astrophysics. In addition to the GANIL facility, the SPIRAL-2[5] project expand the laboratory's capabilities, featuring a super-conducting linear accelerator and experimental areas NFS and S3[6]. The accelerator supports intense proton, deuteron, and heavy ion beams, reaching up to 5 mA, with energy ranges up to 40 MeV for deuterons and 14 MeV/A for heavy ions. Comprising two ion sources, an RFQ[7], and 26 super-conducting cavities, the LINAC enabled the creation of the NFS facility [175]. NFS, situated 9.5 m underground like the LINAC, encompasses a neutron production area currently called "converter room" shown in Fig. 5.6 and a time-of-flight experimental chamber.

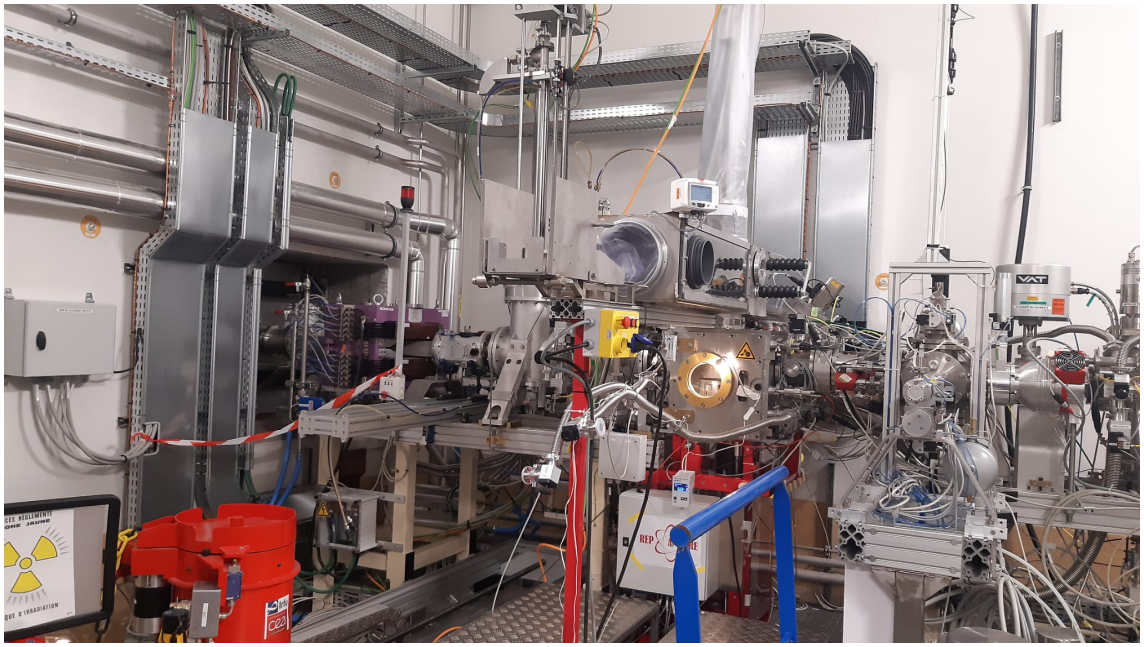

Fig. 5.6. NFS Converter Room.

[5] *Système de Production d'Ions Radioactifs Accélérés en Ligne de 2ème génération (SPIRAL-2)*
[6] *Super Séparateur Spectromètre (S3)*
[7] *Radio-Frequency Quadrupole (RFQ)*

Neutron production at NFS primarily involves the interaction of proton or deuteron beams with lithium or beryllium targets, yielding energetic neutrons. Utilizing thin targets results in quasi-mono-energetic neutron beams due to specific nuclear reactions like $^{7}Li(p,n)^{7}Be$ and $^{9}Be(p,n)^{9}B$. Alternatively, thick beryllium or carbon converters, which fully absorb the incident beam, produce neutrons with continuous energy spectra. NFS employs a rotating beryllium converter and fixed lithium and beryllium converters mounted on a water-cooled target holder. Downstream, a magnet deflects primary beam toward a Faraday cup for intensity measurement. Neutron energies ranging from 0.1 MeV to 40 MeV and flight paths of 5 m to 30 m necessitate a beam period exceeding 1 µs to prevent neutron overlap from successive bunches. Achieving this involves reducing the LINAC frequency of 88 MHz by over 100 or more using a single bunch selector downstream of the RFQ. This setup allows NFS to receive intensities up to 50 µA, corresponding to the maximum intensity authorized at NFS. In that case, for impinging deuteron beam of 40 MeV on a 8 mm tick beryllium target, the neutron flux is estimated to be of the order of $1.8 \cdot 10^{13}$ s^{-1} in 4πsr [176].

5.4.2. Experimental set-up

With the opportunity given by the NFS team, SiC sensors were placed in the NFS experimental area in August 2023, in order to record data during the autumn experimental campaigns where deuteron beams were used to produce neutrons with a thick beryllium target. In the interests of redundancy, and given the uncertainty surrounding the feasibility of such an experiment in this unfamiliar, and unfavorable environment for ToF users, two sensors were positioned, as depicted in Fig. 5.7. Indeed, regarding the locations of the sensors close the beam dump and to magnets, the conditions were not optimal for the sensors, in terms of metrological conditions, with the presence of magnetic fields and scattered neutrons. The thinner sensor, S60, was placed on the tube guide, while the thicker sensor, was positioned on a chassis under the magnet.

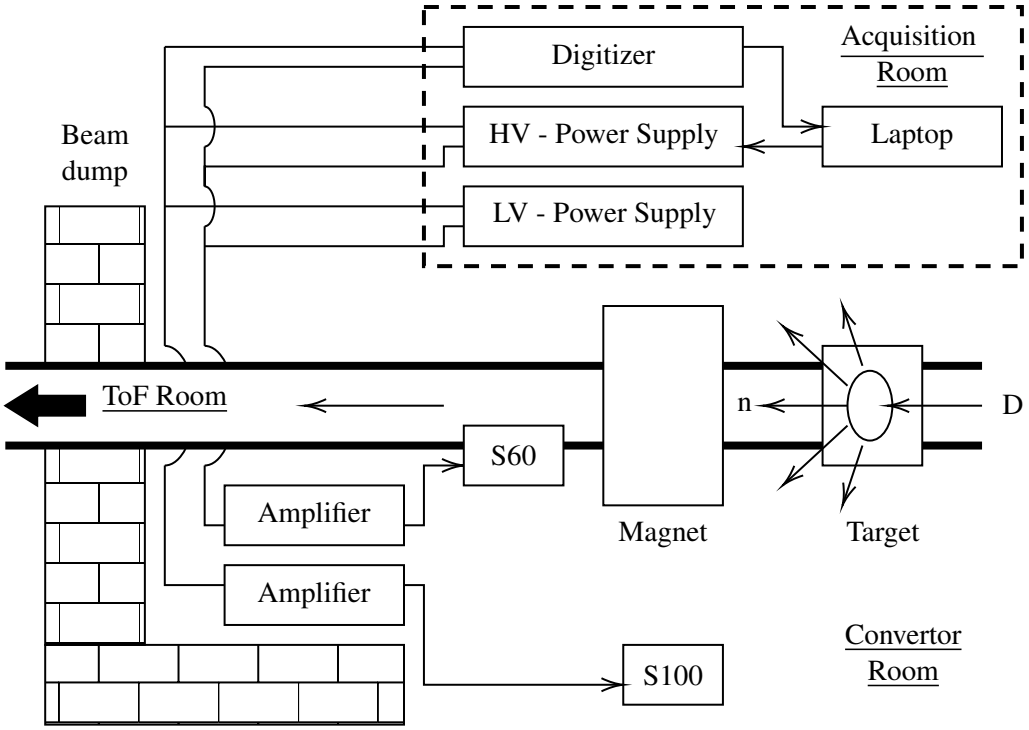

Fig. 5.7. Diagram of the NFS setup. The dashed rectangle represents the remote acquisition room. For sake of simplicity, only one output cable is shown for each amplifier devices. S60 and S100 stand for the SiC sensors of thickness 60 and 100 μm, respectively.

The two sensors under study were placed at an approximate distance of 120 cm from the target, while the preamplifiers were located at a distance of 10 cm from the sensor. It was agreed that the sensors could not be positioned as precisely as desired, due to the high level of activity in the convertor room area. Regarding the other devices, the digitizer was situated at a distance of 20 m from the preamplifier, in the acquisition room.

The amplifier choice was made with regard to the following cross-cutting objectives of the experiments:

- Constructing the response matrix for the neutron flux unfolding process
- Investigating the degradation of the sensors in the harsh environment and high neutron and photon fluxes of the NFS facility
- Studying the deposited charge within the sensor, while getting a first dataset for possible future implementation of the PSD method using current pulses.

Hence, while charge amplifiers are generally used for their ability to maintain the integrity of voltage signals over long distances, providing also better energy resolution, the choice of a current amplifier was made for the dedicated measurement system due to the flexibility it affords regarding the objectives of the experiments, and the questions raised by this unfavorable environment.

5.4.3. Tof principle

The ToF method is a well-established technique for measuring the energy of particles, including neutrons. The principle is based on the time taken for a particle to travel a known distance between a source and a detector. The time of particle creation, t_0, cannot be directly measured and must be determined relative to other events. It corresponds to the moment when deuterons strike the target as described in Fig. 5.8. The spallation products then travel a distance d, at the speed of light c for the gamma, reaching the sensor location where they are detected as a gamma-flash at time t_γ. Signals detected at later times t_n, are therefore associated with neutron-induced reactions.

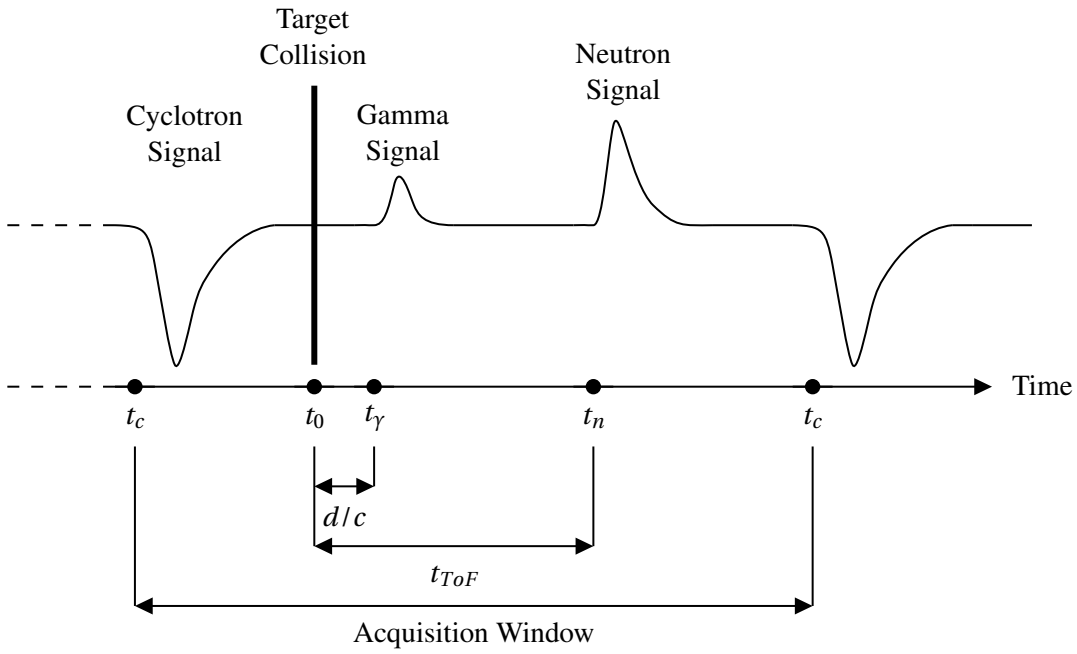

Fig. 5.8. Schematic diagram of the time-of-flight measurement principle.

Consequently the neutron ToF is calculated as the difference between the time of detection of the neutron and the time of detection of the gamma flash according to the following equation:

$$t_{ToF} = t_n - t_\gamma + \frac{d}{c} \tag{5.13}$$

The precision of ToF measurements is limited by the time resolution of the detector. Timing properties of electronic significantly impact neutron energy resolution mainly at short ToF i.e. for high energy neutron.

5.4.4. Acquisition chain requirements

In order to perform ToF measurements at NFS, the acquisition chain had to be able to manage the high frequency of the proton beam, up to 1 MHz. Then concerning the requirements on data storage and processing time, this large amount of data could lead to a detrimental dead time, which represent the main challenge of the preparatory work for the ToF measurements at NFS

Fortunately, the acquisition card identified at the early stage of the study, the Acqiris SA230, could handle such high frequency and large amount of data appropriately. The digitizer firmware was therefore configured to perform a peak detection and to store only the peak descriptors with the purpose of reducing the data size. Hence signal record acquisition and analysis can proceed concurrently with the reading of the outcome from the preceding record, effectively reducing the dead time between analyses of successive records. This approach enables the real-time analysis of a larger volume of signal data, outputting only the key features of significant waveform peaks. Additionally, in instances of input saturation, the system supplies the count of samples exceeding the range.

The dedicated PeaK Listing (PKL) firmware used with the digitizer offers a collection of programmable parameters for peak determination, allowing for real-time identification and listing of peak characteristics in the DDR4 SDRAM[8] memories as peak descriptors. With each new trigger event enabled, a 256-bit trigger descriptor is generated within the marker stream, which includes complete timestamp information related to the absolute time of occurrence of this new ADC record at a resolution of picosecond. For each detected peak within this ADC record, a 256-bit peak descriptor is created that contains metadata pertaining to the peak such as the peak position, peak amplitude and peak width. This peak descriptor is time-related to the previous trigger descriptor using relative timestamp information. The firmware is schematically represented in Fig. 5.9.

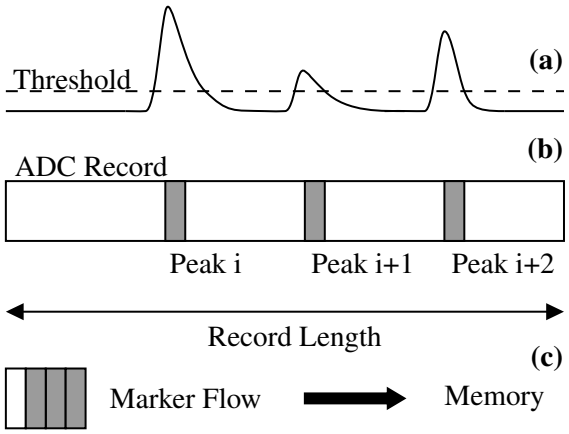

(a) The threshold is set to a value that is above the noise level

(b) The digitizer records the ADC signal when the threshold is crossed

(c) The driver returns the time-stamp and characteristics of each selected pulse, in a stream of descriptor.

Fig. 5.9. The dedicated peak list firmware used for the ToF experiment.

[8] *Double Data Rate 4th generation Synchronous Dynamic Random Access Memory (DDR4 SDRAM)*

A dedicated HCI was developed using LabVIEW to manage the digitizer PKL firmware and control the acquisition chain and data storage. Designed to be user-friendly as shown in Fig. 5.10, the graphical interface allows for configuring the digitizer, setting the acquisition window duration and trigger information, and storing data in a binary format. The HCI also displays the number of records to be stored, pending records, and records to be analyzed.

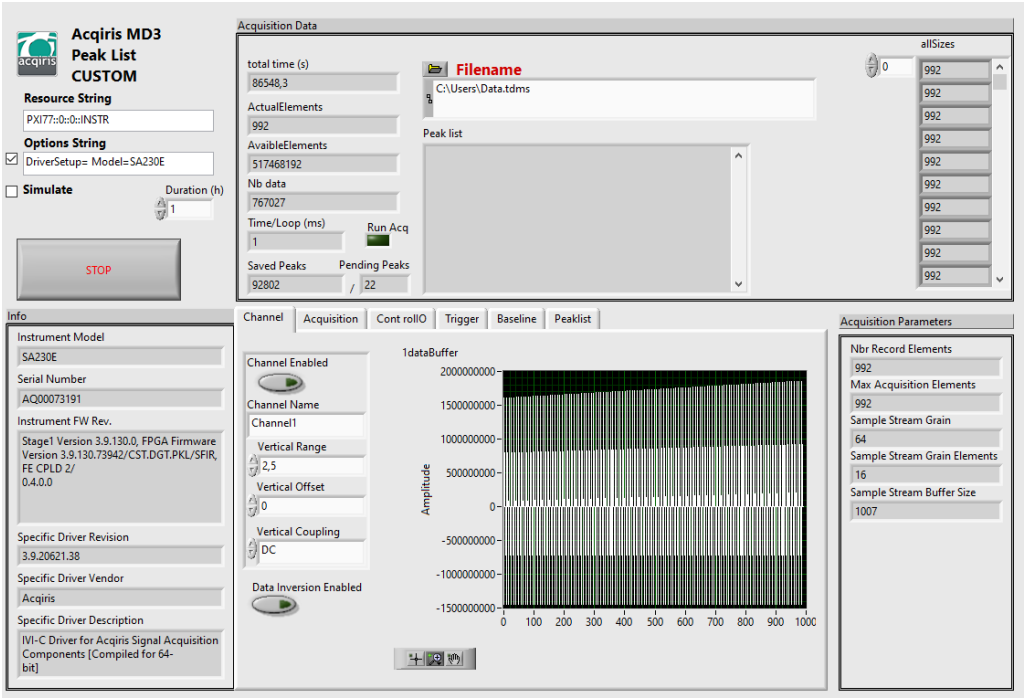

Fig. 5.10. Graphical User Interface for the Acqiris digitizer PKL firmware.

The design of the system, featuring independent triggering aligned with any beam structure, effectively minimizes deadtime in data acquisition. To enhance the timing accuracy of each channel and compensate for timing discrepancies, a filtering technique was applied to the waveforms after data collection. A pulse is identified based on the signal samples transitioning described in Fig. 5.11.

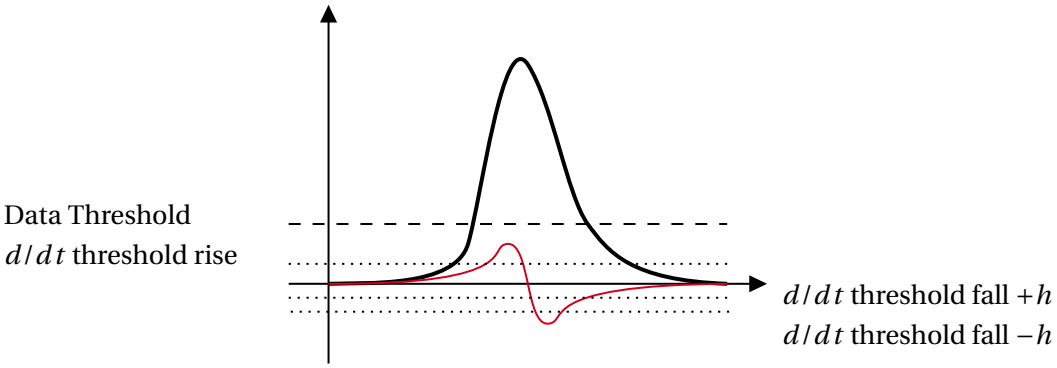

Fig. 5.11. Pulse detection scheme for the PKL method. The red curve represents the derivative of the signal.

It consists of several steps:

- The rising edge occurs when the sample values surpass a set data threshold and the rate of change of these values exceeds a predetermined derivative threshold for rising
- The falling edge is reached when the rate of change of the sample values is lower than the set derivative threshold for falling, adjusted by subtracting a predefined hysteresis value
- The end of the pulse is marked when the rate of change of the sample values goes above the derivative threshold for falling as depicted in Fig. 5.11, after adjusting by adding the same hysteresis value.

To enhance measurement accuracy, the determination of peak time and amplitude is refined through interpolation using a second-degree polynomial applied to three points surrounding the peak identified by the detection algorithm.

5.5. ToF measurement results

5.5.1. Context

During the NFS campaign, two weeks of data were collected using SiC sensors from october 5th to october 20th, 2023 as displayed in Fig. 5.12.

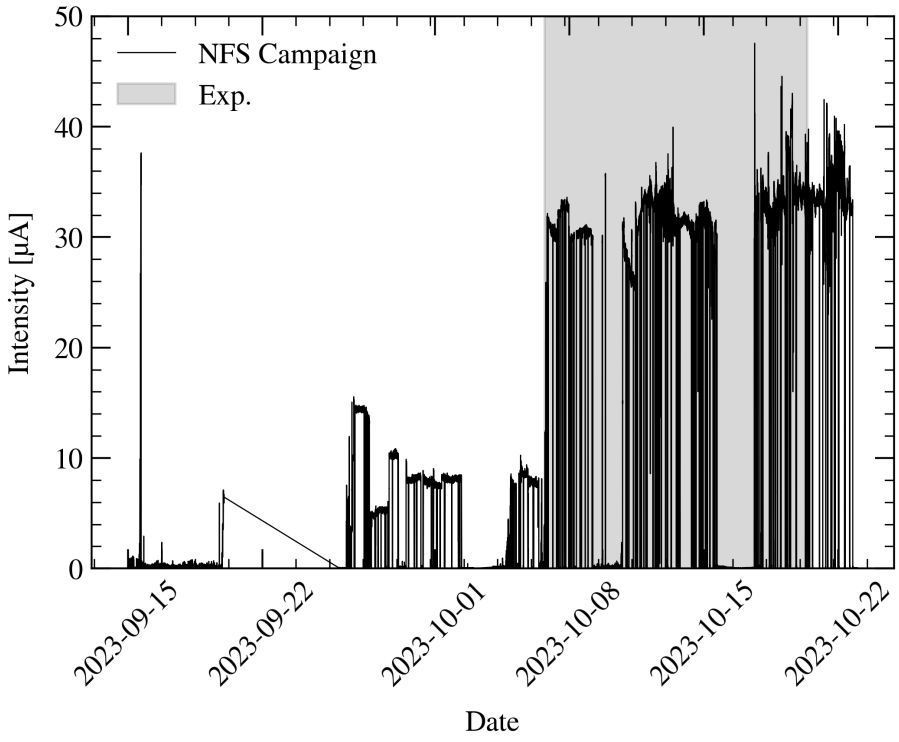

Fig. 5.12. Beam intensity as a function of time during NFS autumn campaign. The shaded area represents the time during which data were acquired.

Since the digitizer under study does not provide two channels, only one sensor was connected to the digitizer at a time. With regard to the objectives assessed in the previous section, the data were collected using the two firmware configurations used previously, the first one with the peak detection and the second one with the waveform recording. An overview of the data recorded, according to the sensor thickness and the firmware configuration, is presented in Table 5.1.

	S60	S100
PKL	Construction of the response matrix[a], 420 min from 10/07/23 - 00:07 to 10/07/23 - 07:25. Monitoring the effects from 10/10/23 to 10/20/23.	Construction of the response matrix[a], 820 min from 10/08/23 - 14:09 to 10/09/23 - 04:55. Monitoring the effects from 10/20/23 - 09:48 to 10/20/23 - 11:20.
PSA	Study of the background noise and shape[b], at the beginning 20 min the 10/08/23. Study of the background noise and shape at the end[c], the 10/20/23.	Study of the background noise and shape[b], at the beginning 20 min the 10/08/23. Study of the background noise and shape at the end[c], the 10/20/23.

[a] *A fraction of these data are analyzed in Section 5.5.3.*
[b] *These data are presented in Section 5.5.2.*
[c] *These data are presented in Section 7.3, Chapter 7.*

Table 5.1. Overview of the data recorded during the NFS campaign for the two sensors of thickness 60 µm and 100 µm and the two firmware configurations.

5.5.2. Experimental data

As explained in the previous Chapter, using current amplifier with digitizer firmware configured to record waveform of the signals, current pulses are recorded. The later are characterized by a peak, corresponding to the neutron-induced or gamma-induced reaction as displayed in Fig. 5.13. The current pulses are defined by their amplitude, width, and shape, which are influenced the charge carriers transport collection. This point is studied in detail in Chapter 6 dedicated to the effects of temperature on charge carrier collection dynamics. Nevertheless, the background noise and the trigger threshold is studied as a first initial step, before going through the acquisition with the PKL firmware.

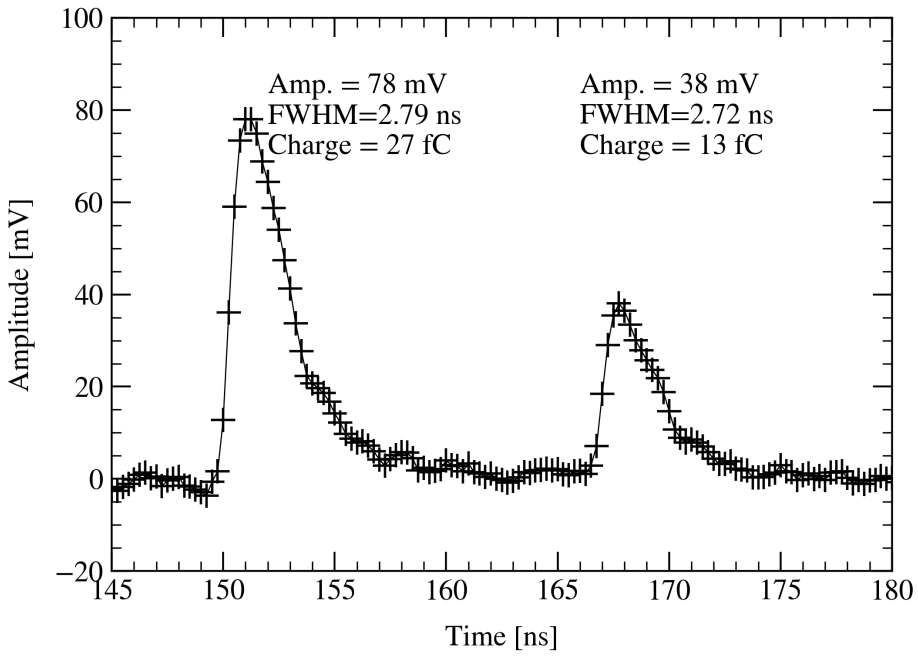

Fig. 5.13. Sample of current pulses recorded with the S60 sensor.

During the production of a pulsed ion beam such as proton or deuteron in the case of our study, not all deuterons bunches are effectively redirected by the internal beam pulse selector. This results in the formation of secondary images, or "satellite peaks," within the pulse height versus ToF distribution. Such occurrences, which represent on average 0.5% of all events as explained in Appendix E, are not detrimental to the unfolding process using the data at the beginning of the campaign.

Hence, due to the variation in the neutron beam intensity during the experimental campaign as depicted in Fig. E.5, and due to the presence of satellite peaks, a segment with stable beam intensity was selected for the unfolding process study. Even if data were acquired during the entire campaign, only the segment with stable beam intensity around 30.4 µA was retained, corresponding to 420 min recorded during 7th, october.

5.5.3. Data analysis

In order to use the experimental data for the construction of the sensor response matrix, the data were analyzed following a specific procedure, described in the following.

5.5.3.1. Distribution of the events according to the trigger timestamps.

In order to compute the neutron time of flight required for the neutron energy calculation, the flash of gamma rays produced by the spallation reactions has to be distinguished. The gamma flash peak is identified once the current pulses analyzed by the PKL firmware, as the first peak in the pulses timestamp distribution according to Fig. 5.14.

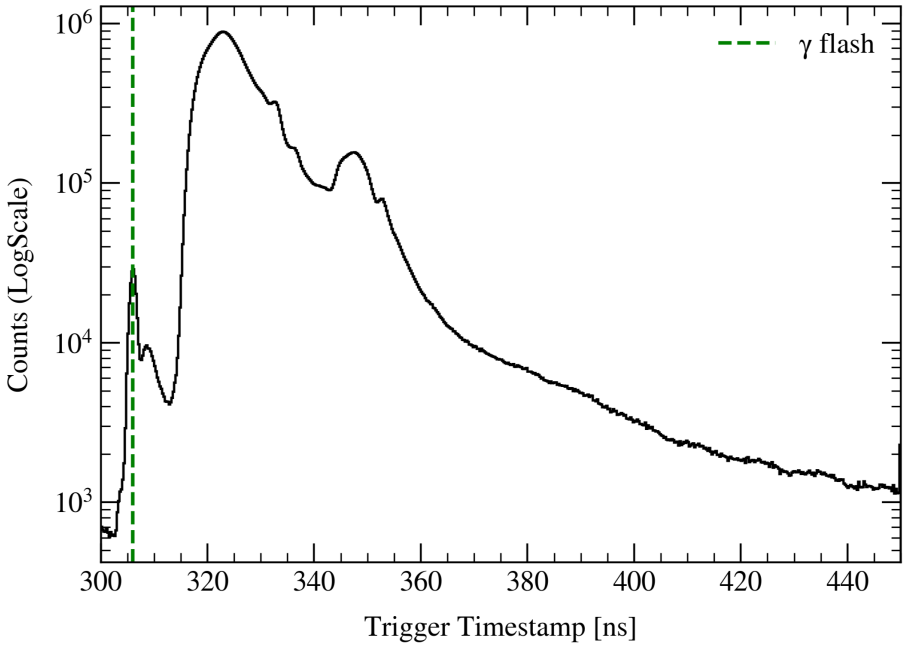

Fig. 5.14. Pulses timestamp distribution. The dashed lined guides the eyes to the prompt gamma flash peak.

The other contributions close to the first peak displayed with the dashed line are attributed to delayed gamma. In this study, the FWHM of the prompt gamma-flash peak is estimated to be around 2 ns according to the experimental results, which establishes the timing accuracy of the detectors used.

This representation gives first insights into the pulse distribution under study in the NFS neutron field. The plot highlighting the distribution of the timestamp of the events reveals the various reaction channels influencing the ToF spectrum. Pulses with timestamp values around 320 ns correspond to the highest energy neutrons once corrected with the distance and gamma flash time of flight, while the lower energy neutrons are detected at later times.

Hence, these first results confirm the primary remark that the sensor response strongly depends on the neutron kinetic energy, as expected from the nuclear reactions involved in the wide energy range of the NFS neutron field.

5.5.3.2. Energy calibration

The transformation of the neutron time of flight into neutron energy is based on the relativistic expression for the total energy such that:

$$E_n = m_n c^2 \cdot \left(\frac{1}{\sqrt{1-\beta^2}} - 1 \right) \tag{5.14}$$

With $\beta = v/c$, the ratio of the neutron velocity to the speed of light and m_n the neutron mass at rest.

Hence, the distance between the target and the sensor appears to be a crucial parameter for the ToF measurements. The computation of the neutron energy distribution is performed using an approximate distance of 124 cm as shown in Fig. 5.15. This neutron energy distribution, function of the sensor distance has to be calibrated. One way to achieve this is to compare the neutron energy distribution with the neutron reaction cross sections which exhibit resonances at specific energies as displayed in Fig. 5.16. Neutron scattering cross section on ^{12}C and neutron scattering cross section on ^{28}Si are few orders of magnitude higher than the neutron capture cross section. In addition, the elastic scattering reaction cross section on ^{12}C exhibits broader resonances, than the scattering reaction cross section on ^{28}Si for the energy range under study, which is interesting for the calibration of the neutron energy distribution.

Therefore, the computed neutron energy distribution is compared with the convolution of the neutron elastic scattering cross section, using the theoretical neutron spectrum at the sensor location as shown in Fig. 5.17. The results are shown for the first approximate distance of S100 sensor at 124 cm and for the corrected distance at 120 cm. With the corrected distance, the broader resonances of the neutron elastic scattering cross section are well matched with shapes of the peaks in the neutron energy distribution, indicating the neutron energy calibration is reliable. It should be noticed that the convolution is not performed taking account the efficiency of the sensor, since the computation of the later requires the knowledge of the neutron energy distribution which is the goal of the first step of this analysis.

A similar comparison is performed in Fig. 5.18, for the neutron energy distribution up to 1 MeV compared with the $^{28}Si(n,\gamma)^{29}Si$ reaction cross section. The resonances are also well matched with the cross section, especially the ones at 68 keV and at 87 keV, confirming once again that the neutron energy calibration is reliable.

The experimental data being well calibrated according to the neutron energy, the sensor response matrix can be constructed using the data recorded for both S60 and S100 sensors. In the following, the results obtained with the S60 sensor are presented, since the sensor was located at the smallest angle with respect to the beam axis, leading to a higher neutron flux.

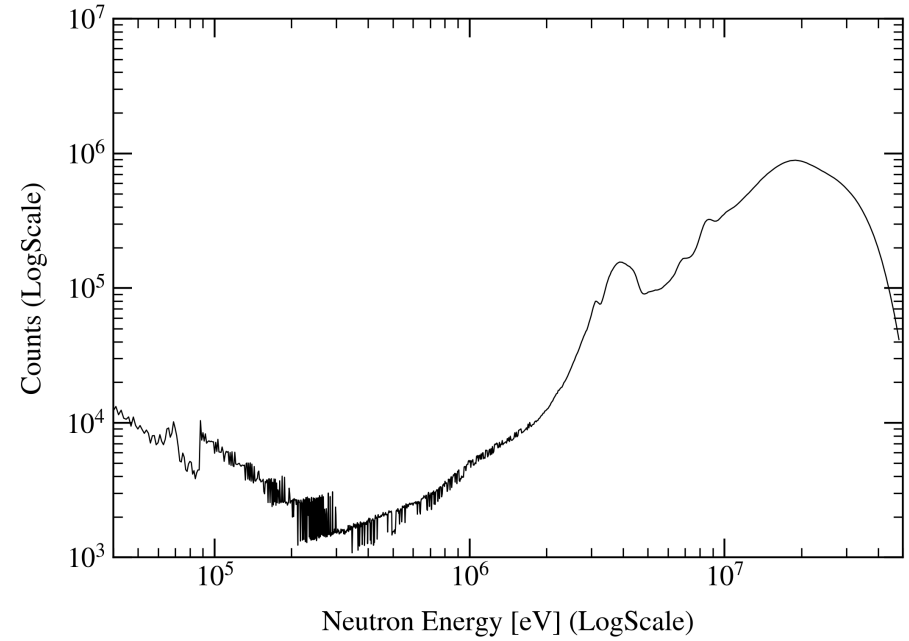

Fig. 5.15. Neutron energy distribution for S100 computed using an approximate distance of 124 cm.

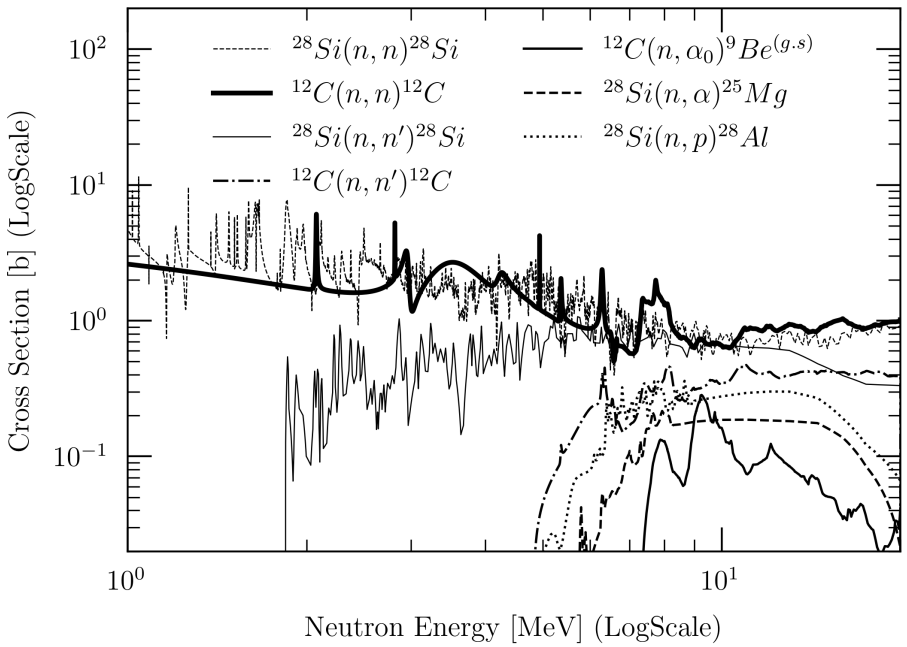

Fig. 5.16. Neutron reaction cross sections as a function of neutron energy for scattering and capture on ^{12}C and ^{28}Si.

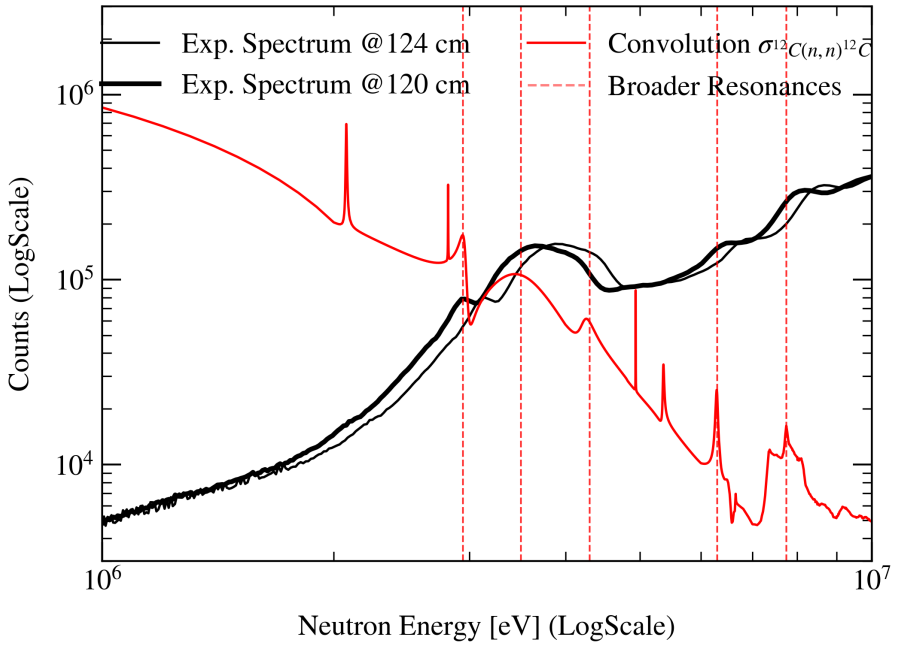

Fig. 5.17. Neutron energy distribution compared with the convolution of the neutron elastic scattering cross section. The results at the approximate distance of 124 cm and the corrected distance of 120 cm are shown. The dashed line guide the eyes to the broader resonances matching the neutron energy distribution shape.

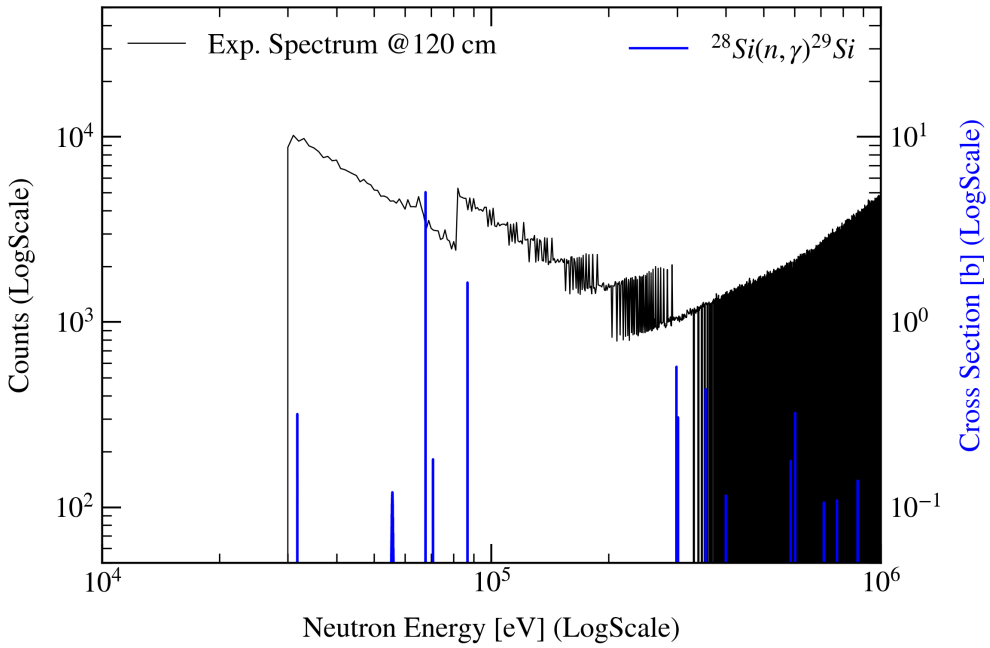

Fig. 5.18. Detected neutron energy distribution at 120 cm up to 1 MeV, compared with the $^{28}Si(n,\gamma)^{29}Si$ cross section on the right side. Cross sections are taken from the ENDF/B-VIII.0.

5.5.4. Construction of a response matrix

The sensor response matrix is derived from the experimental data collected during the segment under study. Its main function is to map the relationship between neutron energy and the energy deposited in each interaction. For a specific incident neutron energy that triggers nuclear reactions and produces charged particles releasing energy within the sensor, the sensor response matrix shows the number of corresponding events. Thus, for a given neutron energy determined through time-of-flight measurements, the collected charge from the current pulses is used to populate the bins of the sensor response matrix, as illustrated in Fig. 5.19.

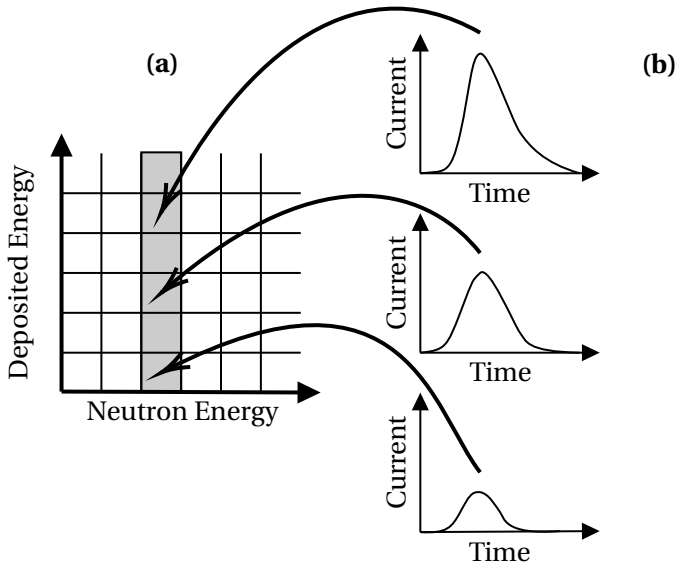

(a) The response matrix is a 2D histogram of the deposited energy versus the neutron energy

(b) Which is filled by the current versus time pulses for each incident neutron given energy.

Fig. 5.19. Response matrix construction scheme.

Finally, the count in each bin of the two-dimensional matrix corresponds to a coefficient R_{ij}, representing the response of the sensor to the neutron flux at energy E_i in energy bin j. This relationship was previously discussed in the context of the convolution between the neutron spectrum and sensor response in Section 5.2. Given the constraints on the proximity of the sensor to the target and the limitations of the resolution of the digitizer and sampling rate, the sensor response matrix is constructed with a bin width of 2 MeV. This bin width is chosen to ensure comprehensive coverage of the entire neutron energy range of the NFS neutron field, utilizing an equally spaced energy binning approach. Regarding the deposited energy distributions, the bin width is set to 0.1 MeV to ensure a fine-grained representation of the deposited energy versus neutron energy relationship. Hence, the sensor response matrix constitutes of 20 neutron energy bins and 300 deposited energy bins is displayed in Fig. 5.20.

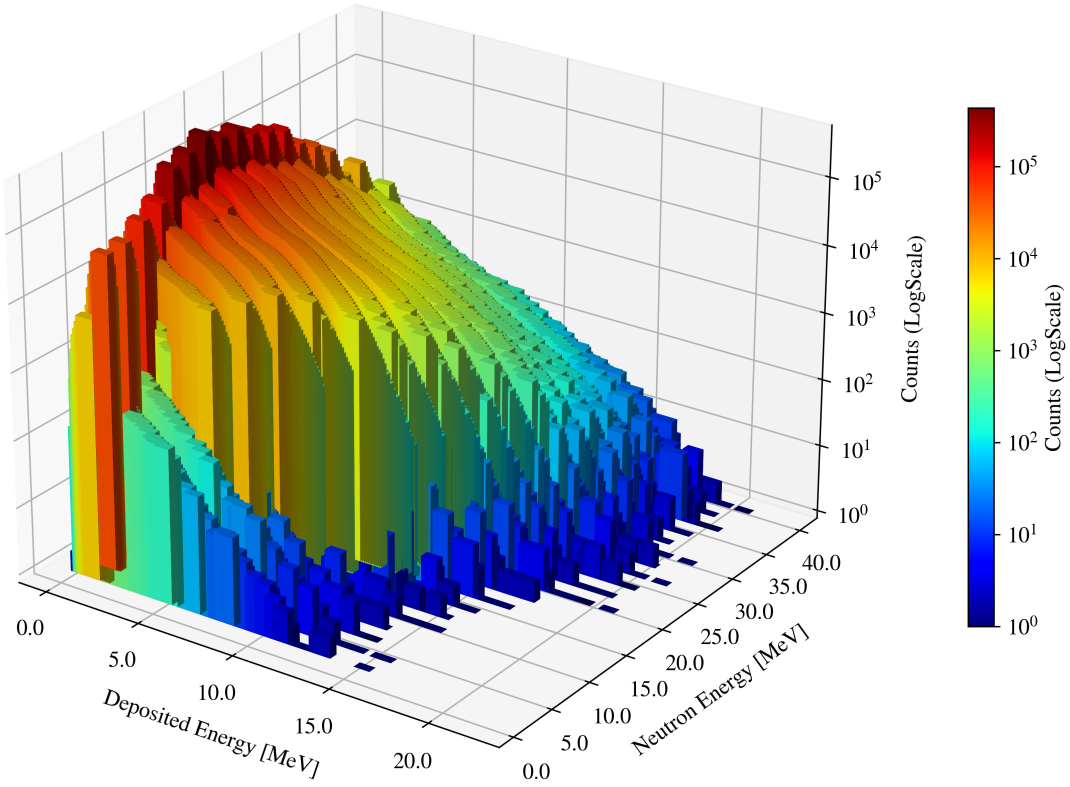

Fig. 5.20. Experimental response matrix of the S60 sensor. The data are computed from the segment under study.

Such a response matrix exhibits a broad distribution of the deposited energy versus the neutron energy, with coefficients R_{ij} varying from 1 to $4.3 \cdot 10^5$ counts.

5.5.5. Calculation versus Experiment comparison

To compare the experimental results with the calculated response matrix of the sensor, we use the GEANT4 modeling scheme presented in Section 4.2, Chapter 4. Such model has been employed to simulate the sensor response to mono-energetic neutron fields. But, due to the missing evaluated nuclear data on the sequential decay reaction leading to the production of three alpha particles, the GEANT4 model was adjusted to accommodate the multistage decay mode supplanting results from dedicated experiments conducted at the PTB facility. Such model was then used to simulate the sensor response to mono-energetic neutron fields and validated with the experimental data for 14 MeV neutrons from D–T neutron generator.

Using this model, the sensor response matrix is calculated for both sensors S60 and S100, taking as input the calculated neutron spectrum at the sensor location from the MCNP model of the NFS convertor room shown in Fig. 5.21.

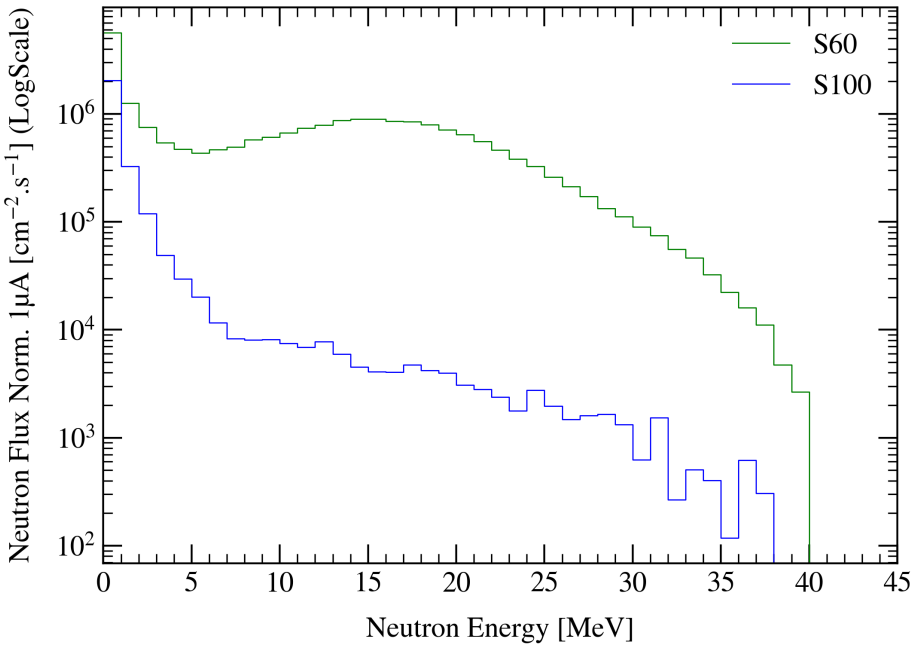

Fig. 5.21. Calculated neutron spectra at sensors locations [177]. Neutron fluxes are normalized to 1 µA of deuteron beam intensity on the berillium target.

The results are normalized to one neutron per energy group by dividing each neutron energy bin distribution by the total number of neutrons in the associated bin. The bidimensional histogram of deposited energy versus neutron energy is then compared. First, as previously discussed, the experimental response matrix of the sensor, shown in Fig. 5.22, exhibits background contributions at low energies up to 5 MeV, where events deposit more energy than the neutron energy associated with the bin. This is consistent with the sensor's sensitivity to fast neutrons scattering off surrounding structures and the satellite contributions discussed in Section 5.5.3. In contrast, the calculated response matrix of the sensor, shown in Fig. 5.23, obtained by simulating the sensor with a 60 µm thickness within the calculated MCNP neutron spectrum, does not show such background contributions. This can be attributed to the fact that the neutron source was modeled as planar and positioned adjacent to the active sensor region. However, discrepancies between the experimental and simulated data above 20 MeV are noted. These discrepancies are attributed to nuclear data uncertainties and the lack of evaluated nuclear data for some interactions in a neutron field with a wide energy range up to 40 MeV, as explained in Section 5.2.1.

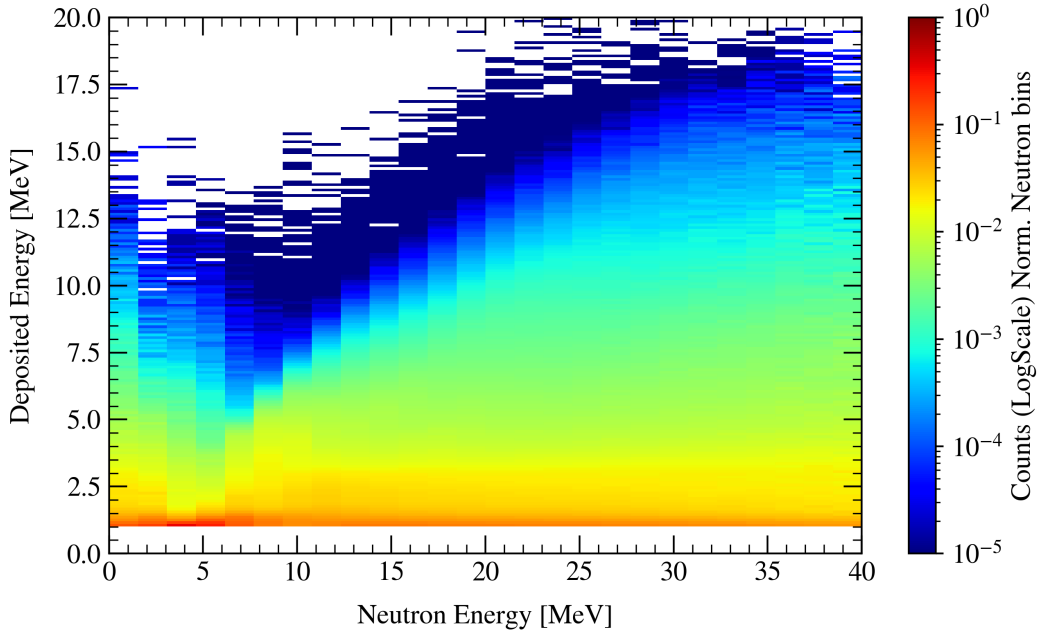

Fig. 5.22. Experimental bidimensional histogram of the deposited energy versus the neutron energy obtained with the sensor S60. Data are normalized to one neutron per energy group.

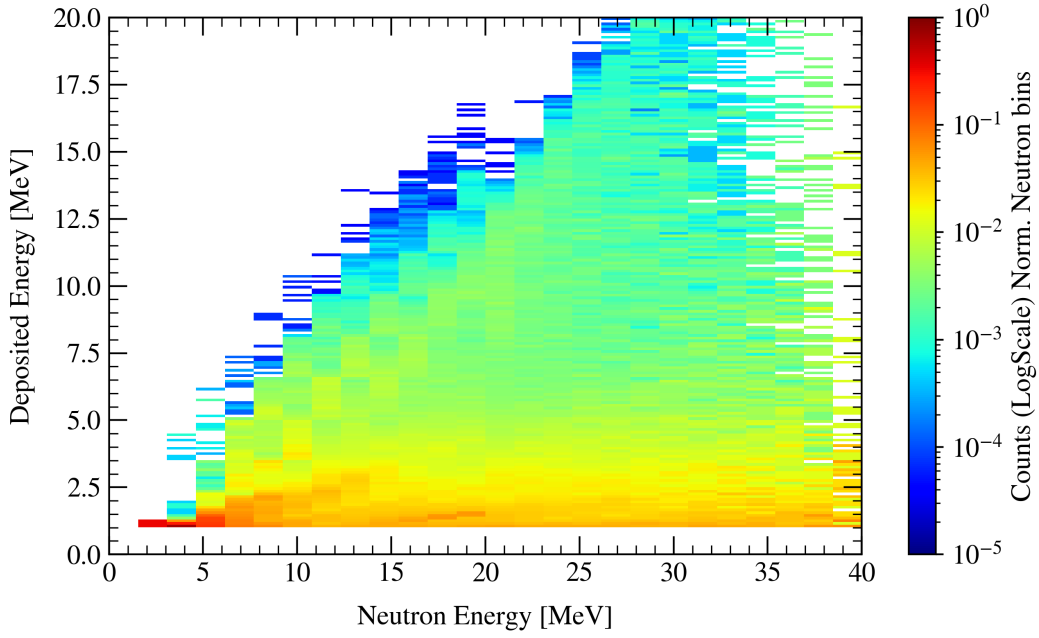

Fig. 5.23. Calculated bidimensional histogram of the deposited energy versus the neutron energy obtained with GEANT4. Simulated data are obtained modeling the sensor with a 60 µm thickness within the calculated MCNP neutron spectrum. Data are normalized to one neutron per energy group.

Therefore, given that the modeling scheme has been previously validated with experimental data for mono-energetic neutron fields in Section 4.4, the comparison between the measurement and the calculated response is feasible but challenging for other energy bins. To perform such a comparison across the entire neutron energy range, a more accurate understanding of the "real" neutron spectrum at the sensor location is necessary. This would require a dedicated experiment with metrological standards to verify the area of the neutron spectrum. However, considering the objectives of this experiment within the context of this phD thesis, the primary goal is to demonstrate the feasibility of using ToF measurements to construct a response matrix and to use it to unfold a neutron spectrum. Therefore, it is not possible to further investigate the biases and uncertainties in the calculations or measurements without a calibration spectrum. There it is, any further analysis of uncertainty or calculated results would be unwarranted given the limited knowledge of the data.

The response functions are now available, based on the neutron energy bin division shown in the sensor response matrix diagram in Fig. 5.24. The next step is to use these sensor response functions with the iterative inversion method to unfold the neutron spectrum. For a specific neutron energy, the spectrum shape is deemed accurate based on these experimental data, provided satellite events are rejected. However, the intensity of the neutron energy bins remains questionable due to the absence of a calibration spectrum.

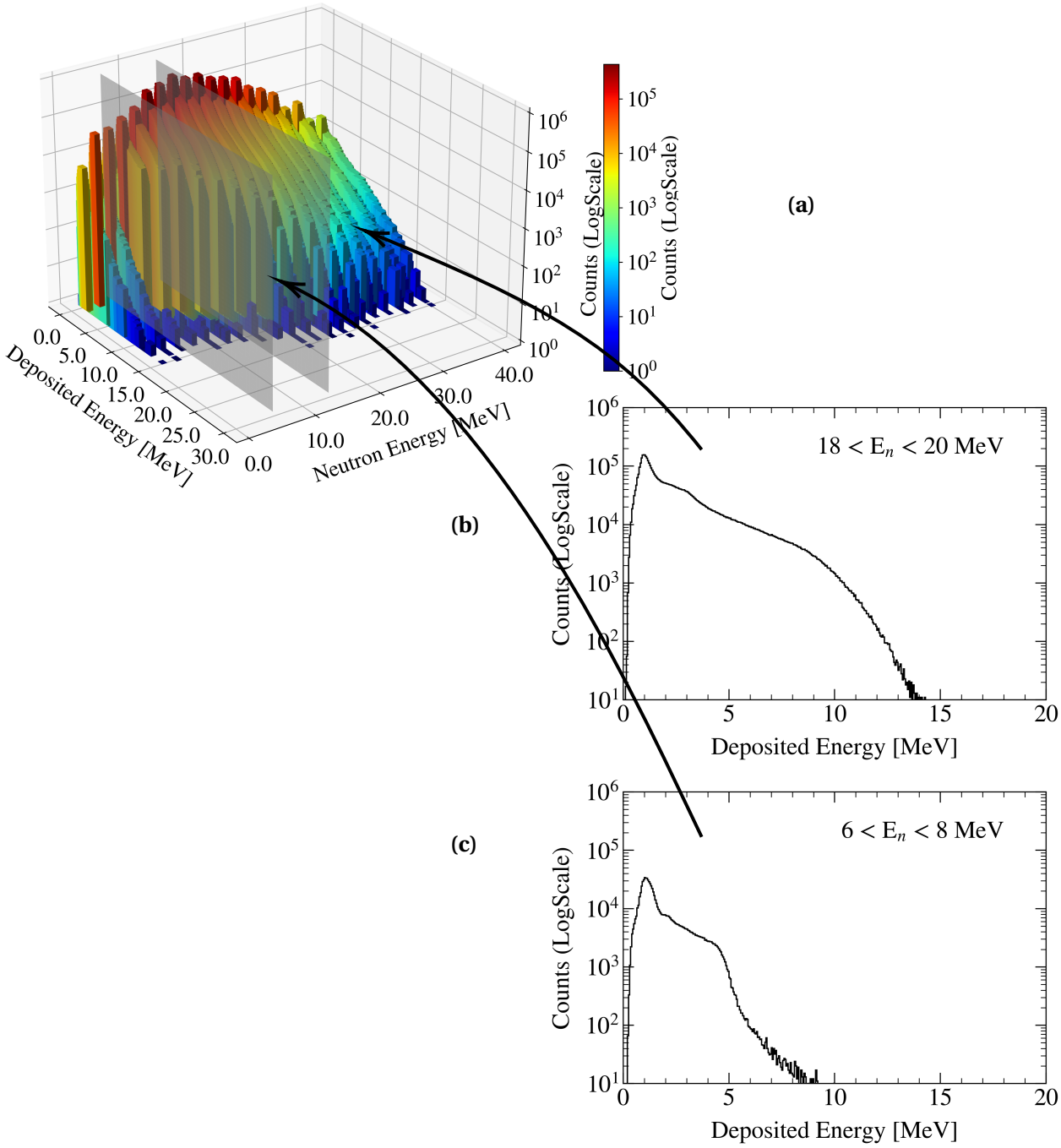

(a) Experimental response matrix

(b) Response function for the 18 MeV to 20 MeV neutron energy bin

(c) Response function for the 6 MeV to 8 MeV neutron energy bin.

Fig. 5.24. Draw up of the sensor responses functions.

5.6. Application of the deconvolution method and calculation versus experiment comparison

To test this initial construction step of the sensor response matrix, the unfolding method is applied using the experimental data from sensor S60, with high confidence that we will revert to the entry spectrum.

5.6.1. Deposited energy distribution

The measured deposited energy distribution shown in Fig. 5.25 is now considered for the deconvolution method. As presented in introduction Section 5.1, based on the kinematic study carried out in Chapter 4, the deposited energy distribution in such a continuous neutron field with neutron energy up to 40 MeV is broad, and does not exhibit any specific features like peaks associated to full energy deposition signatures of some reactions as in the case of mono-energetic neutron fields studied the previous Chapter.

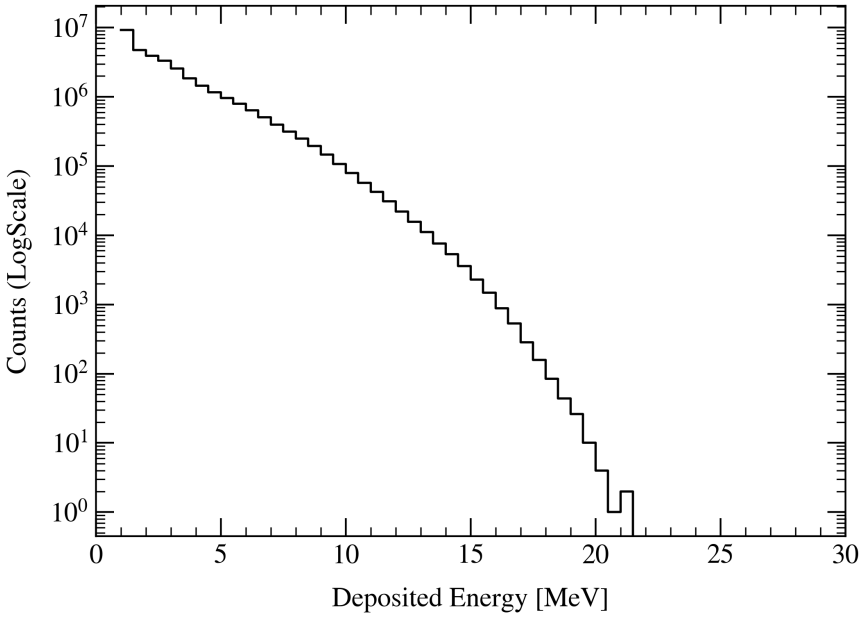

Fig. 5.25. Deposited energy distribution obtained with SiC sensor of 60 µm thickness at NFS for the acquisition segment under study.

5.6.2. Calculation versus experiment comparison

The unfolded neutron spectrum obtained with the SiC sensor of 60 µm thickness in NFS neutron field is shown in Fig. 5.26 considering 2 MeV neutron energy bins. The comparison of the unfolded neutron spectrum with the previous calculated MCNP spectrum is presented in Fig. 5.27. Firstly, the unfolded neutron spectrum is in good agreement with the calculated MCNP spectrum, especially in the energy range above 5 MeV where the deviations are less than 10 %. However, discrepancies are observed at lower energies where the calculated neutron energy bins tend to overestimate the neutron flux. This outcome can be attributed to the geometrical considerations regarding the sensor location and the reference flux spectrum. Consequently, it leads to correlated discrepancies in the sensor efficiency vector computation, used in the unfolding process. Regarding the relative uncertainties in the deviation distribution, the propagation of uncertainties in the unfolded spectra and the uncertainties in the calculated spectra

must be taken into account. However, concerning the uncertainties in the calculated spectra, the latter are underestimated due to the lack of information in the modeling scheme with the neutron source as thin beryllium non rotating target, and the lack of information in the nuclear data libraries uncertainties contribution. Concerning the uncertainties in the unfolded spectra, the uncertainties in the sensor efficiency vector computation are not well defined for the same reasons as the calculated spectra. The total uncertainties are finally underestimated, and the error bars, consequently, are not displayed in Fig. 5.27.

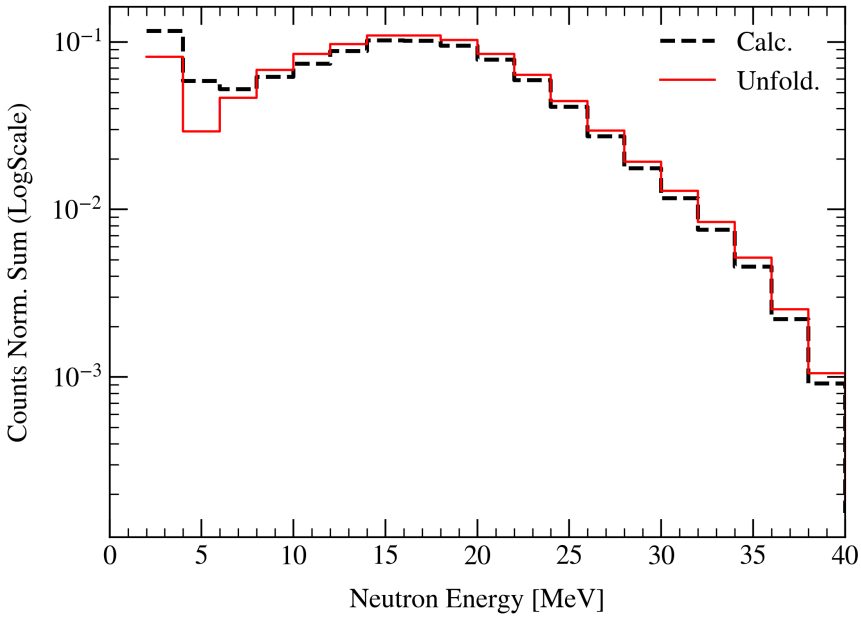

Fig. 5.26. Calculated versus Unfolded NFS neutron spectrum comparison. The spectrum are normalized to the sum of the spectrum.

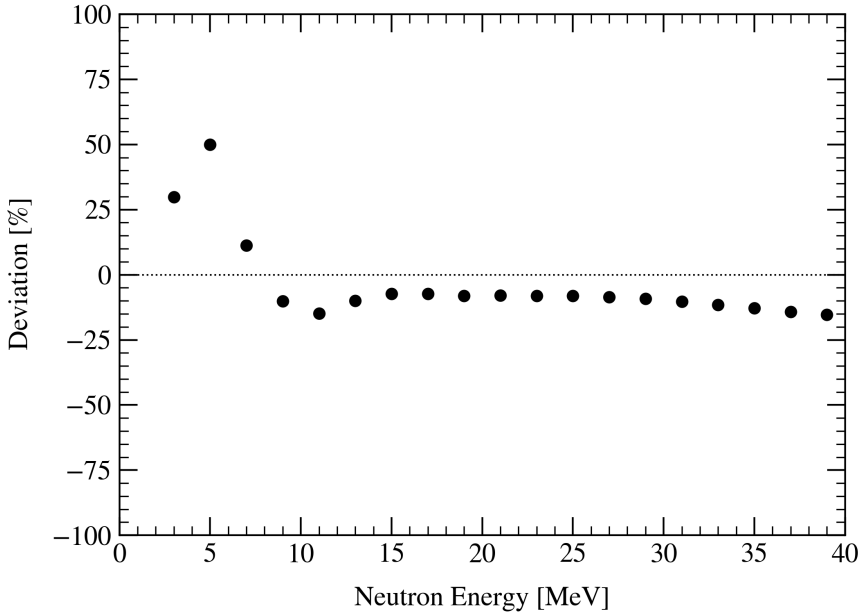

Fig. 5.27. Calculated versus Unfolded NFS neutron spectrum deviation computation. The differences displayed are computed as the ratio of the difference between the calculated and unfolded neutron spectra to the calculated neutron spectrum.

Overall, the results are promising on almost the entire energy range of the neutron spectrum, demonstrating the capability of the sensor to estimate neutron flux in a high-energy field with low discrepancies, as expected, around 10 % across most of the spectrum energy range. The primary goal of constructing a response matrix in this work is to develop an effective deconvolution method and to complete the unfolding process by formatting the data. Ideally, a zero deviation would be achieved when comparing with the theoretical spectrum derived from the facility model calculations. However, discrepancies remain at the end of this initial test. Therefore, a thorough study of the input parameters of the numerical method, such as the choice of energy binning, is necessary in a subsequent phase.

Nonetheless, the objective which was to demonstrate the feasibility of the deconvolution method using an experimental response matrix based on this initial test has been achieved. The results are promising, regarding to the comparison of the unfolded neutron spectrum with other published results in the literature, as shown in Fig. 5.28.

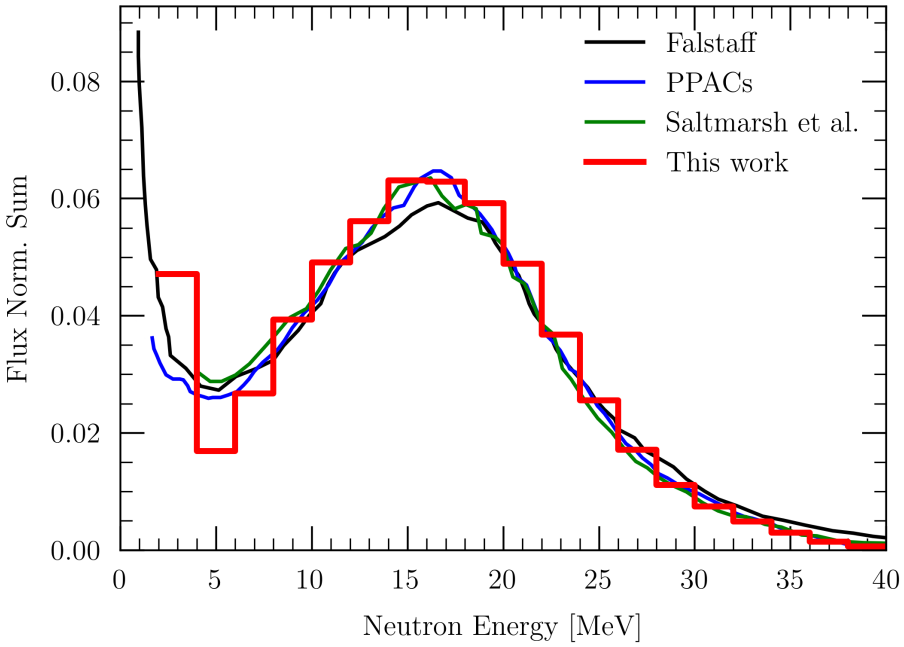

Fig. 5.28. Comparison of the unfolded NFS neutron spectrum with other results from ToF measurements at 0°, for a neutron field generated by a 40 MeV deuteron beam on an 8 mm beryllium target. The spectra are normalized based on their respective areas, above 6 MeV according to the previous discussion about discrepancies of the unfolded spectrum at low energy. The data are from [178] and adapted from [179, 180].

Further progress cannot be made at this stage regarding the estimation of uncertainties in the unfolded spectra. While the results are encouraging, additional work is required to enhance the numerical resolution process and to incorporate realistic uncertainties in the final processing step.

5.6.3. JHR spectrum

Due to the constraints of the proposed timetable for the various experiments in this thesis, obtaining experimental results in a fission spectrum was not feasible. Therefore, the GEANT4 modeling scheme was employed to determine the energy distribution deposited in the sensor. Hence, a neutron spectrum representative of the JHR reactor, as presented in the introduction

Section 1.2, and shown in Fig. 5.29, was used as input to the GEANT4 model to simulate the sensor response.

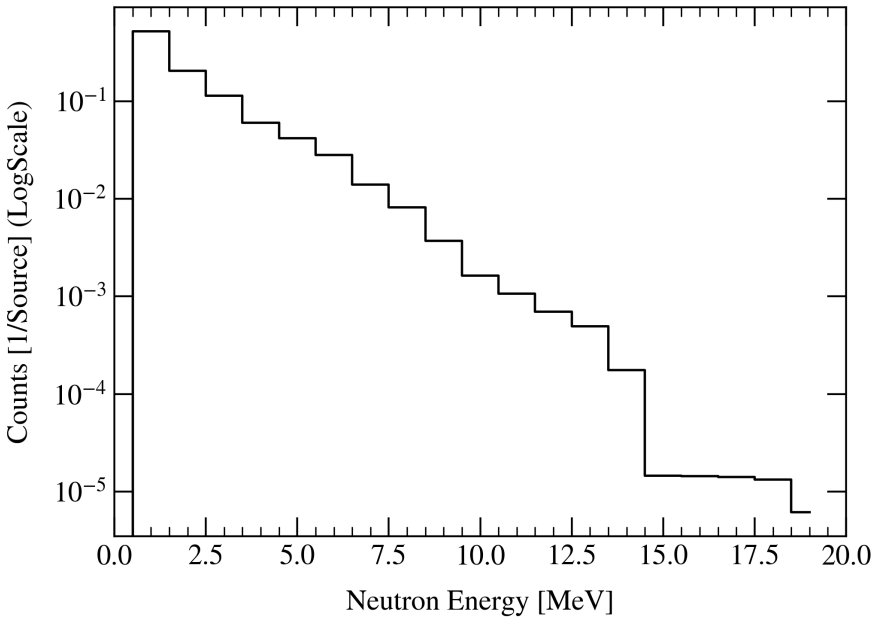

Fig. 5.29. Calculated neutron spectrum of the JHR reactor. Only the fast component above 1 MeV is displayed. Data are normalized to the number of neutron source particles.

The energy distribution deposited in the SiC sensor with a thickness of 60 µm, as calculated using the GEANT4 model in the JHR neutron field, is illustrated in Fig. 5.30.

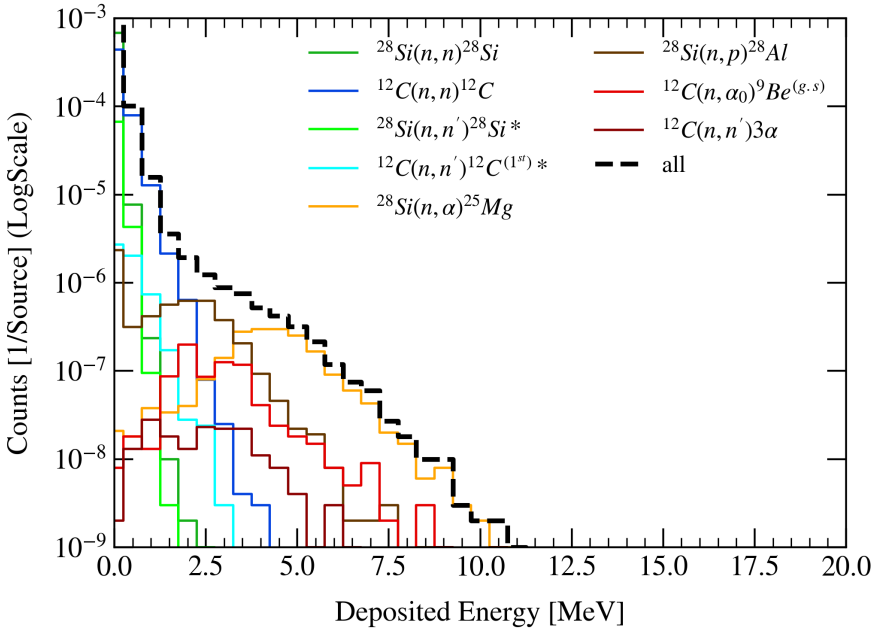

Fig. 5.30. Deposited energy distribution in a 60 µm thick SiC sensor, modeled with GEANT4 in the JHR neutron field. Data normalized to neutron source particles.

This distribution is broad and lacks distinct features such as peaks that would indicate full energy deposition from specific reactions, as discussed in the previous section. The GEANT4 results highlight that neutron scattering reactions predominantly contribute to the total deposited energy distribution, which aligns with the characteristics of the neutron field in the JHR reactor.

However, it is expected that this sensor can still be utilized with the previously established response functions. A neutron fission reactor spectrum typically features a high thermal neutron flux and a high fast neutron field with a Maxwellian distribution in the range of a few MeV, along with a contribution above 2 MeV from native uranium fission reactions that have not interacted with surrounding structures. This is relevant since the sensor is insensitive to thermal neutrons and can, therefore, detect this native contribution above 2 MeV to a first approximation. This implies that the use of the sensor would not, in principle, be location-dependent. In other words, detecting a certain number of counts above a threshold of specific energy deposition, at a given reactor power in one location, suggests that detecting the same number of counts in another location, assuming environmental non-dependence, indicates as a first approximation an equivalent neutron flux with energy above 2 MeV.

Conclusion

All in all, regarding the perspectives of the experiment, the results are encouraging, and the sensor demonstrates its ability to construct a response matrix through ToF measurements and to use it to unfold a neutron spectrum. Nonetheless, a complementary measurement of the neutron flux is strongly recommended to provide a better knowledge of the neutron spectrum at the sensor location. Firstly, regarding the shape of the neutron spectrum, the use of a Bonner sphere, or a fission chamber would allow to provide a more confident measurement of the area, in order to emancipate from the interrogation related to the accelerator beam structure or maintenance operations. Secondly, regarding the area of the neutron spectrum, the use of NAS allows to provide a more confident measurement of the fluence received by the sensor during the measurement campaign.

Regarding the sensor location, in order to reduce the contribution of scattered neutrons, and to avoid the contribution of delayed gamma rays produced by the interaction of neutrons with the surrounding materials, the sensor should be placed in the ToF hall, at a distance close to the collimator in order to reach the highest neutron flux accessible in the ToF room. Such a location would also reduce the satellite contributions due to the deuterons beam structure as experienced and depicted in the Section 5.5.2, and avoid parasitic contributions due to EMC that can arise in an environment with a high electromagnetic field. In order to reduce the technological uncertainties, the use of a charge preamplifier should be considered to improve the energy resolution of the sensor response. However it requires the sensor to be placed in the ToF room for the reasons explained in Section 5.4.4.

All things considered, the experimental campaign has demonstrated the ability of the sensor to measure the neutron flux in a high-energy and continuous neutron field through the use of an experimental response matrix constructed with ToF measurements. Hence, it has been shown that a Tof measurement is essential to obtain a response matrix with a sufficient number of neutron energy bins to envisage an iterative method of spectrum unfolding. The calibration of these response functions could also be envisaged on facilities such as AMANDE or PTB. The unfolding process has provided encouraging results, with discrepancies of the order of 10 % over most of the spectrum energy range compared to the calculated MCNP spectrum of the NFS neutron field at sensor location. However in order to perform a more accurate comparison, taking into account all the sources of uncertainties, another experimental campaign is required using metrological standards to verify the area of the neutron spectrum over the entire energy range, and in particular in the low energy range where the discrepancies are observed. In order

to apply this unfolding method to fission reactor neutron field, in addition to the experimental deposited energy distribution, the use of a response matrix emphasizing the low energies is recommended.

Regarding the reduction of the uncertainties in the calculated spectra, the uncertainties on the nuclear data should be taken into account using covariance matrices. Indeed, enhanced assessments of reactions on specific stable nuclei, crucial for inputs in MCNP and GEANT4 simulations, are essential to precisely forecast experimental backgrounds. This includes a particular emphasis on acquiring more comprehensive double differential cross-section data that accounts for the discrete excitation of states. This general problem is related to the needs highlighted in the previous Chapter 4 regarding the definition of effective capture cross-sections.

To conclude this second Part dedicated to the estimation of the fast neutron flux, the first study dedicated to the response of the sensor in a mono-energetic neutron field has shown a complex behavior of the sensor in terms of deposited energy, and the need to develop a response matrix to unfold a multi-energy neutron spectrum. The feasibility of the construction of such a response matrix has been demonstrated in the context of the NFS neutron field using ToF measurements. Then, an iterative unfolding process has been applied showing encouraging and promising results, with interesting prospects for using this sensor to estimate the neutron flux spectrum of the fast component in fission reactor spectra.

The next Part of this manuscript will focus on the study of the sensor behavior in a hostile environment with high temperature and a high flux of neutrons.

Part III.

Evaluation of the Sensor response to Integration Constraints

6 Study of the effects of temperature on measurements **187**

6.1 Study of the analytical model of the charge carriers dynamics in the SiC 187
6.2 Development of a numerical model to simulate the charge carriers collection . . 193
6.3 Study of mechanisms induced by an ionizing particle via finite element method . 197
6.4 Dedicated 14 MeV neutron generator measurement campaign with a heating device 203
6.5 Evaluation of the model for the charge carrier collection 220
6.6 Perspectives 224

7 Study of the effects of defects on measurements **226**

7.1 Study of the analytical model of defect creation 226
7.2 Application of finite element simulation to study defect activation mechanisms 228
7.3 Neutron induced defects experimental results 232
7.4 Application of thermally activated defect analysis to diamond 239
7.5 Evaluation of the model for the charge carrier trapping 244
7.6 Perspectives 248

6. Study of the effects of temperature on measurements

The aim of this Chapter is to study the effects of temperature on the sensor measurement. Firstly, an analytical model of the charge carriers dynamics in the 4H–SiC is presented, which provides the physical models necessary for the experimental results. Then, the experimental data analysis is presented, which is used to determine the parameters and coefficients of the physical models with increasing temperature. Finally, a numerical model is developed to simulate the complex charge carriers collection dynamics in the sensor with increasing temperature. It provides a fundamental insight into the performance and operation of a device by calculating and visually representing internal profiles such as fields, carrier concentrations, and current densities. These internal characteristics, which are often inaccessible through experimental methods, can be comprehensively understood through simulations.

6.1. Study of the analytical model of the charge carriers dynamics in the SiC

On the basis of the intrinsic properties description provided in Chapter 3, in order to obtain realistic simulation results, proper physical model and their parameter values in the case of using 4H–SiC or other large band-gap semiconductor material must be applied in the Technology Computer-Aided Design (TCAD) simulator. Consequently a group of physical models for 4H–SiC is configured using parameters derived from some latest findings in published literature.

6.1.1. Bandgap energy

The general model for the band gap energy as a function of temperature was proposed by Varshni in 1967 [181], based on theoretical considerations by Vasileff [182] and Adams [183], such that:

$$E_g(T) = E_g(0) - \frac{\alpha T^2}{T + \beta} \tag{6.1}$$

Where, $E_g(0)$ is the band gap energy at 0 K and α and β are materials parameters. The currently used parameters, based on latest literature publications for 4H–SiC, are registered in Table 6.1 below. Since E_{g_0} differs for different band gap models which handle differently the band gap narrowing, it can be written such as:

$$E_g(0) = E_{g,0} + \delta E_{g,0} \tag{6.2}$$

With $E_{g,0}$ an adjustable parameter and $\delta E_{g,0}$ an adjustable parameter different for all models.

This default bandgap model, is used to describe the band gap energy as a function of temperature, as seen in Fig. 6.1.

Symbol	Parameter
$E_{g,0}$ [eV]	3.285 [a]
$\delta E_{g,0}$ [eV]	-4.795e-3 [b]
α [eV/K]	0.033 [b]
β [K]	$1 \cdot 10^5$ [b]

[a] *At* 4 K, *from [184].*
[b] *From [185].*

Table 6.1. Default band gap model coefficients of (6.1) for 4H–SiC.

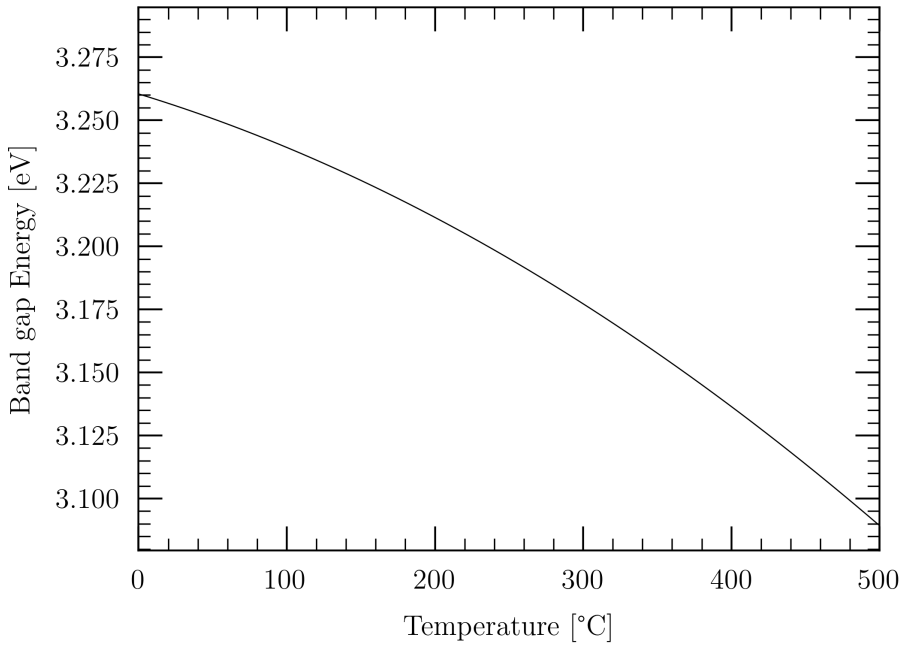

Fig. 6.1. Band gap energy as a function of temperature in degree Celsius for default model, computed with (6.1).

The accurate description of the band gap energy is essential for the simulation of the charge carriers collection with increasing temperature in the sensor. Indeed, as introduced in the preliminary discussion in Chapter 3, Section 3.2, increasing temperature results in crystal lattice vibratory phenomena of expansion and contraction due to phonons emissions. Thus, for instance when an electron from the VB acquires sufficient kinetic energy to overcome the potential energy that holds it in its VB, it can cross the band of forbidden energy which separates it from the bottom of the BC. Therefore, it is straightforward to understand that this effect is increased tenfold, and can become detrimental to the measurement when the band gap decreases too sharply. However, in the case of large band gap semiconductors such as SiC, even if the band gap decreases from room temperature to 500 °C by about 10%, the band gap remains large enough above 3 eV. Hence, it prevents the electrons from crossing the band gap, reducing the risk of leakage current, detrimental to the measurement.

6.1.2. Intrinsic carrier concentration

As a reminder, from the demonstration presented in Appendix A.2, the intrinsic carrier concentration in [cm^{-3}] is given by:

$$n_i = \sqrt{N_C(T) \cdot N_V(T)} \cdot \exp^{-E_g/2k_BT} \tag{6.3}$$

With N_C and N_V respectively the effective density of states of conduction band and valence band, and E_g the energy band gap.

Thus, the intrinsic carrier density is resolutely dependent on temperature, since the effective density of states and energy gap are function of temperature such that:

$$\begin{cases} N_C(T) = N_{C,300} \cdot (T/300)^{3/2} \\ N_V(T) = N_{V,300} \cdot (T/300)^{3/2} \end{cases} \tag{6.4}$$

With $N_{C,300}$ and $N_{V,300}$ estimated in literature with value registered in Table 6.2, by measuring the effective mass of electron and holes density of states.

Symbol	Parameter
$N_{C,300}$ [cm^{-3}]	$1.7193 \cdot 10^{19}$
$N_{V,300}$ [cm^{-3}]	$2.5094 \cdot 10^{19}$

Table 6.2. Intrinsic carrier concentration coefficients. From [186].

Hence, as a result of thermal expansion of the lattice and electron-phonon coupling n_i has an exponential dependence with temperature as represented in Fig. 6.2.

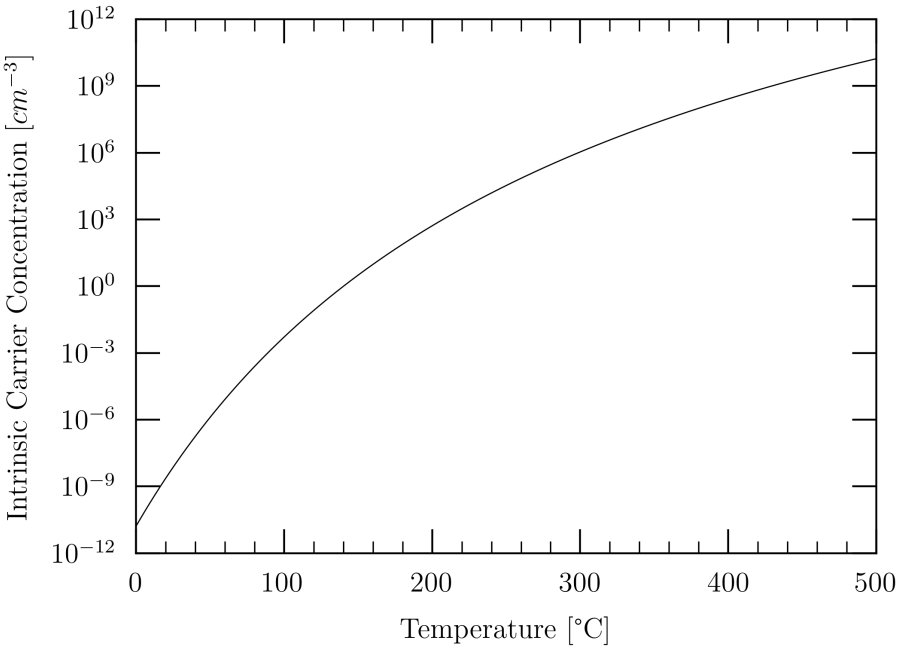

Fig. 6.2. Intrinsic carrier concentration as a function of temperature in degree Celsius using default model description for the band gap, computed with (6.3).

It is of importance in high-temperature applications, because $p-n$ junctions leakage current is directly related to the intrinsic carrier concentration. However, even if the intrinsic carrier

concentration increases by about seven orders of magnitude, the intrinsic carrier concentration remains still lower than other large band-gap semiconductors such as Ge or Si. Hence it is expected that the leakage current remains low, and the sensor remains operational at high temperatures providing signal-to-noise ratio compatible with the measurement requirements of small amount of generated charge carriers in the sensor.

6.1.3. Carrier mobility

In doped semiconductors, various phenomena influence carrier mobility, resulting in multiple dependencies that degrade it. TCAD program uses then a modular approach for the description of the carrier mobilities with several levels of precision that can be defined according to the description of mobility models. For sake of simplicity, regarding the dimensions of our problem in terms of geometry, doping concentration and electric fields, just a few of the following enumerate items are described.

- Phonon scattering
- Doping-dependence
- Carrier-carrier scattering
- High-field saturation.

Considering the simplest scenario, where only phonon scattering is taken into account, the mobility depends solely on the lattice temperature according to the Debye model [187], as follows:

$$\mu_{const.} = \mu_{max} \cdot \left(\frac{T}{300}\right)^{\alpha} \tag{6.5}$$

With μ_{max} the mobility due to phonon scattering. The associated coefficients are registered in Table 6.3 below.

Symbol	Electrons	Holes
μ_{max} $[cm^2/Vs]$	950 [a]	125 [a]
α	2.5 [b]	2.2 [b]

[a] *Commonly agreed value [188, 189].*
[b] *Mobility models are fitted with the measured data from [190].*

Table 6.3. Constant mobility model coefficients.

However, it is important to note that the constant mobility model (6.5) is applicable only to undoped materials. In doped materials, carriers scatter with charged impurity ions, resulting in reduced mobility since carriers are randomly scattered due to Coulomb interaction. To describe this effect, a doping dependent mobility degradation is thus introduced and proposed in several models described in Appendix F.1 and listed below:

- The Arora model [191]
- The Masetti model [192]
- The Philips unified mobility model [193].

In the current study, the Arora model is proposed to be studied as a reference, since it has been shown that Masetti model is not completely temperature dependent [194], and since the Philips unified model is not rigorously calibrated.

The degradation of the mobility with increasing doping concentration is represented for hole carriers as a function of acceptor concentration in Fig. 6.3. Hence, mobility models incorporate the donor and acceptor concentrations as part of its equations to capture the influence of impurities on charge carrier mobility. Thus the donor and acceptor concentration influence the overall carrier scattering mechanisms and concentration dependent effects.

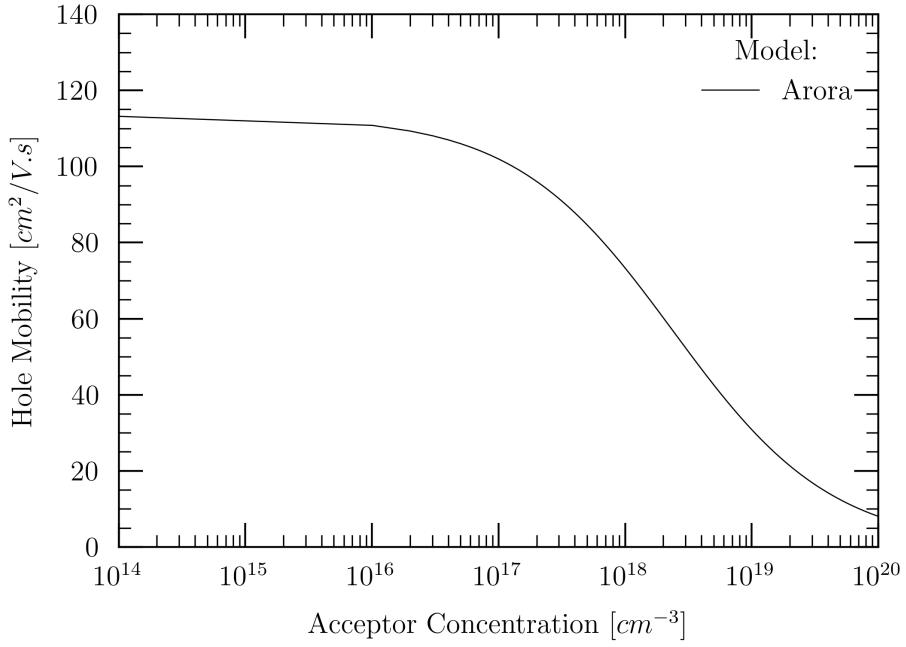

Fig. 6.3. Hole mobility as a function of acceptor atoms concentration in the p type region, computed with the Arora model in Appendix F.1.2.

Finally, regarding the definition of v_{drift} introduced in the presentation of the classical concept of electrical characterization of the sensor in Chapter 3 Section 3.1.2, such as $\vec{v}_{drift} = \mu \cdot \vec{E}$, the equation shows a divergent asymptotic behavior that cannot correspond to a physically possible phenomenon. Indeed, the theoretical framework of the Drude model describing the transport properties of electrons in materials anticipates a linear relationship between drift velocity and electric field strength. However, this linear dependence is applicable primarily under low field strengths. As the electric field intensifies, the drift velocity saturates, approaching a limit denoted as $v_{sat.}$. This saturation occurs as carriers gain higher kinetic energy from the field, which in turn increases the likelihood of scattering events with lattice atoms, impurities and phonons in the case of vibration of the crystal lattice.

Hence, carriers cannot gain significant additional average velocity due to the frequent scattering events which counteract the acceleration from the electric field. Therefore, the rate of charge drift reaches saturation level $v_{sat.}$ such that:

$$\mu(E) = \frac{\mu_0}{1 + \frac{\mu_0 \cdot E}{v_{sat.}}} \tag{6.6}$$

With μ_0 the low field mobility. Which leads to an updated expression for the drift velocity as a function of the electric field:

$$\vec{v}_{drift} = \mu(E) \cdot \vec{E} \tag{6.7}$$

TCAD supports two models for the description of this effect:

- The Canali model [195]
- The Meinerzhagen Engl model [196], mainly used for hydrodynamic simulations.

The general expression of mobility as a function of field strength is described for both models in Appendix F.1.3. In the following, the Canali model is chosen as a reference in our study, since the Meinerzhagen Engl model is mainly used for hydrodynamic simulations. The drift velocity saturation as the electric field intensifies is represented in Fig. 6.4. The effect of the high field saturation is clearly visible in the Canali model, in comparison to the constant drift velocity model which does not take into account the saturation effect. Both room temperature and 500 °C are displayed, since the low field mobility μ_0 is temperature dependent, as already discussed with the Arora model.

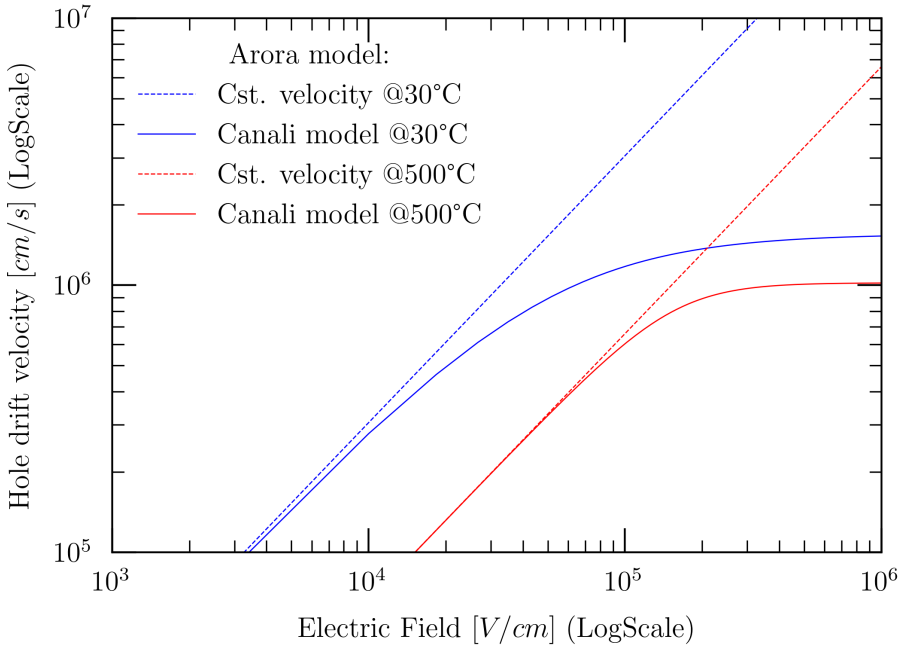

Fig. 6.4. Hole drift velocity as a function of electric field for two mobility models, and two temperatures, computed with the Canali model (6.6).

All things considered, the Arora model is chosen as a reference in our study to take into account the doping concentration dependence of the mobility. In addition, the Canali model is chosen to take into account the high field saturation effect in the mobility model. It is important to note that the Canali model, like any mobility model is an empirical model derived from experimental data and fits. Its purpose is to provide a mathematical representation of carrier mobility under various conditions for accurate device simulations. The specific equations and parameters in the model can vary depending on the semiconductor material and device characteristics.

Physical models to represent the physic intrinsic to the charge carriers dynamics has been exposed in the previous section. High field saturation models as well as the degradation of the mobility by scattering on the lattice have to be taken into account. The latter have to be implemented in TCAD programs, before going though finite element simulation described below.

6.2. Development of a numerical model to simulate the charge carriers collection

6.2.1. Finite element simulation

6.2.1.1. TCAD programs

The two main components of a computer-aided design process are geometry simulations in Sentaurus Structure Editor (SDE) files and process simulations in Sentaurus Device (SDevice) files. The main current suppliers of TCAD tools are Synopsys[197], Silvaco[198] and Crosslight[199]. In the following study, the techniques for simulating semiconductor structures are carried out using the Synopsys tool suite. This includes tools for constructing geometries, choosing meshes and visualizing electrical characteristics.

6.2.1.2. TCAD worflow

The Physics section allows a selection of the physical models to be applied in the device simulation. In summary, the multi step process of TCAD program is described in the scheme presented in Fig. 6.5.

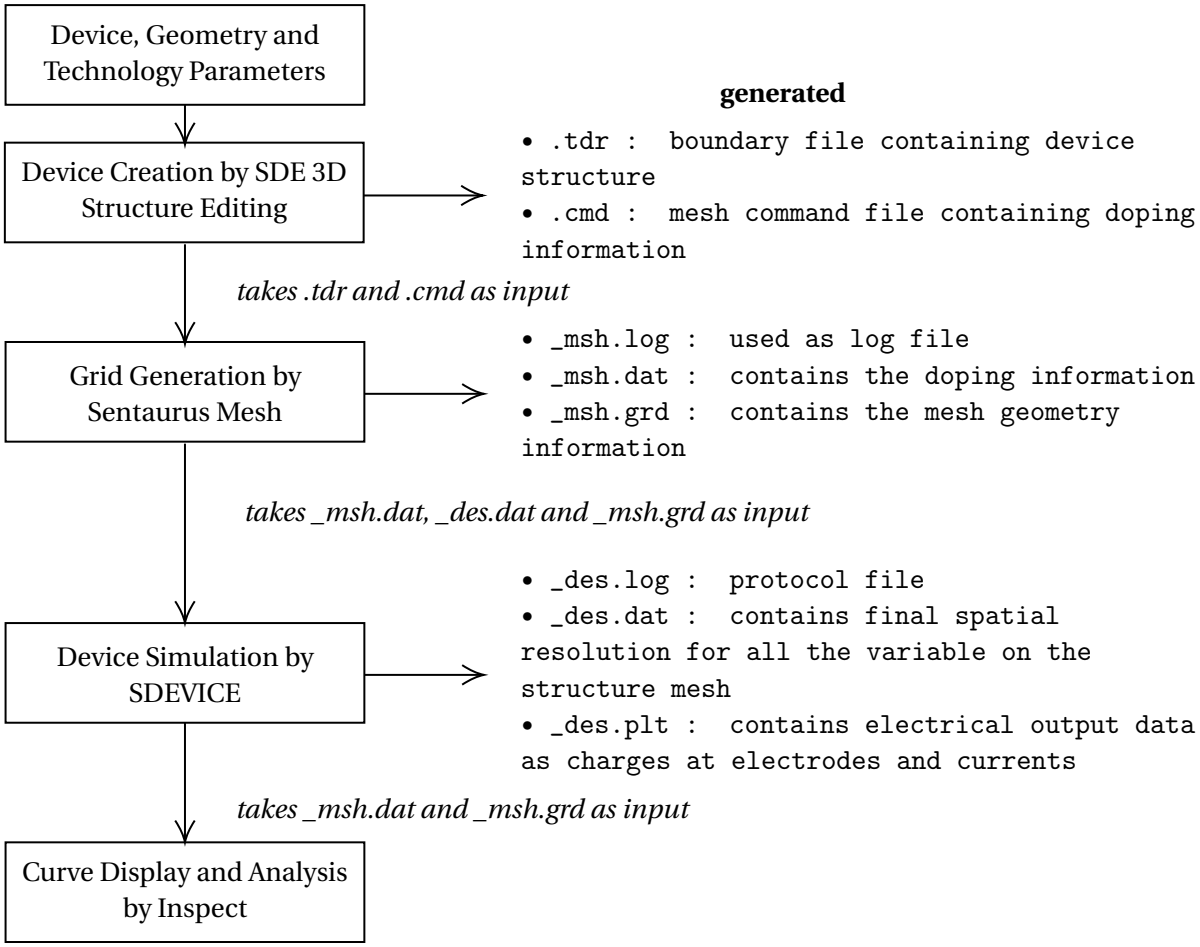

Fig. 6.5. Workflow diagram of device simulation using TCAD Synopsys.

6.2.2. Sensor geometry

6.2.2.1. Abrupt junction

Firstly, the aim is to study the simple case of the $p-n$ junction modeling. As seen in Chapter 3 and displayed in Fig. 6.6. It is composed of two regions of homogeneous semiconductors. One doped with acceptor atoms in the p region and the other doped with donor atoms in the n region. The transition region between the two types of semiconductors is supposed thin, the junction is then called abrupt.

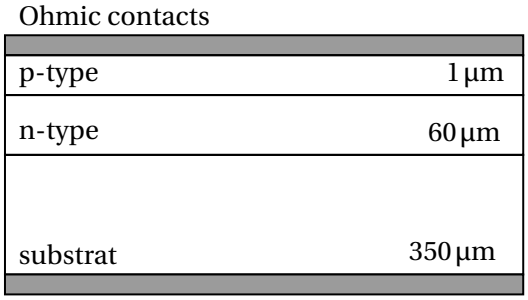

Fig. 6.6. p-n junction scheme modeled in TCAD.

Initially, the p–n junction is modelled such that the p region has a thickness of 1 μm and the n region a thickness of 60 μm. This junction sits on a substrate with the same surface area and thickness of 350 μm. The doping levels considered to be homogeneous are the input data for the simulation and are shown in Table 6.4.

Region	Doping Atoms	Concentration [cm^{-3}]
p	Aluminium	$1 \cdot 10^{19}$
n	Nitrogen	$1 \cdot 10^{14}$
Substrate	Nitrogen	$5 \cdot 10^{18}$

Table 6.4. Doping type for model diode.

6.2.2.2. Ohmic contacts

Semiconductor contacts are inherently Ohmic by nature, exhibiting a resistance of 0.001 Ω only when linked to a circuit node and no resistance in absence of such a connection. At these Ohmic contacts, both charge neutrality and equilibrium conditions are presumed such that:

$$\begin{cases} n_0 - p_0 = N_D - N_A \\ n_0 p_0 = n_i^2 \end{cases} \tag{6.8}$$

With n_0 and p_0 the equilibrium carrier densities, N_D and N_A the donor and acceptor densities, and n_i the intrinsic carrier density.

The Ohmic contacts are modelled as a region of 1 μm thickness at the extremities of the p and n regions. The contacts are then connected to the substrate considering the approximation $n = n_0$ and $p = p_0$ for concentrations at the Ohmic contacts in the approximation where electron or hole recombination velocity is not specified.

6.2.3. Structuring numerical resolution

6.2.3.1. Electrostatic potential and transport equation

By definition[1], conduction currents are proportional to carrier concentration and bias voltage, while diffusion currents are proportional to carrier concentration gradients. The charge carrier currents therefore correspond to the sum of the conduction current associated with the charge velocity drift v_{drift}, and the diffusion current such that:

$$\begin{cases} \vec{J_p} = p \cdot q\mu_p \vec{E} - qD_p \vec{\nabla} p \\ \vec{J_n} = n \cdot q\mu_n \vec{E} + qD_n \vec{\nabla} n \end{cases} \tag{6.9}$$

With p and n respectively the holes and electrons densities, $\vec{J_p}$ et $\vec{J_n}$ the hole and current density vectors, then D_p and D_n the diffusion constants.

The first term of the current equation takes into account the contribution due to the spatial variation of the electrostatic potential, the band gap and the electron affinity. The second term takes into account the contribution of the gradient of concentration and the spatial variation of the effective masses m_n and m_p. The diffusivity coefficients D_n and D_p can be obtained using the Einstein relationship such that:

$$\begin{cases} D_n = kT \cdot \mu_n \\ D_p = kT \cdot \mu_p \end{cases} \tag{6.10}$$

Charge conservation for electron hole pairs implies that the time evolution of carriers densities must obey to continuity equations such that:

$$\begin{cases} -\vec{\nabla} \cdot \vec{J_p} = qR_p + q\frac{\partial p}{\partial t} \\ +\vec{\nabla} \cdot \vec{J_n} = qR_n + q\frac{\partial n}{\partial t} \end{cases} \tag{6.11}$$

With $\vec{J_p}$ and $\vec{J_n}$ the holes and electrons current density vectors, then R_p and R_n the carrier recombination rate.

The system of equations implies then four equations for five unknowns which are p, n, $\vec{E}$, $\vec{J_p}$ and $\vec{J_n}$. But it is necessary to take into account the electrostatic potential equation and Poisson equation which link the potential to the carrier density such that:

$$\begin{cases} \vec{E} & = -\vec{\nabla} V \\ \Delta V & = -\frac{\rho}{\epsilon} \end{cases} \tag{6.12}$$

The system of equations is now composed of six equations for six unknowns, adding electrostatic potential V. Currents densities equations (6.9) are thus introduced in continuity equations (6.11) constituting then the system coupling charge carrier density and electrostatic potential that the finite element simulation is enabled to solve. Initial guess for electrostatic potential is made for each doping wells. Then the semiconductor device is divided into number of regions based on doping and contacted region.

[1] *These brief and synthetic explanations are intended to introduce the main concepts associated with transport equations. For a full discussion of the demonstrations relating to these balance equations, please refer to the references [89, 200]*

6.2.3.2. Finite differences method

Hence, three equations have to be solved locally at any point:

- The Poisson equation
- The continuity equation for holes
- The continuity equation for electrons.

These equations are non-linear and coupled, which means that the variables associated with the charge carrier densities depend non-linearly on the potential. To solve these equations numerically, it is necessary to replace infinitesimal differences by finite differences. For spatial variations, these finite differences are defined between the nodes of a predefined grid. The latter, commonly known as a mesh allows a structure to be spatially discretized into elementary cells as seen in Fig. 6.7.

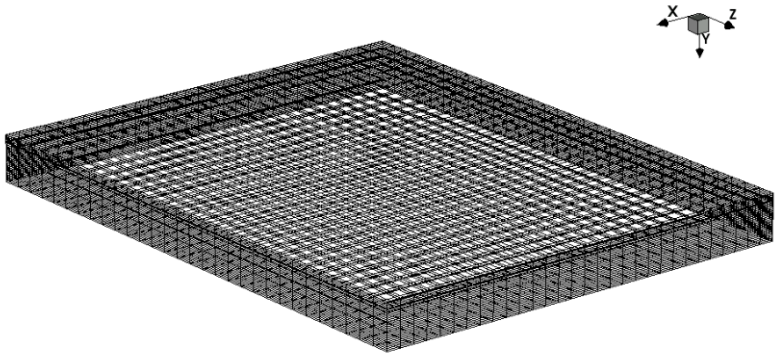

Fig. 6.7. Illustration of the mesh in black, of the diode studied with dimensions 4 $mm \times 5\ mm \times 411\ \mu m$.

The triangles are used as building blocks for the basic mesh used by the simulator to solve the partial differential equations. The accuracy of the mesh must be adapted to the variations in physical quantities, such as doping, that can occur within the structure. The mesh is then refined in areas where the physical quantities vary rapidly.

The overall discussion on the mesh is presented in the following Section 6.3 dedicated to the simulation of a charge particle within the material. The accuracy of calculations increases when derivatives are substituted with ratios of small increments. Consequently, the accuracy of the solutions provided by the simulator depends on the number of nodes used in the mesh. However, it should be noted that the number of nodes is limited by the memory capacity of the computer or by the computing time available. Defining the mesh is therefore a critical step in the simulation development process. For a given number of nodes, accuracy is better if the mesh is denser in areas with high gradients, whereas it may be less dense in areas where low spatial variations are expected. An initial mesh is generally used, which is refined until sufficient accuracy is achieved, observing that the results stabilize as the number of nodes increases. Ultimately, it is necessary to find a compromise between the accuracy of the various sensitive areas and the total number of nodes.

These explanations motivate the choice of a specific mesh for the simulation of each charged particle according to its depth of penetration into the material. These concepts of range and stopping power have already been covered in Chapter 3, Section 3.3.2, and lead to the development of a specific mesh for the simulation of each ionizing particle, according to its penetration depth into the material.

6.3. Study of mechanisms induced by an ionizing particle via finite element method

6.3.1. Simulating a charged particle

6.3.1.1. Linear energy transfer

The interaction of charged particles with matter is a complex phenomenon that can be described by the Linear Energy Transfer (LET). The LET, as introduced in the introductory Part in Chapter 3 is defined as the energy transferred by a charged particle to the material per unit length of its trajectory. Usually expressed in MeV/cm, the SDE file allows the user to define the LET expressed in pairs/cm^3 or in pC/µm in order to express the dimensions of the problem in µm. The LET is therefore a key parameter in the study of the effects of ionizing radiation on semiconductors leading to the quantification of the number of electron–hole pairs generated by the passage of a charged particle through the material.

Function of the penetration depth of the particle, as shown in Fig. 6.8 for a 5 MeV alpha particle, the LET curve is characterized by a peak at the end of the trajectory of the particle, corresponding to the maximum energy transfer to the material. This charged particle is taken as an example for the following study.

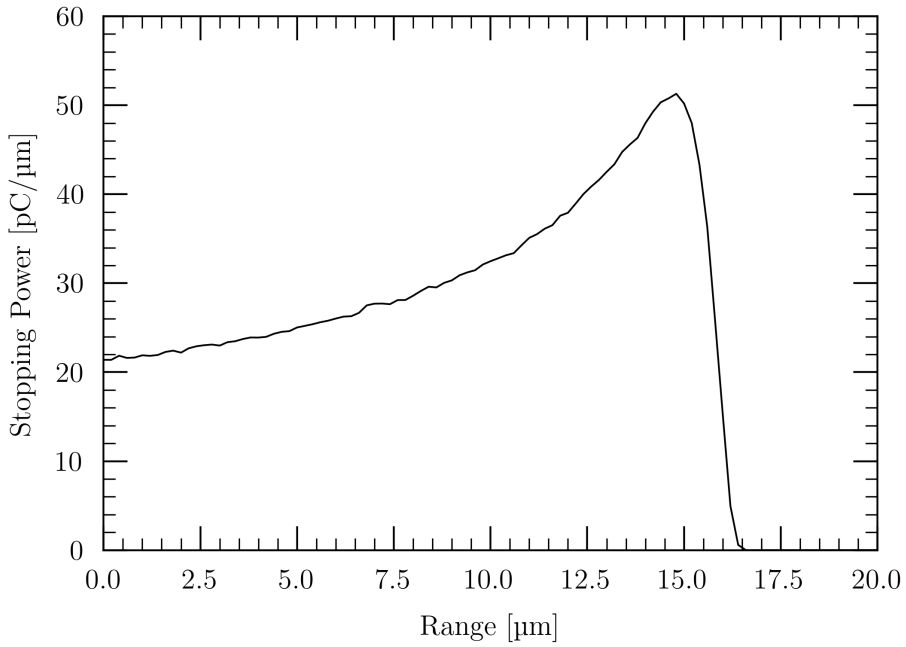

Fig. 6.8. Linear energy transfer as a function of the penetration depth of a 5 MeV alpha particle in 4H–SiC, from SRIM calculation.

6.3.1.2. Generation rate computation

The creation of electron–hole pairs is integrated by TCAD using the generation rate G, which represents the number of pairs generated per cubic centimeter per second. So, for each point in the trajectory of the ion, it is necessary to define a function that describes the spatial and temporal distribution of the created pairs. Given the velocity of the particle and the dimensions of the components, the interaction time between the ion and the target is very short, in the picosecond range. Consequently, the propagation of the generation along the trajectory can be neglected and it can be considered that it follows the same time law at all points along

the trajectory. Finally, because of the axial symmetry of the problem, the spatial distribution function depends only on the distance r from the ion track.

Therefore a generation term G due to the simulated ionizing charged particle, should be added to the charge carrier generation term in the continuity equations presented above, such that:

$$G(l,r,t) = G_{LET}(l) \times R(r,l) \times T(t) \tag{6.13}$$

With l the distance along the track of the charged particle, r the radial distance of the point with respect to the trace and t the time.

The generation term is a product of three terms:

- $G_{LET}(l)$, the linear energy transfer generation density expressed as the number of electron/hole pairs per cm^3 as a function of the penetration distance of the ionizing particle.
- $R(r,l)$, is a function that describes spatial variations in the generation rate. This is defined using an exponential function by default, or a Gaussian function such as:

$$R(r,l) = \exp\left(-\frac{r}{r_t(l)}\right) \tag{6.14}$$

$$R(r,l) = \exp\left(-\left(\frac{r}{r_t(l)}\right)^2\right) \tag{6.15}$$

  With r defined as the radius perpendicular to the ion trace and r_t a characteristic distance specific to the ion and that can be a function of the penetration distance l, as seen in Fig. 6.9.

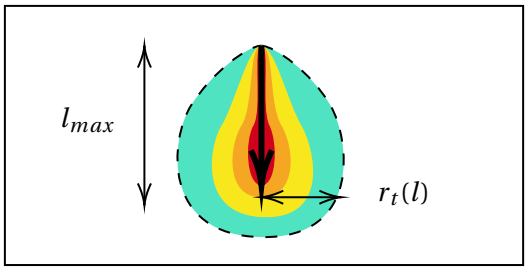

Fig. 6.9. Basic diagram of the junction under study, with an ionizing particle track represented by a bold arrow.

  The Gaussian distribution reflects the symmetry of the concentration with respect to the axis of penetration of the particle, with a maximum value at the centre of the trace. To a first approximation, the standard deviation of this Gaussian determines the diameter of the trajectory of the ionizing particle.

- $T(t)$, is a function that describes temporal variations in the generation rate. It is defined using a Gaussian function, such that:

$$T(t) = \frac{2 \cdot \exp\left(-\left(\frac{t-t_0}{\sqrt{2}\cdot\sigma}\right)^2\right)}{\sqrt{2}\cdot\sigma\sqrt{\pi}\cdot\left(1+\mathrm{erf}\left(\frac{t_0}{\sqrt{2}\cdot\sigma}\right)\right)} \tag{6.16}$$

  With t_0 the initial time of penetration of the ionizing particle, and σ the characteristic value of the Gaussian whose default value is $2 \cdot 10^{-12}$ s.

A more accurate definition would have involved the use of a Dirac function. In fact, the analytical description of nuclear interactions discussed in Part II showed that charged particles generated in SiC travel a typical distance of several µm in a period of approximately 10 ps. However, the instantaneous nature of this event, ideally described by a Dirac function, poses problems of compatibility with the numerical resolution method used by simulators based on finite increments.

The simulator thus represents the passage of an ionizing charged particle through the semiconductor by adopting an approach where a column of charges is used. The ion is then modelled using a three-dimensional configuration, like a cylinder containing electron-hole pairs aligned along the axis corresponding to the trajectory of the particle within the diode as seen in Fig. 6.10.

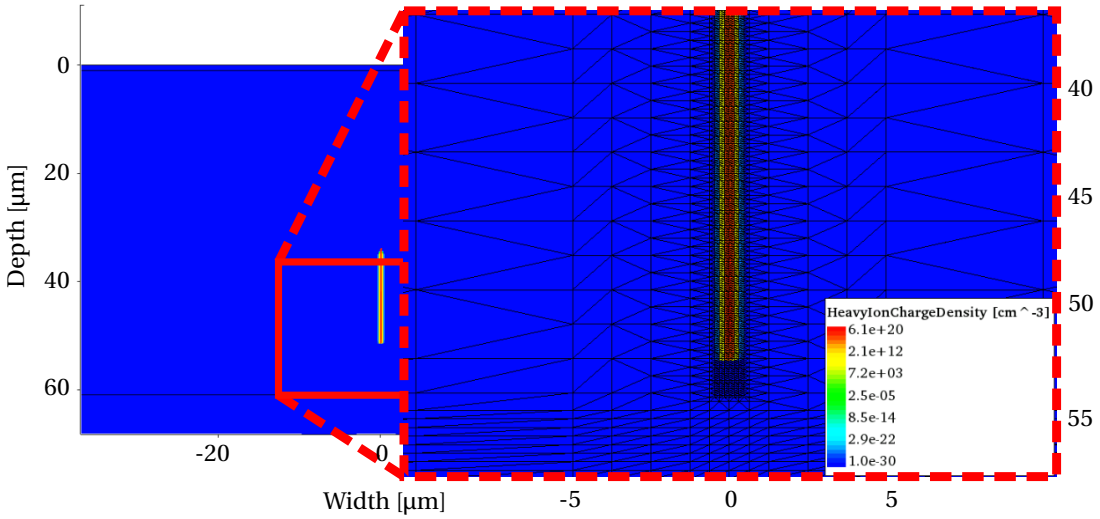

Fig. 6.10. Ion density profile of a 5 MeV alpha particle in SiC. The left image is a cut of the ion density profile at the center of the sensor, while the right image is a zoomed-in view of the mesh region.

The fundamental objective of this method is to establish a correlation between the generation rate G and an experimental or theoretical LET curve in relation to the distance l traveled by the ion. In order to achieve this, the mesh must be adapted to the dimensions of the ion trace, and the number of nodes must be sufficient at the collection electrodes. This is the reason why the mesh is refined up to 0.2 µm in the region of the ion trace as seen in Fig. 6.10, to ensure that the mesh is fine enough to capture the spatial variations in the generation rate. However, due to the high computational cost of the simulation, the mesh is coarser in the rest of the structure. The summary of the modeling scheme regarding the number of nodes in the nodes in the mesh, of segments connecting these nodes and the number of distinct corner points in the mesh is presented in Table 6.5.

Model	Counts
Grid point	45377
Edges	307598
Vertices	45961
Processors	12
total CPU time	24h 30min[a]

[a] *Multiple users running CPU-intensive simulations on the same server degrade performance compared to a single job occupying the entire machine.*

Table 6.5. Summary of the mesh used for the simulation of the passage of a charged particle through the diode.

6.3.2. Charge carrier collection simulation

6.3.2.1. Simulation of the mechanisms involved in energy deposition

In this section, the mechanisms that govern the evolution of the density of charge carriers created by a charged particle are under study. The aim is therefore to study the dynamics of these carriers and the process of charge collection leading to the simulation of the current pulse. The following deals with the case of a reverse-polarized *p*–*n* junction, considering the geometry presented in Section 6.2.2. It is worth recalling at this stage that subjects related to the description and choice of physical models for the simulation of carrier creation and transport in a semiconductor junction are still being studied by the international community. This applies in particular to the description of the radial charge distribution along the trace of the incident charged particle. For instance, as part of the development of radiation-hardened integrated circuits, CEA-DAM has integrated a silicon model into the GEANT4 code [201], within the framework of international collaboration around its development. In addition, this effort has been recently expanded to include models for approximately ten additional materials, in collaboration with Onera and the University of Paris-Saclay [202].

The current study does not take into account these latest advances in the field. The modeling scheme is based on the most favorable case based on the commonly used generation rate description [203, 204]. Potential improvements could be suggested, but they are not the main focus of this study, which concentrates on the dynamics of charge carriers collection rather than the modeling of radial charge distribution.

As explained, the simulation of the passage of the ionizing particle through the semiconductor junction is based on the generation rate G introduced in the previous Section 6.3.1. Hence, once the charged particle is modelled, the simulator calculates the number of electron–hole pairs generated. Then the simulator solves the continuity equations and the Poisson equation to determine the distribution of the charge carriers created. Finally, TCAD program calculates the current pulse by solving the drift-diffusion equations at each point in the structure and at each time step. The charge carrier collection under the influence of an electric field is then simulated. The distribution of the charge carriers created by the passage of a charged particle in the depletion region can therefore be modelled as a function of time as seen in Fig. 6.11 for the holes current density, just after the passage of the particle, and Fig. 6.12 after 1.5 ns. Hence, at each point in the structure, and each time step, charge cloud dynamics are simulated by solving the drift-diffusion equations.

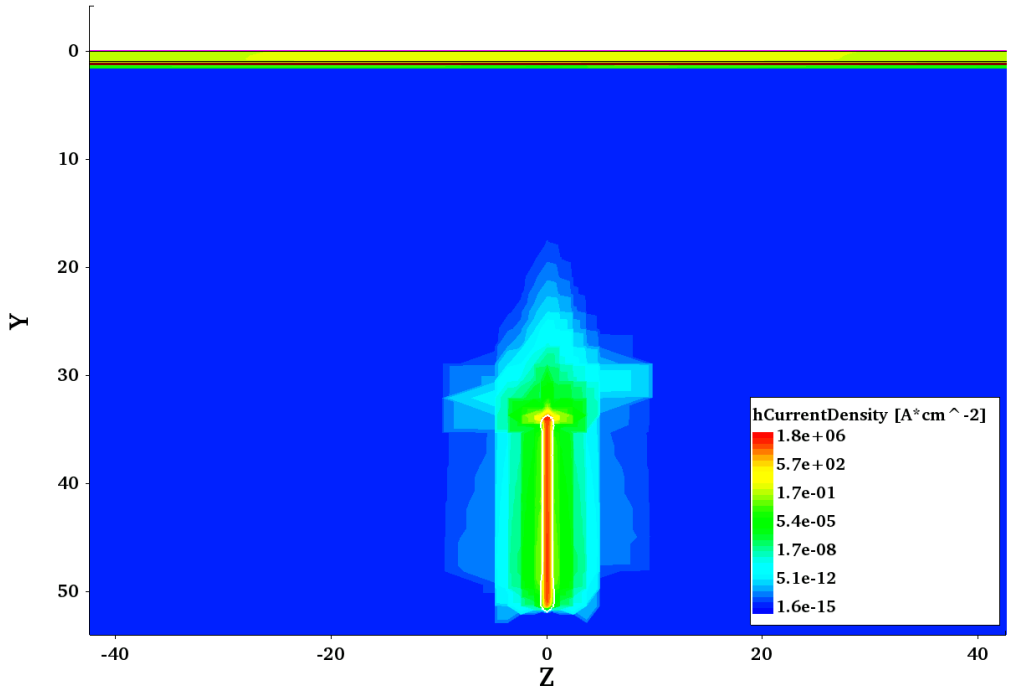

Fig. 6.11. Hole current density distribution map in the 60 µm SCR at 0.5 ns after the passage of the 5 MeV alpha particle. Y and Z labels stand for the depth and the width of the diode respectively in [µm].

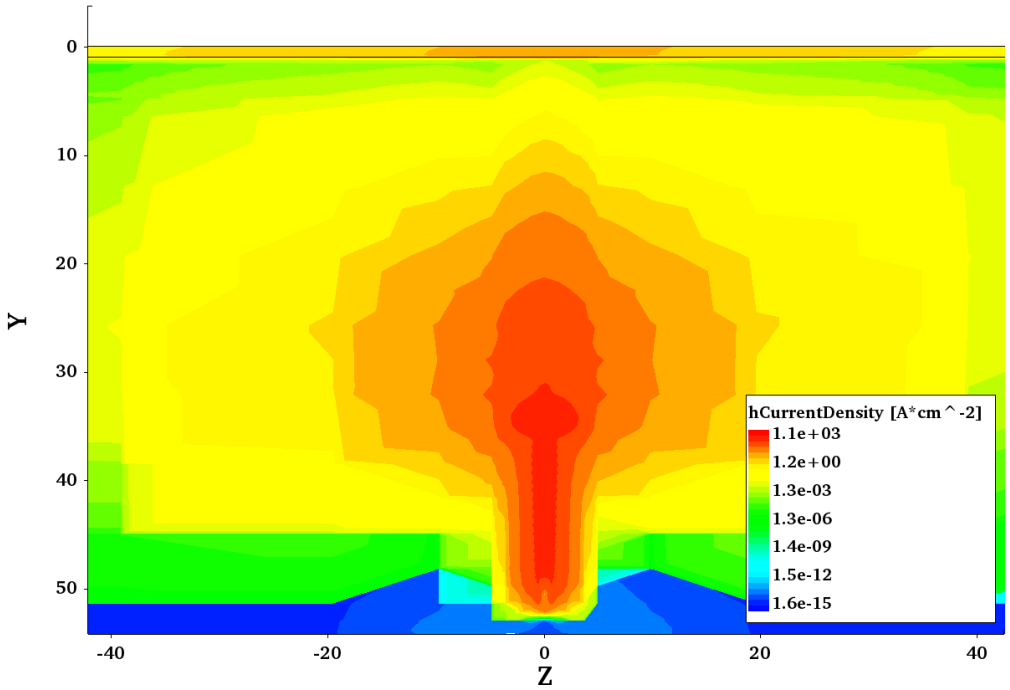

Fig. 6.12. Hole current density distribution map in the 60 µm SCR at 1.5 ns after the passage of the 5 MeV alpha particle. Y and Z labels stand for the depth and the width of the diode respectively in [µm].

6.3.2.2. Simulation of the current pulse

Non-linearities in the governing equations solved by Synopsys are caused by factors such as electric field-dependent quantities and the exponential relationship between carrier concentration and energy bands. Additionally, the nonuniform distribution of carrier concentrations and doping profiles, as well as carrier recombination and generation processes, contribute to these non-linearities. However, the default initial values in the solver only provide rough estimates for the carrier concentration under no applied voltages or currents. Therefore, to solve stationary models accurately, it is recommended to ramp up the voltages or currents to their operating values. The simulation of the current pulse is then based on the drift-diffusion equations at each point in the structure and at each time step. The charge carrier collection as a function of time under the influence of an electric field is then simulated, leading to the current pulse shown in Fig. 6.13.

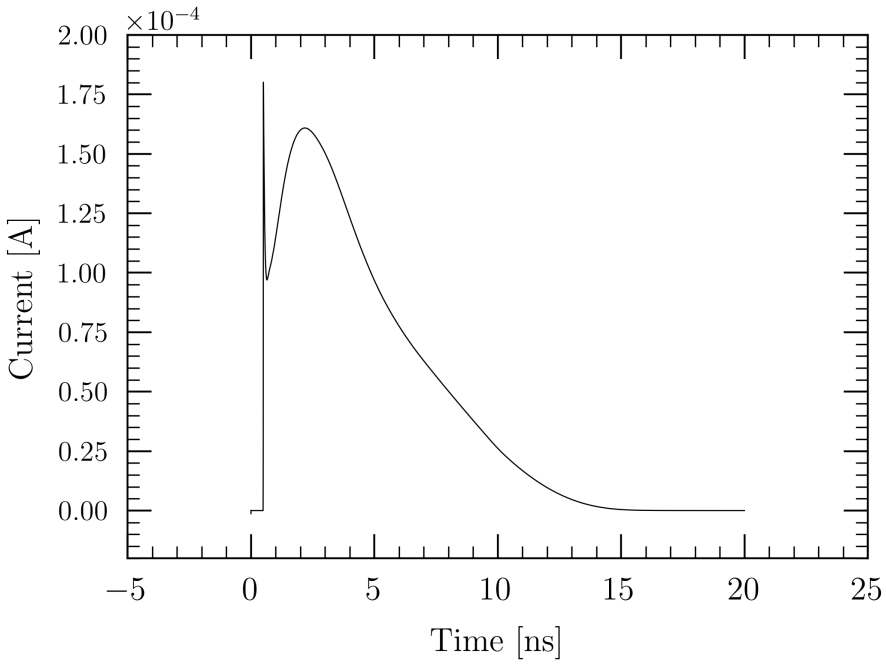

Fig. 6.13. Simulated current pulse for a 5 MeV alpha particle generated at 35 µm from the collection electrode. The additional peak is caused by the short drift of the carriers close to the collection electrode.

When considering the simulation of a charged particle at the boundary of the depletion region, the current pulse is dominated by the drift of the opposite charge carrier through the junction since the time taken for the charge carriers close to the boundary to reach the collection electrode is of the order of few picoseconds. Hence it can be seen an additional peak caused by the short drift of the carriers close to the collection electrode. The current pulse is then characterized by the drift of the opposite charge carriers through the junction, until the complete carriers collection.

6.4. Dedicated 14 MeV neutron generator measurement campaign with a heating device

6.4.1. Protocole and Methodology

Regarding literature data as well as temperature operating domain requirements in ITER, the objectives with regards to this dedicated experiment using an heating device in a neutron field are twofold:

- To refine and adjust the empirical models selected from the literature to use it as input for the numerical simulation using TCAD programs
- To compare the stability in detection performance between SiC and diamond based sensors, within the temperature range of interest for fusion and fission application.

Indeed, in the existing literature, there is notable variability in the reported drift mobility values for both electron and hole carriers in SiC samples in particular regarding the *pn* junction devices. Empirical models derived from experimental data and fits has been introduced in Section 6.1 in order to provide a mathematical representation of carrier dynamic parameters under various conditions for accurate device simulations. However, the specific equations and parameters in these models can vary depending on the semiconductor design and device characteristics. To address this issue, the detector response under different bias voltages and temperatures was analyzed in order to quantify these effects. Through these experiments, the transit time values for holes was estimated, allowing to establish the temperature-dependent relationships for drift velocity, saturation velocity, and low-field drift mobility.

In addition, the aim of the experiment was also to reproduce real irradiation in fast neutron field in order to study the stability of the sensor and so, its ability to be used as a neutron flux monitoring in neutron field with high temperatures. It was also established in preliminary words, the relationship between deep defect activation energy regarding the temperature. The latter point is covered in detail in a dedicated discussion in Chapter 7. This question is of interest regarding the use of semiconductor based sensors for high temperature environment, as introduced in Part I.

Pulse Shape Analysis (PSA) is a direct measurement method of the charge carrier collection dynamics as a function of applied bias voltage and temperature. Indeed, the durations of these current pulse are equal to the time needed for the ionization charges to drift through the sensor in an uniform electric field and hence to be collected at the electrodes. From this transit time, if the characteristic electronic time constant and RC constant are low enough regarding the duration of the pulse, PSA can provide information on the dynamics of the collection such as the velocity drift or the mobility of the carriers are extracted. This method is called the Transient Current Technique (TCT).

To summarize the discussion introduced in Chapter 3, Section 3.1.3, it can be said that the polarity of the bias voltage affects the type of charge carrier collected first and thus impact the shape and duration of the resulting current pulse. The overall discussion is displayed in Fig. 6.14, considering a negative bias voltage applied to the junction, with the charge carriers generated close to the electrodes. The diagram provides a simplified representation, as the actual pulse shape is more intricate due to the electric field, which causes the drift velocity to be higher near the anode of the $p-n$ junction. Schematically, electron move faster than holes due to their higher mobility, hence in the case where they are collected first as in Fig. 6.14(i), it leads to an initial faster rise in the signal. Then the subsequent collection of holes add to the signal but in a longer duration due to their lower mobility.

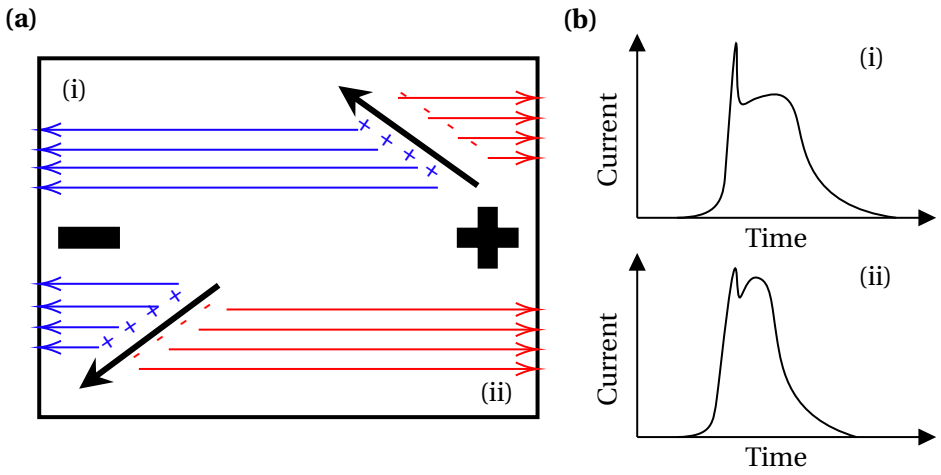

Fig. 6.14. Draw up diagram of a $p-n$ junction with a negative bias voltage applied to the left electrode. (a) Junction with charge clouds generated. (b) Current response to the collection of generated carriers. Both situations are represented as (i) and (ii), when the pulses are dominated by the drift of holes and electrons, respectively.

However, due to the shaping induced by the signal reading electronics, in practice the contribution of the charge carrier drifting towards the input electrode is never observed. This contribution is attenuated. So, depending on the polarization used, the hole or electron transport properties can be studied independently by selecting the charge carrier that drift through almost the entire thickness of the detection volume.

Regarding our study, the FWHM of the current pulse is used to measure the transit time of the charge carriers. Although the experimental base width of the measured current pulse is influenced by time constants as explained in Chapter 3, Section 3.1.3.2, the FWHM is preferred for relative comparison to the transit time because it is less affected by the time constant of the system and baseline noise.

6.4.1.1. Experimental protocol

The neutron generator installation was described in the Chapter 4, Section 4.3, along with the acquisition set up used. As a reminder, the measurement chain includes in the experimental room:

- A broadband amplifier with 2 GHz analog bandwidth and 40 dB gain
- A digitizer with sampling rate of 4 GS/s
- A 12 V power supply
- An encapsulated semiconductor sensor as seen in blue color in Fig. 6.15, surrounded by the heating device seen in Fig. 6.16.

An improved version of housing for study under vacuum conditions was designed and manufactured in the IRFM workshop, as seen in Fig. 6.17 and Fig. 6.18. The results obtained with these vacuum conditions are consistent with those obtained in air, and are not presented for the SiC sensor in this manuscript.

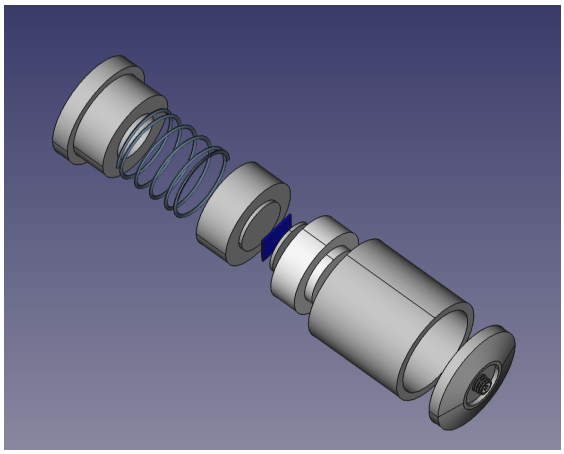

Fig. 6.15. Scheme of the encapsulated semiconductor sensor within ceramic insulator in steel housing. Custom-made by LDCI and manufactured in IRFM workshop, using a flange from Neyco company [205].

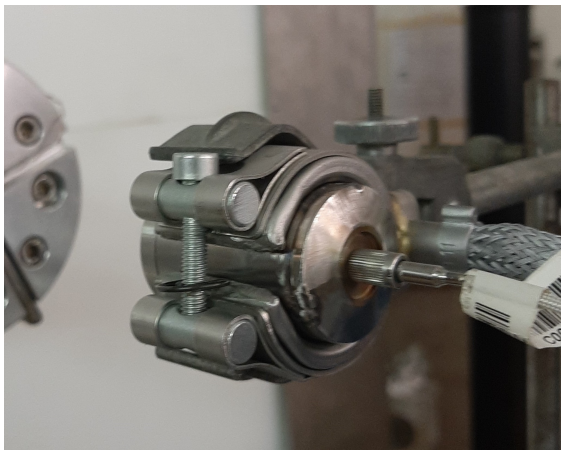

Fig. 6.16. Picture of the sensor housing, with heating device, a tubular cartridge heater from Celtic company [206].

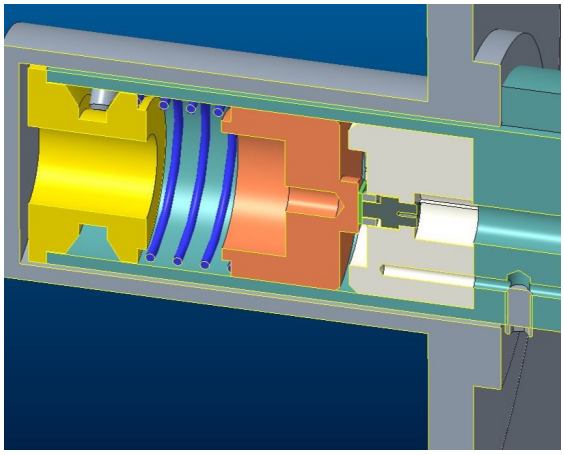

Fig. 6.17. Scheme of the encapsulated semiconductor sensor in green, within ceramic insulator in bronze housing. Manufactured in IRFM workshop.

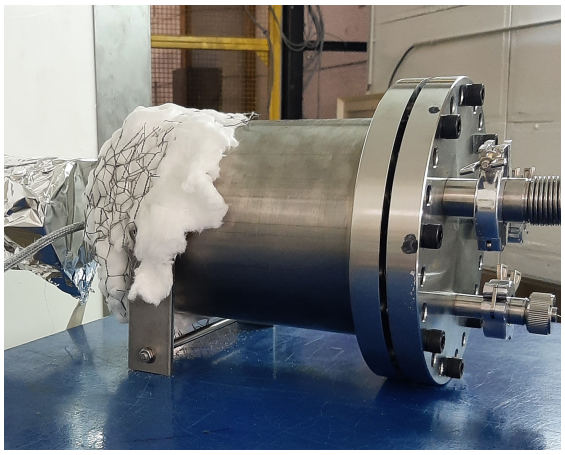

Fig. 6.18. Picture of the vacuum chamber housing, with heating device. Sensor inserted inside, facing the beam.

Regarding the acquisition system, the measuring chain used is the same as the one presented in Chapter 4, Section 4.3.2.1. Hence, fast current preamplifier from CIVIDEC instrumentation are used to amplify signals acquired with high sampling rate digitizer from Acqiris instrumentation which enable finally the acquisition of fast current pulses with a FWHM of few nanoseconds and a high signal-to-noise ratio. In order to design the experiment, in term of time optimization for beam schedule, just one type of carrier has been studied. Therefore, the following analysis and model-based fits focus only on the drift of holes. However, at the contrary to gas filled detectors — where electrons mobility is much more higher than ions mobility — the holes mobility in SiC and Diamond is of the same order of magnitude than electron mobility. Hence, studying the behavior of just one carrier type is not detrimental for the whole understanding of the effect of

temperature on the charge collection dynamic.

Finally, concerning the following data analysis, it should be noticed here, that in TCT measurements performed, since the solid sensor is operated in an energetic neutron beam, the ionizing particles are created at random location within the depleted region of the sensor. In addition, in this separate measurement of electron and hole signals method presented, the deposited ionization charge can be regarded as a thin charge layer generated close to one electrode, which then drifts through the whole detector active region. Hence, in order to compare the transit time of the charge carriers that drift on the same distance, given that charged particles are generated randomly, the PSA which is conducted, necessitates an initial data processing step. This step is essential for selecting data that correspond to the charge cloud formed near the electrode. Bi-dimensional histograms are therefore used to select data according to the charge deposited and the FWHM. This step is not necessary in the proper TCT measurement protocol, since it uses directly collimated charged particles like alpha sources. However, according to the dual objectives of representativeness of our experiment, it is the more relevant way to study charge collection efficiency with increasing temperature as well as variation of mobility parameters in a high neutron field, characteristic of fusion reactors.

6.4.2. Quantification of the effects - SiC

6.4.2.1. Pulse Shape Analysis at room temperature

Before going through the parametric study as a function of temperature, it is useful to re-contextualise the study in terms of the input data available experimentally. The aim of this first experiment is to study the charge collection dynamics in the 4H–SiC sensor. Individual raw waveforms current signals are acquired during two minutes long acquisition in order to have a sufficient statistics for the reaction. The well known peak associated to the $^{12}C(n,\alpha_0)^9Be^{(g.s)}$ events observed in the collected charge distribution in Fig. 6.19, around 185 fC, is used as a tool for analysis. In addition, since the charge carriers are created randomly, the FWHM of the pulses is distributed as seen in Fig. 6.20 according to the drift distance of the charge cloud.

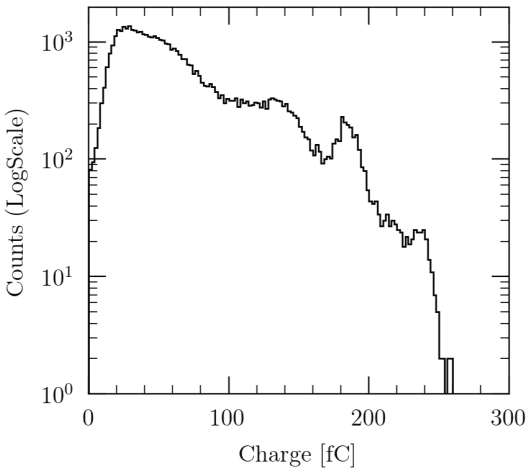

Fig. 6.19. Distribution of the collected charge, with bias voltage of −300 V.

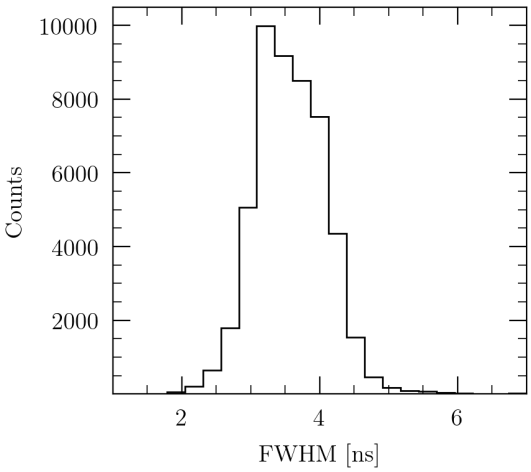

Fig. 6.20. Distribution of the FWHM of the pulses, with bias voltage of −300 V.

Therefore, bi-dimensional histograms of the collected charge within the sensor as a function of FWHM of the pulses are computed as seen in Fig. 6.21. Hence, it allows the selection in a first hand, of the events within the $^{12}C(n,\alpha_0)$ peak that deposit all of their energy i.e. 185 fC, and in a second hand, since the charge particles are created randomly, it allows the selection of the events that drift the longest distance in the sensor, according to their FWHM.

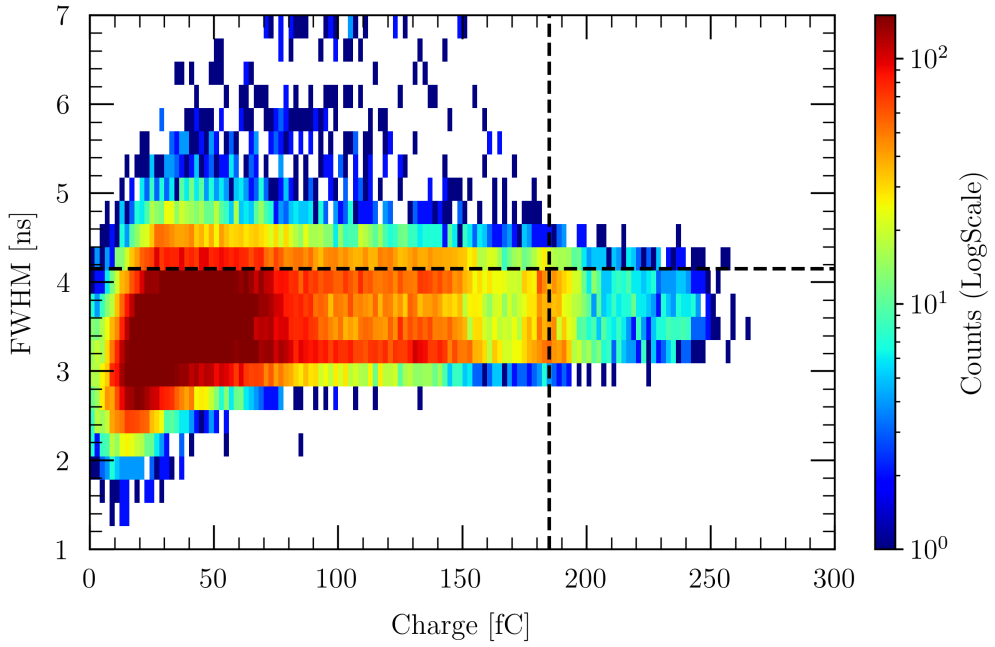

Fig. 6.21. Bi-dimensional histogram of the deposited charge as a function of the FWHM of the pulses, with bias voltage of −300 V. The dashed lines guide the eye to the events that deposit all of their energy and drift the longest distance in the sensor.

Then, regarding the objective of this study, the charge collection efficiency is considered as a function of the bias voltage. As a reminder, in order to collect the total amount of carriers generated by the secondaries particles produced by nuclear reactions such as the $^{12}C(n,\alpha_0)^9Be^{(g.s)}$ reaction, the sensor must be sufficiently depleted so that the total kinetic energy of the particles is deposited within the sensor. For instance, in the case of 14 MeV neutrons, the kinematic study carried out in Chapter 4, led to the conclusion that the kinetic energy of the reaction products is distributed as detailed in Table 6.6.

	$E_{k_{min}}$ [MeV]	$E_{k_{max}}$ [MeV]
α_0	2.74	7.91
$^9Be^{(g.s)}$	0.39	5.55

Table 6.6. Minimum and maximum kinetic energy in [MeV] of reaction products $^{12}C(n,\alpha_0)^9Be^{(g.s)}$ for $\theta = 0$ or $\theta = \pi$ between the incident neutron direction and the emitted alpha particle, considering 14 MeV incident neutrons.

Hence, according to SRIM calculation displayed in Fig. 6.22, the range of the reaction products as a function of their kinetic energy is computed. Consequently, considering the α_0 emitted with a maximum kinetic energy of 7.91 MeV, and the Be nucleus in its ground state with a minimum kinetic energy, the range of the alpha particle in 4H–SiC is 32 µm.

Therefore, a SCR of 32 µm is sufficient to start collecting the total amount of carriers generated by the $^{12}C(n,\alpha_0)Be^{(g.s)}$ reaction, regardless the angle of emission of the alpha particle. According to the distribution of the collected charge in Fig. 6.23, the position of the associated peak, remains at constant value of 185 fC once a bias voltage of 50 V is applied.

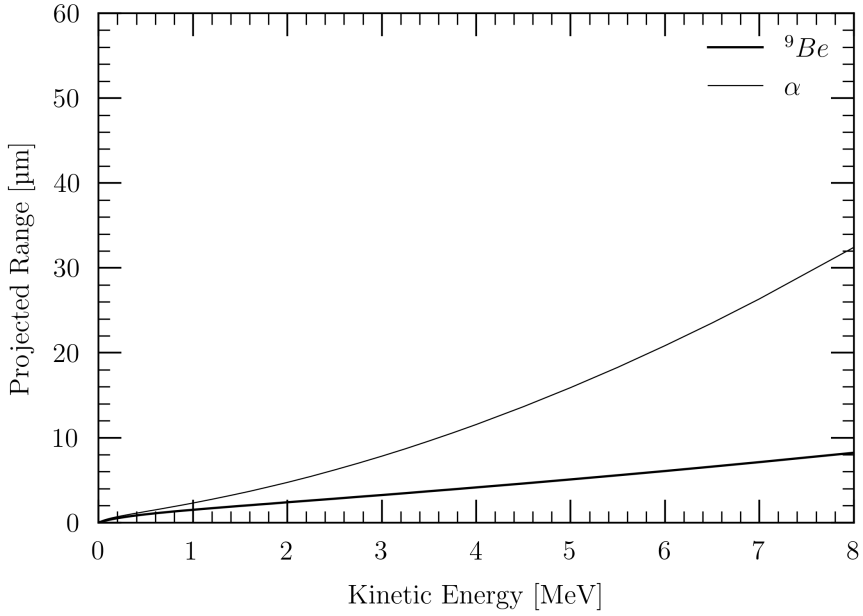

Fig. 6.22. Projected Ranges of $^{12}C(n,\alpha_0)^9Be^{(g.s)}$ reaction products within 4H–SiC as a function of their kinetic energy.

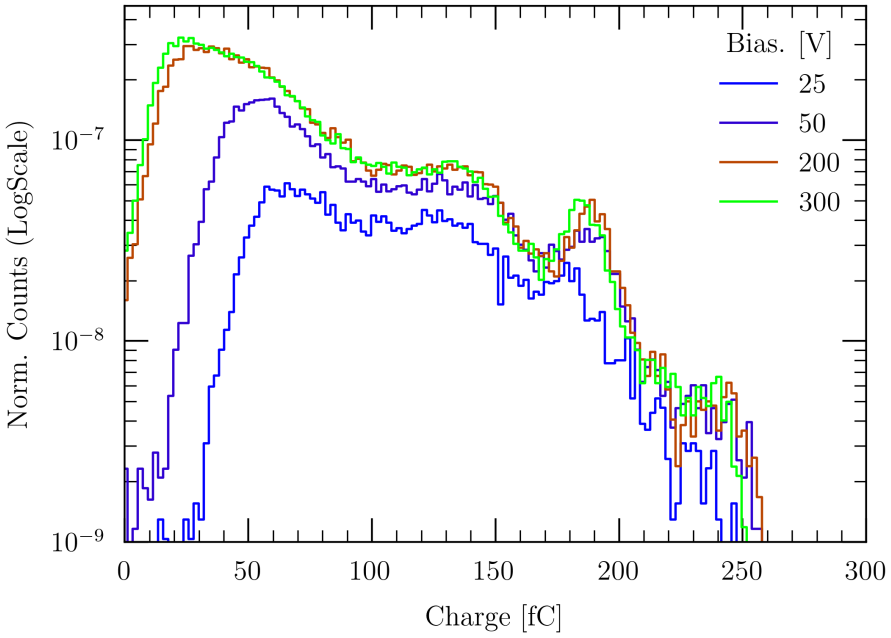

Fig. 6.23. Distribution of the deposited charge in the 60 µm sensor for several bias voltages applied. The data are acquired within two minutes acquisition and the counts are normalized with respect to the neutron intensity.

However, even if this bias voltage is sufficient to collect the total amount of carriers generated by the $^{12}C(n,\alpha_0)Be^{(g.s)}$ reaction, the polarization is not optimal. The application of a bias voltage is said to be optimal if it meets the following two considerations:

- The sensor is fully depleted, improving the CCE by reducing the edge effects

- The drift velocity of the charge carriers is maximized, which is necessary as mobility is expected to decrease with increasing temperature.

Considering the first point, the evolution of the count rate with increasing the reverse bias voltage is examined. As a reminder, it has been demonstrated in Appendix A Section A.1, the analytical expression of the SCR depletion width denoted W_{SCR}. The variation of the number of counts acquired is read on the left vertical axis of Fig. 6.24, while the W_{SCR} is superposed on the right vertical axis.

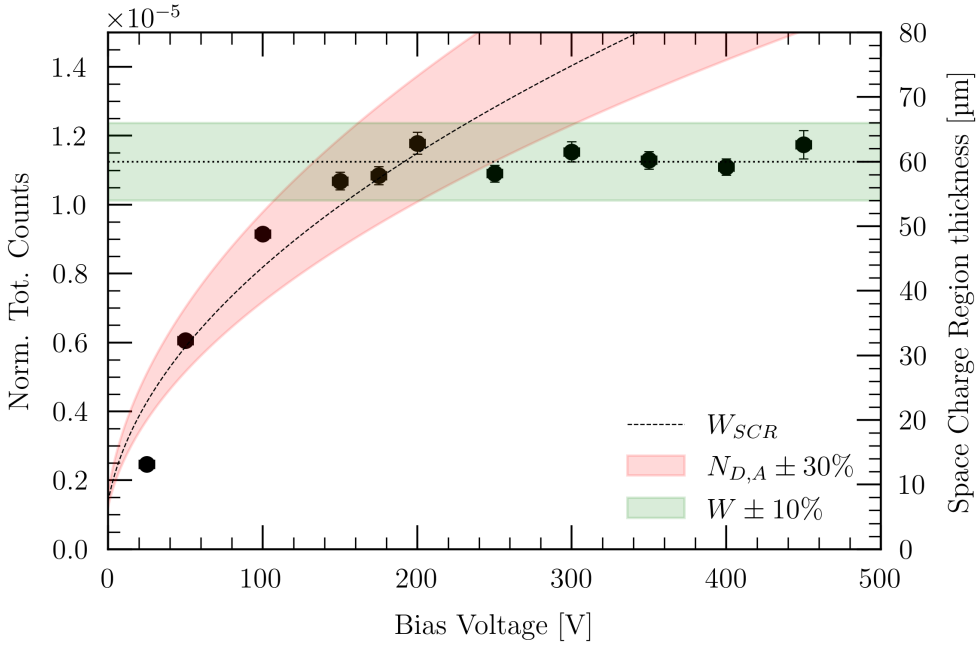

Fig. 6.24. Variation of the total counts number and of the SCR thickness as a function of the reverse bias voltage. The dashed curve represents the SCR thickness W_{SCR}, the filled red area represents the uncertainty on the SCR thickness, according to the uncertainties on the doping acceptation range $N_{D,A}$. The dotted line indicates the W_{SCR} value of 60 µm, and the green filled area represents the uncertainty on the total thickness of the sensor, according to the manufacturer specification for p-type and n-type layers.

Hence the full depletion voltage diode under study, is equal to 150 V since the counts number remains constant after this. The variation of the SCR thickness, represented with a dashed curve, is also well described analytically by the previous expression of W_{SCR} taking into account the uncertainties regarding the doping acception range $N_{D,A}$ of ±30% and the total thickness acceptation range of ±10% given by the constructor according to the manufacturer specification in Appendix C. Therefore, applying a bias voltage of 150 V is sufficient to fully deplete the 60 µm sensor and to collect the total amount of carriers generated by the $C(n,\alpha_0)Be^{(g.s)}$ reaction.

However, the saturation curve of Fig. 6.24 does not provide direct information on the charge carrier drift velocity behavior. Applying a bias voltage of 150 V, although sufficient to fully deplete the sensor, does not necessarily guarantee the maximum drift velocity of the charge carriers. The PSA performed, already used to select the events that deposit all of their energy and drift the longest distance in the sensor, is then used to study the rise time, amplitude and fall time, directly related to the charge carrier dynamics. With the rise time representing the duration it takes for all free charge carriers to move through the junction, and the fall time representing the longest drift time for a carrier to be collected by the electrode.

Hence, considering the average shape of the pulses of the peak of collected charge under study, Fig. 6.25 shows that the amplitude of the pulses increases with the bias voltage, while their duration decreases, even at a bias voltage of 150 V.

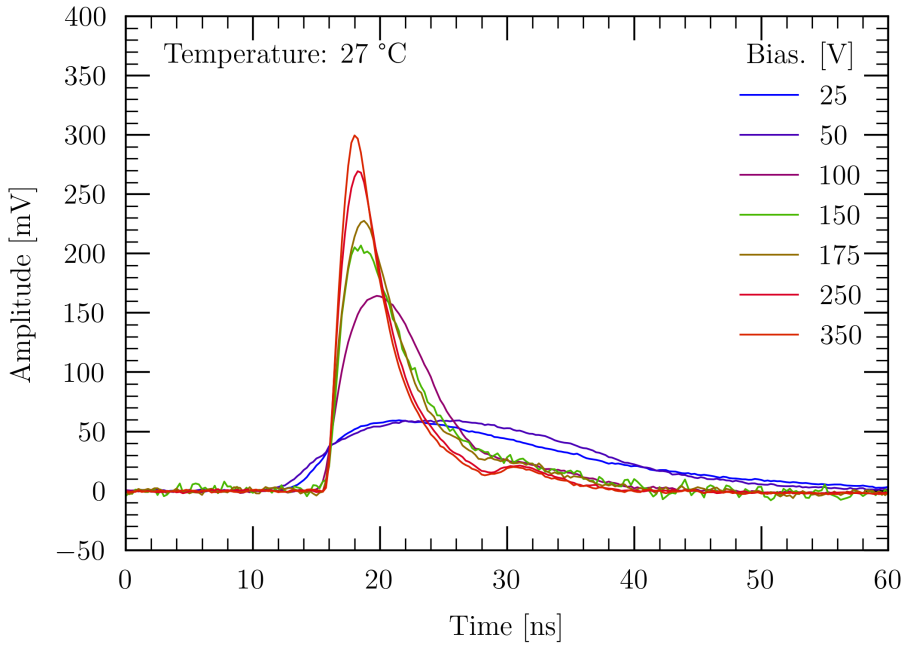

Fig. 6.25. Average SiC pulses shapes for events within the peak of collected charge under study, with charge carriers cloud drifting the longest distance in the sensor, as a function of negative bias voltages.

Since the rise time and fall time of the signal are shaped by time constants, in practice the study of the FWHM for these fast rising signals is more relevant. As explained previously, the charge carriers velocity drift v_{drift} is by definition increasing with the internal electric field for a given temperature. The carrier drift time t_{drift} in the detector volume is then reduced with increasing the bias voltage since the velocity drift can be expressed as:

$$\mu E = v_{drift} = \frac{d}{t_{drift}} \tag{6.17}$$

With d the drift distance between the location at the creation of the carrier and the collecting electrode, which is in our case lower or equal than the space charge region width.

Following the same reasoning as previously, the study of the position of the peak in the PHA spectrum associated mainly to the events of the $C(n,\alpha)$ reaction (according to Chapter 4), that deposit all of their energy and drift the longest distance in the sensor, is performed. Fig. 6.26 shows the bi-dimensional histogram of the pulse height amplitude as a function of the FWHM of the pulses, required to perform TCT analysis. The amplitude and FWHM of the pulses associated to the events under study are extracted and are shown in Fig. 6.27 as a function of the reverse bias voltage.

Hence, because the FWHM directly correlates with the drift time of the charge carriers, a decrease in FWHM with an increase in bias voltage is observed. Consequently, as previously observed, the collected charge associated with these events remains constant once a bias voltage of 50 V is applied. Therefore, an increase in the electric field value results in a corresponding increase in the induced current, in accordance with the Ohm law.

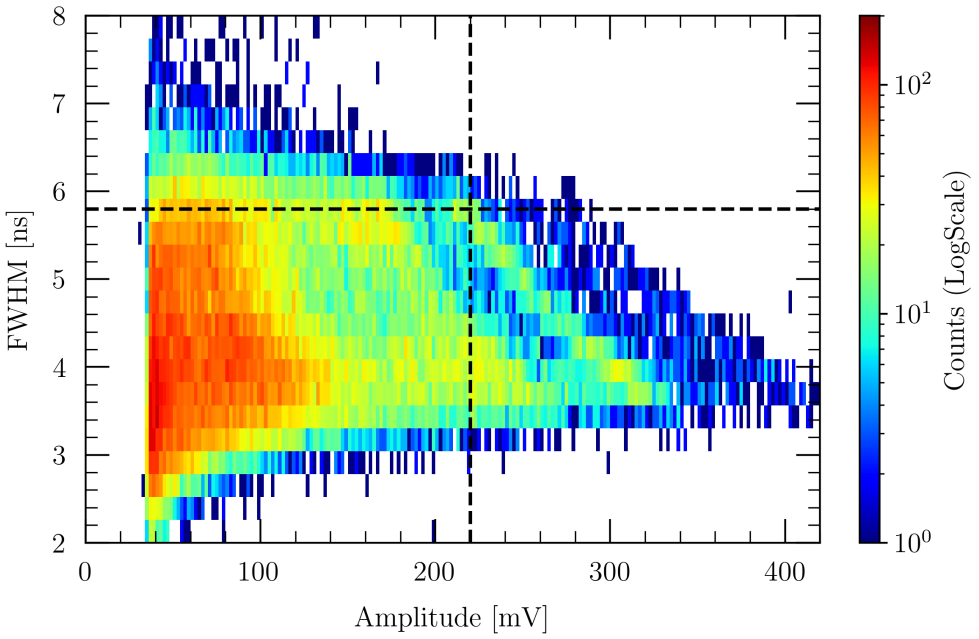

Fig. 6.26. Bi-dimensional histogram of the pulse height amplitude as a function of the FWHM of the pulses under −150 V reverse bias voltage. The dashed lines guide the eye to the $^{12}C(n,\alpha_0)Be^{(g.s)}$ events that deposit all of their energy and drift the longest distance in the sensor.

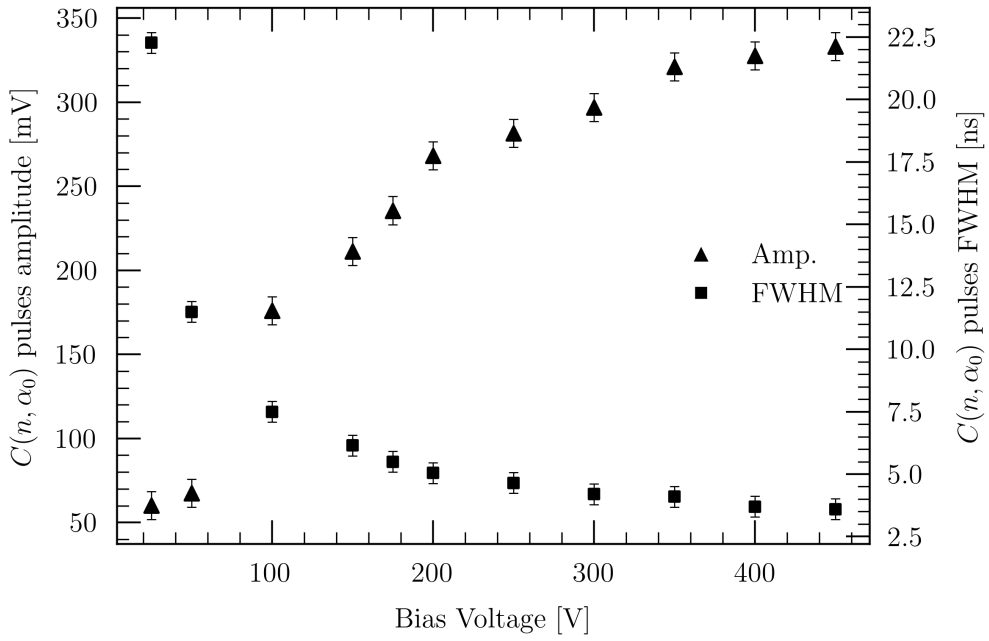

Fig. 6.27. Amplitude and FWHM of the pulses associated to the $^{12}C(n,\alpha_0)Be^{(g.s)}$ events under study, depicted in Fig. 6.26, as a function of the negative reverse bias voltage.

Then, taking into account the previous results, the relative variation of the pulses FWHM can be superposed to the velocity drift computed using the mobility defined previously. For the charge carriers from the $C(n,\alpha)$ events drifting on their maximum path to the electrode it can be observed in Fig. 6.28 that the velocity drift increases at low field strength. Then, for higher fields, the velocity drift tends towards a saturation value as expected in Section 6.1.3. The error bars are computed once again, taking into account the standard deviation of the Gaussian distribution of the amplitude and FWHM of the events associated to the peak of collected charge selected in Fig. 6.26.

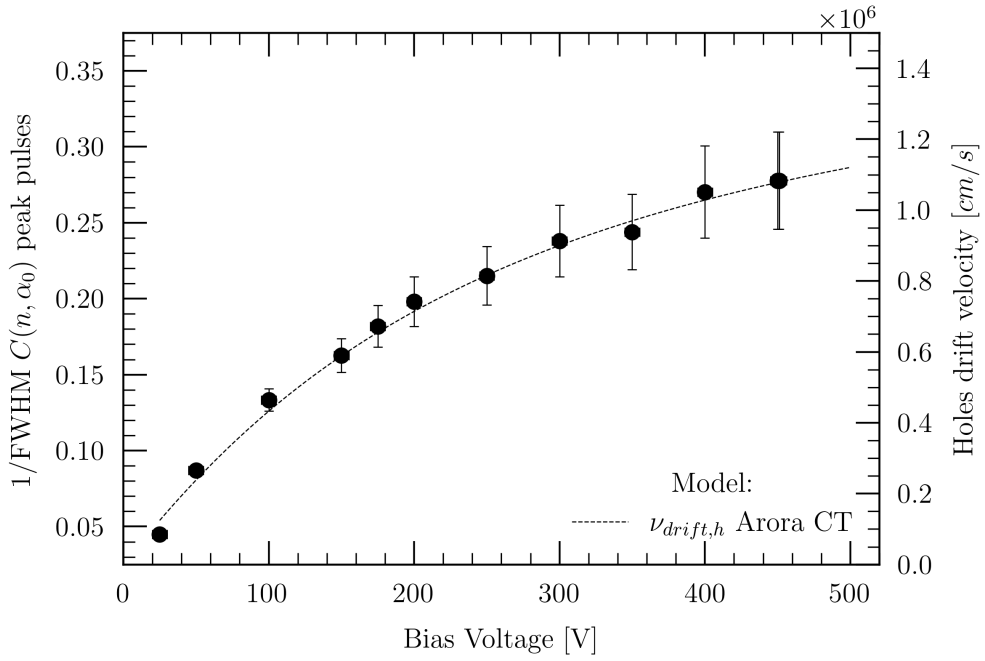

Fig. 6.28. Holes velocity drift of 60 µm thickness as a function of bias voltage.

This curve is fitted by the empirical Arora model [191] using Canali model [195] presented in Appendix F Section F.1, leading to the refined coefficients:

$$\nu_{sat,0} = 1 \cdot 10^6 \,\mathrm{cm\,s^{-1}}$$
$$\nu_{sat,exp} = 0.15$$

It can then provide the charge carrier mobility value at low field as well as the saturation velocity for holes such as:

$$\mu_{low} = 30.85 \,\mathrm{cm\,V^{-2}\,s^{-1}}$$
$$\nu_{sat} = 1.58 \cdot 10^6 \,\mathrm{cm\,s^{-1}}$$

The study of the $C(n,\alpha)$ charge cloud transit time has provided a direct measurement of the average drift velocity as a function of the applied electric field at room temperature. In the following results, the first comparison of the collected charge distributions and count rate as a function of the temperature is performed before investigating the effects of variations in the electric field.

6.4.2.2. Increasing temperature - Overall view of the results

According to the previous experimental protocol, raw pulse waveforms are acquired for each two minutes acquisition slot, in order to have a sufficient statistics. Then, as presented in Section 6.4.2.1, the events are selected according to the charge deposited and the FWHM of the pulses so that the charge carriers drift the longest distance in the sensor. It can be distinctly observed in Fig. 6.29 that the pulses shapes are as expected dependent on the temperature. The following section presents a quantitative analysis of the effects observed on the FWHM and amplitude with increasing temperature.

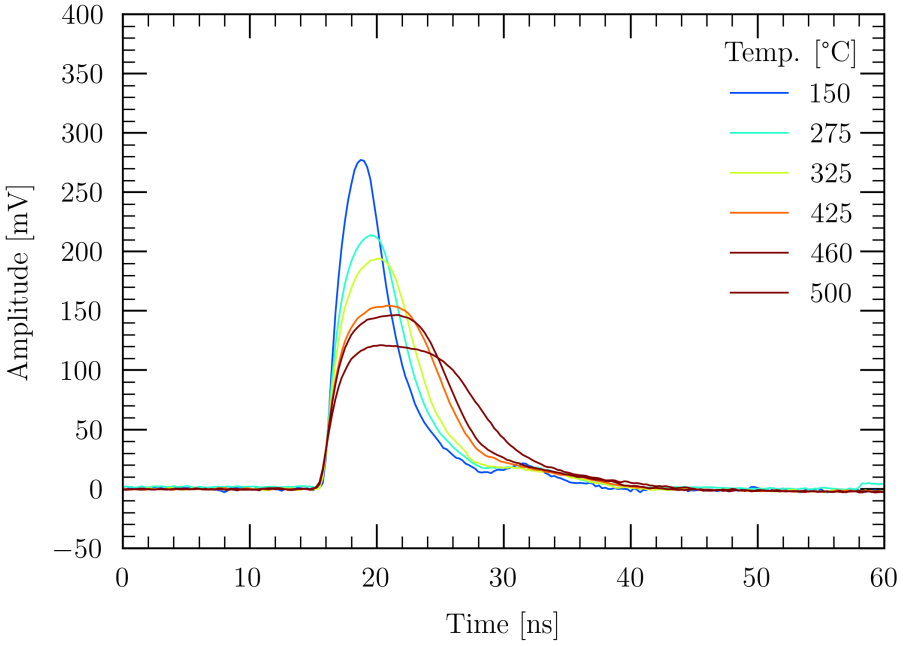

Fig. 6.29. Average SiC pulses shapes for events within the peak of collected charge under study, with charge carriers cloud drifting the longest distance in the sensor, as a function of temperature.

Taking into account all the interactions within the sensor, it can be observed with Fig. 6.30, a decrease of the pulses amplitude distribution toward lower values with increasing temperature. However, according to Fig. 6.31, the position of the peak under study in the distribution of the pulse charge does not fall with increasing temperature, and is even subject to a slight increase which is explained in the following. This is the first significant result regarding the stability of the detector performances. In addition, the decrease in the pulses amplitude with increasing temperature while maintaining a constant collected charge must be correlated with an increase of the FWHM which constitutes the first hypothesis that must be verified and discussed.

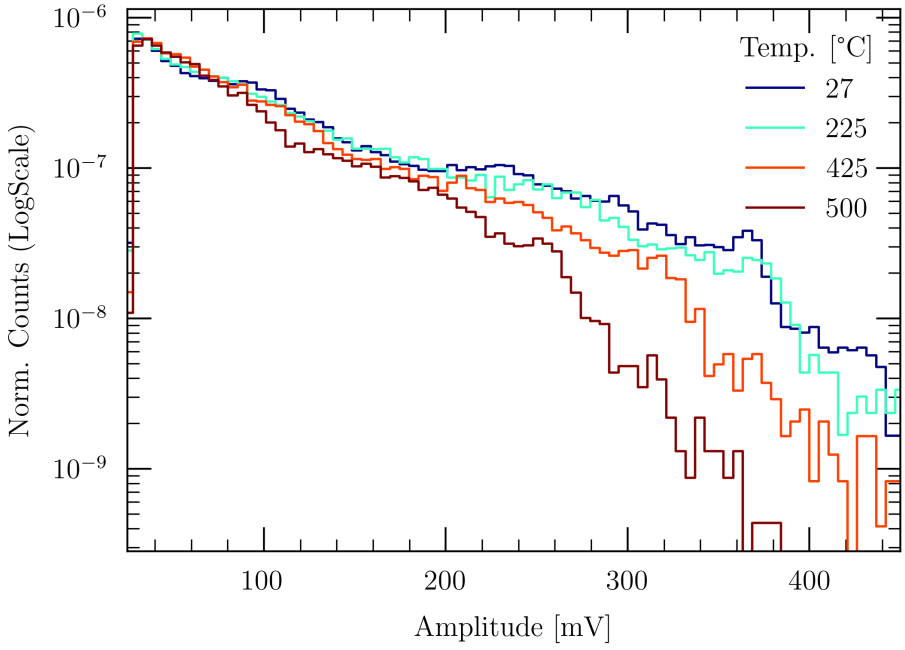

Fig. 6.30. Amplitude distribution of current pulses as a function of temperature based on 2 minutes acquisitions, with a bias voltage of −300 V.

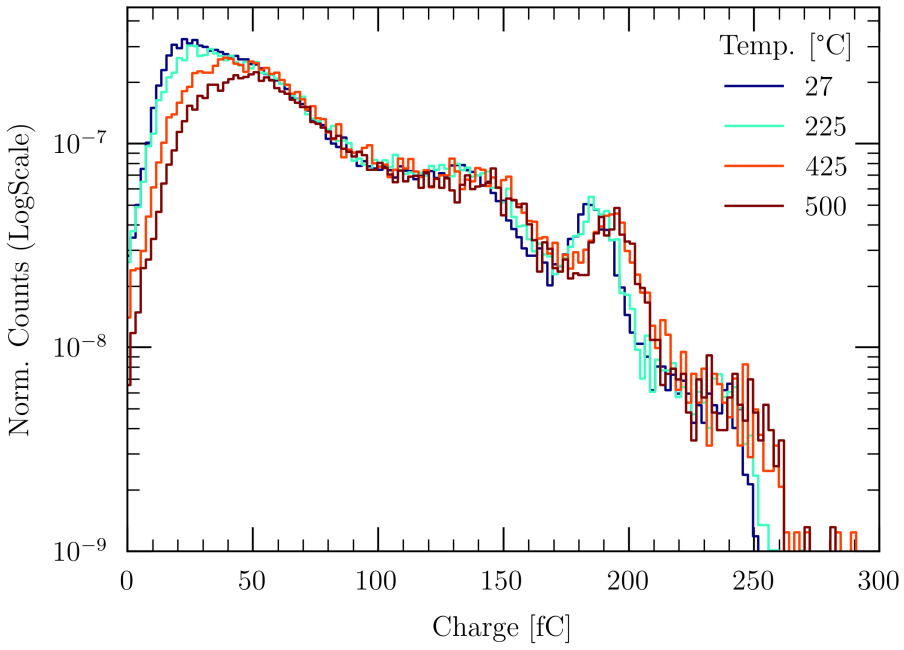

Fig. 6.31. Charge distribution of current pulses as a function of temperature based on 2 minutes acquisitions, with a bias voltage of −300 V.

6.4.2.3. Count rate study

In addition to the constant CCE displayed previously with the peak associated to the $^{12}C(n,\alpha_0)^9Be^{(g.s)}$ reaction, the variation in the count rate as a function of the temperature and bias voltage is studied. The count rate is normalized in the following to the neutron source beam intensity. Due to the specification of the neutron generator presented in Chapter 4 Section 4.3.1, the neutron source can experiment a variation of the intensity during an experiment day. Moreover, the uncertainties of the neutron source beam have to be taken into account on each segment of two minutes acquisition. Thus 1 σ standard deviation is considered for the neutron beam intensity during the acquisition time in order to normalized the count rate to the neutron source.

Regarding the total counts number above the threshold, Fig. 6.32 shows a slight decrease of the order of 21 % from 27 °C to 500 °C. The p-value lower than 0.05 rejects the null hypothesis and leads to the conclusion that the total counts number is decreasing with increasing temperature.

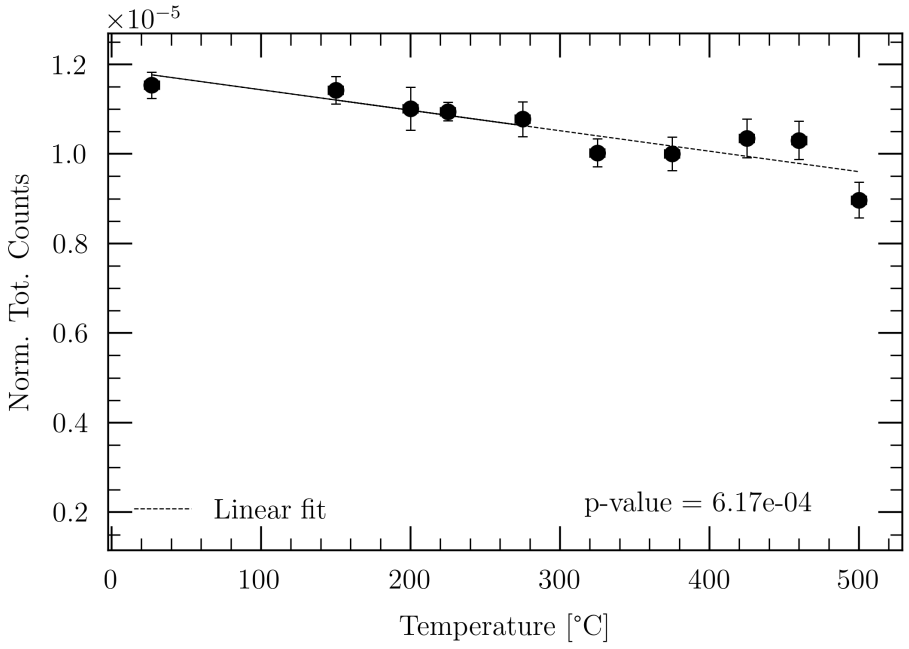

Fig. 6.32. Total count number normalized with the neutron intensity.

At the same time, the number of counts within the peak associated to the $^{12}C(n,\alpha_0)^9Be^{(g.s)}$ reaction is also considered, as represented in Fig. 6.33. The p-value is also computed to test the null hypothesis that the slope is zero. With respect to the error bar, the p-value higher than 0.05 does not reject the null hypothesis and hence does not lead to the conclusion that the number of counts within the peak is decreasing. Thus, it can be said that within the null-hypothesis, the number of counts remains constant, within the uncertainty of the neutron source beam intensity, from 27 °C to 500 °C.

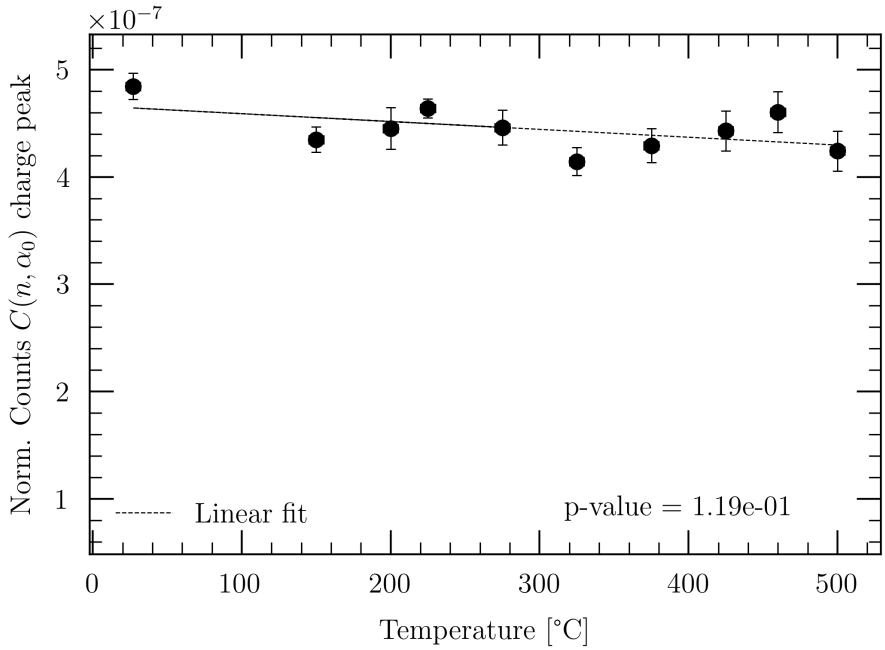

Fig. 6.33. Counts number of the charge distribution peak normalized with the neutron intensity.

Concerning the decrease in total count number, it has been previously introduced with the overall view of the results the general effect of increasing the temperature on the shape of the pulses. Indeed, a decrease in amplitude is observed without experiencing a decrease in the charge collected. Hence a flattening of the signals is observed which as a result, is responsible for the loss of the pulses of lower amplitude because of the amplitude threshold of the acquisition set up. The following effect of temperature on the shape of the signal is discussed in detail and quantified in the following section.

6.4.2.4. Pulse Shape Analysis as a function of the temperature

The flattening of the signal is now studied in detail, performing a dedicated PSA for the pulses associated to the $C(n,\alpha)$ events that deposit all of their energy, as a function of temperature for a given polarisation. Firstly, regarding the CCE, it can be noticed that the position of the centroid peak around 185 fC in the charge distribution does not fall and presents a slight increase of few femtocoulomb in the position of the peak, with increasing temperature as explicitly seen in Fig. 6.34, and previously observed in Fig. 6.31,

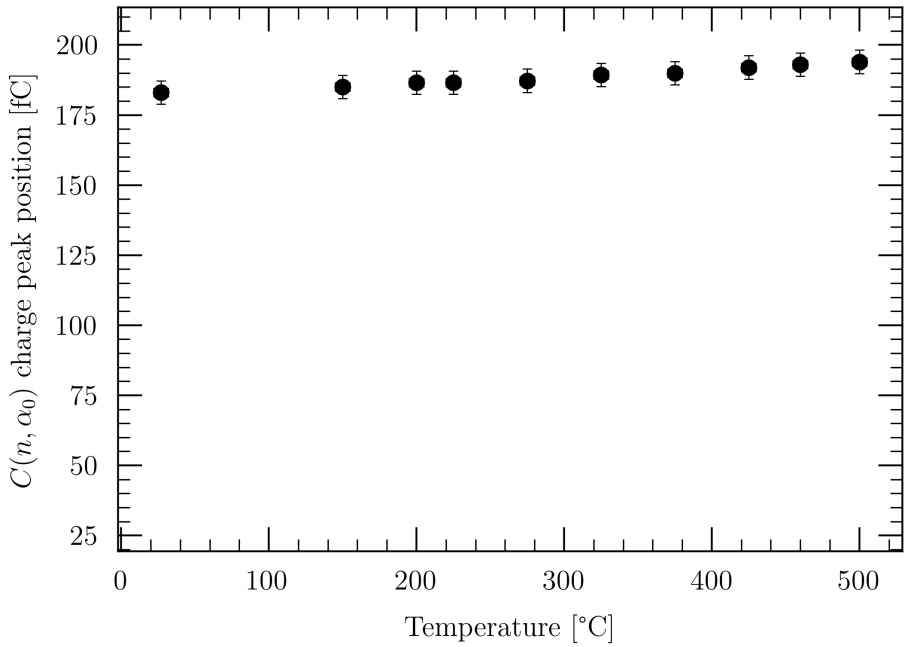

Fig. 6.34. Position of the peak associated with the $^{12}C(n,\alpha_0)^9Be^{(g.s)}$ events in the charge distribution as a function of temperature.

The latter is related to the variation of the mean ionization energy for electron-hole pair generation with increasing temperature. To comprehend this temperature dependence, the Klein model should be introduced [207]. In accordance with theoretical models of pair production, the radiation ionization energy E_W is correlated to the band gap energy E_{gap} such that:

$$E_W = E_{gap} + E_{ph.} + E_{th.} \tag{6.18}$$

With $E_{ph.}$ the reflective phonon loss, and $E_{th.}$ the thermalization losses.

Initially, the release of kinetic energy into the system leads to an irregular distribution of mobile carriers by prompting transitions from the VB to the CB. This initial phase occurs rapidly, in the order of 10 ps, with potential competition between impact ionization and phonon generation. The second phase involves the transfer of excess kinetic energy to the crystal lattice, requiring a significantly longer time. The term representing phonon loss is derived from the observation that charge carriers, which can influence the behavior of phonons, are associated with optical modes and can emit Raman phonons. Thermalization losses arise because the deposition of radiation energy results in the production of electrons and holes that cannot induce further ionization. Consequently, these carriers are bound to convert their remaining energy into lattice vibrations.

The decrease of the band gap energy with temperature has been previously described in Section 6.1.1. Therefore, the mean ionization energy for electron-hole pair generation follows the same trend as the band gap energy with temperature, as illustrated in Fig. 6.35, with a decrease of the order of 0.4 eV from 27 °C to 500 °C.

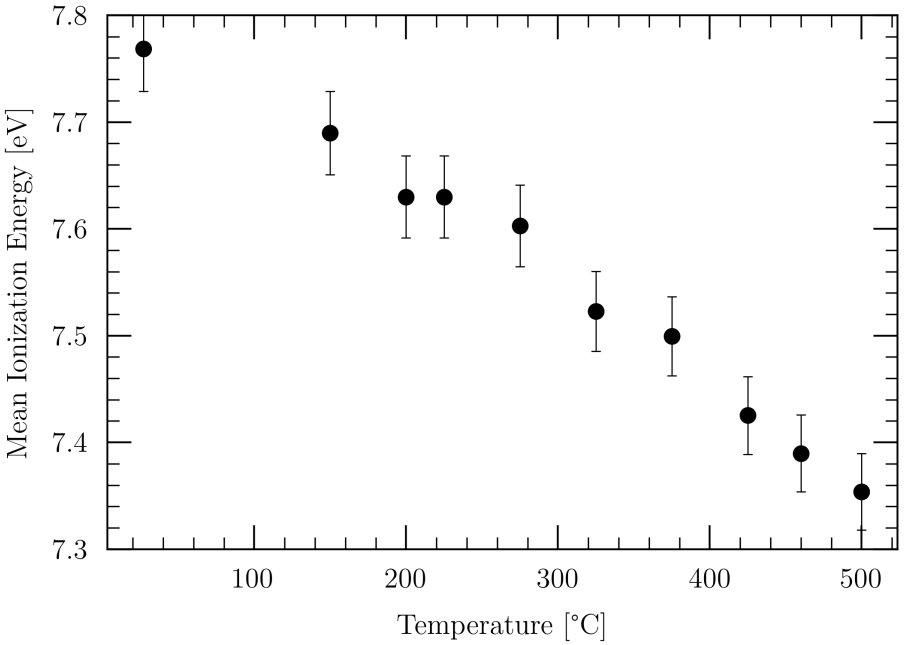

Fig. 6.35. Mean ionization energy as a function of temperature. These experimental points have been computed using the given energy deposition by the $C(n,\alpha_0)$ events and the associated collected charge displayed in Fig. 6.34.

Hence, the decrease in the mean ionization energy leads to an increase in the number of charge carriers for a given energy deposition, which leads to a slight increase in the ${}^{12}C(n,\alpha_0){}^{9}Be^{(g.s)}$ peak position within the charge distribution of current pulses, as noticed in Fig. 6.34. The FWHM of the pulses associated to the ${}^{12}C(n,\alpha_0){}^{9}Be^{(g.s)}$ events, that deposit all of their energy and drift the longest distance in the sensor, increases as a function of temperature as seen in Fig. 6.36.

Indeed, the FWHM is proportional to the charge carrier drift time. Therefore, increasing the temperature reduces mobility and drift velocity, leading to longer pulse duration and an increase in the FWHM. As previously explained, the reduction in amplitude observed in Fig. 6.37 is due to decreased mobility, which lowers both drift velocity and electrical conductivity.

The decrease in pulse amplitude with increasing temperature can be understood through Ohm's law, indicating that the current of charge carriers within the sensor is influenced by the strength of the electric field and the electrical conductivity of the material, which is highly sensitive to temperature changes.

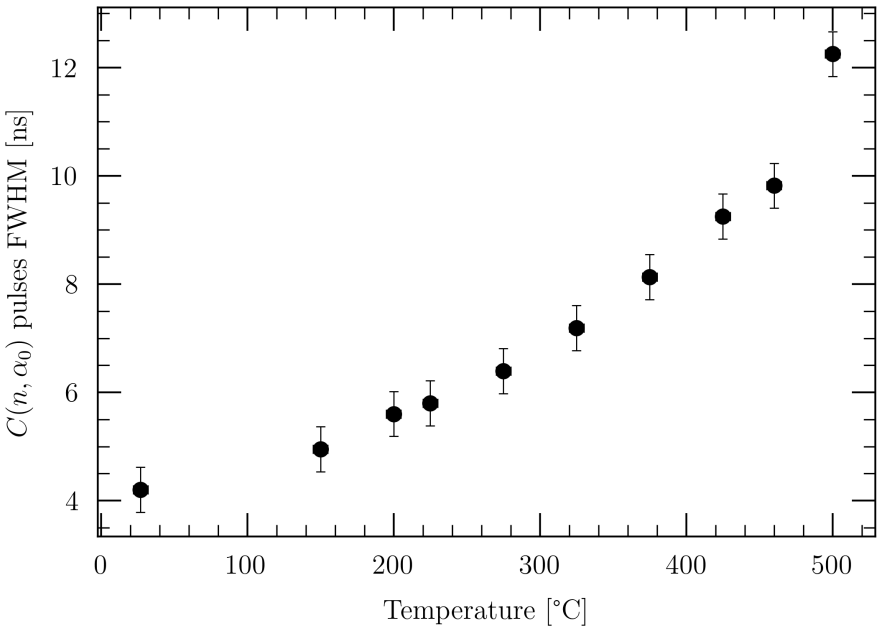

Fig. 6.36. FWHM of the pulses associated to the $^{12}C(n,\alpha_0)^9Be^{(g.s)}$ events under study as a function of temperature.

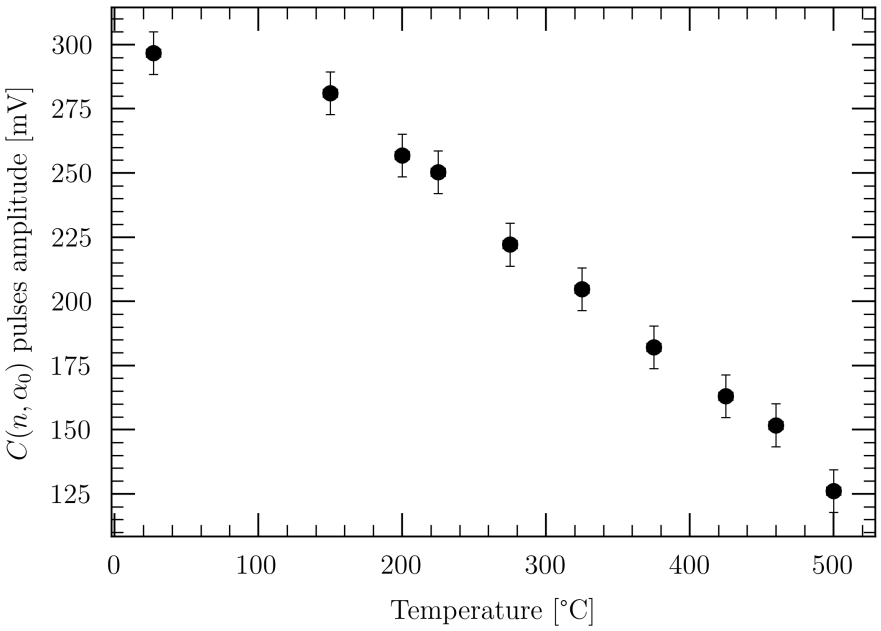

Fig. 6.37. Amplitude of the pulses associated to the $^{12}C(n,\alpha_0)^9Be^{(g.s)}$ events under study as a function of temperature.

6.5. Evaluation of the model for the charge carrier collection

The previous experimental results led to the quantification of the effects of temperature on the drift velocity of charge carriers in SiC. Hence, before going further in the use of the numerical results provided by the TCAD simulations presented in Section 6.2, it is necessary to adjust and validate the models used to describe the charge carrier mobility in SiC.

6.5.1. Charge carrier dynamics and Temperature

6.5.1.1. Full Width at Half Maximum Study

In the conducted study, calibration coefficients for SiC and diamond were suggested, utilizing empirical models to ascertain saturation drift velocities. Consequently, the Arora model was recommended for integration into TCAD simulations due to its applicability in scenarios involving high temperatures and high doping concentrations. This model effectively merges lattice and ionized impurity scattering mobilities to calculate mobility values across a broad spectrum of doping concentrations and temperature ranges.

The calibrated values for the samples yield a dependable prediction of drift velocity under the operational conditions of the detector. Notably, drift velocity is observed to approach a saturation point with increasing temperature, as illustrated in Fig. 6.38. This behavior aligns well with the predictions of the Canali model, which accurately describes mobility under high field conditions in accordance with experimental data. Additionally, the Arora model effectively catches the influence of temperature on drift velocity variations, as demonstrated in Fig. 6.39. It is important to note that, regardless of the electric field strength induced by the applied bias voltage, a decrease in drift velocity is typically observed in semiconductor materials. This reduction is mainly attributed to scattering processes involving optical phonons, with the degree of velocity decrease being influenced by factors such as the energy of optical phonons, charge carrier density, and the relative trapping durations for electrons and holes.

Therefore, the experimental data describing both the low field mobility and the high field velocity saturation are used to adjust coefficients within the Canali model framework.

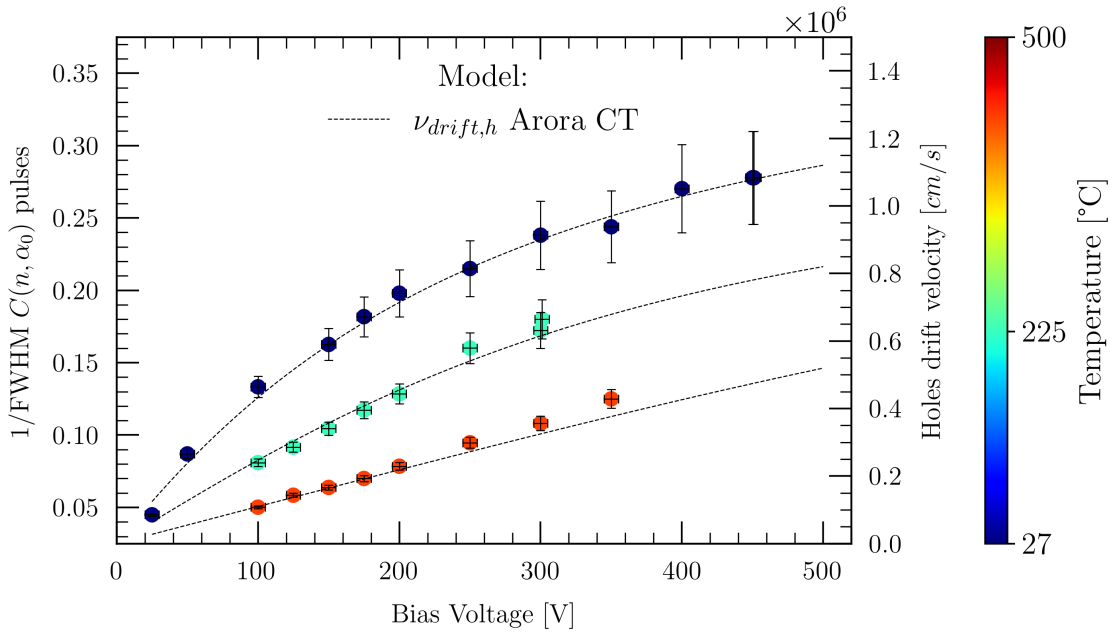

Fig. 6.38. Holes drift velocity as a function of the bias voltage in 60 µm SiC sensor. The color bar indicates the device temperature associated to each data series. The dashed curve represents the semi-empirical model.

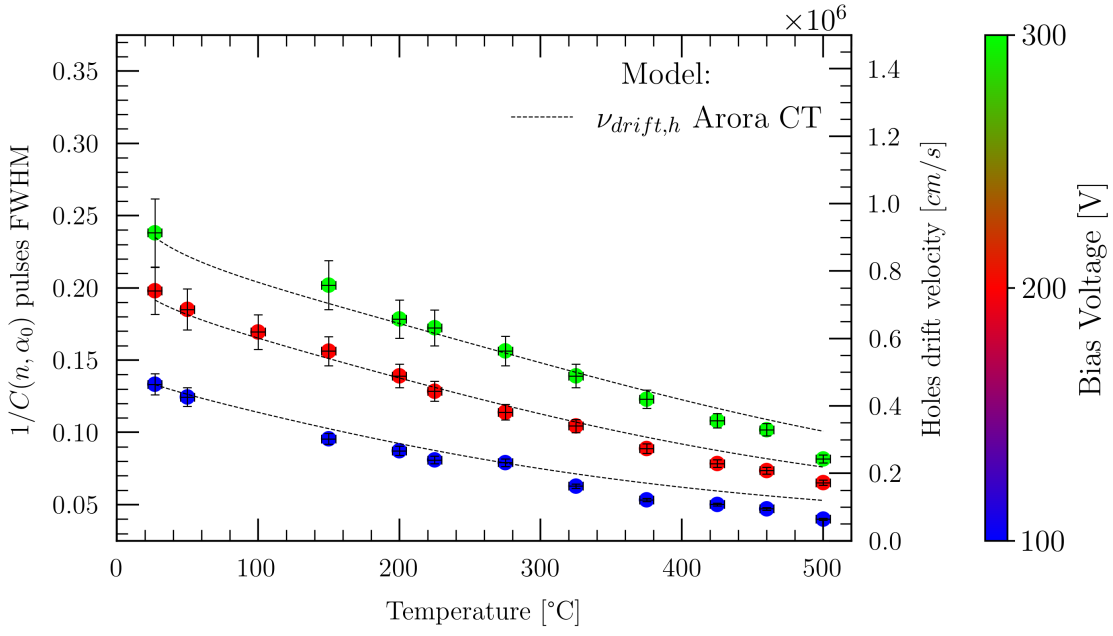

Fig. 6.39. Holes drift velocity as a function of the temperature in 60 µm SiC sensor. The color bar indicates the given applied voltage associated to each data series. The dashed curve represents the semi-empirical model.

6.5.1.2. Mobility models comparison

Arora model represents the scattering effects from impurities and phonons with increasing temperature in an interestingly accuracy within the errors bars. The discrepancies observed could be resolved using a more complete model. For instance, in Section 6.1.3, the Philips Unified Mobility model, was presented as a model offering a complete description of the scattering mechanisms as well as carriers/carriers scatterings. However this model is actually not referenced in 4H–SiC literature. But further investigations could lead to adjusted coefficients to propose an integration of this model within TCAD programs, allowing hence to reduce the discrepancies at high temperatures. This point is not addressed in this study but could be a perspective for future work.

6.5.2. TCAD results

Once the empirical models coefficients have been adjusted with the experimental data, which led to the values presented in Table 6.7, a dedicated modeling scheme is used to simulate the charge carrier collection within the sensor as a function of the temperature.

Parameter	Value
$\nu_{sat,0}$ [cm$\cdot$s^{-1}]	$1\cdot10^{6}$
$\nu_{sat,exp}$	0.15
μ_{low} [cm$^{2}\cdot$V$^{-1}\cdot$s^{-1}]	30.85
ν_{sat} [cm$\cdot$s^{-1}]	$1.58\cdot10^{6}$

Table 6.7. Canali empirical model coefficients adjusted with experimental data.

With the considerations of the application case presented in Section 6.3, the TCAD Synopsys program was used to simulate as a function of the temperature, the charge carrier collection created by a 5 MeV alpha particle generated at 35 µm from the top of the junction. The simulated current pulse are depicted in Fig. 6.40. The additional peak caused by the short drift of the carriers close to the collection electrode is noticeable and has already been discussed. The FWHM of the pulses is then computed and compared to the drift velocity model implemented in the TCAD program. The results are presented in Fig. 6.41. The comparison of the inverse of the FWHM of the pulses with the drift velocity shows a good agreement within the error bars of the model estimated at 10%[2]. Therefore, TCAD simulations provide a promising depiction of the collection process of charge carriers within the sensor, enabling the interpretation of experimental outcomes beyond the scope of available measurement data. In addition, TCAD software is capable of delivering an in-depth analysis of charge carrier dynamics, detailing their collection over time and across different sensor locations which is crucial for understanding the response of the sensor to ionizing radiation, and future optimization of the device design and performance.

[2] *The uncertainty in the FWHM computation is estimated at* 10%*, due to factors like numerical precision, mesh size, and time step in the simulation.*

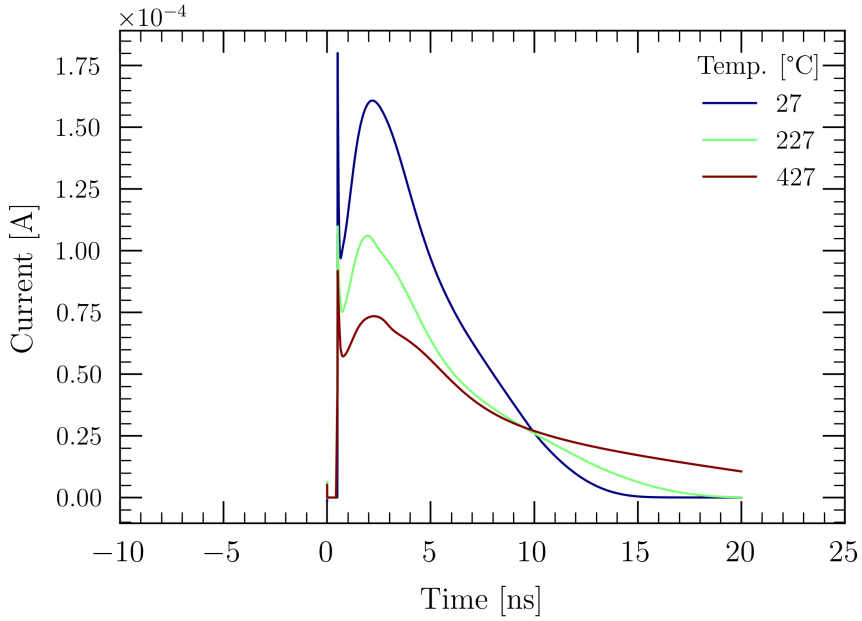

Fig. 6.40. Simulated current pulse for a 5 MeV alpha particle as a function of the temperature in 60 µm SiC sensor. The additional peak is caused by the short drift of the carriers close to the collection electrode.

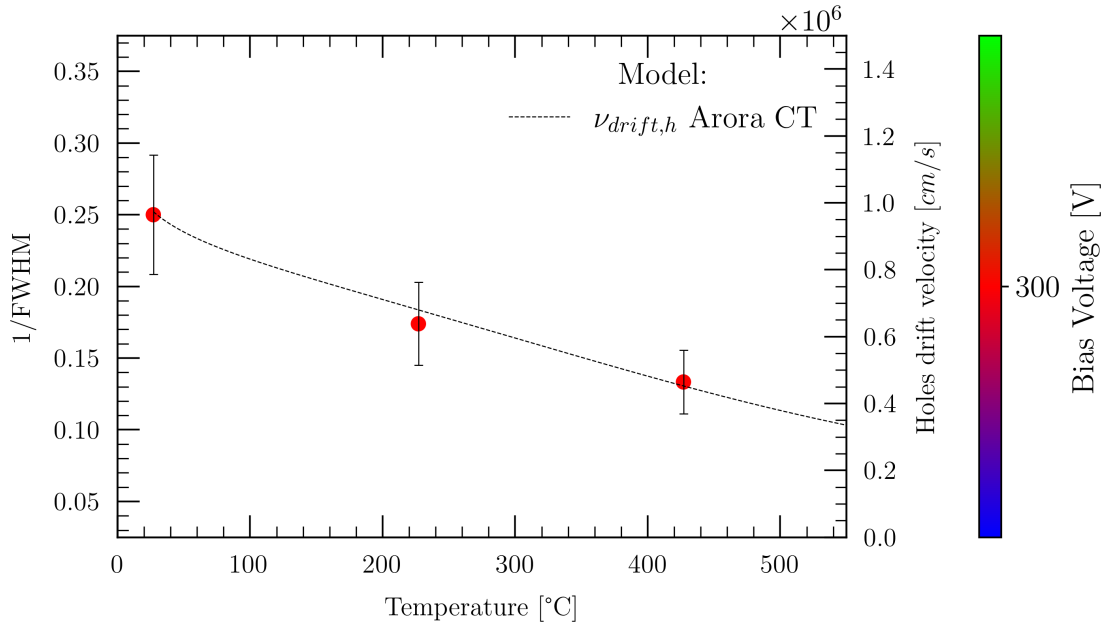

Fig. 6.41. Holes drift velocity as a function of the temperature in 60 µm SiC sensor. The data are computed from the simulated current pulses of Fig. 6.40, and the dashed curve represents the semi-empirical model studied for the drift velocity.

6.6. Perspectives

To provide a comprehensive modeling scheme as a detailed and powerful tool for design optimization and interpretation of current pulse measurements, from the device description in a neutron field to the charge carrier collection leading to current pulse formation, a coupling of the presented GEANT4 model with the TCAD Synopsys program is proposed.

The following workflow diagram described in Fig. 6.42 provides an overview of the modeling schemes coupling which takes into considerations inputs and outputs of device simulations.

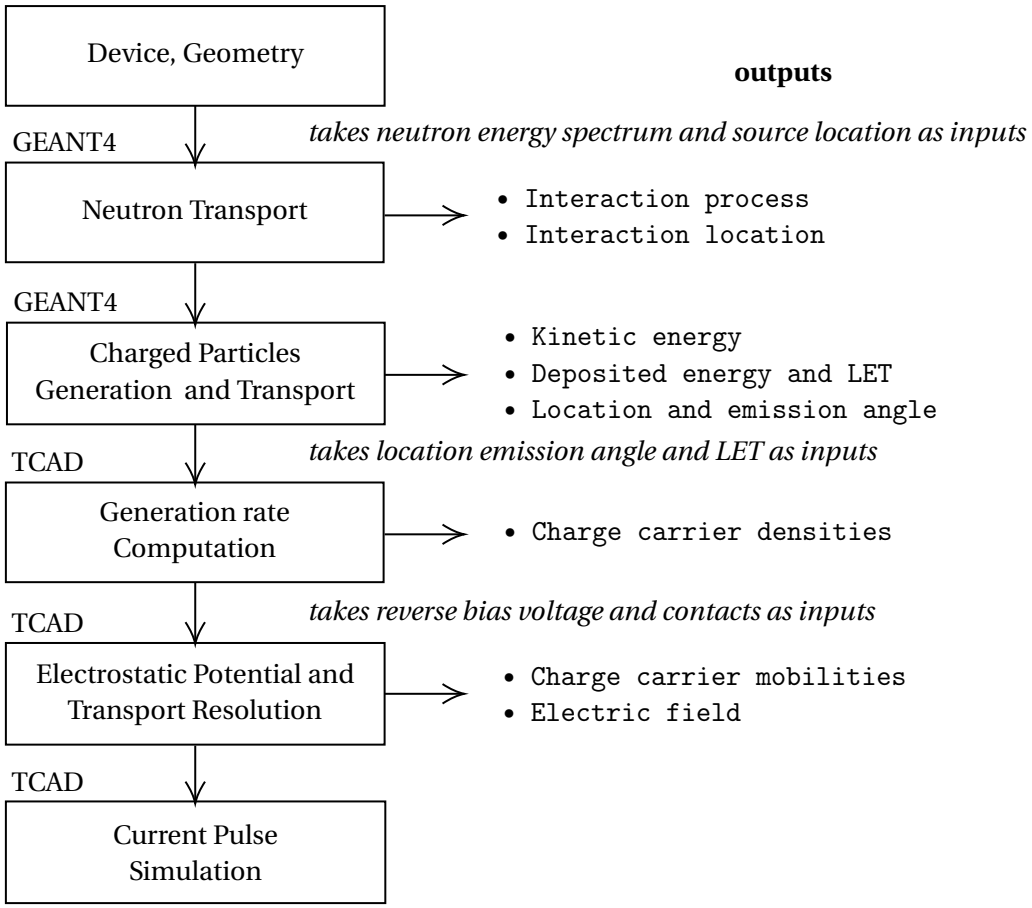

Fig. 6.42. Workflow diagram of the coupling of modeling schemes for the generation of charged particles and charge carriers in solid state sensors .

Promising results were achieved with the simulation of the sensor in a neutron field. The GEANT4 modeling scheme presented in Chapter 4 was used to compute the deposited energy within the sensor for each event, i.e., each impinging neutron. Consequently, the location of the produced charged particles and their kinetic energy were obtained as simulation outputs. With the kinetic energy, location, emission angle, and LET of the charged particles known, the TCAD Synopsys program was employed to model the charge carrier collection, leading to the simulation of current pulses.

Conclusion

Regarding the charge collection dynamics with increasing temperature, numerous experimental works examining the mobility of charge carrier within SiC material are published. Hence, the mobility degradation with increasing temperature had already been well described in terms of charge carriers scattering. However, empirical models calibrated coefficients used to describe this temperature effect with regard to the dependence of the mobility with carrier concentration and doping concentration are infrequent in comparison to the commonly used silicon models. To proceed with the numerical simulation of charge carrier collection, the empirical model coefficients were adjusted to achieve reliable simulation results using the device structure under study in the temperature range of interest up to 500 °C.

Finally, the objectives regarding this temperature effect study were reached. Firstly the demonstration of the stability of the detection performances of the SiC in the temperature range of interest in comparison to diamond sensor. Secondly, PSA performed with increasing temperature was presented to described the effect of the mobility degradation on the charge carrier velocity drift.

Such conclusions open the door to promising future studies regarding the issue of fast neutron sensors integration for high temperature environment presented in the first Part of this manuscript. In addition, the use of the results of the second Part of this work, regarding the neutron interaction description, and charge deposition within the sensor suggest an interesting approach that could be developed regarding chaining both modeling scheme from GEANT4 and TCAD programs. Therefore, it could open another door to the experimental current pulse interpretation for particles identification, discrimination and hence fast neutron fluence rate estimation using machine learning with current pulses of various shapes especially in high temperature environment.

7. Study of the effects of defects on measurements

In this chapter, the study of the effects of defects on measurements is presented. The comprehension of such effects is crucial for the understanding of the sensor response to neutron field representative of the fusion and fission reactor environment.

This chapter is divided into several sections. First the study of the analytical model of defect creation is presented. Then the application of component simulation to study the mechanisms induced by defects activation is discussed. Finally, as certain inherent effects on semiconductor materials, like charge carrier trapping, still need to be validated under real experimental conditions, the results of experiments on neutron-induced defects and thermally activated defects are presented. The later results are based on the experimental campaigns performed at the GENESIS and NFS facilities. Therefore, by providing new insights into the effects of defects on the sensor response, this chapter aims to identify the limitations of the sensor response to neutron irradiation regarding the specific environment of fusion and fission reactors.

7.1. Study of the analytical model of defect creation

In Chapter 3, the various types of native and induced defects were presented, in Section 3.1, and their effects on the CCE, in Section 3.2, caused by trapping and recombination phenomena. Most primary defects can recombine and disappear, while others form deep levels in the energy band gap. These defects can remain isolated as point defects such as vacancies and interstitials or bind to each other forming Frenkel pairs or to impurities, forming aggregates. Defects add levels to the energy band gap are generally classified into two categories based on their position, deep defects and superficial defects. as presented in Fig. 7.1.

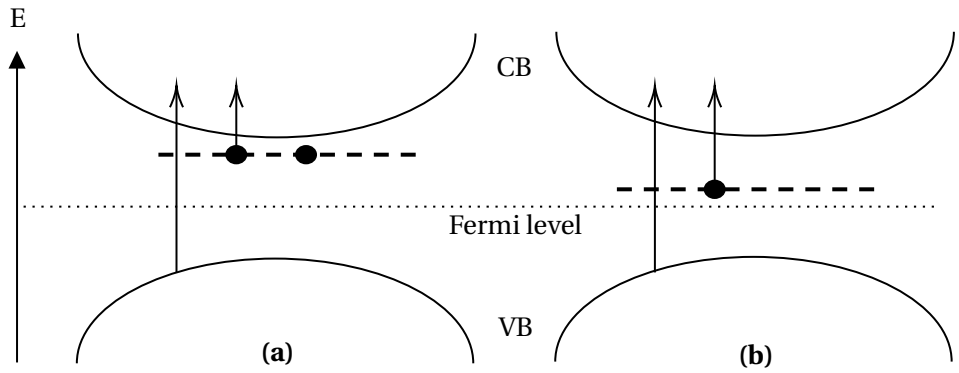

Fig. 7.1. Scheme of the band diagram of a semiconductor. The dotted line represents the Fermi level, and the dashed lines the trap levels, positioned according to their energy level, for (a) shallow and (b) deep traps.

Superficial defects, also called shallow defects, are located near the VB or CB, of the order of 0.1 eV from the band edges, while deep defects are located in the middle of the band gap, of the order of 1 eV from the band edges. While superficial defects might only affect the surface properties by introducing minor perturbations, deep defects can have a significant impact on

the sensor response by trapping charge carriers and reducing the CCE. The following sections focus on the effects of deep defects on the sensor response to neutron irradiation.

7.1.1. Neutron induced defects

Despite being the main way that charged particles transfer energy, ionizing energy loss has a minimal impact on radiation damage in silicon or diamond detectors. Instead, radiation damage is primarily caused by Non Ionizing Energy Loss (NIEL), which results from nuclear interactions leading to lattice defects. When neutrons interact with the atoms of the semiconductor, they create recoils that can displace atoms from their lattice sites if the energy transferred to the initially displaced atom exceeds the displacement threshold energy. This process can continue, resulting in a cascade of displacements and forming a region with a high concentration of defects. Hence, this NIEL creates vacancies, interstitials and other defects in the crystal structure which lead to an adjustment of surrounding atoms, creating localized electronic states in the band gap as described in Fig. 7.1.

The presence of these deep levels can have a significant impact on the performance of the sensor. When charge carriers are trapped in these localized electronic states, they are no longer able to contribute to the electrical output of the device. In addition, NIEL induced defects often have deeper energy levels within the band-gap of the semiconductor material, making it more difficult for the trapped charge carriers to escape. As a result, the sensor becomes unsuitable for online measurement in steady-state conditions within harsh environments.

7.1.2. Thermally activated defects

At high temperature, lattice vibrations become more pronounced allowing defects such as vacancies and interstitials to migrate and form complex configuration including deep level traps. While at room temperature charge carriers can move freely between the valence band and conduction band, at high temperatures, thermal energy can activate deep level defects creating traps for the charge carriers. This activation occurs because the increased thermal energy allows electrons to overcome the energy barrier, required to occupy these deep level states, effectively trapping them between the VB and CB.

While the effects of increasing temperature on the carriers mobility and intrinsic semiconductors properties were previously introduced in Chapter 6. The impact of rising temperature on carrier lifetime, relative to transit time, must be discussed, particularly concerning recombination and trapping issues. In Chapter 3, Section 3.2.1.2, the analytical model of charge carrier lifetime reduction was presented which led to first conclusions related to recombination and charge carriers trapping on CCE. The capture time constant, which determines the time it takes for a trap to capture a charge carrier, is defined by the simplified equation governing the carrier lifetime as follows:

$$\tau_c = \frac{1}{N_t \sigma_h \langle \nu_h \rangle} \tag{7.1}$$

With N_t the trap density, σ_h the capture cross-section and $\langle \nu_h \rangle$ the thermal velocity for holes. This capture time constant is inherently linked to the charge carrier lifetime.

Indeed, for a given trap type, increasing the density of traps will decrease the capture time constant, leading to a decrease in the charge carrier lifetime. Hence, based on the dynamics of charge carrier collection, a charge carrier lifetime shorter than the transit time results in a reduced CCE. This reduction in CCE is a primary issue affecting sensor performance, leading to a lower signal amplitude, which in turn diminishes both the signal-to-noise ratio and the detection efficiency.

7.2. Application of finite element simulation to study defect activation mechanisms

In order to study the effects of defects on the sensor response, the TCAD simulation software is used to model the trapping of charge carriers by deep level traps. While the description of the trapping process is based on theoretical considerations, the practical applicability involves empirical parameters such as the defect energy levels, or capture cross-section that need to be determined experimentally. In addition, with regard to our study, the temperature dependence of such models has to be presented in order to provide a dedicated modeling scheme for the sensor response. Finally, by comparing simulation results with experimental data, the model can be evaluated and the effects of defects on sensor response can be quantified, leading to a better understanding of material quality in order to improve sensor performance.

7.2.1. Recombining and trapping

7.2.1.1. Recombination processes

Direct recombination of electron-hole pairs is not typically considered in SiC due to its indirect band gap nature. In SiC, the CB minimum and VB maximum are at different points in the Brillouin zone [208], requiring phonons to conserve momentum during recombination. This makes direct recombination, which involves simultaneous changes in energy and momentum, less probable.

Regarding the indirect recombination process, it happens through intermediate energy level called trapping center, present within the band gap as explained previously. Two types of centers are distinguished:

- If a defect that has captured an electron is more likely to capture a hole than to re-emit the electron back to the CB, it captures the hole and thus causes the recombination of the electron-hole pair. This center is called a recombination center.
- Conversely, if the defect that has captured an electron is more likely to re-emit the electron back to the CB than to capture a hole, it has solely temporarily trapped an electron. This center is called a trapping center.

Trapping centers play an important role in the current within the semiconductor as they temporarily reduce the density of free carriers but do not play a specific role in carrier recombination. The calculation of the recombination rate associated with these centers is described by Shockley Read Hall (SRH) theory [209], defined such that:

$$R_{net}^{SRH} = \frac{np - n_{i,eff}^2}{\tau_p(n + n_t) + \tau_n(p + p_t)} \tag{7.2}$$

With p and n the hole and electron concentrations, $n_{i,eff}$ the effective intrinsic carrier concentration, τ_p and τ_n the hole and electron lifetimes, and n_t and p_t the hole and electron densities when the quasi-Fermi[1] levels aligns with the defect level E_t, making the recombination rate maximum. It is defined such that:

$$\begin{cases} n_t = n_{i,eff} exp\left(\dfrac{E_t}{kT}\right) \\ p_t = n_{i,eff} exp\left(\dfrac{-E_t}{kT}\right) \end{cases} \tag{7.3}$$

[1] *The quasi-Fermi level is the Fermi level for electrons and holes in a non-equilibrium state.*

With E_t the difference between the Fermi level and the defect level, $n_{i,eff}$ the effective intrinsic carrier concentration, τ_p and τ_n the hole and electron lifetimes.

7.2.1.2. Carrier lifetime

Doping dependence of SRH lifetimes is modeled in TCAD with the Scharfetter relation [210], described in Appendix F.2.2. The lifetime decreases with the increase of the doping concentration following the power law as seen in Fig. 7.2.

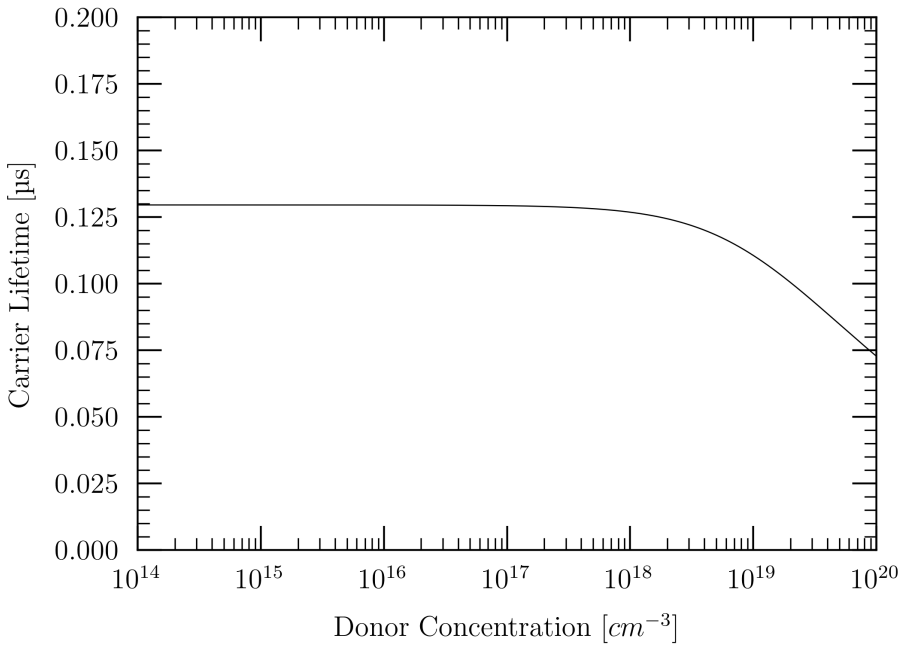

Fig. 7.2. Hole lifetime as a function of the donor concentration at room temperature, computed using the Scharfetter relation described in Appendix F.2.2.

Regarding the temperature dependence of SRH lifetimes, there is no consensus since the temperature behavior is highly dependent on the nature of the recombination centers. But it was concluded from measurements of the recombination lifetime [211] [212], that it can be modeled by a power law defined such that:

$$\tau_{SRH}(T) = \tau_{SRH}(300\text{K}) \cdot \left(\frac{T}{300\text{K}}\right)^{\alpha} \tag{7.4}$$

Here, $\alpha = -3/2$ which represents the expected decrease in minority carrier lifetimes as temperature increases, and $\tau_{SRH}(T)$ computed with the recombination rate (7.2) and Scharfetter relation in Appendix F.2.2.

All things considered, the SRH recombination model, using the Shockley-Read-Hall theory and the Scharfetter relation, is used to describe the recombination processes in the sensor. In addition, it has been demonstrated that the effective carrier lifetimes due to recombination in the SCR of several $p-n$ junction have the same dependence with increasing temperature [213]. Hence, it means that traps of the same type are responsible for recombination processes within the semiconductor junction. Therefore, charge carrier trapping has to be presented to comprehend this result.

7.2.1.3. Trapping and stationary charges

In the framework of TCAD simulation, traps play a crucial role as doping the material add additional traps and enhance recombination. While recombination models like the SRH recombination introduced earlier, implicitly rely on traps, they do not actually simulate them. Hence, models need to be defined in order to consider the occupation of traps and the charge stored in it. Additionally, the notion of fixed charges has to be presented.

Thereby, several trap types can be distinguished:

- Acceptor traps which carry the charge of one electron when entirely occupied and remains uncharged when unoccupied
- Donor traps which carry the charge of one hole when entirely occupied and remains uncharged when unoccupied.

Depending on the type of traps and its nature, the energetic distribution of traps can be implemented, following:

- A Gaussian distribution
- An exponential distribution
- An uniform distribution
- A single-energy level.

Then, the energy of the center the trap distribution E_t^0 is defined such that:

$$E_t^0 = \begin{cases} E_C - E_t & \text{from the energy edge of the CB} \\ \frac{E_C + E_V + k_B T \ln N_V / N_C}{2} + E_t & \text{from mid band gap} \\ E_V + E_t & \text{from the energy edge of the VB} \end{cases} \tag{7.5}$$

With E_C and E_V respectively the CB and VB energies, and E_t the energy level of the trap.

7.2.2. Dynamics of trap occupation

The occupancy level of a trap by a carrier j, which ranges from 0 to 1, varies as a result of electron or hole capture and emission processes i such as:

$$\frac{\partial f^j}{\partial t} = \sum_i {r_i}^j \tag{7.6}$$

With f^j the occupancy level of the trap, r_i the rates of all processes such as the capture rates denoted by c_i and emission rates denoted by e_i, displayed in the Fig. 7.3.

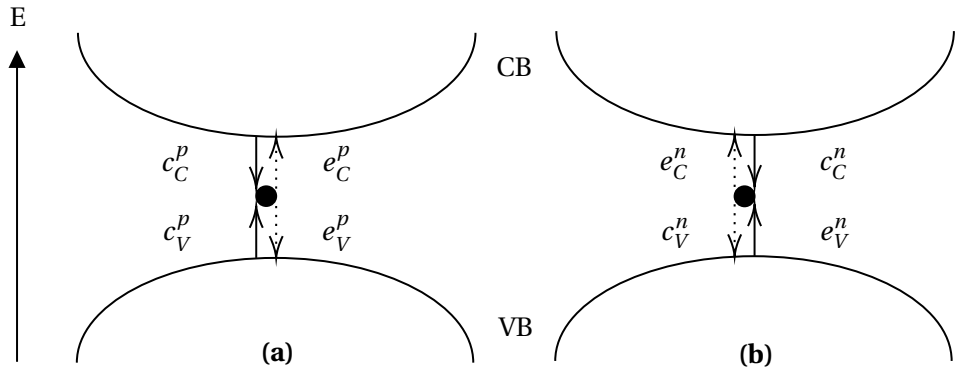

Fig. 7.3. Scheme of a deep trap occupation dynamic, for (a) hole and (b) electron. Emissions are represented with dotted arrows and captures with black arrows. The transitions from the valence band to the trap level are represented by e_V^p and e_V^n, and from the conduction band to the trap level by e_C^p and e_C^n.

The net rate of change of the trap occupancy is then defined such that:

$$r_i^j = \underset{\text{capture}}{(1-f^j)c_i^j} - \underset{\text{emission}}{f^j e_i^j} \tag{7.7}$$

With the first term representing the rate at which carriers are captured by the trap if the trap is currently unoccupied, $(1-f)$ being the probability that the trap is empty. And the second term representing the rate at which carriers are emitted from the trap if the trap is currently occupied.

The sum (7.6) extends over all the processes that can affect the occupancy level of the trap i.e. the capture and emission processes, and the recombination processes. Therefore, the capture of an electron from the VB is distinct from the capture of an electron from the CB. Considering a stationary state, the total rate of capture is equal to the total rate of emission. Hence, from (7.6) and (7.7), it comes:

$$\sum (1-f^j){c_i}^j = \sum f^j {e_i}^j \tag{7.8}$$

Solving the equilibrium condition leads to the expression of the following occupancy probability:

$$f^j = \frac{\sum {c_i}^j}{\sum ({e_i}^j + {c_i}^j)} \tag{7.9}$$

Hence the expression of the net capture rate (7.7) due to the process m is computed using (7.9), which expands and simplifies to:

$$r_m^j = \frac{c_m^j \sum e_i^j - e_m^j \sum c_i^j}{\sum ({e_i}^j + {c_i}^j)} \tag{7.10}$$

Each capture and emission interaction links the trap with a carrier reservoir. If a solitary process prevails, the trap, in a stationary state, would reach equilibrium with the reservoir specific to that process. This notion, known as the principle of detailed balance, establishes a relationship between the capture and emission rates such that:

$$e_i = \frac{c_i}{g} \exp\left(-\frac{E_t - {E_F}^i}{kT_i}\right) \tag{7.11}$$

With g the degeneracy factor of the trap level, E_T the energy of the trap level, E_F the Fermi level, k the Boltzmann constant and T_i the temperature of the carrier reservoir.

Therefore, the trap occupancy level is determined by the balance between the capture and emission rates. The aim of such a description for large band gap semiconductors, is to manage the complex dynamics of traps with shallow and deep levels that can be activated by temperature or induced by irradiation, at several energy levels within the band gap, with different energies from the edges of the CB or VB.

7.3. Neutron induced defects experimental results

7.3.1. Counts rate evolution with irradiation

As previously presented in Chapter 5, the NFS campaign was held during two weeks in October 2023. The S60 and S100 sensors were irradiated with two different neutron fluences, according to their respective positions. While a time slot of the data recorded under stable beam conditions was used in the previous Chapter 5 to provide a quantitative analysis of the sensor response within a multi-energy field environment, all the data recorded during the NFS campaign were used to study the effects of neutron irradiation on the sensor response. The counts rate evolution as a function of the irradiation date for the two sensors S60 and S100 is displayed in Fig. 7.4.

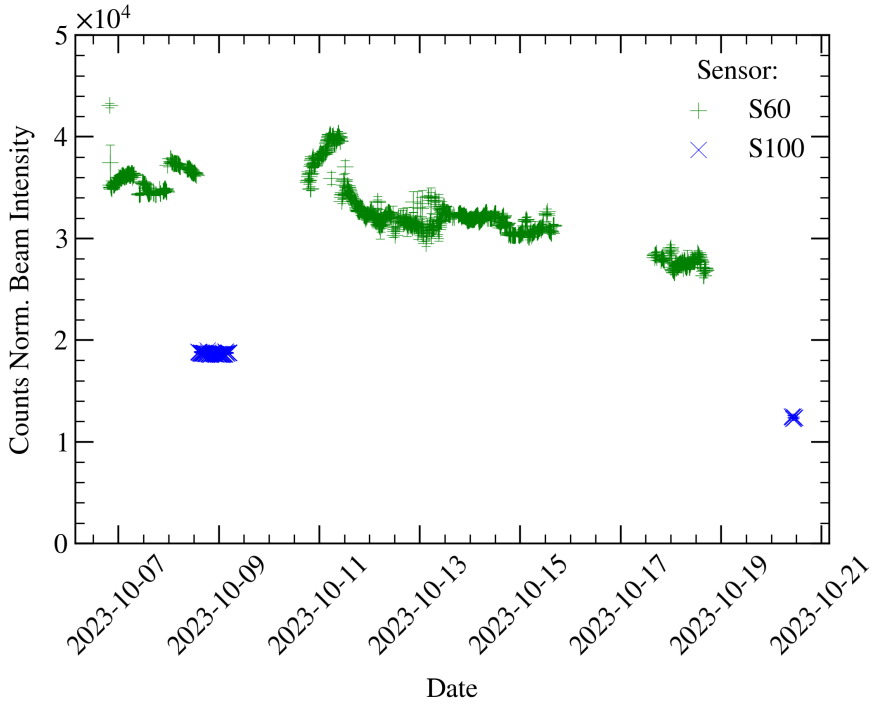

Fig. 7.4. Counts rate evolution as a function of the irradiation date for the two 4H–SiC sensors S60 and S100.

The latter is decreasing with the irradiation date for both sensors, with some local variation of the counts rate due to some bunch selector malfunction as explained in Appendix E. The count rate evolution is in agreement with the overall understanding of the effects of neutron irradiation on the sensor response described in section 7.1. However, while the behavior over time appears similar, the behavior over fluence does not follow the same pattern as seen in Fig. 7.5.

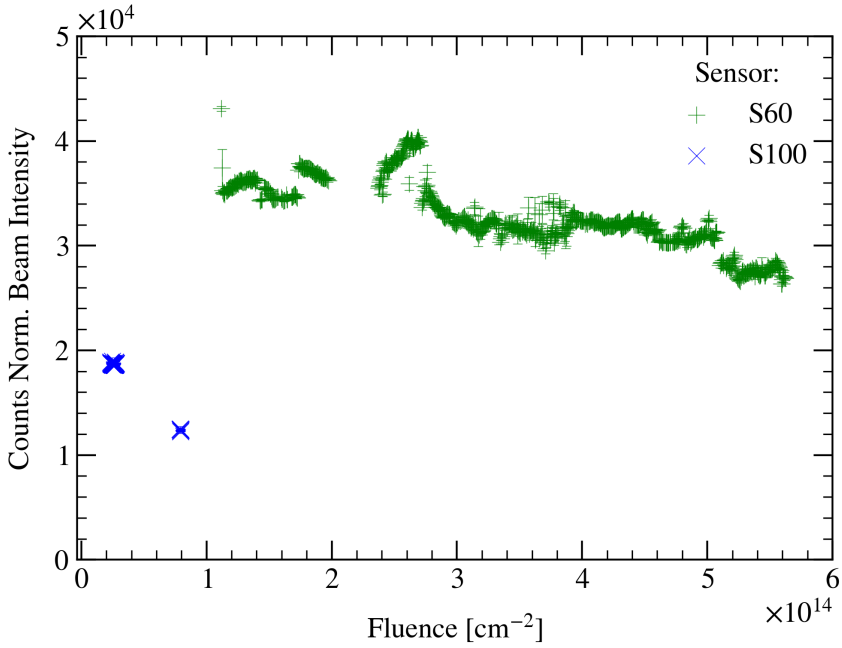

Fig. 7.5. Counts rate evolution as a function of the irradiation date for the two 4H–SiC sensors S60 and S100.

This indicates that the total neutron fluence across the entire energy range does not fully account for the decrease in the count rate. As mentioned previously, this effect is likely due to induced defects. Therefore, the primary objective in interpreting and studying this result is to utilize a normalization tool to make the neutron spectra at the two sensor locations comparable. Considering the displacement damage process as the most important cause of default creation in the bulk of the sensor, the evaluation of the displacement damage is performed through the basis of the NIEL hypothesis. The objective is to assess the relative damage potential of different particle types, enabling the prediction of the total damage potential for a specific particle energy spectrum. This scaling can be simplified to the concept of the 1 MeV equivalent fluence defined as the fluence of 1 MeV particle that causes the same level of damage as a given neutron beam characterized by a specific spectral distribution $\phi(E)$ and fluence Φ. Hence, for solid-state sensors, the NIEL-scaling hypothesis, which is grounded in the concept of non-ionizing energy loss, has been found to be effective for a wide range of particle spectra [214]. This hypothesis suggests that the efficiency of a detector diminishes in proportion to the number of lattice displacements caused by particles. The efficiency of any particle with a given kinetic energy can then be described by the hardness factor K defined as the ratio of the Energy spectrum Displacement Kerma (EDK) taking into account Kinetic Energy Released in MAtter (KERMA) definition, such that:

$$K = \frac{EDK}{EDK(1MeV)} \tag{7.12}$$

While the EDK (1 MeV) is available in the literature, the EDK is computed for the neutron energy spectrum such that:

$$EDK = \frac{\int D(E)\phi(E)dE}{\Phi(E)dE} \tag{7.13}$$

With $D(E)$ the displacement cross section [MeV·mb] shown in Fig. 7.6,

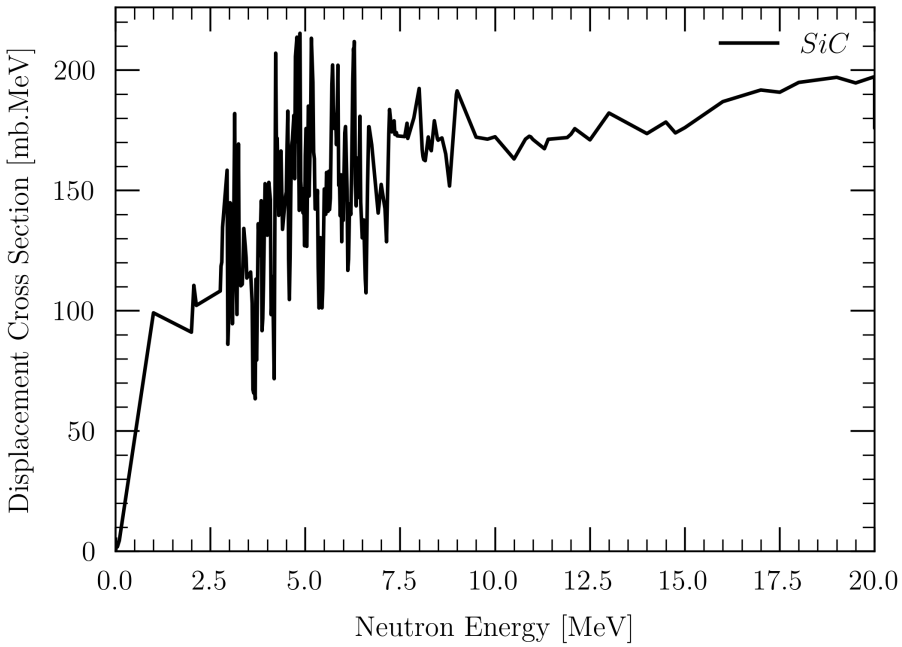

Fig. 7.6. Displacement damage cross section as a function of neutron energy for SiC compound. Data are from ENDF/B.VIII.

This displacement cross section can be defined analytically in a more general way with (7.14) or computed using Monte Carlo simulation scheme like GEANT4 under study or FLUKA [215], following (7.15), such that:

$$D(E) = \sum_i \sigma_i(E) \cdot \int dE_R f_i(E, E_r) P(E_r) \tag{7.14}$$

With σ_i the cross section of reaction i, $f_i(E, E_r)$ the probability of the incident particle to produce a recoil particle of energy E_r in reaction i, and $P(E_r)$ the partition function corresponding to the part of the recoil energy deposited in displacement.

$$D(E) = \frac{NIEL \cdot M}{d \cdot \rho \cdot \mathcal{N}_A} \cdot 1000 \cdot 1 \cdot 10^{27} \tag{7.15}$$

With $NIEL$ the non-ionizing energy loss computed with GEANT4, M the molar mass, d the thickness of the material, ρ the density, and $\mathcal{N}_A$ the Avogadro number.

Finally, the computation of the hardness factor is used as multiplication factor for the neutron fluence distribution such that:

$$\Phi_{\text{eq}}^{1\,MeV} = \Phi \cdot K \tag{7.16}$$

The neutron equivalent fluence at 1 MeV is used to assess the displacement damage caused by neutron irradiation. Consequently, the neutron equivalent fluence at 1 MeV is calculated for the neutron spectra at the S60 and S100 sensor positions. Given the comparable equivalent fluence, both sensors experienced the same level of displacement damage, which accounts for the similar decrease in count rate observed in Fig. 7.7.

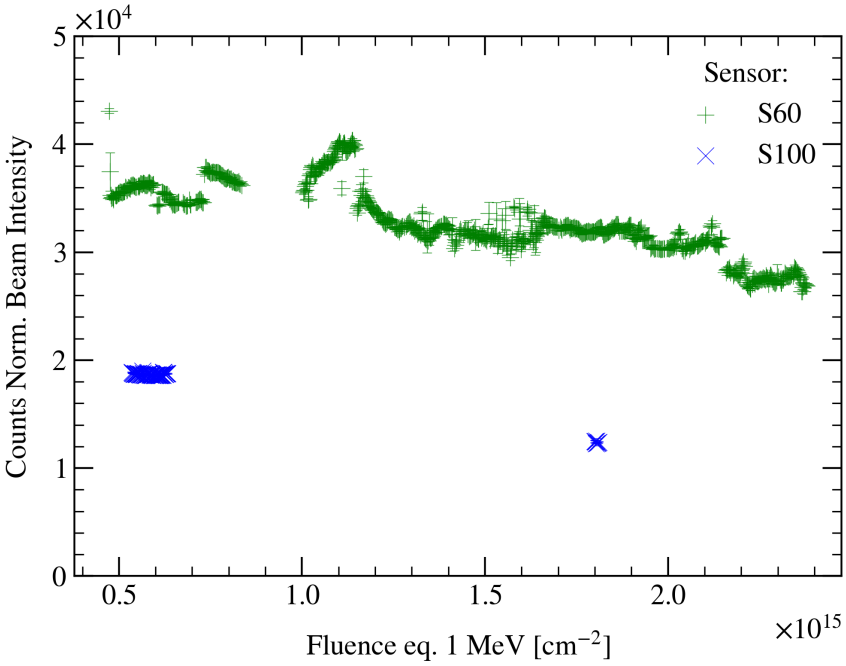

Fig. 7.7. Count rate evolution as a function of the 1 MeV equivalent fluence for the two 4H–SiC sensors S60 and S100.

In the following, the study focuses on the analysis of the current pulses from the sensor S60 in order to interpret and quantify the effects of irradiation on charge collection.

7.3.2. Pulse shape analysis with irradiation

To study the effect of such displacement damage on the sensor response, the pulse shape analysis is performed on the data recorded during the NFS campaign. The PSA of the pulses is displayed in the Fig. 7.8 and Fig. 7.9 for the sensor at the start and at the end of the NFS campaign.

These bidimensional histograms showing the pulse amplitude as a function of the pulse width, give an insight into the sensor response to neutron irradiation. The pulse amplitude and pulse width are decreasing with the the equivalent neutron fluence, which is in agreement with the overall understanding of the effects of neutron irradiation on the sensor response described in Section 7.1. Indeed, for a given data sample of the same amount of pulses, the results show that the pulses of higher amplitude, above 150 mV approximately, associated to a width larger than 8 ns at the beginning of the NFS campaign, are no longer present at the end of the campaign. This can be explained by the analysis carried out above, in terms of creation of defects in the sensor material, which act as deep level traps for the charge carriers. This form factor evolution has to be taken into account in the following charge collection efficiency study with irradiation.

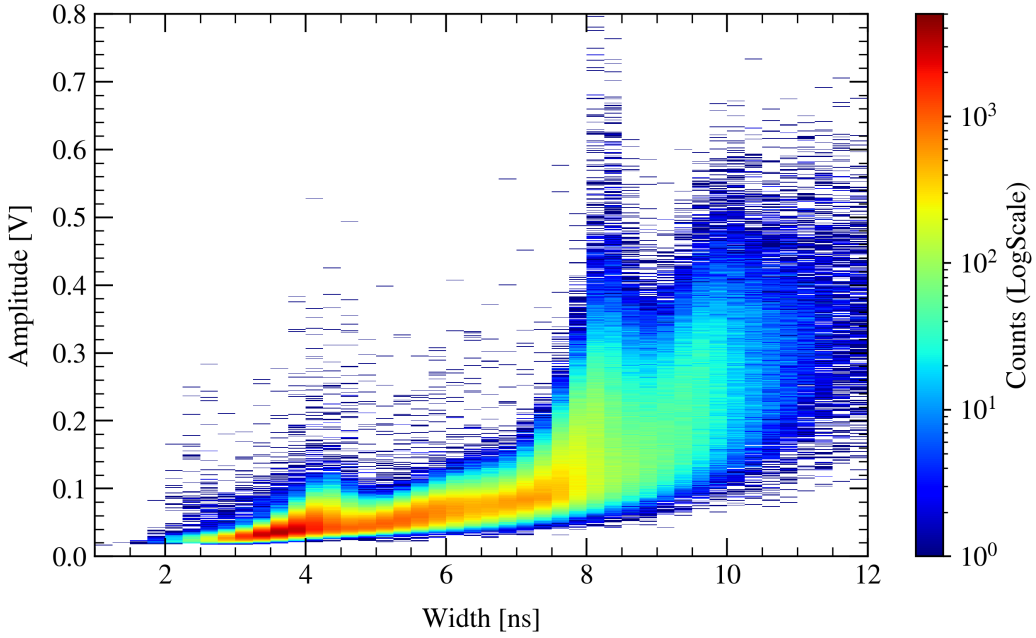

Fig. 7.8. Bidimensional histogram of the pulse amplitude as a function of the pulse width for the sensor at the start of the NFS campaign. Sample of data recorded on the 7th of October 2023, equivalent 1 MeV neutron fluence of $0.5 \cdot 10^{15}$ cm^2.

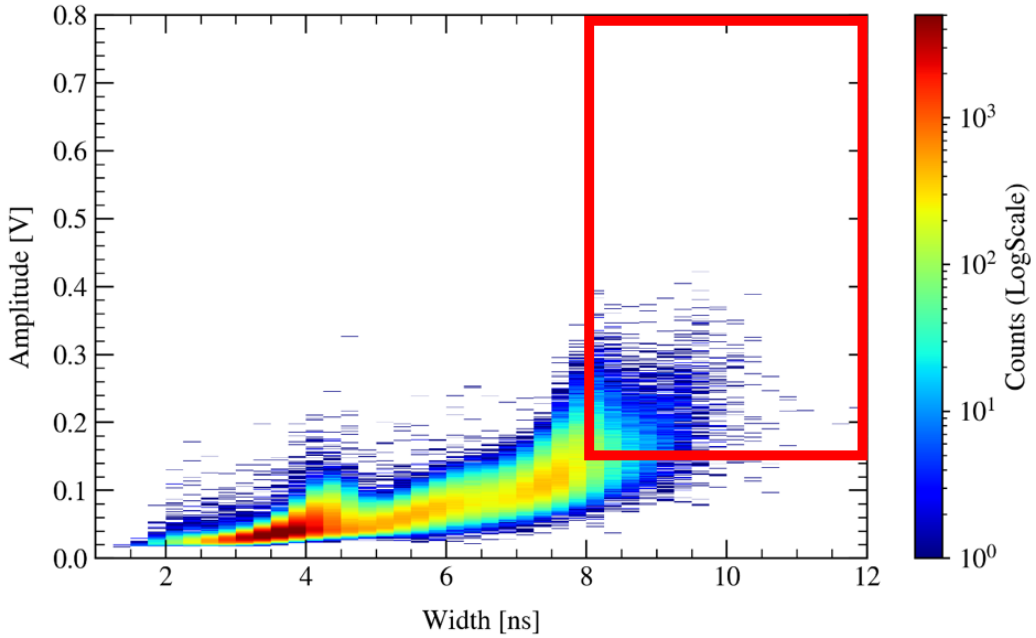

Fig. 7.9. Bidimensional histogram of the pulse amplitude as a function of the pulse width for the sensor at the end of the NFS campaign. Sample of data recorded on the 18th of October 2023, equivalent 1 MeV neutron fluence of $2.3 \cdot 10^{15}$ cm^2. The red rectangle highlights the region of interest where pulses are missing compared to the beginning of the campaign.

7.3.3. Charge collection efficiency study with irradiation

Since neutron induced defects in the sensor material act as deep level traps for the charge carriers, two hypothesis were formulated according to the experimental data:

- The traps carriers probability is proportional to the density of traps
- The density of traps is proportional to the neutron fluence.

These hypotheses result in a first-order attenuation in the collection of charge carriers as a function of drift distance. Since the attenuation constant is proportional to the trap density, the effective distance d_{eff} for charge carrier collection is inversely proportional to the trap density. Given that trap density is proportional to irradiation fluence, both pulse heights and the collected charge are then inversely proportional to irradiation fluence as illustrated in Fig. 7.10 for a charge cloud encountering a cluster of traps.

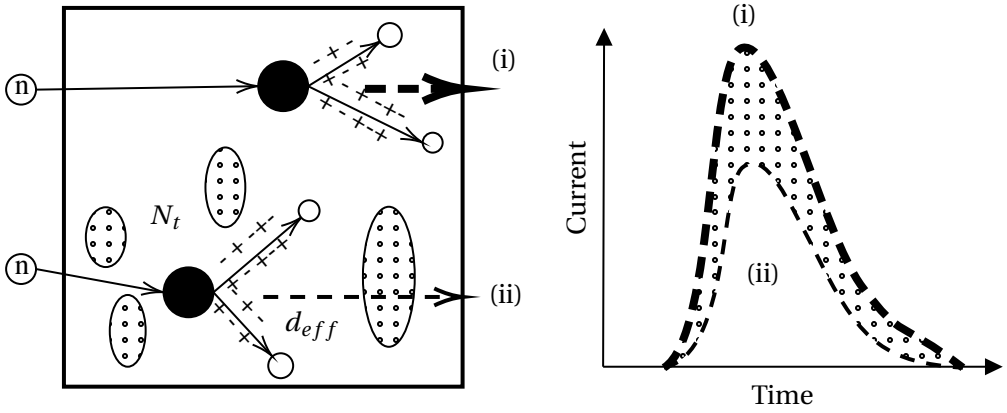

(a) Interaction scheme and traps locations **(b)** Current pulse scheme

Fig. 7.10. Scheme of the charge carrier trapping effect on the current pulse. (i) The charge carriers are not trapped and the current pulse is not delayed.
(ii) A fraction of the charge carriers are trapped in a cluster of traps. N_t stands for the trap density and d_{eff} for the effective drift distance.

This relationship is shown in Fig. 7.11 for the collected charge distribution as a function of the 1 MeV equivalent neutron fluence, leading to a decrease in the collected charge with increasing neutron fluence with time. Regarding the study of the charge collection efficiency, the mean charge collected as a function of the equivalent fluence at 1 MeV is displayed in Fig. 7.12, showing once again the same decrease for both sensors for the same level of equivalent fluence.

The collected charge distribution aligns with the PSA observations, and the mean charge collected as a function of the equivalent fluence at 1 MeV provides a quantitative analysis of the response of the sensor to neutron irradiation. Firstly, both sensors exhibit the same reduction in mean charge collected as the equivalent fluence increases. Secondly, this reduction reaches approximately 35 % for the sensor S60 at an equivalent fluence of $2.5 \cdot 10^{15}$ cm^2, consistent with the overall results reported in the literature [216].

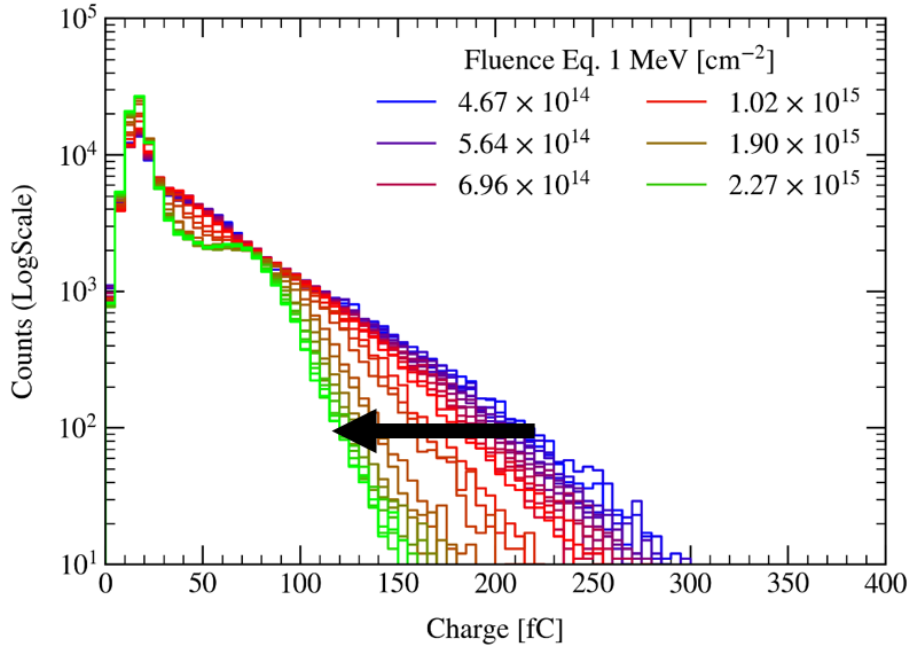

Fig. 7.11. Collected charge distribution as a function of the 1 MeV equivalent neutron fluence. Few samples of data recorded during the NFS campaign are displayed. The bold arrow highlights the decrease of the collected charge with the increase of the equivalent fluence.

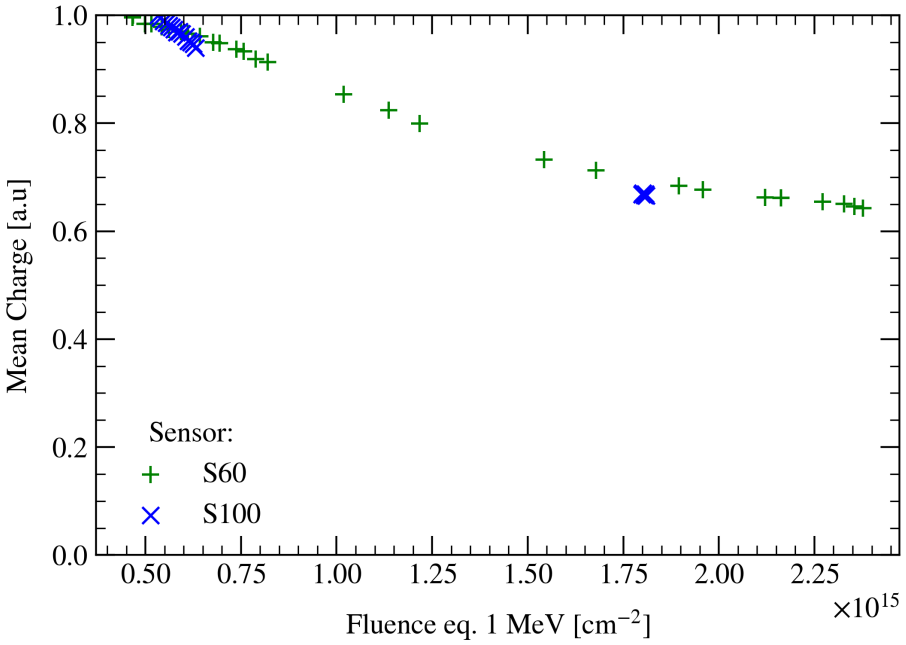

Fig. 7.12. Variation of the mean charge collected as a function of the equivalent fluence at 1 MeV. Both sensors S60 and S100 are displayed.

7.4. Application of thermally activated defect analysis to diamond

The following analysis is not presented for the 4H–SiC sensors. Indeed, the study carried out and presented in last Chapter 6, showed that the 4H–SiC sensors are stable up to 500 °C in terms of charge collection efficiency, which did not reveal the presence of thermally activated defects. Hence, the analysis below is dedicated to the diamond sensor response to increasing temperature. It should be noted that in order to reject any hypothesis of altered performance due to oxidation of the device components, the assembly was carried out in a primary vacuum.

7.4.1. Counts rate evolution with temperature

The methodology used to study the effects of increasing temperature on the sensor response to neutron irradiation is the same as the one used for the SiC sensors. The sensor is placed in a vacuum chamber and the temperature is increased from room temperature up to 300 °C. The counts rate is recorded at each temperature step —after a stabilization time —by the temperature controller reading a thermocouple inserted a few millimeters into the ceramic insulator. The results for a 500 µm thick diamond sensor are shown in Fig. 7.13. It is evident that the count rate decreases as the temperature increases. Specifically, from 50 °C to 300 °C, the count rate drops by 90 %.

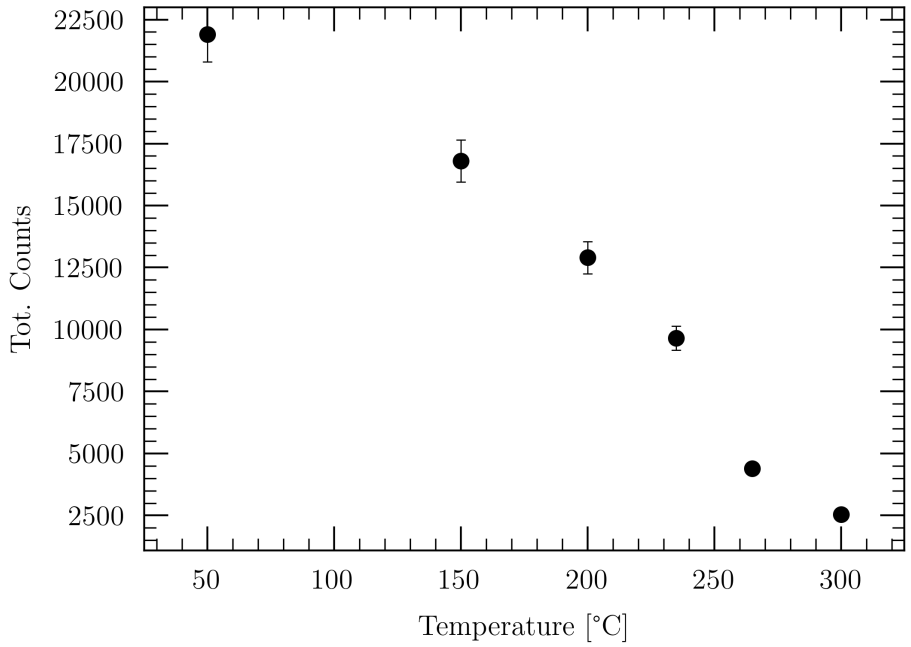

Fig. 7.13. Counts rate evolution as a function of the temperature for 500 µm diamond sensor thickness. The error bar takes into account a systematic error of 5 % on the counts rate due to the neutron source instability.

Although a reduction in the total counts rate has been previously observed with solid-state detectors, such as the 4H–SiC sensors discussed in Chapter 6, Section 6.4.2.3, the reduction observed with diamond sensors is three times greater than observed with 4H–SiC sensors in Fig. 6.32, page 215. Hence, the decrease in the counts rate cannot be solely attributed to the reduction in signal amplitude caused by the well-known decrease in drift velocity.

7.4.2. Pulse shape analysis with temperature

Thus, the PSA is conducted to gather additional insights into the cause of the reduction in the count rate. The results obtained at room temperature in Fig. 7.14 are in agreement with the results obtained in the previous Chapter 6 using SiC sensors.

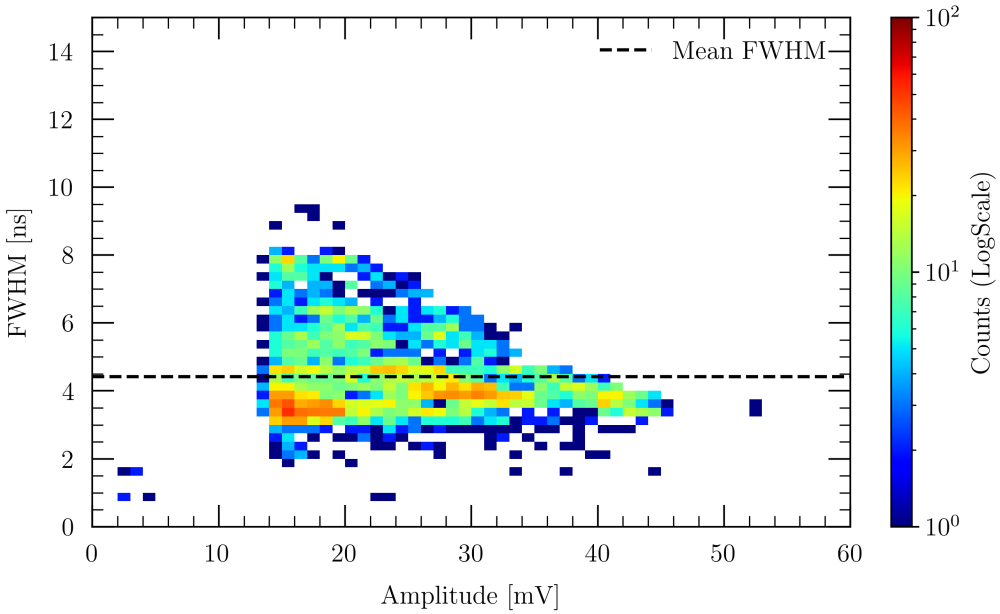

Fig. 7.14. Bidimensional histogram of the pulse amplitude as a function of the pulse width in the diamond sensor at 28 °C.

FWHM and amplitude are distributed based on the charge collection process, drift distance, and reaction type such as elastic/inelastic scattering, and non-radiative capture reactions, $^{12}C(n,\alpha_0)^9Be^{(g.s)}$ or $^{12}C(n,n')3\alpha$, already explained in Chapter 4. However, the results obtained at 300 °C in Fig. 7.15 show a significant modification of the pulse shape.

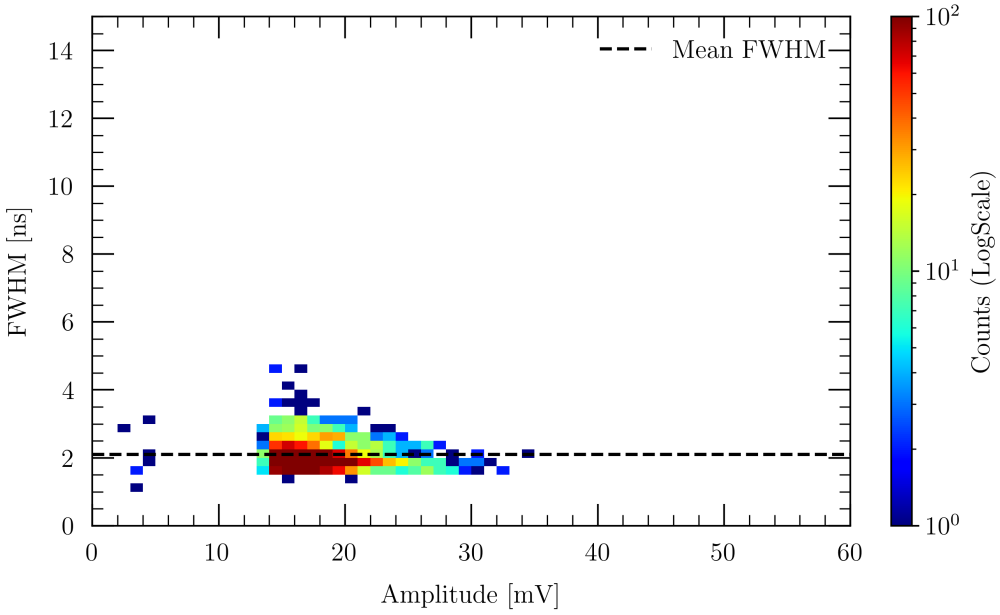

Fig. 7.15. Bidimensional histogram of the pulse amplitude as a function of the pulse width in the diamond sensor at 300 °C.

Firstly, the maximum amplitude of the pulses is reduced by a factor of 2 compared to the amplitude of the pulses at room temperature. Secondly, the pulses with highest FWHM are no longer present in the distribution. This indicates that the charge carriers are no longer able to drift over the same distance as at room temperature. One last point to note is that the mean FWHM of the pulses drifting the smallest distance at room temperature, is now reduced by almost a factor of 2 at 300 °C. Hence, the dispersion in charge arrival time tends to make the signal narrower because charges that would have contributed to the tail of the signal are no longer collected since they are delayed or trapped and so, do not contribute to the signal at the same time.

Consequently, these results on the PSA show that the charge carrier collection process is altered at 300 °C. The combination of the decrease of the amplitude and FWHM indicates that the charge carriers are no longer able to drift over the same distance as at room temperature. A phenomenon of charge carrier trapping along the drift path is the only assumption that can explain such a decrease. The later makes the interpretation of the charge collection more complex, since the net useful signal associated with a particular reaction such as $^{12}C(n,\alpha_0)Be^{(g,s)}$ is no longer discernible from the leftover of the signals. A general and homogeneous recombination phenomenon throughout the volume causes a considerable loss of charges for all the clouds collected, depending on their location in the detection volume. Although it is difficult to analyze precisely the phenomena involved in this complex process of charge trapping by studying experimental data, the degradation in detection performance can be studied in terms of charge collection efficiency.

7.4.3. Charge collection efficiency study with temperature

It has been presented that charge carrier trapping is at the root of degradation in detection performance as displayed with the previous PSA results with pulses distribution compared at room temperature and 300 °C. The dynamic of the charge collection efficiency is then studied as a function of the temperature. One way to represent the effect on charge collection efficiency is through the distribution of the collected charges. This distribution as a function of temperature is shown in Fig. 7.16.

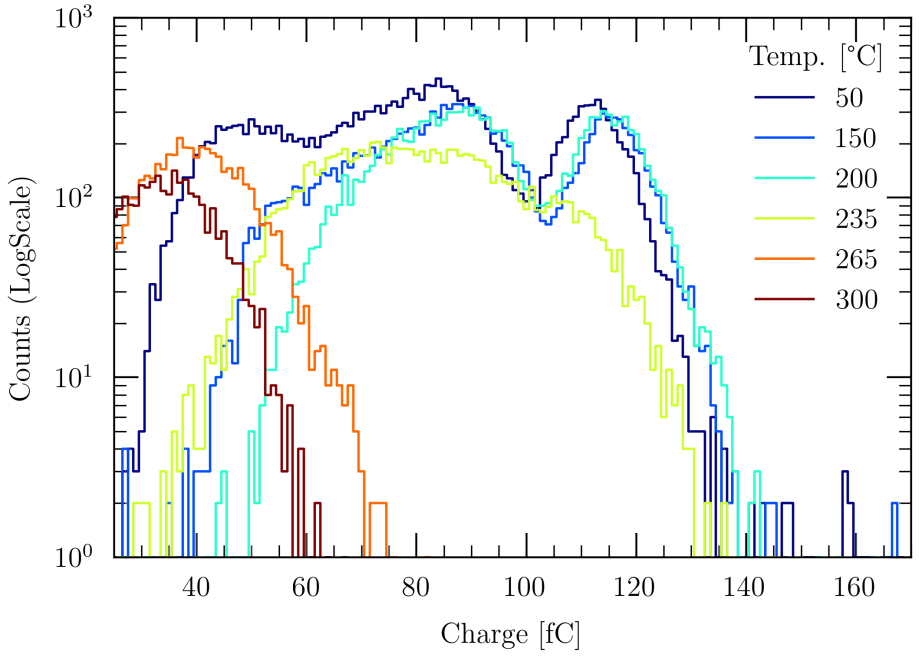

Fig. 7.16. Diamond collected charge distribution as a function of the temperature.

Up to 200 °C, the collected charges distribution behaves similarly to that of the 4H–SiC sensor. The peak position associated with the $^{12}C(n,\alpha_0)^{9}Be$ reaction remains largely unchanged, except for a slight shift towards higher collected charges due to the temperature dependence of the band gap, as described in section 6.4.2.4, page 216. For small quantities of collected carriers, below 80 fC, the distribution indicates a reduction in the number of recorded pulses. This is explained by the decrease in pulse amplitude due to reduced drift velocity, resulting in signals that are no longer triggered by the acquisition system. This behavior is reflected in the previous count rate evolution with temperature up to 200 °C, as seen in Fig. 7.13. However, above 235 °C, the number of pulses with low collected charge increases, whereas the number of pulses with high collected charge decreases. This supports the hypothesis that there is a threshold temperature beyond which the charge collection process is significantly disrupted. The maximum collected charge as a function of temperature is shown in Fig. 7.17, indicating a decrease in the mean collected charge with increasing temperature. This decrease becomes more pronounced above 235 °C, with a reduction of 60 % in the maximum collected charge between 150 °C and 300 °C.

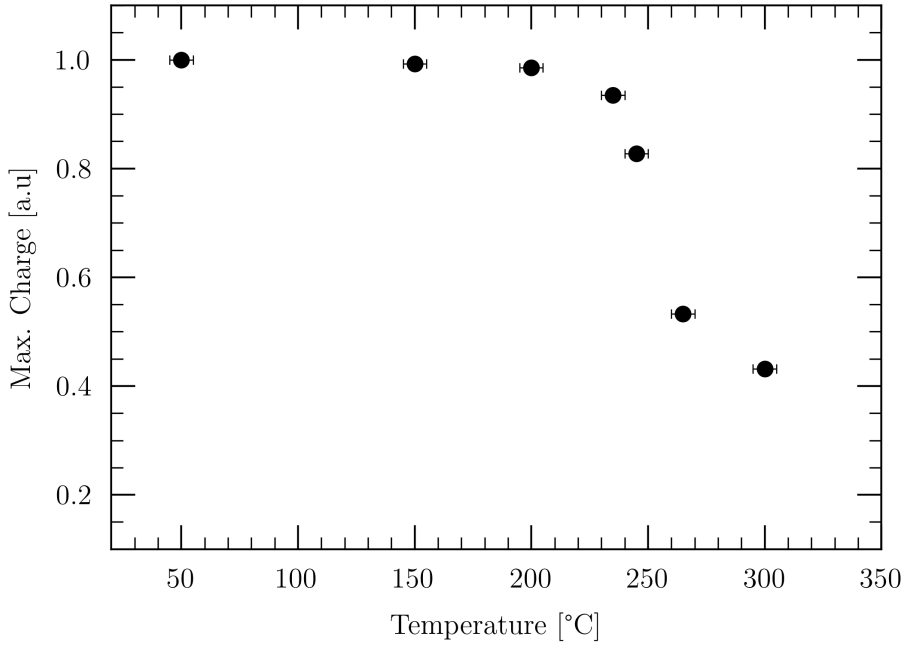

Fig. 7.17. Maximum collected charge with diamond as a function of temperature.

Concerning this threshold temperature of deep traps activation, it has been reported in several works from the literature that thermal spectroscopy is the only technique which enables to determine the capture cross section of the traps and the associated activation energy. Techniques such as PICTS[2] measurements or DLTS[3] measurements are usually performed as shown in Fig. 7.18 for a diamond.

[2] *Photoinduced Current Transient Spectroscopy (PICTS)*
[3] *Deep Level Transient Spectroscopy (DLTS)*

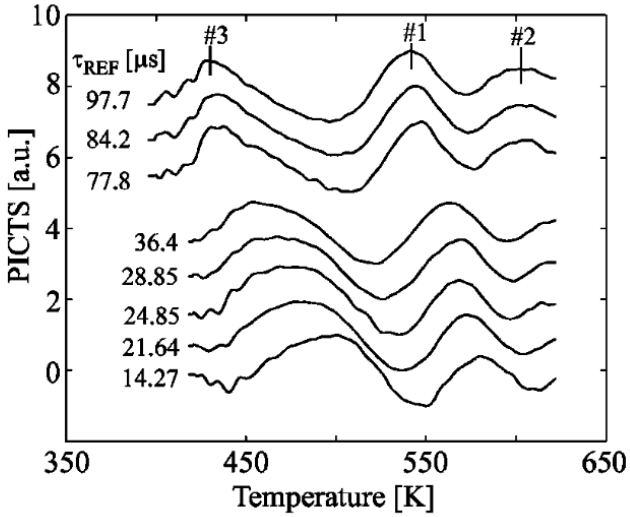

Fig. 7.18. PICTS spectra for a CVD diamond of 608 µm thickness. The dominant peaks are associated by the author to the deep levels numbered [217].

In the temperature range under study from room temperature up to 375 °C, three dominant deep levels traps have been identified and associated to three peaks in PICTS spectra signatures of Fig. 7.18. The relevant information related to these three states are registered in the following Table 7.1. It should be noticed that the trap concentration was also determined by the authors by performing TSC[4] measurements.

Deep Level	E_a [eV]	N_t [cm^{-3}]	σ_c [cm^2]	τ_c [s]	τ_e
1	1.14	$\approx 1 \cdot 10^{16}$	$4 \cdot 10^{-13}$	$20 \cdot 10^{-12}$	≈13 h
2	1.23	$\approx 1 \cdot 10^{16}$	$9.5 \cdot 10^{-14}$	$82 \cdot 10^{-12}$	≈76 days

Table 7.1. Deep levels parameters obtained from PICTS measurements. Data are from [217].

Hence, it can be understood from the levels number 1 and 2, that the energy needed for the activation of such deep trapped with energy higher than 1 eV is reached respectively between 520 K-550 K and 600 K-620 K. This means that once this temperature is reached, electrons have enough energy to overcome the potential barrier and fall into the localized electronic states, which are created by the adjustment of surrounding atoms due to these native defects. Being trapped in these deep levels, the collected charge is then reduced.

Moreover, carriers trapping by such traps appears really problematical within the framework of our study since the emission rate times, which is the time constant required for the charge carriers to be released from the traps, are of the order of hours and days. Hence, without considering any emission, according to the balance equation presented previously, charge carriers can be considered as almost irreversibly immobilized. The second effect to take into account is related to the capture cross sections. The previous table has presented high values for the later, leading then to very low capture time constants. Consequently the capture time constants of the order of magnitude of few picoseconds are considered in any case as lower than the charge carrier drift time of the order of few nanoseconds across the sensor thickness of few hundred of microns. Therefore both of these conclusions will lead to the CCE diminution as described with the Hecht equation in Section 3.2, page 69, governing the charge collection efficiency of the sensor.

[4] *Thermally Stimulated Currents (TSC)*

Finally, the previous description of deep trap activation available in reference articles from the literature can be used to determine the validity of our hypothesis regarding the counts rate drop using the diamond at high temperature. Indeed, it can be ruled that the activation of such deep traps at specific high temperature around 520 K to 540 K is responsible for the CCE diminution observed in the analysis of the experimental results obtained using a CVD diamond of 500 µm since the charge carriers are trapped and recombined within the material.

Moreover, in order to mitigate these polarization effects due to charge trapping within materials, one can enhance growth, processing, and fabrication methodologies of detectors. This involves then reducing defects and impurities concentration, which is not a straightforward endeavor. The experiments performed in this study also pointed out the fact that applying an opposite bias to the sensor was not sufficient to restore the charge collection efficiency of the 500 µm thickness diamond sensor under study. The fact that this performance degradation is not reversible is a strong indication that the traps are not only filled but also that the charge carriers are trapped within the material. In addition, since the SiC sensor did not show any degradation in charge collection efficiency up to 500 °C, the hypothesis of a limit temperature associated to deep level traps activation is confirmed. Above this threshold temperature specific to diamond, the charge collection process becomes strongly disrupted, making it impossible to estimate a neutron flux or monitor neutron intensity.

However, the same measurement was performed the day after, showing a recovery of the charge collection efficiency. This observation is in agreement with the charge carrier trapping in deep level defect hypothesis, since the emission time constants are of the order of thirteen hours for the deep level under study, showing one more time that active measurements in steady state are not possible with diamond sensors at high temperature.

7.5. Evaluation of the model for the charge carrier trapping

In order to evaluate the model developed in the previous sections, the TCAD simulation tool has been used to simulate the charge collection efficiency of the 4H–SiC sensor under study.

7.5.1. Traps distribution

The model is based on the hypothesis that the charge carriers are trapped in deep level defects, leading to a decrease in the charge collection efficiency. In addition, TCAD simulation tool allows to study the effect of external parameters such as electric field modification, which are not easily accessible experimentally.

In order to simulate accurately the effect of charge carrier trapping on the charge collection efficiency, a simple case is examined. Considering the same sensor geometry as the one previously used in the simulation of temperature effect, in Chapter 6, an alpha particle is generated at the bottom of the p-n junction, taking care to implement a sufficiently fine mesh to correctly simulate the linear energy transfer of the alpha particle. The traps are implemented using a gaussian distribution centered on the alpha particle trajectory, in order to take advantage of the fine mesh, to reduce the simulation time. Consequently, the resulting distribution of trapped holes, centered on the alpha particle trajectory, is shown in Fig. 7.19. A concentration of $1 \cdot 10^{16}$ traps per cubic centimeter is considered as a starting point, with an energy level of 0.68 eV and a capture cross section of $5 \cdot 10^{-15}$ cm^2, which are typical values for deep level $Z1$ defect in 4H–SiC [218, 219].

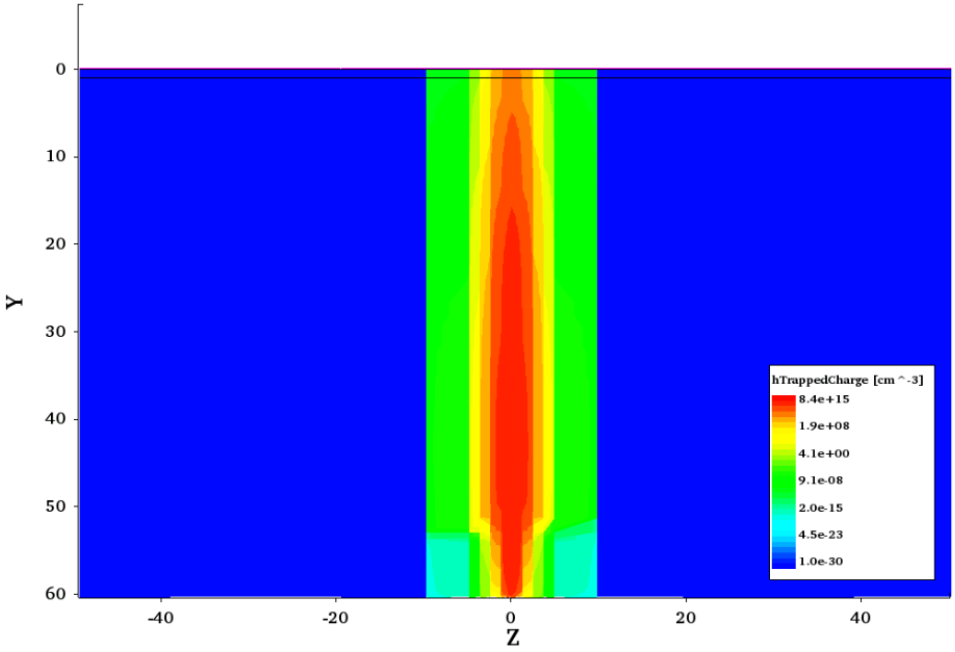

Fig. 7.19. Concentration of trapped holes along the thickness of the sensor. The substrate , is not shown in this figure.

7.5.2. Electric field modification

When traps are filled, they create localized states where charge carriers can become trapped. This effect appears whenever traps are already filled for two main reasons:

- Filled traps can act as recombination centers, where charge carriers can recombine instead of being extracted
- Filled traps can influence the distribution and mobility of charge carriers.

Therefore, even though the traps themselves are filled and no longer actively trapping charge carriers, their presence can still hinder the performance of the device by affecting the charge carrier transport and recombination processes. As a consequence, the electric field distribution within the device can be altered, leading to changes in the charge carrier mobility and drift. The electric field profiles along the thickness of the sensor 4 ns after the charge particle generation, with and without the presence of filled traps, are shown in Fig. 7.20. The presence of filled traps leads to a significant decrease in the electric field strength along the thickness of the sensor, which is in agreement with the investigation results obtained in a similar study of the performance degradation of 4H–SiC neutron detectors published recently [220]. The concentration of defects in a semiconductor can affect the collected current and space charge plays a significant role in this effect. By definition, space charge is the electric charge density that is not balanced by an equal amount of opposite charge. In the case of a semiconductor, space charge can be generated by the presence of charged defects, such as traps, that are not compensated by an equal number of free charge carriers. This can lead to the formation of regions of perturbed electric field, which can affect the drift velocity of charge carriers and their ability to contribute to collected current.

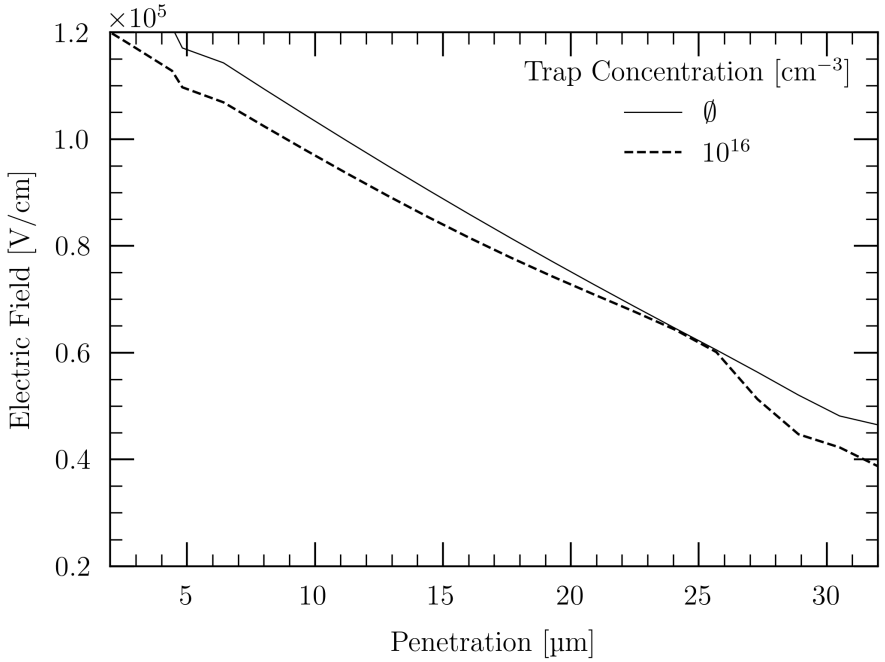

Fig. 7.20. Simulated electric field profiles along the thickness of the sensor 4 ns after the charge particle generation, with and without the presence of filled traps.

The space charge as a function of the sensor thickness for a vertical cut centered on the trap distribution is shown in Fig. 7.21. The presence of filled traps leads to an increase in the space charge density along the thickness of the sensor, with a maximum at the center of the gaussian distribution of traps at 30 µm from the edge of the junction, as shown in Fig. 7.19.

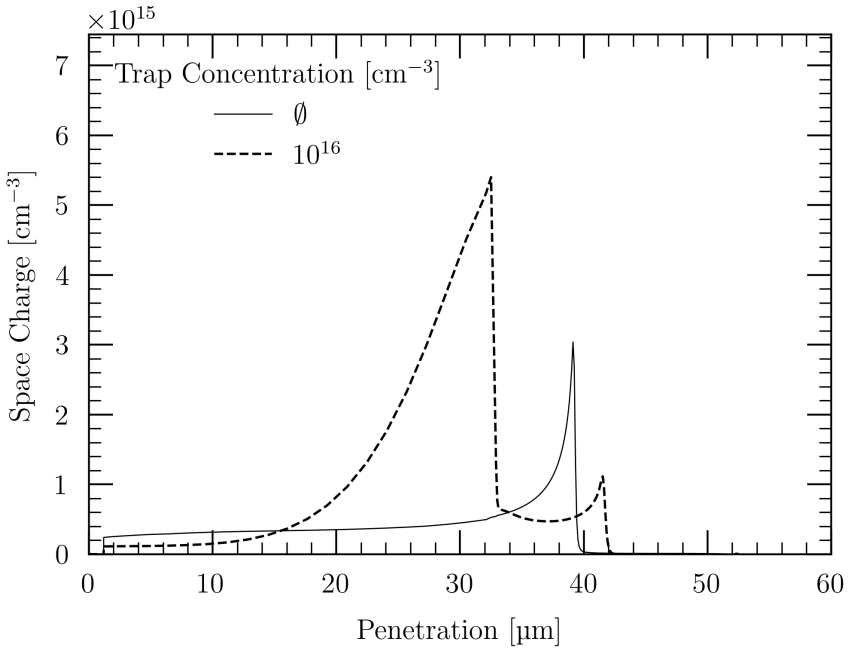

Fig. 7.21. Simulated space charge distribution in the sensor for a vertical cut centered on the trap distribution, 4 ns after the charge particle generation.

To summarize, when traps are filled, it creates localized regions of altered properties. These regions can affect the electric field distribution within the device, leading to changes in charge carrier mobility and drift. Additionally, the presence of filled traps can introduce scattering mechanisms that hinder the motion of charge carriers, reducing their overall mobility and making it more difficult for them to contribute to the output signal. This can result in a decrease in the charge collection efficiency of the device, as the charge carriers are less able to reach the electrodes and be collected. This decrease in charge collection efficiency can be observed in the simulation results with the decrease in the current pulse amplitude, as shown in Fig. 7.22. Integrating the current pulse over time, the total collected charge is reduced by 40 % in the presence of a concentration of $1 \cdot 10^{16}$ traps per cubic centimeter.

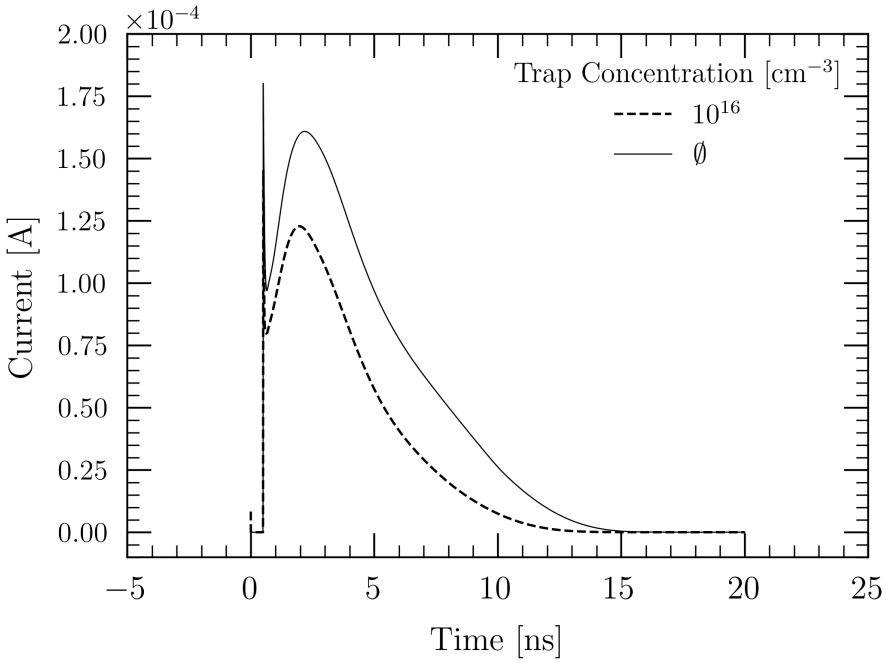

Fig. 7.22. Simulated current pulse of a 5 MeV alpha particle at 300 K with and without the presence of filled traps.

Using this first modeling scheme, the simulation results are in agreement with the experimental data obtained with the diamond sensor. Indeed, the diamond CCE showed a 40 % decrease in charge collection efficiency, as illustrated in Fig. 7.17 on page 242. This decrease occurred after the activation of deep level traps at 520 K to 540 K, corresponding to native defects in the material with a concentration of $1 \cdot 10^{16}$ per cubic centimeter, and is consistent with the simulation results. In a way, the results dealing with the evolution of 4H–SiC charge collection efficiency as a function of 1 MeV equivalent neutron fluence can be correlated. Although these induced defects are different from thermally activated defects, both correspond to deep levels. In addition, the decrease of 35 % in the charge collection efficiency of 4H–SiC observed after an equivalent 1 MeV neutron fluence of $2.5 \cdot 10^{15}/\text{cm}^2$ could be explained by a concentration of traps reaching $1 \cdot 10^{16}$ per cubic centimeter, as shown in the simulation results. However, further investigation are needed to provide an accurate estimation of the trap concentration after the irradiation campaign.

7.6. Perspectives

Due to the deep levels defects considered in this study, overcoming the potential barrier of these traps and facilitating charge carrier emission requires increased electric field strength or temperature. Estimating the electric field required to empty the traps involves considering the energy levels of traps and the energy needed to release the trapped charges. Generally, deeper traps require stronger electric field to empty them. Therefore, the study can be extended using model such as SRH model presented previously, which describes carrier capture and emission process, and can be used to estimate the electric field required to empty the traps.

In addition, another viable approach to empty the traps is to increase the temperature of the semiconductor. Indeed, by increasing the temperature, the thermal energy of the lattice increases allowing trapped charges to gain enough energy to overcome the potential barrier of the trap and escape into the VB or CB. Hence, in theory, it effectively reduces the occupancy of the traps improving the charge collection efficiency of the semiconductor as demonstrated in the literature [221, 222], but seems insufficient to completely correct the decrease in CCE with neutron fluence. This study could thus be extended to investigate the relationship between temperature and trap emptying, through the use of the Arrhenius equation which relates the rate of trap emptying to the temperature of the semiconductor, in order to estimate the temperature required to empty the traps and restore the charge collection efficiency of the sensor.

Both approaches encounter significant challenges due to the operational difficulties of handling bias voltages over 1 kV to achieve high electric field strengths, and temperatures above 500°C, particularly concerning proximity electronics and signal cables, respectively.

Conclusion

In summary, the effects of radiation and temperature on the charge collection efficiency of CVD diamond and 4H–SiC sensors have been studied. The 60% decrease in charge collection efficiency of the diamond sensor at high temperatures has been attributed to charge carrier trapping caused by thermally activated defects, which become active at 250 °C. The same charge carrier trapping mechanism has been also considered to explain the 35% decrease in charge collection efficiency observed in the 4H–SiC sensor as 1 MeV equivalent neutron fluence increases up to $2.5 \cdot 10^{15}$ cm^{-2}.

The numerical model developed with TCAD software to explain the charge carrier trapping has provided encouraging results. The simulation results are in agreement with the experimental data obtained in a first approximation, considering a concentration of traps of $1 \cdot 10^{16}$ per cubic centimeter, and could lead to a future validation of the model. Nonetheless it provided a good understanding of the charge carrier trapping process and its explanation through the electric field modification and the space charge effect that cannot be easily accessible experimentally.

Mitigation strategies have been proposed to reduce the impact of charge carrier trapping on the charge collection efficiency of semiconductor detectors.Finally, given the environmental constraints, the 4H–SiC sensor is better suited for high-temperature operation than diamond. Indeed, the charge collection efficiency of the 4H–SiC sensor remains stable up to 500 °C. In contrast, the diamond sensor suffers from charge carrier trapping due to thermally activated defects at 250 °C, with charge carriers becoming trapped for over twelve hours. As a result, active steady-state measurements are no longer feasible which makes it impossible to estimate a neutron flux or monitor neutron intensity.

General Conclusion **250**

Bibliography **254**

List of acronyms **271**

Appendices **275**

A SiC Junction - Demonstrating the main variables 275
B Kinematic study - Demonstrating the main expressions 284
C NovaSiC Epitaxy quotation - technical details 287
D Reaction Products level scheme and de-excitation 288
E NFS Campaign: Ghost Events 301
F TCAD Modeling 303

General Conclusion

This project has been carried out within the framework of the partnership between the CEA (IRESNE, IRFM) and Aix-Marseille University (ISFIN) through the LIMMEX joint laboratory. Since 2012, several doctoral students have contributed respectively, to the development of the solid-state neutron detector based on silicon carbide [70], to the study of the sensor response to neutron irradiation in a zero power reactor [223], and in a research reactor up to 250 kW power [74].

The PhD thesis presented here, has focused on the study, testing, and qualification of solid-state miniaturized neutron detectors based on silicon carbide 4H-SiC for fast neutron detection and monitoring in a representative nuclear fusion and fission environment. The main objectives were to propose a method for estimating the fast neutron flux, as well as to evaluate the effect of environmental constraints on the detector response. A particular attention was given of each step of the detector development, from the design to the characterization in a representative environments of fusion and fission reactors.

Silicon carbide 4H-SiC as a neutron detector material

To this end, the environmental constraints were carefully considered. The review of the state-of-the-art of neutron detectors showed that wide bandgap semiconductors are promising materials for neutron detection in harsh environments, with the potential to overcome the limitations of current detectors, and offering promising performances in terms of neutron spectrometry and the possibility of miniaturization. The choice of silicon carbide was motivated by its radiation hardness, thermal stability, and compatibility with high temperatures and magnetic fields present in fusion reactors facilities. Then, the use of the silicon carbide 4H-SiC as a radiation sensor was presented, with a detailed description of the detection principle and the neutron detection mechanism. It emphasized the complexity of the sensor response to neutron irradiation, but at the same time, the promising performances for neutron spectrometry due to the numerous nuclear threshold reactions. It led to the definition of the design requirements to develop a solid-state neutron detector based on silicon carbide 4H-SiC to be used in a fast neutron field, as well as the technical specifications required for the manufacturing of the detector. After a description of the manufacturing process, the detectors were characterized in terms of electrical characteristics, showing leakage current levels compatible with the expected operating conditions for radiation detection.

Online monitoring of neutron flux

The primary objective of this thesis was to propose a method for estimating the fast neutron flux using a silicon carbide detector. The initial step of the study involved the absolute estimation of the fast neutron flux in a mono-energetic neutron field of 14 MeV. A dedicated experimental setup was developed to study the detector response to mono-energetic neutrons from DT reactions. In order to interpret the experimental detector response, a model was developed to simulate the sensor within the monoenergetic field and to simulate the generation of charged particles and energy deposition in the active region of the sensor. After a comparison between the analytical model and the calculation results from the GEANT4 Monte-Carlo code, the model was validated and used to estimate the fast neutron flux. Experimental validation was required

for the hypotheses concerning the sequential decay of excited states in Beryllium-9 and Carbon-12 nuclei and silicon neutron capture reactions. The SiC sensor calibration method involved correction factors that relate energy deposition to the active region geometry of the sensor. Hence two correction factors were introduced to account for the deconvolution of the sensor response, and the edge effects in the active region. Combined uncertainties in experimental reaction rate and calculated correction coefficients were evaluated to estimate the measured flux against a theoretical reference flux value, accounting for various sources of uncertainty and biases.The results has shown that the experimental flux is within the 1σ uncertainty range of the reference value at the location of the sensor with a C/E ratio of 1.04 and a relative uncertainty of 22.2% at 1σ.

Highlighting the sensor capability to measure neutron flux in a mono-energetic field using threshold reactions $^{12}C(n,\alpha)^{9}Be$ and $^{28}Si(n,\alpha)^{25}Mg$, has yielded to initial encouraging results. This method is applicable to neutron generators or tokamak neutron sources in D-T scenarios. However, qualifying the sensor response across a broad energy range in a multi-energy field has been shown in all its complexity. The solution to this challenge was presented with the use of response functions. Due to simulation limitations, experimental data are necessary for neutron spectrum deconvolution through the use of response matrix. Calibration of these response functions could have been performed at facilities like AMANDE or PTB facilities with mono-energetic neutron beams. However, time of flight measurement technique has appeared essential for obtaining a response matrix with sufficient neutron energy bins for iterative spectrum unfolding. Thus, a dedicated acquisition chain for neutron measurements using time of flight method at the GANIL facility, was presented. The experimental data were interpreted, and a deconvolution method for spectrum derivation was applied to estimate the neutron flux using the constructed response matrix. The experimental campaign has demonstrated the ability of the sensor to measure neutron flux in a continuous neutron field using an experimental response matrix constructed with time of flight measurements.

Environmental constraints of fusion and fission reactors

In a third part, the effects of environmental constraints on the detector response were evaluated. Regarding the effects of temperature on sensor measurements, an analytical model of charge carrier dynamics in 4H-SiC was first presented, providing the necessary physical models for interpreting experimental results. Concerning the charge collection dynamics with increasing temperature, numerous studies have examined the mobility of charge carriers within SiC material. However, empirical models with calibrated coefficients describing this temperature effect, considering carrier concentration and doping concentration, are less common compared to silicon models. To achieve reliable simulation results for charge carrier collection, the empirical model coefficients were adjusted for the 4H-SiC device structure under study in the temperature range up to 500 °C. Hence, the experimental data analysis were used to determine the parameters and coefficients of these models with increasing temperature. Finally, a numerical model using finite element method led to the simulation of the complex charge carriers collection dynamics in the sensor with increasing temperature, offering insights into device performance by calculating and visually representing internal profiles such as fields, carrier concentrations, and current densities, which are often inaccessible experimentally. The objectives of this temperature effect study were successfully achieved. Firstly, pulse shape analysis with increasing temperature described the effect of mobility degradation on charge collection dynamics. Then the stability of 4H-SiC detection performance in the temperature range of interest was demonstrated.

Finally, the problem of defects within the sensor was addressed. The analytical model of defect creation and carriers recombination were presented, followed by the application of finite element method simulation to study the trapping mechanisms. Then, by presenting the results

of experiments on neutron-induced defects and thermally activated defects, the limitations of sensor response to neutron irradiation in the specific environment of fusion and fission reactors were identified, emphasizing the benefits of using silicon carbide 4H-SiC in comparison to diamond sensors for high temperature applications.

Perspectives

All things considered, the results of this thesis are promising for the development of solid-state neutron detectors based on silicon carbide 4H-SiC for neutron detection and monitoring in a representative nuclear fusion and fission environment. The proposed methods for estimating the fast neutron flux using a silicon carbide 4H-SiC detector are a significant step towards the development of a reliable and accurate neutron detector for spectrometry and monitoring.

Regarding the proposed approach for estimating an absolute fast neutron flux value, the method presented using a Monte-Carlo model to simulate the sensor response to mono-energetic does not address the final stage of sensitivity analysis. However the later is crucial for identifying the most influential input data uncertainties affecting output data uncertainties. This information can help to pinpoint input data with the highest potential to reduce uncertainty. In addition, it has been shown that handling uncertainties is challenging due to the high interconnection among many entries, requiring advanced methods for assessing output uncertainties. Specialized software like URANIE [6] can automate tasks such as Monte-Carlo uncertainty propagation and sensitivity analysis. Additionally, a Monte Carlo sensitivity study using Sobol indexes [167], could identify the most critical input uncertainties impacting the overall results. Finally, to address the significant uncertainty in neutron flux estimation due to nuclear data, a new evaluation of the carbon neutron capture cross-sections leading to sequential decay would be beneficial. This would help reduce the overall uncertainty in neutron flux estimation.

Concerning the neutron spectrum unfolding method, the results of the experimental campaign at the NFS facility are promising, demonstrating the capability of the 4H-SiC sensor to construct a response matrix through time of flight measurements and use it to unfold the neutron spectrum. Nevertheless, it is highly recommended to perform an additional measurement of the neutron flux to gain a clearer understanding of the neutron spectrum at the sensor location. Firstly, for the neutron spectrum shape, using a Bonner sphere would provide a more reliable measurement, mitigating concerns related to the accelerator beam structure or maintenance operations. Secondly, for the neutron spectrum area, employing neutron activation techniques would offer a more accurate measurement of the fluence received by the sensor during the measurement campaign. Regarding the sensor location, to minimize the contribution of scattered neutrons and avoid delayed gamma rays produced by neutron interactions with surrounding materials, the sensor should be positioned in the experimental hall, near the collimator, to achieve the highest neutron flux. For more accurate comparisons, another experimental campaign using metrological standards would be relevant to verify the neutron spectrum over the entire energy range, especially in the low energy range where discrepancies were observed. Lastly, applying this unfolding method to fission reactor neutron fields would require a response matrix emphasizing low energies.

Regarding the defect study, the results have shown that the sensor response to neutron irradiation is limited by the accumulation of deep level traps in the sensor material. For native defects, the sensor response is constrained by the thermal activation of deep-level defects, which has been observed and explained in diamond sensors but was not in 4H-SiC sensors. Then, regarding the induced defects, a 1 MeV neutron equivalent fluence of $2.4 \cdot 10^{15}$ cm^{-2} led to a decrease of 35% of the charge collection efficiency in the sensor, which was attributed to the accumulation of deep level defects created by non ionizing radiation damage. As a result, such

a solid state sensor should be used with caution in environments with high neutron fluence, taking into account this degradation effect on the sensor response.

However, the study of the effect of temperature on the response of the 4H-SiC sensor has yielded promising results, demonstrating stable performance down to 500 °C with a study of the charge collection dynamics in the sensor described by a modeling approach. Combining the results from GEANT4 and TCAD programs for neutron interaction and charge deposition provides a promising method for interpreting experimental current pulses for particle identification and discrimination. This approach is effective for identifying fast neutron interactions, modeling thermal neutron interactions with a converter layer, and discriminating gamma interactions through a detailed study of electron generation and ionization. Coupling these programs offers a powerful tool for optimizing geometry and improving radiation discrimination. This approach corresponds to a comprehensive sensor model that bridges from neutron interaction to charge collection and signal processing. The latter could be used to develop a real-time monitoring system for neutron detection and spectrometry in a fusion environment using machine learning techniques to identify and classify the neutron interactions in the sensor based on pulse shape analysis.

Bibliography

[1] G. Lutz. *Semiconductor Radiation Detectors: Device Physics*. Springer Berlin Heidelberg, 2007. ISBN: 9783540716785 (cit. on pp. 7, 72).

[2] S.M. Sze. *Semiconductor Devices: Physics and Technology*. John Wiley & Sons Singapore Pte. Limited, 2012. ISBN: 9780470873670 (cit. on pp. 7, 72).

[3] *Champs neutroniques monoénergétiques, l'installation AMANDE*. https://www.irsn.fr/recherche/champs-neutroniques-monoenergetiques-linstallation-amande (cit. on p. 9).

[4] *2 MV - Tandetron*. https://www.ptb.de/cms/en/ptb/fachabteilungen/abt6/fb-64/641-ion-accelerators/2-mv-tandetron.html (cit. on p. 9).

[5] *NFS – Neutrons for Science*. https://www.ganil-spiral2.eu/scientists/ganil-spiral-2-facilities/experimental-areas/nfs/ (cit. on p. 9).

[6] Jean-Baptiste Blanchard et al. "The Uranie platform: an open-source software for optimisation, meta-modelling and uncertainty analysis". In: *EPJ N - Nuclear Sciences & Technologies* 5 (Jan. 2019), p. 4. DOI: 10.1051/epjn/2018050. URL: https://cea.hal.science/cea-02052632 (cit. on pp. 14, 153, 252).

[7] John Wesson. *Tokamaks*. OUP Oxford; 3e édition, 2011. ISBN: 0199592233 (cit. on p. 21).

[8] J.M. Rax. *Physique des Tokamaks*. École polytechnique: Physique. Éditions de l'École polytechnique, 2011. ISBN: 9782730215800 (cit. on p. 21).

[9] *Schematic of ITER*. www.iter.org (cit. on p. 22).

[10] Brown DA et al. "ENDF/B-VIII.0: The 8th Major Release of the Nuclear Reaction Data Library with CIELO-project Cross Sections, New Standards and Thermal Scattering Data". In: *NUCLEAR DATA SHEETS* 148 (2018), pp. 1–142. ISSN: 0090-3752. DOI: 10.1016/j.nds.2018.02.001 (cit. on pp. 23, 123).

[11] Jakob Eriksson. "Neutron Emission Spectrometry for Fusion Reactor Diagnosis: Method Development and Data Analysis". PhD thesis. Uppsala University, 2015 (cit. on p. 23).

[12] Rebeca Juarez et al. "A full and heterogeneous model of the ITER tokamak for comprehensive nuclear analyses". In: *Nature Energy* 6 (Feb. 2021), pp. 1–8. DOI: 10.1038/s41560-020-00753-x (cit. on pp. 23, 24).

[13] J.-Ch. Sublet et al. "FISPACT-II: An Advanced Simulation System for Activation, Transmutation and Material Modelling". In: *Nuclear Data Sheets* 139 (2017). Special Issue on Nuclear Reaction Data, pp. 77–137. ISSN: 0090-3752. DOI: https://doi.org/10.1016/j.nds.2017.01.002. URL: https://www.sciencedirect.com/science/article/pii/S0090375217300029 (cit. on pp. 24, 34).

[14] E. Rajendra Kumar. *ITER-TBM Program activities in Europe, China and India*. 24th FEC, San Diego, CA, USA. 2012 (cit. on p. 27).

[15] Robert Arnoux. *Tritium: Changing lead into gold*. 2016. URL: https://www.iter.org/fr/mag/8/single#56 (visited on 02/01/2016) (cit. on p. 26).

[16] C.J. Werner, J.S. Bull, C.J. Solomon, F.B. Brown, G.W. McKinney, M.E. Rising, D.A. Dixon, R.L. Martz, H.G. Hughes, L.J. Cox, A. J. Zukaitis, J.C. Armstrong, R. A. Forster, L. Casswell. *MCNP6.2*. Version 6.2. 2018. URL: https://mcnp.lanl.gov/mcnp_manual.shtml (cit. on p. 28).

[17] E. Brun, F. Damian, C.M. Diop, E. Dumonteil, F.X. Hugot, C. Jouanne, Y.K. Lee, F. Malvagi, A. Mazzolo, O. Petit, J.C. Trama, T. Visonneau, A. Zoia. *CEA, EDF and AREVA reference Monte Carlo code*. 2015. URL: https://www.cea.fr/energies/tripoli-4/Pages/Accueil.aspx (cit. on p. 28).

[18] Prasoon Raj et al. "Computational study of a chromium self-powered detector for neutron flux monitoring in the test blanket module of ITER". In: *Nuclear Instruments and Methods in Physics Research Section A: Accelerators, Spectrometers, Detectors and Associated Equipment* 908 (2018), pp. 10–17. ISSN: 0168-9002. DOI: https://doi.org/10.1016/j.nima.2018.08.020. URL: https://www.sciencedirect.com/science/article/pii/S0168900218309641 (cit. on p. 28).

[19] Vladislav Plyusnin et al. "Study of runaway electron generation during major disruptions in JET". In: *Nuclear Fusion* 46 (Jan. 2006), p. 277. DOI: 10.1088/0029-5515/46/2/011 (cit. on p. 29).

[20] Krista Dulon. *Toward a common basis for TBM systems*. 2011. URL: https://www.iter.org/fr/newsline/-/784 (visited on 07/01/2011) (cit. on p. 29).

[21] Robert Arnoux. *Under construction: Reactor Jules Horowitz*. 2008. URL: https://www.iter.org/fr/newsline/38/771 (visited on 06/30/2008) (cit. on p. 31).

[22] S.GAILLOT L. FERRY. *Latest information provided by the JHR consortium concerning the devices, irradiation locations, PIE facilities and transport capabilities*. part 1 of the work Package N°1 of the JHOP 2040. 2021 (cit. on pp. 32, 33).

[23] Bong Goo Kim et al. "Review Paper: Review of Instrumentation for Irradiation Testing of Nuclear Fuels and Materials". In: *Nuclear Technology* 176 (Nov. 2011), pp. 155–187. DOI: 10.13182/NT11-A13294 (cit. on p. 32).

[24] G. Ithurralde J.-P. Dupuy G. Perotto. "Présentation du réacteur Jules Horowitz". In: *Evolution des réacteurs nucléaires : moyens de recherche et d'essais* 2 (2006), pp. 101–113. DOI: https://doi.org/10.1051/rgn/20062101 (cit. on p. 32).

[25] David BLANCHET. *Etude neutronique du four OCCITANE équipé de l'expérience REF-RJH dans son emplacement d'irradiation*. Tech. rep. CEA, 2021 (cit. on pp. 34, 37).

[26] Rob Bamber et al. "Conceptual design of test devices for the JHR tailored to the needs of the nuclear fusion community". In: *Fusion Engineering and Design* 122 (2017), pp. 113–123. ISSN: 0920-3796. DOI: https://doi.org/10.1016/j.fusengdes.2017.09.003. URL: https://www.sciencedirect.com/science/article/pii/S0920379617308037 (cit. on p. 34).

[27] D. Leichtle et al. "The F4E programme on nuclear data validation and nuclear instrumentation techniques for TBM in ITER". In: *Fusion Engineering and Design* 89.9 (2014). Proceedings of the 11th International Symposium on Fusion Nuclear Technology-11 (ISFNT-11) Barcelona, Spain, 15-20 September, 2013, pp. 2169–2173. ISSN: 0920-3796. DOI: https://doi.org/10.1016/j.fusengdes.2014.02.056. URL: https://www.sciencedirect.com/science/article/pii/S0920379614001537 (cit. on p. 35).

[28] Commissariat à l'énergie atomique et aux énergies alternatives. *Research Nuclear Reactors*. Monographies DEN. Commissariat à l'énergie atomique et aux énergies alternatives, 2012. ISBN: 9782281115635. URL: https://books.google.fr/books?id=BPOGuQEACAAJ (cit. on p. 36).

[29] Yi-Kang Lee. "Analysis of the ITER Computational Shielding Benchmark with the Monte Carlo TRIPOLI-4 Neutron Gamma Coupled Calculations". In: *Fusion Engineering and Design* 109-111 (2015), pp. 1163–1168. DOI: 10.1016/j.fusengdes.2015.12.062. URL: https://hal.archives-ouvertes.fr/hal-02429495 (cit. on p. 37).

[30] R. Mitteau et al. "Allowable heat load on the edge of the ITER first wall panel beryllium flat tiles". In: *Nuclear Materials and Energy* 12 (2017). Proceedings of the 22nd International Conference on Plasma Surface Interactions 2016, 22nd PSI, pp. 1067–1070. ISSN: 2352-1791. DOI: https://doi.org/10.1016/j.nme.2017.02.001. URL: https://www.sciencedirect.com/science/article/pii/S2352179116300734 (cit. on p. 37).

[31] Tomás Junquera et al. "Electromagnetic studies of effects produced by disruption events inside ITER European diagnostic port plugs". In: *Fusion Engineering and Design* 168 (July 2021), p. 112422. DOI: 10.1016/j.fusengdes.2021.112422 (cit. on p. 37).

[32] D. Iracane, Pascal Chaix, and Ana Alamo. "Jules Horowitz Reactor: a high performance material testing reactor". In: *Comptes Rendus Physique - C R PHYS* 9 (Apr. 2008), pp. 445–456. DOI: 10.1016/j.crhy.2007.11.003 (cit. on p. 37).

[33] *jhrreactor*. https://jhrreactor.com/ (cit. on p. 37).

[34] L.M. Giancarli et al. "Overview of the ITER TBM Program". In: *Fusion Engineering and Design* 87.5 (2012). Tenth International Symposium on Fusion Nuclear Technology (ISFNT-10), pp. 395–402. ISSN: 0920-3796. DOI: https://doi.org/10.1016/j.fusengdes.2011.11.005. URL: https://www.sciencedirect.com/science/article/pii/S0920379611006090 (cit. on p. 37).

[35] Philippe Filliatre et al. "Reasons why Plutonium 242 is the best fission chamber deposit to monitor the fast component of a high neutron flux". In: *Nuclear Instruments and Methods in Physics Research Section A: Accelerators, Spectrometers, Detectors and Associated Equipment* 593 (Aug. 2008), pp. 510–518. DOI: 10.1016/j.nima.2008.05.049 (cit. on p. 41).

[36] Ludo Vermeeren et al. "In-Pile SubMiniature Fission Chambers Testing in BR2". In: (June 2003). DOI: 10.1142/9789812705563_0045 (cit. on p. 41).

[37] Mayu Yamauchi et al. "Development of in-vessel neutron monitor using micro-fission chambers for ITER". In: *Review of Scientific Instruments* 74 (Mar. 2003), pp. 1730–1734. DOI: 10.1063/1.1534397 (cit. on p. 41).

[38] Masao Ishikawa, Keigo Takeda, and Kiyoshi Itami. "Development of in-vessel neutron flux monitor equipped with microfission chambers to withstand the extreme ITER environment". In: *Fusion Engineering and Design* 109 (Dec. 2015). DOI: 10.1016/j.fusengdes.2015.12.012 (cit. on p. 41).

[39] Martin Ohmes et al. "Development of Micro-Pocket Fission Detectors (MPFD) for near-core and in-core neutron flux monitoring". In: *Proc SPIE* 5198 (Jan. 2004). DOI: 10.1117/12.513852 (cit. on p. 41).

[40] Douglas McGregor et al. "Micro-pocket fission detectors (MPFD) for in-core neutron flux monitoring". In: *Nuclear Instruments and Methods in Physics Research Section A: Accelerators, Spectrometers, Detectors and Associated Equipment* 554 (Dec. 2005), pp. 494–499. DOI: 10.1016/j.nima.2005.06.086 (cit. on p. 41).

[41] Michael Reichenberger et al. "Micro-Pocket Fission Detectors (MPFDs) for In-Core Neutron Detection". In: *Annals of Nuclear Energy* 87 (Jan. 2016), pp. 318 –323. DOI: 10.1016/j.anucene.2015.08.022 (cit. on p. 41).

[42] Ludo Vermeeren et al. “Irradiation tests in BR2 of miniature fission chambers in pulse, Campbelling and current mode”. In: (June 2011). DOI: 10.1109/ANIMMA.2011.6172885 (cit. on p. 41).

[43] *Fission Chambers for in-core use*. https://www.exosens.com/products/fission-chambers-core-use. Accessed: 2019-03-27 (cit. on p. 41).

[44] Christian Jammes et al. “Progress in the development of the neutron flux monitoring system of the French GEN-IV SFR: Simulations and experimental validations”. In: Apr. 2015. DOI: 10.1109/ANIMMA.2015.7465647 (cit. on pp. 41, 53).

[45] Iec and Pub. “High-Voltage Test Techniques - Partial Discharge Measurements”. In: 60270 (Jan. 2000), pp. 2000–12 (cit. on p. 41).

[46] Lutz Niemeyer. “Generalized approach to partial discharge modeling”. In: *Dielectrics and Electrical Insulation, IEEE Transactions on* 2 (Sept. 1995), pp. 510 –528. DOI: 10.1109/94.407017 (cit. on p. 41).

[47] H. HAMRITA et al. “Rejection of partial-discharge-induced pulses in fission chambers designed for sodium-cooled fast reactors”. In: *Nuclear Instruments and Methods in Physics Research Section A: Accelerators, Spectrometers, Detectors and Associated Equipment* 848 (Nov. 2016). DOI: 10.1016/j.nima.2016.11.055 (cit. on pp. 41, 53).

[48] Ms. Chenaud et al. “Progress in the design of the ASTRID nuclear island”. In: *ICAPP 2018*. Charlotte, United States: ICAPP 2018, Apr. 2018. URL: https://hal.science/hal-02415487 (cit. on p. 42).

[49] Takeo Nishitani et al. “In-Vessel Neutron Monitor Using Micro Fission Chambers for ITER”. In: Jan. 1998, pp. 491–500. ISBN: 978-1-4613-7442-8. DOI: 10.1007/978-1-4615-5353-3_60 (cit. on p. 42).

[50] Terumasa Hayashi, Takeo Nishitani, and Mitsuteru Ishikawa. “First measurement of time-resolved neutron yield on JT-60U using a microfission chamber”. In: *Review of Scientific Instruments* 75 (Oct. 2004), pp. 3575–3577. DOI: 10.1063/1.1785261 (cit. on pp. 42, 53).

[51] Commissariat à l’énergie atomique et aux énergies alternatives. *L’instrumentation et la mesure en milieu nucléaire*. Monographies DEN. Commissariat à l’énergie atomique et aux énergies alternatives, 2019. ISBN: 9782281143034. URL: https://books.google.fr/books?id=MOLMxgEACAAJ (cit. on pp. 43, 45).

[52] Loïc Barbot et al. “Calculation to experiment comparison of SPND signals in various nuclear reactor environments”. In: *2015 4th International Conference on Advancements in Nuclear Instrumentation Measurement Methods and their Applications (ANIMMA)*. 2015, pp. 1–7. DOI: 10.1109/ANIMMA.2015.7465558 (cit. on p. 43).

[53] *Thermal & sensing solutions for nuclear industry*. https://www.thermocoax.com/market/thermal-sensing-solutions-for-nuclear-industry/nuclear-spnd/. Accessed: 2015-04-24 (cit. on p. 44).

[54] M. Angelone et al. “Development of self-powered neutron detectors for neutron flux monitoring in HCLL and HCPB ITER-TBM”. In: *Fusion Engineering and Design* 89 (Oct. 2014). DOI: 10.1016/j.fusengdes.2014.01.077 (cit. on p. 44).

[55] K. Goetz, S. Cetiner, and C. Celik. “Development of a Fast-Spectrum Self-Powered Neutron Detector for Molten Salt Experiments in the Versatile Test Reactor”. In: *EPJ Web of Conferences* 253 (Jan. 2021), p. 05006. DOI: 10.1051/epjconf/202125305006 (cit. on p. 44).

[56] Luigi Lepore, Romolo Remetti, and Antonino Pietropaolo. "A proposal for an alternative use of prompt-Self Powered Neutron Detectors: Online spectral-deconvolution for monitoring high-intensity neutron flux in LFRs". In: *Nuclear Engineering and Design* 322 (Oct. 2017), pp. 536–546. DOI: 10.1016/j.nucengdes.2017.07.028 (cit. on p. 44).

[57] William H. Sr. Todt. "Characteristics of self-powered neutron detectors used in power reactors". In: Sept. 1998, pp. 1–8 (cit. on pp. 44, 53).

[58] J. Ziebermayr and H. Bock. "High temperature incore tests of self-powered neutron detectors". In: Jan. 1976, pp. 1–8 (cit. on p. 44).

[59] Helmuth Böck and Juha Rantanen. "Temperature and radiation tests with Pt- and Rh-self-powered neutron detectors". In: *Nuclear Instruments and Methods* 164.1 (1979), pp. 205–207. ISSN: 0029-554X. DOI: https://doi.org/10.1016/0029-554X(79)90455-5. URL: https://www.sciencedirect.com/science/article/pii/0029554X79904555 (cit. on p. 44).

[60] F. Brooks, R. Pringle, and B. Funt. "Pulse Shape Discrimination in a Plastic Scintillator". In: *Nuclear Science, IRE Transactions on* NS-7 (July 1960), pp. 35 –38. DOI: 10.1109/TNS2.1960.4315733 (cit. on p. 46).

[61] Matthieu Hamel et al. "A fluorocarbon plastic scintillator for neutron detection: Proof of concept". In: *Nuclear Instruments and Methods in Physics Research Section A Accelerators Spectrometers Detectors and Associated Equipment* 768 (Dec. 2014), pp. 26–31. DOI: 10.1016/j.nima.2014.09.029 (cit. on p. 46).

[62] Tsahi Gozani, John Stevenson, and Michael King. "Neutron threshold activation detectors (TAD) for the detection of fissions". In: *Nuclear Instruments and Methods in Physics Research Section A: Accelerators, Spectrometers, Detectors and Associated Equipment* 652 (Oct. 2011), pp. 334–337. DOI: 10.1016/j.nima.2011.01.029 (cit. on p. 46).

[63] V. Ryzhikov et al. "Detection of gamma-neutron radiation by novel solid-state scintillation detectors". In: Apr. 2015, pp. 1–5. DOI: 10.1109/ANIMMA.2015.7465541 (cit. on p. 46).

[64] Michal Košťál et al. "Measurement and calculation of fast neutron and gamma spectra in well defined cores in LR-0 reactor". In: *Applied Radiation and Isotopes* 120 (Nov. 2016). DOI: 10.1016/j.apradiso.2016.11.004 (cit. on p. 46).

[65] Takayuki Yanagida et al. "Temperature Dependence of Scintillation Properties of Bright Oxide Scintillators for Well-Logging". In: *Japanese Journal of Applied Physics* 52 (July 2013), pp. 6401–. DOI: 10.7567/JJAP.52.076401 (cit. on p. 46).

[66] Noriaki Kawaguchi et al. "Temperature dependence of scintillation responses in rare-earth-ions-doped LiCaAlF6 single crystals". In: *Nuclear Instruments and Methods in Physics Research Section A: Accelerators, Spectrometers, Detectors and Associated Equipment* 954 (Nov. 2018). DOI: 10.1016/j.nima.2018.10.196 (cit. on p. 46).

[67] Christian Graf and for collaboration. "Performance of a Highly Granular Scintillator-SiPM Based Hadron Calorimeter Prototype in Strong Magnetic Fields". In: (Nov. 2017) (cit. on p. 47).

[68] Seung Lee et al. "Fast Neutron Detector for Fusion Reactor KSTAR Using Stilbene Scintillator". In: (Dec. 2011) (cit. on pp. 47, 53).

[69] A Lyoussi et al. "I _SMART a collaborative project on innovative sensor for material ageing and radiation testing: European innovative project for SiC applications in harsh media". In: *KIC_Innoenergy, CCAV, I_SMART Proposal/Exhibit* 1 (2012) (cit. on p. 48).

[70] Fatima Issa. "Réalisation de Détecteurs de Neutrons en Carbure de Silicium". PhD thesis. Aix Marseille University, Feb. 2015 (cit. on pp. 48, 250).

[71] D. Szalkai et al. “First tests of silicon-carbide semiconductors as candidate neutron detector for the ITER Test Blanket Modules”. In: June 2013, pp. 1–4. ISBN: 978-1-4799-1047-2. DOI: 10.1109/ANIMMA.2013.6728038 (cit. on pp. 48, 49).

[72] Ruddy, F H, Seidel, J G, Blue, T E, and Miller, D W. *Reactor power monitoring using silicon carbide fast neutron detectors*. 2006 (cit. on p. 49).

[73] Vanessa Vervisch et al. “Thermal neutron detection enhancement by 10B implantation in silicon carbide sensor”. In: *MRS Proceedings* 1693 (Jan. 2014). DOI: 10.1557/opl.2014.691 (cit. on p. 49).

[74] Valentin Valero. “Étude de détections neutroniques, photoniques et de débit de dose absorbée en conditions sévères par détecteurs semi-conducteurs et capteurs calorimétriques”. PhD thesis. Aix Marseille University, Dec. 2023 (cit. on pp. 49, 250).

[75] Jerzy Cetnar and Igor Królikowski. “Methodology development for SiC sensor signal modelling in the nuclear reactor radiation environments”. In: June 2013, pp. 1–7. ISBN: 978-1-4799-1047-2. DOI: 10.1109/ANIMMA.2013.6727995 (cit. on p. 49).

[76] Fausto Franceschini, F.H. Ruddy, and Bojan Petrovic. “Simulation of the Response of Silicon Carbide Fast Neutron Detectors”. In: (Aug. 2009). DOI: 10.1142/9789814271110_0020 (cit. on p. 49).

[77] Jie Liu et al. “Simultaneous measurement of energy spectrum and fluence of neutrons using a diamond detector”. In: *Scientific Reports* 12 (July 2022), p. 12022. DOI: 10.1038/s41598-022-16235-x (cit. on p. 49).

[78] James Ziegler, M.D. Ziegler, and J. Biersack. “The Stopping and Range of Ions in Mater”. In: *Nuclear Instruments and Methods in Physics Research Section B: Beam Interactions with Materials and Atoms* 268 (June 2010), pp. 1818–1823. DOI: 10.1016/j.nimb.2010.02.091 (cit. on p. 50).

[79] R. V. Babcock and H. C. Chang. “SiC neutron detectors high temperature operation, neutron dosimetry”. In: *Proc. Symp. Neutron Detection, Dosimetry Standard* 1 (1963), 613–622 (cit. on p. 50).

[80] Evgenia Kalinina, Alexander Ivanov, and N. Strokan. “Performance of p- n 4H-SiC film nuclear radiation detectors for operation at elevated temperatures (375 °C)”. In: *Technical Physics Letters - TECH PHYS LETT* 34 (Mar. 2008), pp. 210–212. DOI: 10.1134/S1063785008030103 (cit. on p. 50).

[81] Benjamin Kraus et al. “Charge carrier properties of single-crystal CVD diamond up to 473 K”. In: *Nuclear Instruments and Methods in Physics Research Section A: Accelerators, Spectrometers, Detectors and Associated Equipment* 989 (Dec. 2020), p. 164947. DOI: 10.1016/j.nima.2020.164947 (cit. on p. 50).

[82] C. Weiss et al. “High-temperature performance of solid-state sensors up to 500 °C”. In: *Nuclear Instruments and Methods in Physics Research Section A: Accelerators, Spectrometers, Detectors and Associated Equipment* 1040 (July 2022), p. 167182. DOI: 10.1016/j.nima.2022.167182 (cit. on p. 50).

[83] Timothy Garcia et al. “Electron-Hole Pair Generation in SiC High-Temperature Alpha Particle Detectors”. In: *Applied Physics Letters* 103 (Aug. 2013), p. 152108. DOI: 10.1063/1.4824774 (cit. on p. 50).

[84] D. Szalkai et al. “Fast Neutron Detection With 4H-SiC Based Diode Detector up to 500 °C Ambient Temperature”. In: *IEEE Transactions on Nuclear Science* 63 (June 2016), pp. 1491–1498. DOI: 10.1109/TNS.2016.2522921 (cit. on pp. 51, 53).

[85] F.H. Ruddy et al. “Fast Neutron Spectrometry Using Silicon Carbide Detectors”. In: (June 2003). DOI: 10.1142/9789812705563_0043 (cit. on p. 51).

[86] G. Nemtsev et al. “Diagnostic of fusion neutrons on JET tokamak using diamond detector”. In: *AIP Conference Proceedings* 1612 (Aug. 2014), pp. 93–96. DOI: 10.1063/1.4894030 (cit. on p. 51).

[87] B. Hong et al. “Diagnostic of fusion neutrons on EAST tokamak using 4H-SiC detector”. In: *IEEE Transactions on Nuclear Science* 69 (Mar. 2022), pp. 1–1. DOI: 10.1109/TNS.2022.3146180 (cit. on pp. 52, 53).

[88] Elsa Dupin et al. “Theory and modelling for the design of a selective fast neutron self-powered detector for applications in water pool type reactors”. In: Nov. 2023, pp. 1–1. DOI: 10.1109/NSSMICRTSD49126.2023.10338117 (cit. on p. 53).

[89] D. Neamen. *Semiconductor Physics And Devices*. McGraw-Hill Series in Electrical and Computer Engineering. McGraw-Hill Education, 2003. ISBN: 9780072321074 (cit. on pp. 54, 195).

[90] G. Lutz. *Semiconductor Radiation Detectors: Device Physics*. Springer Berlin Heidelberg, 2007. ISBN: 9783540716785 (cit. on p. 54).

[91] S.M. Sze, Y. Li, and K.K. Ng. *Physics of Semiconductor Devices*. Wiley, 2021. ISBN: 9781119429111 (cit. on p. 54).

[92] Vadim Emtsev et al. “Frenkel pairs in silicon and germanium”. In: *Radiation Effects and Defects in Solids - RADIAT EFF DEFECT SOLID* 111-112 (Dec. 1989), pp. 99–118. DOI: 10.1080/10420158908212986 (cit. on p. 56).

[93] W. Brown, W. Augustyniak, and T. Waite. “Annealing of Radiation Defects in Semiconductors”. In: *Journal of Applied Physics* 30 (Sept. 1959), pp. 1258 –1268. DOI: 10.1063/1.1735303 (cit. on p. 57).

[94] P. Drude. “Zur Elektronentheorie der Metalle”. In: *Annalen der Physik* 306.3 (1900), pp. 566–613. DOI: https://doi.org/10.1002/andp.19003060312. eprint: https://onlinelibrary.wiley.com/doi/pdf/10.1002/andp.19003060312. URL: https://onlinelibrary.wiley.com/doi/abs/10.1002/andp.19003060312 (cit. on p. 60).

[95] M. Costato, S. Fontanesi, and L. Reggiani. “Electron energy relaxation time in Si and Ge”. In: *Journal of Physics and Chemistry of Solids* 34.3 (1973), pp. 547–564. ISSN: 0022-3697. DOI: https://doi.org/10.1016/0022-3697(73)90050-4. URL: https://www.sciencedirect.com/science/article/pii/0022369773900504 (cit. on p. 60).

[96] Shoma Yamashita and Tsunenobu Kimoto. “Analysis of carrier lifetimes in n-type 4H-SiC by rate equations”. In: *Applied Physics Express* 13.1 (Dec. 2019), p. 011006. DOI: 10.7567/1882-0786/ab5b42. URL: https://doi.org/10.7567/1882-0786/ab5b42 (cit. on p. 63).

[97] Lindefelt Galeskas Grivickas. *Silicon Carbide, III-nitrides and Related Materials: ICSCIII-N97 : Proceedings of the 7th International Conference on Silicon Carbide, III-Nitrides and Related Materials, Stockholm, Sweden*. Materials science forum. Trans Tech Publications, 1998. ISBN: 9780878497904 (cit. on p. 63).

[98] S. Ramo. “Currents Induced by Electron Motion”. In: *Proceedings of the IRE* 27.9 (1939), pp. 584–585. DOI: 10.1109/JRPROC.1939.228757 (cit. on p. 65).

[99] W. Shockley. “Currents to Conductors Induced by a Moving Point Charge”. In: *Journal of Applied Physics* 9.10 (Oct. 1938), pp. 635–636. ISSN: 0021-8979. DOI: 10.1063/1.1710367. URL: https://doi.org/10.1063/1.1710367 (cit. on p. 65).

[100] H. Pernegger et al. “Charge-carrier properties in synthetic single-crystal diamond measured with the transient-current technique”. In: *Journal of Applied Physics* 97.7 (Mar. 2005), p. 073704. ISSN: 0021-8979. DOI: 10.1063/1.1863417. eprint: https://pubs.aip.org/aip/jap/article-pdf/doi/10.1063/1.1863417/10659061/073704_1_online.pdf. URL: https://doi.org/10.1063/1.1863417 (cit. on p. 67).

[101] Martin Green. “Intrinsic Concentration, Effective Density of States and Effective Mass of Silicon”. In: *Journal of Applied Physics* 67 (Apr. 1990), pp. 2944 –2954. DOI: 10.1063/1.345414 (cit. on p. 68).

[102] Alistair Sproul and Martin Green. “Intrinsic carrier concentration and minority-carrier mobility of silicon from 77 to 300 K”. In: *Journal of Applied Physics* 73 (Mar. 1993), pp. 1214 –1225. DOI: 10.1063/1.353288 (cit. on p. 68).

[103] J.B. Casady and R.W. Johnson. “Status of silicon carbide (SiC) as a wide-bandgap semiconductor for high-temperature applications: A review”. In: *Solid-State Electronics* 39.10 (1996), pp. 1409–1422. ISSN: 0038-1101. DOI: https://doi.org/10.1016/0038-1101(96)00045-7. URL: https://www.sciencedirect.com/science/article/pii/0038110196000457 (cit. on p. 68).

[104] W.J. Choyke. “OPTICAL PROPERTIES OF POLYTYPES OF SiC: INTERBAND ABSORPTION, AND LUMINESCENCE OF NITROGEN-EXCITON COMPLEXES**The research reported in this paper was sponsored in part by the Air Force Cambridge Research Laboratories, Office of Aerospace Research, under Contract AF 19(628)-68-C-0272, but the report does not necessarily reflect endorsement by the sponsor.” In: *Silicon Carbide–1968*. Ed. by H.K. HENISCH and R. ROY. Pergamon, 1969, S141–S152. ISBN: 978-0-08-006768-1. DOI: https://doi.org/10.1016/B978-0-08-006768-1.50018-8. URL: https://www.sciencedirect.com/science/article/pii/B9780080067681500188 (cit. on p. 68).

[105] Filippo Nava et al. “Electron effective masses and lattice scattering in natural diamond”. In: *Solid State Communications* 33 (Jan. 1980), pp. 475–477. DOI: 10.1016/0038-1098(80)90447-0 (cit. on p. 69).

[106] Karl Hecht. “Zum Mechanismus des lichtelektrischen Primärstromes in isolierenden Kristallen”. In: *Zeitschrift fur Physik* 77.3-4 (Mar. 1932), pp. 235–245. DOI: 10.1007/BF01338917 (cit. on p. 69).

[107] Zheng Li and H.W. Kraner. “Modeling and simulation of charge collection properties for neutron irradiated silicon detectors”. In: *Nuclear Physics B - Proceedings Supplements* 32 (1993), pp. 398–409. ISSN: 0920-5632. DOI: https://doi.org/10.1016/0920-5632(93)90052-8. URL: https://www.sciencedirect.com/science/article/pii/0920563293900528 (cit. on p. 70).

[108] Gary L. Harris and Inspec. “Properties of silicon carbide”. In: 1995. URL: https://api.semanticscholar.org/CorpusID:93027729 (cit. on p. 71).

[109] P. Bergonzo et al. “Improving diamond detectors: A device case”. In: *Diamond and Related Materials* 16.4 (2007). Proceedings of Diamond 2006, the 17th European Conference on Diamond, Diamond-Like Materials, Carbon Nanotubes, Nitrides and Silicon Carbide, pp. 1038–1043. ISSN: 0925-9635. DOI: https://doi.org/10.1016/j.diamond.2006.11.099. URL: https://www.sciencedirect.com/science/article/pii/S0925963506004870 (cit. on p. 72).

[110] G.F. Knoll. *Radiation Detection and Measurement*. Wiley, 2010. ISBN: 9780470131480 (cit. on pp. 75, 85).

[111] Dermott E. Cullen. “A Survey of Photon Cross Section Data for use in EPICS 2017”. In: 2017. URL: https://api.semanticscholar.org/CorpusID:106398326 (cit. on p. 75).

[112] M.J. Berger et al. "XCOM: Photon cross sections database". In: *NIST Standard Reference Database* 8 (Jan. 2009), pp. 87–3597 (cit. on pp. 76, 77).

[113] H. Bethe. "Zur Theorie des Durchgangs schneller Korpuskularstrahlen durch Materie". In: *Annalen der Physik* 397.3 (Jan. 1930), pp. 325–400. DOI: 10.1002/andp.19303970303 (cit. on p. 78).

[114] M J Berger. *ESTAR PSTAR ASTAR, Stopping Power and Range of Electrons, Protons, Alpha*. June 1995 (cit. on pp. 78, 79).

[115] James F. Ziegler, M. D. Ziegler, and J. P. Biersack. "SRIM - The stopping and range of ions in matter (2010)". In: *Nuclear Instruments and Methods in Physics Research B* 268.11-12 (June 2010), pp. 1818–1823. DOI: 10.1016/j.nimb.2010.02.091 (cit. on pp. 79–84).

[116] P. Sigmund. *Stopping of Heavy Ions: A Theoretical Approach*. Springer Tracts in Modern Physics. Springer Berlin Heidelberg, 2004. ISBN: 9783540222736 (cit. on p. 79).

[117] M. Ahsan Zeb et al. "Electronic Stopping Power in Gold: The Role of *d* Electrons and the **H**/He Anomaly". In: *Phys. Rev. Lett.* 108 (22 May 2012), p. 225504. DOI: 10.1103/PhysRevLett.108.225504. URL: https://link.aps.org/doi/10.1103/PhysRevLett.108.225504 (cit. on p. 79).

[118] Rafi Ullah et al. "Electronic stopping power in a narrow band gap semiconductor from first principles". In: *Phys. Rev. B* 91 (12 Mar. 2015), p. 125203. DOI: 10.1103/PhysRevB.91.125203. URL: https://link.aps.org/doi/10.1103/PhysRevB.91.125203 (cit. on p. 79).

[119] James F. Ziegler and Jochen P. Biersack. "The Stopping and Range of Ions in Matter". In: *Treatise on Heavy-Ion Science: Volume 6: Astrophysics, Chemistry, and Condensed Matter*. Ed. by D. Allan Bromley. Boston, MA: Springer US, 1985, pp. 93–129. ISBN: 978-1-4615-8103-1. DOI: 10.1007/978-1-4615-8103-1_3. URL: https://doi.org/10.1007/978-1-4615-8103-1_3 (cit. on p. 80).

[120] J. R. Comfort et al. "Energy Loss and Straggling of Alpha Particles in Metal Foils". In: *Phys. Rev.* 150 (1 Oct. 1966), pp. 249–256. DOI: 10.1103/PhysRev.150.249. URL: https://link.aps.org/doi/10.1103/PhysRev.150.249 (cit. on p. 83).

[121] A. Lyoussi. *Détection de rayonnements et instrumentation nucléaire*. Génie Atomique. EDP Sciences, 2012. ISBN: 9782759809127 (cit. on p. 85).

[122] *NOVASiC*. https://www.novasic.com/. Accessed: 2023-02-22 (cit. on p. 91).

[123] *Soitec*. https://www.soitec.com/fr/ (cit. on p. 91).

[124] Werner Kern. "The Evolution of Silicon Wafer Cleaning Technology". In: *Journal of The Electrochemical Society* 137.6 (June 1990), pp. 1887–1892. DOI: 10.1149/1.2086825. URL: https://doi.org/10.1149/1.2086825 (cit. on p. 92).

[125] Farah Laariedh. "Technologie d'intégration monolithique des JFET latéraux". PhD thesis. EEA de Lyon, Jan. 2013 (cit. on p. 92).

[126] Michael Houry. *Solid State Sensor*. CEA, 2000 (cit. on p. 97).

[127] A. Michalowicz. *Cinématique des réactions nucléaires*. Monographies Dunod. Dunod, 1964 (cit. on p. 100).

[128] B. Antolković and Z. Dolenec. "The neutron-induced 12C(n, n')3alpha reaction at 14.4 MeV in a kinematically complete experiment". In: *Nuclear Physics A* 237 (Jan. 1975), pp. 235–252. DOI: 10.1016/0375-9474(75)90422-4 (cit. on p. 100).

[129] B. Antolkovic, Günther Dietze, and H. Klein. "Reaction Cross Sections on Carbon for Neutron Energies from 11.5 to 19 MeV". In: *Nuclear Science and Engineering; (United States)* 107:1 (Jan. 1991). DOI: 10.13182/NSE91-A23777 (cit. on p. 100).

[130] F.H. Ruddy and John Seidel. "The effects of intense gamma-irradiation on the alpha-particle response of silicon carbide semiconductor radiation detectors". In: *Nuclear Instruments & Methods in Physics Research Section B-beam Interactions With Materials and Atoms - NUCL INSTRUM METH PHYS RES B* 263 (Oct. 2007), pp. 163–168. DOI: 10.1016/j.nimb.2007.04.077 (cit. on p. 105).

[131] Keitaro Kondo et al. "Measurement and analysis of neutron-induced alpha particle emission double-differential cross section of carbon at 14.2 MeV". In: *Journal of Nuclear Science and Technology* 45 (Feb. 2008), pp. 103–115. DOI: 10.1080/18811248.2008.9711420 (cit. on p. 111).

[132] M. Shamsuzzoha Basunia. "Nuclear Data Sheets for A = 28". In: *Nuclear Data Sheets* 114.10 (2013), pp. 1189–1291. ISSN: 0090-3752. DOI: https://doi.org/10.1016/j.nds.2013.10.001. URL: https://www.sciencedirect.com/science/article/pii/S0090375213000653 (cit. on pp. 112, 113).

[133] D.A. Brown, M.B. Chadwick, R. Capote, et al. "ENDF/B-VIII.0: The 8th Major Release of the Nuclear Reaction Data Library with CIELO-project Cross Sections, New Standards and Thermal Scattering Data". In: *Nuclear Data Sheets* 148 (2018). Special Issue on Nuclear Reaction Data, pp. 1 –142. ISSN: 0090-3752. DOI: https://doi.org/10.1016/j.nds.2018.02.001. URL: https://www.sciencedirect.com/science/article/pii/S0090375218300206 (cit. on pp. 112, 115, 116, 124).

[134] E. Rutherford. "LXXIX. The scattering of alpha and beta particles by matter and the structure of the atom". In: *The London, Edinburgh, and Dublin Philosophical Magazine and Journal of Science* 21.125 (1911), pp. 669–688. DOI: 10.1080/14786440508637080. eprint: https://doi.org/10.1080/14786440508637080. URL: https://doi.org/10.1080/14786440508637080 (cit. on p. 119).

[135] Laurie S. Waters et al. "The MCNPX Monte Carlo Radiation Transport Code". In: *AIP Conference Proceedings* 896.1 (Mar. 2007), pp. 81–90. ISSN: 0094-243X. DOI: 10.1063/1.2720459. eprint: https://pubs.aip.org/aip/acp/article-pdf/896/1/81/11572103/81_1_online.pdf. URL: https://doi.org/10.1063/1.2720459 (cit. on p. 121).

[136] Alfredo Ferrari et al. "FLUKA: A multi-particle transport code (Program version 2005)". In: (Oct. 2005). DOI: 10.2172/877507 (cit. on p. 121).

[137] Stefano Agostinelli et al. "GEANT4-a simulation toolkit". In: *Nuclear Instruments and Methods in Physics Research Section A Accelerators Spectrometers Detectors and Associated Equipment* 506 (July 2003), p. 250. DOI: 10.1016/S0168-9002(03)01368-8 (cit. on p. 121).

[138] Koji Niita et al. "PHITS: A particle and heavy ion transport code system". In: *Radiat. Meas.* 41 (2006), pp. 1080–1090. DOI: 10.1016/j.radmeas.2006.07.013 (cit. on p. 121).

[139] Fausto Franceschini, F.H. Ruddy, and Bojan Petrovic. "Simulation of the Response of Silicon Carbide Fast Neutron Detectors". In: (Aug. 2009). DOI: 10.1142/9789814271110_0020 (cit. on p. 121).

[140] Alberto Milocco et al. "Monte Carlo simulation of the experimental pulse height spectra produced in diamond detectors by quasi-mono-energetic neutrons". In: *Nuclear Instruments and Methods in Physics Research Section A: Accelerators, Spectrometers, Detectors and Associated Equipment* 720 (Aug. 2013), 74–77. DOI: 10.1016/j.nima.2012.12.031 (cit. on p. 121).

[141] Plompen A et al. “The Joint Evaluated Fission and Fusion Nuclear Data Library, JEFF-3.3”. In: *EUROPEAN PHYSICAL JOURNAL A* 56 (2020), p. 181. ISSN: 1434-6001 (online). DOI: 10.1140/epja/s10050-020-00141-9(online). URL: https://rdcu.be/b5CJV (cit. on p. 123).

[142] L. Thulliez, C. Jouanne, and E. Dumonteil. “Improvement of Geant4 Neutron-HP package: From methodology to evaluated nuclear data library”. In: *Nuclear Instruments and Methods in Physics Research Section A: Accelerators, Spectrometers, Detectors and Associated Equipment* 1027 (2022), p. 166187. ISSN: 0168-9002. DOI: https://doi.org/10.1016/j.nima.2021.166187. URL: https://www.sciencedirect.com/science/article/pii/S016890022101055X (cit. on p. 123).

[143] G. Folger, VN Ivanchenko, and Johannes Wellisch. “The Binary Cascade: Nucleon nuclear reactions”. In: *The European Physical Journal A - Hadrons and Nuclei* 21 (Sept. 2004), pp. 407–417. DOI: 10.1140/epja/i2003-10219-7 (cit. on p. 123).

[144] Aatos Heikkinen, Nikita Stepanov, and J. P. Wellisch. *Bertini intra-nuclear cascade implementation in Geant4*. 2003. arXiv: nucl-th/0306008 [nucl-th] (cit. on p. 123).

[145] C. L. Dunford. “Evaluated Nuclear Data File, ENDF/B-VI”. In: *Nuclear Data for Science and Technology*. Ed. by Syed M. Qaim. Berlin, Heidelberg: Springer Berlin Heidelberg, 1992, pp. 788–792. ISBN: 978-3-642-58113-7 (cit. on p. 123).

[146] F. Hoyle. “On Nuclear Reactions Occuring in Very Hot STARS.I. the Synthesis of Elements from Carbon to Nickel.” In: *Astrophysical Journal Supplement* 1 (Sept. 1954), p. 121. DOI: 10.1086/190005 (cit. on p. 124).

[147] M. Freer and H.O.U. Fynbo. “The Hoyle state in 12C”. In: *Progress in Particle and Nuclear Physics* 78 (2014), pp. 1–23. ISSN: 0146-6410. DOI: https://doi.org/10.1016/j.ppnp.2014.06.001. URL: https://www.sciencedirect.com/science/article/pii/S0146641014000453 (cit. on p. 124).

[148] Randall S. Caswell and J. Joseph Coyne. “Interaction of Neutrons and Secondary Charged Particles with Tissue: Secondary Particle Spectra”. In: *Radiation Research* 52.3 (1972), pp. 448–470. ISSN: 00337587, 19385404. URL: http://www.jstor.org/stable/3573505 (visited on 06/01/2024) (cit. on p. 124).

[149] Keiichi SHIBATA et al. “JENDL-4.0: A New Library for Nuclear Science and Engineering”. In: *Journal of Nuclear Science and Technology* 48.1 (2011), pp. 1–30. DOI: 10.1080/18811248.2011.9711675. eprint: https://doi.org/10.1080/18811248.2011.9711675. URL: https://doi.org/10.1080/18811248.2011.9711675 (cit. on p. 124).

[150] G. Dietze and H. Klein. *NRESP 4 and NEFF 4, Monte Carlo codes for the calculation of neutron response functions and detection efficiencies for NE 213 scintillation detectors*. Bericht: ND. Bundesanst., 1982 (cit. on pp. 124, 125).

[151] Aczel García et al. “New physics model in GEANT4 for the simulation of neutron interactions with organic scintillation detectors”. In: *Nuclear Instruments and Methods in Physics Research Section A: Accelerators, Spectrometers, Detectors and Associated Equipment* 868 (June 2017). DOI: 10.1016/j.nima.2017.06.021 (cit. on p. 125).

[152] Francesca Villa. *GENEPI2 : générateur de neutrons pulsés*. Journée Dispositifs et Installations Instrumentales Orientés Détecteurs (Fabrication, Tests, Calibration). Poster. June 2015. URL: https://hal.in2p3.fr/in2p3-01171928 (cit. on p. 131).

[153] Benjamin Cheymol. *GENEPI2 Simulations*. Tech. rep. UNIVERSITE GRENOBLE ALPES, Laboratoire de Physique Subatomique et de Cosmologie, Mar. 2023 (cit. on p. 133).

[154] Pavel Bem et al. “Angular Anisotropy of the 3H(d, α) n Reaction at Deuteron Energies Below 200 keV”. In: *Few-Body Systems* 22 (1997), pp. 77–89. URL: https://api.semanticscholar.org/CorpusID:124881480 (cit. on p. 133).

[155] Alberto Milocco and Andrej Trkov. “Modelling of the Production of Source Neutrons from Low-Voltage Accelerated Deuterons on Titanium-Tritium Targets”. In: *Science and Technology of Nuclear Installations* 2008 (Jan. 2008). DOI: 10.1155/2008/340282 (cit. on p. 134).

[156] M. Rajput et al. “Tritium-titanium target degradation due to deuterium irradiation for DT neutron production”. In: *Nuclear Fusion* 63.6 (May 2023), p. 066033. DOI: 10.1088/1741-4326/accd80. URL: https://dx.doi.org/10.1088/1741-4326/accd80 (cit. on p. 134).

[157] *Cividec Instrumentation*. https://cividec.at/ (cit. on p. 135).

[158] *Cividec Instrumentation - Signal Acquisition Solutions*. https://acqiris.com/ (cit. on p. 136).

[159] Q. Potiron, C. Destouches, L. Dubus, M. Houry, O. Llido, A. Lyoussi, L. Ottaviani, C. Reynard-Carette. “Modelling of a SiC Based Detector for the Interpretation of 14.1 MeV Neutrons Measurements”. In: *EPJ Web of Conferences* 288 (Nov. 2023), p. 03001. DOI: 10.1051/epjconf/202328803001 (cit. on pp. 139, 142).

[160] Q. Potiron and C. Destouches and M. Houry and O. Llido and A. Lyoussi and C. Reynard-Carette. “Comparison of Solid-State Neutron Detectors for 14 MeV Neutron Measurement under High Temperature up to 500°C.” In: (2024). Submitted for publication to *SOFT2024* September 2024 (cit. on p. 139).

[161] Q. Potiron, C. Destouches, L. Dubus, M. Houry, O. Llido, A. Lyoussi, L. Ottaviani, C. Reynard-Carette, F.H. Ruddy. “Estimation of the Fast-Neutron Fluence Rate with a 4H-SiC Based Detector in a 14.1 MeV Mono-Energetic Field”. In: *IEEE Transactions on Nuclear Science* PP (Dec. 2023), pp. 1–1. DOI: 10.1109/TNS.2023.3348147 (cit. on pp. 142, 151).

[162] Shifan Zhao, Georgia Lioliou, and A. Barnett. “X-ray spectrometer with a low-cost SiC photodiode”. In: *Nuclear Instruments and Methods in Physics Research, Section A: Accelerators, Spectrometers, Detectors and Associated Equipment* 887 (Apr. 2018), pp. 138–143. DOI: 10.1016/j.nima.2018.01.054 (cit. on p. 146).

[163] Alessandro Giudice et al. “Average energy dissipated by mega-electron-volt hydrogen and helium ions per electron-hole pair generation in 4H-SiC”. In: *Applied Physics Letters* 87 (Nov. 2005), pp. 222105–222105. DOI: 10.1063/1.2135507 (cit. on p. 146).

[164] Sandeep Chaudhuri, Kelvin Zavalla, and Krishna Mandal. “Experimental determination of electron-hole pair creation energy in 4H-SiC epitaxial layer: An absolute calibration approach”. In: *Applied Physics Letters* 102 (Jan. 2013), p. 31109 (cit. on p. 146).

[165] F.H. Ruddy et al. “The fast neutron response of 4H silicon carbide semiconductor radiation detectors”. In: *Nuclear Science, IEEE Transactions on* 53 (July 2006), pp. 1666 –1670. DOI: 10.1109/TNS.2006.875151 (cit. on p. 146).

[166] G.F. Knoll. *Radiation Detection and Measurement*. Radiation Detection and Measurement vol. 415. Wiley, 1979. ISBN: 9780471495451 (cit. on p. 146).

[167] I.M Sobol. “Global sensitivity indices for nonlinear mathematical models and their Monte Carlo estimates”. In: *Mathematics and Computers in Simulation* 55.1 (2001). The Second IMACS Seminar on Monte Carlo Methods, pp. 271–280. ISSN: 0378-4754. DOI: https://doi.org/10.1016/S0378-4754(00)00270-6. URL: https://www.sciencedirect.com/science/article/pii/S0378475400002706 (cit. on pp. 153, 252).

[168] Luca Dioni. “Development of a Multi-purpose Fast Neutron Spectrometric Capability in the MASURCA Facility”. Thèse de doctorat. Aix Marseille Université, 2017 (cit. on pp. 158, 161).

[169] Augusto Di Chicco. “Characterization of a stilbene organic scintillator for use as a broad-band neutron spectrometer in mixed radiations fields”. Thèse de doctorat. Aix Marseille Université, 2022 (cit. on pp. 158, 161).

[170] A. N. Tikhonov. “Solution of incorrectly formulated problems and the regularization method”. In: *Soviet Math. Dokl.* 4 (1963), pp. 1035–1038 (cit. on p. 160).

[171] Per Christian Hansen. “The truncatedSVD as a method for regularization”. In: *BIT* 27.4 (Dec. 1987), 534–553. ISSN: 0006-3835. DOI: 10.1007/BF01937276. URL: https://doi.org/10.1007/BF01937276 (cit. on p. 161).

[172] G. D’Agostini. “A multidimensional unfolding method based on Bayes’ theorem”. In: *Nuclear Instruments and Methods in Physics Research Section A: Accelerators, Spectrometers, Detectors and Associated Equipment* 362.2 (1995), pp. 487–498. ISSN: 0168-9002. DOI: https://doi.org/10.1016/0168-9002(95)00274-X. URL: https://www.sciencedirect.com/science/article/pii/016890029500274X (cit. on p. 161).

[173] James Bourbeau and Zigfried Hampel-Arias. “PyUnfold: A Python package for iterative unfolding”. In: *The Journal of Open Source Software* 3.26 (June 2018), p. 741. DOI: 10.21105/joss.00741. URL: https://doi.org/10.21105/joss.00741 (cit. on p. 162).

[174] R. Alfaro et al. “All-particle cosmic ray energy spectrum measured by the HAWC experiment from 10 to 500 TeV”. In: *Phys. Rev. D* 96 (12 Dec. 2017), p. 122001. DOI: 10.1103/PhysRevD.96.122001. URL: https://link.aps.org/doi/10.1103/PhysRevD.96.122001 (cit. on p. 162).

[175] X. Ledoux et al. “The Neutrons for Science Facility at SPIRAL-2”. In: *Nuclear Data Sheets* 119 (2014), pp. 353–356. ISSN: 0090-3752. DOI: https://doi.org/10.1016/j.nds.2014.08.097. URL: https://www.sciencedirect.com/science/article/pii/S0090375214006310 (cit. on p. 163).

[176] X. Ledoux et al. “First beams at neutrons for science”. In: *The European Physical Journal A* 57.8 (Aug. 2021). ISSN: 1434-601X. DOI: 10.1140/epja/s10050-021-00565-x. URL: http://dx.doi.org/10.1140/epja/s10050-021-00565-x (cit. on p. 164).

[177] Xavier Ledoux. *NFS Simulations*. Tech. rep. CEA/DRF - CNRS/IN2P3, Oct. 2023 (cit. on p. 176).

[178] M.J. Saltmarsh et al. “Characteristics of an intense neutron source based on the d+Be reaction”. In: *Nuclear Instruments and Methods* 145.1 (1977), pp. 81–90. ISSN: 0029-554X. DOI: https://doi.org/10.1016/0029-554X(77)90559-6. URL: https://www.sciencedirect.com/science/article/pii/0029554X77905596 (cit. on p. 182).

[179] Xavier Ledoux. “The Neutrons For Science Facility”. In: JEFF nuclear data week, 22-26 April 2024, 2024 (cit. on p. 182).

[180] Diane Doré. “T235U fission fragment study with Falstaff at NFS”. In: 2024 (cit. on p. 182).

[181] Y.P. Varshni. “Temperature dependence of the energy gap in semiconductors”. In: *Physica* 34.1 (1967), pp. 149–154. ISSN: 0031-8914. DOI: https://doi.org/10.1016/0031-8914(67)90062-6. URL: https://www.sciencedirect.com/science/article/pii/0031891467900626 (cit. on p. 187).

[182] H. D. Vasileff. "Electron Self-Energy and Temperature-Dependent Effective Masses in Semiconductors: *n*-Type Ge and Si". In: *Phys. Rev.* 105 (2 Jan. 1957), pp. 441–446. DOI: 10.1103/PhysRev.105.441. URL: https://link.aps.org/doi/10.1103/PhysRev.105.441 (cit. on p. 187).

[183] E. N. Adams. "Vasileff's Calculation of Electronic Self-Energy in Semiconductors". In: *Phys. Rev.* 107 (3 Aug. 1957), pp. 671–671. DOI: 10.1103/PhysRev.107.671. URL: https://link.aps.org/doi/10.1103/PhysRev.107.671 (cit. on p. 187).

[184] Lyle Patrick, Wolfgang Choyke, and D. Hamilton. "Luminescence of 4H SiC, and Location of Conduction-Band Minima in SiC Polytypes". In: *Physical Review* 137 (Mar. 1965). DOI: 10.1103/PhysRev.137.A1515 (cit. on p. 188).

[185] Martin Lades. "Modeling and Simulation of Wide Bandgap Semiconductor Devices: 4H/6H-SiC". Available at https://api.semanticscholar.org/CorpusID:107268524. PhD thesis. Munich, Germany: Technischen Universitat Munchen, 2000 (cit. on p. 188).

[186] G. Wellenhofer and U. Rössler. "Global Band Structure and Near-Band-Edge States". In: *physica status solidi (b)* 202.1 (1997), pp. 107–123. DOI: https://doi.org/10.1002/1521-3951(199707)202:1<107::AID-PSSB107>3.0.CO;2-9. eprint: https://onlinelibrary.wiley.com/doi/pdf/10.1002/1521-3951%28199707%29202%3A1%3C107%3A%3AAID-PSSB107%3E3.0.CO%3B2-9. URL: https://onlinelibrary.wiley.com/doi/abs/10.1002/1521-3951%28199707%29202%3A1%3C107%3A%3AAID-PSSB107%3E3.0.CO%3B2-9 (cit. on p. 189).

[187] P. Debye. "Zur Theorie der spezifischen Wärmen". In: *Annalen der Physik* 344.14 (1912), pp. 789–839. DOI: https://doi.org/10.1002/andp.19123441404. eprint: https://onlinelibrary.wiley.com/doi/pdf/10.1002/andp.19123441404. URL: https://onlinelibrary.wiley.com/doi/abs/10.1002/andp.19123441404 (cit. on p. 190).

[188] William Schaffer et al. "Conductivity Anisotropy in Epitaxial 6H and 4H Sic". In: *MRS Proceedings* 339 (Jan. 1994). DOI: 10.1557/PROC-339-595 (cit. on pp. 190, 303).

[189] Tesfaye Ayalew. "SiC Semiconductor Devices, Technology, Modeling, and Simulation". Available at https://repositum.tuwien.at/handle/20.500.12708/20405. PhD thesis. Wien, Austria: Technishen Universitaet Wien, 2004 (cit. on pp. 190, 303).

[190] Wolfgang Choyke and G. Pensl. "Physical Properties of SiC". In: *MRS Bulletin* 22 (Mar. 2013), pp. 25–29. DOI: 10.1557/S0883769400032723 (cit. on pp. 190, 303).

[191] Narain Arora, John Hauser, and David Roulston. "Electron and Hole Mobilities in Silicon as a function of Concentration and Temperature". In: *Electron Devices, IEEE Transactions on* 29 (Mar. 1982), pp. 292 –295. DOI: 10.1109/T-ED.1982.20698 (cit. on pp. 190, 212, 303).

[192] Masetti Guido, Mirko Severi, and Sandro Solmi. "Modeling Of Carrier Mobility Against Carrier Concentration In Arsenic-, Phosphorus-, and boron-doped silicon". In: *Electron Devices, IEEE Transactions on* 30 (Aug. 1983), pp. 764 –769. DOI: 10.1109/T-ED.1983.21207 (cit. on pp. 190, 303).

[193] D.B.M. Klaassen. "A unified mobility model for device simulation—I. Model equations and concentration dependence". In: *Solid-State Electronics* 35.7 (1992), pp. 953–959. ISSN: 0038-1101. DOI: https://doi.org/10.1016/0038-1101(92)90325-7. URL: https://www.sciencedirect.com/science/article/pii/0038110192903257 (cit. on p. 190).

[194] Hiu Wong. "TCAD Simulation Models, Parameters, and Methodologies for beta-Ga2O3 Power Devices". In: *ECS Journal of Solid State Science and Technology* 12 (May 2023). DOI: 10.1149/2162-8777/accfbe (cit. on p. 190).

[195] C. Canali et al. "Canali, C., Majni, G., Minder, R. Ottaviani, G. Electron and hole drift velocity measurements in silicon and their empirical relation to electric field and temperature. IEEE Trans. Electron. Dev. 22, 1045-1047". In: *Electron Devices, IEEE Transactions on* 22 (Dec. 1975), pp. 1045 –1047. DOI: 10.1109/T-ED.1975.18267 (cit. on pp. 192, 212, 304).

[196] B. Meinerzhagen and Walter Engl. "The influence of the thermal equilibrium approximation on the accuracy of classical two-dimensional numerical modeling of silicon submicrometer MOS transistors". In: *Electron Devices, IEEE Transactions on* 35 (June 1988), pp. 689 –697. DOI: 10.1109/16.2514 (cit. on pp. 192, 305).

[197] Synopsys technology. *Synopsys*. URL: https://www.synopsys.com/ (cit. on p. 193).

[198] Silvaco. *Silvaco*. URL: https://silvaco.com/ (cit. on p. 193).

[199] Crosslight. *Crosslight*. URL: https://crosslight.com/ (cit. on p. 193).

[200] S.M. Sze and M.K. Lee. *Semiconductor Devices: Physics and Technology*. J. Wiley & Sons., 2013. ISBN: 9788126556755 (cit. on p. 195).

[201] Mélanie Raine et al. "Improved Simulation of Ion Track Structures Using New Geant4 Models—Impact on the Modeling of Advanced Technologies Response". In: *IEEE Transactions on Nuclear Science* 59.6 (2012), pp. 2697–2703. DOI: 10.1109/TNS.2012.2220783 (cit. on p. 200).

[202] Q. Gibaru et al. "Geant4 physics processes for microdosimetry and secondary electron emission simulation: Extension of MicroElec to very low energies and 11 materials (C, Al, Si, Ti, Ni, Cu, Ge, Ag, W, Kapton and SiO2)". In: *Nuclear Instruments and Methods in Physics Research Section B: Beam Interactions with Materials and Atoms* 487 (2021), pp. 66–77. ISSN: 0168-583X. DOI: https://doi.org/10.1016/j.nimb.2020.11.016. URL: https://www.sciencedirect.com/science/article/pii/S0168583X20304973 (cit. on p. 200).

[203] Maria Rizzi, Michele Maurantonio, and Beniamino Castagnolo. "3D- finite element model for GaAs alpha-particles pixel detector". In: (Feb. 2005), p. 16 (cit. on p. 200).

[204] Ke Li et al. "Simulation of heavy ion irradiation effect on 3D MOSFET". In: *AIP Advances* 13.2 (Feb. 2023), p. 025143. ISSN: 2158-3226. DOI: 10.1063/5.0131345. URL: https://doi.org/10.1063/5.0131345 (cit. on p. 200).

[205] *Neyco*. https://www.neyco.fr/en. Accessed: 2023-01-12 (cit. on p. 205).

[206] *Heating elements for electrical heating technology*. https://www.electricalheat.com/. Accessed: 2023-01-12 (cit. on p. 205).

[207] Claude A. Klein. "Bandgap Dependence and Related Features of Radiation Ionization Energies in Semiconductors". In: *Journal of Applied Physics* 39 (1968), pp. 2029–2038. URL: https://api.semanticscholar.org/CorpusID:120874058 (cit. on p. 217).

[208] Lyle Patrick, W. J. Choyke, and D. R. Hamilton. "Luminescence of 4*H* SiC, and Location of Conduction-Band Minima in SiC Polytypes". In: *Phys. Rev.* 137 (5A Mar. 1965), A1515–A1520. DOI: 10.1103/PhysRev.137.A1515. URL: https://link.aps.org/doi/10.1103/PhysRev.137.A1515 (cit. on p. 228).

[209] W. Shockley and W. T. Read. "Statistics of the Recombinations of Holes and Electrons". In: *Physical Review* 87.5 (Sept. 1952), pp. 835–842. DOI: 10.1103/PhysRev.87.835 (cit. on pp. 228, 305).

[210] D.L. Scharfetter and H.K. Gummel. "Large-signal analysis of a silicon Read diode oscillator". In: *IEEE Transactions on Electron Devices* 16.1 (1969), pp. 64–77. DOI: 10.1109/T-ED.1969.16566 (cit. on pp. 229, 305).

[211] M.S. Tyagi and R. Overstraeten. "Minority Carrier Recombination in Heavily-Doped Silicon". In: *Solid-State Electronics* 26 (June 1983), pp. 577–597. DOI: 10.1016/0038-1101(83)90174-0 (cit. on p. 229).

[212] Holger Goebel and K. Hoffmann. "Full dynamic power diode model including temperature behavior for use in circuit simulators". In: Feb. 1992, pp. 130 –135. DOI: 10.1109/ISPSD.1992.991249 (cit. on p. 229).

[213] P.A. Ivanov et al. "Temperature dependence of the current gain in power 4H-SiC NPN BJTs". In: *IEEE Transactions on Electron Devices* 53.5 (2006), pp. 1245–1249. DOI: 10.1109/TED.2006.872701 (cit. on p. 229).

[214] Angela Vasilescu. *Notes on the fuence normalisation based on the NIEL scaling hypothesis*. National Institute for Nuclear Physics and Engineering Horia Hulubei, Bucharest, 2000 (cit. on p. 233).

[215] Moritz Guthoff, Wim de Boer, and Steffen Müller. "Simulation of beam induced lattice defects of diamond detectors using FLUKA". In: *Nuclear Instruments and Methods in Physics Research Section A: Accelerators, Spectrometers, Detectors and Associated Equipment* 735 (2014), pp. 223–228. ISSN: 0168-9002. DOI: https://doi.org/10.1016/j.nima.2013.08.083. URL: https://www.sciencedirect.com/science/article/pii/S0168900213012291 (cit. on p. 234).

[216] F Nava et al. "Silicon carbide and its use as a radiation detector material". In: *Measurement Science and Technology* 19.10 (Aug. 2008), p. 102001. DOI: 10.1088/0957-0233/19/10/102001. URL: https://dx.doi.org/10.1088/0957-0233/19/10/102001 (cit. on p. 237).

[217] Mara Bruzzi et al. "Deep levels and trapping mechanisms in chemical vapor deposited diamond". In: *Journal of Applied Physics - J APPL PHYS* 91 (May 2002). DOI: 10.1063/1.1461891 (cit. on p. 243).

[218] Alexander A. Lebedev. "Deep level centers in silicon carbide: A review". In: *Semiconductors* 33 (1999), pp. 107–130. URL: https://api.semanticscholar.org/CorpusID:96550291 (cit. on p. 244).

[219] C.M. Zetterling and Institution of Electrical Engineers. *Process Technology for Silicon Carbide Devices*. EMIS processing series. INSPEC, 2002. ISBN: 9780852969984. URL: https://books.google.fr/books?id=BYhgjUMPU_sC (cit. on p. 244).

[220] Yongbo Sun et al. "Investigation of the Performance Degradation of 4H-SiC Neutron Detectors Using MCNP and TCAD". In: *IEEE Sensors Journal* 24 (Feb. 2024), pp. 4432–4441. DOI: 10.1109/JSEN.2023.3345407 (cit. on p. 245).

[221] F.H. Ruddy, A.R. Dulloo, and J.G. Seidel. "Study of the radiation resistance of silicon carbide radiation detectors, invited". In: *Transactions of the American Nuclear Society* 90 (Jan. 2004), pp. 348–349 (cit. on p. 248).

[222] Frank H. Ruddy, Sandeep K. Chaudhuri, and Krishna C. Mandal. "A Review of the Effects of Fast-Neutron Irradiation on the Performance of 4H-SiC Schottky Barrier Detectors". In: *IEEE Transactions on Nuclear Science* 71.5 (2024), pp. 1056–1063. DOI: 10.1109/TNS.2024.3355293 (cit. on p. 248).

[223] Olga Obraztsova. "Comparaison du Diamant et du Carbure de Silicium (SiC) pour la détection de neutrons en milieux nucléaires". PhD thesis. Aix Marseille University, Oct. 2018 (cit. on p. 250).

[224] Lucas de Arruda. *BG neutron problem report*. Tech. rep. GANIL, Jan. 2024 (cit. on p. 301).

[225] F Gagnon-Moisan, M Reginatto, and A Zimbal. "Results for the response function determination of the Compact Neutron Spectrometer". In: *Journal of Instrumentation* 7.03 (Mar. 2012), p. C03023. DOI: 10.1088/1748-0221/7/03/C03023. URL: https://dx.doi.org/10.1088/1748-0221/7/03/C03023 (cit. on p. 301).

[226] Sudarshan Khrishnamoothy. *Simulation of Wide Band-Gap Devices SiC and GaN*. Synopsys, Inc., 2008 (cit. on p. 304).

[227] Tetsuo Hatakeyama, Kenji Fukuda, and Hajime Okumura. "Physical Models for SiC and Their Application to Device Simulations of SiC Insulated-Gate Bipolar Transistors". In: *Electron Devices, IEEE Transactions on* 60 (Feb. 2013), pp. 613–621. DOI: 10.1109/TED.2012.2226590 (cit. on p. 304).

[228] D.M. Caughey and R.E. Thomas. "Carrier mobilities in silicon empirically related to doping and field". In: *Proceedings of the IEEE* 55 (Jan. 1968), pp. 2192 –2193. DOI: 10.1109/PROC.1967.6123 (cit. on p. 304).

[229] M. Ruff, H. Mitlehner, and R. Helbig. "SiC devices: physics and numerical simulation". In: *IEEE Transactions on Electron Devices* 41.6 (1994), pp. 1040–1054. DOI: 10.1109/16.293319 (cit. on p. 306).

List of acronyms

ADC

Analog to Digital Converter. 134

ANI

Active Neutron Interrogation. 43

API

Application Programming Interface. 159

ASTRID

Advanced Sodium Technological Reactor for Industrial Demonstration. 39

BR2

Belgian Reactor 2. 38

CB

Conduction Band. 51

CCFE

Culham Centre for Fusion Energy. 31

CEA

Commissariat à l'Énergie Atomique et aux énergies alternatives. 5

CSDA

Continuous Slowing Down Approximation. 76

CVD

Chemical Vapor Deposition. 45

DDR4 SDRAM

Double Data Rate 4th generation Synchronous Dynamic Random Access Memory. 163

DEMO

DEMOnstration power plant. 24

DESY

Deutsches Elektronen-SYnchrotron. 44

DLTS

Deep Level Transient Spectroscopy. 239

EAST

Experimental Advanced Superconducting Tokamak. 48

ECORCES

Energetic COmputation of Reaction rate from Cross section and nEutron Spectrum. 27

ECR

Electron Cyclotron Resonance. 128

EDK

Energy spectrum Displacement Kerma. 230

EMC

ElectroMagnetic Compatibility. 32

ENEA

Energia Nucleare ed Energie Alternative. 41

FC

Fission Chamber. 33

FLUKA

FLUktuierende KAskade. 118

FNDS

Fast Neutron Detection System. 38

FPGA

Field-Programmable Gate Array. 133

FWHM

Full Width at Half Maximum. 38

GANIL

Grand Accélérateur National d'Ions Lourds. 152

GEANT

GEometry ANd Tracking. 118

GENEPI2

GEnérateur à NEutrons Pulsés Intenses. 128

GENESIS

GEnerator of NEutrons for Science and IrradiationS. 128

HCI

Human-Computer Interface. 134

HCPB

Helium Cooled Pebble Beds. 25

HV

High Voltage. 132

IM2NP

Institut Matériaux Microélectronique Nanosciences de Provence. 5

IN2P3

Institut National de Physique Nucléaire et de Physique des Particules. 128

IRESNE

Institut de REcherche sur les Systèmes Nucléaires pour la production d'Energie bas carbone. 5

IRFM

Institut de Recherche sur la Fusion Magnétique. 5

ISFIN

Institut Sciences de la Fusion et de l'Instrumentation en Environnements Nucléaires. 5

IT

Isomeric Transition. 98

ITER

International Tokamak Experimental Reactor. 18

JAERI

Japan Atomic Energy Research Institute. 38

JHR

Jules Horowitz Reactor. 18

JSI

Jožef Stefan Institute. 46

JT-60

JAERI - Tokamak 60. 39

KERMA

Kinetic Energy Released in MAtter. 230

KSTAR

Korea Superconducting Tokamak Advanced Research. 44

LabVIEW

Laboratory Virtual Instrument Engineering Workbench. 134

LDCI

Laboratoire de Dosimétrie, Capteurs et Instrumentation. 50

LET

Linear Energy Transfer. 194

LIMMEX

Laboratoire d'Instrumentation et de Mesures en Milieux EXtrêmes. 5

LINAC

LINear ACcelerator. 45

LLCB

Lithium-Lead Ceramic Breeder. 23

LPSC

Laboratoire de Physique Subatomique et Cosmologie. 128

LR-0

Light water zero power Reactor. 43

MCNP

Monte Carlo N-Particle. 25

MCNPX

Monte Carlo N-Particle eXtended. 118

MPFD

Micro-Pocket Fission Detectors. 38

MTR

Material Testing Reactors. 28

N/A

Not Assessed. 50

NBI

Neutral Beam Injection. 26

NCL

Neutron Converter Layer. 44

NFS

Neutron For Science. 152

NIEL

Non Ionizing Energy Loss. 224

NNDC

National Nuclear Data Center. 97

OSIRIS

Origins, Spectral Interpretation, Resource Identification, and Security. 29

PCIe

Peripheral Component Interconnect Express. 133

PEREN

Plateforme d'Etude et de Recherche sur l'Energie Nucléaire. 128

PHA

Pulse Height Analysis. 134

PHITS

Particle and Heavy Ion Transport code System. 118

PICTS

Photoinduced Current Transient Spectroscopy. 239

PKL

PeaK Listing. 163

PSA

Pulse Shape Analysis. 200

PSD

Pulse Shape Discrimination. 43

PTB

Physikalisch-Technische Bundesanstalt. 121

RFQ

Radio-Frequency Quadrupole. 160

S3

Super Séparateur Spectromètre. 160

SCK-CEN

StudieCentrum voor Kernenergie-Centre d'étude de l'Énergie Nucléaire. 38

SCR

Space Charge Region. 55

SDE

Sentaurus Structure Editor. 190

SDevice

Sentaurus Device. 190

SiC

Silicon Carbide. 45

SNR

Signal-to-Noise Ratio. 133

SPIRAL-2

Système de Production d'Ions Radioactifs Accélérés en Ligne de 2ème génération. 160

SPND

Self Powered Neutron Detectors. 39

SRH

Shockley Read Hall. 225

TAPIRO

TAratura PIla Rapida di potenza 0. 41

TBM

Test Blanket Modules. 22

TBR

Tritium Breeding Ratio. 26

TCAD

Technology Computer-Aided Design. 184

TCT

Transient Current Technique. 200

TDMS

Technical Data Management System format. 137

ToF

Time oF Flight. 152

TOKAMAK

TOroidalnaïa KAmera s MAgnitnymi Katouchkami. 18

TRIPOLI

TRIdimensionnel POLIcinétique. 25

TSC

Thermally Stimulated Currents. 240

VB

Valence Band. 51

Appendices

A. SiC Junction - Demonstrating the main variables

A.1. Space Charge Region

Considering a semiconductor shown in Fig. A.1 the concentration is a function of x and the doping is non-uniform.

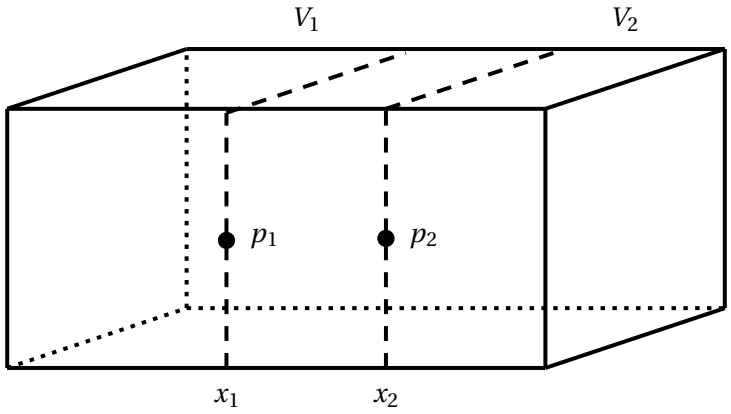

Fig. A.1. Semiconductor with non-uniform doping.

Since no external bias voltage is applied across the junction, the total current flowing through it must therefore be zero such that:

$$J = J_n + J_p = 0 \tag{A.1}$$

But because of the concentration gradient of p along the x axis, there is a non-zero diffusion current such that:

$$\begin{cases} J_n = q\mu_n nE + qD_n \dfrac{dn}{dx} \\ J_p = q\mu_p nE - qD_p \dfrac{dp}{dx} \end{cases} \tag{A.2}$$

With μ_n and μ_p the electron and hole mobility, D_n and D_p the diffusion constants of each type of carrier, and q the electric charge.

So for the total current (A.1) to be zero, there must exist an equal and opposite current in the form of a drift current such that:

$$J_n = q\mu_n nE + qD_n \frac{dn}{dx} = 0 \tag{A.3}$$

As such:

$$D_n \frac{dn}{dx} = \mu_n nE$$
$$\frac{D_n}{\mu_n}\frac{dn}{dx} = nE$$

But as a reminder, the unidimensional electric field is defined such that $E = -\frac{dV}{dx}$ and with the following Einstein relationship between the diffusion current density D and the charge carrier mobility μ it comes:

$$\frac{D_n}{\mu_n} = \frac{D_p}{\mu_p} = V_T \tag{A.4}$$

Hence:

$$\begin{aligned} V_T \frac{dn}{dx} &= -n \frac{dV}{dx} \\ -V_T \frac{dn}{n} &= dV \\ \int_{V_1}^{V_2} dV &= -V_T \int_{n_1}^{n_2} \frac{dn}{n} \\ V_{21} &= V_T \ln \frac{n_1}{n_2} \end{aligned}$$

And the electron concentration n is obtained at $x = x_1$ such that:

$$n_1 = n_2 \exp\left(-\frac{V_{21}}{V_T}\right) \tag{A.5}$$

And a similar reasoning is applied to get the hole concentration p, at $x = x_1$ such that:

$$p_1 = p_2 \exp\left(\frac{V_{21}}{V_T}\right) \tag{A.6}$$

Hence:

$$n_1 p_1 = n_2 p_2 = np = n_i^2 \tag{A.7}$$

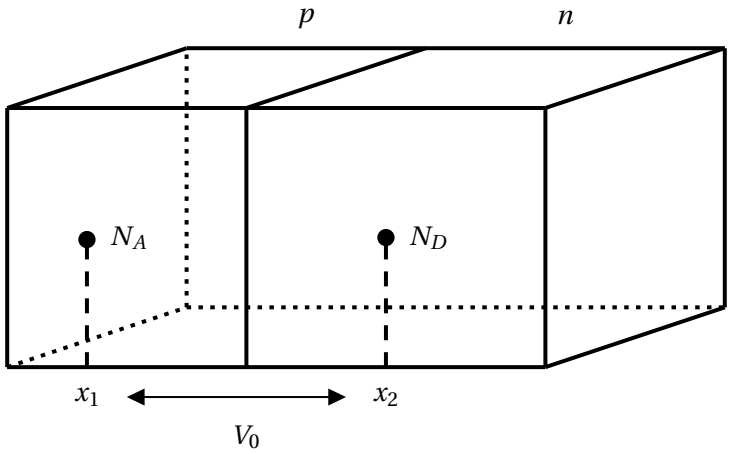

Fig. A.2. *p-n* junction in a semiconductor.

In a semiconductor device with a *p-n* junction as illustrated with the Fig. A.2, the density changes abruptly from p-doped region to n-doped region. The contact potential V_0 at the junction is given by:

$$V_0 = V_T ln\left(\frac{p_{p_0}}{p_{n_0}}\right) \tag{A.8}$$

With V_T the integrated potential equals to $k_B T/q$, p_{p_0} the hole concentration at thermal equilibrium in p-doped region, and p_{n_0} the hole concentration at thermal equilibrium in n-doped region.

With $p_{p_0} \approx N_D$:

$$N_A p_{n_0} = n_i^2 \tag{A.9}$$

$$p_{n_0} = \frac{n_i^2}{N_A} \tag{A.10}$$

Then with the equality (A.8), it comes:

$$\boxed{V_0 = V_T ln\left(\frac{N_D N_A}{n_i^2}\right)} \tag{A.11}$$

Because of the density gradient across the *p*-*n* junction, the holes will diffuse to the right across the n-doped region of the junction and the electrons in the opposite direction. Holes, which carry a positive charge, and electrons, which carry a negative charge, will therefore neutralize each other by recombining.

As a result, the positively charged holes that neutralized the acceptor ions near the junction in the p-type region disappeared as they recombined with the electrons that passed through the junction. Similarly, the electrons that neutralized the donor ions in the *n* region recombined with holes that passed through the junction from the *p* material. Ions that have not been neutralized in the vicinity of the junction are called non-neutralized charges. As the region of the junction is depleted of mobile charge, it is called the "depletion region", "space charge region" or "transition region". In this very narrow space charge layer, there are no mobile carriers. To the left of this region, the concentration of carriers is $p \approx N_A$, and to its right, it is $p \approx N_A$.

At the junction, the charge carriers that are no longer compensated must be equal, so it comes:

$$qN_D S x_{n_0} = qN_A S x_{p_0} \tag{A.12}$$

$$N_D x_{n_0} = N_A x_{p_0} \tag{A.13}$$

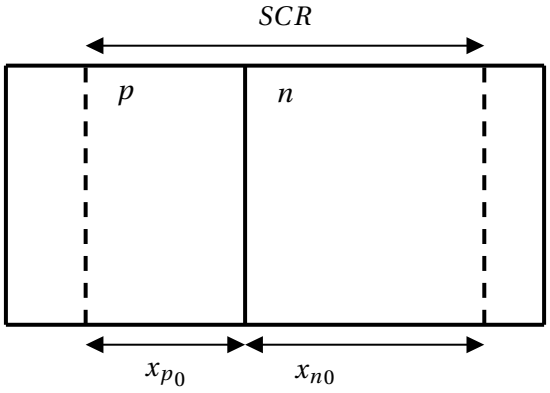

Fig. A.3. Diagram of the transition region, i.e. the depletion region.

Hence, it can be defined W the thickness of this space charge region as illustrated in the Fig. A.3 such that:

$$W = x_{n_0} + x_{p_0} \tag{A.14}$$

In the case where $N_D < N_A$ the space charge zone penetrates more into the *n* region than into

the p region as schematically represented in the Fig. A.4, leading to $x_{p_0} < x_{n_0}$. Hence, it comes from the Poisson equation:

$$\frac{d^2V}{dx^2} = -\frac{\rho_V}{\epsilon}$$
$$\frac{d}{dx}\left(\frac{dV}{dx}\right) = -\frac{\rho_V}{\epsilon}$$

But, since the unidimensional electric field is defined sch that $E = -\dfrac{dV}{dx}$, it comes:

$$\frac{dE}{dx} = \frac{\rho_V}{\epsilon} \tag{A.15}$$

With ρ_V the volume charge density associated with the charge present per unit volume, defined as the product of the concentration of carriers per unit volume multiplied by the charge of the carrier, such that $\rho = nq$.

It comes the following system of equations, depending on the region studied:

$$\rho_V = \begin{cases} -qN_A & \text{for } -x_{p_0} < x < 0, \\ +qN_D & \text{for } 0 < x < x_{n_0}, \\ 0 & \text{otherwise.} \end{cases}$$

The charge density profile within the junction is then depicted with the Fig. A.4b. Then using (A.15), it comes:

$$\frac{dE}{dx} = \begin{cases} -\dfrac{qN_A}{\epsilon} & \text{for } -x_{p_0} < x < 0, \\ +\dfrac{qN_D}{\epsilon} & \text{for } 0 < x < x_{n_0}, \\ 0 & \text{otherwise.} \end{cases}$$

To obtain the expression for the electric field, the previous expressions need to be integrated. For $-x_{p_0} < x < 0$:

$$\begin{aligned} E(x) &= \int_{-\infty}^{x} -\frac{qN_A}{\epsilon} dx \\ &= \int_{-\infty}^{-x_{p_0}} 0 \; dx + \int_{-x_{p_0}}^{x} -\frac{qN_A}{\epsilon} dx \\ &= -\frac{qN_A}{\epsilon}(x + x_{p_0}) \end{aligned}$$

The electric field expression at the junction is thus obtained such that:

$$E(x = 0) = -\frac{qN_A}{\epsilon} x_{p_0} = E_0 \tag{A.16}$$

And the electric field expression at the beginning of the SCR such that:

$$E(x = -x_{p_0}) = -\frac{qN_A}{\epsilon}(-x_{p_0} + x_{p_0}) = 0 \tag{A.17}$$

For $0 < x < x_{n_0}$:

$$\begin{aligned} E(x) &= \int_{-\infty}^{x} \frac{qN_D}{\epsilon} dx \\ &= \int_{-\infty}^{-x_{p_0}} 0 \; dx + \int_{-x_{p_0}}^{0} -\frac{qN_A}{\epsilon} dx + \int_{0}^{x} -\frac{qN_D}{\epsilon} dx \\ &= 0 - \frac{qN_A}{\epsilon} x_{p_0} + \frac{qN_D}{\epsilon} x \qquad \text{and with (A.16) it comes:} \\ &= E_0 + \frac{qN_D}{\epsilon} x \end{aligned}$$

The expression for the electric field on either side of the junction is :

$$E(x) = \begin{cases} -\dfrac{qN_A}{\epsilon}(x + x_{p_0}) & \text{for } -x_{p_0} < x < 0, \\ +\dfrac{qN_D}{\epsilon} x + E_0 & \text{for } 0 < x < x_{n_0}, \\ 0 & \text{or.} \end{cases}$$

The profile of the electric field in the junction is then represented as seen in the Fig. A.4c. Then, by integrating the electric field at the junction between $-x_{p_0}$ and x_{n_0}, it comes:

$$V_0 = -\int_{-x_{p_0}}^{x_{n_0}} E(x)\, dx$$

Since the area under the curve represented in the Fig. **??** is interpreted as the value of the integral, the expression for the potential V_0 is obtained by summing the area of the two right-angled triangles such that:

$$\begin{aligned} V_0 &= -\left(\frac{1}{2} x_{p_0} E_0 + \frac{1}{2} x_{n_0} E_0 \right) \\ &= -\frac{1}{2} E_0 (x_{p_0} + x_{n_0}) \qquad \text{with the definition (A.14) it comes,} \\ &= -\frac{1}{2} E_0 W \end{aligned}$$

Then with the expression (A.16) and the charge equilibrium at the junction obtained in (A.13) it comes:

$$V_0 = -\frac{1}{2}\left(-\frac{qN_D}{\epsilon} x_{n_0} \right) W \tag{A.18}$$

We can therefore determine the expression for the boundaries of the SCR, i.e. the edges of the junction at x_{p_0} and x_{n_0}, as a function of the thickness W of the junction and the concentrations of donor atoms N_D and acceptors N_A. With (A.16) and (A.13) it comes :

$$\begin{aligned} W &= x_{n_0} \frac{N_D}{N_A} + x_{n_0} \\ &= x_{n_0} \left(\frac{N_D}{N_A} + 1 \right) \end{aligned}$$

Hence, the two following expressions are obtained:

$$\begin{cases} x_{n_0} &= W\left(\dfrac{N_A}{N_D+N_A}\right) \\ x_{p_0} &= W\left(\dfrac{N_D}{N_D+N_A}\right) \end{cases} \tag{A.19}$$

If $N_D < N_A$, it implies respectively that $\dfrac{N_D}{N_A} < 1$ and $\dfrac{N_A}{N_D} > 1$, and so consequently $x_{n_0} > x_{p_0}$. Hence, using the expression (A.18) it comes:

$$\begin{aligned} V_0 &= \frac{1}{2}\frac{qN_D}{\epsilon}x_{n_0}W \\ &= \frac{1}{2}\frac{qN_DN_A}{\epsilon(N_D+N_A)}W^2 \end{aligned}$$

and with the expression (A.19) it comes,

Isolating W and by taking the root, the expression for the thickness of the space charge region in a steep junction semiconductor is then obtained such that:

$$\boxed{W = \sqrt{\frac{2\epsilon V_0}{q}\cdot\left(\frac{N_D+N_A}{N_DN_A}\right)}} \tag{A.20}$$

With V_0 the potential determined above (A.11) such that:

$$\boxed{V_0 = V_T\, ln\left(\frac{N_DN_A}{n_i^2}\right)}$$

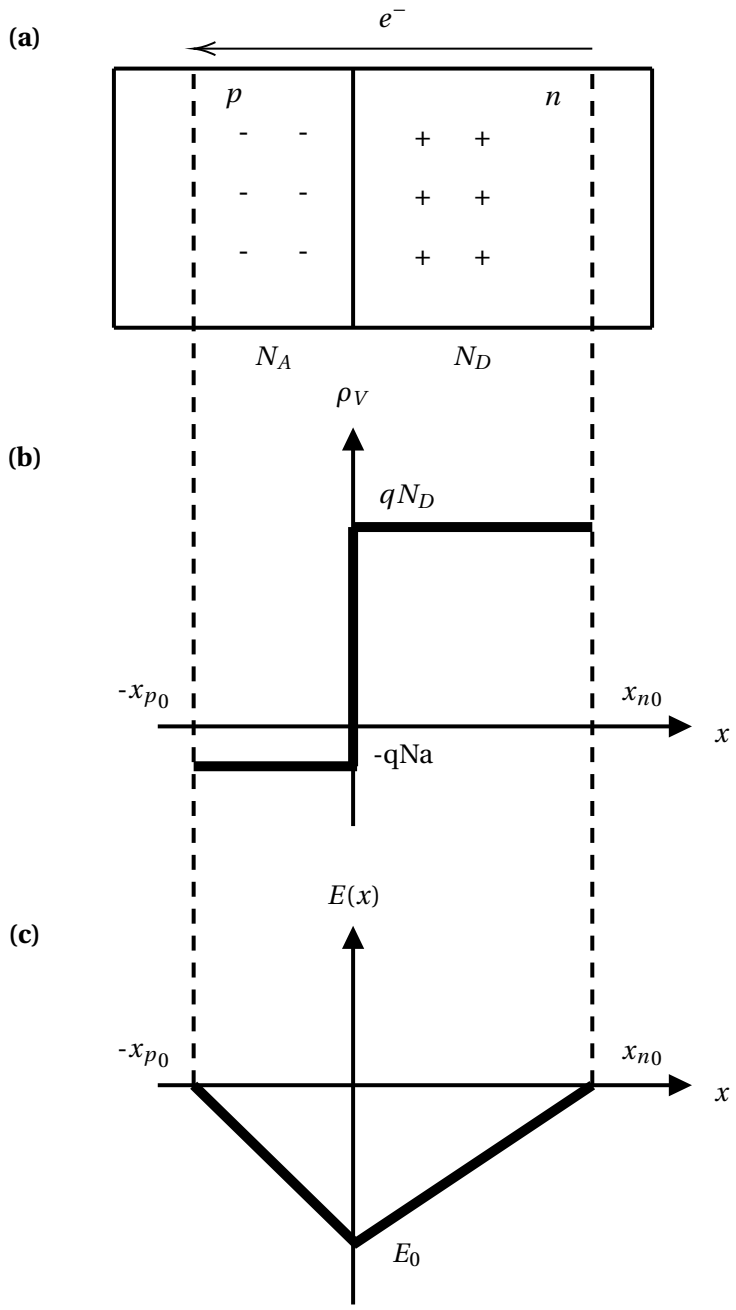

(a) p-n junction in open circuit

(b) Charge density profile in the junction

(c) Electric field profile in the junction.

Fig. A.4. Draw-up of the p-n junction.

A.2. Free carriers concentration

The number of holes and electrons in the semiconductor is given by the product of the density of state by a distribution function. It is the Fermi-Dirac distribution function that gives the number of electrons in the conduction band and the number of holes in the valence band. Let $f(E)$ be this probability distribution function. The equation to which Fermi statistics applied to the mathematical process of filling the energy levels E by electrons leads is given by:

$$f(E) = \frac{1}{1 + e^{\frac{E - E_F}{kT}}} \tag{A.21}$$

With E_F the Fermi level, which is the energy level at which the probability of occupation of the state is equal to 1/2. This probability distribution function is applied to know the occupation by electrons of the possible energy levels in the bands that are allowed to them. As the energy levels within a band are so tight that they must be considered as continuous, it is easy to conceive that if in the vicinity of the energy E, the density of permitted state is $N(E)$ per unit of volume, for a small interval dE of energy, the number of states actually occupied will be, by virtue of the Pauli principle of 2 possible occupations per state:

$$2f(E)N(E)dE \tag{A.22}$$

The number of charges in the conduction band extending from the lower value E_C to infinity, and in the valence band extending from the upper value E_V to minus infinity, is given by:

$$\begin{cases} n = \displaystyle\int_{E_C}^{\infty} 2f(E)N_C(E)dE \\ p = \displaystyle\int_{-\infty}^{E_V} 2f'(E)N_V(E)dE \end{cases} \tag{A.23}$$

With $f'(E) = 1 - f(E)$. Indeed, given that the probability of the presence of a charge $-q$ in a state of energy E is $f(E)$, the probability of the absence of a charge $-q$ in this state, that is to say the probability of the presence of a charge +q, in this same state, is $1 - f(E)$.

These integrals can be solved by assuming that in practice the energy levels occupied in the CB by the charges are very close to E_C and E_V respectively. The simplified calculation therefore allows the introduction of the quantities N_C and N_V which are respectively the number of energy states that can be occupied by charges $-q$ and $+q$ in the CB and VB per unit volume. Hence, using (A.21), it comes:

$$\begin{cases} n = 2N_C \cdot \dfrac{1}{1 + e^{\frac{E_C - E_F}{kT}}} \\ p = 2N_V \cdot \dfrac{1}{1 + e^{\frac{E_F - E_V}{kT}}} \end{cases} \tag{A.24}$$

The product np is then given by:

$$np = 4N_C N_V \cdot \frac{1}{1 + e^{\frac{E_C - E_F}{kT}} + e^{\frac{E_F - E_V}{kT}} + e^{\frac{E_C - E_V}{kT}}} \tag{A.25}$$

And since E_F is at the mid-gap, it comes:

$$E_C - E_F = -(E_F - E_V) \tag{A.26}$$

Hence, by setting:

$$u = \frac{E_C - E_F}{kT} \gg 1 \tag{A.27}$$

It comes:

$$\frac{1}{1 + e^{u} + e^{-u} + e^{2u}} \sim e^{-2u} \tag{A.28}$$

And so, the product np is given by:

$$\boxed{np = N_C N_V e^{-E_g/kT}} \tag{A.29}$$

B. Kinematic study - Demonstrating the main expressions

B.1. Two bodies

As a reminder, when a particle is referred to by its mass, it is always the mass at rest in the reference system under consideration. Mass is an invariant. And the Einstein law of equivalence between mass and energy is written as : $M = mc^2$

However, the use of this relativistic relationship does not imply the use of a relativistic formalism for nuclear shock kinematics calculations. In the case of the following study, where the kinetic energy is always smaller than the mass at rest, the classical formalism is sufficient and it can be introduced the following expressions:

$$T = \frac{1}{2}mv^2 \tag{B.1}$$

$$p = mv \tag{B.2}$$

With T the kinetic energy and p the momentum.

$$T = \frac{1}{2}\frac{p^2}{m} \tag{B.3}$$

With p the momentum defined such that $P = pc$ it comes:

$$P = \sqrt{2MT} \tag{B.4}$$

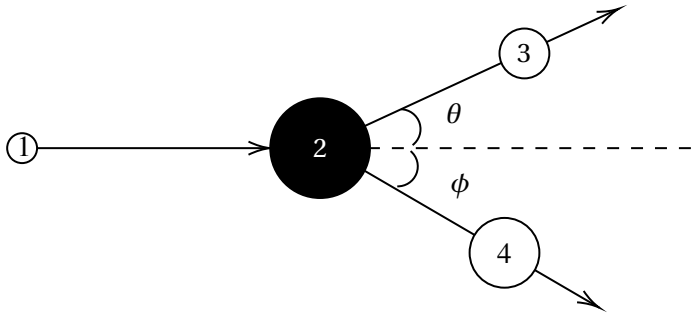

Fig. B.1. Diagram of the interaction between an incident particle and a target particle.

Considering the following two bodies problem, the conservation of mass equation gives:

$$m_1c^2 + T_1 + m_2c^2 + T_2 = m_3c^2 + T_3 + m_4c^2 + T_4$$

Then, considering the particle 2 at rest, so with null kinetic energy, it comes the Q value for the reaction such that:

$$Q = (m_1 + m_2 - m_3 - m_4)c^2 = T_3 + T_4 - T_1 \tag{B.5}$$

Then, with the definition of momentum using the non-relativistic approximation since the kinetic energy of neutrons involved in this study is much smaller than their rest mass energy[1], it comes the equation for the conservation of moments in the x and y directions such that:

$$\begin{cases} P_1 = P_3 cos\theta + P_4 cos\phi \\ 0 = P_3 sin\theta + P_4 sin\phi \end{cases} \tag{B.6}$$

[1] *Approximately* 935.5 MeV/c^2.

By squaring it comes,

$$\begin{cases} P_1^2 = P_3^2 cos^2\theta + 2P_3P_4 cos\theta cos\phi + P_4^2 cos^2\phi \\ 0 = P_3^2 sin2\phi + 2P_3 sin\theta P_4 sin\phi + P_4^2 sin^2\phi \end{cases} \tag{B.7}$$

Using (B.6) it comes:

$$\begin{cases} \begin{cases} P_1^2 = P_3^2 cos^2\theta + 2P_3 cos\theta(P_1 - P_3 cos\theta) + P_4^2 cos^2\phi \\ 0 = P_3^2 sin2\theta + 2P_3 sin\theta(-P_3 sin\theta) + P_4^2 sin^2\phi \end{cases} \\ \\ \begin{cases} P_1^2 = P_3^2 cos^2\theta + 2(P_1 - P_4 cos\phi)P_4 cos\phi + P_4^2 cos^2\phi \\ 0 = P_3^2 sin2\theta - (2P_4 sin\phi)(P_4 sin\phi) + P_4^2 sin^2\phi \end{cases} \end{cases}$$

Then adding the first lines to the second lines and using the trigonometric relation $cos^2\beta + sin^2\beta = 1$, it comes:

$$\begin{cases} P1^2 + P_3^2 - 2P_3P_1 cos\theta = P_4^2 \\ P1^2 + P_4^2 - 2P_1P_4 cos\phi = P_3^2 \end{cases} \tag{B.8}$$

And using the definition of P (B.4) as-well as the definition of Q (B.5), it comes:

$$\begin{cases} 2M_1T_1 + 2M_3T_3 - 2\sqrt{2M_1T_1}\sqrt{2M_3T_3}cos\theta = 2M_4(Q - T_3 + T_1) \\ 2M_1T_1 + 2M_4T_4 - 2\sqrt{2M_1T_1}\sqrt{2M_4T_4}cos\theta = 2M_3(Q - T_4 + T_1) \end{cases} \tag{B.9}$$

Isolating Q value and dividing respectively by M_4 and M_3 leads to the Q equation describing the relationship between the particle leaving the system and the angle at which it is emitted as represented in Fig. B.1. This is a quadratic equation of the second degree such that:

$$\begin{cases} \underbrace{\left(\frac{M_3}{M_4}+1\right)}_{a}\left(\sqrt{T_3}\right)^2 \underbrace{-\frac{2}{M_4}\sqrt{M_1M_3T_1}cos\theta}_{b}\sqrt{T_3} + \underbrace{\left(\frac{M_1}{M_4}-1\right)}_{c}T_1 - Q = 0 \\ \underbrace{\left(\frac{M_4}{M_3}+1\right)}_{a}\left(\sqrt{T_4}\right)^2 \underbrace{-\frac{2}{M_3}\sqrt{M_1M_4T_1}cos\theta}_{b}\sqrt{T_4} + \underbrace{\left(\frac{M_1}{M_3}-1\right)}_{c}T_1 - Q = 0 \end{cases} \tag{B.10}$$

Solving this second-degree equation leads to :

$$\sqrt{T_3} = \frac{\frac{2}{M_4}\sqrt{M_1M_3T_1}cos\theta \pm \sqrt{\frac{4}{M_4^2}M_1M_3T_1cos^2\theta - 4\left(\frac{M_3}{M_4}+1\right)\left(\left(\frac{M_1}{M_4}-1\right)T_1 - Q\right)}}{\left(\frac{M_3}{M_4}+1\right)} \tag{B.11}$$

$$= \frac{\sqrt{M_1M_3T_1}cos\theta}{M_3+M_4} \pm \frac{1}{M_3+M_4}\sqrt{M_1M_3T_1cos^2\theta - (M_3+M_4)M_4\left(\left(\frac{M1-M_4}{M_4}\right)T_1 - Q\right)} \tag{B.12}$$

Finally it comes the general solution of the equation (B.11):

$$\boxed{\sqrt{T_{3_\pm}} = A \pm \sqrt{A^2 + B}}$$

With :

$$A = \frac{\sqrt{M_1 T_1 M_3}}{M_3 + M_4} cos\theta$$

$$B = \frac{QM_4 - (M_1 - M_4)T_1}{M_3 + M_4}$$

The later can be simplified in the case of elastic scatterings such that:

$$Q = 0 \qquad M_1 = M_3 \qquad M_2 = M_4 \tag{B.13}$$

C. NovaSiC Epitaxy quotation - technical details

Name	S60	S100
Substrate material	4H-SiC	4H-SiC
Diameter [mm]	100	100
Epi side surface orientation	Si-face	Si-face
Mis-orientation	4°	4°

Table 1. Substrates specifications

Name	S60	S100
target thickness (layer 1) [μm]	0.5	0.5
target doping (layer 1)	n>=$1 \cdot 10^{18}$	n>=$1 \cdot 10^{18}$
target thickness (layer 2) [μm]	60.0	100.0
target doping (layer 2)	n<$1 \cdot 10^{14}$	n<$1 \cdot 10^{14}$
target thickness (layer 3) [μm]	1.3	1.3
target doping (layer 3)	p>$1 \cdot 10^{19}$	p>$1 \cdot 10^{19}$
Tot. thickness acceptation range	+/- 10%	+/- 10%
Doping acceptation range	+/- 30%	+/- 30%

Table 2. Epilayers specifications

D. Reaction Products level scheme and de-excitation

D.1. Be

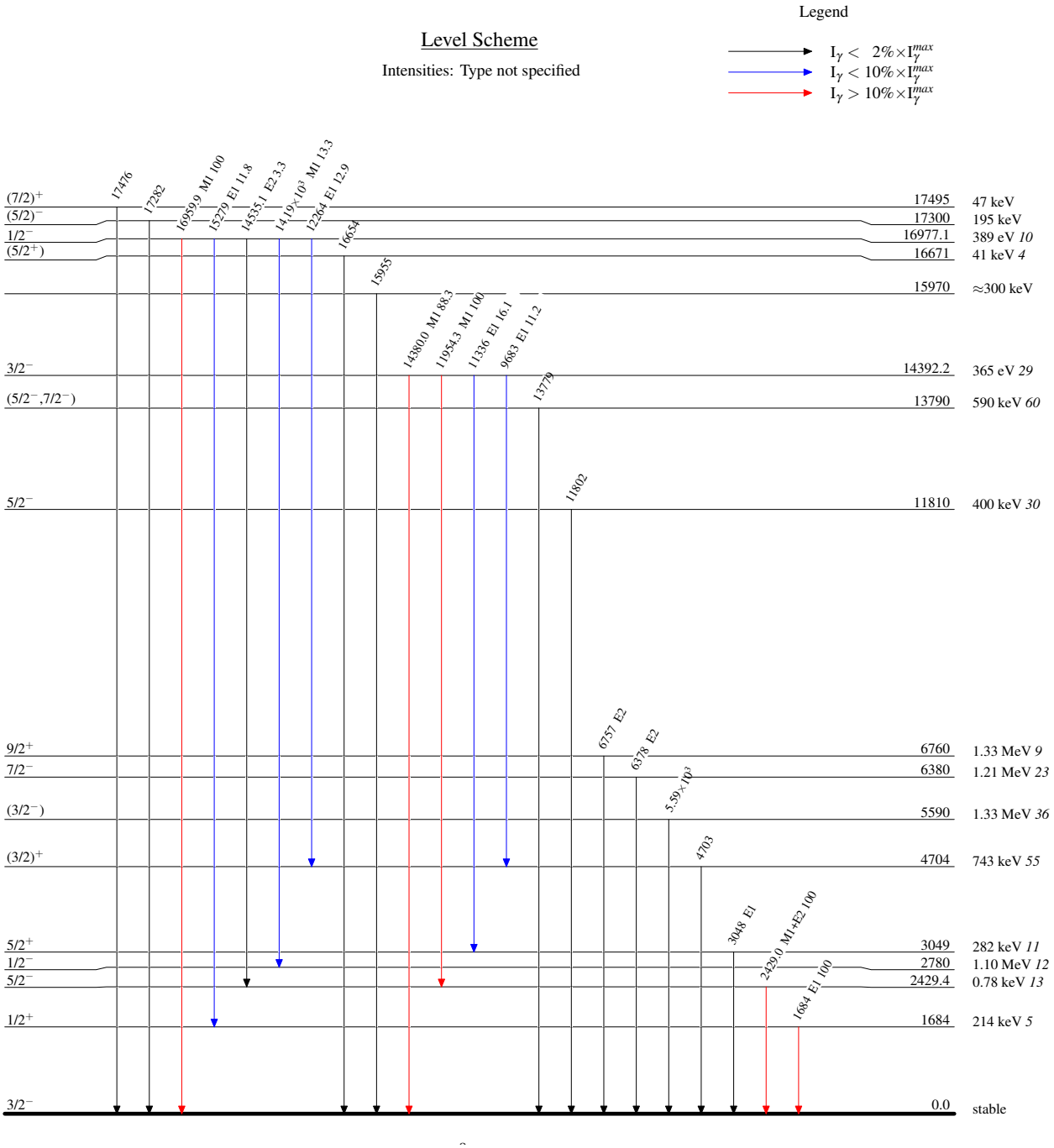

Fig. D.1. Level scheme of ^{9}Be with the excited states considered in the study. The energy levels are in [MeV].

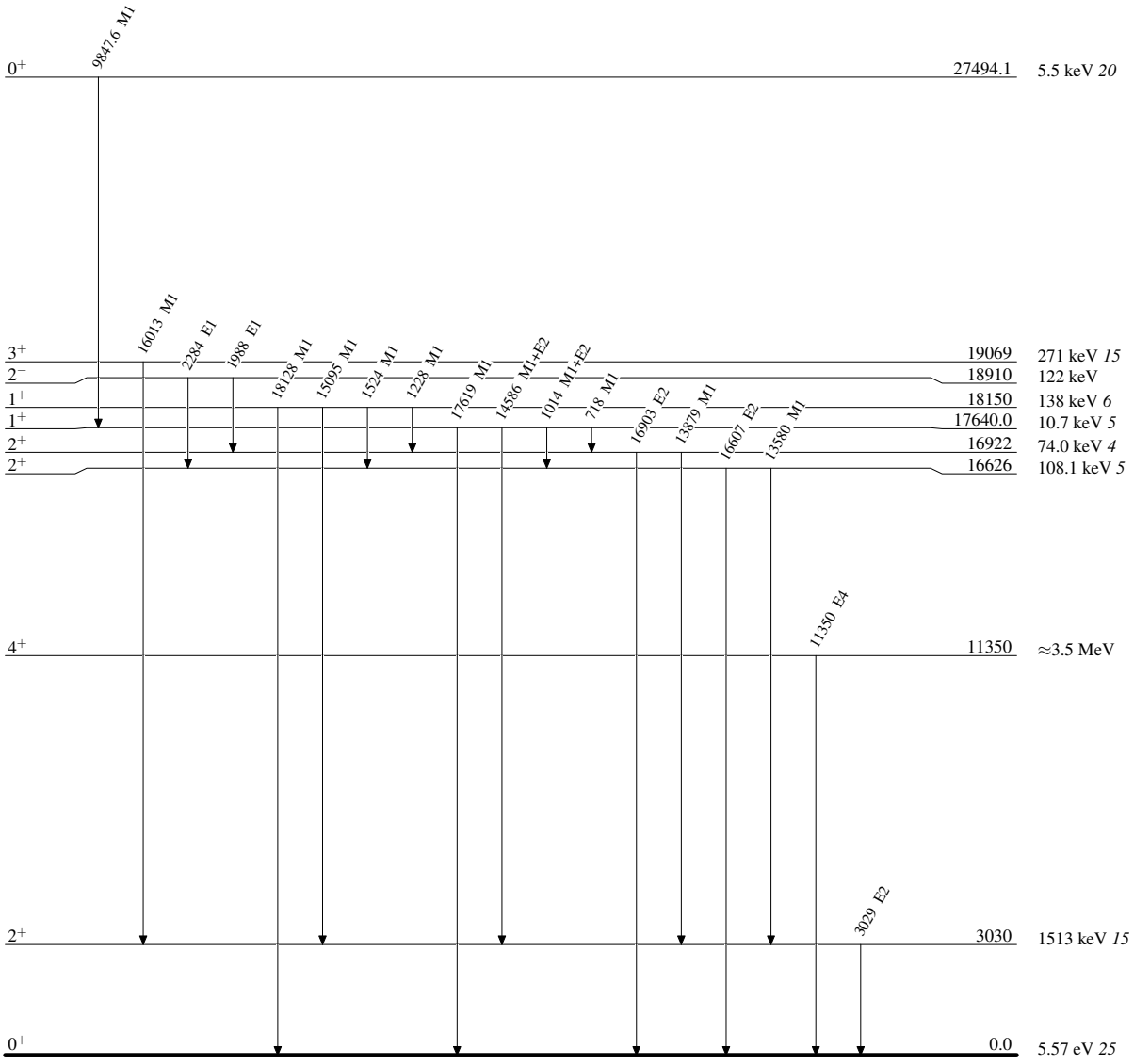

Fig. D.2. Level scheme of ^{8}Be with the excited states considered in the study. The energy levels are in [MeV].

D.2. Mg

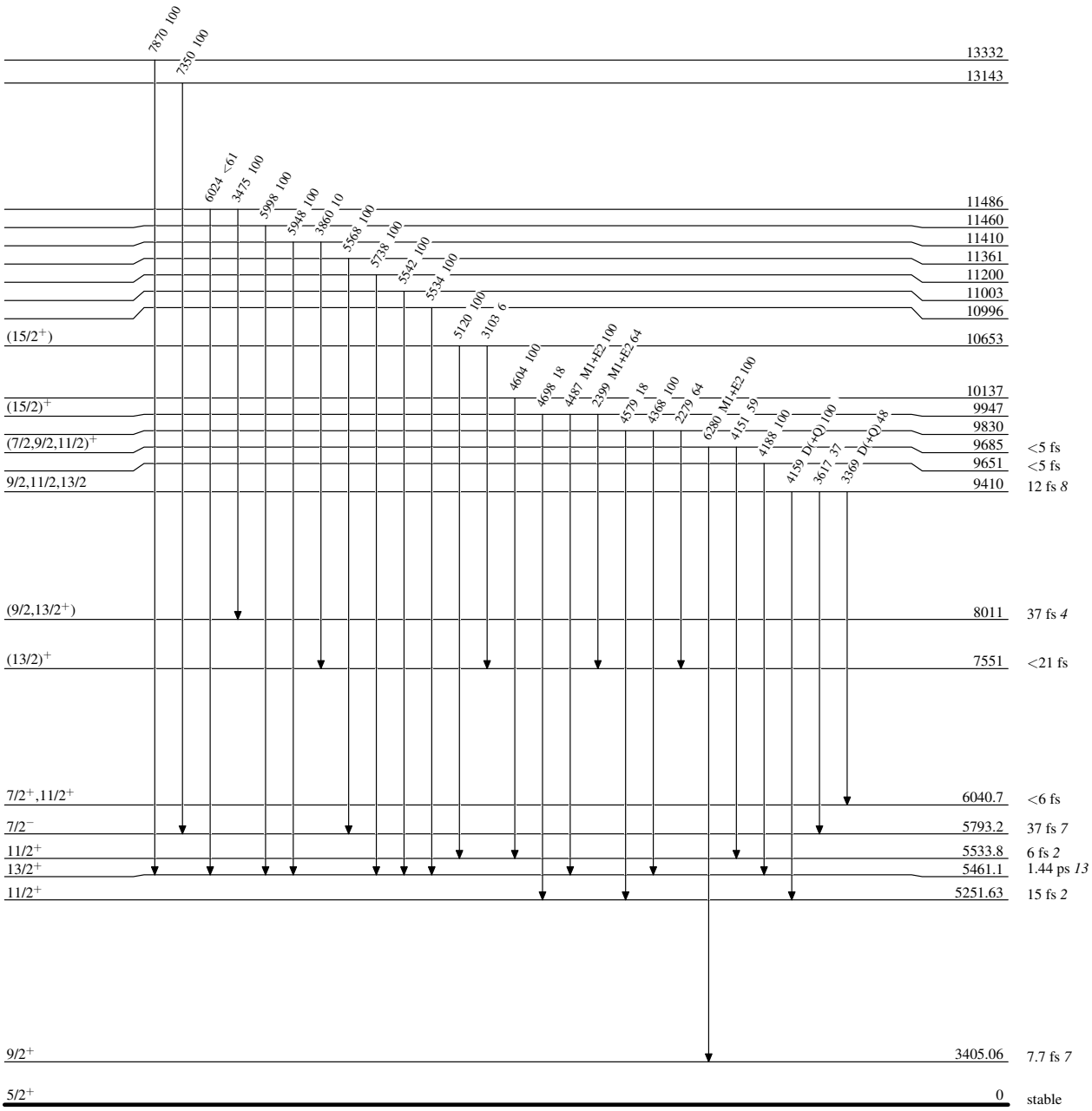
Level Scheme
Intensities: Relative photon branching from each level
7870 100
7350 100
6024 <61
3475 100
5998 100
5948 100
3860 10
5568 100
5738 100
5542 100
5534 100
5120 100
3103 6
4604 100
4698 18
4487 M1+E2 100
2399 M1+E2 64
4579 18
4368 100
2279 64
6280 M1+E2 100
4151 59
4188 100
4159 D(+Q) 100
3617 37
3369 D(+Q) 48
13332
13143
11486
11460
11410
11361
11200
11003
10996
(15/2+)
10653
10137
(15/2)+
9947
9830
(7/2,9/2,11/2)+
9685
<5 fs
9651
<5 fs
9/2,11/2,13/2
9410
12 fs 8
(9/2,13/2+)
8011
37 fs 4
(13/2)+
7551
<21 fs
7/2+,11/2+
6040.7
<6 fs
7/2−
5793.2
37 fs 7
11/2+
5533.8
6 fs 2
13/2+
5461.1
1.44 ps 13
11/2+
5251.63
15 fs 2
9/2+
3405.06
7.7 fs 7
5/2+
0
stable

Level Scheme (continued)

Intensities: Relative photon branching from each level

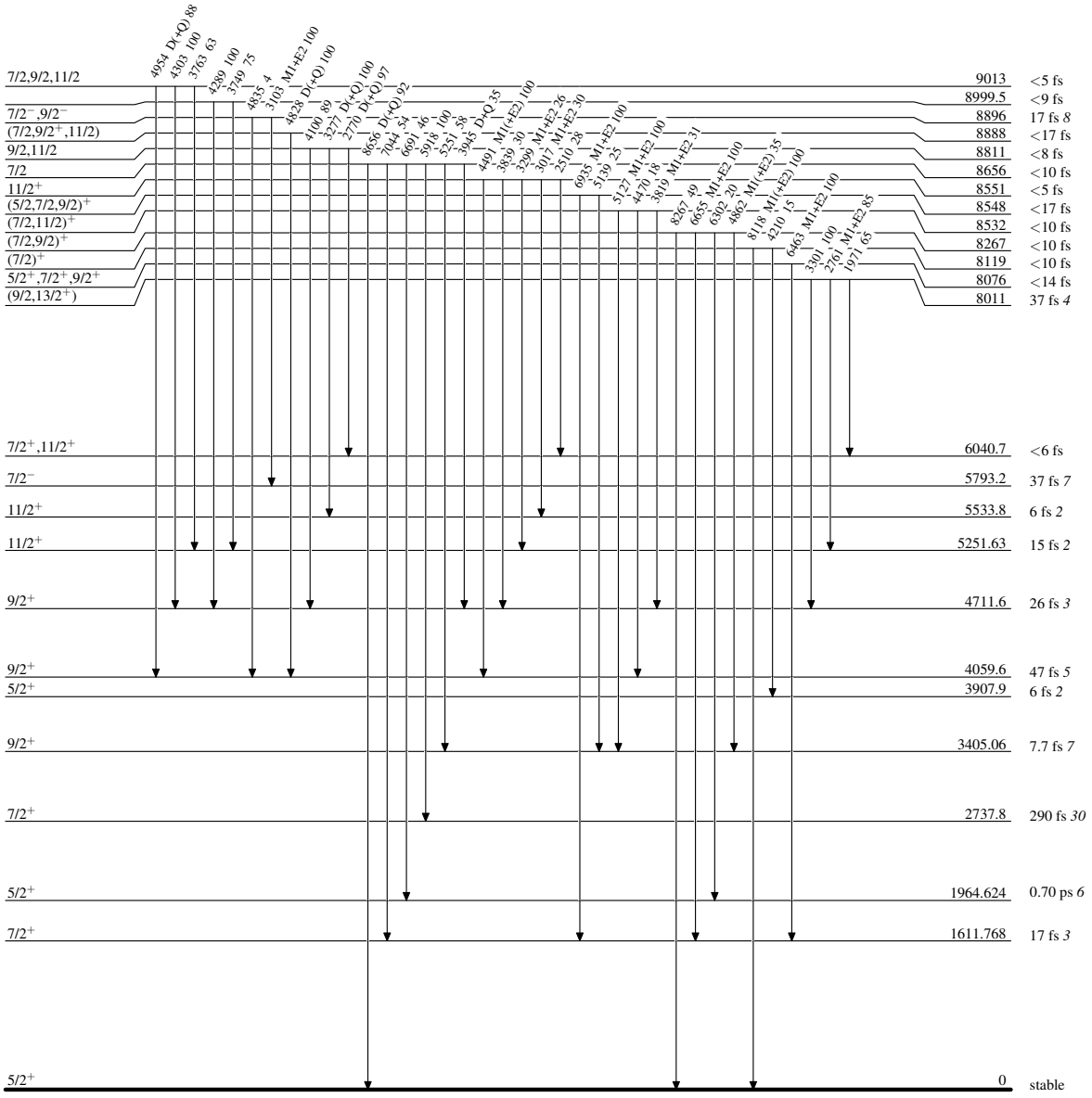

Level Scheme (continued)

Intensities: Relative photon branching from each level

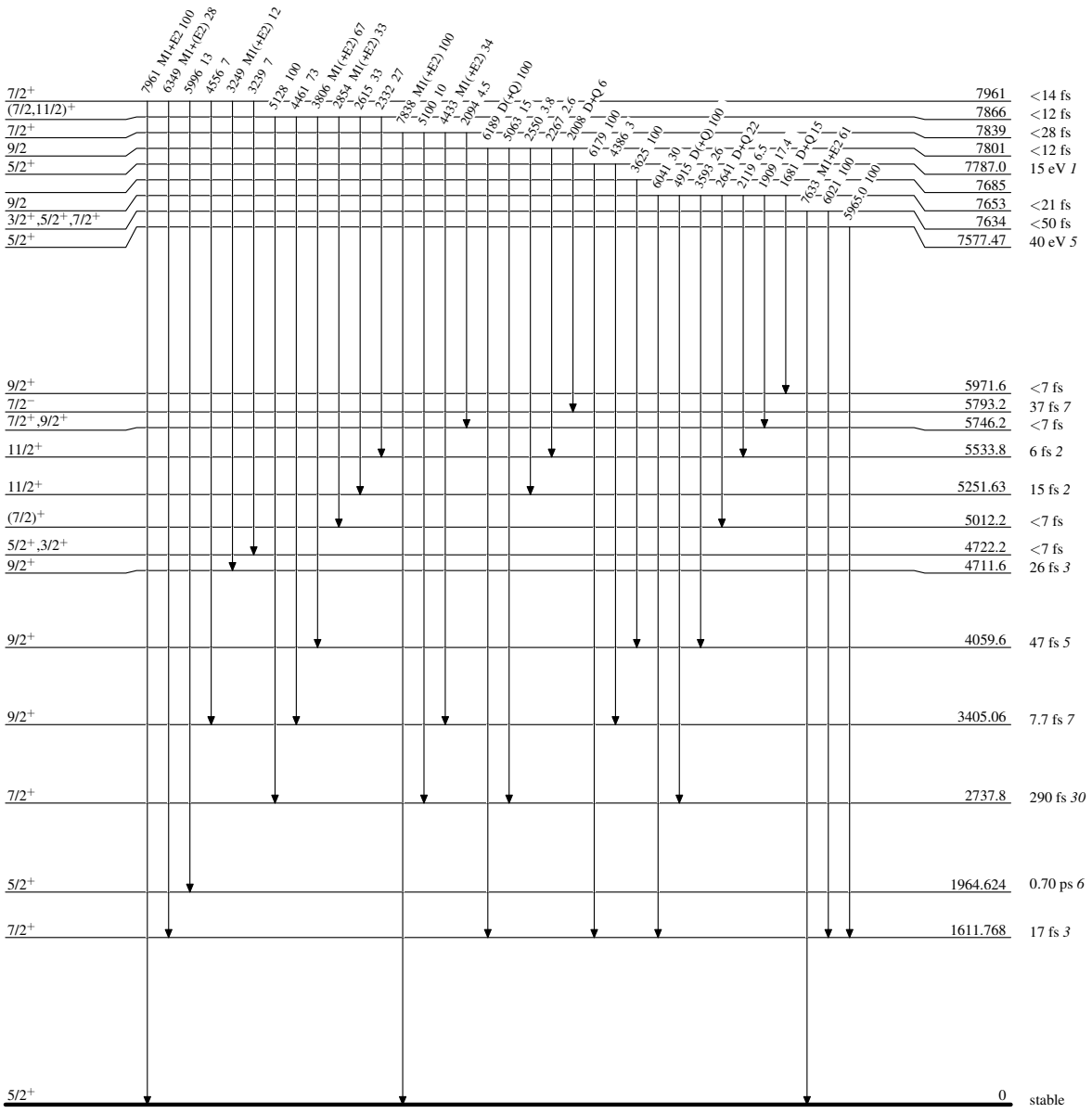

Level Scheme (continued)

Intensities: Relative photon branching from each level

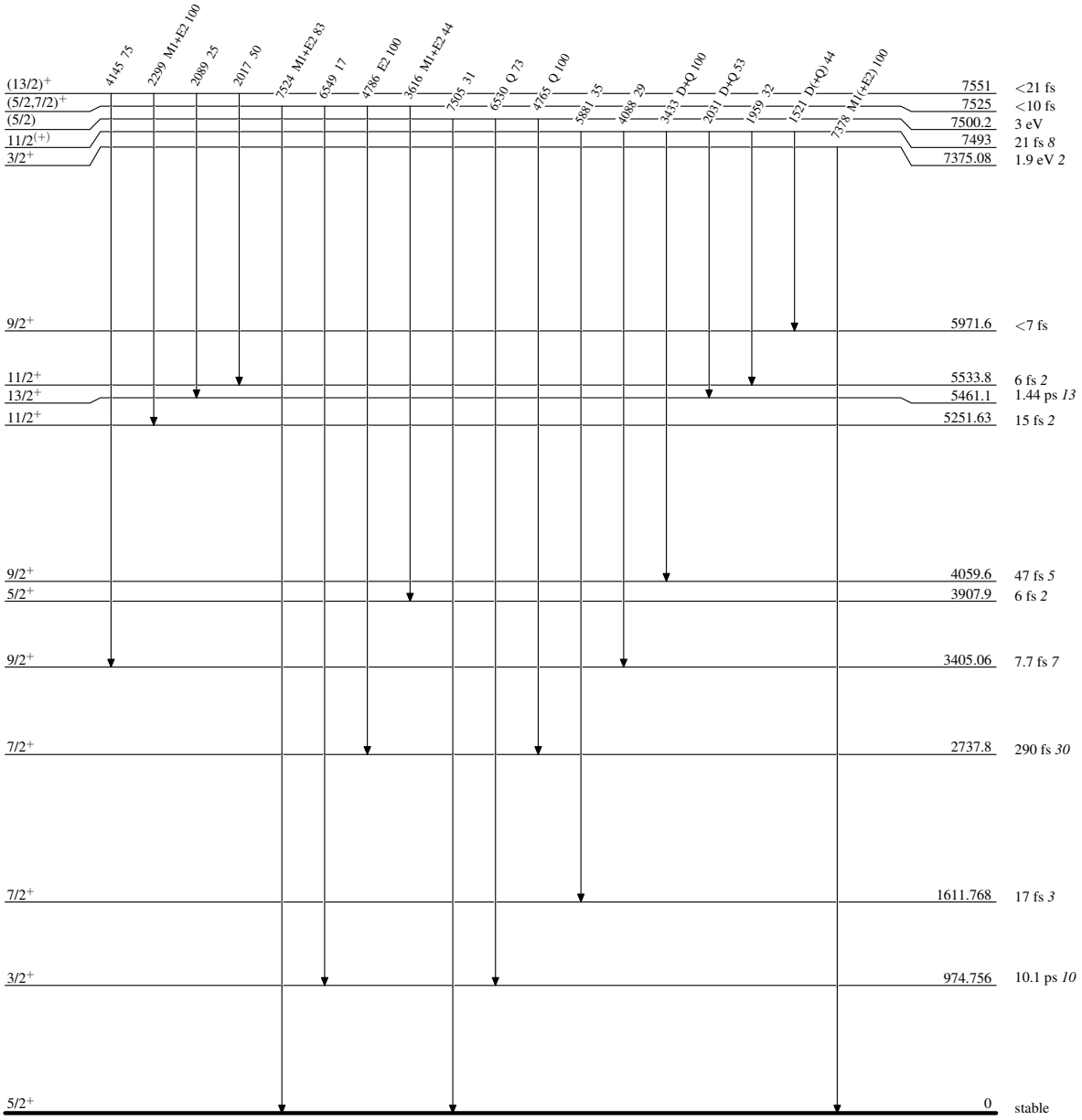

Adopted Levels, Gammas

Level Scheme (continued)

Intensities: Relative photon branching from each level

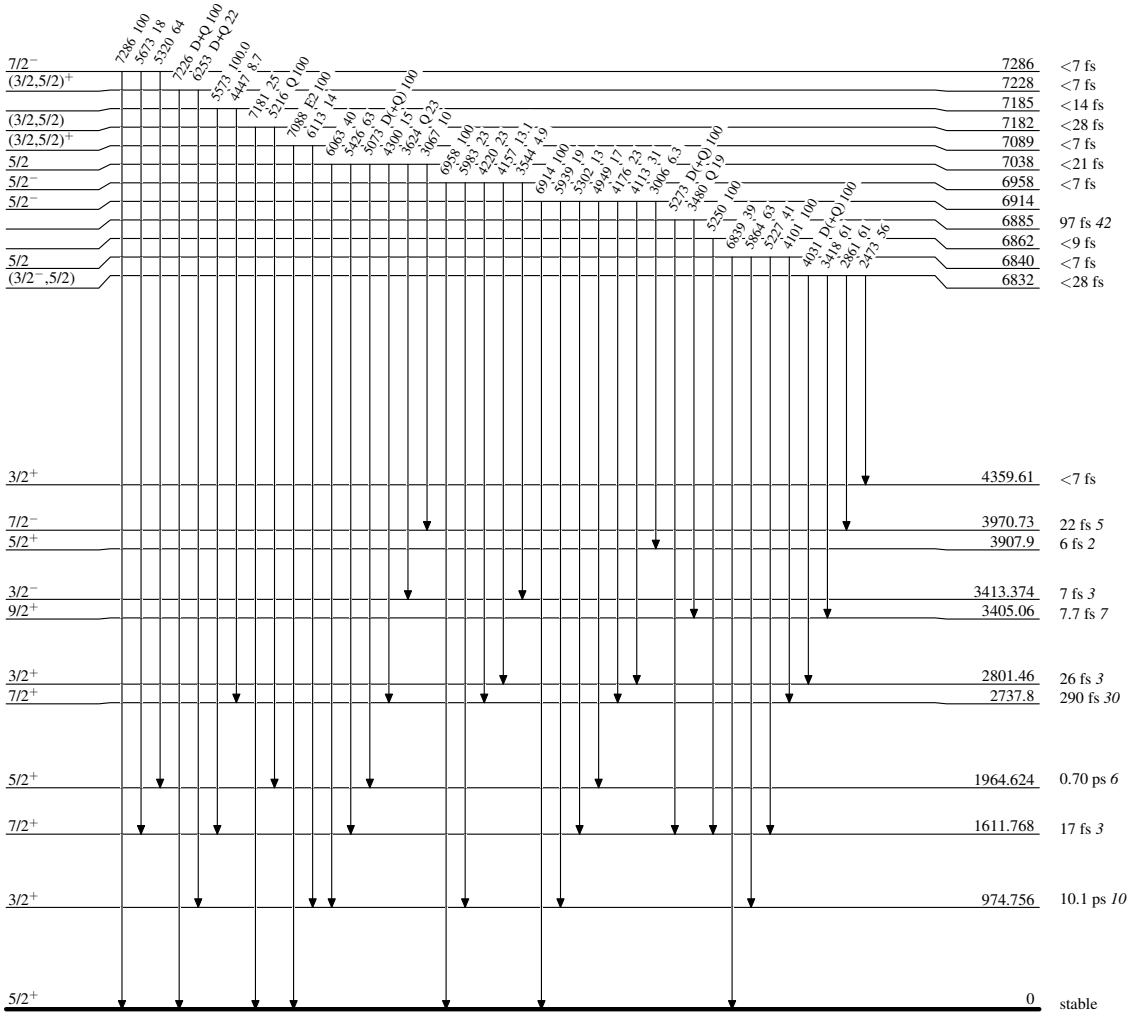

Adopted Levels, Gammas

Level Scheme (continued)

Intensities: Relative photon branching from each level

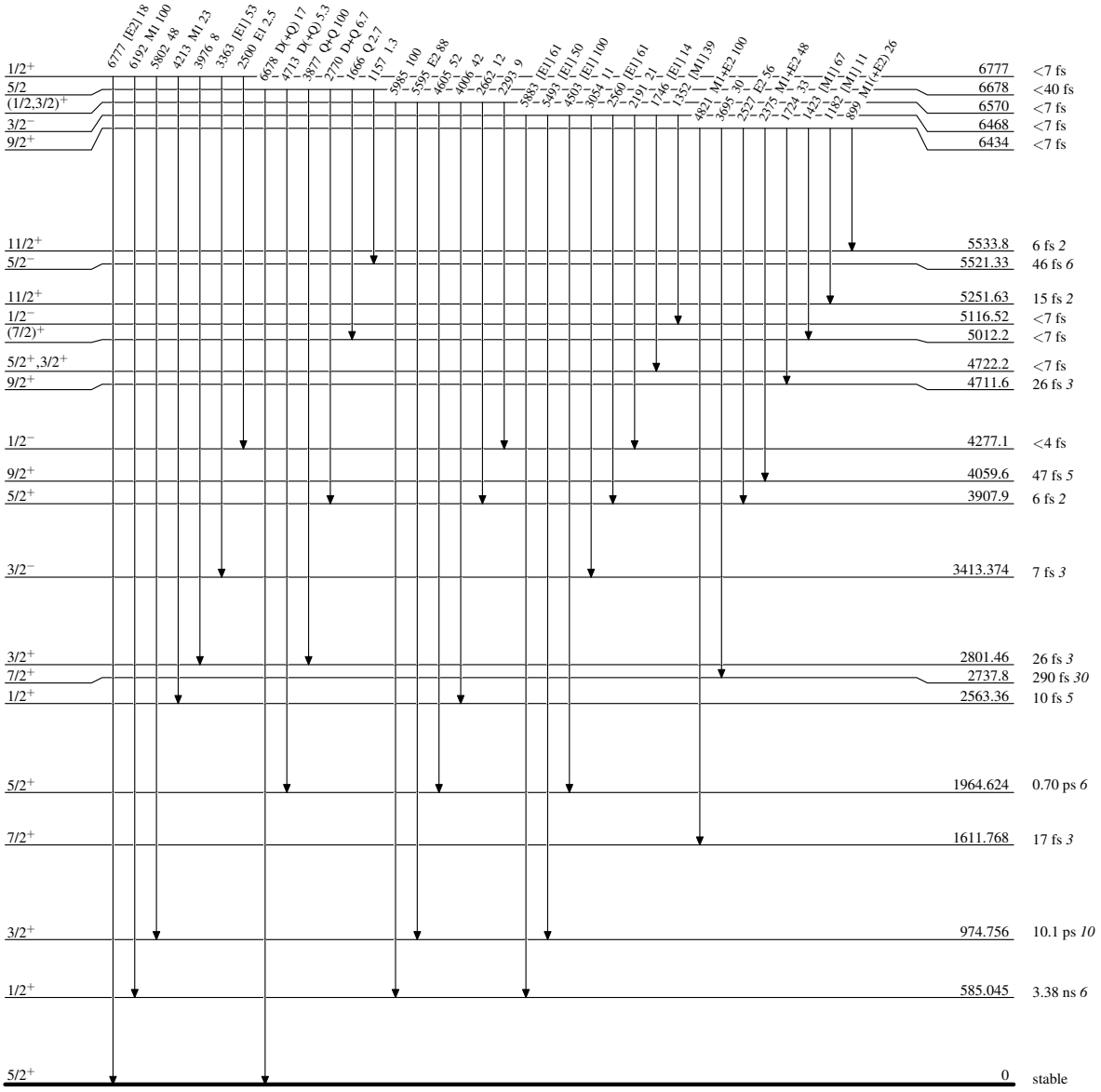

Adopted Levels, Gammas

Level Scheme (continued)

Intensities: Relative photon branching from each level

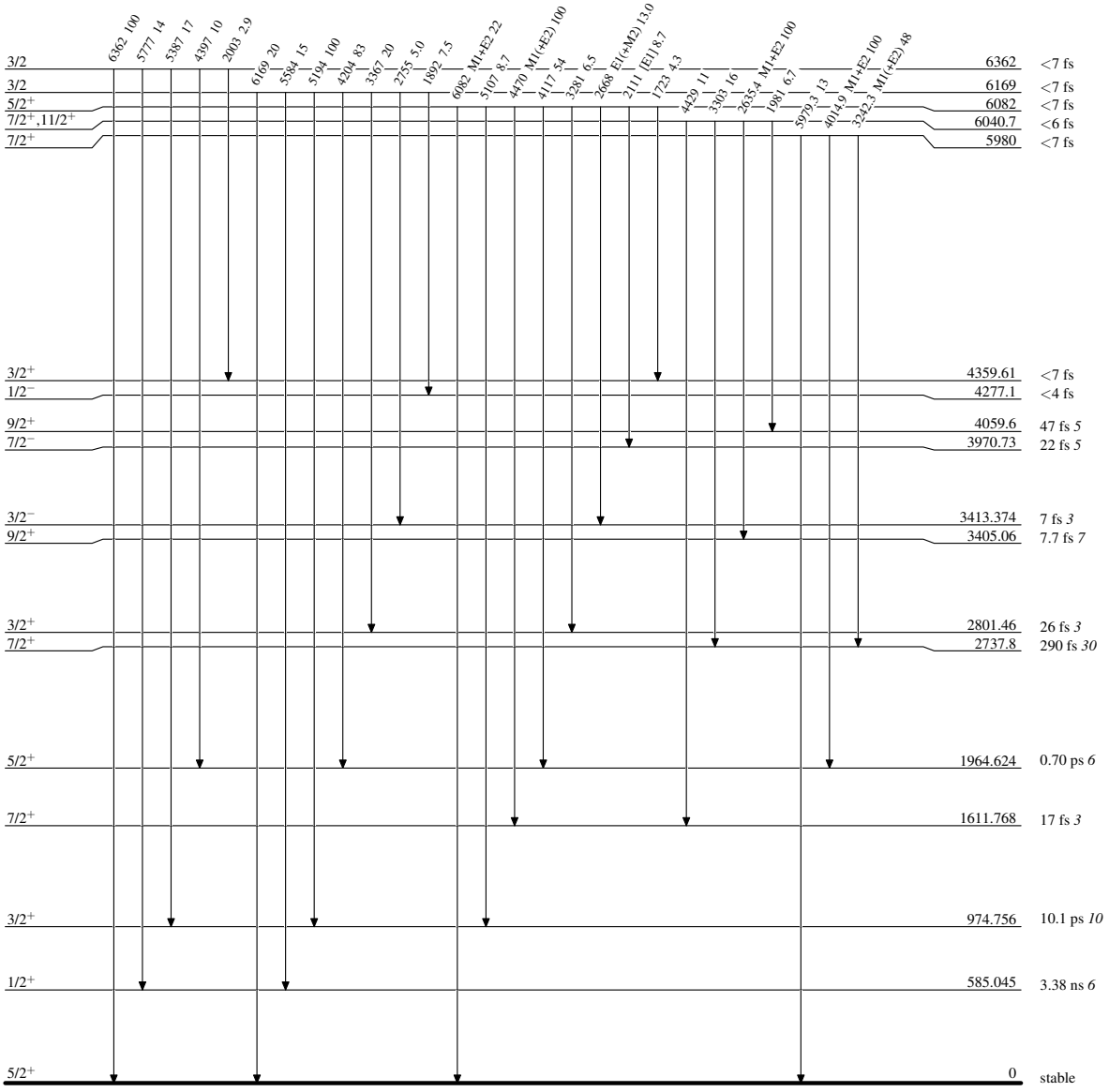

Legend

Level Scheme (continued)

Intensities: Relative photon branching from each level

γ Decay (Uncertain)

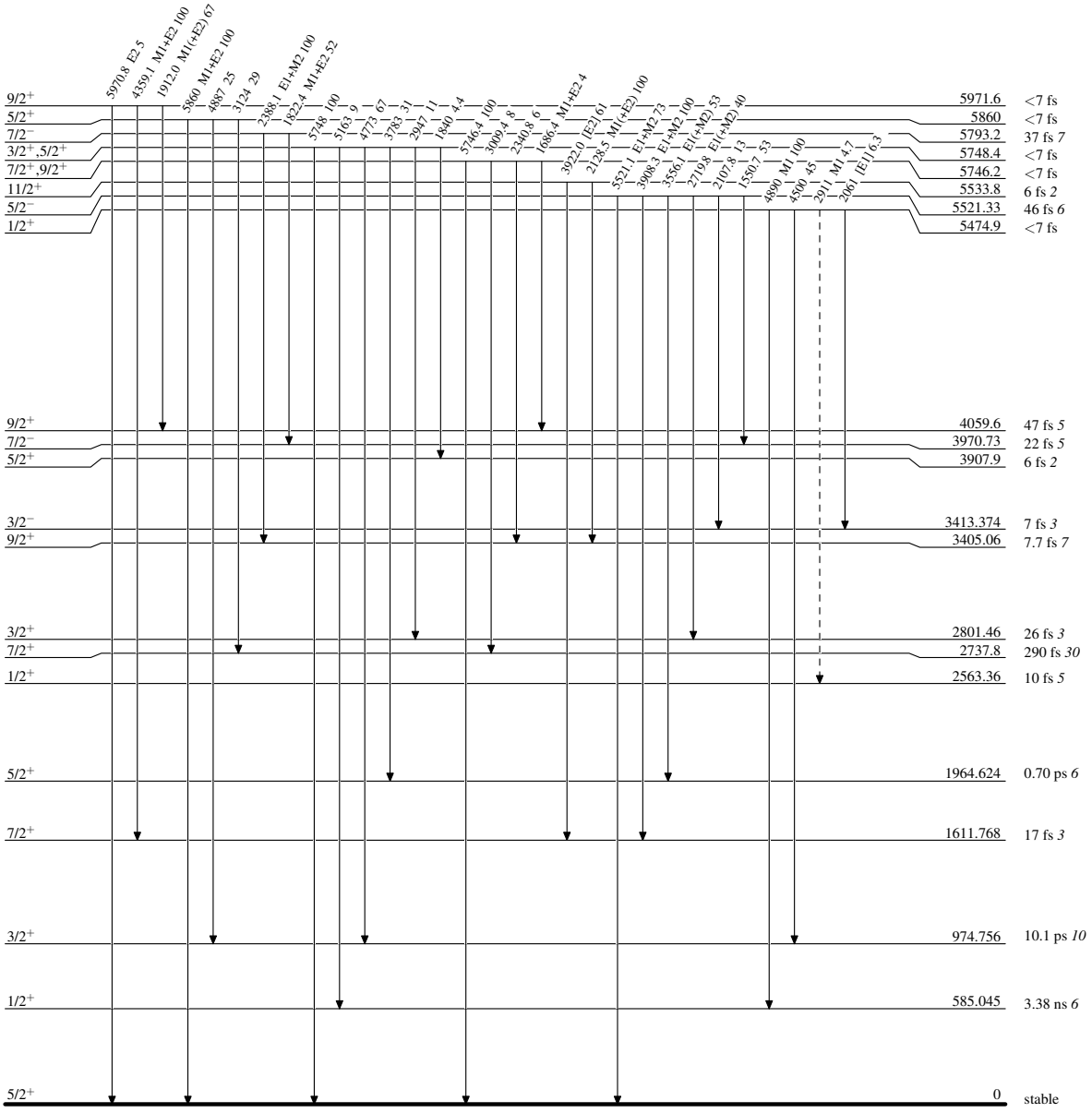

Adopted Levels, Gammas

Level Scheme (continued)

Intensities: Relative photon branching from each level

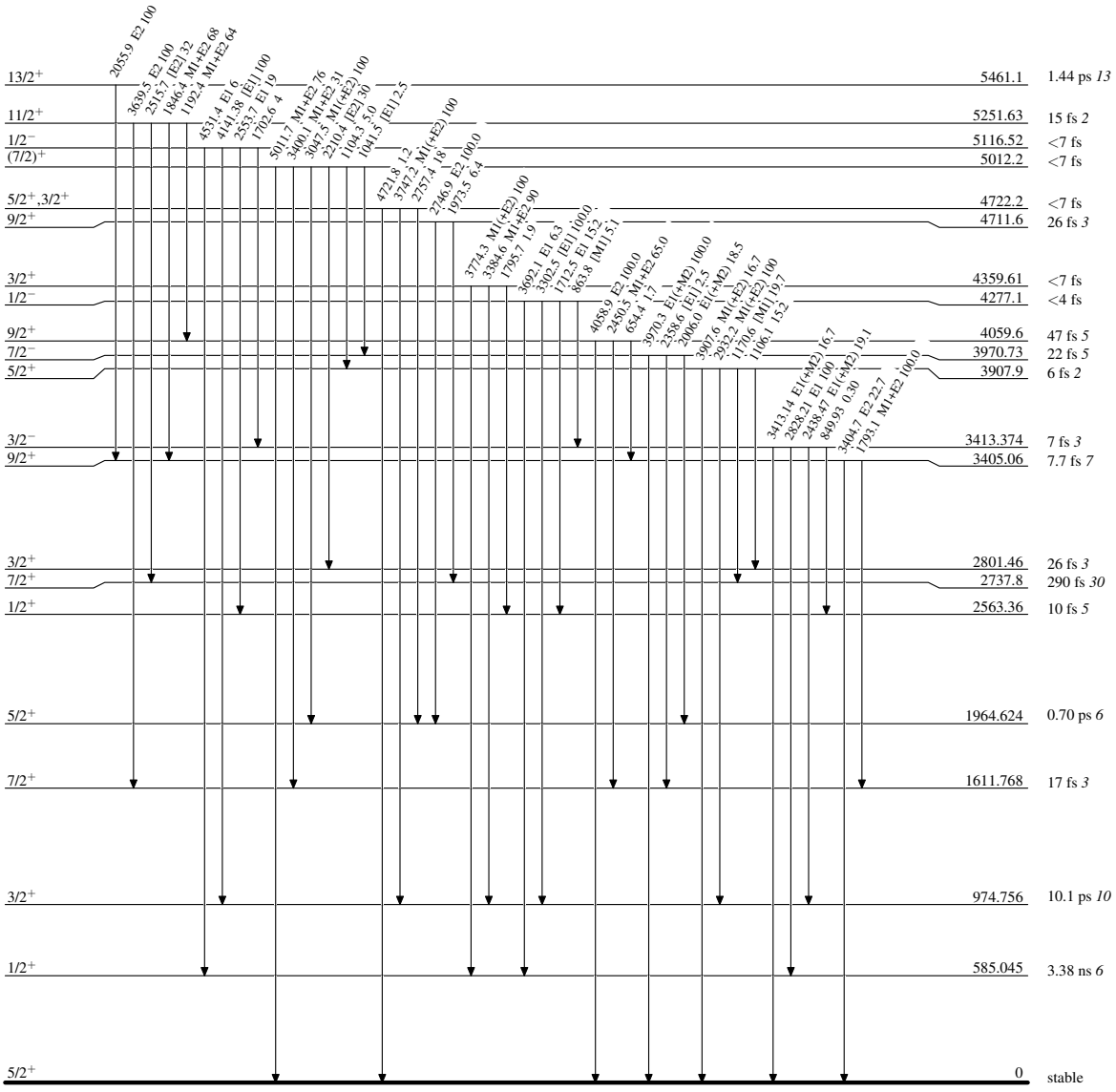

Level Scheme (continued)

Intensities: Relative photon branching from each level

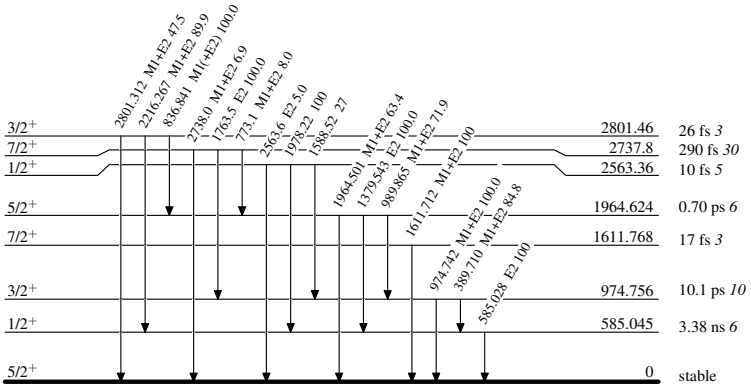

$^{25}_{12}\mathrm{Mg}_{13}$

D.3. Al

Level Scheme

Intensities: Relative photon branching from each level
& Multiply placed: undivided intensity given

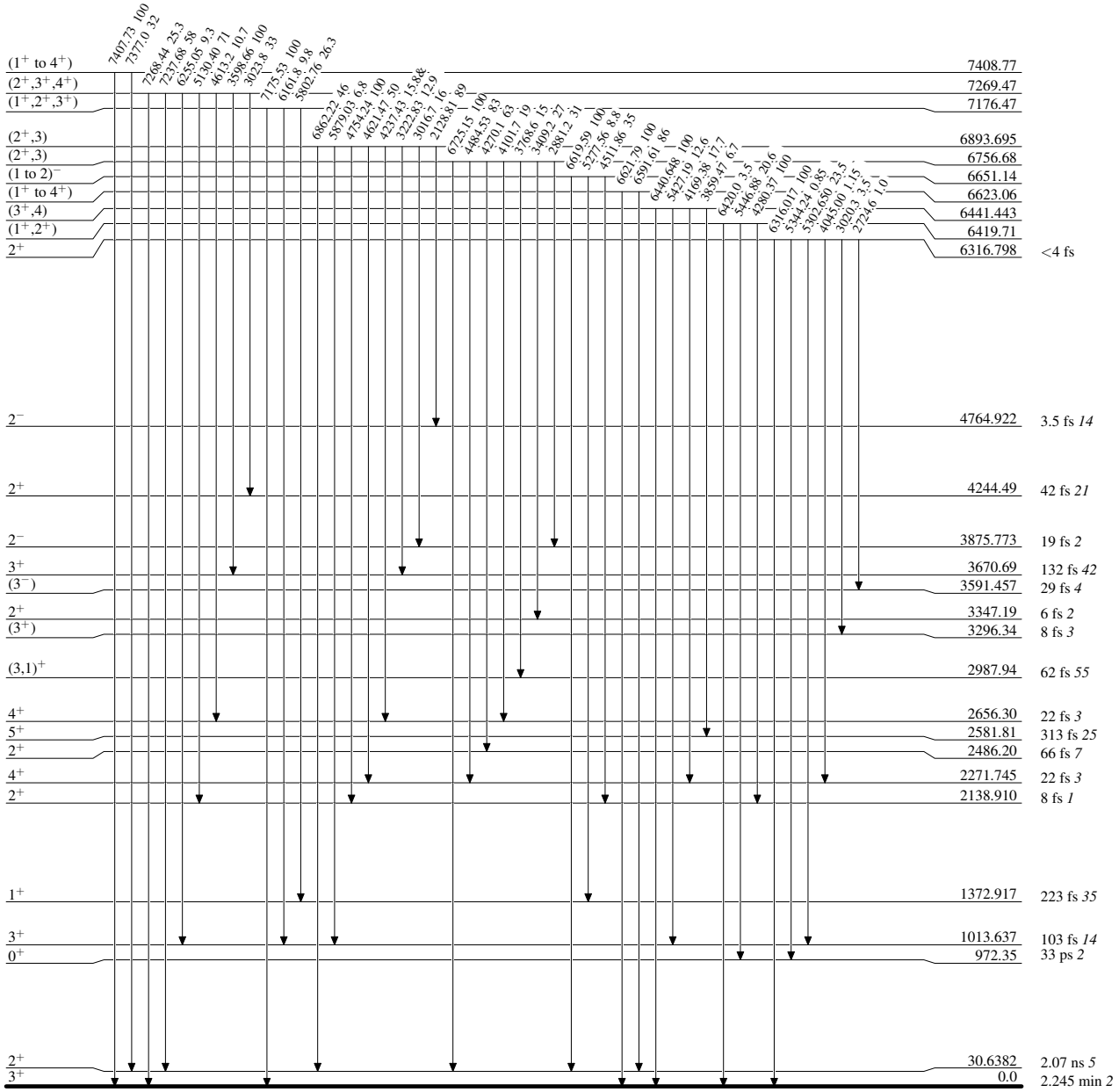

E. NFS Campaign: Ghost Events

Events exhibiting anomalous ToF characteristics, marked by a periodic temporal pattern, were detected as displayed in Fig. E.3. The amplitude of the FFT result against the frequency bins is displayed in Fig. E.4, showing the frequency components of the energy deposition signal. Peak at specific frequency around 87.5 MHz suggest the presence of periodic components in the background recorded signals.

These occurrences align with the operational frequency of the LINAC of 88 MHz, translating to a cycle duration of approximately 11.36 ns, which can be observed in the ToF distribution shown in Fig. E.3. The prevailing theory suggests that the observed anomalies may stem from a malfunction in the bunch selector [224]. Such occurrences, which represent on average 0.5% of all events as displayed in Fig. E.5, are not detrimental to the unfolding process using the data at the beginning of the campaign. However, in the case of a beam monitoring during the entire duration of an experimental campaign, the later must be excluded from the analysis due to inaccurate ToF assessments. To address this, a random selection process is employed to eliminate a subset of events based on their likelihood of being associated with a satellite peak [225].

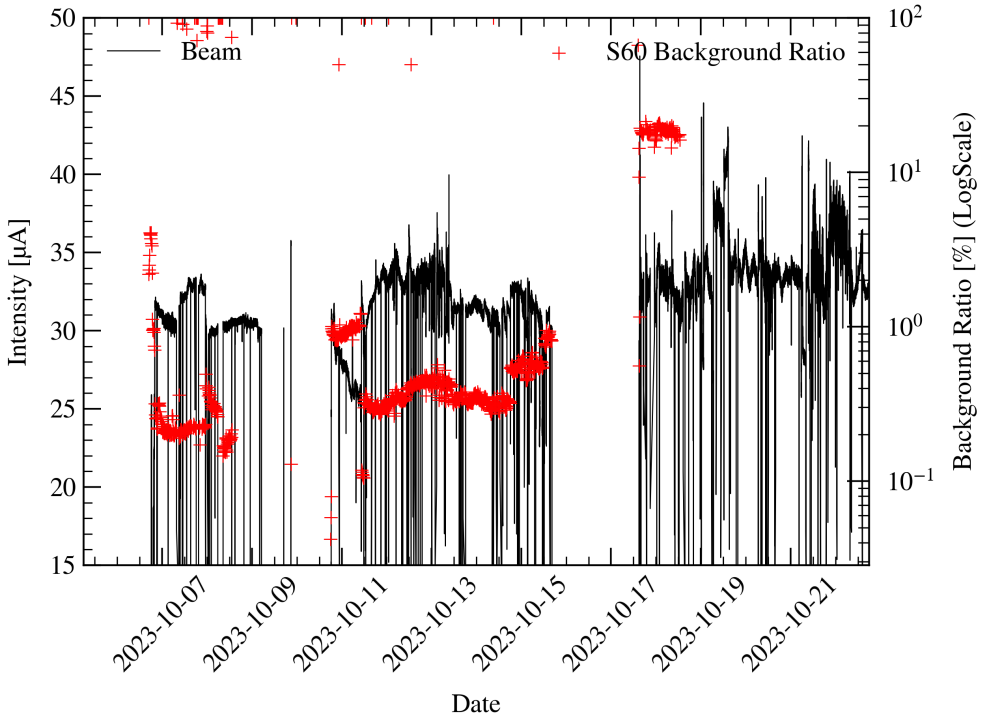

Fig. E.5. Comparison of the neutron beam intensity and the background noise during the NFS campaign. The red markers refers to the ratio between the number of satellite events and the total number of events.

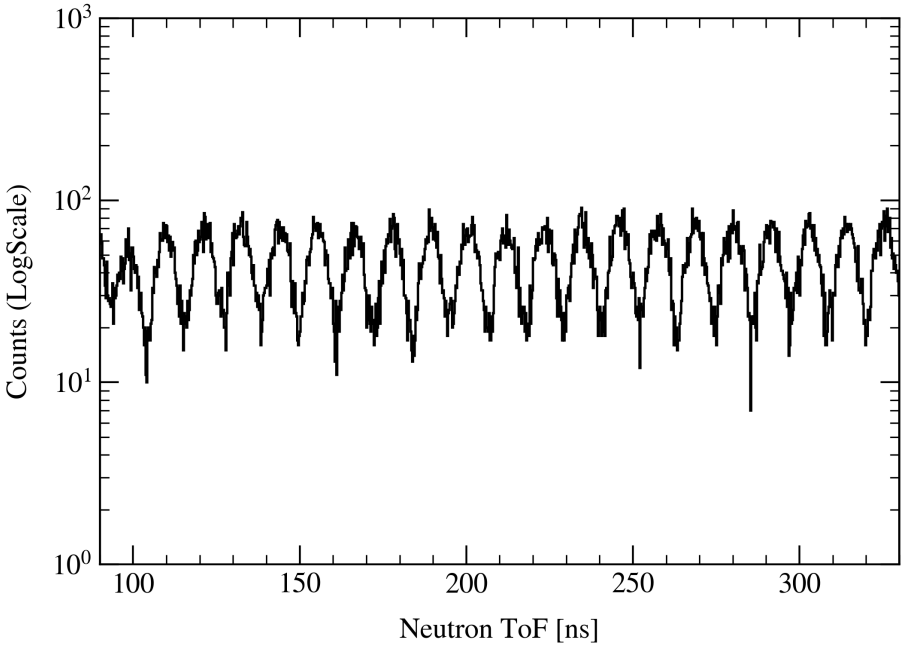

Fig. E.3. Distribution of the events according to their time of flight, after the main neutron contribution.

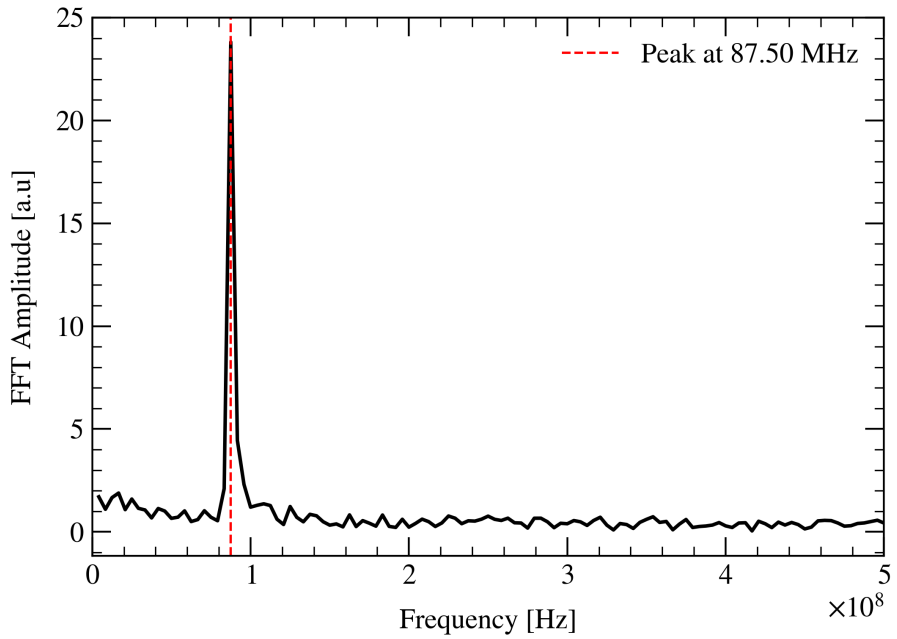

Fig. E.4. FFT amplitude of the signal temporal distribution within the acquisition window after the main neutron contribution. The dashed line indicates the FFT peak frequency.

F. TCAD Modeling

F.1. Mobility Models

F.1.1. Phonon Scattering

$$\mu_{const.} = \mu_{max} \cdot \left(\frac{T}{300\text{K}} \right)^{\alpha} \tag{F.1}$$

With μ_{max} the mobility due to phonon scattering. The associated coefficients are registered in the Table 3 below.

Symbol	Electrons	Holes
μ_{max} $[cm^2/Vs]$	950 [a]	125 [a]
α	2.5 [b]	2.2 [b]

[a] *Commonly agreed value [188] [189]*
[b] *Mobility models are fitted with the measured data from [190]*

Table 3. Constant mobility model coefficients.

F.1.2. Doping Dependant

Masetti Model

The Masetti model [192] is defined as follows:

$$\mu_{dop} = \mu_{min1} \exp\left(-\frac{P_c}{N_{A,0} + N_{D,0}} \right) + \frac{\mu_{cons} - \mu_{min2}}{1 + \left(\frac{N_{A,0} + N_{D,0}}{C_r} \right)^{\alpha}} - \frac{\mu_1}{1 + \left(\frac{C_s}{N_{A,0} + N_{D,0}} \right)} \tag{F.2}$$

Arora Model

The Arora model [191] is defined as follows:

$$\mu_{dop} = \mu_{min} + \frac{\mu_d}{1 + \left(\frac{N_{A,0} + N_{D,0}}{N_0} \right)^{A^*}} \tag{F.3}$$

With μ_{min} the minimum mobility value expected, μ_d the difference between the maximum and minimum mobility value expected, N_0 a reference concentration and A^* an exponential factor that controls the slope around $N = N_{ref}$, with N_{ref} the reference concentration sets as a threshold for when the carrier density starts to affect the mobility. The previous variables are defined such that:

$$\mu_{min} = A_{min} \cdot \left(\frac{T}{300\text{K}} \right)^{\alpha_m} \tag{F.4}$$

$$\mu_d = A_d \cdot \left(\frac{T}{300\text{K}} \right)^{\alpha_d} \tag{F.5}$$

And:

$$N_0 = A_N \cdot \left(\frac{T}{300\text{K}}\right)^{\alpha_N} \tag{F.6}$$

$$A^{star} = A_a \cdot \left(\frac{T}{300\text{K}}\right)^{\alpha_a} \tag{F.7}$$

The associated coefficients are registered in the Table 4 below:

Symbol	Electrons[a]	Holes[b]
A_{min}	40	0
A_d	910	113.5
α_m	-1.536	-0.57
α_d	-2.397	-2.6
N_0	$2.0 \cdot 10^{17}$	$2.4 \cdot 10^{18}$
α_N	0.75	2.9
A_a	0.76	0.69
α_a	0.722	-0.2

[a] *Commonly agreed values [226]*
[b] *Commonly agreed values [227]*

Table 4. Arora mobility model coefficients.

F.1.3. High-Field Saturation Models

Canali Model

The Canali model [195] originates from the Caughey–Thomas formula [228], but has temperature-dependent parameters, which were fitted up to by Canali et al.:

$$\mu(E) = \frac{(\alpha+1)\mu_{low}}{\alpha + \left[1 + \left(\frac{(\alpha+1)\mu_{low}E}{v_{sat}}\right)^{\beta}\right]^{1/\beta}} \tag{F.8}$$

With μ_{low} which denotes the low-field mobility according to the described mobility model chosen previously. It should be noticed that the exponent β is also temperature dependant such that:

$$\beta = \beta_0 \left(\frac{T}{300\,\text{K}}\right)^{\beta_{exp}} \tag{F.9}$$

Velocity saturation are defined aswell according to several description, like the one provided by Canali such that:

$$v_{sat} = v_{sat,0} \left(\frac{300\,\text{K}}{T}\right)^{v_{sat,exp}} \tag{F.10}$$

Which takes into account the temperature dependence of the parameter through equation

(F.12) and (F.13) such that:

$$\mu(E) = \frac{\mu_{low}}{\left[1 + \left(\frac{\mu_{low} \cdot E}{v_{sat.}}\right)^{\beta}\right]^{1/\beta}} \tag{F.11}$$

$$\beta = \beta_0 \left(\frac{T}{300}\right)^{\beta_{exp}} \tag{F.12}$$

$$v_{sat.} = v_{sat.0} \left(\frac{300}{T}\right)^{v_{sat.,exp}} \tag{F.13}$$

Meinerzhagen–Engl Model

The Meinerzhagen–Engl model [196] is defined as:

$$\mu = \frac{\mu_{low}}{\left[1 + \left(\mu_{low} \frac{3k}{2q} \frac{(T_c - T)}{\tau_{e,c} v_{sat}^2}\right)^{\beta}\right]^{1/\beta}} \tag{F.14}$$

F.2. Recombination Rate

F.2.1. Shockley-Read-Hall Recombination Rate

The Shockley-Read-Hall recombination rate [209] is defined as:

$$R_{net}^{SRH} = \frac{np - n_{i,eff}^2}{\tau_p(n + n_t) + \tau_n(p + p_t)} \tag{F.15}$$

With p and n the hole and electron concentrations, $n_{i,eff}$ the effective intrinsic carrier concentration, τ_p and τ_n the hole and electron lifetimes, and n_t and p_t the hole and electron densities when the quasi-Fermi levels aligns with the defect level E_t, making the recombination rate maximum. It is defined such that:

$$\begin{cases} n_t = n_{i,eff} exp\left(\frac{E_t}{kT}\right) \\ p_t = n_{i,eff} exp\left(\frac{-E_t}{kT}\right) \end{cases} \tag{F.16}$$

With E_t the difference between the Fermi level and the defect level, $n_{i,eff}$ the effective intrinsic carrier concentration, τ_p and τ_n the hole and electron lifetimes.

F.2.2. Carriers lifetime doping dependance

Doping dependence of SRH lifetimes is modeled in TCAD with the Scharfetter relation [210] defined such that:

$$\tau_{dop}(N_{A,0} + N_{D,0}) = \tau_{min} + \frac{\tau_{max} - \tau_{min}}{1 + \left(\frac{N_{A,0} + N_{D,0}}{N_{ref}}\right)^{\gamma}} \tag{F.17}$$

With τ_{max} the maximum lifetime of the minority carriers in the epitaxially grown layer. It is process dependant since its value can be degraded with the damage induced by ion implant

process during the manufacturing of the device.

Symbol	Parameter
τ_{max} [s]	$0.5 \cdot 10^{-6}$ [a]
τ_{min} [s]	0.0
γ	0.3 [a]
N_{ref} [cm^{-3}]	$1 \cdot 10^{17}$ [a]

Table 5. Coefficients for the Scharfetter relation for the SRH recombination rate in 4H-SiC. From [229].